



**TARGETING THE COMPLETE RANGE OF SOOT
COMPONENTS THROUGH THE CATALYTIC
OXIDATION OF DIESEL PARTICULATES**

**Thesis submitted in accordance with the
requirements of Cardiff University for the degree
of**

Doctor of Philosophy

Ragini Ramdas

March 2014

DECLARATION

This work has not been submitted in substance for any other degree or award at this or any other university or place of learning, nor is being submitted concurrently in candidature for any degree or other award.

Signed (candidate) Date

STATEMENT 1

This thesis is being submitted in partial fulfillment of the requirements for the degree of Doctor of Philosophy

Signed (candidate) Date

STATEMENT 2

This thesis is the result of my own independent work/investigation, except where otherwise stated. Other sources are acknowledged by explicit references. The views expressed are my own.

Signed (candidate) Date

STATEMENT 3

I hereby give consent for my thesis, if accepted, to be available for photocopying and for inter-library loan, and for the title and summary to be made available to outside organisations.

Signed (candidate) Date

STATEMENT 4: PREVIOUSLY APPROVED BAR ON ACCESS

I hereby give consent for my thesis, if accepted, to be available for photocopying and for inter-library loans **after expiry of a bar on access previously approved by the Academic Standards & Quality Committee.**

Signed (candidate) Date

I wish to dedicate this thesis to my aunt, **Annette** (a fighter, with a never say die attitude), whom I lost to breast cancer but who believed I could be what I am today, a good researcher.

"The whole of science is nothing more than a refinement of everyday thinking"

-Albert Einstein

Abstract

While total exhaust emissions from individual road vehicles continue to be reduced, it is becoming increasingly important to identify and quantify the residual chemical compounds in tail-pipe emissions that are potential hazards to the environment and to human health. Diesel particulate matter (DPM) is known to consist mostly of carbonaceous soot together with minor components, such as volatile organic fractions (from unburned fuel), lubricating oil, and inorganic compounds that include ash and sulphur compounds. Polycyclic aromatic hydrocarbons (PAHs) are invoked as the key intermediates in diesel soot formation. These are mutagenic air pollutants formed as by-products of combustion. PAH-precursors identified in soot include single ring structures such as benzene and toluene. Soot nucleation and growth gradually leads to the formation of five to six membered ring structures, such as benzopyrene, dibenzopyrene and coronene.

Several methods have been devised to reduce the emissions of DPM, which include the use of a diesel particulate filter, or a technology which combines selective catalytic reduction of NO_x with a regenerating particulate trap in a single unit. These oxidise the combustible content of the particulate matter collected on the filter through a non-catalytic reaction with NO₂. As an alternative, the more difficult catalysed oxidation of soot by direct reaction with O₂ has been gaining a lot of attention. Several studies have shown that the oxidation of soot requires a redox catalyst, such as CeO₂, CeO₂-ZrO₂ and CeO₂-ZrO₂-Al₂O₃, or other reducible metal oxides including perovskites and spinels.

In the past, proposed mechanisms have assumed that exhaust soot is simply graphitic carbon, and so have not taken into account the other organic components. In this work, we have carried out a speciation of soot that has been sourced from a diesel particulate trap. The soluble components have been identified by GC-MS, following extraction by Soxhlet and ultrasonication techniques. The speciation has been repeated as a function of temperature during the non-catalysed and catalysed combustion of the soot, allowing the conversion of individual components to be tracked. The results provide important catalyst design information, which should allow the formulation of materials that will be catalytically active in the combustion both of graphitic carbon and the complete range of retained organic species.

Acknowledgement

I wish to begin by thanking God for giving me the strength and courage to complete my Ph.D. successfully and to the best of my ability. I would like to express my heartfelt gratitude to my supervisor, Prof. Stanislaw E. Golunski, for his constant supervision and guidance throughout these three years of my Ph.D. I wish to thank Dr. Andrew York at Johnson Matthey, for his constructive suggestions and supervision, from the start to the end of my doctoral research. My sincere thanks to Johnson Matthey for giving me this wonderful opportunity to carry out my research in U.K. I wish to thank Prof. Stuart Taylor and Dr. David Willock, for their constant mentoring and advice. Industrial expertise and suggestions from Dr. Dave Thompsett (JM), Dr. Paul Collier (JM), Prof. Athanos Tsolakis (University of Birmingham) and Prof. Edman Tsang (Oxford University) have been very valuable in shaping my research project. I wish to sincerely thank Dr. Robert Jenkins and Dr. Ewa Nowicka, for the great ideas, guidance and the invaluable support they have given me throughout the project and for bringing out the best in me. I also thank Dr. David Sellick for his help in this project. A major part of my project would not have been successfully completed without the resourceful help offered by Mr. Steve Morris, Mr. Alun Davies, Mr. Robin Hicks and Mr. Dave Walker.

I wish to thank Dr. P. Manikandan for being a great mentor and for being instrumental in encouraging me to pursue my research career. I express my sincere thanks to Dr. Sivaram Pradhan for his constant encouragement. I also wish to extend my thanks to my colleagues at work, Rob, Sara, Rebecca and Yingyu.

I wish to thank Mr. Mahesh Mani, for being a great friend and a brother to me. Words are not enough to express how grateful I am to god for giving me my biggest strength-my parents and my grandmother. I wholeheartedly wish to thank them for their undying faith in me and for their constant encouragement. I wish to specially thank my mother, for being one of my best friends and understanding me through my thick and thin. I wish to thank my in-laws, for their prayers and good wishes. Last but most important, I wish to express my sincere thanks to my fiancé Dr. Sreevathsan Ramanathan, who has been my best friend, philosopher and guide always. I thank him for the constant love and trust he has bestowed upon me and for understanding me so well at all times.

Glossary

B(a)P	Benzo(a)pyrene
BET	(Brunauer, Emmett, Teller) Surface Area Analysis
DCM	Dichloromethane
EPA	Environmental Protection Agency
FTIR	Fourier Transform Infrared spectroscopy
GC	Gas Chromatography
HPLC	High Performance Liquid Chromatography
HSQC	Heteronuclear Single-Quantum Correlation Spectroscopy
IR	Infrared spectroscopy
MS	Mass Spectrometry
NMR	Nuclear Magnetic Resonance
PAH	Polyaromatic Hydrocarbon
SEM	Scanning Electron Microscopy
TGA	Thermogravimetric Analysis
TEF	Toxic Equivalency Factor
TEM	Transmission Electron Microscopy
XPS	X-Ray Photoelectron Spectroscopy
XRD	X-Ray Diffraction

Table of contents

Declaration	iii
Abstract	v
Acknowledgement	vi
Glossary	vii
1. Introduction to Catalysis	1
1.1 Catalysts and Catalysis	1
1.2 Kinetics of catalysed reactions	2
1.3 Classification of catalytic systems	4
1.4 Introduction to exhaust gas analyses	4
1.4.1 Exhaust Gas Analysis	6
1.4.2 Diesel particulate matter	7
1.4.2.1 Size distribution of diesel particulate matter	8
1.4.2.2 Toxicological Effects	10
1.4.3 Diesel soot formation	11
1.4.4 Poly aromatic hydrocarbons	15
1.4.4.1 Sources of PAH	17
1.4.4.2 Physicochemical properties	17
1.4.4.3 Toxicological effects	18
1.4.5 Diesel emissions legislation	20
1.4.6 Diesel exhaust gas treatment technologies	23
1.4.6.1 Diesel oxidation catalysts (DOCs)	23
1.4.6.2 Diesel particulate filter (DPF)	24
1.4.6.3 Continuous regenerating trap (CRT)	25
1.4.6.4 SCRT	26
1.5 Literature review	27
1.5.1 Noncatalysed soot oxidation	27
1.5.2 Catalytic soot oxidation	28
1.5.3 Type of Contact	31
1.5.4 Redox catalysts	32
1.5.4.1 Catalysts used in this project- Mixed metal oxides –CeO ₂ -ZrO ₂ -Al ₂ O ₃	33
1.5.4.2 Introduction of diffusion barrier concept	35
1.5.4.3 Role of alkali and alkaline earth metals as promoters in soot oxidation	35
1.5.5 Silver impregnation on CeO₂ for soot oxidation	37
1.5.6 Soot extraction techniques	40
1.5.7 Aims of the project	41
References	42
2. Experimental	52
2.1 Introduction	52
2.2 Catalyst Preparation- Mixed metal oxide	52
2.2.1 Catalyst support preparation – Wet impregnation	53

2.2.2	Catalyst support preparation- Co-precipitation using Na₂CO₃, NH₄OH, NaOH	53
2.2.2.1	Catalyst support preparation - Co-precipitation using urea	54
2.2.3	Catalyst support preparation - Co-precipitation using Na₂CO₃ -Varying method of preparation	54
2.2.4	Silver supported catalysts	55
2.2.5	Alkali and Alkaline earth metal supported CeO₂-ZrO₂-Al₂O₃ samples	55
2.2.5.1	Different potassium salts- KOH, K ₂ CO ₃ , KNO ₃ , KCl	55
2.2.5.2	Varying the weight loading of potassium on CeO ₂ -ZrO ₂ -Al ₂ O ₃	55
2.2.5.3	Comparison of alkali and alkaline earth metals	55
2.2.6	Effect of varying the content of Ag and K on CeO₂-ZrO₂-Al₂O₃	56
2.2.6.1	Combination of Silver and Potassium on the support	56
2.2.6.2	Optimization of the catalyst	57
2.2.7	Pt/SiC for naphthalene oxidation	57
2.2.7.1	Modification of the catalyst for PAH-soot combustion	57
2.2.8	Preparation of Ag-CeO₂ and 10%K/Ag-CeO₂ catalysts via co-precipitation and dry impregnation	57
2.3	Reactor design	58
2.3.1	Catalyst screening using Thermogravimetry	58
2.3.2	Reactor schematic - qualitative analysis –Soot oxidation reactor	59
2.3.2.1	Overview of design	59
2.3.2.2	Reaction conditions	61
2.3.2.3	Product analysis using High Performance Liquid Chromatography (HPLC)	63
2.3.2.4	Product identification and quantification	65
2.3.3	Reactor schematic – Quantitative analysis	67
2.3.3.1	Overview of design	67
2.3.3.2	Reaction conditions	68
2.3.3.3	Sample delivery	70
2.3.3.4	Valve sequence and temperature programme	71
2.3.3.5	Data handling	71
2.3.4	Gas analysis by Fourier Transform Infrared (FTIR) spectroscopy	72
2.3.5	Mass spectrometry (MS)	74
2.3.5.1	Techniques coupled with MS	77
2.3.5.1.1	Gas chromatography- Mass Spectrometry (GC-MS)	77
2.3.5.1.2	Liquid Chromatography-Mass Spectrometry (LC-MS)	78
2.4	Characterization	78
2.4.1	X-Ray diffraction- Principle	78
2.4.1.1	Experimental	80
2.4.1.2	In-situ XRD	81
2.4.2	Raman Spectroscopy – Principle	81
2.4.2.1	Experimental	83
2.4.3	Nuclear Magnetic Resonance (NMR) spectroscopy-Principle	83
2.4.3.1	Two dimensional NMR spectroscopy	85
2.4.4	Infrared spectroscopy-Principle	85
2.4.5	Temperature Programmed Reduction (TPR)-Principle	86
2.4.5.1	Experimental	87

2.4.6	Thermogravimetric analysis (TGA) - Principle	87
2.4.6.1	Experimental	88
2.4.7	Brunauer Emmet Teller surface area determination - Principle	88
2.4.7.1	Experimental	90
2.4.8	Scanning Electron Microscopy (SEM) - Principle	90
2.4.8.1	Experimental	92
2.4.9	Transmission electron microscopy (TEM)	92
2.4.10	Porosimetry	92
2.4.10.1	Experimental	92
2.4.11	X-ray photoelectron spectroscopy (XPS)	93
2.4.11.1	Experimental	93
2.4.12	Elemental analysis	94
	References	94
3.	Catalyst screening for soot oxidation	96
3.1	Catalyst support- Varying ratios of Ce:Zr in Ce_xZr_{1-x}Al_{0.5}O_{1.75}	97
3.1.1	Characterization	97
3.1.2	Soot oxidation	100
3.1.2.1	Soot oxidation activity -Varying Ce:Zr ratios	102
3.1.2.2	Catalyst support - Varying ratios of Ce:Zr in Ce _x Zr _{1-x} Al _{0.5} O _{1.75}	104
3.2	Catalyst support preparation- Co-precipitation using Na₂CO₃, NH₃, NaOH	106
3.2.1	Characterization	106
3.2.2	Soot oxidation activity	116
3.3	Catalyst support -variation of preparation method	119
3.3.1	Characterization	119
3.3.2	Soot oxidation activity	124
3.4	Supported metal oxides- Impregnation of Ag on Ce_xZr_{1-x}Al_{0.5}O_{1.75}	127
3.4.1	Characterization	127
3.4.2	Soot oxidation activity	136
3.5	Alkali metal promotion over CZA	138
3.5.1	Characterization - Varying different alkali metal (K) salts and their effects on different support	138
3.5.1.1	Study on different supports	141
3.5.2	Soot oxidation activity	144
3.5.2.1	Variation of potassium salt precursor on CeO ₂ -ZrO ₂ -Al ₂ O ₃	144
3.6	Varying the weight loading of potassium on CeO₂-ZrO₂-Al₂O₃	149
3.6.1	Characterization	149
3.6.2	Soot oxidation	158
3.7	Comparison of alkali and alkaline earth metals	161
3.7.1	Characterization	161
3.7.2	Soot oxidation activity - Comparison between alkali and alkaline earth metal supported CeO₂-ZrO₂-Al₂O₃	163
3.8	Combination of Silver and Potassium on the support	165
3.8.1	Catalyst characterisation	166
3.8.2	Soot oxidation activity	176
3.8.3	Ag-K direct impregnation on CZA- characterization	177
3.8.3.1	Optimization of the catalyst	178
3.9	Variation in the content of Ag-K on CZA	202
3.10	Catalyst durability	205

References	209
4. Soot oxidation studies-quantitative analysis	212
4.1 Introduction	212
4.2 Soot characterization	213
4.2.1 TEM /STEM	213
4.2.2 CHNS analyses	215
4.2.3 Raman spectroscopy	216
4.2.4 NMR	219
4.2.5 IR	222
4.2.6 Porosimetry	223
4.3 Rate of uncatalysed soot oxidation in the presence of synthetic air flow	224
4.3.1 Varying O ₂ /He flow rate	225
4.3.2 Varying O ₂ /He concentrations	226
4.4 Study on the rate of catalysed soot oxidation in the presence of synthetic air flow	227
4.4.1 Varying O ₂ /He concentrations and flow rates	228
4.4.2 Variation of O ₂ /He concentration	229
4.4.3 Soot oxidation- N ₂ atmosphere-rate of reaction	229
4.4.4 Catalysed soot oxidation- effect of catalyst-soot contact	230
4.4.5 In-situ XRD studies on Ag-K/CZA+soot-O ₂ /He	231
4.5 Model soot oxidation	232
4.5.1 Norit charcoal-O ₂ /He	232
4.5.2 Graphite - O ₂ /He	232
4.5.3 Phenanthrene-graphite model- O ₂ /He	233
4.5.3.1 Contributions of graphite, phenanthrene towards CO ₂ production in the presence and absence of catalysts	233
4.6 Testing using synthetic exhaust mix	236
4.6.1 Uncatalysed soot oxidation- exhaust gas mix-with 300 ppm NO	236
4.6.2 Combustion of soot to CO ₂ - Mass balance	237
4.6.3 Catalysed soot oxidation- exhaust gas mix	238
4.6.3.1 Ag-K/CZA+soot	238
4.6.3.2 Pt/SiC	242
4.6.3.3 Ag-K/CZA+Pt/SiC	244
4.6.4 Extracted soot- with and without NO	247
4.7 Catalyst characterization	249
4.7.1 Pt/SiC	249
4.7.2 Pt/SiC+Ag-K/CZA	255
4.8 Conclusions	262
References	264
5. Speciation of diesel soot: Identification and quantification of polyaromatic hydrocarbons	265
5.1 Introduction	265
5.2 Soot - Direct insertion into the Mass Spectrometer	266
5.3 Diesel soot extraction techniques	266
5.3.1 Crude extraction using DCM and acetone	267

5.3.2	Minimising experimental error	267
5.3.3	GC-MS analysis on crude soot extracts	268
5.3.4	HPLC - Identification of polyaromatic hydrocarbons	270
	5.3.4.1 HPLC analysis of the polyaromatic hydrocarbon standard	270
	5.3.4.2 HPLC analysis on 4 step extracted soot combined with ultrasonication	272
	5.3.4.3 HPLC analysis on Soxhlet extracted diesel soot	273
5.4.	Quantification of Polyaromatic hydrocarbons	275
	5.4.1 Quantification of PAHs in soot - Extraction	275
	5.4.2 Quantification of PAHs in soot during oxidation	279
5.5	Desorption of Polyaromatic hydrocarbons on thermal treatment	280
	5.5.1 Desorption upon soot treatment with helium	280
	5.5.2 Desorption of PAHs during soot oxidation under 20% O ₂ /He	283
	5.5.3 Desorption of PAHs during soot oxidation under CO ₂ atmosphere	289
	5.5.4 Desorption of PAHs during soot oxidation under NO atmosphere	293
	5.5.5 Desorption of PAHs during soot oxidation under exhaust gas atmosphere	296
	5.5.6 Conclusions	299
	5.5.7 Comparison of extracted soot and pre-treated soot during oxidation	306
5.6	Modification of catalyst for total PAH combustion	308
	5.6.1 Testing for Pt/SiC for naphthalene oxidation	308
	5.6.2 Optimization of the ratio of Pt/SiC: Ag-K/CZA for efficient PAH combustion	309
	5.6.3 Desorption of PAHs during soot oxidation under 20%O ₂ /He	311
	5.6.4 Desorption of PAHs during soot oxidation under CO ₂ /He	313
	5.6.5 Desorption of PAHs during soot oxidation under NO atmosphere	314
5.7	Phenanthrene bound to graphite: An ideal soot model	316
	5.7.1 Desorption of PAHs during soot oxidation under 20% O ₂ /He atmosphere	317
5.8	Mechanisms of certain PAHs under various oxidative atmospheres	324
5.9	Conclusions	328
	References	330
6.	Final Conclusions and future work	333
6.1	Final conclusions	333
6.2	Future work	335
7.	Appendix	336

Chapter 1

Introduction

1. Introduction to Catalysis

1.1 Catalysts and Catalysis

Catalysis is a scientific discipline which is an important phenomenon for our modern industrial economy. Several important discoveries in chemistry and physics were made in the early years of the 19th century, when it was noticed that a number of chemical reactions were taking place in the presence of a substance that was not being consumed in the reaction and that led to the enhancement in the rates of the reaction. Traces of acid were found to bring about the hydrolysis of starch [1], decomposition of hydrogen peroxide occurred in the presence of low concentrations of metal ions, noble metals such as platinum were found to oxidize hydrogen which was later developed by J.W. Dobereiner into a lamp-lighter. In 1831, platinum was yet again used for the oxidation of sulphur dioxide by Peregrine Philips, whose patent was later used as the basis of sulphuric acid manufacture [1].

Thermodynamics helped to define a rational approach towards catalytic processes. The definition of a catalyst in a thermodynamic sense was suggested by Ostwald as the material that will leave the equilibrium of the reaction unchanged. In the recent past, molecular basis of catalysis was understood and thermodynamics helped in the understanding of processes such as the Haber-Bosch process for ammonia synthesis in the early 20th century. Sabatier who had received the Nobel prize for catalytic hydrogenation, making the production of hydrogen cheaper through the use of coal, provided the molecular view of catalytic reaction as a series of reaction steps in which intermediate complexes were formed between the catalyst and reagent and this complemented Ostwald's physicochemical approach towards catalysis [2]. Later, Berzelius coined the term 'catalysis'. The word 'catalysis' originated from the Greek words 'cata' meaning 'down' and the verb 'lysein' meaning to 'split or break', thus defining it as a substance that breaks down the normal forces that inhibit the reaction of molecules. A catalyst may thus be defined simply as a substance that increases the rate

at which a chemical reaction approaches equilibrium without undergoing any chemical change or being consumed in the process [1].

1.2 Kinetics of catalysed reactions

The Sabatier principle states that when there is optimum interaction of the reactant and products with the catalyst, the catalytic rate is maximum. The rate of reaction is maximum when the rate of reactant activation to form a surface intermediate equals the formation of products from the intermediates. According to the transition theory, rate coefficient is given by,

$$k = \frac{kT}{h} \exp\left(-\frac{\Delta G}{RT}\right)$$

Where, k is the Boltzmann constant, ΔG is the Gibbs free energy of activation and h is the Planck's constant. The catalyst aims to decrease the free energy of activation of the reaction which is composed of enthalpy and entropy of activation [1]. The entropy of a catalysed reaction is less than that of an uncatalysed reaction as the transition state tends to get immobilised on the catalyst surface resulting in a loss of translational freedom, in turn leading to a decrease in the enthalpy of activation in order to compensate for this.

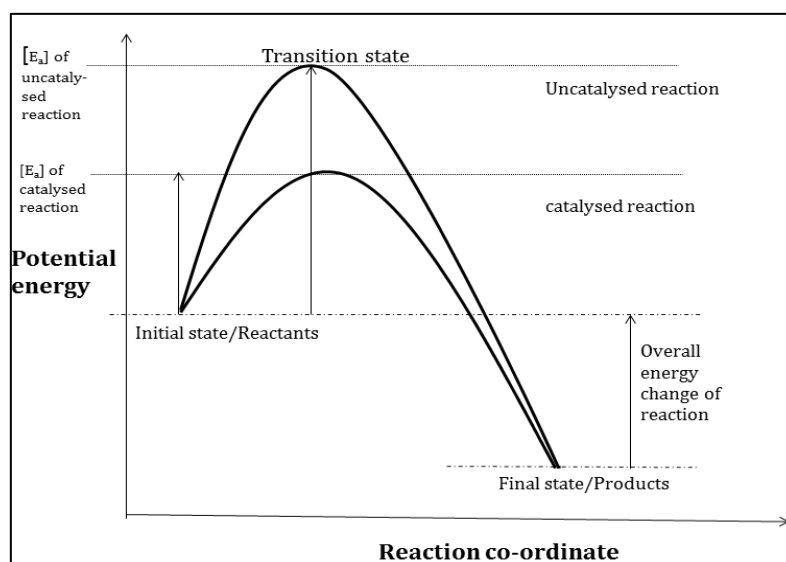


Figure 1.1 Activation energy barrier determining the rate of the reaction [1]

A catalysed reaction as shown in the figure 1.1 can be 10million times faster than a non-catalysed reaction. In the energy profile shown above, there may be a succession of

intermediate products formed sequentially, each being more stable than its precursor. According to the Arrhenius' equation the dependence of the rate constant 'k' of a chemical reaction on the absolute temperature 'T' (in kelvin), where 'A' is the pre-exponential factor, E_a is the activation energy, and 'R' is the universal gas constant.

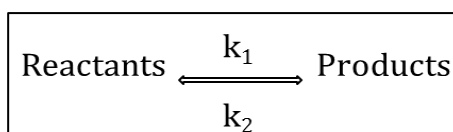
$$k = Ae^{-E_a/RT}$$

The catalyst proceeds through an alternative pathway for a reaction that requires a lower overall activation energy barrier (E_a). The presence of a catalyst does not alter the equilibrium constant or position in a reversible reaction. Thus the quotient of the rates for the forward and reverse reactions must also remain unchanged. The Gibbs free energy ΔG° is a state function that can have only one value for the standard Gibbs free energy change ΔG° for a reaction.

Since,

$$-\Delta G^\circ = RT \ln K$$

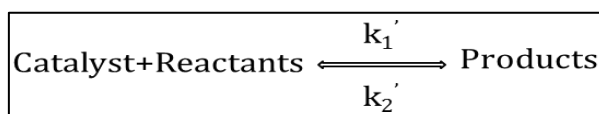
where, K is the equilibrium constant, K can have only one value. In an uncatalysed reaction as shown below:



The equilibrium coefficient can be defined as:

$$K = \frac{k_1}{k_2}$$

where, k_1 and k_2 are the rate constants for the forward and reverse reaction respectively. In the case of a catalysed reaction the rate coefficient may be given as



$$K = k_1' / k_2'$$

The standard Gibbs free energy change for an uncatalysed reaction is

$$-\Delta G^\circ T = RT \ln \left(\frac{k_1}{k_2} \right)$$

And the standard Gibbs free energy change for a catalysed reaction is

$$-\Delta G^\circ T' = RT \ln \left(\frac{k_1'}{k_2'} \right)$$

$$-\Delta G^\circ T = -\Delta G^\circ T'$$

where, $-\Delta G^\circ T$ is the standard free energy change at T° Kelvin, therefore

$$\left(\frac{k_1}{k_2}\right) = \left(\frac{k_1'}{k_2'}\right)$$

A catalyst can therefore accelerate the rate of a thermodynamically feasible reaction [3].

1.3 Classification of catalytic systems

Catalytic reactions may be broadly categorised as *homogeneous* or *heterogeneous* catalysts. If a catalyst is in the same phase as the reactants and products and no phase boundary exists, the reaction is described as *homogeneous*. This can occur in the gas phase, as in the case of sulphur dioxide oxidation in the presence of nitrogen oxide, and in case of the liquid phase, when the acids and bases catalyse the mutarotation of glucose. It is usually difficult to separate the catalyst from the reactant/product mixture after a homogeneous reaction is complete.

Heterogeneous catalysis may be defined as the reaction that occurs where a phase boundary separates the catalyst from the reactants [1]. It is often the preferred type of catalysis for large-scale continuous manufacturing processes.

Table 1.1 Examples of heterogeneous catalysis

Catalyst	Reactant	Example
Liquid	Gas	Alkene polymerization catalysed by phosphoric acid
Solid	Liquid	Hydrogen peroxide decomposition by gold
Solid	Gas	Iron catalysed ammonia synthesis
Solid	Liquid-Gas	Pd catalysed hydrogenation of nitrobenzene to aniline.

1.4 Introduction to exhaust gas analyses

The consumption of fossil fuels such as coal, natural gas and oil has led to the industrial development of the world. These consist of carbon, hydrogen and sulphur containing compounds. The incomplete or partial combustion of these constituents leads to harmful emissions of nitrogen oxides (NO_x), carbon monoxide (CO), sulphur oxides (SO_x), NH_3 and unburned hydrocarbons. These contribute significantly to the issue of global warming and to environmental pollution. This kind of incomplete or partial combustion may be attributed to the combined effect of high temperature and low air to fuel ratio or due to combustion under sub stoichiometric oxygen conditions

[4]. These pollutants emitted are from mobile sources such as automobiles, aeroplanes etc. and stationary sources such as power plants, industrial effluents, combustion of waste and domestic burning as shown in figure 1.2.

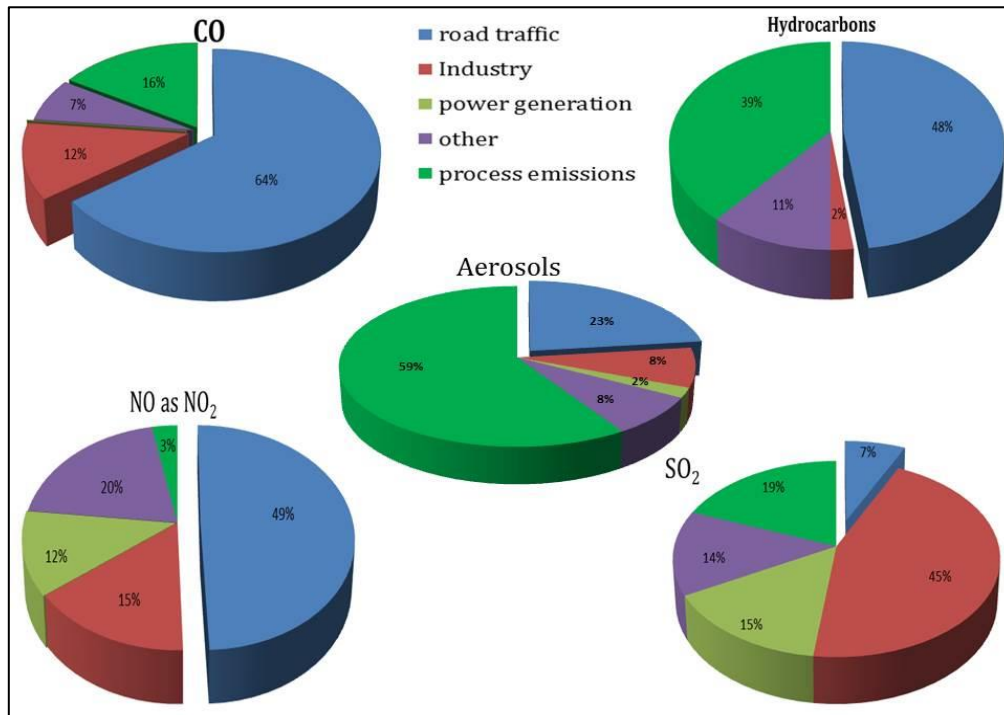


Figure 1.2 Relative contributions of emission sources to air pollution [5]

Diesel engines are the power source behind commercial transport such as buses, trains, ships and trucks as well as in industrial vehicles such as excavation and mining equipment. Almost 50% of the cars in Europe run on diesel engines. These engines have high efficiency, low operating costs, high durability and reliability due to which they are used in construction and industrial activities. These engines despite their advantages are one of the largest contributors to environmental pollution. The exhaust of the diesel engines contains a far higher amount of particulate matter and NO_x than the petrol engines and secondly, the exhaust is far leaner with lesser unburned hydrocarbons and carbon monoxide (CO) than a typical exhaust from petrol engines. Thus nowadays, the need is to focus on the reduction of harmful diesel emissions such as particulate matter (DPM) and reduction of NO_x, particularly difficult to reduce in the presence of excess O₂. Although this problem has been present since 1940s, with the ever growing demand for vehicles and urbanization, the exhaust gas emissions have started to pose a dangerous threat to the environment and human life [6].

Over the last few decades concerns have grown regarding the harmful effects of DPM on human health due to which these emissions have been subjected to several restrictions and various emission reduction technologies. These have led to the reduction of legislated total particulate mass but have not accounted for low-mass but high-number emissions, which because of their size or composition may have a higher impact on health [7]. Thus there is a need for absolute filtration alongside the complete combustion of hydrocarbons. Particulate filter traps can be used for efficient filtration but there is a need for filter regeneration to prevent an increase in back pressure and filter plugging. Current filters rely on NO_2 (passive) or a large exothermic (active) regeneration. The development of a filter coated with a noble metal based catalyst, combining retention and oxidation of the emitted particulate matter has been used widely. Most of these are expensive and vulnerable to further price increases upon increasing demand as the noble metals such as Pt, Pd and Au are expensive to procure. Thus the search for an inexpensive catalyst with or without the use of these noble metals is gaining attention in the past few decades.

1.4.1 Exhaust Gas Analysis

The combustion of fuels such as natural gas, gasoline, fuel oil, diesel or coal results in the emission of exhaust gas or flue gas which is discharged into the atmosphere through a propelling nozzle, exhaust pipe or flue gas stack. The principal pollutants of engine exhaust gas include atmospheric oxides of nitrogen such as nitric oxide (NO), nitrogen dioxide (NO_2), nitrous oxide (N_2O -very small concentrations produced in the engine), of which NO and NO_2 are collectively referred to as NO_x , CO and unburned hydrocarbons. This is illustrated in table 1.2.

Table 1.2 Typical diesel exhaust composition [6]

Sl.No	Component	Concentration
1	CO	100-10000 ppm
2	HC	50-500 ppm
3	NO_x	30-1000 ppm
4	SO_x	proportional to fuel S content
5	DPM	20-200mg/m ³
6	CO_2	2-12 vol %
7	NH_3	2 mg/mile
8	Cyanides	1 mg/mile
9	Benzene	6 mg/mile
10	Toluene	2 mg/mile
11	PAH	0.3 mg/mile

These belong to a class of legally *regulated* vehicle exhaust emissions which means they should meet the legislative requirements in industrialized countries. The *unregulated* class of compounds are those that are not subject to any specific legislative limit. The other gases include H₂, NH₃, CO₂, SO_x that are present in smaller amounts [8]. The complex mixture of particulates arises depending on a variety of factors such as driving condition, type of engine, vehicle speed, content of sulphur in the fuel, as in the case of sulphate particulate and so on. The group of polyaromatic hydrocarbons (PAH) belong to this group [8].

1.4.2 Diesel particulate matter

Diesel particulates are defined by the US Environmental Protection Agency (EPA) as “all compounds collected on a pre-conditioned filter, in diluted diesel exhaust gases at a maximum temperature of 325 K (125°F)” which includes diesel soot and aerosols such as ash particulates, metallic abrasion particles, sulphates and silicates [2]. A tiny portion of the fuel and the atomised and evaporated lubrication oil escape oxidation and get adsorbed onto particles which are known as the *soluble organic fraction* (SOF). Polyaromatic hydrocarbons containing oxygen, nitrogen and sulphur belong to this class of SOFs. The sulphur in the fuel gets oxidised to SO₂ but a small fraction gets oxidised to SO₃ that leads to the formation of sulphuric acid and sulphate aerosol. The metal compounds in the fuel and lubrication oil lead to the formation of inorganic ash [9, 10]. The common particulate bound compounds include the linear and branched chain hydrocarbons with 14-35 carbon atoms, alkylated benzenes, polynuclear aromatics, nitro-PAH and several polar, oxygenated PAH derivatives. These compounds are reported as potential mutagens/carcinogens [11]. The soluble organic fraction can be determined by chemical extraction methods such as Soxhlet extraction that help in identifying the adsorbed hydrocarbon speciation. The size ranges of particulate matter (PM) are from less than 10nm to more than 10µm, i.e. from nanoparticles to PM₁₀ particles.

Diesel soot can be defined as agglomerates of carbonaceous particles of 10-80nm, forming “clusters” that can be larger than 10µm, composed of thousands of particles. They are mainly composed of carbon, with some absorbed hydrocarbons, sulphur and nitrogen compounds and trace elements [2]. The composition of the exhaust particulates depends on how and where they are formed. The exhaust gas gets diluted

and cooled and eventually the processes of nucleation, condensation and adsorption lead to the transformation of the volatile material to the solid and liquid phases but as the temperature of the exhaust increases, there is a formation of gaseous volatile matter [6].

According to a review by Kittleson *et al.*, a typical particle composition of a heavy duty diesel engine tested under a heavy duty transient cycle is as shown in figure 1.3.

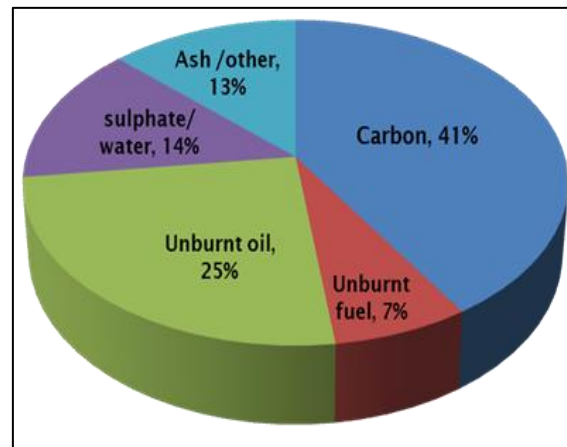


Figure 1.3 Composition of particles from a heavy-duty diesel engine [12]

In the recent decades there has been an increase in the measurements of particulate matter using source measurement studies for the development of pollution abatement strategies, characterisation of air quality and studies related to health and ecological studies, in a number of areas. These help to determine the particulate matter concentrations in air and in turn help to understand the adverse health effects associated with the exposure to particulate matter [6].

1.4.2.1 Size distribution of diesel particulate matter

Particles found in the atmosphere are either emitted directly into the atmosphere as *primary particles* or are formed in the atmospheric reactions such as nucleation and condensation of gaseous precursors to give rise to the *secondary particles*. Their shapes, sizes and chemical composition vary depending on the process of their formation and any atmospheric processes they might have experienced. The size of the particles is an important parameter so as to understand the deleterious health effects of PM, as these influence the depth to which they are inhaled. Particles with a diameter larger than $10\mu\text{m}$ are filtered out in the upper respiratory tract itself, while particles smaller than $10\mu\text{m}$ (PM₁₀) penetrate further into the lungs [13, 14].

Particles that possess a diameter of $1\mu\text{m}$ or less can penetrate as far as the alveoli, where they are deposited and potentially enter the circulatory system [15].

Diesel particulates possess a bimodal size distribution consisting of *nuclei mode* and *accumulation mode*. Particles in the nuclei mode are in the range of $0.007\text{-}0.04\mu\text{m}$ that are formed from primary carbon spherules in the combustion chamber. Nucleation of hydrated sulphuric acid particles gives rise to sulphate particulates that are also formed in the nuclei mode [16, 17]. The accumulation mode consists of chainlike aggregates of primary soot particles and associated hydrocarbons while the coarse mode contains re-entrained agglomerates of the chainlike aggregates as seen in figure 1.4.

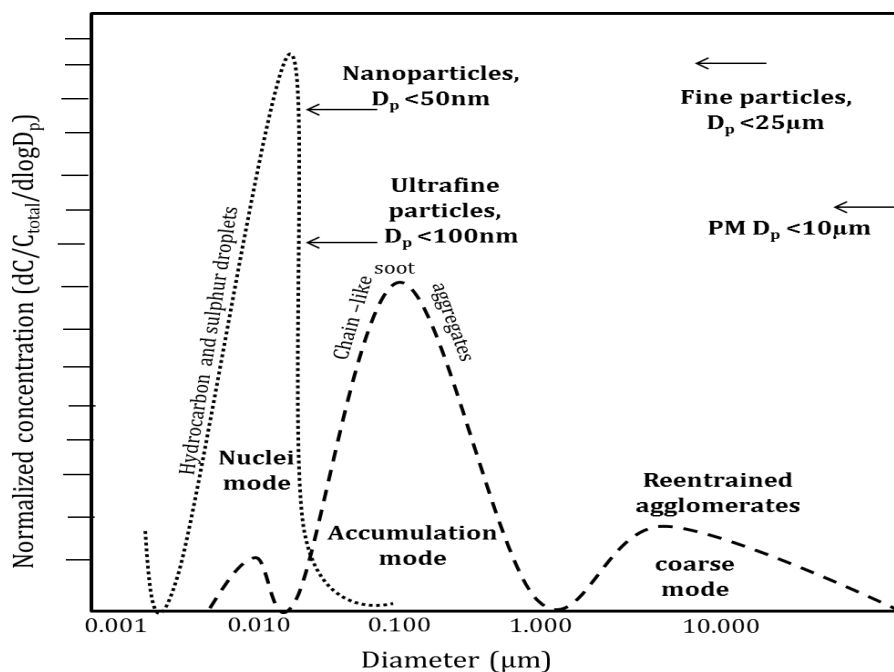


Figure 1.4 Typical particle size distribution in a diesel exhaust [7].

The hydrocarbons condense via two different pathways as shown in figure 1.5.

- a) Nucleation leads to formation of new particles onto which particles get adsorbed;
- b) In the accumulation mode, fewer particles are emitted and thus the surface area for adsorption of the hydrocarbons onto the exhaust gas decreases, thus leading to further nucleation of particles in the nuclei mode and a subsequent increase in the number of particles [4].

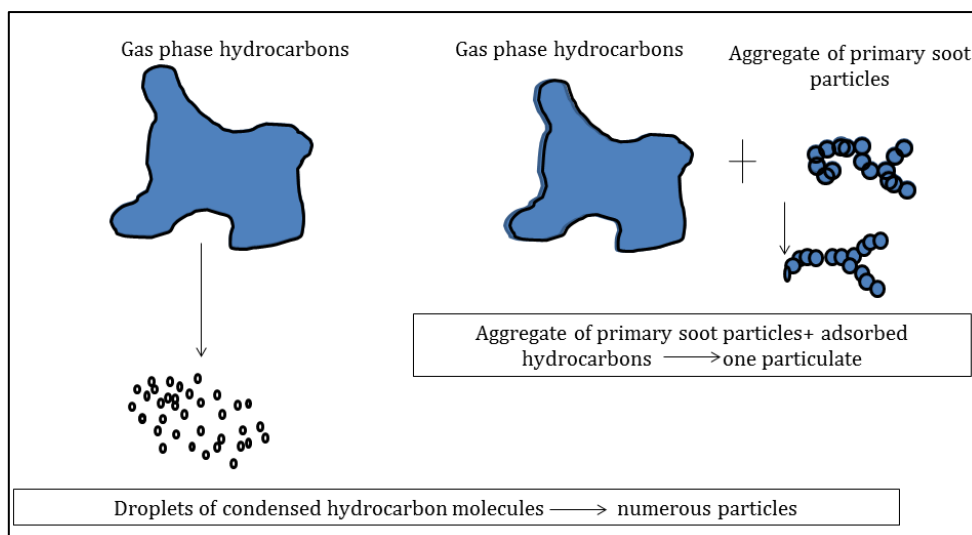


Figure 1.5 Different pathways for hydrocarbon condensation [7]

1.4.2.2 Toxicological Effects

Vehicle exhaust emissions are known to have a detrimental effect on human life and on the environment. The vast majority of these particulates are less than $1\mu\text{m}$ [3, 18] in diameter and most of the mass falls in the range of $0.1\text{-}1\mu\text{m}$ which is the accumulation mode size fraction. Most particles that are respirable and enter into the lungs and eventually into the bloodstream and brain are less than $0.1\mu\text{m}$ nanoparticles [3, 14, 19]. Several organizations such as (National Institute for Occupational Safety and Health, NIOSH); International Agency for Research on Cancer (IARC), Health Effects Institute (HEI); World Health Organization (WHO), California EPA, US EPA etc. have conducted epidemiological and experimental studies on diesel engine exhaust and have classified exhaust emissions as 'potential', 'likely', 'probable', or 'definite' carcinogens to human health [3,20]. The carcinogenic compounds in the exhaust include formaldehyde, acetaldehyde, dioxins and several polyaromatic hydrocarbons such as benzopyrene [3, 21]. The soot also combines with other air pollutants and forms atmospheric brown clouds that have other adverse effects on human health and on the environment. Long term occupational exposure to DPM has known to be associated to 40% increase in the risk of lung cancer [3, 22]. The possible health effects depend on a number of factors such as dose, duration and frequency of exposure, surrounding environmental conditions, overall health of the population etc. The estimated numbers of deaths due to exposure to DPM are estimated to be 4.6 million per annum in the world [5, 23].

Pope *et al.* have concluded that long term exposure to ultrafine particles ($PM_{2.5}$) may be associated with increased cardiopulmonary and lung cancer mortality [5, 24]. Pagano *et al.* have found that mutagenic activity was inversely proportional to the particle size as according to their study on mutagenic activity on size distributed particle fractions from DPM in urban areas [5, 25]. A given mass of ultrafine particles will affect a larger surface area of lung tissue than an equal mass of larger particles [26]. The coarse soot particles, 2.5-10 μm inhaled, settle in the windpipe and cause irritation and frequent coughing. The DPM10 particles are found to enter the nose, throat and lungs, causing irritation but can be removed from the body by sneezing or coughing. This sort of distribution of these particulates is shown in figure 1.6.

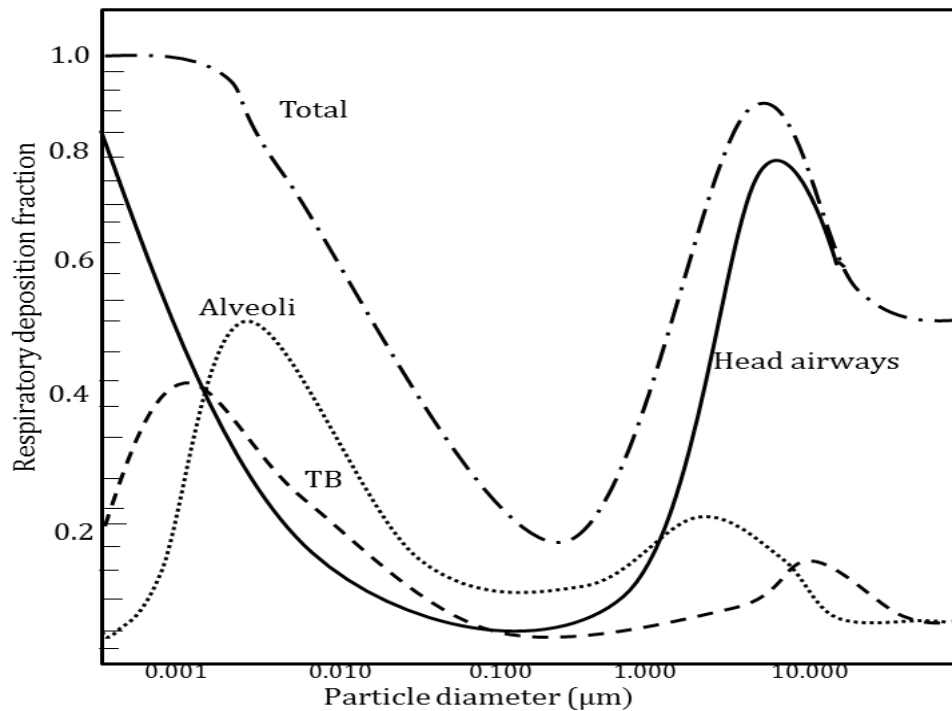


Figure 1.6 Distribution of various DPM in the human respiratory tract [7].

1.4.3 Diesel soot formation

Soot can be defined as agglomerates of carbonaceous particles of 10-80 nm, forming “clusters”, larger than 10 μm , composed of thousands of particles, with some adsorbed hydrocarbons, sulphur and nitrogen compounds and trace elements, formed due to incomplete combustion of hydrocarbons, as described in section 1.4.2. Figure 1.7 shows the composition of soot particulates.

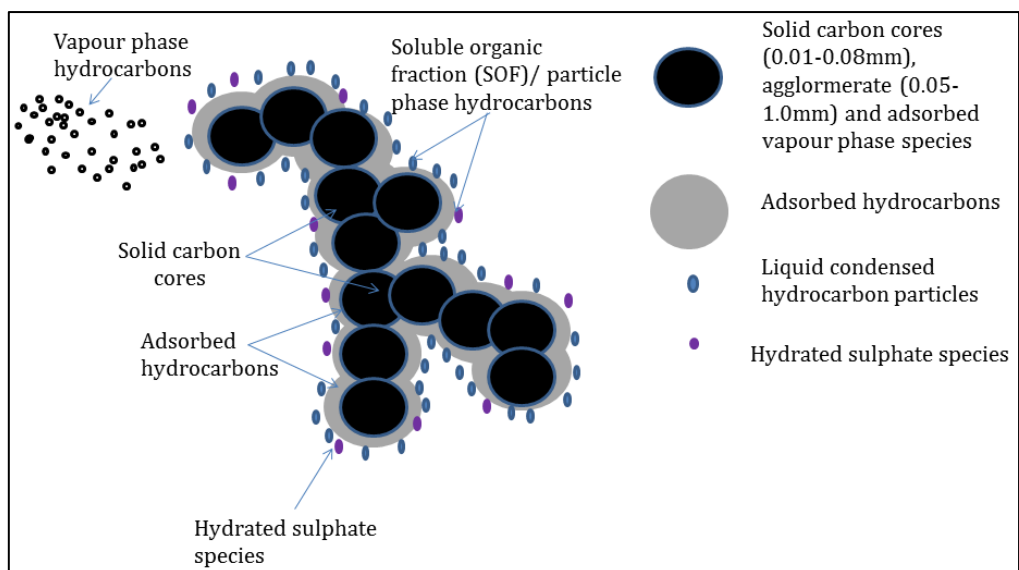


Figure 1.7 Schematic structure of a chainlike aggregate of primary soot particles and associated compounds [27]

The Euro V legislations (from effect since September 2009) for particulate matter in diesel and gasoline powered passenger cars is 0.005g/km and the Total hydrocarbon content (THC) is 0.1g/km. The Euro VI legislations to come into effect from September 2014, instruct the same levels to be maintained for the particulate matter and THC. Thus it is necessary to understand the formation and composition of soot [4].

Polycyclic aromatic hydrocarbon (PAH) molecules have often been invoked as key intermediates in the chemistry of soot formation and growth. There is a chemical reaction wherein there is a transformation of gaseous phase to condensed phase particles. The particle growth inception may be due to the formation of a chemical bond by release of heat energy or an entropy increase due to the formation of gaseous species. This is because of the formation of carbon through the release of H_2 from saturated alkanes leading to an increase in entropy of the system, eventually responsible for the particle growth as mentioned above.

The physical phenomenon involves the dimerization of PAHs leading to further condensation and particle growth. In the case of flame soot formation, acetylene is the dominant hydrocarbon formed during fuel rich combustion [28, 29]. This causes an increase in entropy due to dehydrogenation and overall reduction in Gibbs free energy (figure 1.8). The process beyond is exothermic, thus the formation of benzene from

acetylene is under reduced entropy. The Gibbs free energy gradually reduces on formation of PAHs from benzene, as shown in the figure 1.8. The titania is formed from titanium vapour when a flame doped with the precursor titanium salt ignited. The heat from the flame causes the precursor to dissociate giving rise to titania. The titania formation in flames was accompanied by an entropy reduction, owing to bond formation and crystallization from gas-phase species, unlike the case of carbon formation [30].

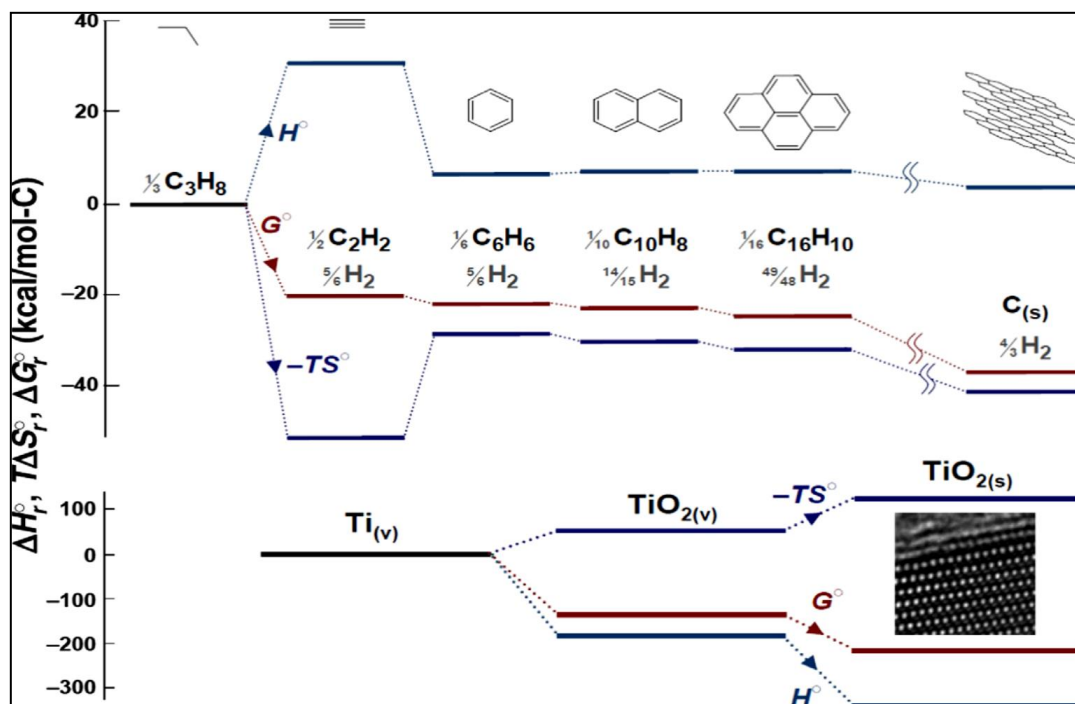


Figure 1.8 Formation of heavier polycyclics from smaller hydrocarbons [28, 30]

The acetylene may polymerise to polyethyne and other polycyclic structures led by ring closure. These polycyclics are called *platelets* that stack together to form *crystallites*, which subsequently stack together to form *turbostratic particles*. Particle coagulation and surface growth caused by the addition of precursor gas-phase molecule leads to the increase in size of the particles. The space between the coagulated particles is filled by surface growth and because of this the coagulated particles attain a spherical shape. The growth of the particles stops with an inhibition to surface growth. This eventually leads to the formation of *primary soot particles* that continue to coagulate to form chain like *aggregates*. These clot together to form *agglomerates*. This was

proposed by Smith as the fundamental steps in soot formation as shown in figure 1.9 [5].

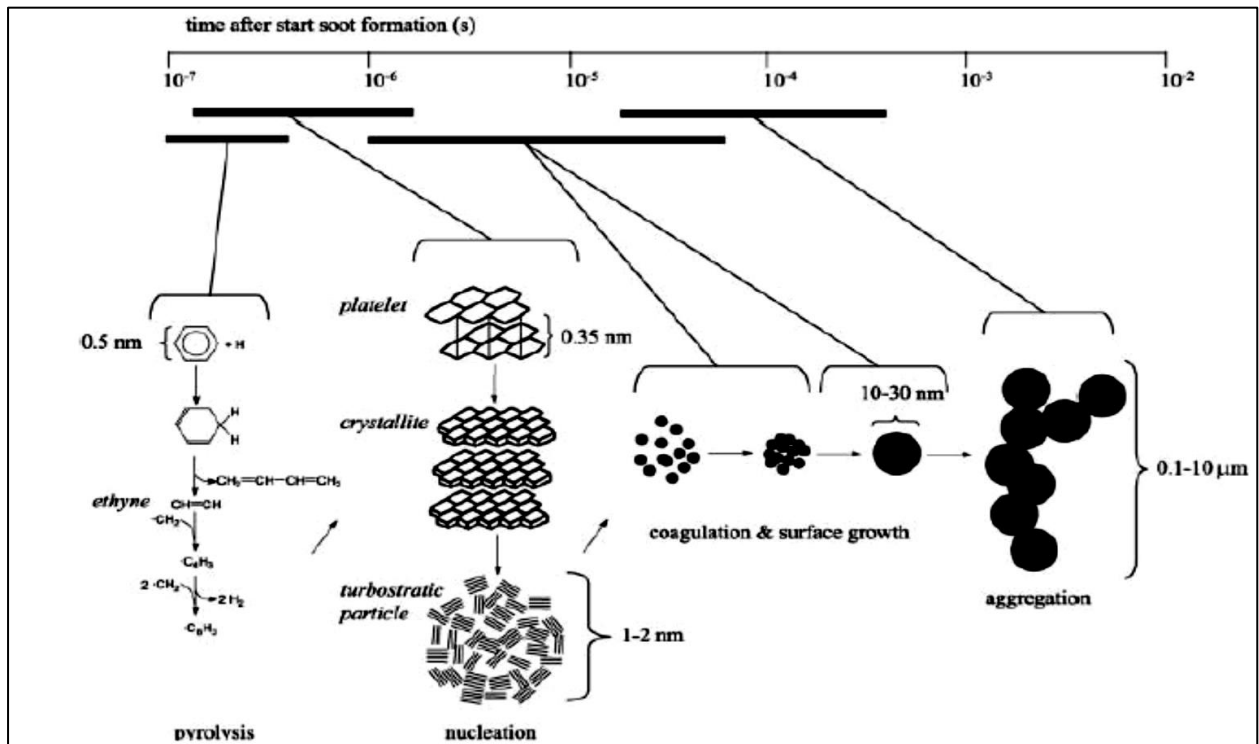


Figure 1.9 Process of soot formation [7]

The process of soot formation occurs at different times scales ranging from few microseconds in the initial nucleation stage to a few milliseconds when the soot oxidation is complete. This is given in figure 1.10 as a function of time where, n is the total number of nuclei per cylinder volume. This generally occurs in the high temperature region, fuel rich reaction zone around individual droplets, where the hydrocarbons are oxidised under sub stoichiometric oxygen conditions.

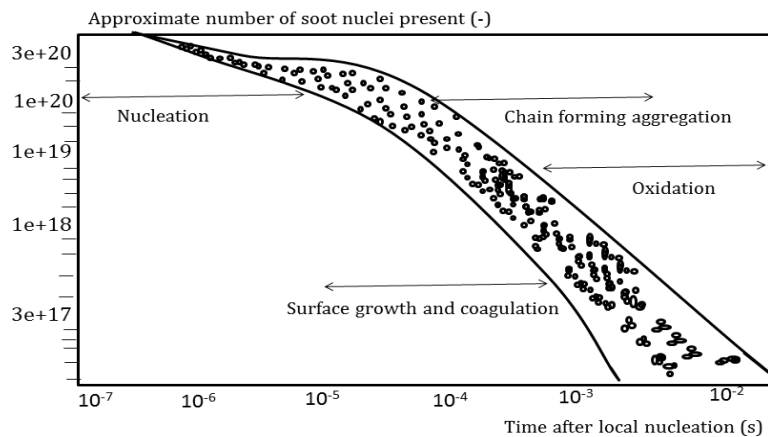


Figure 1.10 Particulate number density as a function of time [31]

The process includes the following stages:

1. Pyrolysis - In this process soot precursor molecules are formed from gas phase molecules through free radical mechanisms. The two kinds of pyrolysis that occur are: a) Pyrolysis in the oxygen free reaction zone; b) Pyrolysis in the oxygen containing reaction zone. In both these processes the aromatic and aliphatic molecules first break down into olefins and then form acetylene which is the precursor of soot formation [32-34].
2. Nucleation/Inception - At this stage the soot precursor molecules grow into soot nuclei. As the pyrolysis occurs at high temperatures, high concentration of the ions and radicals of the hydrocarbons (O. and .OH) is formed. The decomposition rate of the soot nuclei is lower than the rate of reaction with unsaturated, charged hydrocarbons, leading to the growth of soot nuclei [5, 30].
3. Surface growth - In this stage the precursor molecules tend to grow from 1-2nm to 10-20nm within few micro seconds to 0.05ms of formation of nuclei. There is a rapid addition of acetylene/polyacetylene molecules. There is a decrease in the H:C ratio in this zone as the addition of polyacetylene has much lesser H:C than the original nuclei. Alongside this process, coagulation occurs which causes the molecules to collide, coalesce and form larger, spherical particles [5, 30].
4. Aggregation - This process leads to the formation of fractal structures that are formed when soot spheres collide at a rate proportional to the square number of spheres. These chain like structures that are a few 100nm usually form within 0.02-0.07s of nucleation [5, 30].

1.4.4 Poly aromatic hydrocarbons

Polycyclic aromatic hydrocarbons, PAHs, are a large group of organic compounds made of two or more fused aromatic rings containing carbon and hydrogen atoms. These are referred to as *alternant PAHs*. The unsaturated -four, -five or six-membered rings are called *non alternant PAHs*. The addition of rings and alkylation increases the number of possible isomers. The incomplete combustion of organic matter such as coal, oil, wood or tobacco leads to the formation of these ubiquitous environmental air pollutants. In order to understand the toxic effects of these PAHs on

humans, it is necessary to identify the sources, the types of substances they emit and also evaluate the physical and chemical reactivity of these substances in the atmosphere. It is also necessary to describe the existing methods for collecting, separating, detecting and quantifying these PAHs.

A list of some of the commonly known PAHs is given in the figure below.

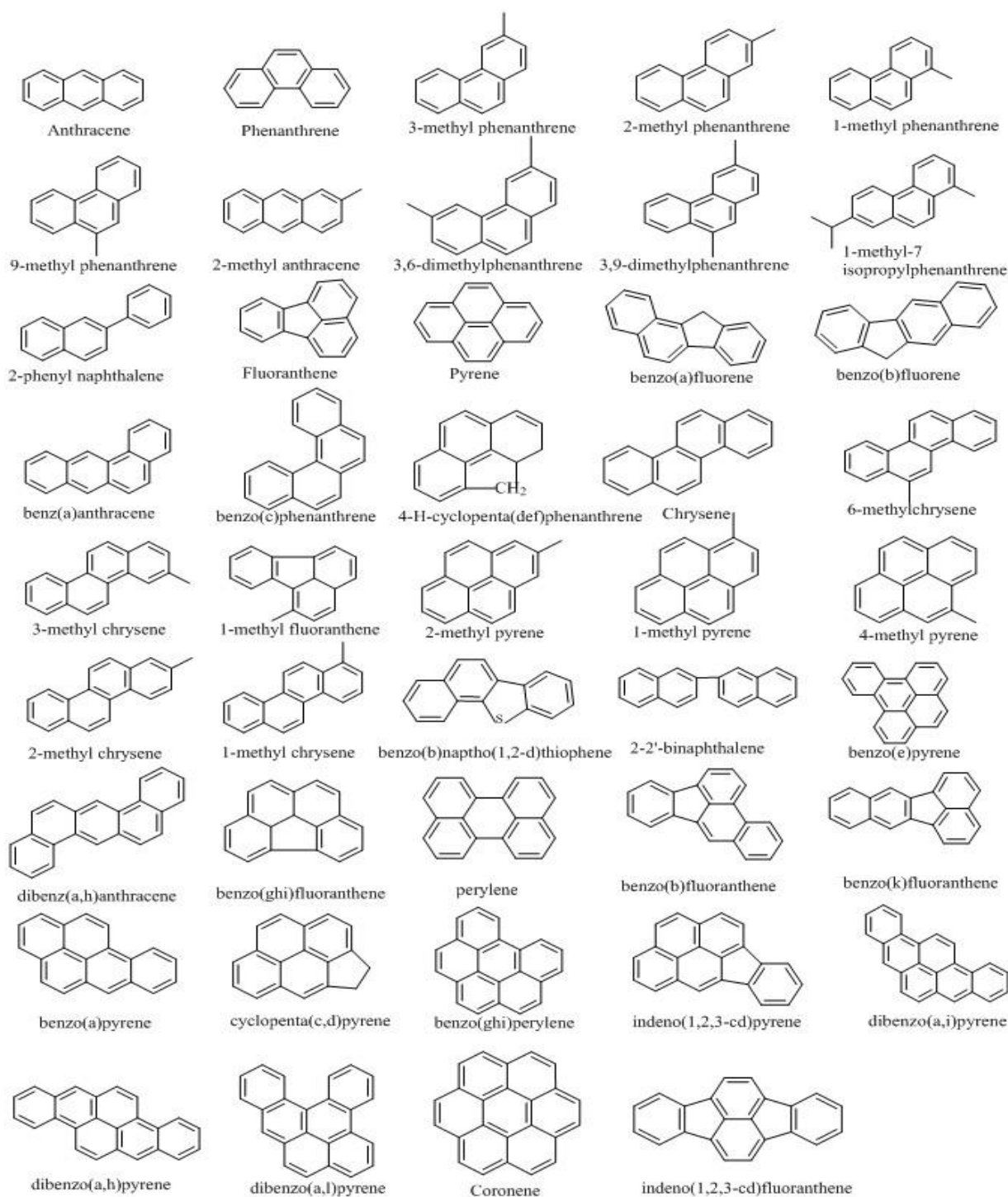


Figure 1.11 List of PAHs found in the atmosphere [8]

1.4.4.1 Sources of PAH

The major natural sources of PAHs include fossil fuels such as crude oil, coal, oil shale, volcanoes and forest fires, while the anthropogenic sources are vehicle exhausts, industrial processes, waste incineration and domestic waste. The amount of emission varies widely from low emissions over controlled and efficient combustion to high emissions due to incomplete combustion. Oxygenated PAH (O-PAH) are volatile organic air pollutants and have been identified in samples from gasoline, diesel, coal, wood and municipal waste incineration [35-39]. The photo-oxidation of PAH also produces O-PAH.

The concentrations of PAH are in the range of 0.1-39ng/m³ and this tends to vary between sampling sites and duration of sampling. Various factors that affect the concentration of PAH include proximity to sources, source types, wind speed, wind direction, temperature, concentration of other pollutants and precipitation. The concentrations of O-PAH in the atmospheric sampling studies have shown concentrations to be in the range of 0.1-10ng/m³ [40-43].

1.4.4.2 Physicochemical properties

PAHs are known to have molecular weights ranging from 116-302 g/mol, corresponding to 2-6 membered ring structures [5, 44]. These compounds are relatively inert and slightly polar in nature. They derive their chemical stability from their conjugated π system. Their occurrence is in the solid state with boiling points higher than n-alkanes consisting of the same number of carbon atoms [45, 46]. They have relatively low vapour pressures which decreases with the increase in the number of rings.

The factors such as ambient temperature, relative humidity, concentration of the PAHs and composition of the aerosol particles effect the partitioning of these PAHs between gas and particle phase [5, 47]. The distribution of PAHs occurs such that 2-3 ringed PAHs mainly occur in the gas phase while 5-6 ringed PAHs get adsorbed onto the particles and 4-ringed PAHs are found in both the gas phase and adsorbed on the particles [5, 48]. The increase in ring size causes a decrease in volatility and solubility of PAHs.

1.4.4.3 Toxicological effects

The interest to understand PAHs emanated from the understanding of the toxicological and epidemiological effects of these compounds on human health and animals. They have been shown to cause mutations in cells and cancer in animals [32, 49-51]. The first report to be published on this subject dates back to 1775, in which British surgeon, Sir Percivall Pott described his hypothesis on scrotal cancer related to occupational exposure to soot from chimney sweeps [5, 52]. This was later discovered to be caused by PAHs in soot. von Volkman and Bell later reported the increase in skin cancer incidents affecting workers in the coal tar industry [53, 54].

Benzo(a) pyrene in coal tar was discovered as a causal agent by Cook *et al.* in the 1930s [55]. The first carcinogenic activity of pure PAH compounds were reported by Kennaway and Hieger, when they found that dibenz(a,h) anthracene and dibenz (a,j) anthracene produced cancer when painted on mouse skin [56, 57]. At around the same time, Heiger showed the carcinogenicity from a mass of yellow powder obtained from two tonnes of coal tar pitch. These were further fractionated to yield two crystalline products – B(a)P and benzo(e)pyrene [58]. Several PAHs are considered to be tumour initiators and promoters. B(a)P has been found to be the only existing PAH that is carcinogenic to humans by the International Agency for Research on Cancer (IARC) [59].

However, there are other carcinogenic PAHs that have been identified but lack strong evidence for their carcinogenicity. Many organizations such as the IARC, World Health Organization (WHO) and the US Department of Health and Human Services (US-HHS) [60] have suspected several PAHs as potential carcinogens. A recent review shows that the carcinogenic effects from vehicle exhausts (Diesel and Otto engines), cigarette smoke, hard coal combustion condensates, and used motor oil, on mouse skin and rat lung, may be attributed entirely to PAHs [61]. The PAHs with 4 rings and more were shown to contribute to 70-90% of the carcinogenic potential.

Durant *et al.* observed that PAHs with high MWs of 302 such as dibenzo(a,e)pyrene and dibenzo(a,i)pyrene were shown to contribute to approximately 30% of the total PAH mutagenic activity as tested using the chromatographically fractionated Soxhlet extracts of urban PM using a line of human B-lymphoblastoid cells [62]. The concentrations of dibenzopyrene isomers in ambient air or in vehicle emissions are found to be lower than the low molecular weight PAHs. Their abundance in comparison

to other PAHs could be low but their relative concentrations alone do not provide an indication of the toxicity of these compounds, for which the individual concentrations of these compounds needs to be combined with its Toxic Equivalency Factor (TEF). The TEF value can be used to denote the cancer potency of specific PAHs relative to the potency of benzo(a)pyrene. TEF of B(a)P is set to unity according to the definition. The values higher than 1 are set for compounds having carcinogenic potencies higher than benzo(a)pyrene and values lower than 1 for compounds having potencies lower than B(a)P.

Table 1.3 The degree of evidence for carcinogenicity of PAHs in animal experiments and overall evaluations of carcinogenicity to humans [8, 49-51]

Sl. No	Compound	Molecular weight (M.W)	IARC		WHO	TEF
			ANIMAL	HUMAN		
1.	Phenanthrene	178	I	3	(+/-)	0.0005
2.	Anthracene	178	I	3	-	0.0005
3.	Fluoranthene	202	I	3	+	0.05
4.	Pyrene	202	I	3	(+/-)	0.001
5.	benzo(ghi)fluoranthene	226	I	3	-	
6.	benzo(c) phenanthrene	228	I	3	(+/-)	
7.	cyclopenta(c,d) pyrene	226	L	3	+	
8.	benzo (a) anthracene	228	S	2A	+	0.005
9.	Chrysene	228	L	3	+	0.03
10.	benzo(b) fluoranthene	252	S	2B	+	0.075
11.	benzo(k) fluoranthene	252	S	2B	+	0.075
12.	benzo(e) pyrene	252	I	3		
13.	benzo(a)pyrene	252	S	2A	+	1
14.	perylene	252	I	3	(-)	
15.	indeno(1,2,3-cd)pyrene	276	S	2B	+	0.1
16.	dibenz(a,h) anthracene	278	S	2A	+	
17.	benzo(ghi)perylene	276	I	3	-	0.02
18.	dibenzo(a,l)pyrene	302	S	2B	+	
19.	Coronene	300	I	3	(+/-)	
20.	dibenzo(a,i)pyrene	302	S	2B	+	
21.	dibenzo(a,h)pyrene	302	S	2B	+	

TEF: Toxic equivalency factors for selected PAHs, I: inadequate evidence; L: limited evidence; S: sufficient evidence; 2A: probably carcinogenic to humans; 2B: possibly carcinogenic to humans; 3: not classifiable; -: negative; +: positive; +/-: questionable; (): limited number of studies. IARC

1.4.5 Diesel emissions legislation

The international concerns over several aspects of environmental pollution caused by several polluting sources increase the need for stringent regulations in order to control the emission of these toxic pollutants that pose big threats to ecology. Therefore, several leaders from many developed countries met at different time frames to execute these regulations. U.S Federal Government regulations were introduced in the 1970s, although the first government legislations for the permissible exhaust emission standards were effectively enforced in Europe and USA in 1992, for light duty and heavy duty engines. In the US, emission standards are managed by the Environmental Protection Agency (EPA) on a national level while the state and local governmental bodies play a subsidiary role [4].

According to the European legislations, the emission standards for light-duty vehicles that include passenger cars of 1305 kg and vans with a gross weight of 3500 kg are represented in g/km. In the case of heavy-duty vehicles such as trucks and buses moving with an average speed of 25 km/h with a gross weight of 3500kg and off-road engines emission standards are expressed in g/kWh [7]. According to the European Union standards these stepwise legislations are referred to as Euro standards as listed in Table 1.4. For passenger cars and heavy duty vehicles, the engine certification for the light duty vehicles is done using a chassis dynamometer that simulates the actual driving behaviour or over a defined test cycle. Exhaust emission standards and test cycles differ from country to country and over a year.

Table 1.4 European Union emission standards for gasoline and diesel powered (within bracket) passenger cars (g km^{-1}) [4]

Sl.No	Tier	Time frame	CO	THC	NMHC	NO _x	HC+NO _x	PM
1	Euro I	1992	2.72 (2.72)	-	-	-	0.97 (0.97)	- 0.14
2	Euro II	1996	2.2 (1.0)	-	-	-	0.5 (0.7)	- (0.08)
3	Euro III	2000	2.3 (0.64)	0.20 (-)	-	0.15 (0.50)	- (0.56)	- (0.05)
4	Euro IV	2005	1.0 (0.50)	0.10 (-)	-	0.08 (0.25)	- (0.30)	- (0.025)
5	Euro V	2009	1.0 (0.50)	0.10 (-)	0.068 (-)	0.060 (0.180)	- (0.230)	0.005 (0.005)
6	Euro VI	2014	1.000 (0.500)	0.100 (-)	0.068 (-)	0.060 (0.080)	- (0.170)	0.005 (0.005)

Euro V and VI regulations have stricter emission for NO_x and PM, since it adopts a new PM mass emission measurement method developed by the UN/ECE Particulate Measurement Programme (PMP). PMP method introduces a particle number emission limit, in addition to the mass-based limits. Number-based PM limits would prevent the possibility that in the future open filters are developed that meet the PM mass limit but enable a high number of ultra fine particles to pass [63].

The emission test cycles determine vehicle emissions and the test procedures for light duty vehicles vary slightly from that for medium plus heavy duty engines. This also varies from country to country. Table 1.5 describes the test points under the European 13-mode test for heavy duty engines where the emissions are monitored at 13 speed and load points, giving an overall emission calculated using weighting factors. While in USA, this is carried out using transient test cycles where the speed and load of a vehicle are measures as a function of time. This is used in Europe as well for light duty vehicles [5].

Table 1.5 Speed, load and relative weight factor of the 13 points in the European 13-mode test

Mode	Speed	Load %	Weighting Factor
1.	Idle	0	0.083
2.	Intermediate	10	0.080
3.	Intermediate	25	0.080
4.	Intermediate	50	0.080
5.	Intermediate	75	0.080
6.	Intermediate	100	0.25
7.	Idle	0	0.083
8.	Rated	100	0.100
9.	Rated	75	0.020
10.	Rated	50	0.020
11.	Rated	25	0.020
12.	Rated	10	0.020
13.	Idle	0	0.083

The New European Driving Cycle (NEDC) is used to certify the light duty vehicles in Europe (figure 1.12) during which a fraction of the diluted exhaust is continuously collected in special ‘Tedlar bags’, the contents of which were then analysed for CO, hydrocarbons and NO_x. Particulate matter can be sampled via filter samplers made of Teflon coated glass fibre, connected to the sampling line through which a small portion of the diluted exhaust is drawn out from the dilution tunnel using a sampling probe. Upon collection onto the filters, particulate matter is determined gravimetrically [64].

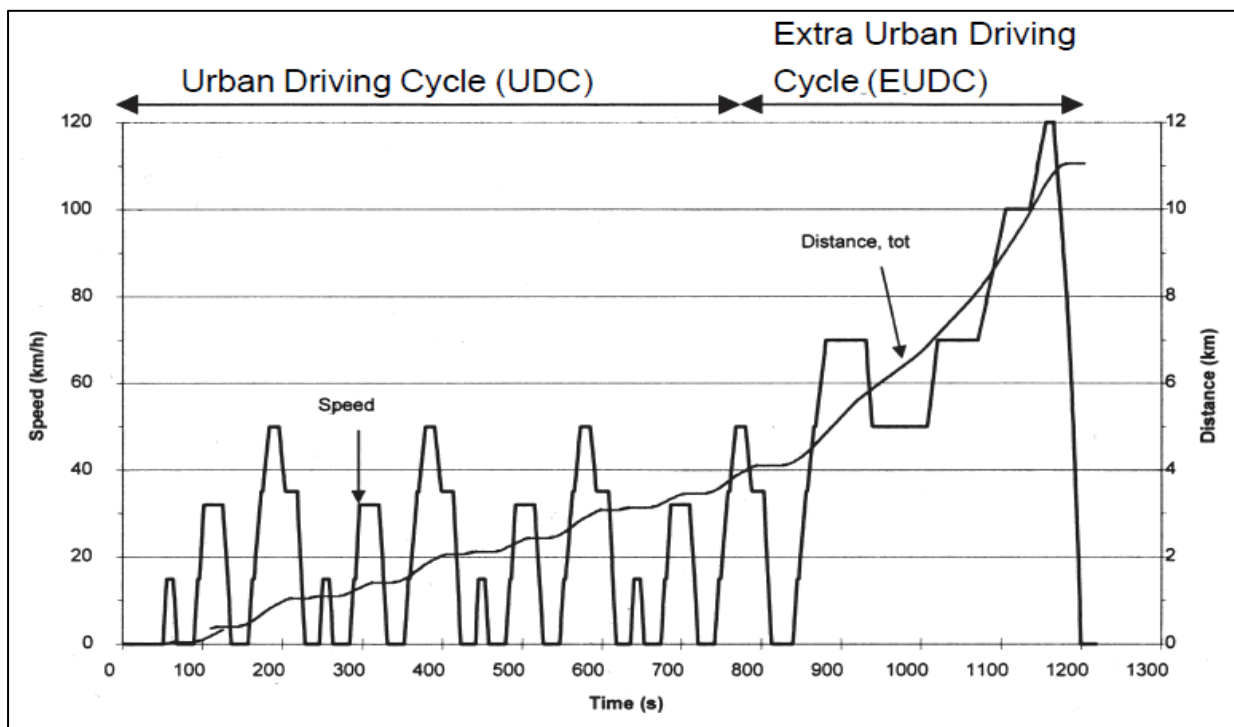


Figure 1.12 New European Driving Cycle [64]

There are several techniques that have been adopted in the US and Europe to reduce these emissions from diesel engines such as using modified or alternative fuels, by trying to correlate emission level with fuel specifications in order to optimize fuel composition generating low emissions. Another effective method is to carry out some engine modifications that have been implemented in recent years. At the same time, considerable effort has been directed at developing catalytic after treatment for diesel vehicles, especially for the removal of NO_x and particulate matter. These have been discussed in the section below.

1.4.6 Diesel exhaust gas treatment technologies

The largest application of heterogeneous catalysis has been in the area of catalytic exhaust gas after-treatment. This involves several automobile manufacturers, government agencies, catalyst suppliers, petroleum refiners etc. Several primary measures which include modification in engine, fuel and operating conditions in order to regulate the emissions from diesel exhausts have not been successful in keeping up the set legislations in the developed and developing countries. Thus there is a need for secondary measures that have been adopted as the tail pipe treatment technologies that include:

1.4.6.1 Diesel oxidation catalysts (DOCs)

In the early stages of the development of automotive catalysts, non-noble metals were evaluated because of their low costs and availability, but it was soon realised later that these base metal oxides of Ni, Co, Cu, Mn etc. were not durable and lacked intrinsic reactivity and resistance to poisoning[65-69]. Thus the need to use noble metals due to their excellent thermal stability and low tendency to react with support materials has gained recognition. These metals, generally Pt and Pd, are impregnated onto an alumina washcoat about 20-40 μ in thickness. Pt catalysts are preferred over Pd ones because the exhaust stream of a diesel engine is a highly oxidising environment and Pd under these conditions gets converted to less catalytically active palladium oxide (for soot oxidation), while Pt remains in its metallic form.

A diesel oxidation catalyst (DOC) oxidises the CO, unburnt hydrocarbons as well as the SOF of particulate matter, over the precious metal. They also oxidize SO₂ present in the exhaust from the combustion of sulphur containing fuels, which leads to a significant increase in the total particulate emissions. Thus modern oxidation catalysts are being synthesized to balance high HC and SOF activity alongside low SO₂ activity. The emissions are reduced upto 60-90% for HCs, CO and upto 20-40% for DPM using these DOCs. The temperature of the exhaust is very high but the oxidation of particulates in the presence of the catalyst tends occur at temperatures between 300-600°C. The point at which this occurs is called the *light-off temperature* [3, 6, 70]. Most DOCs are designed to have a low light off temperature when the engine has just started. However over time the catalytic performance in the DOC is known to deteriorate gradually throughout the lifetime of the vehicle as there may be a build-up of a variety

of sulphur compounds on its surface that causes poisoning and decrease in its performance, resulting in the need for a more efficient technology to keep these emissions under control. Thus modern technologies rely on particulate filter trap as more efficient methods of controlling emissions by trapping the soot.

1.4.6.2 Diesel particulate filter (DPF)

These filters help to trap DPM on a large honeycomb structured monolith made of cordierite ($2\text{MgO}-2\text{Al}_2\text{O}_3-5\text{SiO}_2$) or silicon carbide [71,72], adjacent channels of which are plugged at one end to force the particulates through the porous substrate walls as shown in figure 1.13. The porosity of these walls helps the exhaust gas to pass through without creating a large pressure drop while collecting the particulates as well. These filters need to be regularly regenerated as they can become blocked by particulate species from the exhaust stream and this causes a back pressure to build up which could lead to possible engine and/filter failure [73]. Regeneration is usually done by oxidizing (burning) the trapped particulates.

There are two modes of regeneration-active and passive. Active regeneration is usually done by injecting some fuel into the DOC which generates a large exotherm. In the active regeneration mode, the PM gets oxidized periodically once the soot loading on the filter reaches a set limit (approx. 40%) This creates a pressure drop across the DPF which is monitored by a back pressure sensor. This occurs in the presence of heat supplied from a flame based burner or an electric heater which burns the soot above 600°C . This has several problems such as instability due to melting of the filter material at high temperatures and thermal regeneration requires lot of energy, which makes it an expensive and tedious process.

The passive regeneration mode on the other hand has a continuous self-regenerative process in the presence of a catalyst coated on the trap itself or the catalyst in the case of the CRT system is lodged upstream of the trap. This process is fuel efficient, inexpensive and simple as compared to the active mode [74]. The challenge is to find a suitable catalyst that is capable of decreasing the soot combustion temperature from 600°C to diesel exhaust temperatures ($200-400^\circ\text{C}$).

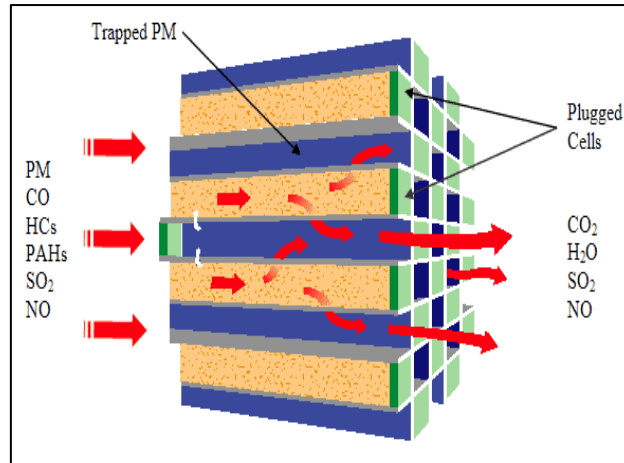


Figure 1.13 Diesel particulate filter [71, 72]

1.4.6.3 Continuous regenerating trap (CRT)

The CRT works on the principle that a diesel oxidation catalyst coated on a monolith can oxidize NO to NO₂ that reacts with the deposited soot on the filter forming CO₂ and NO as shown in figure 1.14. This helps in continuously regenerating the trap, and thus the term CRT. This has been patented by Johnson Matthey and is the most widely used DPF. Moulijn *et al.* developed a TU Delft catalytic filter where Pt on ceramic foam is mounted on a wall flow monolith. This helps in deep filtration on the foam where the NO is oxidized to NO₂ and most of the NO₂ is used to oxidize the soot. A portion of this NO₂ slips out, which is used to oxidize further in-flow of particulates onto the trap. This process of NO₂ assisted soot oxidation occurs on surface of the wall monolith [6].

Due to the continuous process of regeneration, the stability of the system is maintained as the temperatures are not very high in this process but the problem in this system was that the NO_x is not totally reduced efficiently. Also, the performance of this system is best at low sulphur (<50ppm) content and the SO₂ formed is oxidized by the Pt catalyst adding more to the particulate mass. The ideal ratio of NO_x:PM is considered to be 20:1. This condition is applicable to light duty engines such as in the case of passenger cars running on gasoline and not diesel. This is not feasible to use in the case of heavy duty diesel engines as low sulphur fuel is not widely used in these vehicles [6].

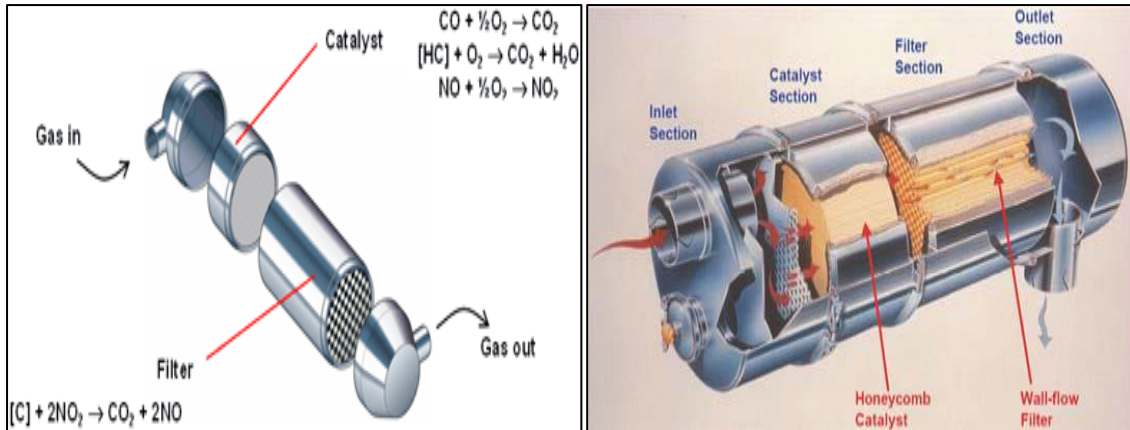


Figure 1.14 Continuous regenerating trap (CRT) technology [6]

1.4.6.4 SCRT

This system was also developed by Johnson Matthey which is a combination of SCR (Selective Catalytic Reduction) with CRT (Continuous Regenerating Trap) technology. This efficiently oxidizes the CO, hydrocarbons and particulate matter. The NO₂ content of the gases is enhanced and the effective SCR system helps to reduce the NO_x content. In the SCR, there is a controlled amount of urea being injected into the exhaust which is hydrolysed to NH₃. In the presence of NH₃, the NO_x is reduced to N₂ and H₂O [6]. Over an SCR catalyst, the excess NH₃ was removed using an NH₃ slip catalyst by converting it into N₂ and water as shown in figure 1.15.

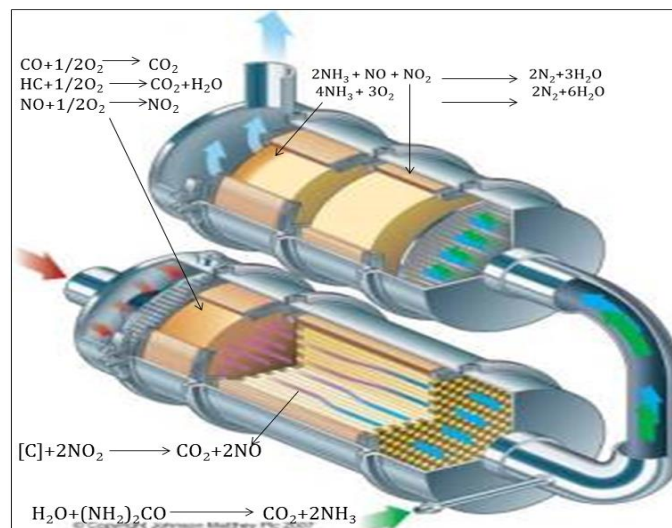


Figure 1.15 SCRT system [6]

1.5 Literature review

Diesel soot oxidation has been widely studied since the early 20th century. In the early 1980s, diesel particulate trapping techniques were developed and it was observed that three way catalysts were not suitable for this purpose as they function at lower temperatures in the exhaust, while the onset temperatures for the soot oxidation was between 400-450°C. The strategy that was followed in the case of non-catalysed soot oxidation was to trap the soot and ignite it at high temperatures and then turning the heat off. Thus the exothermic soot combustion reaction helped to maintain the high temperature for the reaction. This technique was called *self-supporting flame propagation* [75]. There are several factors such as temperature, deposited soot amounts, flow rate of the gas, oxygen concentration etc. that effect this process and the need for trap regeneration during all driving conditions was also essential. Higuchi *et al.* observed that the regeneration efficiency was poor and about 35% of the soot remained on the filter leading to a build-up which eventually lead to the poor performance of the filter [76]. Thus there was a need to oxidize the soot efficiently and thus uncatalysed and catalysed soot oxidation were studied

1.5.1 Non-catalysed soot oxidation

Moulijn et al. proposed a reaction mechanism for the carbon–oxygen reactions on the active surface area in different carbon materials which according to them depended on several factors such as crystallite size, orientation, vacancy concentration, impurity type, location and concentration [7, 77-80]. The following steps occurred as shown in the figure:

- a) A surface semiquinone group and a physically adsorbed oxygen atom are formed when the graphite containing a ketone surface-oxygen complex reacts with the oxygen in the gas phase. This semiquinone complex is a stable surface oxygen complex as the bond strength of the C-C bond is only slightly weaker than the C-C bond strength in graphite.
- b) The electronegativity of the oxygen atoms on the semiquinone complex allows the carbon atom between the CO groups to bond with the oxygen, resulting in a semiquinone complex with off-plane oxygen which lowers the C-C bond strength of the neighbouring C atoms.

c) Graphite with a carbonyl group is formed when the complex decomposes and thus the carbon atom next to the carbonyl group is a target for bonding with oxygen due to the electronegativity of the oxygen atom in the carbonyl group, which eventually leads to the formation of a carbonyl complex with off-plane oxygen attached to it.

d) There is a reduction in the C-C bond strength of the neighbouring C atom with the formation of the new complex.

e) CO is released and the cycle restarts from the carbonyl group again.

This mechanism does not explain the oxidation of all carbonaceous substances but gives an insight into the oxidation process.

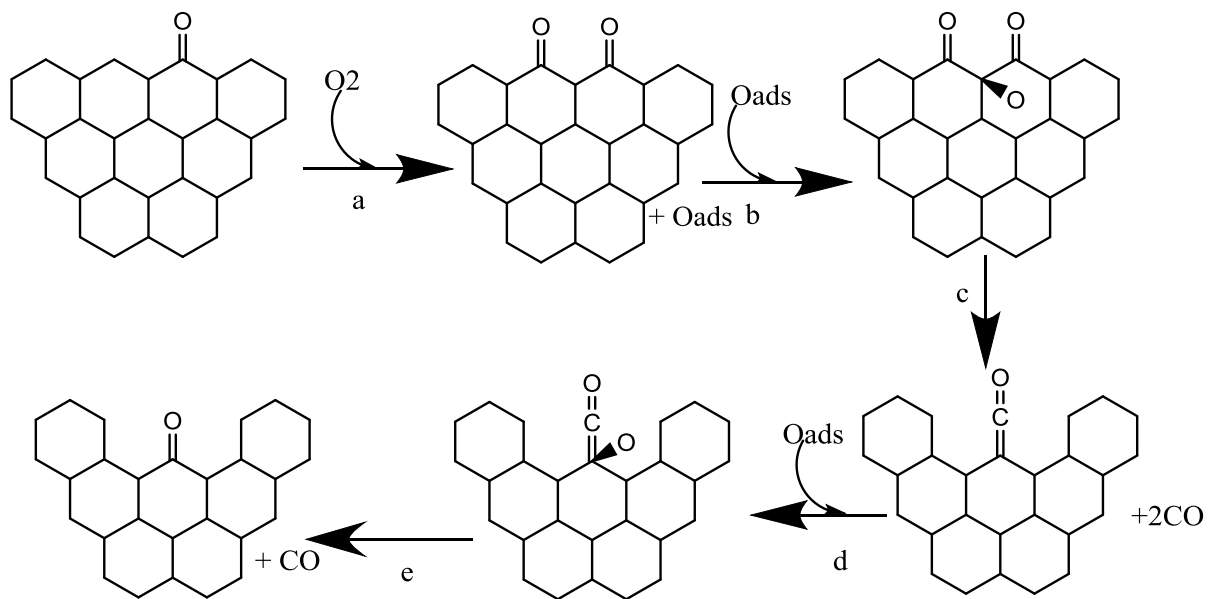


Figure 1.16 Reaction mechanism of the noncatalytic oxidation of carbon [7]

1.5.2 Catalytic soot oxidation

The two main factors that influence catalytic soot oxidation are type of catalyst and the type of contact between the soot and catalyst. There are two groups of catalysts usually preferred in this case:

1. *PGM catalysts* - These catalysts are very active for soot oxidation in the presence of NO stream [81, 82]. Most commercial filters have been made using Pt combined with promoters. The NO present in exhaust gas is converted into NO₂ over the Pt catalyst that oxidizes the soot at temperatures between 300-500°C. This observation was made by Cooper and Thoss [83]. Several other metals such as Pd, Rh, and Ru [84] have been used but the disadvantages of these PGM are their high cost (Pt being most expensive) and production of sulphate particles upon oxidation of sulphur in the fuel. Studies by

Uchisawa and co-workers on Pt supported catalysts showed that the catalytic activity was measured using a temperature programmed oxidation profile which detected the CO₂ signal as a function of temperature [85].

Pt impregnation using Pt (NH₃)₄(OH)₂ onto a MO_x/SiC where MO_x is TiO₂, ZrO₂ and Al₂O₃ have shown high activity and durability at high temperatures and sulphate exposure. Pt catalysts generally tend to oxidize the SO₂ to H₂SO₄ but when supports with low basicity are used this is reduced. Kim *et al.* [86] and Liu *et al.* [87] have studied the effects of vanadium in Pt based catalysts for diesel emission reduction as the SO₂ molecules tend to adsorb onto hydroxyl groups of TiO₂ and are promoted by V₂O₅. These molecules migrate to the Pt particles and react with the oxygen. The PGM catalysts operate on a balance between NO₂ and soot in the exhaust. It is thus clear that Pt based catalysts have the ability to oxidize soot by delivering 'active oxygen' to the soot-catalyst interface and also oxidizes the NO to NO₂ based on the conditions predominant in the exhaust.

2. *PGM free catalysts*- The use of non-noble metals have gained significant importance due to their high activity towards soot oxidation at cheaper costs for production. Transition metal oxide based catalysts such as Co-Ni [88], Cu-Fe [89], K-Cu, K-Co [90], Co-Ba-K [91], Cu-K-Mo [92], Cu-V-K [93], Cs-Fe-V [94] and other vanadate based catalysts have been widely studied for the treatment of emissions. Several studies on the use of rare earth metals have been investigated. These include metals oxides such as as Ce-La, La-Cr, Pr-Cr, La-K, La-K-Cr, La-K-Mn-O, La-K-Cu-V and Co-Ce [3].

These catalysts help in reducing the onset temperatures of soot oxidation and improve the activity. An important discovery was the Cu/K/M/Cl (M- V, Mo, Nb) based formulation by Watabe *et al.* which was shown to exhibit high soot oxidation rates at low temperatures which was related to the mobility and volatility of the active copper chloride component [95-97] but this catalyst was inactive at high temperatures as it evaporated under these conditions [98].

The addition of potassium as a promoter has been widely studied by several researchers. Querini *et al.* showed that activity of Co/MgO and Co/K/MgO towards soot oxidation was enhanced by the catalyst mobility increased by the addition of potassium [99]. Barium catalysts were reported by Otto *et al.*, to reduce the temperature at which soot burns by about 100-150K. A comparison between noble metal catalysts and non-noble metals were made by Marinangeli *et al.* in the presence of NO and SO₂ in the gas

feed which was shown in the case of Pt/Pd with Cu/Cr catalysts, and found that the noble metals proved to have higher activity [100].

Watabe *et al.* reported several alkali metal catalysts such as LiCl, LiF, KCl, KF, CsCl to be active for soot oxidation using Al_2O_3 , SiO_2 , and $\text{SiO}_2\text{-Al}_2\text{O}_3$ as supports [101]. Li *et al.* recently reported iron substituted nanometric perovskites-type catalyst ($\text{La}_{0.9}\text{K}_{0.1}\text{Co}_{1-x}\text{Fe}_x\text{O}_{3-\delta}$), that showed the highest activity at $x=0.1$ for simultaneous NO_x -soot removal [102]. The maximum soot oxidation rate was at 362°C . A study on different filters for soot oxidation was carried out by Hoffmann and Rieckmann using base metal oxides and they showed that the type of filter can have a greater influence in the process of soot oxidation. Peralta *et al.*, Zhang *et al.* and Bueno-L'opez *et al.* studied CeO_2 and CeO_2 based mixed oxides that increase the soot oxidation rate by providing for the active oxygen in them through a redox mechanism, where the soot is oxidized by the surface active oxygen from the catalyst that is then re-oxidized by the gas phase oxygen [92,99]

Soot oxidation occurs through two different mechanisms as reported so far in literature:

(i) Redox mechanism- the oxidation of carbon occurs through the lattice oxygen from the catalyst which is the reduction step and there is a re-oxidation of the catalyst by oxygen from the gas phase. This is the oxidation step. This follows a *Mars vanKrevelen* mechanism and applies to reducible metal oxide catalysts as shown in figure 1.17.

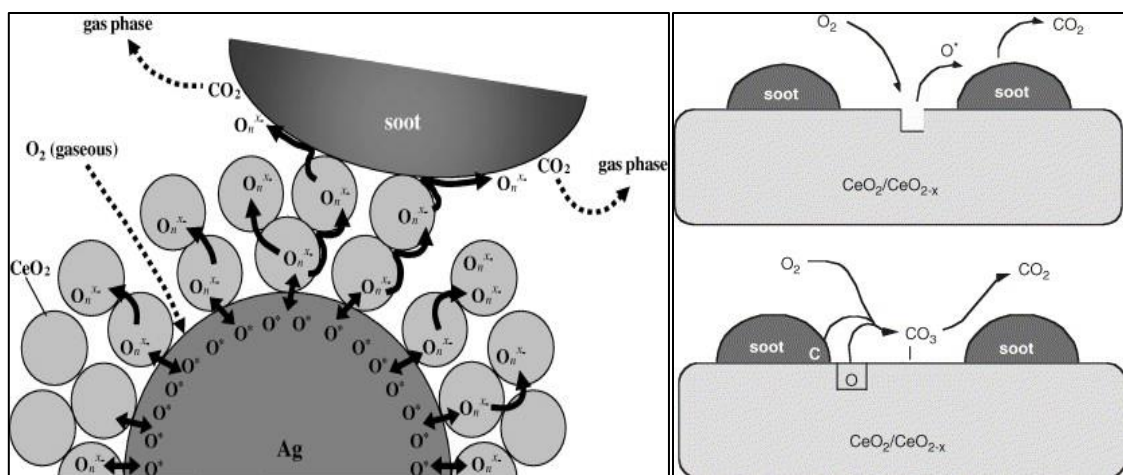


Figure 1.17 Redox mechanism of catalysed soot oxidation [7]

(ii) Spill-over mechanism- Some catalysts can dissociate the adsorbed gas-phase oxygen and surface diffusion to the soot particle occurs where the oxidation occurs as shown in the figure 1.18 [4]. This applies to the metals that can dissociatively adsorb O_2 .

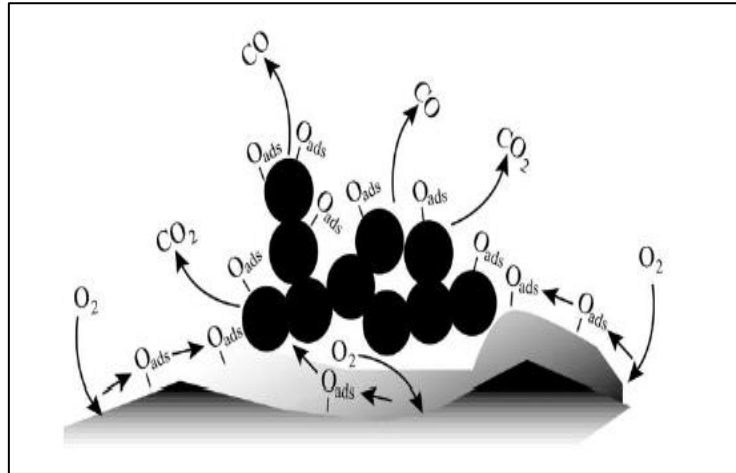


Figure 1.18 Spill over mechanism of catalysed soot oxidation⁷

1.5.3 Type of Contact

The major factor influencing catalytic soot oxidation is the soot-catalyst proximity. Several studies on carbon black with catalysts have been conducted in order to understand the concept of contact driven oxidation. Inui and Otowa discovered the poor contact of deposited soot on the catalytic filter. Neeft *et al.* [4] later investigated the effect of physical contact on the catalytic combustion after which they defined three types of contact- a)Loose contact-Mixing of the catalyst and soot in the right proportions using a spatula, b)Tight contact- Mechanical milling of catalyst and soot together to establish a firm contact between the two components.

c) in-situ contact-Diesel soot was filtered onto a catalyst bed from an exhaust stream

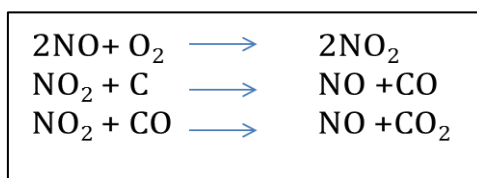
The difference in combustion temperature is as large as $200^{\circ}C$ between loose and tight contact. The studies by Neeft *et al.* revealed that the loose contact conditions were similar to the in-situ contact as is the case in exhaust conditions. Tight contact was more reactive as it established a better contact between the catalyst and soot and the dispersion of catalyst particles are better. This is known to control the mechanism of the reaction. Oxygen spill over mechanism is the predominant one in the case of oxides such as V_2O_5 and MoO_3 under tight contact conditions. Using labelled oxygen techniques, Mul

et al. showed that the spill over and redox mechanism occur simultaneously, depending on the degree of physical contact between the soot and catalyst [4].

On an atomic scale the two mechanisms proposed include electron transfer and oxygen transfer.

- a) Electron transfer: this involves the alteration of the distribution of π electrons in graphite sheets and thus the carbon substrate is prone to oxidation. This was proposed by Long and Sykes, but no conclusive proof for it exists [103].
- b) Oxygen transfer: this involves the metals that can oscillate between the two oxidation states and provide the oxygen stored for soot oxidation. This was proposed by Neumann *et al.* and later developed by Amariglio and Duval [104,105].

The oxidation of soot also occurs without intimate contact between the catalyst and the soot, under loose contact conditions, through the formation of mobile species such as NO_2 , O_{ads} etc. that are far more reactive than O_2 . The two main reaction mechanisms that exist under loose contact are *NO_x aided gas phase mechanism* and the *spill over mechanism* as described above. The NO_x aided gas phase mechanism was suggested by Copper and Thoss that explains the use of gas phase NO_2 as an activated mobile species that helps in soot oxidation. The NO_2 formed from the oxidation of NO helps in oxidizing the carbon through a series of steps as shown below:



1.5.4 Redox catalysts

Recent emission regulations such as Euro VI, LEVII and J-SULEV have enforced more stringent legislations that would demand the reduction in particulate emissions through a more precise and complete combustion of fuel in the engines, resulting in higher exhaust temperatures. Diesel engines have high fuel efficiency with relatively higher air to fuel ratio as compared to gasoline or petrol engines. Thus the conversions of CO and hydrocarbons occur at lower temperatures but the exhaust emits far more particulates that oxidize at higher temperatures. The time of residence of these particulates in the exhaust is very short and thus there is a need of a catalyst that can efficiently oxidize these particulates and simultaneously aid in NO_x reduction in an oxygen rich environment in the exhaust. Due to the detrimental effects of some of these

PM₁₀ particles that are potential carcinogens to human health, there is a greater need to reduce these emissions from being released into the environment, for which several oxidation catalysts are being widely studied. The catalyst should be capable of oxidizing the soot at lower exhaust temperatures, ideally alongside the CO and hydrocarbon oxidation. The contact between the catalyst and soot is usually poor due to the short residence time and thus penetration into the catalyst pores is not possible, thus making filter regeneration more difficult. The function of the catalyst is also over a large exhaust window thus testing the thermal stability of the catalyst [106].

CuO/ γ -Al₂O₃ was known to be efficient in reducing the NO_x with CO due to its high thermal stability and activity but at lower temperatures the activity was unsatisfactory. This was improved by doping it with ceria and other oxides that have proven to be ideal for industrial applications as three way catalysts that play a major role as indispensable oxygen storage sources [107].

1.5.4.1 Catalysts used in this project- Mixed metal oxides –CeO₂-ZrO₂-Al₂O₃

The efficiency of the catalyst is measured by its capacity to supply the oxygen stored in its lattice to the surface of the carbon for its oxidation termed as the oxygen storage capacity (OSC) that is known to fluctuate between the lean and rich states of the exhaust. Most rare earth oxides were investigated for their structural properties and have proven to be electronic promoters that improve the activity, selectivity and thermal stability of the catalysts. A well-known such oxide being CeO₂, undergoes reduction from Ce⁴⁺ to Ce³⁺ thereby supplying the oxygen in its lattice for the soot oxidation [108-110].

In a constantly varying feed stream of fuel rich (O₂ deficient) to lean (O₂ excess) states in the exhaust, CeO₂ donates the O₂ stored in it, to oxidize the CO and hydrocarbons while it re-oxidizes back using O₂, NO and water during the lean cycle. These steps help in the removal of the three major components of CO, hydrocarbons and NO during a normal exhaust cycle. Over higher temperatures, there is formation of O-deficient nonstoichiometric compositions that are produced continuously such as CeO_{2-x} (α phase $0 < x < 0.178$). Despite the formation of oxygen vacancies, CeO₂ retains its fluorite cubic structure and upon exposure to O₂, CeO_{2-x} gets re-oxidized back to CeO₂ [111-112]. A kinetic model below represents the reduction of CeO₂ comprising of 4 steps which has been shown to form hydroxyl groups as seen from FTIR studies. The steps include:

1. Dissociation of chemisorbed H_2 to form hydroxyl groups
2. Formation of anionic vacancies and reduction of neighbouring cations
3. Desorption of water by recombination of hydrogen and hydroxyl groups
4. Diffusion of surface anionic vacancies into the bulk material [113,114].

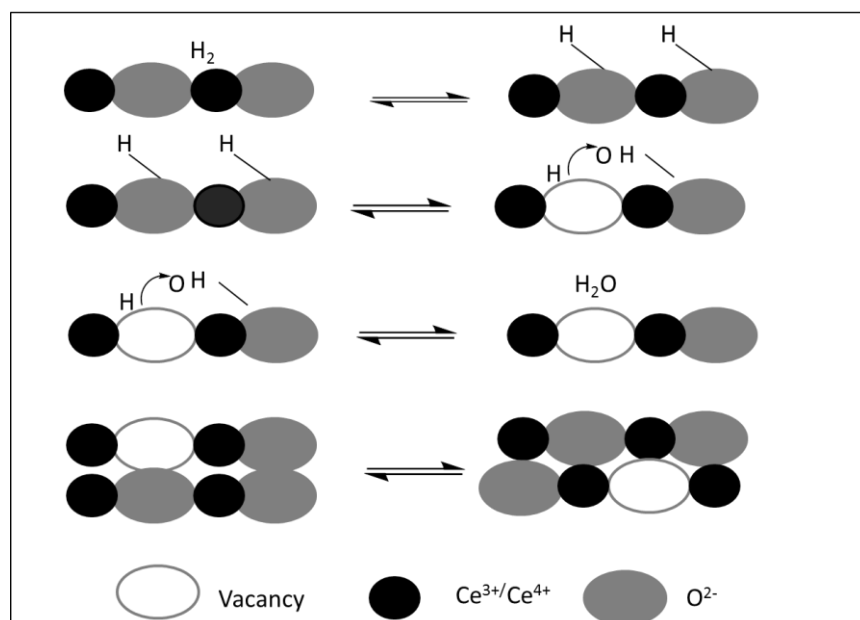


Figure 1.19 Kinetic reduction of CeO_2

The drawback of an oxygen storage source as in the case of pure CeO_2 is its low thermal resistance and poor activity at lower temperatures of the exhaust. The surface area of CeO_2 reduces at temperatures as high as $600-700^\circ C$. The CeO_2 reduction is promoted either by retaining its fluorite structure through noble metal dispersion or by chemically modifying the crystal structure [115-117].

Understanding of the mechanism of oxygen storage has established the fact that increasing the defects, increase in oxygen vacancies and their mobility through the lattice of CeO_2 can help in enhancing the soot oxidation rate. The choice of dopant depends on its ability to substitute one cation with another depending on the dimensions of the guest and host ion and the structure of pure CeO_2 . The method of preparation of these doped mixed oxides also plays a very important role in determining the stability and homogeneity of the solid solution

Several transition metal oxides with CeO_2 are formed, the most common being with Al_2O_3 which is a thermally stable oxide or other oxides such as ZrO_2 , La_2O_3 , SiO_2 , PbO , CuO , MnO_x etc. in solid solutions or as mixed metal oxide phases [118-119]. In the

case of Cu^{2+} and Mn^{2+} the ionic radius is smaller than in CeO_2 which maintain the fluorite structure but form solutions only when in a particular composition range but despite the ionic radius of ZrO_2 (0.84\AA) being smaller than CeO_2 (0.97\AA), it forms solutions very easily and in a larger composition. Zr^{4+} helps in the ease of CeO_2 reduction and thus enhancing the oxygen storage. These features help in conversion of most of the emissions at lower temperatures of the exhaust. The amount of oxygen thermodynamically available at a given temperature relates to the total reduction which is given as the total oxygen storage capacity. The amount of oxygen transferred in a pulse regime while passing the material through a series of reducing and oxidizing cycles gives the oscillations of the exhaust which indicates the specific activity of the material and the kinetics of the redox process [120].

1.5.4.2 Introduction of diffusion barrier concept

This concept was introduced by Morikawa *et al.* which shows that the thermal stability and surface area of $\text{CeO}_2\text{-ZrO}_2$ can be improved by introducing Al_2O_3 . This nanocomposite that they synthesized was termed ACZ. The introduction of Al_2O_3 as shown in figure 1.20 helps to reduce the growth of the $\text{CeO}_2\text{-ZrO}_2$ particles that could sustain interting at higher temperatures of the exhaust by curbing particle growth and indirectly improving the heat resistance and OSC performance of $\text{CeO}_2\text{-ZrO}_2$ [121].

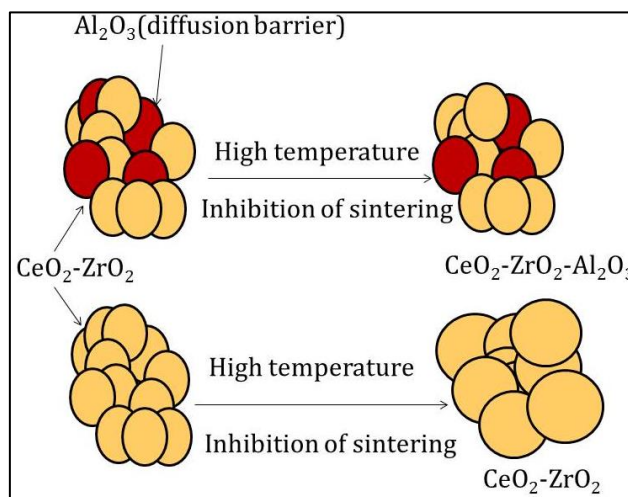


Figure 1.20 Diffusion barrier concept upon introduction of Al_2O_3 [121]

1.5.4.3 Role of alkali and alkaline earth metals as promoters in soot oxidation

The alkali metals are known to enhance the soot combustion activity due to their ability to form carbonate species when reacted with soot. Potassium was amongst the

most widely used alkali metal due to the low melting points of the compounds such as KOH, KNO₃ or its formation of eutectics with other catalytic components that favours a good contact. It is an electron donor and keeps the reducibility and dispersion of transition metals intact. It helps to trap and release the gaseous NO_x involved in soot combustion and they form intermediate carbonate species and provide a route for CO₂ release [122]. This was studied by Liu *et al.*, (2002), Jim'enez *et al.*, (2006) and Wang *et al.*, (2008). Potassium promoted catalysts have been widely studied as in the case of Co, K/MgO catalysts and also the effect of K on perovskites such as La_{1-x}K_xCoO₃ and La_{2x}K_xCu_{0.95}V_{0.05}O₄ [123-124], La_{0.4}Sr_{0.6}MnO₃, La_{0.9}K_{0.1}MnO₃ [125] and spinel-type Cu_{1-x}K_xFe₂O₄ [126] The addition of K and Cs lowered the soot oxidation temperatures [127,128]. Alkali metal nitrates supported on ZrO₂ also proved to be active for particulate matter oxidation [129]. Alkaline earth metals have also been widely investigated but their higher melting points as compared to alkali metals leads to their lower activity. They are quite stable catalysts as shown by Pisarello who studied the activity of 22%Ba/CeO₂ and compared this to 7%K/CeO₂ catalyst [130]. Other alkaline earth metal catalysts include BaCoO₃ perovskites, Co, Ba, K/CeO₂ and K-V with appropriate amounts of alkaline earth metal supported on Al₂O₃ showing the presence of KNO₃, KCaVO₄, Ca₃(VO₄)₂ phases in the case of K-V-Ca catalysts in the molar ratio of 6:1:1 [131].

The mechanism in the case of potassium supported metal oxide catalysts has been observed to be due to the reduction of alkali compounds to the metal state that in turn favours the oxidation of carbon [132,133]. At higher temperatures there could be sublimation and enhancement of mobility of the catalyst that eventually leads to loss of the catalyst [134,135]. These alkali metal salts might also cause damage to the DPF filter wall due to their increased solubility in water and thus exhibit enhanced alkalinity around the DPF wall. For this purpose supports such as K/MgO, potash glass etc. are being used, that have good catalytic activity and stability for potassium catalysts. Thermal treatment on K₂CO₃ impregnated on nano sized sodalite showed enhanced activity at very high temperatures (800°C) [136].

Mechanistic studies involving the role of potassium and other alkali metals in soot oxidation have shown that an oxygen containing species plays an important role in enhancing the activity. Two such mechanisms were put forward, one suggesting a redox mechanism correlated to the redox cycle of CeO₂ where the oxidation -reduction is

related to K_xO_y and K_xO_{y+1} states [137,138]. K_xO_y is oxidized by O_2 to K_xO_{y+1} which then transfers the O_2 to reduced Ce^{3+} to restore Ce^{4+} which can subsequently oxidize the soot.

In the other mechanism, there is a formation of carbonate species formed through a chemisorption of molecular O_2 or an oxygen exchange mechanism in which C-O-AM (AM-Na, K, Rb, Cs) carbon oxygen complexes are formed that are the active sites, which react with the carbon in the soot to form CO_2 and in turn a reduced form is created [139-141]. This gets re-oxidized by molecular oxygen to form C-O-AM. The redox mechanism is true as in the case of redox active supports such as CeO_2 but for inactive supports such as TiO_2 and ZrO_2 , the oxygen exchange mechanism is favourable as this is proven with the help of understanding the CO profiles from TPR profiles of these catalysts showing the formation of carbonates in the reaction [101,142-144].

The order of reactivity based on the efficiency of oxygen transfer from the catalyst to carbon and release of carbon-oxygen complexes is $Cs > Rb \sim K > Na$. In the case of Cs, lower electronegativity shows a stronger electrostatic attraction with surface O_2 which decreases the possibility of agglomeration and favours dissociative chemisorption of the O_2 that occurs readily on Cs, giving a better dispersion. Aging reduced the activity of the catalysts where there is complete loss of metal at higher temperatures and in the presence of water leading to deactivation [145,146]. There could be the formation of volatile compounds in the presence of water that leads to loss of activity. The role of precursors is also vital in understanding the effect of the alkali metal promoter [140]. The hydroxide and carbonate precursors were more efficient ones as compared to the chloride precursors. This was explained by Moulijn and Kapteijn who suggested that there could be a formation of stable salts in the presence of chloride ions due to its strong interaction with alkali metals. The K^+ in the case of KCl interact with Cl^- and since this interaction is a strong one, the interaction of K^+ is not favourable and so there is only a small amount of carbonate species formed as active sites for the reaction.

1.5.5 Silver impregnation on CeO_2 for soot oxidation

The formation of superoxide species using ESR spectroscopy was demonstrated by Machiada *et al.*, who showed that these species helped to increase the soot oxidation activity of CeO_2 [147]. They may follow two pathways - one through the oxidation by reactive super-oxide species that are adsorbed at the three phase boundary between

soot, reduced CeO_2 and the gas phase. The other mechanism follows a reaction between the soot and lattice oxygen at the soot/ CeO_2 interface. Aneggi *et al.* showed that Ag/ZrO_2 was more active as compared to Ag/CeO_2 . This was probably due to the stabilized interface between $\text{Ag}/\text{Ag}_2\text{O}/\text{CeO}_2$ [148].

A new concept consisting of a nanomaterial made of aggregates of CeO_2 particles around Ag metal represented as $\text{CeO}_2\text{-Ag}$ was synthesized using a one pot selective redox reaction using Ce(III) and Ag(I) . This reaction was auto-catalysed by silver metal without the use of any surfactants or organic compounds. This structure is better than core shell materials as the shell tends to decompose into the catalyst metal. The catalysed soot oxidation in this case is favoured by increasing the silver-ceria interface that helps to activate oxygen species and this in turn increases the contact between ceria and the soot. This aids in the oxidation of soot by the facilitation of spill over of active oxygen onto the soot [149-151]. The presence of silver over the ceria also prevents sintering. The ceria aggregate in the centre has rice ball morphology. SEM image of the $\text{CeO}_2\text{-Ag}$ structure shows numerous spherical balls with diameters of $\sim 100\text{nm}$. On taking a cross sectional image using transmission electron microscopy (TEM), one of the balls was analysed separately to show that the silver metal in the centre was surrounded by fine ceria particles. This was termed rice ball morphology as it resembled a popular Japanese food with pressed rice grains around a central filling called “onigiri” as shown in the figure 1.21.

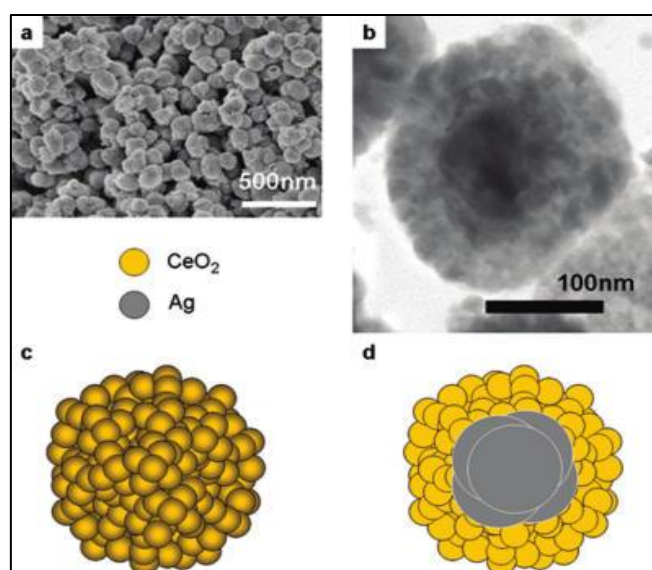


Figure 1.21 Rice ball structure of the Ag@CeO_2 structure [149]

The X-ray diffraction pattern also shows peaks from ceria and silver and the particle sizes for CeO₂ (14nm) and Ag (28nm) predicted from the XRD patterns and TEM matched quite closely. The rice-ball composition is obtained from an equal molar concentration of ceria and silver irrespective of the silver excess on the cerium in the nitrate aqueous solution [152,153]. Ce(OH)₃ and Ag₂O are formed from the co-precipitation of the respective nitrate solutions by an equimolar amount of aqueous NH₃. Alongside these products there is also a formation of [Ag(NH₃)₂]⁺ from Ag₂O due to presence of excess NH₃ at the start of the co-precipitation process. It is the redox between the Ce(OH)₃ and [Ag(NH₃)₂]⁺ that favours this morphology by the formation of Ce(OH)₄ dehydrating to form CeO₂ and Ag.

Ag₂O was the most active among 30 kinds of metal oxides tested under tight contact conditions for the oxidation of soot under the flow of O₂. But was deactivated after the first catalytic run when it was converted to the metallic state. However a loading of 20wt% Ag on CeO₂ showed higher activity and stability as compared to pure CeO₂. Time resolved UV-vis analysis shows that on subjecting the catalyst to repeated reduction and oxidation cycles the Ag enhances the Ce⁴⁺ to Ce³⁺. Aneggi *et al.* have also investigated the potential of silver (Ag⁰) deposited on Al₂O₃, ZrO₂, CeO₂ and SiO₂ for the oxidation of carbon particles in the presence of NO_x and O₂. The activity of Ag on Al₂O₃ and ZrO₂ was better than for CeO₂, with an onset of 500 K for Ag on ZrO₂ and T₅₀ in the range of 600–640 K. This was because the Ag₂O reduction to the Ag⁰ is not rapid and on thermal treatment leads to loss of metal and deactivation at higher temperatures [154]. Thus a combination of these supports as a mixed metal oxide support as in my study could be ideal in synthesizing a stable catalyst capable of oxidizing the soot at lower temperatures.

On using fumed SiO₂ as the support, the activity increases as the surface area is very high (550m²/g) and this favours better contact and more residence time for the soot particles. Thus the differences in relative stabilities of the different oxygen species on the various metal surfaces is due to the differences in electron donating abilities of the metals such as Ag, Cu and Au deposited over SiO₂ for the purpose of diesel soot oxidation. This study was carried out using UV-vis absorption spectroscopy in order to determine the oxidation state of the catalysts. These studies have shown that Ag loaded SiO₂ proved to be good supports as compared to Cu and Au on SiO₂ that were quite inactive for soot oxidation [155].

Ag on SnO₂ catalysts have also shown good activity for soot oxidation. The main factors governing this was their thermal and redox stability which was established as the self-regenerative concept for these catalysts that could provide the stored oxygen to soot particles and later regain original state by getting re-oxidised by gaseous O₂. On thermal aging in air at 1000°C this catalyst was ideal in terms of withstanding the heat treatment and XRD and EXAFS studies showed that due to the presence of Ag-O-Sn bonds at the metal –support interface, there was a resistance to sintering. Also during the redox cycle, upon reduction Ag/SnO₂ formed large Ag₃Sn particles which in the oxidation phase formed metallic Ag. Thus this strong interaction between the Ag and SnO₂ inhibited the sintering at high temperatures [156].

1.5.6 Soot extraction techniques

There are several techniques that have been reported for the extraction of PAHs from soot. These include Soxhlet extraction [157], supercritical fluid extraction [158], microwave assisted extraction [159], ultrasonic assisted extraction [160], accelerated solvent extraction [161], subcritical water extraction [162] etc. The ideal extraction method can be chosen based on several factors such as type of analyse, available equipment and the number of samples to be analysed. The steps post extraction includes a clean-up procedure followed by separation and detection. In my study, Soxhlet extraction, ultrasonic assisted extraction and a crude form of extraction were carried out to analyse the PAHs.

Soxhlet extraction is a very inexpensive method of extraction of PAHs that employs the use of an extraction thimble placed into an extractor fitted to a round bottom flask containing a suitable solvent such as toluene or chloroform/ethanol. The apparatus is heated to a temperature to allow the formation of vapours of the solvent that condense into the extractor thimble containing the soot. Upon reaching a particular level in the extractor the condensate is then automatically siphoned back to the boiling flask. The process is repeated over a span of 16-20hrs, leaving behind the extracts in the end that is then allowed to be evaporated to get rid of the solvent using a rotary evaporator. The extract left behind is analysed by adding about 1ml of acetonitrile to dissolve the extracts in it. This is then analysed using the HPLC and GC-MS.

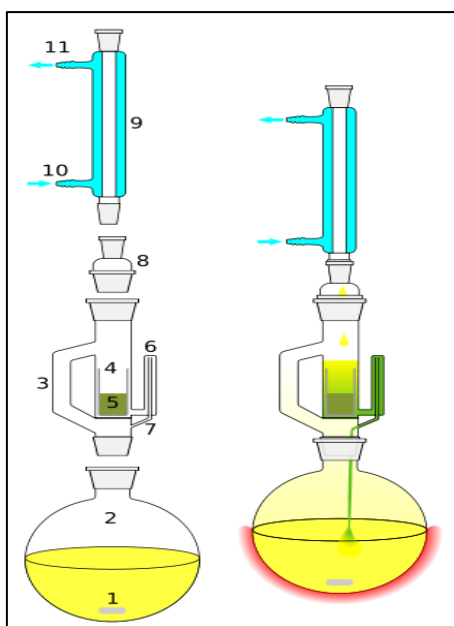


Figure 1.23 Soxhlet extraction [163]

Ultrasonic assisted extraction consisted of the use of acoustic waves with frequencies above 20kHz creating cavitation i.e. formation of very small gas bubbles or cavities in a liquid through a series of compression and expansion. These cavities grow during the low pressure cycle and become compressed during the high pressure cycle [5]. At a certain stage they grow more than they are compressed and they tend to reach a critical size, leading to an implosion that momentarily generates heat and tremendous pressure. This technique allows efficient extraction at faster time periods as compared to the Soxhlet technique. This method was used alongside a crude extraction of soot with a four step solvent extraction. Ultrasonication was done for 15-20 min on the sample of soot along each step. The solvents used were n-heptane, chloroform-ethanol, toluene and methanol, following the same procedure on the same sample of soot with subsequent extractions. Crude extraction was initially carried out on soot using acetone and dichloromethane as preliminary extraction tests for PAHs on soot.

1.5.7 Aims of the project

The project titled 'BAUHAUS' involved a collaboration with Cardiff university, Oxford university and the University of Birmingham, funded by Johnson Matthey, a global speciality chemical company. The aim of this project was to probe the mechanism of soot oxidation in order to try and reduce the toxic and carcinogenic emissions of particulate matter into the atmosphere, through the use of efficient catalyst systems and

filter/ trap regeneration technologies. Thus suitable catalysts have been prepared and optimized for this purpose. A mechanism based on proposed mechanisms in literature and extensive study of the soot under different test conditions has been proposed, considering the complexity of soot.

The study also aims at synthesizing a catalyst suitable as a three way catalyst helping in the oxidation of CO, hydrocarbons and NO_x reduction alongside enhancing the rate of particulate matter (soot) oxidation at lower temperatures in the exhaust. An optimised Ag-K/CeO₂-ZrO₂-Al₂O₃ catalyst was synthesised, characterised and tested for soot oxidation under both tight and loose contact conditions. Several other catalysts were studied to try and understand the effect of Ag and K impregnation on CeO₂ based catalysts. The various physical properties of these catalysts were also analysed using several analytical techniques in order to optimise the catalyst preparation.

An in-depth study on the effect of various oxidants such as NO₂, CO and diesel exhaust feed, on the oxidation of soot, in the presence of the catalyst was carried out. Catalysed soot oxidation under an O₂ atmosphere, quantifying the amount of primary products-CO₂ and CO was carried out alongside estimating the rate of the reaction.

The study also focussed on the oxidation of the adsorbed hydrocarbons on carbonaceous soot particles. Extraction of soot was carried out to identify the various aromatics present and these were quantified using HPLC. The fate of these aromatics upon oxidation were analysed by trapping them in acetone, followed by identification and quantification using HPLC. The aims of this project have been successfully achieved to a large extent in establishing the mechanism of soot combustion.

REFERENCES

1. G. C. Bond, *Heterogeneous catalysis - principles and applications*, second edition, Oxford, **1987**
2. M. Beller, A. Renken, R. A. Santen, *Catalysis from principles to applications*, Wiley-VCH Verlag and Co, Germany, **2012**
3. G. C. Bond, *Principles of Catalysis*, Monographs for teachers, The Royal Institute of Chemistry, **1963**
4. P. Bera, M. S. Hegde, *Journal of the Indian Institute of Science*, 90:2, (**2010**), 299-325
5. J. P. A. Neeft, M. Makkee, J. A. Moulijn, *Fuel Processing Technology*, 47, (**1996**), 1-69

6. R. Prasad, V. R. Bella, *Bulletin of Chemical Reaction Engineering & Catalysis*, 5 (2), (2010), 69 – 86
7. B. A. A. L. van Setten, M. Makkee, J. A. Moulijn, *Catalysis Reviews*, 43(4), (2001), 489–564
8. A. Christensen, *Polycyclic aromatic hydrocarbons in exhaust emissions from mobile sources-Sampling and Determination*, Ph.D. Thesis, Department of Analytical Chemistry, Stockholm University, 2003
9. G. A. Stratakis, *Experimental investigation of catalytic soot oxidation and pressure drop characteristics in wall flow diesel particulate filters*, Ph.D. Thesis, University of Thessaly, 2004
10. D. B. F. Watts, *Review of diesel particulate matter sampling methods, Final report*, Department of Mechanical Engineering, University of Minnesota, Minneapolis, 1999
11. G. H. Schnakenberg, A. D. Bugarski, U.S. Department of health and human services, Public Health Service, National Institute for Occupational Safety and Health(NIOSH), Pittsburgh, *Information Circular*, 9462, (1992), 1-58.
12. M. M. Maricq, *Aerosol Science*, 38, (2007), 1079-1118
13. R. O. McClellan, *Toxicology*, 181-182, (2002), 329-347
14. G. L. Squadrito, R. Cueto, B. Dellinger, W. A. Pryor, *Free Radical Biology and. Medicine*. 31 : 1132-8, 2001
15. M. Sehlstedt, B. Forsberg, R. Westerholm, C. Boman, T. Sandström, *The role of particle size and chemical composition for health risks of exposure to traffic related aerosols - A review of the current literature*, Swedish Road Administration, 2007.
16. J. Pagan, *Study of particle size distributions emitted by diesel engine*, SAE technical paper, US EPA, 1999-01-1141, 1999
17. D. B. Kittelson, *Journal of Aerosol Science*, 29, (1998), 575–588.
18. R. O. McClellan, *Annual Review of Pharmacology and Toxicology*, 27, 198927, (1987), 279-300
19. J. H. Seinfeld, *Air pollution: Physical and chemical fundamentals*, McGraw-Hill, Inc., New York. 1975
20. J. Kagawa, *Toxicology*, 181-182, (2002), 349-353
21. A. C. Lloyd, T. A. Cackette, *Journal of the Air & Waste Management Association*, 51(6), (2001), 809-847

22. E. L. Avol, W. J. Gauderman, S. M. Tan, S. J. London, J. M. Peters, *American Journal of Respiratory and Critical Care Medicine*, 164, (**2001**), 2067-2072.
23. D. Schwela, *Toxicology Letters*, 86, (**1996**), 131-142
24. C. A. Pope, R. T. Burnett, M. J. Thun, E. E. Calle, D. Krewski, K. Ito, G. D. Thurston, *Journal of the American Medical Association*, 287(9), (**2002**), 1132-1141
25. P. Pagano, T. De Zaiacomo, E. Scarcella, S. Bruni, M. Calamosca, *Environmental Science and Technology*, 30(12), (**1996**), 3512-3516
26. G. Oberdörster, R. Gelein, J. Ferin, B. Weiss, *Inhalation Toxicology*, 7 (1), (**1995**), 111-124
27. J. S. Johnson, S. T. Bagley, L. D. Gratz, D. G. Leddy, A review of diesel particulate control technologies and emissions effects-1992 Homing Memorial Award lecture, *SAE Paper No. 940233*, **1994**
28. T. S. Totton, A. J. Misquitta, M. Kraft, *Physical Chemistry Chemical Physics*, 14, (**2012**), 4081-4094
29. J. P. Cain, P. L. Gassman, H. Wang, A. Laskin, *Physical Chemistry Chemical Physics*, 12, (**2010**)5206-5218
30. H. Wang, *Proceedings of the Combustion Institute*, 33, (**2011**), 41-67
31. G. W. Smith, *Kinetic aspects of diesel soot coagulation*, *SAE Paper No. 820466*, **1982**
32. O. I. Smith, *Progress in Energy and Combustion Science*, 7(4), (**1981**), 275-291
33. F. Takahashi, I. Glassman, *Combustion Science and Technology*, 37(1), (**1984**), 1-19
34. S. J. Harris, A. M. Weiner, *Combustion Science and Technology*, 38, (**1984**), 75.
35. J. O. Allen, *Atmospheric Partitioning of Polycyclic Aromatic Hydrocarbons (PAH) and Oxygenated PAH*, *Ph.D. Thesis*, Department of Chemical Engineering, Massachusetts Institute of Technology, **1999**
36. M. Strandell, S. Zakrisson, T. Alsberg, R. Westerholm, L. Winquist, U. Rannug, *Environmental Health Perspectives*, 102, (**1994**), 85-92,
37. T. Spitzer, T. Takeuchi, *Journal of Chromatography A*, 710, (**1995**), 109-116
38. T. Alsberg, U. Stenberg, *Chemosphere*, 8(7), (**1979**), 487-496
39. D. R. Choudhury, *Environmental Science and Technology*, 16, (**1982**), 102-106
40. T. Ramdahl, *Environmental Science and Technology*, 17, (**1983**), 666-670,
41. J. König, E. Balfanz, W. Funcke, T. Romanowski, *Analytical Chemistry*, 55, (**1983**), 599-603

42. M. P. Ligocki, J. F. Pankow, *Environmental Science and Technology*, 23(1), (1989), 75–83
43. S. B. Hawthorne, D. J. Miller, J. J. Langenfeld, M. S. Krieger, *Environmental Science and Technology*, 26(11), (1992), 2251–2262
44. P. Haglund, *Isolation and Determination Methods for Halogenated Polycyclic Aromatic Compounds*, Ph.D. Thesis, Department of Analytical Chemistry, Stockholm University, Stockholm, Sweden, **1991**
45. C. Bergvall, *Methods for Determination of Benzo(a)pyrene and High Molecular Weight (>300 Da) Polycyclic Aromatic Hydrocarbons in Particulate Matter from Ambient Air and Vehicle Exhausts*, Ph.D. Thesis, Department of Analytical Chemistry, Stockholm University, Sweden, **2009**
46. M. L. Lee, M. V. Novotny, K. D. Bartle. *Analytical chemistry of polycyclic aromatic compounds*. Academic Press, New York, **1981**.
47. K. Goss, R. P. Schwarzenbach, *Environmental Science and Technology*, 32, (1998), 2025-2032.
48. S. O. Baek, R. A. Field, M. E. Goldstone, P. W. W. Kirk, J. N. Lester, R. Perry Water, *Air and Soil. Pollution*, 60, (1991), 279-300
49. IARC Working Group on the Evaluation of the Carcinogenic Risk of Chemicals to Humans. *Polynuclear Aromatic Compounds, Part 1: Chemical, Environmental and Experimental Data*, volume 32 of *IARC Monographs on the Evaluation of the Carcinogenic Risk of Chemicals to Humans*, International Agency for Research on Cancer, Lyon, France, **1983**
50. IARC Working Group on the Evaluation of the Carcinogenic Risk of Chemicals to Humans. *Polynuclear Aromatic Compounds, Part 2: Carbon Blacks, Mineral Oils (Lubricant Base Oils and Derived Products) and Some Nitroarenes*, volume 33 of *IARC Monographs on the Evaluation of the Carcinogenic Risk of Chemicals to Humans*. International Agency for Research on Cancer, Lyon, France, **1984**
51. IARC Working Group on the Evaluation of the Carcinogenic Risk of Chemicals to Humans. *Polynuclear Aromatic Compounds, Part 3: Industrial Exposures in Aluminium Production, Coal Gasification, Coke Production and Iron and Steel Founding*, volume 34 of *IARC Monographs on the Evaluation of the Carcinogenic Risk of Chemicals to Humans*. International Agency for Research on Cancer, Lyon, France, **1984**

52. P. Pott, *Chirurgical Observations*, (1775) Reproduced in Journal of National Cancer Institute Monograph, (1963), 7-13
53. R. von Volkman, *Beiträge Zur Chirurgie.*, Leipzig, Germany, 1875
54. J. Bell, *Edinburgh Medical Journal*. 22, (1876), 135-137
55. J. W. Cook, C. L. Hewett, I. Hieger, *Journal of Chemical Society*, (1933), 395.
56. E. L. Kennaway, I. Hieger Carcinogenic substances and their fluorescence spectra. *British Medical Journal*, 1, (1930), 1044-1046
57. E. L. Kennaway, Further experiments on cancer-producing substances. *Biochemical Journal*, 24, (1930), 497-504
58. J. W. Cook, C. L. Hewett, I. Hieger, *Journal of Chemical Society*, (1933), 396-398
59. K. Straif, R. Baan, Y. Grosse, B. Secretan, G. F. El, V. Cogliano, *Lancet Oncology*, 6, (2005), 931-932,
60. US HHS. *Report on carcinogens, eleventh edition*, U.S. Department of Health and Human Services, Public Health Service, National Toxicology Program, <http://ntp.niehs.nih.gov/index.cfm?objectid=32BA9724F1F6>, 2009.
61. J. Jacob, *Polycyclic Aromatic Compounds*, 28, (2008), 242-272
62. J. L. Durant, A. L. Lafleur, E. F. Plummer, K. Taghizadeh, W. F. Busby, W. G. Thilly. *Environmental Science Technology*, 32, (1998), 1894-1906
63. <http://www.dieselnet.com/standards/eu/ld.php> accessed in February 2008.
64. Federal register, Protection of Environment, Code of Federal Regulations, part 81-89, 1986
65. H. S. Gandhi, G. W. Graham, R. W. McCabe, *Journal of Catalysis*, 216 (2003) 433-442
66. M. Shelef, K. Otto, N. C. Otto, *Advances in Catalysis*, 27 (1978) 311-365
67. J. T. Kummer, *Progress in Energy and Combustion Science*, 6 (1980) 177
68. K. C. Taylor, *Catalysis Reviews, Science and Engineering*, 35 (1993) 457-481
69. R. M. Heck, R. J. Farrauto, *Catalytic Air Pollution Control: Commercial Technology*, Van Nostrand Reinhold, 1995
70. A. Russell, W. S. Epling, *Catalysis Reviews, Science and Engineering*, 53, (2011), 337-423
71. T. Kuki, Y. Miyairi, Y. Kasai, M. Miyazaki, S. Miwa, Study on Reliability of Wall-Flow-Type Diesel Particulate Filter. *SAE, 2004-01-0959*, (2004)
72. K. Ohno, N. Taoka, T. Furuta, A. Kudo, T. Komori, Characterization of High Porosity SiC-DPF. *SAE, 2002-01-0325*, (2002)

73. A. M. Stamatelos, *Energy and Commerce Management*, 38, (1997), 83-99.
74. A. P. Walker, *Topics in Catalysis*, 28, (2004), 165-170.
75. G. Hu^othwohl, F. Pischinger, G. Lepperhoff, Self-Supporting Regeneration of Diesel Particulate Traps. SAE paper 870017, 1987
76. N. Higuchi, S. Mochida, M. Kojima, Optimized Regeneration Conditions of Ceramic Honeycomb Diesel Particulate Filters. SAE paper 830078, 1983
77. N. R. Laine, F. J. Vastola, P. L. Walker, *Journal of Physical Chemistry*, 67, (1963), 2030–2034
78. J. P. A. Neeft, T. X. Nijhuis, E. Smakman, M. Makkee, J. A. Moulijn, *Fuel*, 76, (1997), 1129–1136
79. S. G. Chen, R. T. Yang, F. Kapteijn, J. A. Moulijn, *Industrial and Engineering Chemistry Research*, 32, (1993), 2835–2840
80. F. Kapteijn, R. Meijer, J.A. Moulijn, D. Cazorla-Amoro, *Carbon*, 32, (1994), 1223–1231.
81. B. J. Cooper, J. E. Thoss, Role of NO in Diesel Particulate Emission Control, *SAE Paper* 890404, 1989
82. G. Neri, L. Bonaccorsi, A. Donato, C. Milone, M. G. Musolino, A. M. Visco, *Applied Catalysis. B*, 11, (1997), 217-231
83. B. J. Cooper, H. J. Jung, Treatment of diesel exhaust gases, Thoss JE US 4902487, 1990.
84. Z. Dang, Y. Huang, A. Bar-Ilan, Oxidation catalyst on a substrate utilized for the purification of exhaust gases. US 2006/0211569 A1, 2006
85. J. O. Uchisawa, A. Obuchi, R. Enomoto, J. Xu, T. Nanba, S. Liu, S. Kushiyaama, *Applied Catalysis B*, 32, (2001), 257-268
86. M. R. Kim, D. H. Kim, S. I. Woo, , *Applied Catalysis B*, 45, 269-279, 2003
87. S. Liu, A. Obuchi, J. Oi-Uchisawa, T. Nanba, S. Kushiyaama, 2001. *Applied Catalysis B*, 30, (2001), 259-265.
88. B. P. Tarasov, V. E. Muradyan, Y.M. Shul'ga, E. P. Krinichnaya, N. S. Kuyunko, O. N. Efimov, E. D. Obraztsova, D. V. Schur, J. P. Maehlen, V. A. Yartys, H. J. Lai, *Carbon*, 41, (2003), 1357-1364
89. W. F. Shangguan, Y. Teraoka, S. Kagawa, *Applied Catalysis B*, 16, (1998), 149-154
90. N. Nejar, J. M. Garcia-Cortes, C. Salinas-Martínez de Lecea, M. J. Illa'n-Gomez, *Catalysis Communications*, 6, (2005), 263-267,

91. V. G. Milt, C. A. Querini, E. E. Miro, M. A. Ulla, *Journal of Catalysis*, 220, (2003), 424-432
92. P. Bera, S. T. Aruna, K. C. Patil, M. S. Hegde, *Journal of Catalysis*. 186, (1999), 36-44.
93. P. Ciambelli, V. Palma, P. Russo, S. Vaccaro, J. Mol, *Applied Catalysis A*, 204, (2003), 673
94. G. Neri, G. Rizzo, L. Bonaccorsi, C. Milone, S. Galvagno, *Catalysis Today* 100, (2005) 309-313
95. Y. Watabe, C. Yamada, K. Irako, Y. Murakami, Application of catalytic materials for diesel exhaust emission control. *European Patent* 0092023, (1983)
96. P. Ciambelli, V. Palma, P. Russo, S. Vaccaro, *Applied Catalysis B*, 22, (1999), L5-L10, 132
97. G. Mul, F. Kapteijn, J. A. Moulijn, Catalytic oxidation of model soot by metal chlorides. *Applied Catalysis B*, 12, (1997), 33-47
98. C. A. Querini, M. A. Ulla, F. Requejo, J. Soria, U. A. Sedra'n, E. E. Miro', *Applied Catalysis B* 15, (1998), 5-19.
99. C. Badini, G. Saracco, V. Specchia, *Catalysis Letters*, 55, (1998), 201-206
100. R. E. Marinangeli, E. H. Homeier, F. S. Molinaro, *Catalysis and Automotive Pollution Control, Elsevier*, 30, (1987), 457-467.
101. Y. Watabe, K. Irako, T. Miyajima, T. Yoshimoto, Y. Murakami, "Trapless trap"-a catalytic combustion system of diesel particulates using ceramic foam, SAE Paper No. 830082, 1983
102. Z. Li, M. Meng, Q. Li, Y. Xie, T. Hu, J. Zhang, *Chemical Engineering Journal* 164, (2010), 98-105
103. F. J. Long, K. W. Sykes, *Journal of Chemical Physics*, 47, (1950), 361-378.
104. B. Neumann, C. Kro'ger, E. Fingas, D.W Kohlenstoffmitaktivierenden, *Anorgan. Allgemeine Chem.* 197, (1931), 321- 338.
105. D. W. McKee, *Carbon*, 25, (1987), 587-588
106. E. Aneggi, C. de Leitenburg, G. Dolcetti, A. Trovarelli, *Catalysis Today* 136 (2008) 3-10
107. Q. Yua, L. Liua, L. Donga, D. Lia, B. Liua , F. Gaob, K. Sunc, L. Donga, Y. Chena, *Applied Catalysis B: Environmental*, 96 (2010) 350-360
108. A. Trovarelli, C. de Leitenburg, M. Boaro, G. Dolcetti, *Catalysis Today*, 50 (1999) 353-367

109. M. Ricken, J. Nörlting, I. Riess, *Journal of Solid State Chemistry*, 54 (1984) 89
110. J. Zhang, Z. C. Kang, L. Eyring, *Journal of Alloys and compounds*, 192 (1993) 57
111. A. Laachir, V. Perrichon, A. Badri, J. Lamotte, E. Catherine, J. C. Lavalley, J. E. Fallah, L. Hilaire, F. Le Normand, E. Quéméré G. N. Sauvion, O. Touret, *Journal of the Chemical Society, Faraday Transactions*, 87, (1991), 1601 -1609
112. A. Badri, J. Lamotte, J. C. Lavalley, A. Laachir, V. Perrichon, O. Touret, G. N. Sauvion, E. Quemere, *European Journal of Solid State and Inorganic Chemistry*, 28, (1991), 445
113. A. Trovarelli, *Catalysis Reviews: Science and Engineering*, 38 (4), (1996), 439-520
114. J. E. Fallah, S. Boujana, H. Dexpert, A. Kiennemann, J. Majerus, O. Touret, F. Villain, F. Le Normand, *Journal of Physical Chemistry*, 98, (1994), 5522-5533
115. P. Fornasiero, R. Di Monte, G. R. Rao, J. Kaspar, S. Meriani, A. Trovarelli, and M. Graziani, *Journal of Catalysis*, 151, (1995), 168-177
116. B. K. Cho, *Journal of Catalysis*, 131, (1991), 74-87
117. P. Vidmar, P. Fornasiero, J. Kaspar, G. Gubitosa, M. Graziani, *Journal of Catalysis*, 171,(1990),160
118. M. Yashima, H. Arashi, M. Kakihana, M. Yoshimura, *Journal of the American Ceramic Society*, 77, (1994), 1067-1071
119. Y. Zhang, A. Andersson, M. Muhammed, *Applied Catalysis B Environmental*, 6, (1995), 325-337
120. M. Boaro, C. deLeitenburg, G. Dolcetti, A. Trovarelli, *Journal of Catalysis*, 193, (2004), 338-347
121. T. Kanazawa, J. Suzuki, T. Takada, T. Suzuki, A. Morikawa, A. Suda, H. Sobukawa, M. Sugiura, *SAE Paper No. 2003-01-0811* (2003).
122. D. Weng, J. Li, X. Wu, Zhichun Si, *Journal of Catalysis*, 271 (1), (2010), 43-51
123. L. Sui, L. Yu, Y. Zhang, *Journal of Dispersion Science and Technology*, 28 (4), (2007), 607-612
124. Y. Teraoka, K. Nakano, W. F. Shangguan, S. Kagawa, *Catalysis Today*, 27, (1996), 107-113.
125. Y. Teraoka, K. Nakano, S. Kagawa, and W. F. Shangguan, *Applied Catalysis B, Environmental*, 5, (1998), L181-L185.
126. W. F. Shangguan, Y. Teraoka, S. Kagawa, *Applied Catalysis B Environmental*, 16, (1998) 149-154.

127. G. Neri, G. Rizzo, S. Galvagno, A. Donato, M. G. Musolino, R. Pietropaolo, *Applied Catalysis B Environmental*, 42, (2003), 381–391.
128. H. M. An, C. Kilroy, P. J. McGinn, *Catalysis Today*, 98, (2004) 423–429.
129. N. F. Galdeano, A. L. Carrascull, M. I. Ponzi, I. D. Lick, E. N. Ponzi, *Thermochimica Acta*, 421, (2004) 117–121
130. M. L. Pisarello, V. Milt, M. A. Peralta, C. A. Querini, E. E Miro', *Catalysis Today*, 75, (2002) 465–470.
131. L. Sui, L. Yu, Y. Zhang, *Journal of Dispersion Science and Technology*, 28 (4), (2007), 607-612
132. D. W. McKee, *Fuel*, 62, (1983), 170–175.
133. C. Janiak, R. Hoffmann, P. Sjoval, B. Kasemo, *Langmuir*, 9, (1993), 3427–3440
134. H. An, J. P. McGinn, *Applied Catalysis B*, 62, (2006), 46–56.
135. J. M. Saber, J. L. Falconer, L. F. Brown, *Fuel*, 65, (1986), 1356–1359.
136. R. Kimura, S. P. Elangovan, M. Ogura, H. Ushiyama, T. Okubo, *Journal of Physical Chemistry C*, 115 (30), (2011), 14892–14898
137. Z. H. Zhu, G. Q. Lu, *Journal of Catalysis*, 197, (1999), 262.
138. Z. H. Zhu, G. Q. Lu, R. T. Yang, *Journal of Catalysis*, 192, (2000), 77-87
139. M. B. Cerfontain, R. Meijer, F. Kapteijn, J. A. Moulijn, *Journal of Catalysis*, 107, (1987), 173.
140. G. Chen, R. T. Yang, *Journal of Catalysis*, 141, (1993), 102.
141. G. Mul, F. Kapteijn, J. A. Moulijn, *Carbon* 37 (1999) 401.
142. S. J. Yuh, E. E. Wolf, *Fuel*, 63, (1984), 1604.
143. S. J. Yuh, E. E. Wolf, *Fuel* 62 (1983) 252.
144. J. P. A. Neeft, M. Makkee, J. A. Moulijn, *Applied Catalysis B Environmental*, 8, (1996), 57-78
145. R. J. Lang, *Fuel* 65 (1986) 1324
146. J. A. Moulijn, F. Kapteijn, *Carbon*, 33 (1995) 1155.
147. M. Machida, Y. Murata, K. Kishikawa, D. Zhang, K. Ikeue, *Chemistry of Materials*, 20, (2008), 4489-4494
148. K. Shimizua, H. Kawachia, S. Komaib, K. Yoshidac, Y. Sasaki, A. Satsuma, *Catalysis Today*, 175 (2011) 93–99
149. T. Kayama, K. Yamazaki, H. Shinjoh, *Journal American Chemistry Society*, 132 (38), (2010), 13154–13155

150. K. Krishna, A. Bueno-Lo'pez, M. Makkee, J. A. Moulijn, *Applied Catalysis B*, 75, (2007), 189–200.
151. L. Pesant, J. Matta, F. Garin, M. J. Ledoux, P. Bernhardt, C. Pham, C. Pham-Huu, *Applied Catalysis A*, 266, (2004), 21–27
152. I. Pastoriza-Santos, D. S. Koktysh, A. A. Mamedov, M. Giersig, N. A. Kotov, L. M. Liz-Marza'n, *Langmuir*, 16, (2000), 2731–2735.
153. C. M. Y. Yeung, K. M. K. Yu, Q. J. Fu, D. Thompsett, M. I. Petch, S. C. Tsang, *Journal American Chemistry Society*, 127, (2005), 18010–18011.
154. E. Aneghi, J. Llorca b, C. de Leitenburg, G. Dolcetti, A. Trovarelli, *Applied Catalysis B: Environmental*, 91, (2009), 489–498
155. G. Corro, U. Pal, E. Ayala , E. Vidal, E. Guilleminot , *Topics in Catalysis*, 56, (2013), 467–472
156. K. Shimizua, M. Katagirib, S. Satokawac, A. Satsumab, *Applied Catalysis B: Environmental*, 108–109 (2011) 39–46
157. D. Bodzek, K. Luks-Betlej, L. Warzecha, *Atmospheric Environment, Part A: General Topics*, 27(5), (1993), 759-64.
158. T. Paschke, S. B. Hawthorne, D. J. Miller, B. Wenclawiak, *Journal of Chromatography A*, 609(1-2), (1992), 333-340
159. K. K. Chee, M. K. Wong, H. K. Lee, *Environmental Monitoring and Assessment*, 44(1-3), (1997), 391-403
160. C. H. Marvin, L. Allan, B. E. McCarry, D. W. Bryant, *International Journal of Environmental Analytical Chemistry*, 49(4), (1992), 221-30.
161. B. E. Richter, B. A. Jones, J. L. Ezzell, N. L. Porter, N. Avdalovic, C. Pohl, *Analytical Chemistry*, 68, (1996), 1033-1039.
162. S. B. Hawthorne, C. B. Grabanski, E. Martin, D. J. Miller, *Journal of Chromatography A*, 892(2), (2000), 421- 433.

Chapter 2

Experimental

2.1 Introduction

This chapter contains the detailed preparation of supported and unsupported mixed metal oxide catalysts and description of equipment used for the purpose of characterisation and testing of these catalysts. Mixed metal oxides are used as the supports in three way catalysts, because they have the potential to store oxygen in the lattice and undergo reduction to release the stored oxygen under oxygen-lean conditions in the exhaust. This property is referred to as their oxygen storage capacity (OSC). Mixed-metal oxides catalysts can therefore be expected to oxidize diesel soot due to this property.

2.2 Catalyst Preparation- Mixed metal oxide

The main methods of syntheses of mixed metal oxides include co-precipitation and wet impregnation. A simple wetness impregnation method was used for metal supported oxides. Chemicals used in the preparation are listed in the table below.

Table 2.1 Precursors used in the preparation of mixed metal oxides and impregnated metal oxides

Sl. No	Precursor	Source and purity
1.	ammonium cerium(IV) nitrate- $(\text{NH}_4)_2\text{Ce}(\text{NO}_3)_6$	Sigma Aldrich, ACS reagent, $\geq 98.5\%$
2.	zirconium(IV) oxynitrate hydrate- $\text{ZrO}(\text{NO}_3)_2 \cdot x\text{H}_2\text{O}$	Aldrich, 99%
3.	aluminium nitrate nonahydrate - $\text{Al}(\text{NO}_3)_3 \cdot 9\text{H}_2\text{O}$	Sigma Aldrich, ACS reagent, $\geq 98\%$
4.	silver nitrate - AgNO_3	Aldrich, 99.99%
5.	potassium carbonate - K_2CO_3	Fischer Scientific, 99+%, ACS reagent
6.	potassium nitrate - KNO_3	Alfa Aesar, 99%
7.	potassium hydroxide - KOH	Aldrich chemical, 99.99%

8.	potassium chloride –KCl	Sigma Aldrich, 99%, ACS reagent
9.	sodium carbonate – Na ₂ CO ₃	Alfa Aesar, anhydrous, 99.5% ACS
10.	sodium hydroxide –NaOH	Sigma Aldrich, ≥97% pellets
11.	ammonium hydroxide –NH ₃	Fischer Scientific, 35%, analytical reagent grade
12.	urea - CO(NH ₂) ₂	Aldrich, ACS reagent, 99–100.5%,
13.	caesium nitrate – CsNO ₃	Alfa Aesar, 99.8% trace metal basis
14.	sodium nitrate- NaNO ₃	Fischer Scientific, lab reagent grade
15.	barium nitrate – Ba(NO ₃) ₂	Fischer Scientific, analytical reagent grade
16.	magnesium nitrate – Mg(NO ₃) ₂ .6H ₂ O	Sigma Aldrich, 99.9%, trace metal basis
17.	calcium nitrate – Ca(NO ₃) ₂ . 4H ₂ O	Aldrich, ACS reagent, 99%
18.	platinum acetylacetonate Pt (acac) ₂	Aldrich, 99.9% trace metal basis,

2.2.1 Catalyst support preparation – Wet impregnation

The catalyst supports (Ce_xZr_{0.5-x}Al_{0.5}O_{1.75} where x lies between 0.05 and 0.45) with different ratios (atomic %) of Ce:Zr-1:9, 3:7, 5:5, 7:3, 9:1 were prepared by a direct wet impregnation of Al₂O₃ using ammonium cerium (IV) nitrate and zirconyl nitrate hydrate mixed solutions (proportions were dependent on the desired Ce:Zr ratio) at 80°C in a beaker. The resulting slurry was then allowed to dry in an oven overnight at 110°C, before calcination at 500°C for 5 hours (following a heating ramp at a rate of 5°C min⁻¹) under flowing air. The calcined samples were crushed to fine powder to obtain the supports [1, 2, 3]. The preparation was usually made on a 3g batch basis. The following supports were prepared in the above manner:

- Ce_{0.05}Zr_{0.45}Al_{0.5}O_{1.75}- Ce:Zr-1:9
- Ce_{0.15}Zr_{0.35}Al_{0.5}O_{1.75}- Ce:Zr-3:7
- Ce_{0.25}Zr_{0.25}Al_{0.5}O_{1.75}- Ce:Zr-5:5
- Ce_{0.35}Zr_{0.15}Al_{0.5}O_{1.75}- Ce:Zr-7:3
- Ce_{0.45}Zr_{0.05}Al_{0.5}O_{1.75}- Ce:Zr-9:1

2.2.2 Catalyst support preparation- Co-precipitation using Na₂CO₃, NH₄OH, NaOH

The desired quantities (3g support) of aqueous 0.25M solutions of ammonium cerium (IV) nitrate (5.52g), zirconyl nitrate hydrate (0.99g) and aluminium nitrate

nonahydrate (1.79g) were mixed together (100ml water). The pH of the solution (<1) was measured before the solution was heated to 80°C. Then the precipitating agent (0.5M Na₂CO₃/NH₄OH /NaOH) was slowly added drop wise with continuous addition of the warm precursor solution containing the metal salt solution, while the pH was maintained at 9 [4,5,6]. The resulting suspension was aged at 80°C for 1 hour and then allowed to cool. The precipitate was filtered, washed with deionised water 3-4 times and dried in an oven at 110°C. Finally the dried precursor was calcined under an atmosphere of flowing air, by heating to 500°C at 5°C min⁻¹ and dwelling at the maximum temperature for 5 hours. The preparation was usually made on a 3g batch basis.

2.2.2.1 Catalyst support preparation - Co-precipitation using urea

The appropriate amounts of aqueous ammonium cerium (IV) nitrate (5.52g), zirconyl nitrate hydrate (0.99g), aluminium nitrate nonahydrate (1.79g) and urea (40g) in distilled water (200ml) were aged by stirring in a round-bottomed flask for 24h at 120°C [7]. The resulting slurry was filtered, washed with deionised water and dried at 110°C overnight. This was followed by calcination under flowing air, by heating to 500°C at 5°Cmin⁻¹ and dwelling at the maximum temperature for 5 hours.

2.2.3 Catalyst support preparation - Co-precipitation using Na₂CO₃ -Varying method of preparation

The co-precipitation of Ce_xZr_{1-x}Al_{0.5}O_{1.75} with Na₂CO₃ was carried out in several ways. In the first case, the precursor solutions for all the three metal salts were mixed together, before forming the co-precipitate by adding aqueous Na₂CO₃, as described above. In the second method, the precursors for ceria and zirconia were mixed together and precipitated using the base, while Al₂O₃ was separately precipitated, before the two suspensions were thoroughly mixed together, dried at 110°C and calcined under the conditions mentioned above. The third method consists of mixing the dried precursors of CeO₂-ZrO₂ with the dried precursor of Al₂O₃ and calcining the mixture as above. The last method consists of physically mixing the CeO₂-ZrO₂ calcined powder with the calcined Al₂O₃ powder [2].

2.2.4 Silver supported catalysts

The silver supported $\text{CeO}_2\text{-ZrO}_2\text{-Al}_2\text{O}_3$ catalysts were prepared in two ways:

1. Impregnating an AgNO_3 solution (1% - 0.0157g, 2% - 0.0314g and 5wt%Ag- 0.0787g for a 1 g catalyst preparation) onto the support (CZA- Ce:Zr-7:3 -prepared by alumina impregnation on $\text{CeO}_2\text{-ZrO}_2$ precursor solution) [8], at 80°C under constant magnetic stirring, until a viscous suspension remained. This was then dried at 110°C and calcined at 500°C under flowing air, by heating to 500°C at 5°Cmin⁻¹ and dwelling at the maximum temperature for 5 hours.
2. AgNO_3 solution (2wt %) was mixed with the $\text{CeO}_2\text{-ZrO}_2\text{-Al}_2\text{O}_3$ (Ce: Zr-7:3) precursor solution before adding the precipitant (aq Na_2CO_3). The precipitate was isolated, dried at 110°C and then calcined under the same conditions as described above.

2.2.5 Alkali and Alkaline earth metal supported $\text{CeO}_2\text{-ZrO}_2\text{-Al}_2\text{O}_3$ samples

2.2.5.1 Different potassium salts- KOH, K_2CO_3 , KNO_3 , KCl

The appropriate quantities of the different potassium salt solutions mentioned above (10wt% K loading) were impregnated onto CeO_2 , $\text{CeO}_2\text{-ZrO}_2$, $\text{CeO}_2\text{-ZrO}_2\text{-Al}_2\text{O}_3$, $\text{CeO}_2\text{-Al}_2\text{O}_3$, Al_2O_3 (prepared by co-precipitation using Na_2CO_3) by the direct wet impregnation method, dried at 110°C and calcined at 500°C at 5°Cmin⁻¹ and dwelling at the maximum temperature for 5 hours under flowing air [9].

2.2.5.2 Varying the weight loading of potassium on $\text{CeO}_2\text{-ZrO}_2\text{-Al}_2\text{O}_3$

K_2CO_3 (2%-0.06g, 5%-0.17g, 10%-0.35g, 50wt%-1.76g) was impregnated on $\text{CeO}_2\text{-ZrO}_2\text{-Al}_2\text{O}_3$ (0.5-1g), CZA-prepared by co-precipitation using Na_2CO_3) by the direct wet impregnation method as described above, dried at 110°C and calcined at 500°C as mentioned above [9].

2.2.5.3 Comparison of alkali and alkaline earth metals

Various alkali metals such as Cs (0.14g), Na(0.36g), K (0.25g) and alkaline earth metals such as Ba (0.19g), Ca (0.4g) and Mg (0.61g) as nitrate solutions (10wt%) were impregnated on $\text{CeO}_2\text{-ZrO}_2\text{-Al}_2\text{O}_3$ (CZA-prepared by co-precipitation using Na_2CO_3), dried at 110°C and calcined at 500°C as mentioned above [9].

2.2.6 Effect of varying the content of Ag and K on CeO₂-ZrO₂-Al₂O₃

The content of Ag and K on CZA was varied so as to achieve the optimum loading of the two metal supported on CZA in terms of their activity towards soot oxidation.

Table 2.2 Varying weight loading of Ag and K on CZA

Sl.No	%Ag	%K
1.	2 (0.031g)	2 (0.07g)
2.	2 (0.031g)	5 (0.17g)
3.	2 (0.031g)	10 (0.353g)
4	5 (0.07g)	10 (0.35g)
5.	10 (0.15g)	10 (0.35g)

2.2.6.1 Combination of Silver and Potassium on the support

The process of catalyst screening was carried out and a loading of 2wt% Ag (0.031g) and 10wt% K (0.35g) impregnated onto CeO₂-ZrO₂-Al₂O₃ (CZA-prepared by coprecipitation using Na₂CO₃), dried at 110°C and calcined at 500°C at 5°Cmin⁻¹ and dwelling at the maximum temperature for 5 hours under flowing air was found to be ideal for soot oxidation.

Table 2.3 Optimization of calcination conditions for the preparation of 2%Ag10%K/CZA

2%Ag10%K-CZA (CZA-Ce:Zr-7:3- Na ₂ CO ₃ coprep)	Calcination temperature(°C) @ 5°Cmin ⁻¹	Calcination rate at 500°C (°Cmin ⁻¹)	Calcination time at 500°C, @5°Cmin ⁻¹ (h)
	200	1	4
	400	5	5
	500	10	6
	750	20	

2.2.6.2 Optimization of the catalyst

The 2% Ag 10 %K/CZA catalyst was calcined at different temperatures, rates, for different durations and tested for their activity. This was done to identify the best method of preparation of the catalyst. The calcination rates and time were based on the formation of the oxides at 500°C under flowing air as detected using the TGA to understand the temperatures for decomposition of the precursors.

2.2.7 Pt/SiC for naphthalene oxidation

Polyaromatic hydrocarbon (PAH) oxidation was carried out using two catalysts combustion catalysts, consisting of platinum on silicon carbide, with a 2.5wt% loading of platinum. The first method was a modified impregnation method wherein Pt (acac)₂ (0.0504 g, 0.13 mmol) was dissolved in toluene (75 ml), to which SiC (1 g) was added. The resulting mixture was stirred for 24 h. The solvent was evaporated using a rotary evaporator and the resulting solid was dried at 110°C for 16 h. The dried precursor was ground in a mortar and pestle and calcined at 500°C for 5h under static air. The second catalyst was prepared by an incipient wetness method wherein Pt (acac)₂ (0.0504 g, 0.13mmol) was dissolved in toluene (6.5 ml) and added to SiC (1 g), followed by drying the resulting paste at 110°C for 16 h. This was then ground to a fine powder and calcined at 500°C for 5 h under static air [10].

2.2.7.1 Modification of the catalyst for PAH-soot combustion

The Pt/SiC catalyst prepared by incipient wetness and the Ag-K/CZA catalyst prepared as described previously were combined by manual grinding in ratios of 1:2, 1:1 and 2:1 (weight ratios) to give a mixed catalyst - Pt/SiC:Ag-K/CZA. These mixed catalysts were tested for soot oxidation, with the aim of choosing an optimised ratio of mixed catalyst and soot for further testing.

2.2.8 Preparation of Ag-CeO₂ and 10%K/Ag-CeO₂ catalysts via co-precipitation and dry impregnation

The Ag-CeO₂ catalyst was prepared via co-precipitation using silver nitrate (Sigma Aldrich, 74.08mg) as Ag-source and cerium (III) nitrate hexahydrate (Sigma Aldrich, 126.23mg) as Ce-source. The salts were dissolved in H₂O (3.75 mL). An ammonia solution was used as co-precipitating agent (0.98 mL of 25% NH₃) in H₂O (2.5

mL). Both solutions were mixed under stirring for 1 minute, and the black co-precipitate was heated uniformly in an autoclave at 120°C with steam during 10 minutes. The resultant brown co-precipitate was then separated by centrifugation. The precipitate was calcined in flowing air at 500 °C for 5 hours with a ramp rate of 5°C/min to yield a brown powder, 48.5%wt Ag-CeO₂.

The Ag-CeO₂ catalyst was then impregnated with 10%wt K via dry impregnation. K₂CO₃ and Ag-CeO₂ were separately dissolved in a small amount of water. The Ag-CeO₂ suspension was heated up to 80°C under stirring and then, K₂CO₃ was dropwise added. The resultant solution was kept at the mentioned conditions until evaporation of most part of the solvent. After drying overnight at 110°C, the solid was ground and calcined in flowing air at 500°C for 5 hours with a ramp rate of 5°C/min to yield a brown powder, 10%K/Ag-CeO₂.

2.3 Reactor design

2.3.1 Catalyst screening using Thermogravimetry

Soot oxidation activity was tested by mixing catalyst with the soot (Ex-CRT) in different ratios. This process was used to optimize a suitable ratio between the catalyst and soot. The analysis showed that an excess of catalyst over soot in the ratio of 10:3 was ideal for lowering the temperatures of oxidation of soot. The soot and catalyst were mixed together and subjected to thermogravimetric analysis using the Setaram Labsys TG-DTA/DSC instrument. The catalysts were tested in two different ways for soot oxidation-

- a) TIGHT CONTACT- The catalyst was mixed and compressed with the soot, using a pestle and mortar to increase the contact area. This is not an ideal representation of the packing of soot in an exhaust filter, but was chosen for reproducibility of results.
- b) LOOSE CONTACT- The catalyst and soot were mixed together in the optimum ratio using a spatula in a tube. This mimics the likely packing of soot in an exhaust filter, but does not necessarily offer the best catalyst-to-soot contact.

The sample was heated under an atmosphere of flowing air from 30°C to 900°C at 5°C min⁻¹. The onset temperature (T_{on}), extrapolated onset temperature (T_{eo}), temperature corresponding to maximum rate of oxidation (T_p) and the final

temperature (T_f) were recorded from the derivative of the TG plot. The analysis was also carried out under N_2 atmosphere to understand the effect of lattice oxygen stored and available for soot oxidation.



Figure 2.1 Setaram Labsys TGA-DTA/DSC

2.3.2 Reactor schematic - qualitative analysis -Soot oxidation reactor

2.3.2.1 Overview of design

The reactor consisted of 5 mm i.d quartz tube, held inside the furnace governed by a temperature controller. The soot (uncatalysed reaction) and the soot: catalyst mixture (catalysed reaction) was placed at the centre and in between two layers of quartz wool within the reactor tube. The gas feed consisted of: O_2/He (volume% - 20:80); 20% CO_2/He ; 100% CO_2 ; 300 ppm NO/He ; 300 ppm $NO/O_2/He$; 1500 ppm $NO/O_2/He$; or a synthetic diesel exhaust mixture. Each gas feed, which could be mixed as desired (from the respective cylinders labelled 1-5) and regulated using mass flow controllers (8), was fed into the reactor tube (9) containing the catalyst -soot bed (11). A temperature controller (10) controls the temperature of the furnace surrounding the reactor tube. The temperature through the tube was controlled using a thermocouple placed above the soot: catalyst bed (12). A thermally insulated line maintained at $120^\circ C$ (13), consisting of the oxidation products was then sent through a 0.5 micron filter (14) to prevent any particulate matter from entering into the GC and then trapped in a vial with acetone (16) that was placed in an ice acetone bath (17). The line from the reactor

head to the vial with acetone and from the vial to the vent was heated to 120°C to avoid any condensation in the line. The products collected in a vial were allowed to evaporate and 1ml of acetonitrile (ACN) was added to the vial containing the condensed hydrocarbons. Then 0.5ml of this was transferred into a 1ml vial and analysed using HPLC. This was shown in the reactor schematic below in figure 2.2.1.

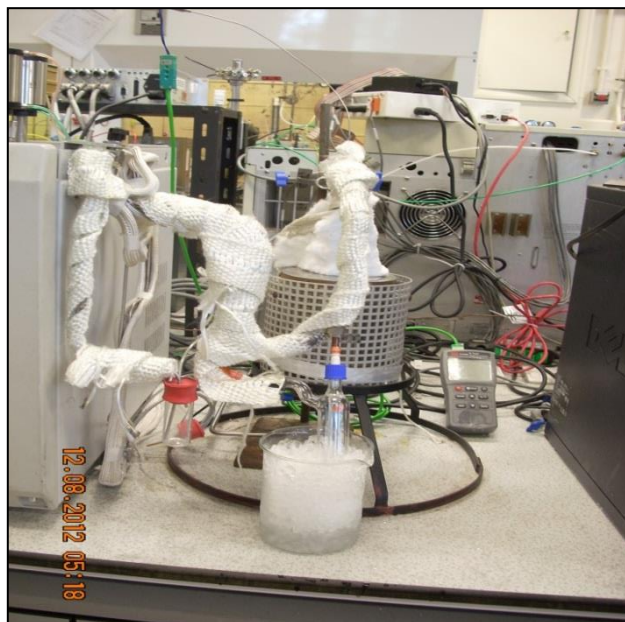


Figure 2.2 Reactor design

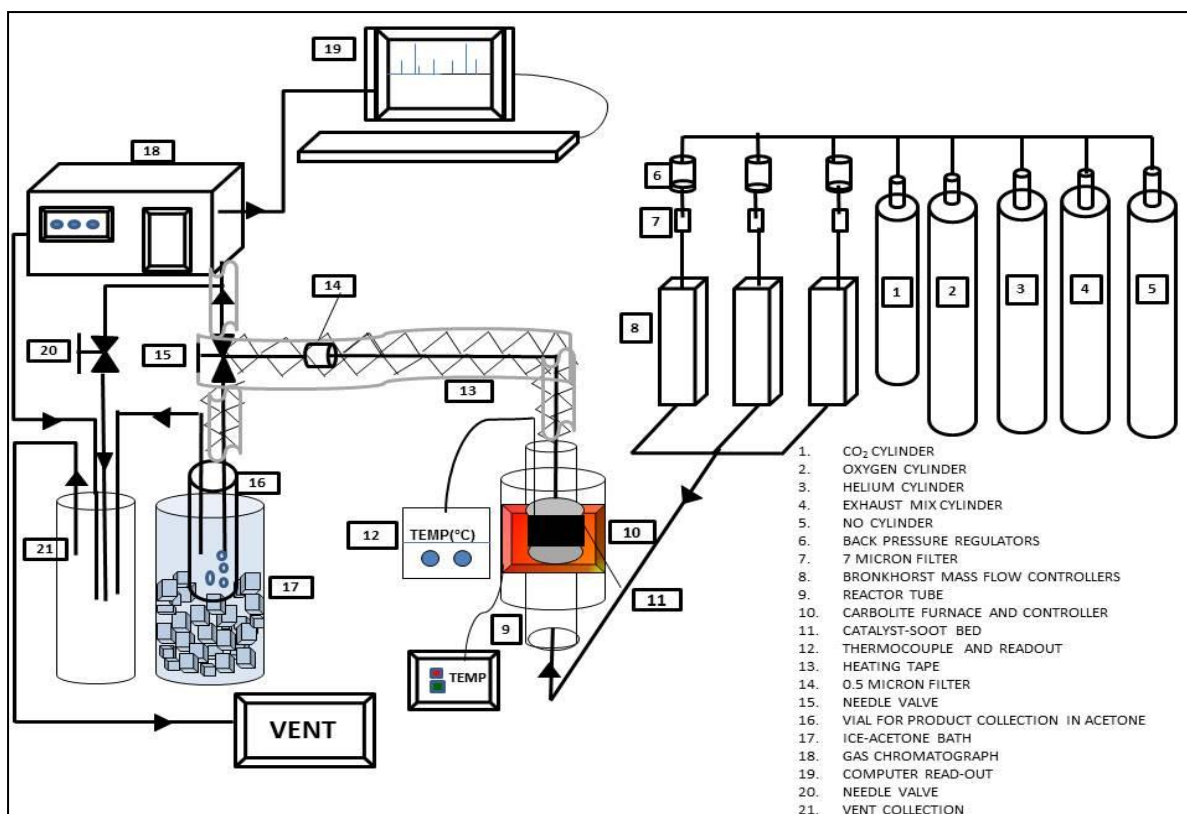


Figure 2.2.1 Reactor schematic illustration for speciation of soot

2.3.2.2 Reaction conditions

Analysis was carried out under oxidative and inert (helium) atmospheres as mentioned above, maintaining a gas hourly space velocity of $30,000\text{h}^{-1}$ with a flow of 50 ml min^{-1} . A ratio of 10:3 (catalyst: soot) was prepared by mixing 0.2 g of catalyst with 0.0061g of soot for the catalysed tests, while 0.00814g of soot was used for the uncatalysed tests. Testing for soot oxidation was also carried out under higher flows (200ml min^{-1}), using a larger soot/catalyst charge in order to maintain the same space velocity. The reaction was carried out at different temperatures – 300 (initial), 400 , 500 , 600 , 700°C (final) for uncatalysed soot oxidation and 300 (initial), 400 , 500 , 600°C (final) for catalysed soot oxidation, with a heating rate of $40^\circ\text{C min}^{-1}$. The reaction was then held at each temperature for an hour and products were collected in acetone.

Testing was also carried out under inert atmospheres such as Helium and N_2 flows to understand the effect of lattice oxygen from the catalyst on soot oxidation and to observe if the PAHs desorbed off the surface at high temperatures as a thermal effect.

Table 2.8 Reaction conditions for the qualitative analysis of soot

Sl. No	Sample	Gas mixture (%)	Flow rate (ml min ⁻¹)	Heating rate (°C min ⁻¹)	Temperature Range (°C)
1		20%O ₂ /He	50,200		
2.		He pre-treated (110°C) 20% O ₂ /He	200		
3.		100% CO ₂	50		
4.		10%CO ₂ /He	200		
5.	Soot	300pm NO	200	40	300,400,500,600,700
6.		300ppmNO/O ₂ /He	200		
7.		1500ppm NO/O ₂ /He	200		
8.		100% He	200		
9.		Exhaust mix (100ppm propane, 230 ppm CO, 300ppm propylene, 9% O ₂ , ≥ 90.93% N ₂)	200		
10.		20%O ₂ /He-loose contact	50,200		
11.		20%O ₂ /He-tight contact	200		
12.		He pre-treated (110°C) 20% O ₂ /He	200		
13.		100% CO ₂	50	40	300,400,500,600
14.	Ag-K/CZA+soot	10%CO ₂ /He	200		
15.		300pm NO	200		
16.		300ppmNO/O ₂ /He	200		
17.		1500ppm NO/O ₂ /He	200		
18.		100% He	200		
19.		Exhaust mix	200		
20.	Norit	20%O ₂ /He	50		
21	Extracted soot	20%O ₂ /He	50	40	300,400,500,600,700

2.3.2.3 Product analysis using High Performance Liquid Chromatography (HPLC)

High performance or high pressure liquid chromatography (HPLC) is a form of column chromatography where the particle sizes of the stationary phase are very small (providing a large surface area for separation of compounds), with the mobile phase being forced under high pressure along the column. This type of chromatography separates complex analyte mixtures with great efficiency, often allowing excellent separation in a very short time span. This gives qualitative and quantitative information as each compound has its own elution time. Thus the peak area and height under a set of conditions is proportional to the amount of the corresponding substance. In the case of reverse phase HPLC, there is an adsorption of hydrophobic molecules onto a hydrophobic solid support in a polar mobile phase. The hydrophobic interaction between the solute and the solid support can be reduced by decreasing the polarity of the mobile phase through the addition of organic solvent thus resulting in desorption. The stationary phase consisting of silica is made non polar by adding 8 or 18 C atoms long hydrocarbon chains to it. Nonpolar compounds in the mixture tend to elute before the polar ones as their interactions with the polar mobile phase is weak [11].

The HPLC system consists of large solvent reservoirs for storage of mobile phase solvents such as acetonitrile, water, methanol, hexane etc. A pneumatic or screw-driven pump delivers the solvent at 20ml min^{-1} and 1000 psi, thus pushing the mobile phase through the column (producing a pressure drop of up to 400 atm). A precolumn is invariably used for the removal of contaminants or impurities from the solvent, and for reconditioning the column with mobile phase so as to avoid the stripping of the stationary phase of its packed material. It is followed by an injection system that consists of a hypodermic needle used to draw the analyte into a valve that has a capacity of 2-100 μl . A self-sealing septum made of silicon or teflon is used at this port. The chromatographic column that follows is made of glass or stainless steel and is of 15- 150 cm in length with an internal diameter of 2-3mm. The packing material used inside is invariably silica gel and sometimes diatomaceous earth or celite. Post separation, the sample is analysed using a detector based on UV, IR absorption, conductance, refractive index, fluorescence, radioactive measurements, and polarography and mass spectrometric measurements [12].

Products of soot oxidation (catalysed and uncatalysed) were trapped in acetone. The solvent was evaporated and 0.5ml of acetonitrile was added to the extracts and used for further analysis on HPLC. A standard PAH calibration mix (Sigma Aldrich) was used for the identification and quantification of the aromatics. It contained 10µg/ml of 16 compounds that included naphthalene, acenaphthalene, acenaphthene, fluorene, phenanthrene, anthracene, fluoranthene, pyrene, benzanthracene, chrysene, benzo(b)fluoranthene, benzo(k)fluoranthene, benzopyrene, dibenzanthracene, benzo(ghi)perylene, indeno (1,2,3-cd) pyrene. The quantification has been described in the section below. The analysis was carried using a reversed phase HPLC system with water: acetonitrile as the mobile phase with a flow rate of 1ml min⁻¹ (for efficient separation) along a gradient program as mentioned below in table 2.9. The compounds were separated on a Zorbax Eclipse Plus phenyl-hexyl 4.6 x 150mm, 3.5µm column. The column temperature was constant at room temperature (25°C) and the injection volume used was 5µl.

Table 2.9 Gradient elution programme of the solvent system for HPLC analysis

Sl. No.	Time (min)	Solvent A (ACN %)	Solvent B (Water %)	Flow(ml min ⁻¹)
1.	0	0	100	1
2.	25	100	0	1
3.	26	100	0	1
4.	27	0	100	1
5.	30	0	100	1

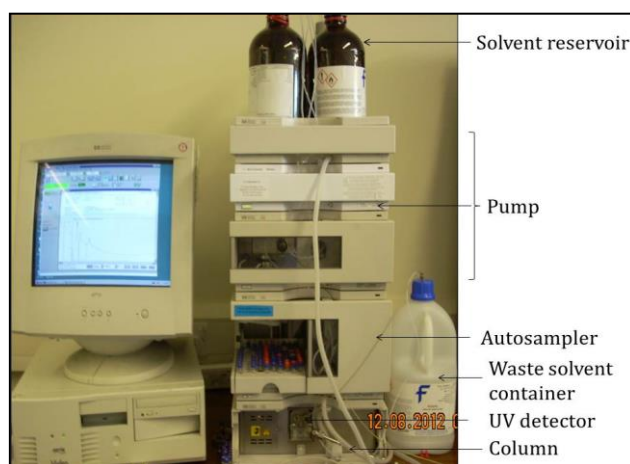


Figure 2.3 HPLC system

An example of HPLC chromatogram of the PAH standard consisting of 16 compounds is illustrated below (Figure 2.4 and 2.5).

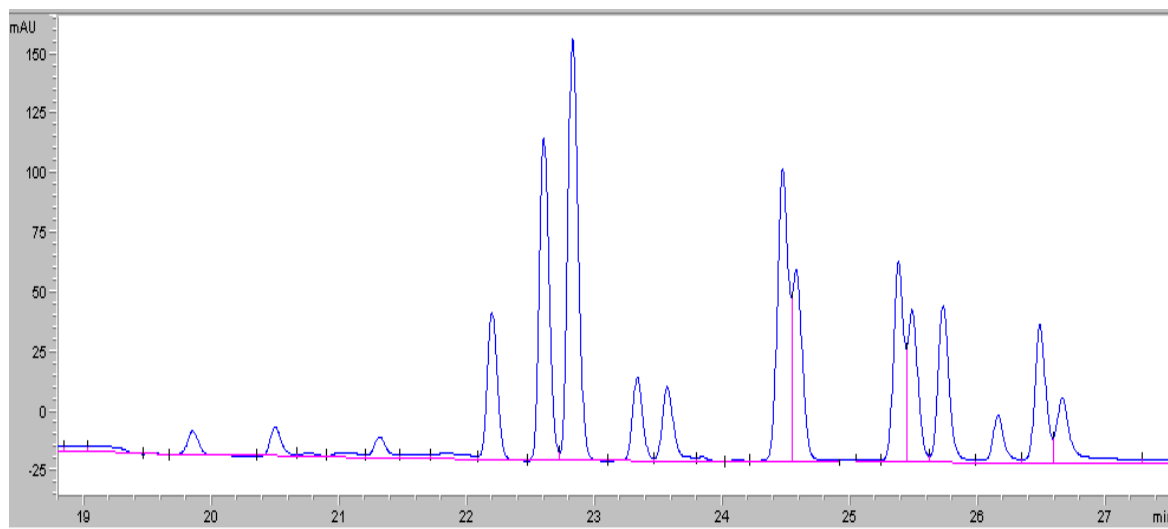


Figure 2.4 HPLC spectrum of PAH calibration mixture

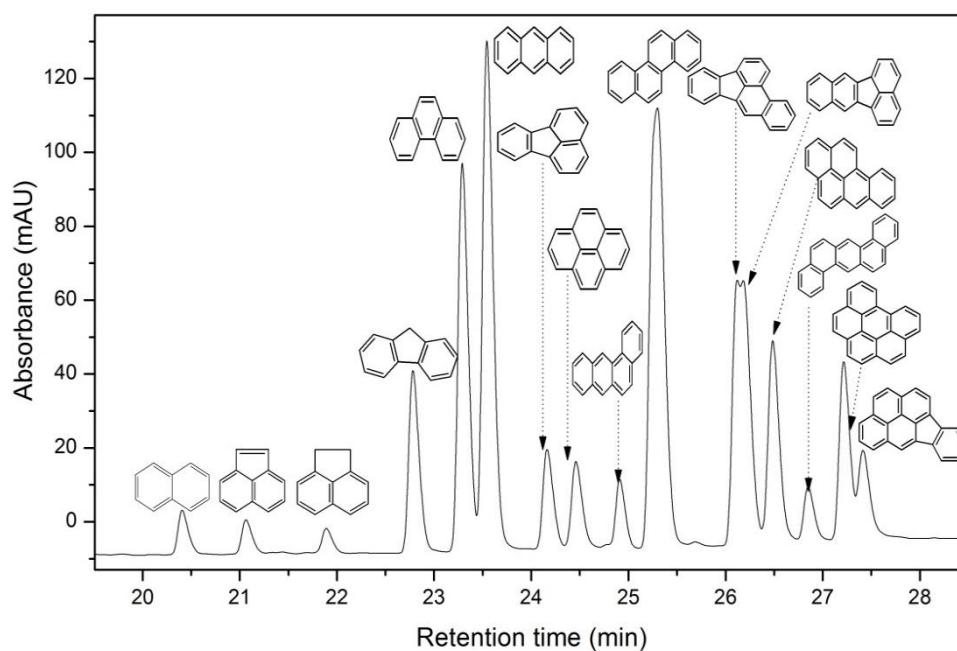


Figure 2.5 Speciation of PAH calibration mixture

2.3.2.4 Product identification and quantification

The PAH standard (5 μ l) was diluted to obtain five standard solutions by taking 0.5ml and adding 0.5ml of ACN each time and they were labelled as PAH std, PAH dil 1, PAH dil2, PAH dil3, PAH dil4 and PAH dil5 which were then injected into the HPLC (shown in figure 2.6).

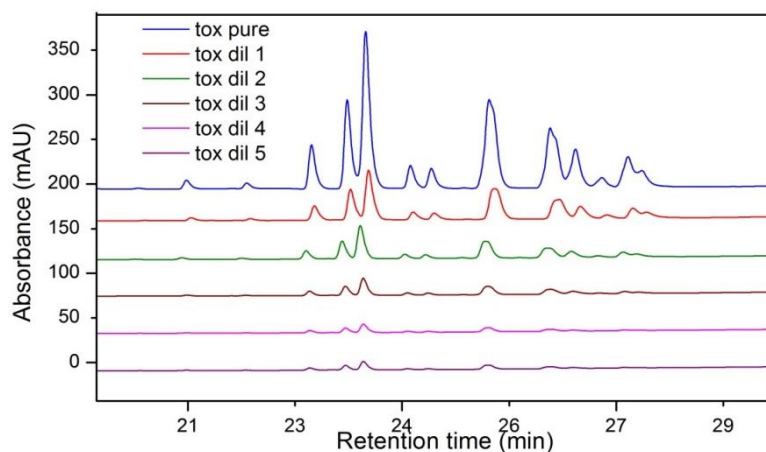


Figure 2.6 Dilution of PAH standard for calibration on HPLC

The calibration plots for each of the 16 compounds eluted were plotted from the values of the peak area of each of the individual compounds. The calibration plot for chrysene as an illustration is given below (figure 2.7). The calibration plots for the other compounds have been shown in the appendix.

Table 2.10 Concentration and peak areas for the PAH calibration mixture and five corresponding dilutions

Sl.No	Concentration (M)	Concentration (mM)	Area
1	0.00004381	0.04381	1002.85352
Diln1	0.00002199	0.02199	453.67685
Diln2	1.09952E-05	0.0109952	210.1317
Diln3	5.49763E-06	0.00549763	103.70542
Diln4	2.74881E-06	0.00274881	50.90343
Diln5	1.3744E-06	0.0013744	24.80263

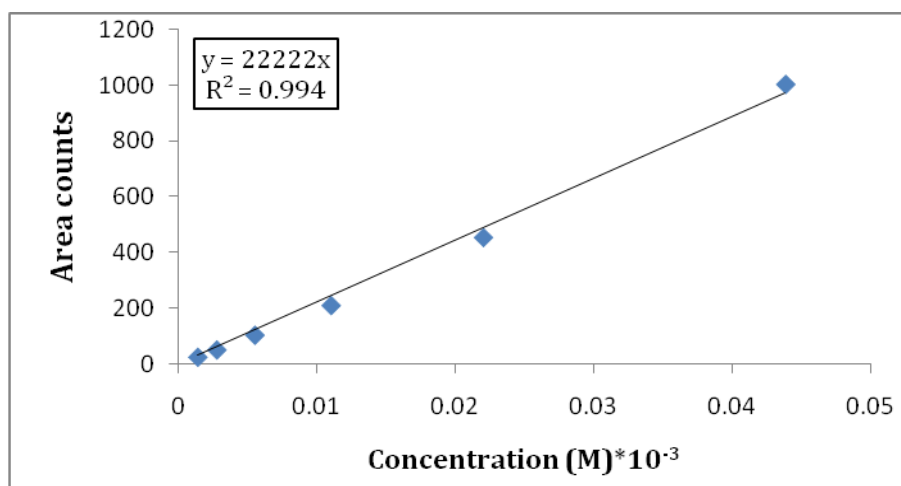


Figure 2.7 Plot of Concentration against area counts for the injected PAH calibration mixture and corresponding dilutions

The unknown concentrations of the aromatics desorbed along the oxidation process was thus calculated from the equation for a straight line,

$$y = mx$$

where, y is the peak area counts and the slope is m,

Therefore, the unknown concentration is given as;

$$x = \frac{y}{m}$$

Thus the identification and quantification of the concentrations of the 16 compounds detected in soot that matched the standard were obtained using this method.

2.3.3 Reactor schematic - Quantitative analysis

2.3.3.1 Overview of design

The reactor consisted of a quartz tube of 5mm i.d (Figure 2.8) placed inside a horizontal tubular furnace, the temperature of which was regulated using a temperature controller. The catalyst and soot were mixed together in a ratio of 10:3 by the loose contact method for most of the analyses as mentioned above unless otherwise specified. the catalyst:soot bed was subjected to individual analyses under varying concentrations and flows of O₂/He, CO₂, NO and exhaust mix and the products obtained along the analysis (primarily CO₂) was sent into the G.C for online analyses. A cold trap

was used on line, along the path so as to condense the PAHs and allow the passage of only CO₂ into the GC. The lines from the reactor head to the GC were heated to about 120°C using a heating cord. The GC was fitted with a thermal conductivity detector (TCD) to quantify the CO₂ concentration.

2.3.3.2 Reaction conditions

The soot oxidation (catalysed and uncatalysed) was studied under the conditions listed in Table 2.11. The flow of O₂, He, NO, CO₂ and exhaust mix was regulated by the use of mass flow controllers to get the desired mix of gases (8). The soot oxidation process was monitored for oxidation products (CO₂) between room temperature (30°C) to 600°C in the presence of catalyst as observed from TGA and 700°C for uncatalysed soot oxidation with a heating rate of 5°C min⁻¹. Various catalysts were also tested for their activity under the same regime for soot oxidation.

Table 2.11 Reaction conditions for the quantitative analysis of soot

Sl. No	Sample	Gas mixture (%)	Flow rate (ml min ⁻¹)	Heating rate (°C min ⁻¹)	Temperature Range
1	Soot	20%O ₂ /He	50,200,500	5	RT-700°C
2		10,20,50, 75,100%O ₂	50	5	
3		20%O ₂ /He	50	5,10,15,20	
4		300ppm NO/He	200	5	
5		20% CO ₂ /He	50	5	
6		300pm NO/O ₂ /He	200	5	
7		Exhaust mix (FTIR)	50,200	5	
8	Ag-K/CZA+soot	20%O ₂ /He	50,200,500	5	RT- 600°C
9		20%O ₂ /He (tight contact)	200	5	
10		10,20,50, 75,100%O ₂	50	5	
11		20%O ₂ /He	50	5,10,15,20	
12		300ppm NO/He	200	5	
13		20% CO ₂ /He	50	5	
14		300pm NO/O ₂ /He	200	5	
15	Exhaust mix (FTIR)	50,200	5		
16	Soot	100% He	50	5	RT-700°C
17	Ag-K/CZA+soot	100% He	50	5	RT-600°C
18	Norit	20%O ₂ /He	50	5	RT-700°C
19	Extracted soot	20%O ₂ /He	50	5	RT-700°C
20	Graphite	20%O ₂ /He	50	5	RT-700°C

2.3.3.3 Sample delivery

The major product of soot oxidation (CO_2) was quantified using a Varian Star online gas chromatograph, a Porapak-Q column and a six port injection valve as shown in figure 2.8 was used for identification of CO_2 and efficient separation from the other components for the separation.

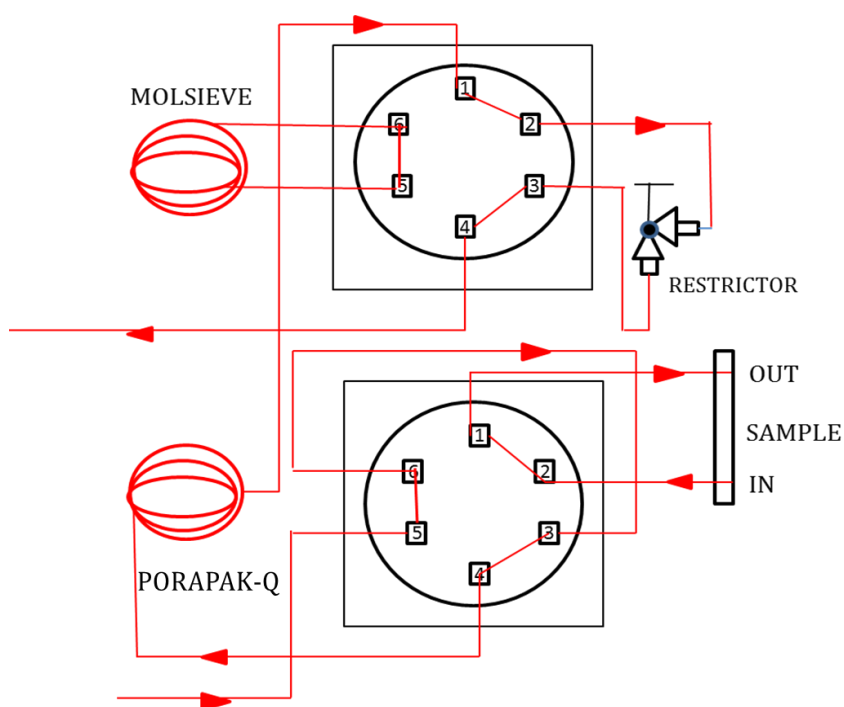


Figure 2.8 Schematic representation of the sample delivery system in the GC

The use of a second column such as a molecular sieve was not needed as this would cause the CO_2 and bulky hydrocarbons to get adsorbed onto the column and would not be separated. The hydrocarbons were trapped in the cold trap set in-line to prevent them from entering the Porapak -Q column and for better separation of CO_2 . The CO_2 after passing through the column was first detected on the TCD. TCD measures the thermal conductivity difference between the analyte gas and the carrier gas (helium). The difference is detected as a change in resistance of a tungsten wire element at elevated temperature. A plot of the change in resistance (or voltage) as a function of time is derived that is communicated as the TCD signal.

The FID detected the bulky hydrocarbons, but considering the complex hydrocarbons that are present in soot these could not be efficiently separated and

detected using an FID. Thus the HPLC was the ideal technique for identification and quantification of the PAHs as mentioned in section 2.4.2.3.

2.3.3.4 Valve sequence and temperature programme

The injection of the sample into the column was controlled by valve 1 (V1) after the loop was filled as shown in table below.

Table 2.12 Valve sequence for valve operation

	V1	V2
Time	Series	Bypass
Initial	Fill	-
0.01	Inject	-

A temperature programme was set on the GC oven and communicated to the computer controlling the GC for efficient separation of CO₂ from the hydrocarbons at the shortest elution time. The programme was carefully set as shown in table 2.13, after calibrating the GC for CO₂ separation, as increasing the oven temperature could result in shortening of the retention time which would cause a poor separation of CO₂. CO₂ elutes usually around 0.7s as according to the programme. The total programme was about 3 min long. Thus an injection every 3 minutes was used with a 0.5s stabilization time.

Table 2.13 Temperature programme for efficient elution of CO₂

Temperature (°C)	Ramp rate (°Cmin⁻¹)	Hold time (min)	Total time (min)
50	---	0.00	0.00
56	2.00	0.00	3.00

2.3.3.5 Data handling

The calibration of CO₂ was carried out using known amounts of pure CO₂ and a response factor was generated which was used for the quantification of CO₂. The response factor for CO₂ was calculated to be 0.000143.

$R_f = \text{Known \% of CO}_2 \text{ injected} / \text{number of counts produced from the peak area.}$

The concentration of CO₂ in ppm or as a percentage was calculated as shown in the appendix. In order to determine the rate of the reaction or CO₂ formation, the ideal gas equation was used. A calibration plot of the ratio of CO₂/He flow against the area counts corresponding to the amount of CO₂, gives the amount of CO₂ produced in mmol min⁻¹, so allowing the rate of the reaction to be measured as a function of time and temperature. This has also been described in the appendix. To determine the conversion of the carbon to CO₂, elemental analysis of the soot was conducted. This revealed that the carbon content in the soot was 91.4% (by mass), which allowed the carbon balance to be calculated accurately.

2.3.4 Gas analysis by Fourier Transform Infrared (FTIR) spectroscopy

Principle: Infrared spectroscopy can be used to analyse a gas-stream, by passing infrared radiation through a gas-sampling cell where some of it is absorbed by the gas sample and the rest is transmitted. A molecular fingerprint of the sample is created from the absorption and transmission obtained in the resulting spectrum. This technique is unique to specific molecules and it can be used to identify unknown materials, determine quality and consistency of a sample and also to determine the amount of components in a given mixture. Providing the gas molecules are IR active, a fingerprint of the sample with absorption peaks corresponding to the frequencies of vibration between the bonds of the atoms present in the sample constitutes an infrared spectrum. A unique combination of atoms is present in each material analysed, no two compounds produce identical spectra. Thus identification of different kinds of species in a compound is possible giving a qualitative analysis of the sample and size of the peaks give a direct indication of the amount of material present [12].

An FTIR gas analyser measures all of the infrared frequencies simultaneously rather than individually. This is done using an interferometer that produces a unique type of signal that encodes all the infrared frequencies and this can be measured very quickly in the order of one second or so. The interferometer consists of a beam splitter that splits the incoming infrared beam into two optical beams, of which one reflects off a flat mirror placed in fixed location. The other beam reflects off a flat mirror based on a mechanism that allows a mirror to move a short distance away from the beam splitter.

The two reflected beams recombine when they meet back at the beam splitter. The signal produced is a result of two beams interfering with each other as one beam travels a fixed length and the other constantly changes as the mirror moves. This signal is referred to as the interferogram and it gives information of every infrared frequency arising from the source. A Fourier transformation is employed to decode the individual frequencies producing data that can be interpreted by the user.

In this study, real-time analysis of complex gas mixtures was carried out using a Gasmet FTIR gas phase spectrophotometer (figure 2.9), with a 400 ml high-temperature sampling cell (180°C). The inlet and outlet gas lines were heated by heating cords. Nitrogen was used as a purge gas through the sampling cell. After recording a background spectrum under the flow of nitrogen through the reactor, the reactant gases were sent into the sampling cell, by-passing the reactor setup. This provided the inlet concentrations of the molecules in the reactant gas-stream. The reactant gas-stream was then fed through the reactor bed. The FTIR had previously been calibrated for the identification and quantification of exhaust-gas components CO, CO₂, propane, propene, NO, NO₂, N₂O, and other gases such as methane, ethane and ethene that could be formed during soot oxidation. Testing was carried out using a feed of exhaust mix and NO for the catalysed and uncatalysed soot oxidation, to understand the effect of NO in soot oxidation. The overlapping of bands was taken into account using the calibration for various gases depending on the gas feeds.



Figure 2.9 FTIR Setup

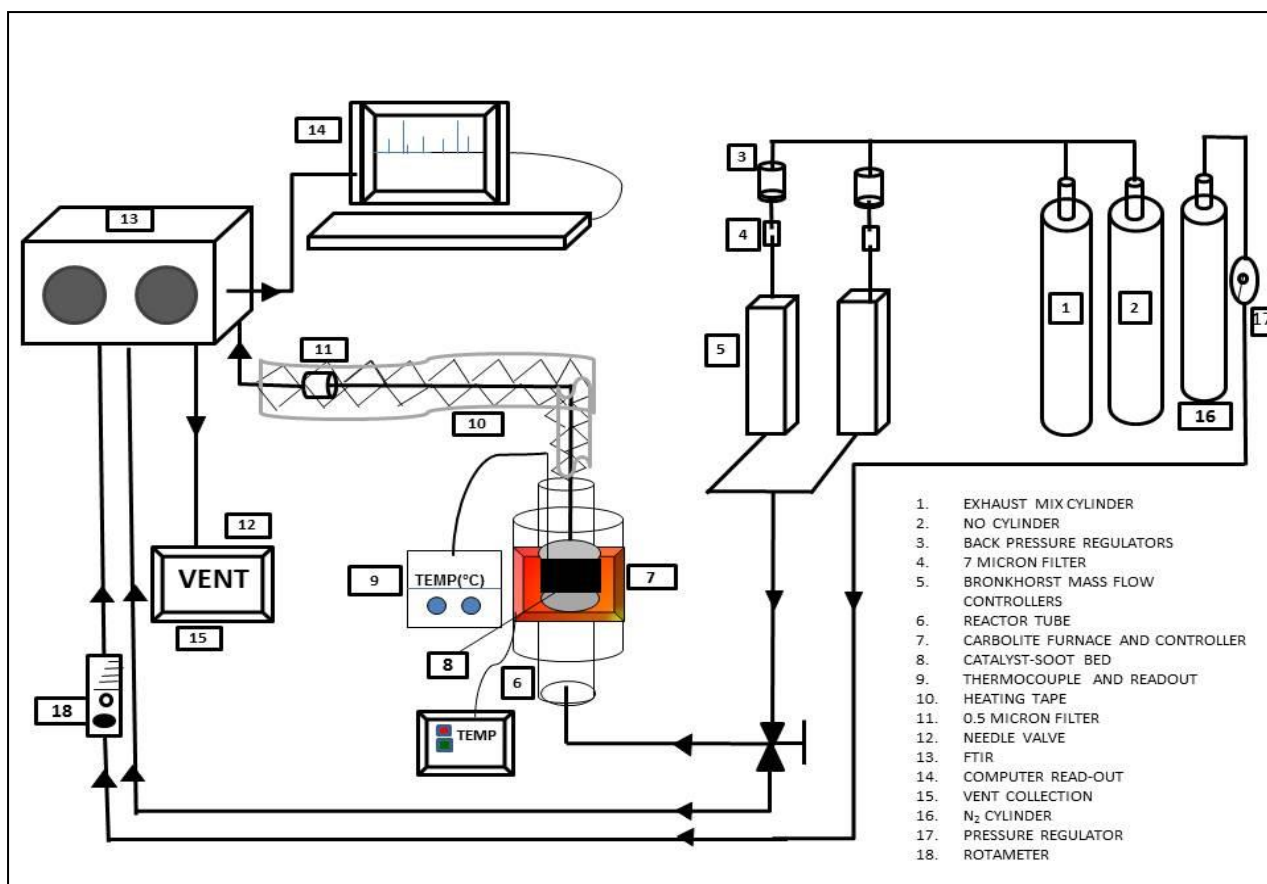


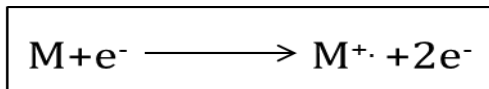
Figure 2.10 Reactor with an inline FTIR

The FTIR system was purged with N₂ gas to flush the system clean at the start of the analysis. The gases regulated using mass flow controllers were fed into the FTIR initially, to obtain the background spectrum. The spectrum for each of the reactant gases is compared against calibrated data for the same. The volume of the FTIR sample cell is 400ml and a flow rate of 200ml min⁻¹ was used to fill the cell. The reactant gases used were pure exhaust mix and NO. The soot oxidation products were monitored using the FTIR for every minute run, with increase in temperature from 200-600°C. A plot of the concentration as a function of temperature was plotted.

2.3.5 Mass spectrometry (MS)

A mass spectrometer is a powerful analytical tool to quantify known materials, to identify unknown compounds and to understand the structure and chemical properties of different molecules. It involves ionization of the sample into gaseous ions with or without fragmentation, followed by quantification of the relative abundance of the ions on the basis of their mass to charge ratios (m/z). There are different ion types formed

depending on the nature of the ionization process. The most common way of production of these ions is by electron impact that induces the loss of an electron from a gaseous atom or molecule.



The product formed is a radical cation referred to as an odd electron species with a positive charge. $\text{M}^{+\cdot}$ has the same mass as the molecular weight of the compound 'M' and is known as the molecular ion. The charge of the ion is the same as that of the electron but on losing an electron, the charge of the ion may always be a multiple of the charge of an electron given as ze .

The instrumentation consists of: a) *an ion source*- this is used to introduce molecules into the mass spectrometer and to convert them into charged or ionized form. This is usually operated under vacuum in order to avoid collision of ions with residual gas molecules during their travel from the ion source to the detector. The distance the ion travels before its collision with the molecules (mean free path) should be ideally longer than the distance from the ion source to the detector. The kinds of ionization processes include electron ionization where gas molecules are bombarded with a stream of electrons. This is a common method for the detection of volatile organic molecules. Electrons produced upon heating by the passage of current through a thin ribbon of metal (e.g. ruthenium) which acts as the cathode, are projected through an ion chamber attracted by the anode, placed on the other end of the cathode. Usually a magnetic field may be applied through the ion source to increase the probability of interaction with the gaseous sample. Collision leads to ionization and formation of the molecular ion. Some molecules possess sufficient energy to ionize while others undergo fragmentation or dissociation.

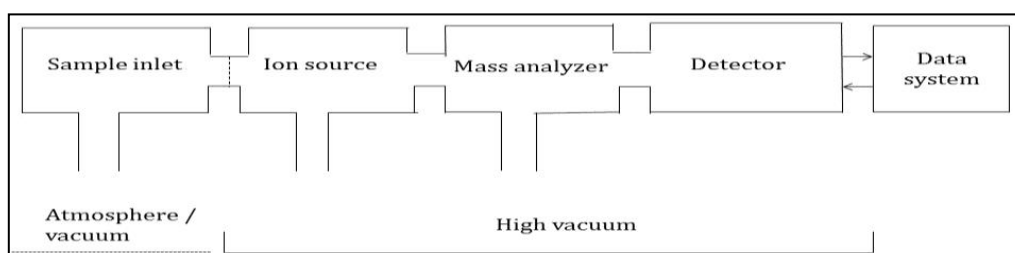


Figure 2.11 Schematic of mass spectrometer

The other methods of ionization include chemical ionization, field and plasma desorption ionization, matrix assisted laser desorption ionization (MALDI) and electrospray ionization

- b) *mass analyser*- this helps to separate the ions based upon their mass to charge ratio through the application of magnetic and electric fields. The different types of analysers include time of flight (TOF), magnetic sector, quadrupole and ion trap.
- c) *ion detectors* – these help to generate an image current when the ions leave the mass analyser and pass through the detector. These include Faraday cup, electron multipliers, array detectors etc. [13, 14, 15].

Soot insertion into the mass spectrometer was performed according to the similar experiment conducted by Norbert Klempier and Hienrich Binder (1984) where they used 0.05 mg of unextracted soot and 0.2 mg of extracted soot (sourced from the micro combustion of purified benzene) for the analysis, by placing it in a capillary at the tip of the insertion system [16]. The exhaust particulates from a diesel engine similar as in this study were used for the analysis. A HP-5930-A dodecapole coupled with an electron impact mass spectrometer was used, with an ion source temperature of 175°C, source pressure of 2×10^{-6} Torr, in order to record an integrated ion current using a strip chart recorder. The aim of their analyses was to detect five ring PAHs with a molecular weight of 252 such as benzo(a)pyrene, benzo(e)pyrene, benzo(b)fluoranthene, benzo(k)fluoranthene and perylene. They were able to detect aliphatic hydrocarbons in diesel soot particulates using this technique with the distinction in peak intensities. The ratio of intensity of m/e 252 to intensity of m/e 253 as a function of temperature was obtained and the peak intensity of aliphatic hydrocarbons at m/e 252 is 80% of the m/e of 253. Any peak greater than the 80% of the 253 peak represented the aromatic hydrocarbons [16]. A similar experiment was conducted and a mass spectrum was obtained as shown in figure 2.12 that indicated the various polyaromatic hydrocarbons in soot ranging from two ringed structures to 6/7 ringed heavy aromatics.

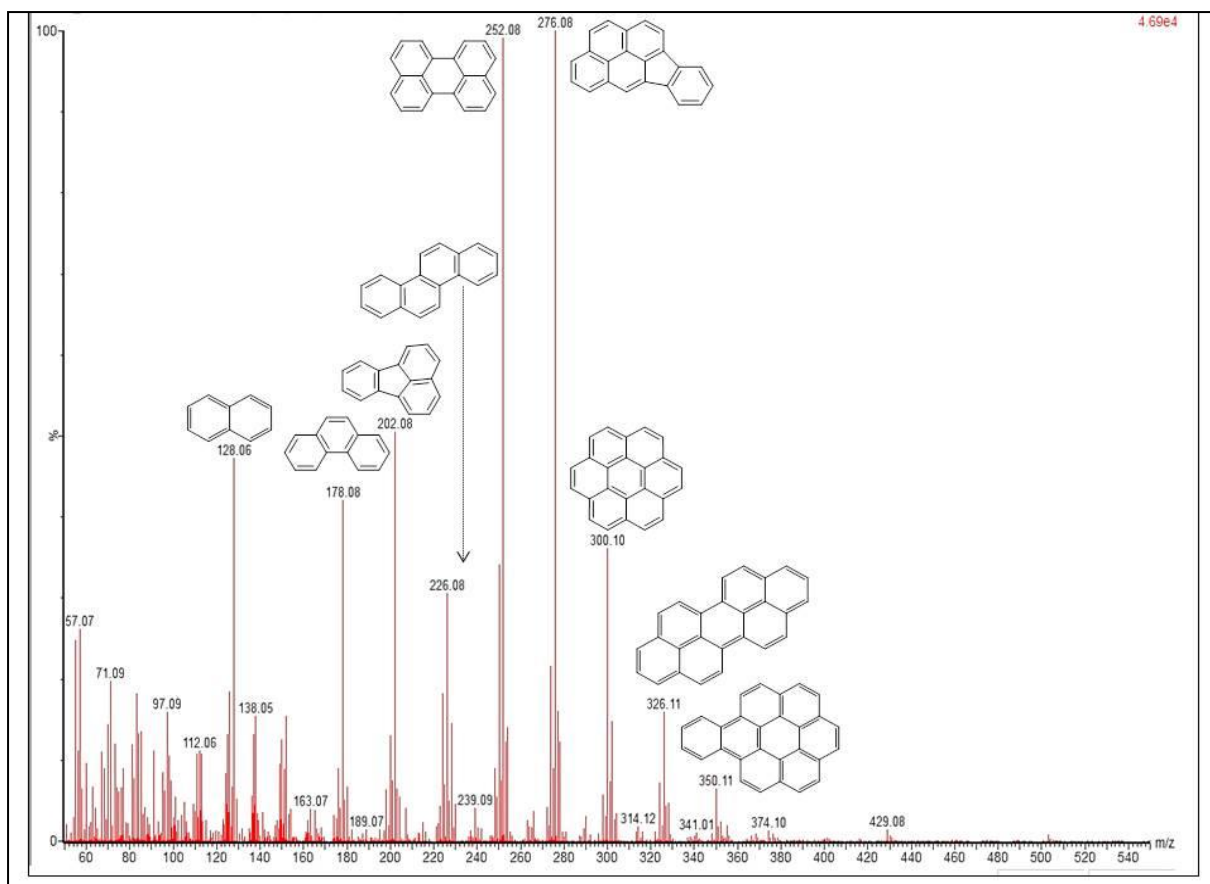


Figure 2.12 Mass spectrum showing the PAHs in diesel ex-CRT soot

2.3.5.1 Techniques coupled with MS

2.3.5.1.1 Gas chromatography-Mass Spectrometry (GC-MS)

Mass spectrometry could be coupled to several techniques like gas chromatography as there is a possibility of ionisation of molecules in this technique. This technique helps to identify volatile compounds from a complex mixture. This is possible through chemical or electron ionization methods and detected as they are released from a GC column. It can detect elements with low molecular weights.

Modern GC-MS uses capillary columns, typically with i.d of 100-500 μ , which provide an efficient separation of very low levels of analytes, while minimizing the amount of carrier gas entering the ion source from the GC, (thus maintaining a low pressure).. For this purpose, high capacity pumping systems are also being used extensively. Most solutions analysed by this technique are organic in nature. The sample is then injected into the GC where it gets vaporized and the carrier gas such as helium helps in the elution of compounds from the mixture, based on their relative interaction with the

column and carrier gas. The end of the column then leads through to a heated transfer line onto the entrance of the ion source of the mass spectrometer where the compounds eluting the column are converted to ions and get separated as they pass through the mass analyser and detectors based on their mass to charge ratio.

The application of this technique is widespread, which includes areas like drug detection, fire investigation, environmental analysis, explosives investigation and identification of unknown samples. It can also be employed in the identification of trace elements in materials that were previously thought to have disintegrated beyond identification [15].

A Waters GCT premier instrument, fitted with an Agilent HP-5MS column, was used to perform GC-MS analyses in this study. The internal diameter and length of the column were 0.25 μ m and 30m, respectively. The temperature program used for the analyses ranged between 40°C to 280°C with a carrier gas of helium (flow 1ml min⁻¹). The mass spectra obtained for the unknown compounds were matched with the spectra in the mass spectral database in order to determine the nature of the compound. In the case of soot analyses, the soot was inserted directly into the mass spectrometer probe.

2.3.5.1.2 Liquid Chromatography-Mass Spectrometry (LC-MS)

This combination of techniques is effective for the separation of compounds (through the use of physical separation capacities of liquid chromatography) followed by the identification of the separated compounds using the mass analysis properties of mass spectrometry. This technique was used to analyse the aromatics formed on oxidation of soot. In particular, when using phenanthrene-graphite as the model for soot oxidation, the oxidative products such as 9, 10 phenanthrene quinone and 2, 2'biphenyl dicarboxylic acid were quantified from the EI+ MS spectrum.

2.4 Characterization

2.4.1 X-Ray diffraction- Principle

X-Ray diffraction is a form of elastic scattering of X-ray photons by the atoms or ions present in a periodic lattice. X-rays have wavelengths in the angstrom range, about the size of an atom or ion, and possess sufficient energy to penetrate solids so providing a method for probing the solid-state structure of materials. When monochromatic X-

rays are scattered, those that are in-phase with one another will produce constructive interference. This was explained by W.L Bragg in 1912 upon observing the X-rays impinging on a crystal surface. These rays were seen to be deflected from atoms on the surface and a portion of the rays tend to penetrate into layers below and are reflected thereafter. Those rays that constructively interfere are said to satisfy the Bragg's equation given below.

$$n\lambda = 2d\sin\theta$$

where,

n is an integer ($n = 1, 2, 3\dots$) also known as the order of the reflection

λ is the wavelength of the X-rays

d is the distance between two lattice planes;

θ is the angle of incidence

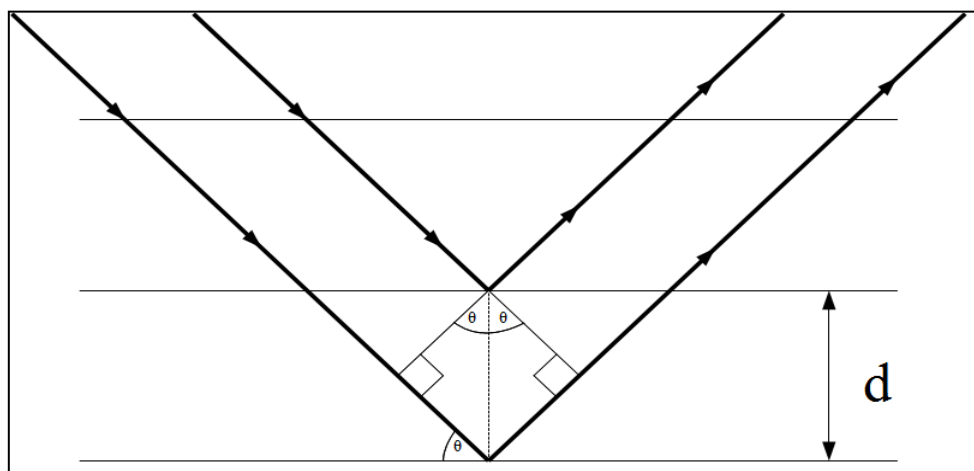


Figure 2.13 X-Ray diffraction pattern based on Bragg's law

Thus only for certain angles of incidence on the crystal these X-rays are in phase and constructively interfere and their path difference is a whole number multiple of the wavelength. This gives the corresponding lattice spacing that is characteristic of a certain compound. At all other angles, the rays will be partly or completely out of phase which is referred to as destructive interference [17].

The instrumentation thus consists of a stationary X-ray source, usually a $\text{CuK}\alpha$ source with energy of 8.04 keV and wavelength 0.154 nm that generates the X-rays or a

beam or electrons striking a metal target. The inner electron from the K shell of the atom of the metal is forced to get ejected and an outer electron from the L shell fills the vacancy created. K_{β} radiation is emitted when the electron from the M shell fills the vacancy. The resultant beam consists of X-rays with different energies which are detected by a movable detector [18].

Crystallite sizes can be determined from the Debye-Scherrer equation:

$$\beta_k = \frac{k\lambda}{d_{hkl}} \cos\theta$$

where, β_k is the peak width ($\beta_k = \beta_{obs} - \beta_{std}$); β_{obs} is the overall peak width and β_{std} is the instrument line broadening component;

K is the shape factor or a constant often taken as 1;

λ is the wavelength of radiation used,

d_{hkl} is the crystallite size;

θ is the peak position

The Scherrer equation depends on the line broadening effect that indicates that the broader peaks tend to appear due to smaller crystallites or measurement at smaller wavelengths gives sharper peaks as the wavelength decreases, with a shift in diffraction angles to lower angles, thereby decreasing the $1/\cos\theta$ term.

2.4.1.1 Experimental

Analysis was performed on a PANalytical, XPERT Pro with $CuK\alpha$ radiation impinging on the samples. The samples were placed in individual holders and the surface exposed was made completely smooth, free of any irregularities to obtain a good diffraction pattern. The analysis was run for 1 hour under a current of 40mA and voltage of 40kV from 2θ ranging from 20-80°. PanAnalytical High score plus was used for the analysis of the data or spectra obtained. The diffractograms obtained were compared with the JCPDS database in the software for the identification of specific phases present in the sample. The crystallite sizes were determined using the Debye Scherrer equation for all the samples.

2.4.1.2 In-situ XRD

Monitoring solid-state changes in a catalyst can help in understanding the surface reaction. This technique consists of a sample cell with windows that are transparent to X-rays and that can hold the analyte sample (soot+catalyst). There is a heating stage that is covered by platinum foil to keep the sample holder with the powdered sample thermally conducted. A simple temperature programmed model of the soot oxidation using O₂ and Helium flows was replicated to understand the kinetics of the reaction [19]. Upon heating to 700°C in the presence of oxygen, the patterns were not modified, which meant that the combustion process did not modify, irreversibly the catalyst structure, in the time scale of XRD measurements which required an hour for each diffractogram collection. Any fast and reversible change in structure occurring for instance, during the soot ignition will not be detected by this in-situ XRD monitoring.

2.4.2 Raman Spectroscopy - Principle

Raman is a form of vibrational spectroscopy based on absorption and emission of infrared and visible light and its interaction with the molecules. It has been observed that when a beam of light is passed through a substance, a small amount of the radiation energy is scattered and, on using a monochromatic radiation source, the scattered energy consists almost entirely of the frequency of incident radiation (Rayleigh scattering) and some discrete frequencies above and below this incident radiation (Raman scattering).

Raman scattering may be explained based on the quantum theory effect that describes the radiation frequency ' ν ' as a stream of photons from a laser beam, possessing an energy of ' $h\nu$ ' (h is Planck's constant) that undergo collisions with the molecules, upon striking the surface of the substance being analysed. A detector is usually employed to analyse the photons after interaction with the sample under analysis.

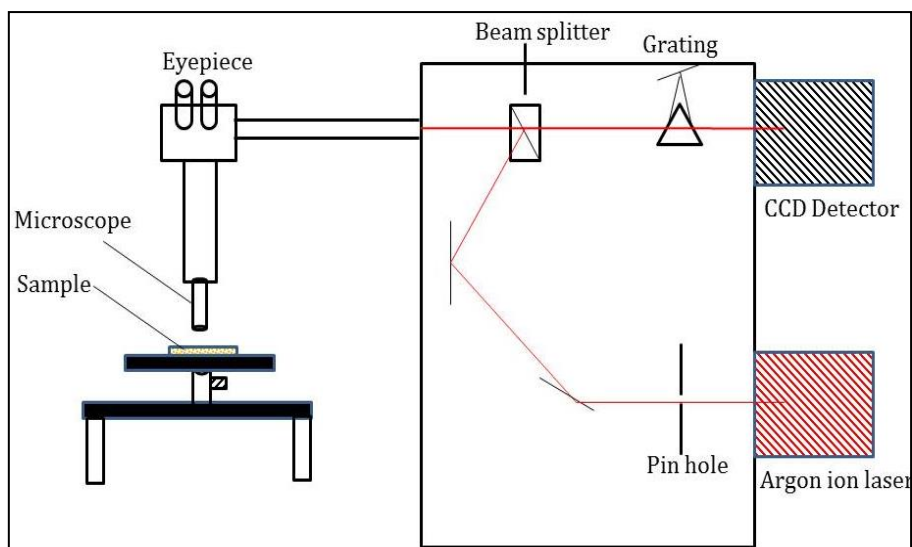


Figure 2.17 Schematic representation of Raman spectrometer

Upon exchanging energy with the incident molecules the collisions become inelastic. Thus if the molecule gains energy ΔE , the photon gets scattered by an energy $h\nu - \Delta E$ and it will possess a frequency of $\nu - \Delta E/h$ and on losing energy the scattered frequency is $\nu + \Delta E/h$. The photon gets scattered by an energy and it will possess a frequency of and on losing energy the scattered frequency is The radiation that is scattered with a frequency lower than that of the incident radiation is referred to as the *Stoke's lines* or radiation which are generally accompanied by the increase in molecular energy. The scattered radiation at higher frequency is referred to as *Anti-stokes lines* or radiation. In this case the molecule is in an excited rotational or vibrational state and involves a decrease in energy [20].

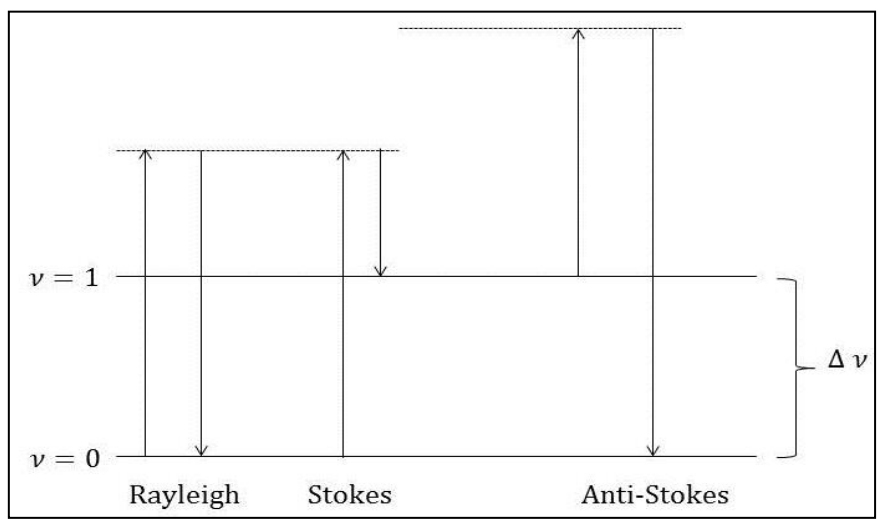


Figure 2.18 Illustration to show the kinds of radiation involved in Raman spectroscopy

On the basis of the classical theory of Raman effect, when a molecule is placed in a static electric field, some form of distortion occurs that causes the positively charged nuclei to be attracted towards the negatively charged pole and the electrons towards the positive pole. This induces an electric dipole moment and polarizes the molecule. The induced dipole can depend on the magnitude of the applied field E and on the ease of distortion. Thus, $\mu = \alpha E$ where α is the polarisability. So for a molecule to be Raman active, a molecular rotation or vibration must cause some change in the polarisability

2.4.2.1 Experimental

The bulk structure of catalysts was characterised using a Renishaw inVia Raman microscope that was equipped with two kinds of lasers, a 514nm Modu-laser (green argon ion) as the active medium and a 784nm (argon laser). A crystalline silica reference material was used for calibration, before the catalyst samples were analysed. The samples were mounted on an aluminium plate, and the surface was flattened out. The laser power was set to a 10mW at the start of each analysis, with an exposure time of 10s for each scan, targeting 100 accumulations of the sample under observation. The laser power was gradually increased depending on the quality of the spectrum.

2.4.3 Nuclear Magnetic Resonance (NMR) spectroscopy-Principle

This spectroscopic technique relies on the magnetic properties of atomic nuclei. An atom possesses negatively charged electrons around a positive nucleus composed of protons and neutrons. Nuclei containing an odd number of protons or neutrons possess a *magnetic moment*. This is seen in the case of ^1H , containing a single proton in its nucleus. On applying a magnetic field this magnetic moment tends to interact in such a way that it directs itself in the direction of the magnetic field or opposite to it. These alignments possess different energies but require the same amount of energy to change the position from one to the other. These nuclei are usually assigned a spin that may be zero, half integral or integral. The NMR active nuclei are those that have the spin, $I \neq 0$ and possessing a magnetic moment ' μ '. The magnetic moment may be '+ μ ' or '- μ ' depending on whether it is parallel or antiparallel to the applied field. Thus the energies of the two alignments are '+ μB_0 ' and '- μB_0 ', the difference of which is ' $2\mu B_0$ ' is needed to invert the proton's magnetic moment from lower to higher energy state. This is given by,

$$\Delta E = h\nu = 2 \mu B_0 ;$$

$$\text{Or } E = -\mu_z B_0 = -m_l \gamma \frac{h}{2\pi} B$$

where, μ is the magnetic moment of the proton,

B_0 is the applied field strength or magnetic flux density;

ν is the frequency or the radiofrequency region of the electromagnetic spectrum for NMR experiments;

m_l = magnetic quantum number;

γ = magnetogyric (gyromagnetic) ratio;

h is the Planck's constant;

For a ^1H or ^{13}C nucleus ' l ' is $1/2$ thus, m_l can either be $\pm 1/2$ and thus only two energy levels are produced.

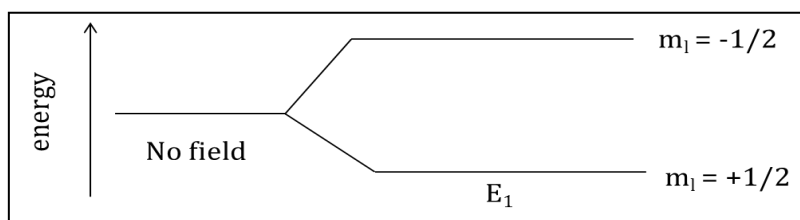


Figure 2.19 Splitting of energy into two levels

In practice, the magnetic field is varied by using a radio frequency oscillator, producing electromagnetic radiation and keeping the applied frequency ' ν ' a constant, so as to achieve the absorption of energy to flip the magnetic moment of the hydrogen atom. The resulting signal can be amplified and fed to a recorder, as a plot of energy against frequency. The frequency shift relative to the standard is called its chemical shift ' δ '. A suitable reference compound for this purpose is tetramethylsilane (TMS) or $\text{Si}(\text{CH}_3)_4$ which possesses a single resonance at a certain position and does not overlap with other signals [14, 21, 22].

^1H NMR spectra were recorded using Bruker 400 MHz and 600 MHz instrument using CDCl_3 , D_2O or DMSO as solvents. The sample preparation involved the evaporation of the solvent used in the soot extraction analyses. The sample was then placed under

vacuum until it was completely dry and a volume of approximately 1ml of deuterated solvent was added to the dry residue to dissolve it. The solution (0.5-0.7 ml) was subsequently transferred to the NMR tube and then placed under the magnetic field.

2.4.3.1 Two dimensional NMR spectroscopy

Due to the development of a variety of computer-controlled pulse sequences consisting of two or more pulses of appropriate length, frequency range, power and phase, two dimensional spectroscopy plays an important role in the identification of chemical compounds. There are a number of different techniques which are widely applied in NMR analysis, here only NMR experiments used in this thesis are mentioned. Heteronuclear single-quantum correlation spectroscopy (HSQC) detects correlations between nuclei of two different types which are separated by one bond.

2.4.4 Infrared spectroscopy-Principle

The basis of this spectroscopic technique is the absorption of discrete IR frequencies by molecules or extended structures, corresponding to the frequencies of stretching and bending vibrations. An increase in amplitude of the vibrational motion of bonds, which have a dipole moment changing as a function of time, will occur when frequencies of infrared radiation match the vibrational frequencies absorbing the radiation. This can be used diagnostically to characterise complex structures [14].

A typical spectrometer consists of a heated filament or laser producing radiation in the form of continuous range of frequencies in the infrared region that is allowed to pass through the sample within a cell. Some of this radiation may be absorbed by the molecules in the sample and then passed through a system of slits and mirrors to emerge as a collimated beam. The grating placed thereafter helps to disperse the beam into different wavelengths which are further converted into an electrical signal by the detector. The detector first senses the ratio between the intensity of the reference and the sample and thus determines the frequencies that have been absorbed by the sample and those that haven't been absorbed. A plot of frequency or wavenumber against the energy absorbed or transmitted is given [17].

In this work, the sample was prepared by mixing very small amount (10-20mg) of dried KBr with 0.1 mg of sample, and grinding together using a pestle and mortar. A small

quantity (0.1mg) of this was placed in a holder and then subjected to a pressure of 8 Torr. The KBr disperses and seals the sample in a matrix in the form of a pellet, which was then mounted inside the holder of the spectrometer. A blank run with no sample was first recorded to obtain the background. This was later subtracted from the spectrum of the sample using the software to achieve the actual absorption spectrum of the sample. The analysis was also carried out for more precision using a Shimadzu IRAffinity-1 Fourier Transform Infrared Spectrophotometer which did not require an elaborate sample preparation. In this case, a background spectrum was recorded and then the sample to be analysed was placed in the field of the radiation to obtain the spectrum. A scan between $400\text{-}4000\text{cm}^{-1}$, under a resolution of 8 was carried out. The spectra recorded were under the transmission mode and for some of the carbon rich samples, absorbance mode was used.

2.4.5 Temperature Programmed Reduction (TPR)-Principle

This technique gives quantitative information about the reducibility of the surface and bulk species in a sample. TPR also gives information on the heterogeneity of the surface. The reduction of metal oxides is the most commonly studied profiles. It begins with the dissociative adsorption of H_2 . The next step depends on how fast this dissociation occurs and based on this the diffusion of atomic hydrogen into the lattice and subsequent reaction with oxygen takes place, leading to the removal of hydroxyl species. In the case of noble metals on oxide supports or defective metal oxides, the activation of H_2 is a relatively fast step as compared to oxide supports alone. In this case the nuclei of reduced metal atoms grow rapidly over the entire surface of the particle and eventually into the shell of reduced metal. The transport of oxygen out of this particle then occurs. Over time the metal reduction is favoured over the metal shell growth. This is the shrinking core or contracting sphere model. In the nucleation model, dissociation of H_2 is a slow step. Upon reduction, the nucleus of the metal acts a site for further reduction, where H_2 is further dissociated causing diffusion to adjacent sites on the surface or lattice and then reduces the oxide. This leads to the growth of the nuclei in three dimensions until the whole surface is reduced. Beyond this the reduction takes place as a shrinking core. The temperature programmed reduction of the catalyst is given as a function of time as the temperature increases at a linear rate [18].

2.4.5.1 Experimental

In this study, a small quantity of sample (100mg) was weighed out and placed into the U tube shaped sample holder, held in the oven of the instrument. The sample was first degassed under a flow of helium at 110°C for about 40 minutes to one hour. This pre-treatment removed any surface absorbed species on the catalyst in order to obtain a pure surface for reduction and to minimize reduction from impurities or other species. The sample was then exposed to a flow of 10% H₂/Ar at 13ml min⁻¹ while it was heated from 30-800°C at 5°C min⁻¹. The measured consumption of H₂ was plotted as a function of temperature.

2.4.6 Thermogravimetric analysis (TGA) - Principle

Thermogravimetry is an analytical technique used to determine the thermal stability of a sample, and to quantify the fraction of any volatile components, by monitoring the change in weight of the material when it is heated. The change in weight is recorded as a function of temperature and time, usually by carrying out the analysis under a flow of air or inert atmosphere such as helium or argon. It is often used to track the decomposition of materials (e.g. under conditions that mimic calcination of a catalyst), and the data can yield kinetic information about the physicochemical processes taking place in the sample. Due to the unique sequence of the physicochemical reactions occurring over specific temperature ranges and heating rates, TG curves are often characteristic of particular compounds. However, as several factors (such as sample mass, volume, physical form, shape and nature of the holder, nature and pressure of the atmosphere in the sample chamber and heating rate) can influence the characteristics of a recorded TG curve, it is essential that a set of standard conditions is used throughout any comparative study.

There are two kinds of balances-vertical and horizontal. In the case of the vertical balance, the sample is usually hanging from the balance or is situated above it on a stem and they need to be calibrated to overcome any buoyancy effects that may arise due to the density and nature of the gas. There is usually only one pan present in this case. A horizontal balance consists of two pans, one for the sample and the other for the reference. In this case the temperature difference between the sample and the reference can be measured (Differential thermal analysis, DTA) or measurement of the

heat flow into the sample pan as compared to the reference pan was carried out. The components of the instrument include a microbalance, furnace, programmer controller, and a computer or data acquisition system [12].

2.4.6.1 Experimental

Setaram Labsys TGA/DTA/DSC equipment was used for this study. A sample mass of 13mg of soot or a mix of 10mg catalyst and 3mg soot was used for the soot oxidation studies while in the case of analyses of the precursors, about 30mg of sample was used. This technique was used to determine a suitable calcination regime for the catalyst support precursors by subjecting these materials to a flow of air (50ml min⁻¹) and heating it from 30-900°C at 5°C min⁻¹ and recording the weight loss upon oxidation of the support as a function of temperature and time. The TGA was also used to screen the catalysts as mentioned in section 2.4.1.

2.4.7 Brunauer Emmet Teller surface area determination – Principle

This method is based on the theory described by Brunauer, Emmet and Teller for the physical adsorption of inert gases on the external and internal surfaces of porous materials. The surface area of the material is considered to have discrete number of adsorption sites and at a certain partial pressure the gas molecules get adsorbed onto these sites forming stacks of layers. Thus a particular material surrounded by a gas with a temperature of ‘T’ and vapour pressure, P/P₀ physically adsorbs a certain amount of gas which is dependent on the vapour pressure of the gas and proportional to the external and internal surfaces of the material. The amount of gas adsorbed and the relative vapour pressure of the gas at a given temperature is indicated by the adsorption isotherm. The Langmuir isotherm, describes the relation between the surface coverage of adsorbate molecules and the pressure of the adsorbate gas, at a given temperature.

$$\theta = \frac{\alpha P}{1 + \alpha P}$$

Where:

θ is the percentage surface coverage of the adsorbate gas

P is the gas pressure

α is the Langmuir adsorption constant (This tends to increase with an increase in binding energy of adsorption, and with a decrease in temperature) [23].

The other physical adsorptions isotherms were classified by Brunauer into five types, out of which the type II and III are only for *non-porous solids* and IV and V, are for *porous materials*. The form of the isotherm depends on the choice of the adsorbate. The BET equation is given as

$$\frac{P}{V(P_o - P)} = \frac{1}{V_m C} + \frac{(C - 1)P}{C V_m P_o}$$

Where:

V is the volume of gas adsorbed.

P_o is the saturation pressure

V_m is the volume of gas adsorbed at (STP) per unit mass of adsorbent, when the surface is covered by a unimolecular layer of adsorbate

C is a constant

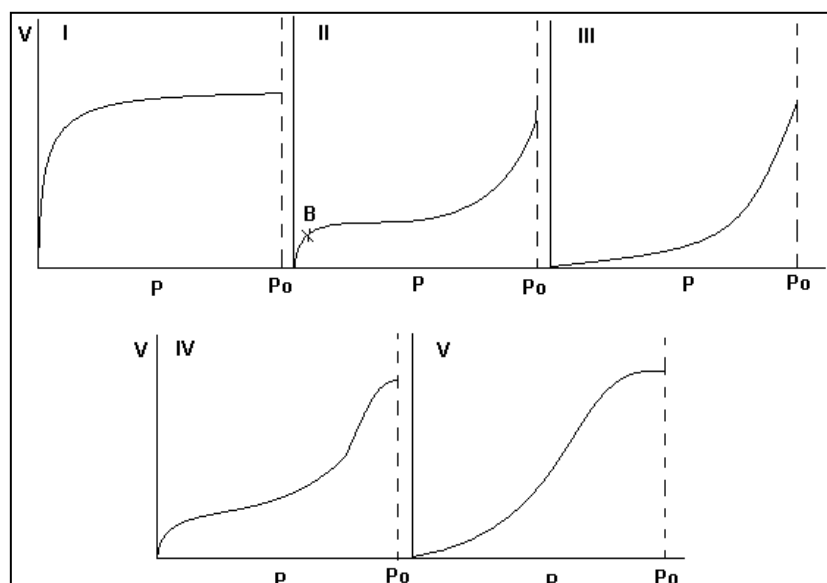


Figure 2.20 Types of Adsorption isotherms

Nitrogen is often used as the adsorbate, because the adsorption of N₂ generally occurs via physisorption around its condensation temperature (77 K). The size of the N₂ molecule determines the monolayer formation on the surface, which is around 0.16nm². The BET equation yields a straight line upon plotting $P/v [(P_0 / P) - 1]$ on the y-axis and P / P_0 on the x-axis, giving the volume of the monolayer on the surface, V_m , and from the size of a N₂ molecule (0.16 nm²), the surface area can be calculated.

2.4.7.1 Experimental

The BET surface area analysis was carried out using a Micromeritics Gemini 2360 surface area analyser. The samples (100mg) were degassed under N₂ for about an hour at 120 °C, to remove moisture and other impurities from the surface and pores of the sample, before analysis. The sample was then subjected to analyses under a vacuum atmosphere. An error of ±10% error was recorded in the values due to the limitations in the technique.

2.4.8 Scanning Electron Microscopy (SEM) - Principle

SEM is based on the acceleration of electrons from a thermionic, Schottky or field emission cathode through a potential difference between the anode and cathode ranging from a low voltage of 0.1 keV to as high as 50 keV. These electrons then pass through a system of apertures and electromagnetic lenses producing a thin beam which scans the surface of the specimen of interest. Electrons possess wavelengths of less than an angstrom (Å) and can efficiently detect atomic details in the specimen (EDX). Based on the sample thickness, a portion of the electron passes through the sample without suffering any energy loss giving rise to a two dimensional projection of the sample. The diffracted particles yield dark field and crystallographic information.

In practice, the instrumentation consists of a high energy beam of electrons produced using an electron gun containing a tungsten filament cathode. The beam then passes through condenser lenses, pairs of scanning coils, an objective lens and apertures that help to focus and deflect the beam allowing it to scan a rectangular area of the sample.

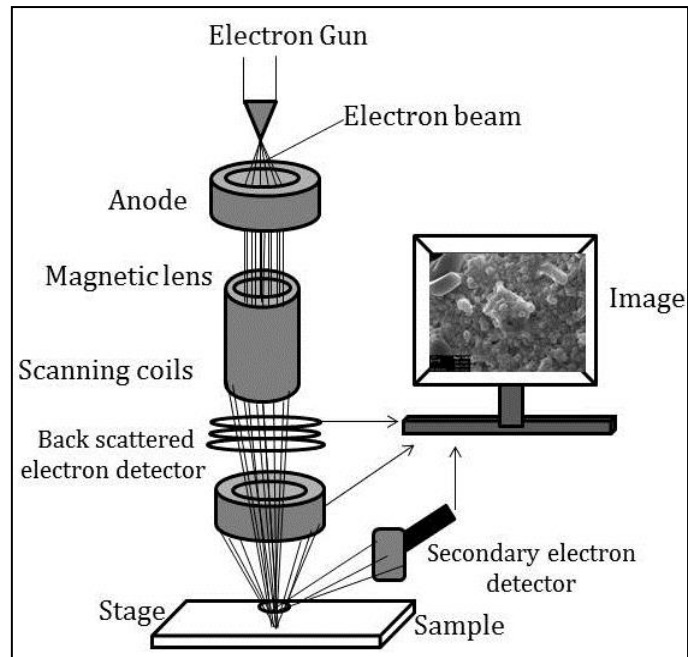


Figure 2.21 Illustration of the schematic for SEM

Electrons tend to lose energy due to the absorption and scattering by the sample when the beam interacts with the surface. The density of the material and the accelerating voltage determines the extent of penetration of the electron beam that results in the production of high energy secondary electrons along with electromagnetic radiation.

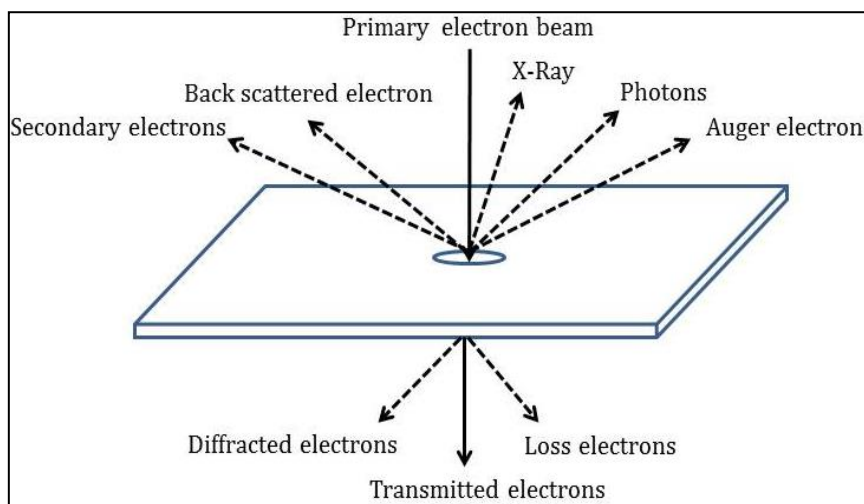


Figure 2.22 Radiations produced in SEM

Upon excitation by an electron beam the inner shell electron in an atom may be ejected and an outer higher energy level electron then fills the vacancy. This difference in

energy gets emitted as an X-ray that can be detected using an energy dispersive spectrometer. The elemental composition of the specimen can therefore also be determined using these X-rays as they are characteristic of a specific atomic structure of the element from which they are emitted [18, 24].

2.4.8.1 Experimental

The analysis was carried out using a Carl Zeiss, Evo 40 microscope. Samples were mounted onto an 8-stub carousel and a vacuum was created inside the equipment prior to the analysis which was done using either the secondary electron or the back-scattered detector.

2.4.9 Transmission electron microscopy (TEM)

This type of microscopic technique uses the high energy primary beam that passes through the condenser to produce parallel rays that impinge on the sample. A bright field image can be produced by the two dimensional projection of the sample mass depending on the density of the sample and a dark field image is obtained from the diffracted electron beam [18]. The analysis was carried out at the School of Optometry to determine the structure and morphology of soot nucleates and in the determination of the elements present on the soot.

2.4.10 Porosimetry

This technique characterises the pores of a material, that including their diameter, total volume, surface area and average size. It involves the intrusion of a non-wetting liquid such as mercury into a material at high pressure. The external pressure is required to force the liquid into the pores against the opposing force of the surface tension of the liquid. Since the technique is usually done under vacuum, the gas pressure begins at zero. Upon increasing the pressure the pore volume also increases. Thus the average pore diameter can be calculated using the pressure and pore diameter where 50% of the total volume is added.

2.4.10.1 Experimental

The samples were initially pre-treated at a 110°C under N₂ flow for an hour, which was done to degas or remove any adsorbed impurity on the sample. The sample

was then analysed by placing it under liquid N₂ overnight and the adsorption of N₂ onto the pore sites occurs followed by desorption that is recorded. The BJH pore size distribution was used to calculate the pore volume, average pore size, surface area and pore size distribution of the particles. The surface areas were also calculated based on a five point method.

2.4.11 X-ray photoelectron spectroscopy (XPS)

This is a surface sensitive technique that gives quantitative information about elements present on the outermost surface of a sample, their oxidation state and relative ratios. It relies on the principle that photoelectrons are emitted from the surface of the sample that is being irradiated by X-rays (from a magnesium or aluminium source) under ultra-high vacuum. These emissions are specific to each element present in the sample. To calculate the binding energy of the photoelectron, the following equation was used:

$$E_{\text{binding}} = E_{\text{photon}} - (E_{\text{kinetic}} + \phi_s)$$

E_{binding} is the electron binding energy of emitted electron

E_{photon} is the energy of irradiating photons

E_{kinetic} is the kinetic energy of the electron

ϕ_s is the spectrometer work function

Owing to the influence of polarisability and chemical potential, each element possessing a specific binding energy can be related to its oxidation state [18].

2.4.11.1- Experimental

The analysis was performed using a Kratos Axis Ultra DLD photoelectron spectrometer, equipped with an aluminium monochromatic source (photon energy=1486.6eV) and a dual Al/Mg achromatic source. The spectra were acquired over an area of 700x300 μ m at pass energy of 40 eV for high resolution scans. All spectra were calibrated to the C (1s) line of adventitious carbon at a binding energy of 284.7 eV.

2.4.12 Elemental analysis

Elemental analysis of the carbon, hydrogen and nitrogen present in soot samples was carried out by a commercial laboratory (Warwick Analytical Services), using a quantitative combustion method [26].

References

1. L. Hongmei, Z. Qingchao, L. Yile, G. Maochu, C. Yongdong, W. Jianli, C. Yaoqiang, *Journal of Rare Earths*, 28, **(2010)**, 794
2. J. Wang, J. Wen, M. Shen, *Journal of Physical Chemistry.C*, 112, **(2008)**, 5113-512
3. C. Chuang, H. Hsiang, J. S. Hwang, T. S. Wang, *Journal of Alloys and Compounds*, **(2008)**, 470(1-2), 387-392
4. D. H. Prasad, J. H. Lee, H. W. Lee, B. K. Kim, J. S. Park, *Journal of Ceramic Processing Research*, 10, **(2009)**, 748-752
5. Z. Ming, C. Shanhu, Z. Xiaoyu, G. Maochu, C. Yaoqiang, *Journal of Rare Earths*, 27, **(2009)**, 728
6. Z. Qingwei, S. Meiqing, W. Jing, W. Jun, F. Yanan, *Journal of Rare Earths*, 26, **(2008)**, 347
7. E. Ntainjua, T. Garcia, B. Solsona, S. H. Taylor, *Catalysis Today*, 137, **(2008)** 373–378
8. G. Ranga Rao, J. Kašpar, S. Meriani, R. D. Monte, M. Graziani, *Catalysis Letters*, 24 (1994) 107.
9. E. Aneggi, C. de Leitenburg, G. Dolcetti, A. Trovarelli, *Catalysis Today*, 136, **(2008)** 3–10
10. D. R. Sellick *et al.*, *Applied Catalysis B: Environmental*, 132, **(2013)**, 98-106
11. V. R. Meyer, *Practical High performance liquid chromatography*, Wiley, **2010**
12. S. M. Khopkar, *Basic concepts of analytical chemistry*, second edition, 1998, reprinted, **2004**
13. K. Downard, *Mass spectrometry, A foundation course*, The Royal Society of Chemistry, **2004**
14. D. L. Pavia, G. M. Lampman, G. S. Kriz, J. A. Vyvyan, *Introduction to spectroscopy*, fourth edition, Brooks /Cole, **2008**
15. W. Henderson, J. S. McIndoe, *Mass Spectrometry of Organic and Organometallic Compounds, Tools-Technique-Tips*, John Wiley & Sons Ltd, **2005**

16. N. Klempier, H. Binder *Analytical Chemistry* 55, (**1983**), 2104-2106
17. S. Duckett, B. Gilbert, *Foundations of Spectroscopy*, Oxford University Press, **2000**
18. J. W. Niemantsverdriet, *Spectroscopy in Catalysis*, third edited and enlarged version, **2007**
19. N. Guilhaume, B. Bassou, G. Bergeret, D. Bianchi, F. Bosselet, A. Desmartin-Chomel, B. Jouguet, C. Mirodatos, *Applied Catalysis B: Environmental*, 119–120, (2012), 287–296
20. C. N. Banwell, *Foundations of molecular spectroscopy*, third edition, Mc Graw Hill, **1983**
21. F. W. Fifield, D. Kealey, *Principles and Practice of Analytical Chemistry*, Blackwell Science Ltd., **2000**
22. H. Friebolin, *Basic One-and Two-Dimensional NMR Spectroscopy*, 4th edition, Wiley-VC, **2005**
23. S. Brunauer, P. H Emmet, E. Teller, *Journal of American Chemical Society*, 60 (**1938**) 309-319
24. J. I. Goldstein, *Scanning electron microscopy and X-ray microanalysis*, 3rd Edition, Springer, New York, (**2003**)
25. Quantachrome Instruments, *Autosorb-1 Operating Manual*, Quantachrome Instruments, **2006**
26. Exeter Analytical, Inc. (University of Warwick), *CE440 Elemental Analyser*, <http://www.eai1.com/theory.htm>, **2009**

Chapter 3

Catalyst screening for soot oxidation

$\text{CeO}_2\text{-ZrO}_2\text{-Al}_2\text{O}_3$ (CZA) mixed oxide supports were prepared using different methods such as impregnation of Al_2O_3 on $\text{CeO}_2\text{-ZrO}_2$ mixed precursor solution, co-precipitation of the precursors and also by varying the method of mixing of the precursors. Studies on soot oxidation have revealed that alkali metals promote the combustion of soot at low temperatures (300-500°C) [1, 2]. Alkali metal on different supports such as CeO_2 , $\text{CeO}_2\text{-ZrO}_2$, $\text{CeO}_2\text{-Al}_2\text{O}_3$, $\text{CeO}_2\text{-ZrO}_2\text{-Al}_2\text{O}_3$ and Al_2O_3 were studied and it was observed that the onset of soot oxidation using 10wt% K on $\text{CeO}_2\text{-ZrO}_2\text{-Al}_2\text{O}_3$ under tight contact conditions of soot with catalyst was at 318°C and the soot was completely combusted by 508°C. Ag on CeO_2 showed good activity previously for soot oxidation [1, 2]. Thus combining the two systems, a more efficient catalyst was prepared by an impregnation of 2wt% Ag and 10wt% K on $\text{CeO}_2\text{-ZrO}_2\text{-Al}_2\text{O}_3$ that promoted the onset of soot oxidation at 309°C and complete oxidation by 453°C.

CZA materials are widely used as supports for three way catalysts due to i) oxygen storage capacity of CeO_2 , ii) the creation of structural defects by ZrO_2 , allowing the movement of O_2 through the lattice, and iii) Al_2O_3 providing the high surface area, thermal stability and preventing the sintering of the $\text{CeO}_2\text{-ZrO}_2$ particles at high temperatures [1,2]. These supports have been widely studied for these properties and have been used as three way catalysts in diesel exhausts. These when supported with precious metals such as Ag and promoted with K resulted in lowering the combustion temperatures. Thus these supports have been prepared in this study using techniques such as co-precipitation and mechanical methods such as hand grinding of the precursors.

On impregnating these supports with alkali and alkaline earth metals the oxidation of soot occurred between 300-500°C. The oxidation of real soot from the CRT of a diesel engine had an onset at 419°C and complete oxidation took place around 720°C. Ag on CZA showed higher oxidation temperatures as compared to the 10wt%K/CZA but the Ag caused the reduction of CeO_2 at a lower temperature of 130°C,

thus aiding in the supply of oxygen stored in the ceria for the soot oxidation. Thus on impregnating 2%Ag and 10%K on CZA, the oxidation of soot was complete by 453°C and the catalyst reduced at around 300°C where the onset of soot oxidation occurred thus providing for the oxygen necessary for soot oxidation.

3.1 Catalyst support- Varying ratios of Ce:Zr in $Ce_xZr_{1-x}Al_{0.5}O_{1.75}$

3.1.1 Characterization

Figure 3.1 shows the X-Ray diffractograms recorded for the Al_2O_3 impregnated onto the CeO_2 - ZrO_2 with different ratios of Ce:Zr.

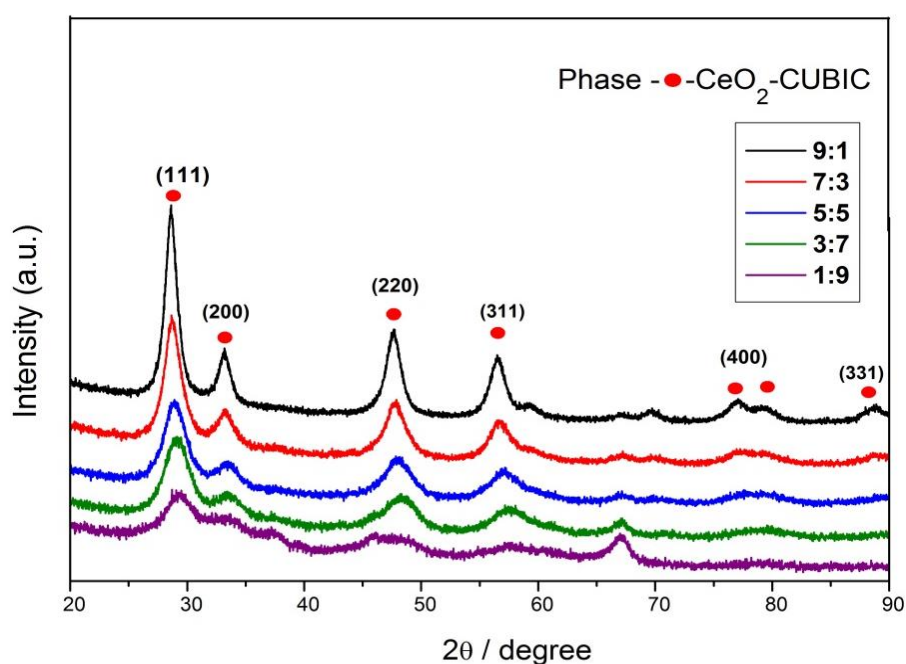


Figure 3.1. X-ray diffractograms for varying Ce: Zr ratios in CZA

All the diffractograms included on figure 3.1 contain the main reflections typical of a fluorite-structured material with an FCC unit cell at 28.5, 33.1, 47.6, and 56.5°, corresponding to the (111), (200), (220) and (311) planes [1]. X-ray diffraction patterns for the varying Ce:Zr ratios showed that the peaks increased in intensity with increase in CeO_2 content. An increase in peak width was observed with increase in ZrO_2 content indicating a decrease in crystallite size as obtained from the Scherrer equation for the (111) plane. In this case the Al_2O_3 was impregnated onto the CeO_2 - ZrO_2 . The change from amorphous to a more crystalline phase was observed with increased CeO_2 content. On incorporation of Zr^{4+} into the lattice, the peak shifted to higher angles as Zr content increased. There have been reports in literature that show that this is due to the

difference in ionic radius between Ce^{4+} (0.97\AA) and Zr^{4+} (0.84\AA) [2]. All samples showed a cubic crystal system, except $\text{Ce}_{0.05}\text{Zr}_{0.45}\text{Al}_{0.5}\text{O}_{1.75}$ that showed a tetragonal structure, more characteristic of ZrO_2 . However, broad peaks in XRD profiles can lead to incorrect assignments, and so Raman spectroscopy can be a good complementary technique to complete the analysis of the phases. Crystallite sizes were seen to decrease with increase in ZrO_2 content.

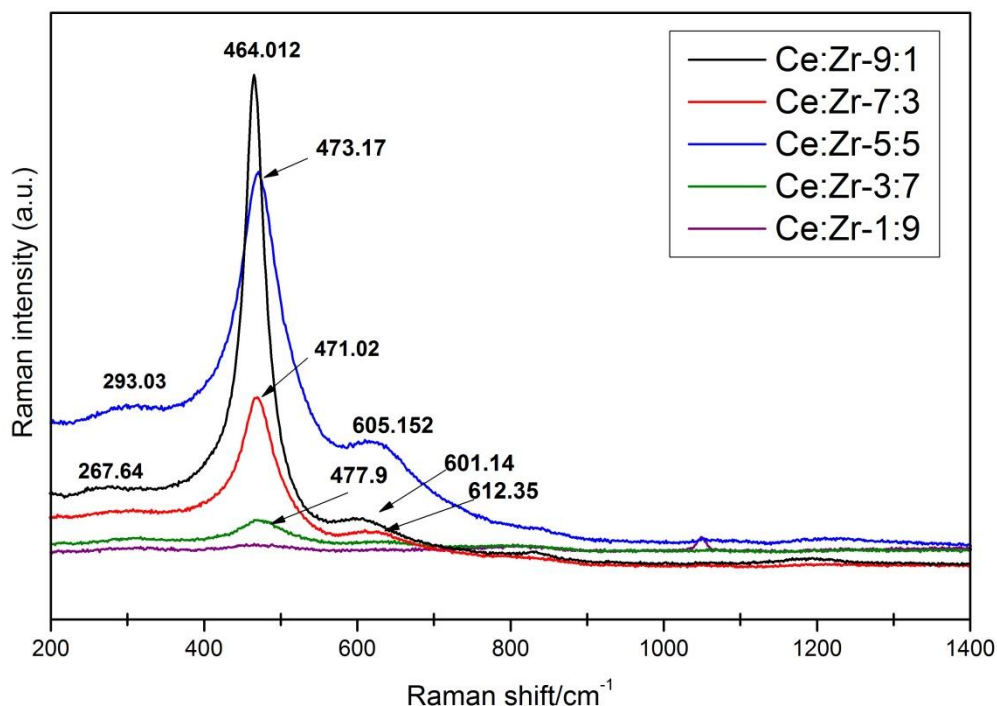


Figure 3.2 Raman spectra for varying Ce: Zr ratios in CZA

Raman spectroscopy supports the conclusions of XRD. The CZA supports presented the typical structure of CeO_2 with the main band at 460 cm^{-1} attributed to the only allowed Raman mode (F_{2g}) of a fluorite-type structure [3]. The Raman spectrum of pure CeO_2 displayed a sharp peak at 465 cm^{-1} that corresponded to the cubic fluorite structure of CeO_2 ($Fm3m$ space group) with an F_{2g} symmetry, regarded as a symmetric O-Ce-O stretching [4]. For the Raman spectrum of the single ZrO_2 phase, the peaks displayed from 170 to 200 cm^{-1} and at 265 , 313 , 460 , 600 and 645 cm^{-1} revealed the presence of monoclinic and tetragonal phases.

The Raman spectra of these fluorite-type oxide structures were dominated by oxygen lattice vibrations and were sensitive to the crystalline symmetry [5]. The presence of Zr^{4+} in the CeO_2 lattice deformed the structure, while the intensity of the

fluorite characteristic peak decreased significantly, as was evident from the change in ratios from CeO₂ rich (Ce-Zr-9:1) to ZrO₂ rich (Ce-Zr-1:9). The peak at 605 cm⁻¹ was attributed to the distortion of the cubic fluorite symmetry of CeO₂. It has been reported that this deformation favours oxygen mobility affecting the redox behaviour of the material [6]. The CeO₂ cubic phase decreased with increase in ZrO₂ content as shown in figure 3.2, resulting in a flat line for ZrO₂ tetragonal phase in Ce_{0.05}Zr_{0.45}Al_{0.5}O_{1.75}.

The TPR profile for CZA showed a bimodal type of reduction profile (figure 3.3). The bimodal TPR profiles shown in figure 3.3 indicated that the surface reduction of smaller CeO₂ crystallites occurred at around 500°C, due to the surface Ce⁴⁺ while the second peak at around 800°C was typical of the reduction of the bulk CeO₂ [7,8,9]. The reduction of surface and bulk occurred concurrently and no clear distinction could be made. An increase in the ZrO₂ content caused the bulk reduction peak to broaden in size. There is a direct correlation between the number of reducible species and the peak area.

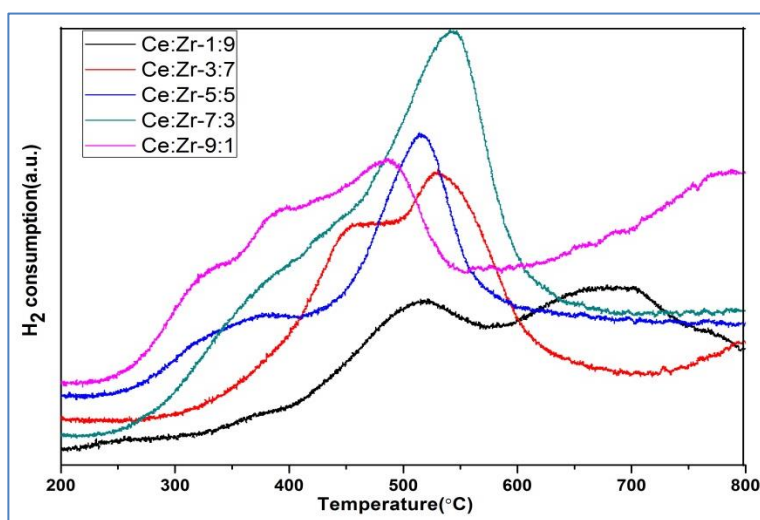


Figure 3.3 TPR profiles showing reduction of the CZA oxides with varying Ce:Zr ratios

In the case of the Ce: Zr-7:3 oxide support represented by the green curve, the peak area was largest and this showed that the surface and bulk reduction occurred nearly simultaneously. Thus more reductive species (ceria) were available at lower temperatures, indicating a stronger reductive capability. The peaks were more intense for the ceria rich mixed CeO₂-ZrO₂ oxide supports with lower reduction temperatures as shown in the figure 3.3 and this suggested enhanced oxygen mobility within the lattice due to the presence of defects created, by the addition of ZrO₂ into the lattice. The

reduction is observed only from CeO₂ as ZrO₂ is non-reducible. The H₂ consumption data has been calculated as shown in the appendix.

Table 3.1 Physical properties of CeO₂-ZrO₂-Al₂O₃ supports with varying Ce: Zr ratios

Sl.No	Catalyst	Surface area (m ² g ⁻¹)	2θ (°)	Crystallite size (nm)	Peak temperature (reduction) °C		H ₂ consumption (μ mol g ⁻¹)	
1.	Ce:Zr - 9:1	54	28.60	8.3	482		385.673	
2.	Ce:Zr - 7:3	98	28.72	6.4	543		152.4 654.3	
3.	Ce:Zr - 5:5	102	29.07	6.6	353.2	516.2	86.2	276.2
4	Ce:Zr - 3:7	117	29.07	4.1	391.2	483.2	222.1	342.4
5.	Ce:Zr - 1:9	133	28.92	4	515	681	161.2	186

An increase in the crystallite size led to an increase in peak-width. This was observed in the case of an increase in ceria content. Several researchers have shown that decrease in crystallite size with peak broadening has been related to the ceria content [5]. The Ce: Zr-1:9 ratio showed smaller crystallites as compared to the Ce: Zr-9:1. This was because the ceria cubic phase showed more intense peak and less broadening indicating smaller crystallites from XRD. The surface area also tends to increase with increase in ZrO₂ content. The mixed oxides with larger crystallites possessed a lower surface area as compared to those made of smaller crystallites with larger surface area. The average crystallite sizes for (Ce: Zr-7:3) were around 6.6 nm with a surface area of 98 m²/g, showed best activity for soot oxidation consisting of a highly homogeneous mixture of CZA.

3.1.2 Soot oxidation

The relative soot oxidation activity has been measured from the derivative of the TG plot as shown in the figure 3.4a. The onset temperature (T_{on}) corresponded to the beginning of soot oxidation, the extrapolated onset temperatures were obtained by extrapolating the steepest part of the dTG curve back to the baseline. The point of

intersection yielded the extrapolated onset temperature (T_{eo}). The maximum rate of soot oxidation was given by the peak temperature (T_p) and the final temperature corresponded to the complete oxidation of the soot (T_f). Ag/CZA was used as an example for illustration as the TG and dTG plots were well defined with less disturbance recorded during the analyses.

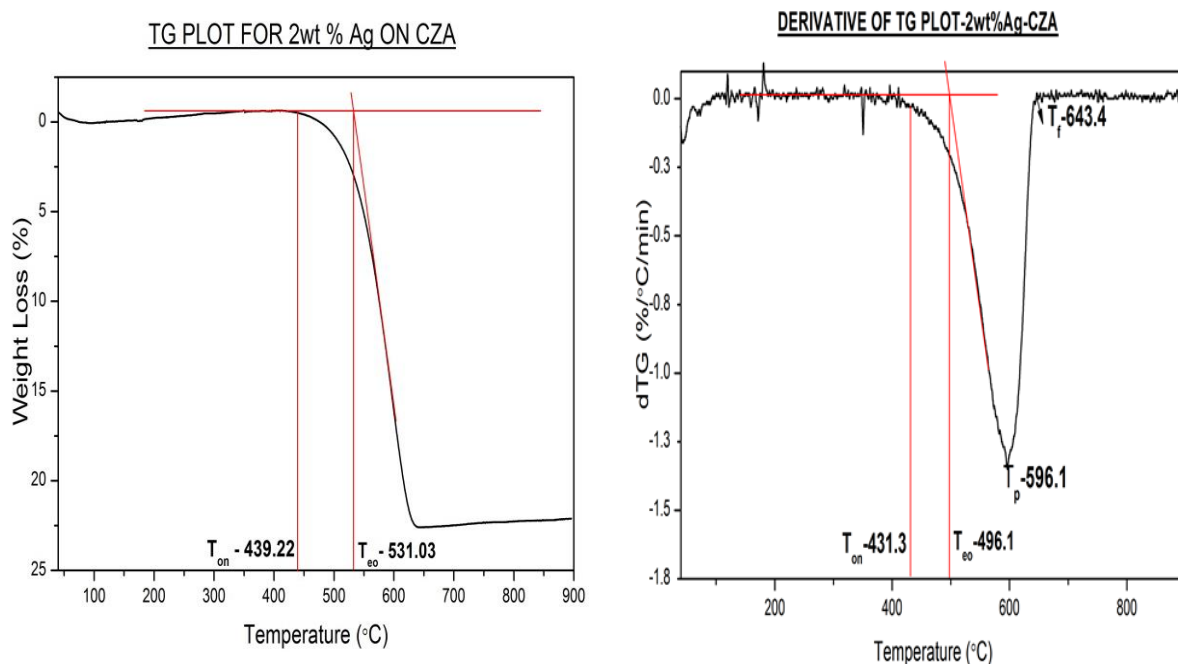


Figure 3.4 a) TG plot indicating onset, extrapolated and final temperatures; b) derivative of TG plots (dTG) indicating the onset, extrapolated onset, peak and final temperatures of soot oxidation

The combustion temperatures obtained were more accurate from the derivative of the weight loss than from the weight change plot. Nevertheless, the two sets of results obtained from the TG and dTG plots were comparable within $\pm 5^\circ\text{C}$. This was used for obtaining all combustion data for the remaining catalysts. Soot oxidation is a highly exothermic process as was observed from the DTA analyses showing the rate of heat flow (Figure 3.5). The reaction slowly began to increase in rate over a temperature range of 400-600°C and at this stage the reaction tended to become highly exothermic. As expected, therefore, the complete combustion resulted in a heat gain as seen in figure 3.5. The soot oxidation process was easily understood from the weight loss pattern while the derivative plots indicated any disturbance occurring during the analysis, leading to a very noise curve.

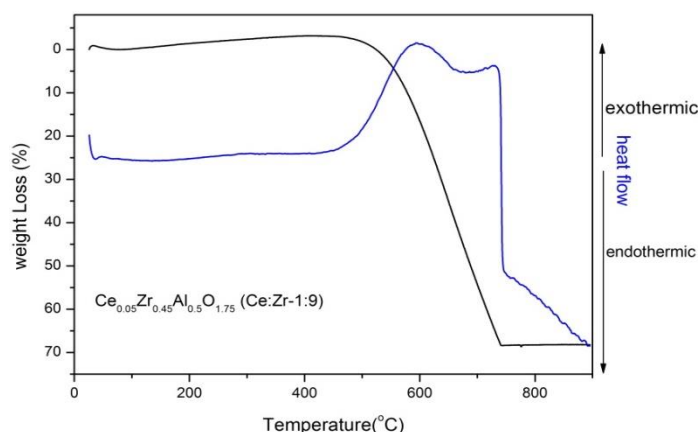


Figure 3.5 represents the weight loss and heat flow (DTA) occurring during soot oxidation as a function temperature for the Ce-Zr-1:9 support.

3.1.2.1 Soot oxidation activity –Varying Ce: Zr ratios

The oxidation activity for the various $\text{CeO}_2\text{-ZrO}_2\text{-Al}_2\text{O}_3$ supports with different Ce: Zr ratios from (1:9 to 9:1) was carried out under flowing air from 30-900°C and then analysed as described in section 3.1.2, to obtain the combustion temperatures. Figure 3.6 showed the loss in weight of soot from the initial 13mg (10mg catalyst + 3mg soot) or no weight loss (0%), at the start to the complete combustion of soot at around 750°C (75%). There was a steady mass loss due to combustion, at its peak between 500-700°C that determined the rate of soot oxidation. There was a small amount of weight loss observed from the catalyst after the first that contributed to the weight loss beyond 23%.

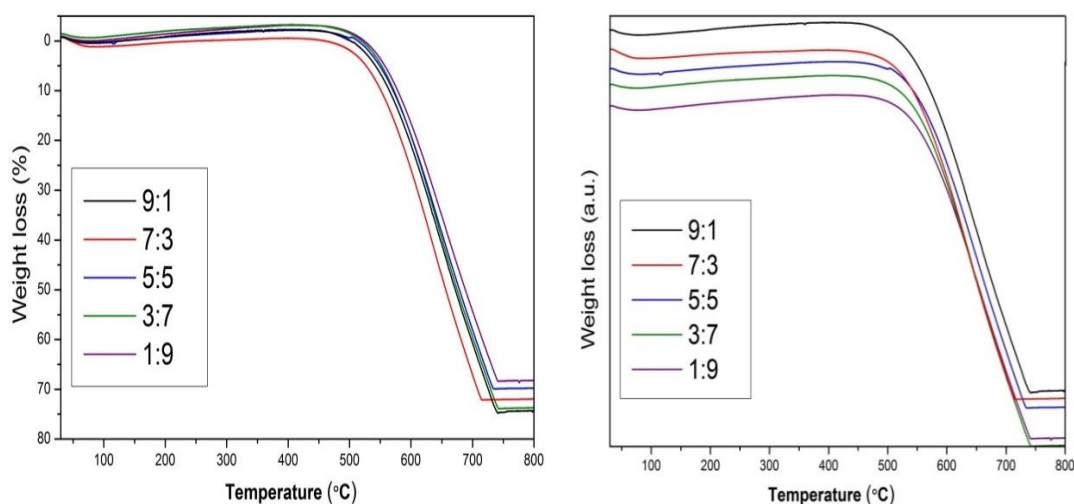


Figure 3.6 Soot oxidation activity for varying Ce:Zr ratios (the same plots on the right have been represented with an offset to identify the profiles distinctly)

The two plots shown in figure 3.6 illustrated the combustion activity. Figure 3.6a compared the five different ratios of Ce-Zr with respect to the loss of soot during oxidation as function of temperature. The red line represented the activity for Ce: Zr-7:3, which showed the best activity as shown in table 3.2.

Table 3.2 Soot oxidation activity for varying Ce: Zr ratios

Sl.No.	Ce:Zr ratios	Onset Temperature (T_{on}) (°C)	Extrapolated Onset Temperature (T_{eo}) (°C)	T_p (°C)	T_f (°C)
1	9:1	458	541	646	747
2	7:3	407	507	597	634
3	5:5	499	544	647	739
4	3:7	491	549	643	747
5	1:9	483	551	651	744

The results showed that the Ce:Zr-7:3 support reduced the temperatures from the reaction temperatures compared to uncatalysed soot oxidation (T_{on} -420°C, T_f - 760°C). This suggested that the support had the right proportion of CeO₂ to provide the lattice oxygen stored within it for the soot oxidation, on coming in contact with soot and also had sufficient Zr⁺ ions incorporated into the lattice, allowing sufficient mobility of the oxygen through these defects. As already discussed, the reducibility of the CZA was shown in the TPR profiles in figure 3.3. The catalysts function by a Mars vanKrevelen mechanism where the Ce⁴⁺ reduces to Ce³⁺ and this allows the O₂ stored in the lattice to traverse through the defects created by the introduction of Zr⁺ ions. The O₂ stored is now available for the soot to undergo oxidation on the surface of the support when it comes in contact with it as it passes through the DPF/CRT. The gaseous O₂ then oxidizes the reduced Ce³⁺ to Ce⁴⁺. This is the most commonly represented mechanism for soot oxidation.

Figure 3.7 illustrates the temperatures at which soot oxidation rate is maximum against Ce-content in the mixed oxide from literature [3, 4, 5]. The profile suggested that Zr⁴⁺ had deformed the lattice, creating more defects which could provide better oxygen

mobility in the structure and so, the changes in CeO₂ during the reaction were faster. The optimum activity was found to be between 0.7-0.9 Ce-content (molar fraction) [10].

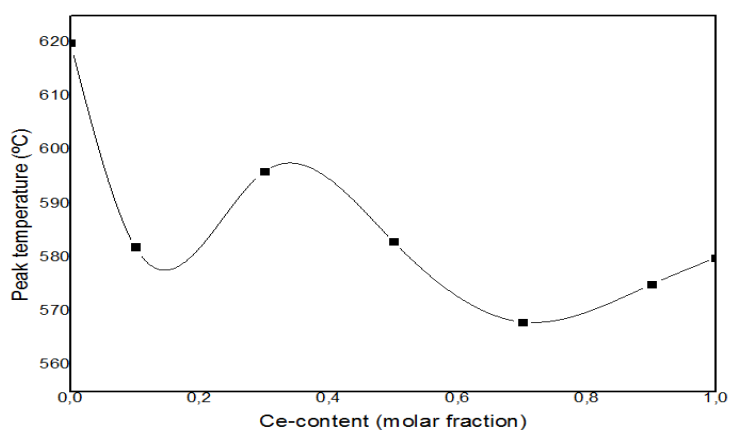


Figure 3.7 Soot activity versus increasing Ceria content [10]

3.1.2.2 Catalyst support - Varying ratios of Ce: Zr in Ce_xZr_{1-x}Al_{0.5}O_{1.75}

The Ce-Zr-7:3 support prepared by co-precipitation was tested for soot oxidation by mixing it with soot in different ratios as shown in figure 3.8. This was carried out to optimize the ratio of catalyst to soot for oxidation. The soot oxidation for ratios 1:12, 2:11, 3:10, 4:9 and 5:8, with a soot excess, was seen to be occurring at higher temperatures as compared to the soot and catalyst mixed with a catalyst excess as shown in table 3.3. The rate of combustion was faster in the case of a catalyst excess over soot.

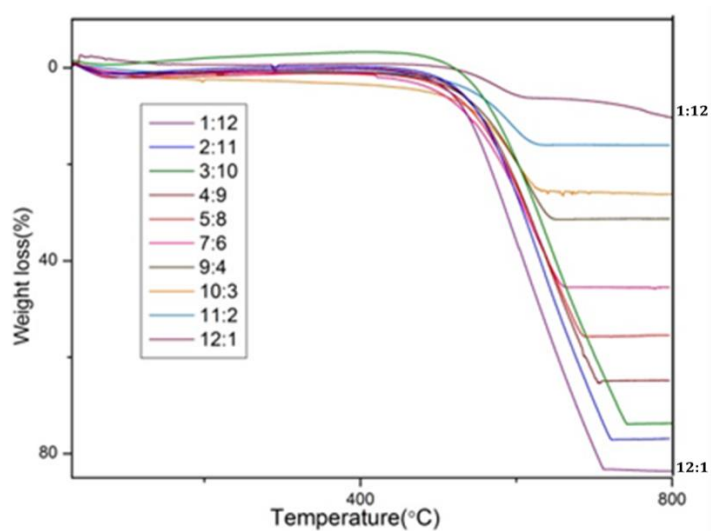


Figure 3.8 Soot oxidation activity for varying soot to catalyst ratios

In an aftertreatment system, the catalyst will be coated onto a filter, so that the soot may only be in contact only for a very short span of time. The oxidation occurs at the interface between the catalyst and soot. Thus an ideal condition would be an excess of catalyst and sufficient amount of soot as shown in the case of the catalyst: soot-10:3. The combustion temperatures reported for this ratio were lower than the others. It has thus been used as a standard for further analyses. The temperatures of oxidation reported showed that the onset and final temperatures were lower than that reported in literature[3,4,5,6] for the uncatalysed oxidation and 10:3 shows a rapid increase in the rate of the reaction between 500-600°C. Table 3.3 represented the oxidation temperatures of varying ratios of catalyst:soot.

Table 3.3 Soot oxidation activity for varying soot to catalyst ratios

Sl.No.	Catalyst:Soot ratios	Onset Temperature (T _{on}) (°C)	Extrapolated Onset Temperature (T _{eo})(°C)	T _p (°C)	T _f (°C)
1	1:12	400.4	490.5	604.5	718.3
2	2:11	413.7	492.7	631.4	727.03
3	3:10	395.4	489.6	625.4	747.1
4	4:9	422.3	484.6	638.5	716.3
5	6:7	411.1	479.9	632.5	697.4
6	7:6	412.5	463.7	621.8	671.7
7	9:4	409.7	496.1	613.7	661
8	10:3	407.5	507.7	597.4	633.8
9	11:2	401.6	497.1	593	642
10	12:1	416	488.04	577.5	634.02

3.2 Catalyst support preparation- Co-precipitation using Na₂CO₃, NH₃, NaOH

3.2.1 Characterization

The X-ray diffractograms for the various CZA supports prepared by the co-precipitation method showed a characteristic CeO₂-ZrO₂ (CZ) mixed phase, when the patterns were compared with the JCPDS database, showing a Ce_{0.75}Zr_{0.25}O₂ phase for the different supports. These were compared with the CeO₂-ZrO₂-Al₂O₃ (Ce:Zr-7:3) prepared by the impregnation method described above. The peaks for CeO₂ were observed in the case of the Al₂O₃ impregnated CZA support. In the case of the co-precipitated supports this was not observed, instead a mixed phase was observed.

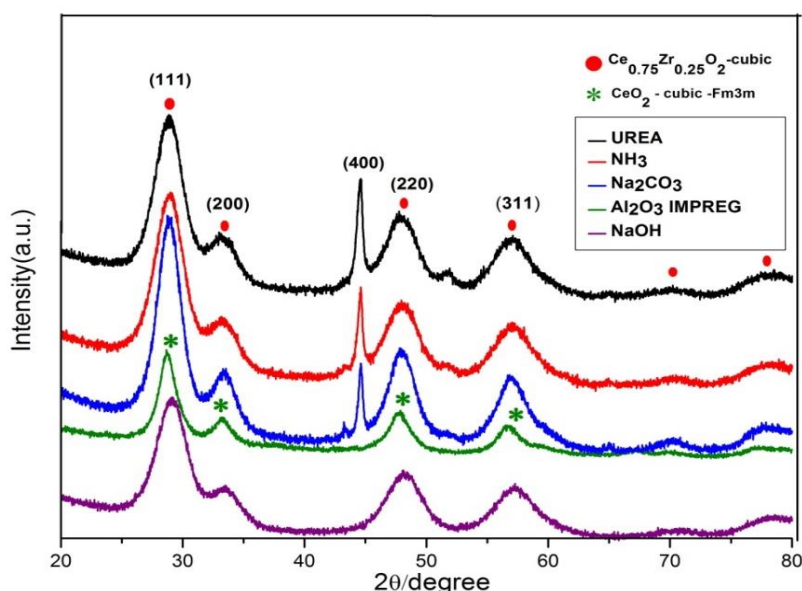


Figure 3.9 X-ray diffractograms for various CZA supports

The X-ray diffractograms showed a consistency in the cubic fluorite symmetry and confirmed the formation of CZ solid solutions. The CZ supports were also prepared in different ratios and compared with CZA to confirm the cubic structure as shown in figure 3.10. There was no individual $\alpha/\beta/\gamma$ -Al₂O₃ phase observed in case of CZA. This implied that the ZrO₂ and Al₂O₃ were well diffused into the CeO₂ crystal lattice, resulting in a perfect blend of the three metal oxides. The various precipitating agents yielded the same structure but CZA-Na₂CO₃ had smaller crystallites and a larger surface area as compared to CZA-Urea and CZA-NH₃.

The conventional co-precipitation method uses NH_3 as a precipitating agent which is not a very environmentally friendly substance and tends to react quite vigorously when introduced into the metal salt solution as compared to Na_2CO_3 [11]. Thus it would not be ideal if the catalyst was to be prepared on a large industrial scale using this precipitating agent. Figure 3.9 showed the formation of slightly more pronounced $\text{CeO}_2\text{-ZrO}_2$ phase peaks for $\text{CZA-Na}_2\text{CO}_3$ with smaller crystallites. Al_2O_3 seemed to be incorporated well into the CZ matrix. The crystallite sizes of these supports were between 6-8nm.

Table 3.4 Physical properties of various CZA supports

Sl.No	Catalyst	Surface area (m^2g^{-1})	Crystallite size (nm)	Peak temperature (reduction) $^\circ\text{C}$	H_2 consumption ($\mu\text{mol g}^{-1}$)
1.	Ce:Zr - Al_2O_3 Impregnation	98	6.4	543	152.3 652
2.	CZA - Na_2CO_3	148	3.1	436	1710
3.	CZA - NaOH	130	3.2	490	1649
4	CZA - NH_3	183	4.7	511	1570
5	CZA - Urea	170	4.2	511	1380

Different precipitating agents yielded $\text{CeO}_2\text{-ZrO}_2\text{-Al}_2\text{O}_3$ particles with varying surface areas and crystallite sizes. The average crystallite sizes were in the range of 3-4 nm (table 3.4). Smallest crystallites (3.1nm) were obtained from co-precipitation using Na_2CO_3 but there was a significant decrease in the surface area when prepared using this method. The surface areas of the support prepared using NH_3 was highest (183 m^2/g). The soot oxidation activity for the CZA-Urea and CZA-NaOH were much lower as compared to CZA- Na_2CO_3 despite having greater surface areas. Al_2O_3 impregnation yielded larger crystallites (6.4nm) as in this method there is a direct impregnation of the Al_2O_3 onto the surface of CZ. Thus it indicated that there was no significant mixing of the precursors solutions that would yield a homogeneous mixture

as in the case of co-precipitated supports. The crystallite sizes were taken as an average of the values obtained from the (111), (220) and (311) planes in the cubic system.

The reflection occurring at 42.5° (figure 3.9) was thought to be a distinct $\gamma\text{-Al}_2\text{O}_3$ phase. However, from examination of the plots below for pure $\text{CeO}_2\text{-ZrO}_2$ and CeO_2 it was thought that this could be due to a $\text{CeO}_2\text{-ZrO}_2$ interaction formed upon incorporation of the ZrO_2 into the CeO_2 crystal lattice and this varied in intensity with the change in preparation method. The diffractograms shown in figure 3.9 was matched with the JCPDS database for Al_2O_3 peak and this did not indicate the presence of any distinct Al_2O_3 phase.

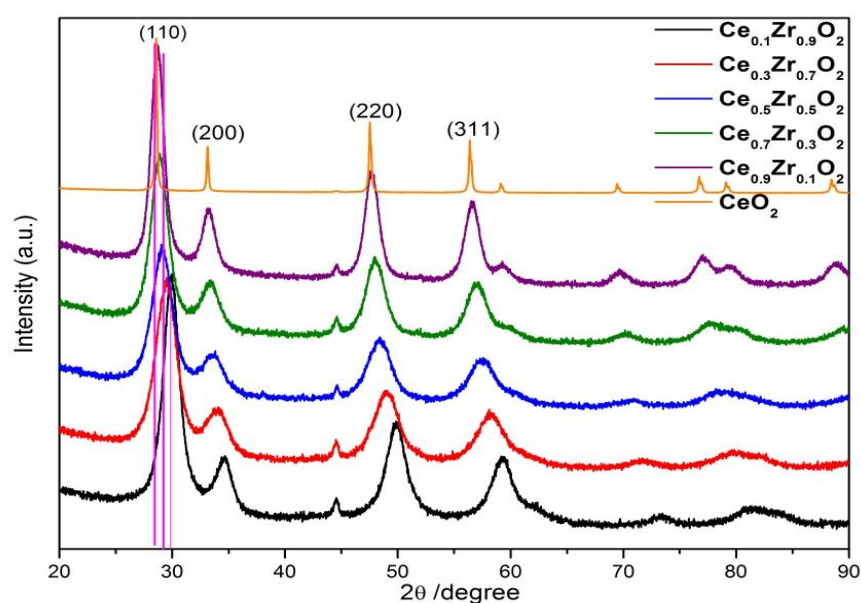


Figure 3.10 X-ray diffractograms for varying Ce: Zr ratios in $\text{CeO}_2\text{-ZrO}_2$ supports - The pink line indicates shift in peak with increase in crystallinity with increase in content of CeO_2

As Ce-content increased, the smaller peaks attributed to other CeO_2 planes were more noticeable: 59.1° , 69.5° , 76.7° , 79.1° and 88.5° . Moreover, the intensity of the peaks was higher in pure ceria as a consequence of a greater order of the atoms within the lattice and far larger crystallite size for CeO_2 [11]. The crystallite sizes for all mixed oxides were very similar except $\text{Ce}_{0.9}\text{Zr}_{0.1}\text{O}_2$ which had slightly larger value. The crystallite sizes of the CZA mixed oxides were smaller than those of the CZ oxides.

Table 3.5 Crystallite sizes for various CZ supports-varying Ce:Zr ratios

Sl.No	Catalyst support	Crystallite size (nm)
1	Ce _{0.1} Zr _{0.9} O ₂	5.7
2	Ce _{0.3} Zr _{0.7} O ₂	5.0
3	Ce _{0.5} Zr _{0.5} O ₂	46
4	Ce _{0.7} Zr _{0.3} O ₂	5.4
5	Ce _{0.9} Zr _{0.1} O ₂	8.0
6	CeO ₂	56.1

The main peak observed in every Raman spectrum (range 460-476 cm⁻¹) corresponded to an F_{2g} mode of a fluorite-type structure with Ce-O bonding (cubic lattice) (figure 3.11)[12]. The oxygen lattice vibrations tend to dominate the Raman spectra in these particular type of oxides, being very sensitive to the crystalline symmetry [11]. It could be clearly observed from the spectra (figure 3.10) that an increase in Ce-content resulted in greater intensity of the mentioned peak, indicating a characteristic cubic CeO₂ phase was more predominant apart from the higher Ce-content. The crystallite sizes for the mixed CZA oxides were smaller with larger surface area due to the incorporation of Al³⁺ into the CZ matrix as compared to the pure CeO₂ or CZ oxide.

The prepared Ce_xZr_{1-x}O₂ mixed oxides showed low surface areas (< 20 m²/g) with an adsorption isotherm characteristic of non-porous materials. Soot oxidation is a contact driven process where the soot comes in contact with the catalyst coated onto a filter. The benefit of a large surface area of catalyst is that it provides more area for contact with the soot. Since the reaction kinetics for soot oxidation is extremely rapid, the need for a large surface area is not a vital prerequisite. The pore sizes of soot particles were usually greater than 100nm and thus were in the range of macroporous particles. These particles would not be accommodated into microporous or mesoporous particles in the catalyst. Thus it is not essential for these catalysts to possess such porosity.

Upon incorporation of Zr⁴⁺ into the ceria, lattice defects could arise due to the smaller size of the Zr⁴⁺ ion as compared to Ce⁴⁺ and this improved the oxygen mobility within the lattice [16]. The size decrease of the fluorite peak is in complete agreement with a change in the lattice toward a more tetragonal phase, characteristic of a ZrO₂

structure [17]. Indeed, if $\text{Ce}_{0.1}\text{Zr}_{0.9}\text{O}_2$ spectrum were to be closely analysed, two additional peaks could be distinguished around 300 cm^{-1} and 600 cm^{-1} , assigned to a typical vibration mode of a tetragonal phase [18]. This fact was in agreement with XRD results that suggested the presence of a tetragonal phase in the $\text{Ce}_{0.1}\text{Zr}_{0.9}\text{O}_2$ with excess ZrO_2 . The peak assigned to a cubic vibration mode was also observed at 476 cm^{-1} , and it is attributed to the small Ce-content. These observations suggested a co-existence of cubic and tetragonal phases for the catalyst with higher Zr-content, whereas the rest of mixed oxides show predominantly cubic crystal systems.

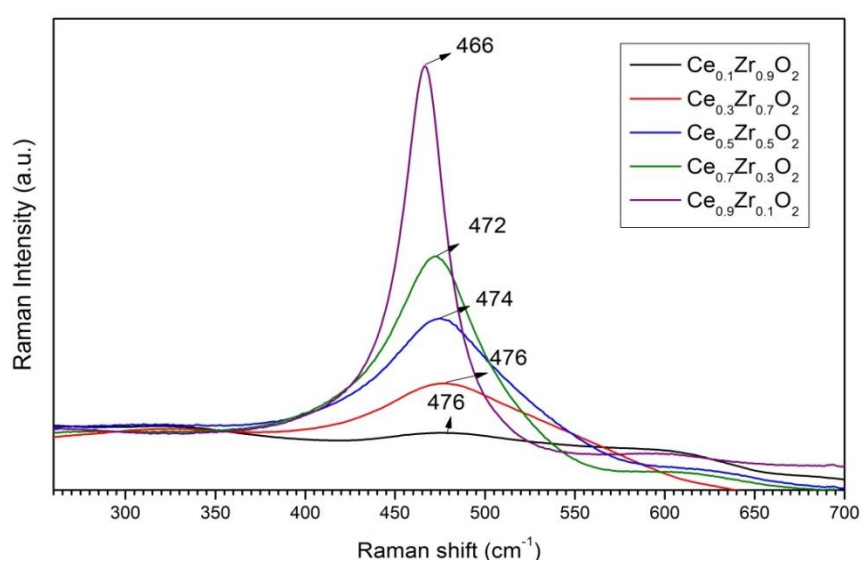


Figure 3.11 Raman spectra for the varying Ce: Zr ratios in $\text{CeO}_2\text{-ZrO}_2$ supports

Zr⁴⁺ incorporation could result in changes in the vibration frequencies of Ce-O bonds in the mixed oxides as a consequence of different ionic radius of cerium and zirconium ions [11]. The smaller ionic radius for Zr⁴⁺ enabled the contraction of the lattice so that vibrations were faster. Hence, the band shifts could be expected at higher frequencies. Raman spectroscopy confirmed the cubic symmetry of the CZ mixed phase for various CZA supports prepared using different precipitating agents. The additional broad bands at 300 and 605 cm⁻¹ were due to the distortion of the Raman active oscillation of cubic, F_{2g} symmetry. The minor peak at 300cm⁻¹ was observed only in the case of CZA-NH₃ but this was not very significant, and thus most of the crystallites were of the same cubic mixed oxide phase.

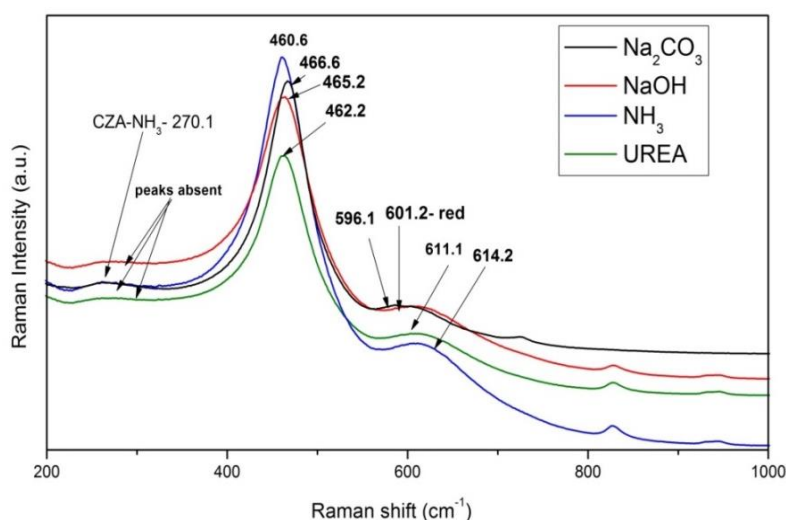


Figure 3.12 Raman spectra for various CeO₂-ZrO₂ supports

The TPR profile for CZA-Na₂CO₃ (figure 3.13) showed that the bimodal nature of CeO₂ reduction was modified and the peak area was larger, thus proving the greater extent of reducibility of this support over other co-precipitated supports. The hydrogen consumption peaks are attributed only to the reduction of Ce⁴⁺ to Ce³⁺ as Zr⁴⁺ and Al³⁺ are non-reducible [13]. The first peak 530°C was related to the reduction of surface ceria and small crystallites, while the second peak (700-800 °C) was linked to the reduction of the bulk constituted of larger crystallites. Some researchers have also studied the reduction properties of ceria mixed oxides. Katta *et al.* observed a single reduction peak in CeO₂-La₂O₃ and CeO₂-ZrO₂ solid solutions and this peak was associated with a more facile reduction of the mixed oxides [11]. The two expected peaks appeared together due to the generation of defects in the structure as a

consequence of the substitution of Ce^{4+} cations by La^{3+} or Zr^{4+} . These modifications lead to the rapid diffusion within the lattice resulting in a single peak in the reduction profile. The single peak for reduction showed that the surface and bulk reduction occurred simultaneously, in the temperature range of 300-590°C, thus providing the O_2 stored in the CZA lattice to migrate through the defects in the lattice. The other supports showed a typical bimodal reduction profile, with the surface reduction occurring at 350°C and bulk reduction occurring at higher temperatures.

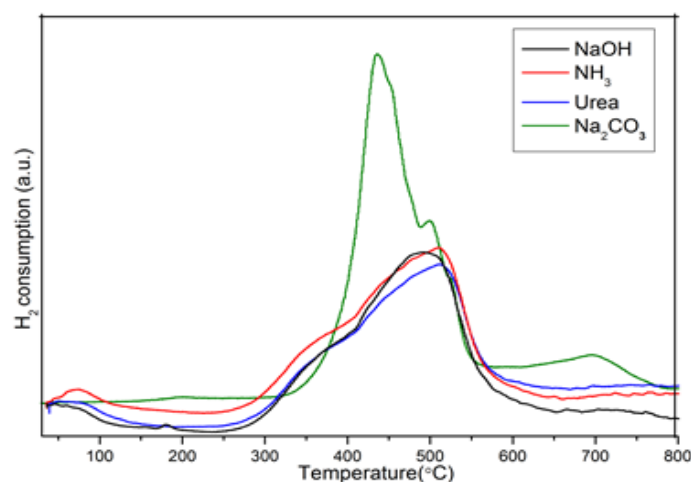


Figure 3.13 TPR profiles for various CZA supports

The main defect centres were the Ce^{3+} ions, with the formation of oxygen vacancies (O^{2-}) neutralising the charge imbalance. The cubic fluorite structure was still maintained even after reduction at such high temperatures. The re-oxidation of CeO_2 when exposed to air at room temperature, indicating the ease of lattice oxygen availability and the retention of the structural feature, was a major factor for the use of these materials as supports in three way exhaust catalysis [8, 13, 14].

An important aspect to be noticed from figure 3.13 was that the hydrogen consumption in the low temperature region tended to increase with increase in surface area of the CZA, thus drawing a linear correlation between the surface area and the amount of hydrogen consumed at low temperatures [15]. The different kinds of O^{2-} ions could be steps, kinks or corners projecting of different co-ordination numbers. A sequence of steps for the ceria reduction which were described previously, as from literature, were summarised below [15, 16]

- (i) The chemisorbed hydrogen dissociated to form a surface hydroxyl group

- (ii) Then there was a formation of anionic vacancies and reduction of neighbouring Ce^{4+} ions.
- (iii) The hydrogen and hydroxyl groups tended to recombine to form water.
- (iv) Surface anionic vacancies diffused into the bulk material.

This was represented in a model shown below in figure 3.14.

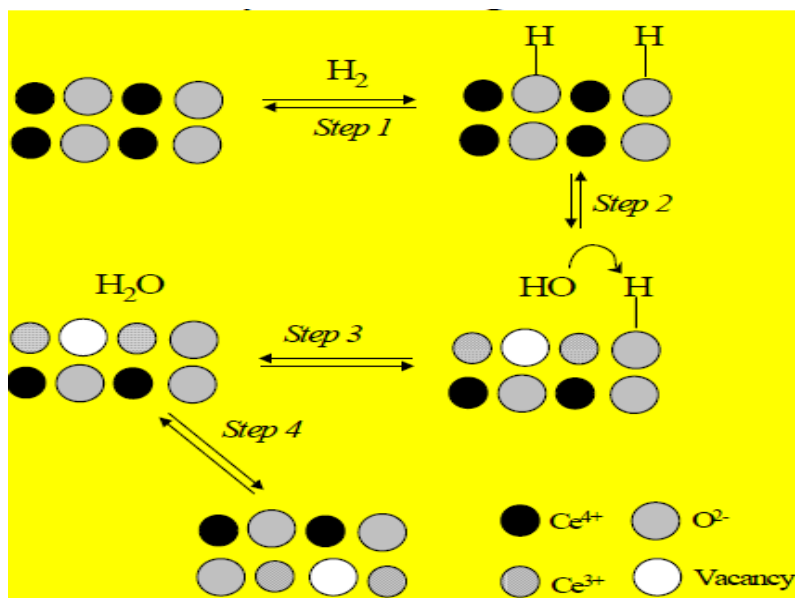


Figure 3.14 CeO_2 reduction model [15]

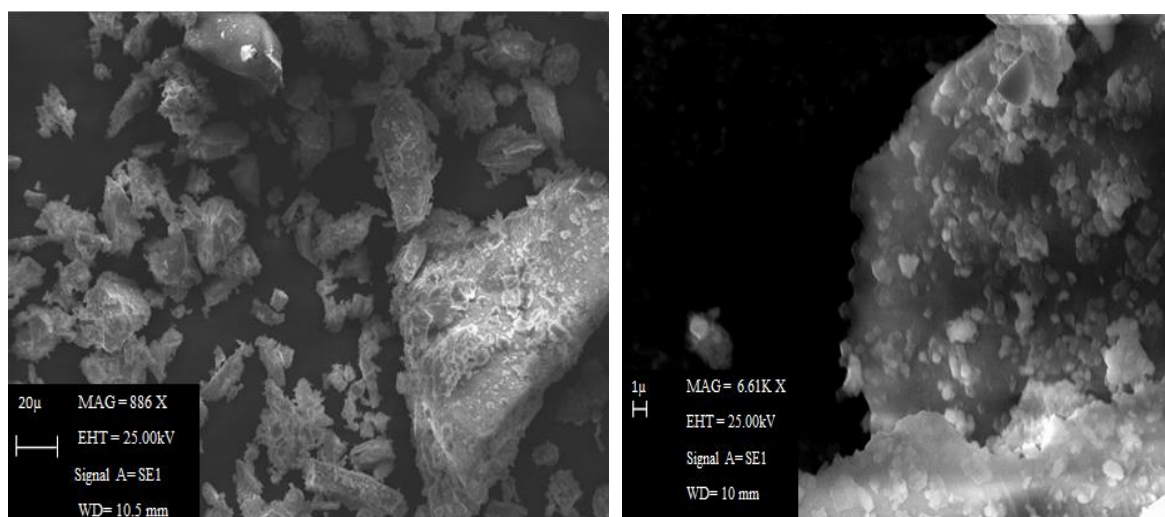


Figure 3.15 SEM micrographs for CZA- Al_2O_3 supports- a)886 X; b)6.61KX

Al_2O_3 impregnated CZA catalysts showed a distinct presence of the Al_2O_3 particles on the CZ surface as was observed by SEM in figure 3.15 and especially at higher

magnification of 6.61KX. The Al_2O_3 particles were seen to be present on the top of the CZ surface. This observation was supported by the EDX analysis (figure 3.16) of a CZA particle that showed a distinct concentration of Al in the form of its oxide as a percentage of weight and as a concentration of atomic percentage. The particles were of the size 1-20 μ . Smaller particles were present atop larger ones.

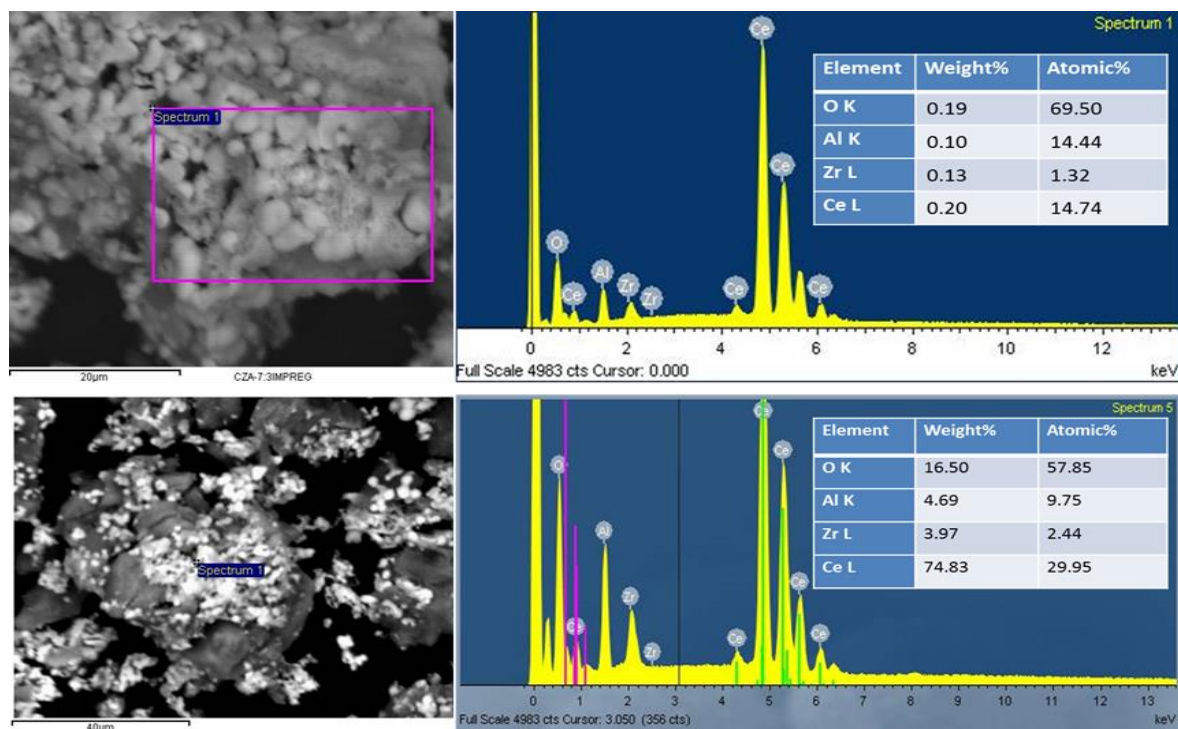


Figure 3.16 EDX a)region, b)point scan showing elemental composition of CZA- Al_2O_3

EDX was used to quantify the amount of CeO_2 and ZrO_2 in the $\text{CZA-Al}_2\text{O}_3$ impregnated material. For this purpose, a point scan was carried out as shown in figure 3.16 that indicated that the major concentration in the case of the Al_2O_3 impregnated catalyst was CeO_2 but there was a trace of Al_2O_3 observed as well. This showed that the mixture may not be completely homogeneous due to the preparation method. The table indicated the concentration of the elements in the area, shown as an inset in figure 3.16. Point analysis and area analysis of the sample particle revealed that ceria was the predominant phase as was seen from the XRD and Raman spectroscopy. Al_2O_3 impregnation onto CZA led to an increase in size of the CZA particles and the crystallites were as big as 6.4nm as compared to the well dispersed $\text{CZA-Na}_2\text{CO}_3$ particles. The Ce:Zr ratio was compared using EDX and XPS against the theoretical weight ratio indicating a

ratio of Ce:Zr-2:1 from both analysis. This was in accordance with the ratio used for preparation.

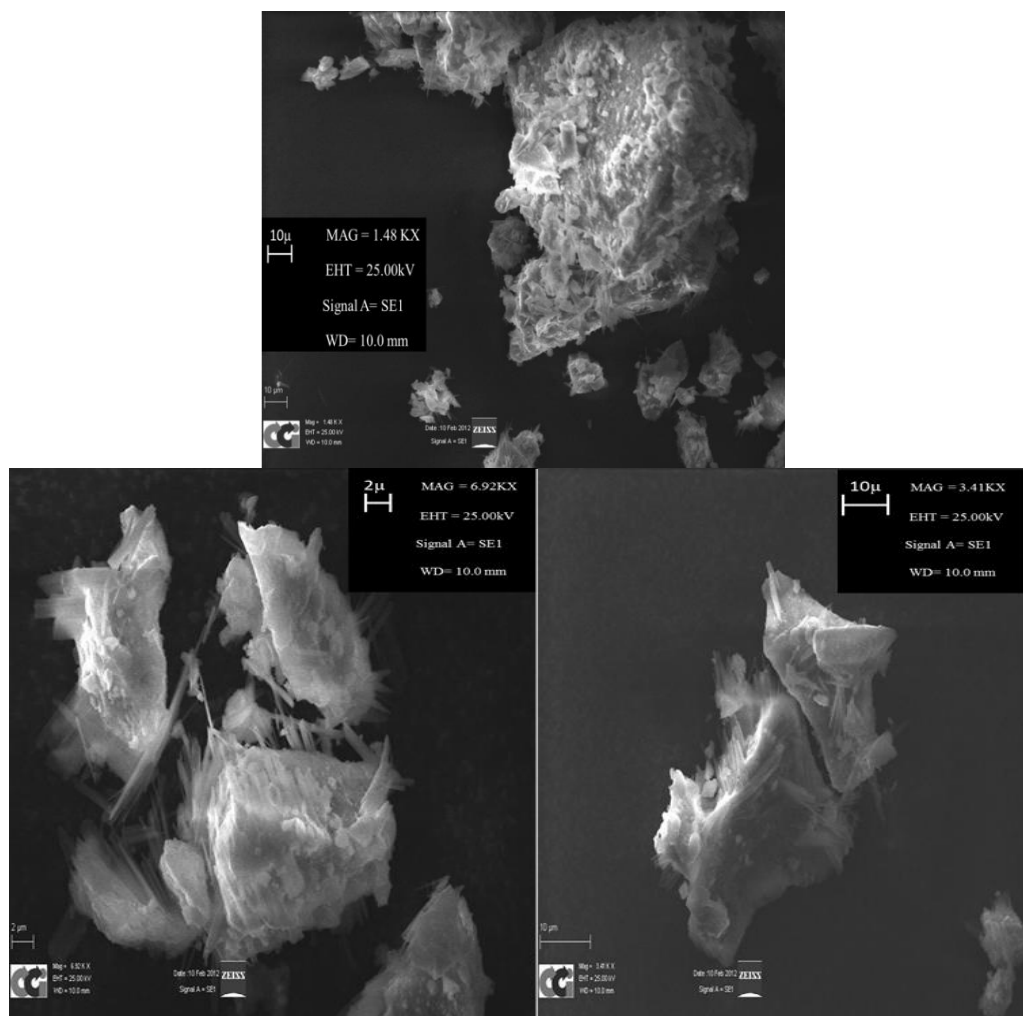


Figure 3.17 SEM micrographs for CZA-Na₂CO₃ precursor - a)1.48KX, b)6.92KX, c)3.41KX

CZA-Na₂CO₃ when calcined from the above precursors at 500°C at 5°Cmin⁻¹ for 5 hours under flowing air resulted in ordered agglomerates of CeO₂-ZrO₂-Al₂O₃ particles with no distinct Al₂O₃ phase present, as was seen from XRD and EDX. There was a distinct presence of cubic CeO₂. The CZA particles were smaller compared to the Al₂O₃ impregnated supports, as there was a thorough mixing of the precursors together. The small support particles were constituted of small crystallites of ~3 nm. Thus the Al₂O₃ incorporation into the CZ matrix, as was seen from XRD, Raman and EDX techniques, indicated that the Al₂O₃ restricted the growth in size of the particle. Several large pores were evident on the support as is indicated in figure 3.18.

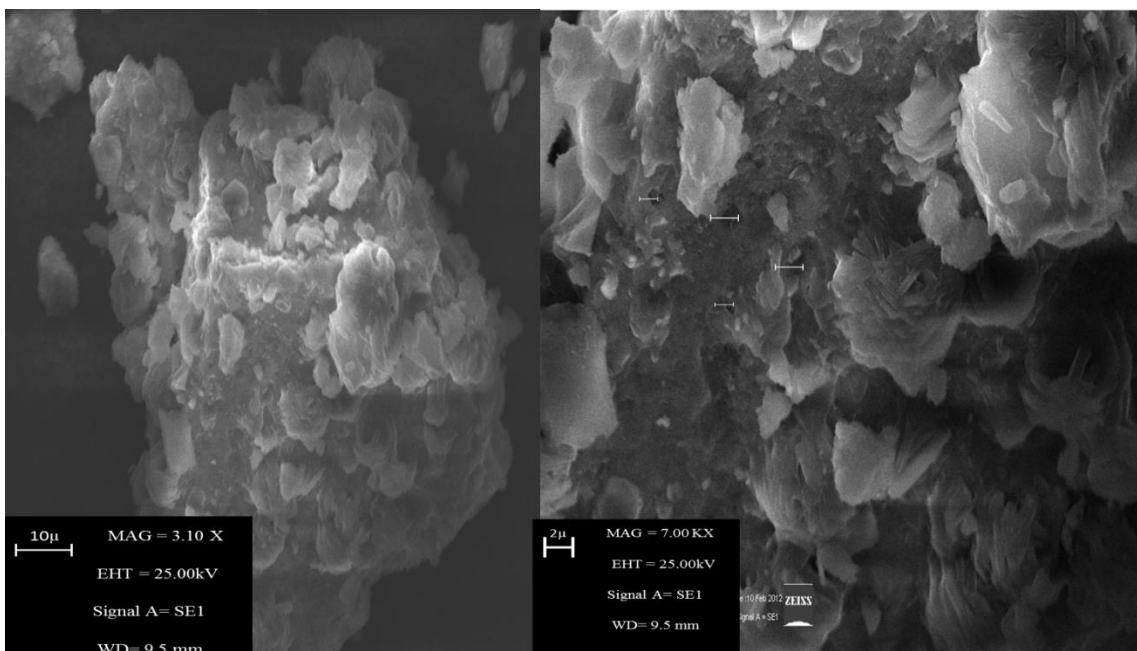


Figure 3.18 SEM micrographs for CZA- Na_2CO_3 calcined supports

CZA- Na_2CO_3 (7:3) particles were made up of particles of the size 1-20 μm . The CZA particles were seen to clump together giving rise to large particles. No bright spots were observed on the back scattered electron detection that would have indicated the distinct CeO_2 and ZrO_2 particles due to the higher atomic mass of cerium particles. But from the figure 3.18 no such spots were observed which was in agreement with the XRD patterns shown earlier, indicating a well dispersed CZA phase.

3.2.2 Soot oxidation activity

The soot oxidation activity was best using the CZA- Na_2CO_3 support indicated by the green line in figure 3.19. The weight loss pattern from the TG and the dTG plots showed that the rate of the oxidation was rapid in the presence of the CZA- Na_2CO_3 material. The onset temperatures for the oxidation was 345 $^\circ\text{C}$ and the combustion was complete by 570 $^\circ\text{C}$ as shown in table 3.6. This showed that the onset of activity had been lowered by 200 $^\circ\text{C}$, compared to the uncatalysed soot oxidation. The CZA-urea support showed the least activity and had higher combustion temperatures for the soot compared to the other co-precipitated supports but there was more loss of catalyst upon using the Al_2O_3 impregnated CZA support as observed from the figure below. Incorporation of Al_2O_3 into the CeO_2 - ZrO_2 matrix helped to reduce the lattice

strain/parameter, due to the formation of Ce-Zr-Al-O solid solutions, with the incorporation of smaller radii Al^{3+} (0.57\AA) in exchange for larger Ce^{4+} (0.97\AA).

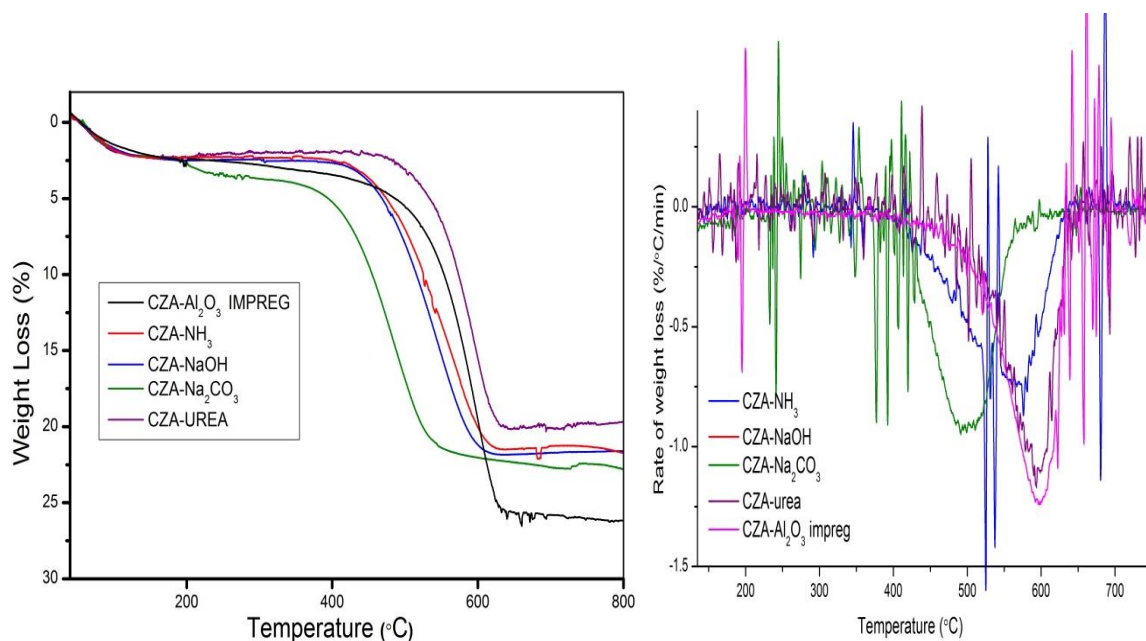


Figure 3.19 Soot oxidation activity for various CZA supports

The CZA-NH₃ and CZA-NaOH showed very similar activities. The use of Na₂CO₃ gave a more homogeneous mixed oxide with smaller crystallites, larger surface and greater reducibility of the support. Smaller crystallites were formed due to the thorough mixing of the precursor solutions and also due to the reduction in the growth of the size of the CZ crystallites, by the introduction of Al₂O₃ as a diffusion barrier. The crystallite sizes of the supports were quite similar. The large surface area for CZA-Na₂CO₃ was expected to provide a larger interface with soot, and so enhanced the rate of oxidation.

Table 3.6 Soot oxidation activity of various CZA supports (catalyst:soot-10:3)

Sl.No.	Precipitating agents	Onset Temperature (T_{on})(°C)	Extrapolated Onset Temperature(T_{eo}) (°C)	T_p (°C)	T_f (°C)
1	NH ₃	374.7	409.3	575	644.3
2	Na₂CO₃	345.3	374.7	485.1	570
3	NaOH	388	410.6	496.4	567.2
4	UREA	474	507	594	634
5	Al ₂ O ₃ IMPREGNATION	407	507	597	634
6.	Pure soot	420	460	652	717

The weight loss occurred as the oxidation took place, and therefore the rate of weight loss (dTG) was a measure of the rate of the reaction as a function of temperature. This data has not been represented as the dTG plots recorded any disturbance reported as noise. At the start of the reaction there was no weight loss. Over time the soot began to get combusted slowly, at the start, and then rapidly around 400°C, which gave rise to the peak temperature. Table 3.7 summarised the data for the comparison between the activities of the mixed (CZ) and pure oxides. The mixed oxides were prepared by co-precipitation using Na₂CO₃ as the precipitating agent.

Table 3.7 Summary of characteristic temperatures in catalysed soot oxidation with Ce_xZr_{1-x}O₂, CeO₂ and ZrO₂.

Catalyst	T_{on} (°C)	T_{eo} (°C)	T_p (°C)	T_f (°C)
ZrO ₂	460	480	620	710
Ce _{0.1} Zr _{0.9} O ₂	420	472	582	623
Ce _{0.3} Zr _{0.7} O ₂	455	477	596	631
Ce _{0.5} Zr _{0.5} O ₂	450	470	583	637
Ce _{0.7} Zr _{0.3} O ₂	463	473	568	631
Ce _{0.9} Zr _{0.1} O ₂	435	465	575	623
CeO ₂	420	475	580	690
Bare soot	420	460	652	717

The onset temperatures revealed that the mixed oxides with the highest Ce- and Zr-content oxides were remarkably more active than other of mixed oxides, but the extrapolated onset temperatures were almost identical in all cases, including those for pure oxides CeO₂ and ZrO₂. However, there were more variations with respect to the peak temperatures, with ZrO₂ showing a peak temperature of 52°C higher than the most active material (Ce_{0.7}Zr_{0.3}O₂). Analysing the value given in Table 3.7 and that for the mixed CZ and CZA oxides, the mixed oxides and CeO₂ showed T_p within 16°C range, being slightly inferior at higher Ce-content. The incorporation of Al₂O₃ also helped reduce the onset temperatures.

The differences among the final temperatures of soot oxidation were very small for all mixed oxides, with pure CeO₂ and pure ZrO₂ showing a very poor performance in this aspect. Thus the thermal stability seemed to be a critical issue for pure CeO₂, as it was seen in early TWCs studies [17]. This has been discussed in detail towards the end of this chapter. Several researchers have tried to improve this property employing different doping-cations such as Ca²⁺, Mg²⁺, La³⁺, Y³⁺, Si⁴⁺ or Zr⁴⁺ among others, [17,18] reporting more stable mixed oxides against sintering for those cations with smaller ionic radii than that of Ce⁴⁺. Thus, CZA was more active than bare CeO₂. Furthermore, it could be said that the lack of reducibility of Zr⁴⁺ in ZrO₂ was responsible for its poor activity.

3.3 Catalyst support –variation of preparation method

3.3.1 Characterization

The CeO₂-ZrO₂-Al₂O₃ support with Ce: Zr – 7:3 prepared by co-precipitation using Na₂CO₃ was identified as having the highest activity for soot oxidation. The method of preparing these co-precipitated supports was varied based on the introduction of the precursors as described in chapter 2. The different supports prepared were named as:

a) *CZA precursor*- in which all the three precursor solutions were mixed together before precipitation; b) *CZ prec. + Al prec.* – in this the CZ precursor solution was precipitated out simultaneously with the Al₂O₃ precursor and the two precipitated solutions were combined together before drying; c) *CZ prec. dried + Al prec. dried* - in which the CZ precursor was precipitated out by the Na₂CO₃ separately dried and then mixed with the

simultaneously precipitated and dried Al_2O_3 precursor. This kind of mixing was attributed to a physical mixing (by hand) of the precursors; d) *CZ prec. (dried+calc.)+Al. prec. (dried+calc.)*-in this case the CZ formed oxide post drying at 110°C and calcination at 500°C for 5 hrs in flowing air was ground physically by hand with Al_2O_3 oxide formed in a similar manner; e) *CZA- Al_2O_3 impregnation*- the above co-precipitated supports were finally compared to the impregnated support.

The CZA supports prepared in different ways showed similarity in phases and possessed a cubic $\text{CeO}_2\text{-ZrO}_2$ mixed phase ($\text{Ce}_{0.75}\text{Zr}_{0.25}\text{O}_2$ - from JCPDS database). But these supports had different crystallite sizes owing to their method of preparation. In the case of mixing all the precursors together before precipitation - case a)CZA-precursor, the crystallite size is 3.1nm and surface area ($148\text{m}^2\text{g}^{-1}$) was larger than for the other supports. This was due to the fact that there was thorough mixing of the precursors before the formation of oxides and no distinct single phases were present, indicating that a homogeneous solid solution is formed.

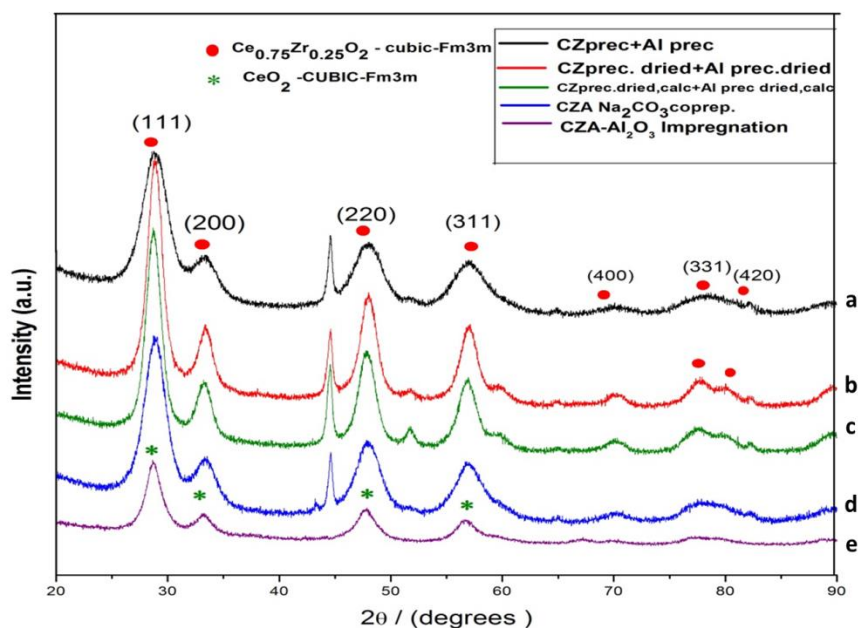


Figure 3.20 X-Ray diffractograms for CZA-varying the preparation methods

The crystallite size could be linked to the peak width, that showed that peaks for CZA-precursor (blue) and in the case b) CZprec. +Al prec. (4.2 nm) shown by the black line were broader and thus had smaller crystallite size (3.1 nm). There was formation of a homogeneous mixture of the precursors leading to a well defined cubic crystal

structure upon calcination. Precipitation of the precursors, all together or separately followed by drying and calcining yielded similar structural properties but slight difference in activity.

In case of c, d and e, the crystallites were larger in size (red-6.4nm, green-6.5 nm, purple-6.4 nm respectively) compared to the others, owing to the fact that physical mixing of the supports and direct impregnation as in case e yielded segregation of phases (as seen in figure 3.20). There was a small peak distinctly observed at $2\theta=52^\circ$, a small shoulder peak observed at $2\theta=61^\circ$ and small peaks at $2\theta=72, 78$ and 80° . These were not representative of the cubic symmetry of the CeO_2 phase or indicative of a mixed $\text{CeO}_2\text{-ZrO}_2$ phase. This could be due to the separation of the ZrO_2 or $\gamma\text{-Al}_2\text{O}_3$ phases from the mixture. The crystallites sizes are given in table 3.8.

Raman spectroscopy for the different supports were quite similar representing the superior F_{2g} vibration mode for cubic fluorite CeO_2 phase. The peaks for the 300 and 600cm^{-1} CeO_2 cubic phase distortion or also known as the Raman active mode for t'' -tetragonal ZrO_2 phase was more distinct in the case of supports prepared by c and d – physical mixing methods, mentioned above. This could be correlated to the increased peak intensity shown by XRD giving rise to larger crystallites.

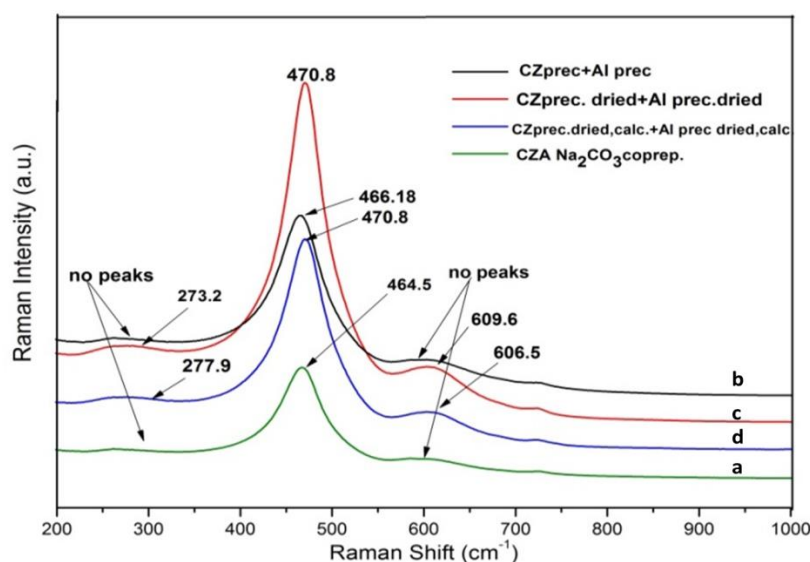


Figure 3.21 Raman spectra for various CZA supports prepared by varying the method of preparation

While in the case of individual precursor mixing followed by precipitation (case b), and co-precipitation of all the precursors mixed together (case a), these peaks were not significant or mostly absent. These were better dispersed supports with smaller crystallites. The Al₂O₃ was incorporated into the CeO₂-ZrO₂ lattice and provided more thermal stability to the supports.

Table 3.8 Physical properties of CZA supports prepared in different ways

Sl.No	Label	Catalyst	Surface area (m ² g ⁻¹)	2θ	Crystallite size (nm)	Peak temperature (reduction) °C	H ₂ consumption (μmol g ⁻¹)
1.	e	CZA -Al ₂ O ₃ IMPREGNATION	98	28.72	6.4	543	152.35 654
2.	a	CZA- Na ₂ CO ₃	148	28.86	3.1	436	1710
3.	b	CZprecursor+Al precursor mix	47	28.79	4.2	458 514	826 1526
4	c	CZ prec.dried+Al prec. dried	27	28.7	6.5	487 501 690	873 763 376
5.	d	CZprec.dried,calc.+ Al prec.dried,calc.	50	28.71	64	489 686	995 452

Table 3.8 reports the surface areas, crystallite sizes and H₂ consumption values for the different CZA supports. The growth of crystallites in nano-crystalline materials can be explained by the coalescence of small neighboring crystallites upon atomic diffusion or the discrete attachment of crystallographically oriented particles [19]. The nano-crystallites with large surface area and low density may coalesce to decrease their surface energy. In this kind of oriented attachment, two small nanocrystallites combined to form a larger crystallite without any atomic diffusion. The probability of contact between the nano-crystallites in appropriate orientations determines the orientation attachment mechanism. In the case of co-precipitation the mixing of the precursors was on an atomic level. Thus the Al³⁺ ions in CZA-Na₂CO₃ tend to prevent the crystallite growth, by suppressing its aggregation through this probable mechanism, thereby giving a more homogeneous catalyst with smaller crystallites as opposed to the

mechanical mixing method where the physical grinding of the precursors did not favour a good contact between the Al^{3+} ions and the CZ matrix leading to larger crystallites.

The TPR profiles for the varied CZA- Na_2CO_3 supports showed that the precursors mixed together, represented by the black line, showed greatest ease in reduction and the peak temperature was 436°C , where the surface CeO_2 (in CZA) was seen to reduce (ZrO_2 and Al_2O_3 non-reducible). A smaller peak representing the bulk reduction occurred at 700°C (figure 3.22). The peak area was maximum in this case and thus the showed greatest extent of reducibility. This support thus exhibited the ease for Ce^{4+} reduction to Ce^{3+} , at temperatures between $400\text{--}800^\circ\text{C}$. The Al_2O_3 in the support also helped to maintain the thermal stability. Zr^{4+} and Al^{3+} incorporation into the CeO_2 lattice introduced structural defects due to the smaller sizes of the two ions in comparison to Ce^{4+} . The charge equilibrium by the insertion of Al^{3+} further enhanced the Ce^{4+} reduction to Ce^{3+} .

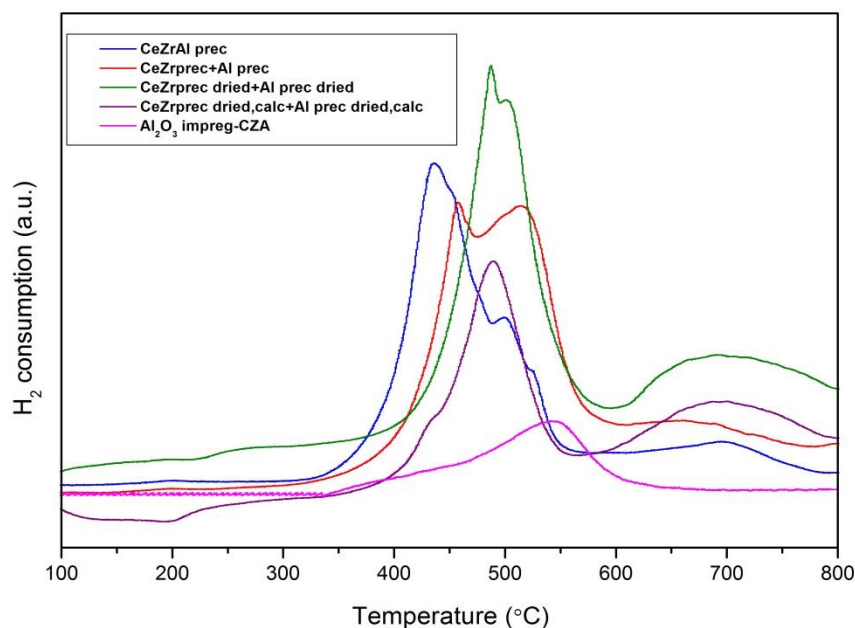


Figure 3.22 TPR profiles for the various CZA supports prepared using various methods

In the case of mixing the precursors of CZ and Al separately, the peak reduction temperatures were slightly higher than for mixing the precursors together (459°C - surface, 690°C - bulk). The reduction profile showed a similar approach as in the case of the CZA-precursor mixing. The physical mixing methods had slightly different reduction profiles. The dried precursors when mixed before calcination showed a high peak

temperature for reduction at (488°C – surface, 690°C - bulk). In the case of the supports physically mixed after drying and calcining, the peak temperature was at (488°C-surface, 690°C-bulk) Thus the reduction of CeO₂ did not occur with ease, due to the poor interaction between the oxides. The ZrO₂ and Al₂O₃ were not well incorporated into the lattice. Physical mixing, by hand, in a pestle and mortar, did not yield very good supports as compared to the co-precipitated ones. The insertion of Al³⁺ into the CZ matrix was poor and thus the thermal stability of these supports was not expected to be high.

3.3.2 Soot oxidation activity

The oxidation temperatures as shown in table 3.9 indicated that the CZA-Na₂CO₃ support was the best method of preparation of the support. The incorporation of the Al³⁺ into the CZ matrix had improved the reducibility and thermal stability of this support, as shown in the last part of this chapter. The CeO₂ reduction to Ce₂O₃ was also readily possible in this case, as shown in the TPR profiles and the temperature of reduction was in the range of the onset, peak and final temperatures of combustion of the soot, when mixed with this support. Thus suggesting that the oxygen stored in the lattice of CZ was readily available as it passed through the defects created in the structure by the incorporation of smaller ions such as Zr⁴⁺ and Al³⁺ into the CeO₂ cubic fluorite structure. Several authors have proposed a Mars-Van Krevelen mechanism as shown in Figure 3.23 [20, 21]. Soot is oxidised by CeO₂ using lattice oxygen produced on its reduction to Ce₂O₃. As the reaction is under air the external oxygen is able to re-oxidise Ce(III) to Ce(IV) which can then undergo another redox cycle by oxidising more of the carbon in soot.

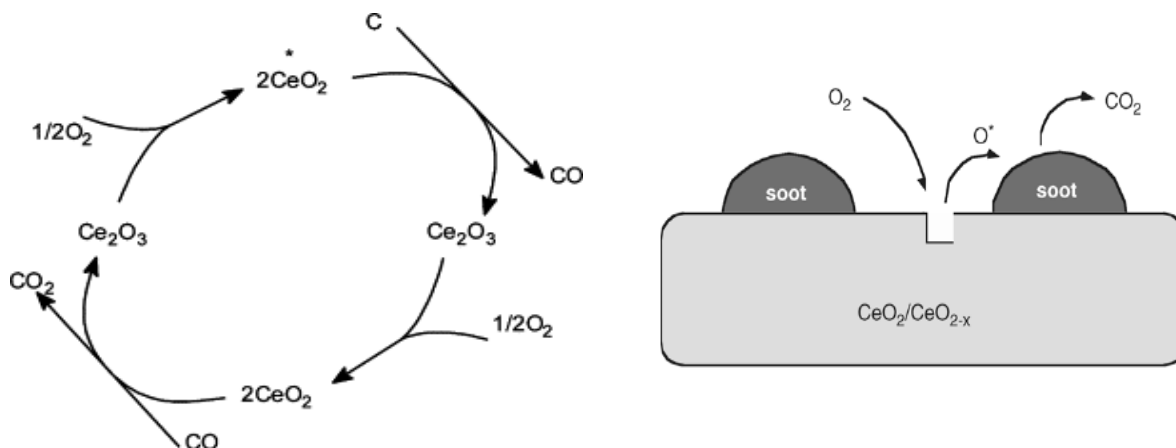


Figure 3.23 Mars vanKrevlen mechanism for the redox reaction of CeO₂ [21]

The impregnated support was not as active as the co-precipitated supports or the physically mixed support. This was probably because of the weakest interaction of the supported Al_2O_3 onto the surface of the CZ structure. Although in the case of physical mixed-dried precursors before calcination, their activity was good, these supports were not very thermally stable (tested using TGA for successive runs with fresh charge of soot) and were made of large crystallites, with lower surface areas. In the case of the physical mixing of the calcined CZ and Al_2O_3 oxides to form the CZA support, the oxidation temperatures of the soot were highest as shown in table 3.9.

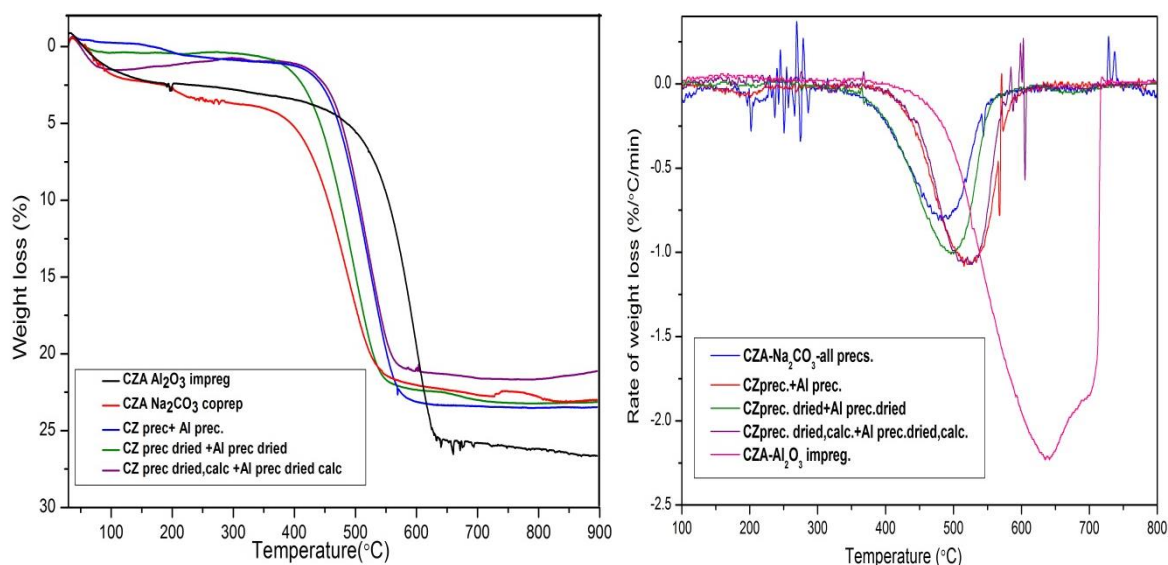


Figure 3.23a Soot oxidation- CZA-varying method of preparation

The ease of reducibility of c,d as seen in figure 3.22 was poor, in the above two cases and this did not facilitate the rapid reduction through the Mars vanKrevelen mechanism, promoting CeO_2 reduction to Ce_2O_3 and re-oxidation by the gaseous O_2 to replenish the reduced CeO_2 . The extent of reduction was also lower in these supports as shown in table3.8. Phase segregation was not suppressed in these cases and gave rise to an increase in particle and crystallite sizes. Al_2O_3 well defined in the CZ lattice as in cases a and b helped in increasing the surface area for improved contact with the soot, thus increasing the rate of the oxidation and also increased the thermal stability of the catalysts, thereby making these supports more suitable for aftertreatment applications.

Table 3.9 Soot oxidation activity of various CZA supports prepared by varying the preparation method

Sl.No.	Label	Preparation method	Onset temperature (T _{on}) (°C)	Extrapolated onset temperature (T _{eo}) (°C)	T _p (°C)	T _f (°C)
1	e	CZA -Al ₂ O ₃ IMPREGNATION	407	507	597	634
2	a	CZA- Na₂CO₃	345.3	375	485.15	563
3	b	CZprecursor+Al precursor mix	350.2	430	497.3	592
4	c	CZ prec.dried+Al prec. dried	363	385.01	523	564.6
5	d	CZprec.dried,calc.+Al prec.dried,calc.	378.2	436.1	521	585.3

Mixing the precursors after precipitation and before drying (b) led to a good support with low soot oxidation onset temperatures and peak temperatures, but with a slightly higher temperature for reduction of the CeO₂ as compared to the CZA-Na₂CO₃ support. This support was ideal for the use as a good support in aftertreatment applications. They possessed small crystallites and high surface area too. For the ease of preparation, the precursors were mixed together at the start and then precipitated dropwise by the addition of the precipitating agent (Na₂CO₃).

3.4 Supported metal oxides- Impregnation of Ag on Ce_xZr_{1-x}Al_{0.5}O_{1.75}

3.4.1 Characterization

The CeO₂-ZrO₂-Al₂O₃ support formed by the impregnation of Al₂O₃ on CZ was chosen for the impregnation of Ag. The CZA-Al₂O₃ support was used for the ease of catalyst preparation (as this support was initially used for Ag impregnation before optimising the preparation methods for CZA supports). The loading of Ag on CZA support was varied from 1, 2, 5wt%. The diffraction patterns shown below represented a characteristic cubic symmetry for CeO₂. There was a distinct phase observed in the case of 5wt% Ag loading this distinct Ag⁰ (111) phase at 2θ=38° was seen. This phase was not observed in the other two loadings which meant the loading was too low to detect its presence by XRD (figure 3.24).

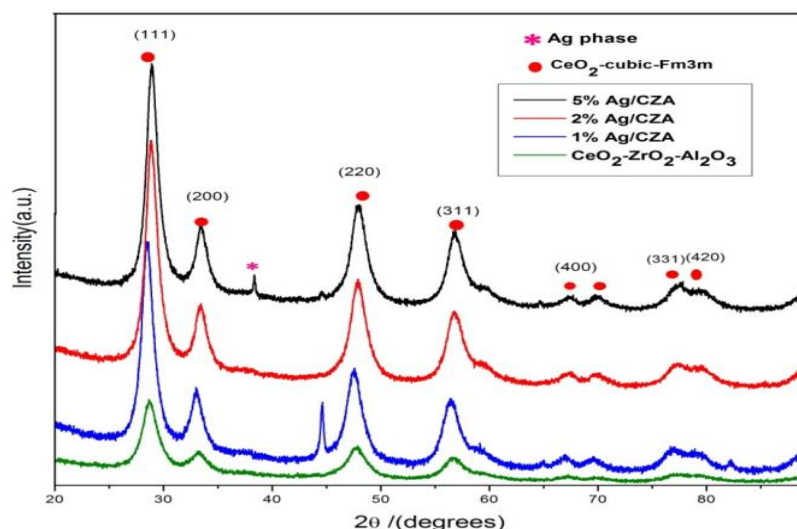


Figure 3.24 X-Ray diffractograms for the Ag impregnated CZA catalysts

The CZA crystallite sizes increased upon Ag impregnation as seen from the diffractograms with an increased crystallinity in the phases and a shift from $2\theta = 28.6^\circ$ to 28.3° . The crystallite sizes tended to increase with loading of silver- $5\% > 2\% > 1\%$. The increase in content of Ag caused the growth of the crystallites as there was a phase separation from CZA, giving rise to a distinct metallic phase of Ag. In all the three cases there was a characteristic CeO_2 cubic phase, with a trace of the Ag- CeO_2 phase ($2\theta = 38^\circ$) observed. Separation of the phases was seen only in 5% Ag/CZA.

The impregnation of the Ag onto the CZA support showed that the weight loading of Ag determined its presence as a distinct phase. The formation of the oxide or Ag^0 through binding energy analysis was not an easy prediction, as in the case of Ag, an Auger correction is required to give an idea of the state.

Table 3.10 XPS representing elemental composition of Ag impregnated CZA catalysts-narrow scan

Atomic % narrow scan									
Sl.no	Catalyst	O 1s (531 ev)	Cl 2p (199ev)	Zr 3d (183 ev)	Al 2p (75 ev)	Ag 3d (368.1, 374 ev)	Ce 3d (884, 901 ev)	Ce:Zr ratio	Ag:Al
1	1%Ag/CZA	48.59	0.54	2.47	28.82	1.10	5.08	$5.08/2.47 = 2.05:1$	$1.10/28.82 = 0.038$
2	2%Ag/CZA	46.41	1.04	2.01	25.78	1.49	4.15	$4.15/2.01 = 2.06:1$	$1.49/25.78 = 0.057$
3	5%Ag/CZA	47.67	1.01	2.25	29.54	4.11	4.82	$4.82/2.25 = 2.14:1$	$4.11/29.54 = 0.139$

The narrow scan for Ag/CZA indicated the concentration of various elements in the three catalysts. From this, the ratio of Ce:Zr was calculated and compared with that obtained from the wide scan using the *area: relative sensitivity* factor. On calculating the Ce:Zr ratios for 1 % Ag/CZA, **Ce:Zr** – 5.08/2.47= **2.05:1** from the narrow scan, and **Ce:Zr**- 5.31/2.16=**2.45:1**, from the wide scan. The narrow scan was a more accurate representation for CZA when compared to the ratio of Ce:Zr-7:3 in Ce_{0.35}Zr_{0.15}Al_{0.5}O_{1.75}. On calculating the ratios from the area and sensitivity factor (narrow scan measurement), we get

$$\text{Atomic \% of Ce} = \text{area/R.S.F} = 6703.45/8.808 = 761.06$$

$$\text{Atomic \% of Zr} = \text{area/R.S.F} = 953.88/2.576 = 370.29$$

$$\text{Therefore, Ce:Zr} = 761.06/370.29 = \mathbf{2.055:1}$$

It was thus concluded that the ratio of Ce:Zr prepared was ~**2.05:1**. The Ce:Zr:Al ratio is 2.05/28.82=0.07:1. This has been maintained in the case of 1,2 and 5% Ag/CZA.

Table 3.11 XPS representing elemental composition of Ag impregnated CZA catalysts-wide scan

		Atomic % wide scan							
		O 1s (531 ev)	Cl 2p (199ev)	Zr 3d (183 ev)	Al 2p (75 ev)	Ag 3d (368.1, 374 ev)	Ce 3d (884, 901 ev)	Ce:Zr ratio	Ag: Al ratio
1	1%Ag /CZA	43.84	0.54	2.16	29.29	0.10	5.31	5.31/2.16 = 2.45:1	0.10/29.29 = 0.0034
2	2%Ag /CZA	47.41	1.04	2.03	20.21	0.77	4.18	4.18/2.03 = 2.05:1	0.77/20.21 = 0.038
3	5%Ag /CZA	43.34	1.01	1.92	29.44	3.49	5.05	5.05/1.92 = 2.63:1	3.49/29.44 = 0.11

The concentration of Ag was seen to change as observed in table 3.11, upon varying the weight loading of Ag onto CZA. Thus a significant increase was observed in figure 3.25 that indicated the increase in intensity of the Ag 3d peak with increase in weight loading. XPS signals of Ag 3d_{5/2} appeared at a binding energy of 368.2 eV with a

splitting of about 6 eV for the 3d doublet. All these demonstrated the metallic nature of the silver core [22]. There is a possibility of electronic transfer that could occur between the Ag core and the CeO₂ shell, despite the fully oxidized Ce⁴⁺ and metallic nature of Ag.

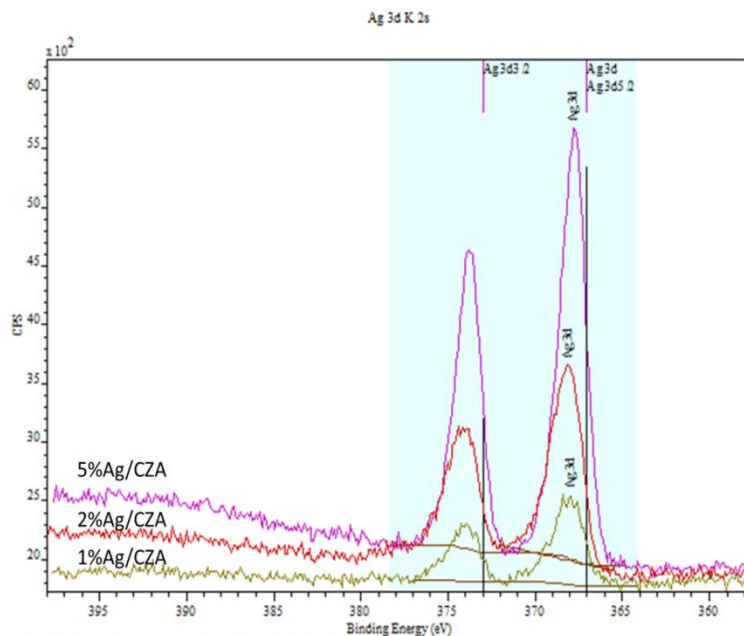


Figure 3.25 XPS showing the varying Ag 3d peak on varying loading of Ag on CZA

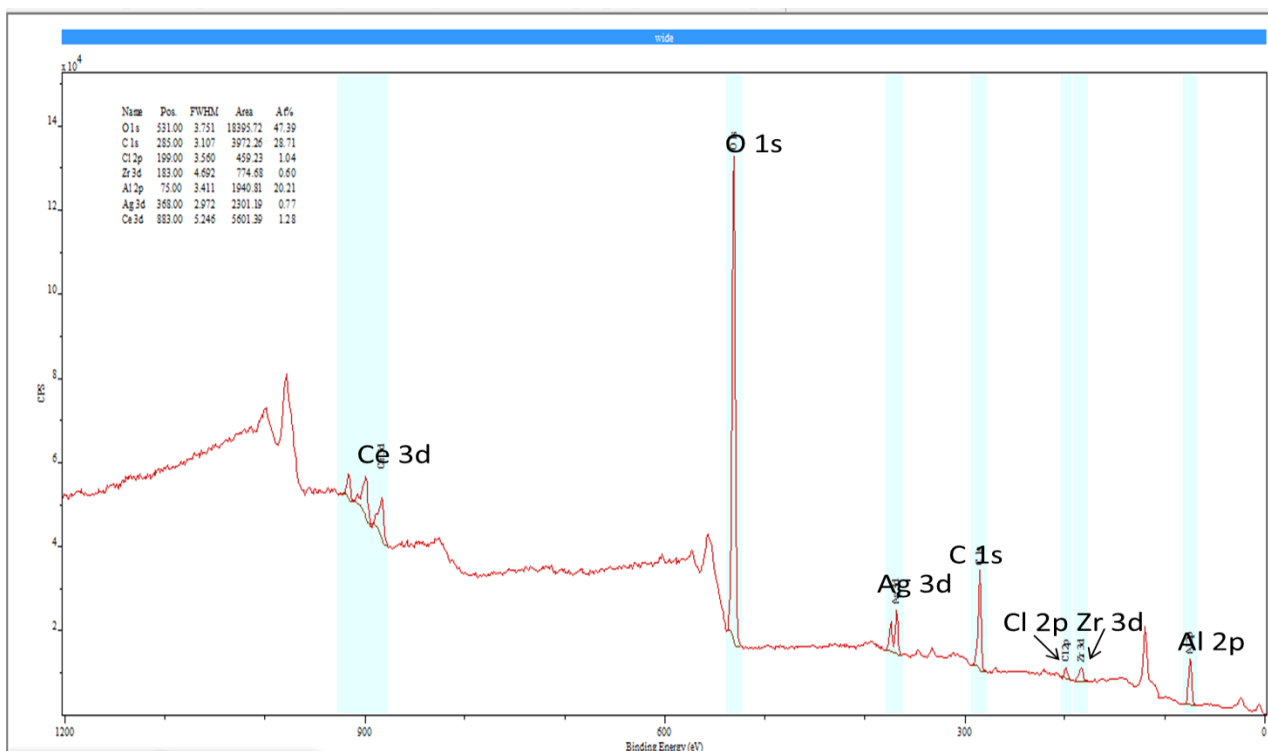


Figure 3.26 Wide scan spectrum shown from XPS indicating the elemental distribution in Ag/CZA

The different phases of the elements Ce, Zr, Al, Ag and O present in the Ag/CZA structure are shown in figure 3.26. The Ce 3d in CeO₂ was observed at 882ev with clear formation of the oxide as CeO₂ (Ce⁴⁺) from the pattern shown in figure 3.27, in all the three cases. The nature of the Ag phase was difficult to interpret as mentioned above (present at 368.2ev).

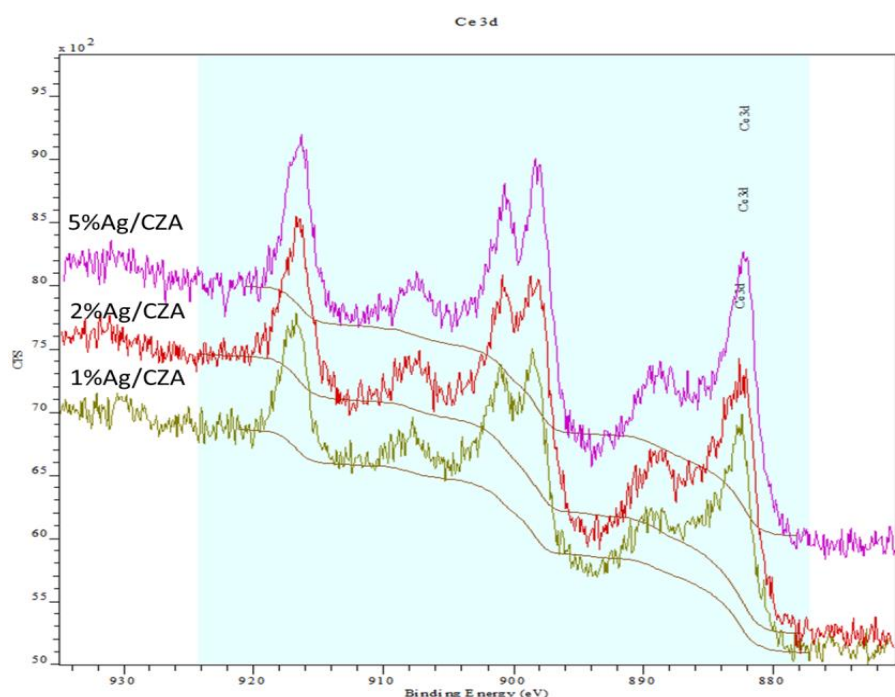


Figure 3.27 XPS spectra representing Ce-3d phases with varying Ag content

Ag–CeO₂ interface was studied by several researchers showed the presence of O_n^{x-} species, when the adsorbed oxygen on the Ag surface migrated to the CeO₂ surface via the Ag–CeO₂ interface and Ag⁰ promoted the formation of superoxide ions. This could be a possible method of diffusion of O₂ through the interface to the surface of the soot, for its oxidation [23, 24].

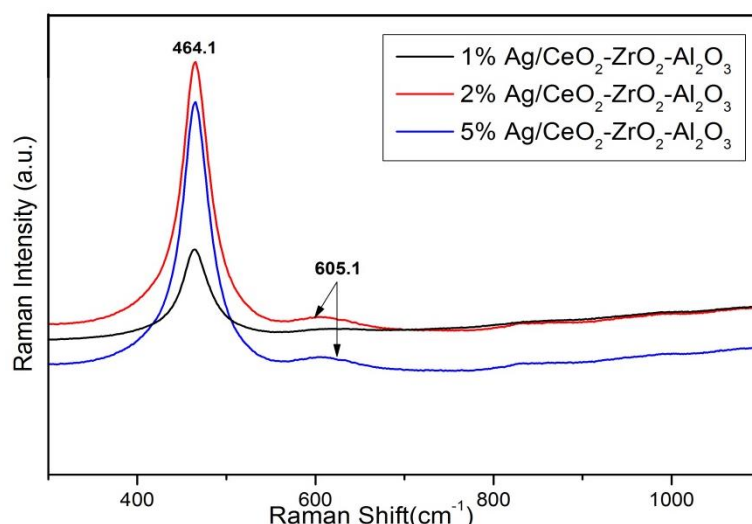


Figure 3.28 Raman spectra of the Ag impregnated CZA supports (not normalised for clear representation of spectra)

Raman spectra showed the F_{2g} cubic fluorite symmetry for CeO_2 at 464 cm^{-1} and distortion of this cubic CeO_2 phase at 605 cm^{-1} for the 2 and 5% Ag-CZA samples. This was not clear in 1% Ag-CZA as there was a predominance of cubic fluorite phase (figure 3.28) and low loading of Ag. This peak intensity increased with weight loading as observed from XRD patterns.

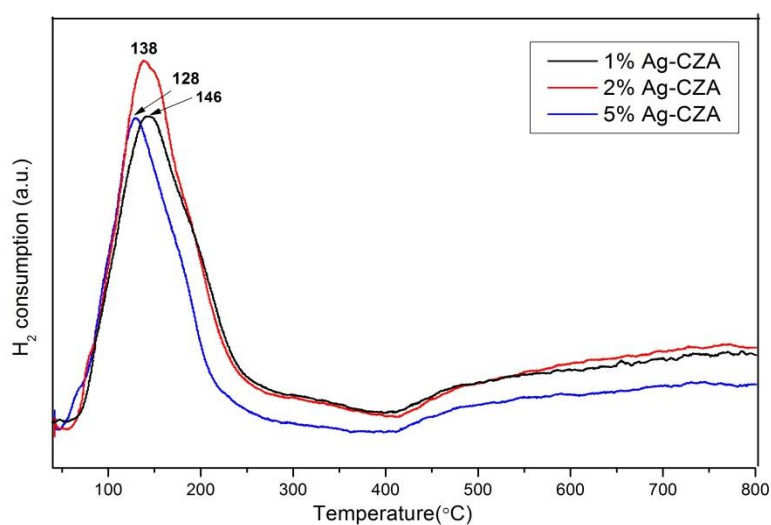


Figure 3.29 TPR profiles for Ag/CZA

Temperature programmed reduction profiles (figure 3.29) showed a decrease in reduction temperature of the CZA in the presence of the Ag in the lattice. The bimodal nature of CeO_2 reduction seen with surface reduction taking place at temperatures as low as $128\text{--}140^\circ\text{C}$ and bulk reduction at around 500°C . This low temperature reduction was assigned to the reduction of surface O_2^- of CeO_2 interacting with silver. The silver promoted the reducibility of surface CeO_2 at low temperatures and this fact was

reported by several researchers [23,24]. The better the interaction of Ag-CeO₂, the lower was the reduction temperature [24]. H₂ TPR profiles of the two catalysts (2,5% Ag/CZA) were very different, and Ag₂O was found to be much more stable on 2wt% Ag/CZA than 5wt% Ag/CZA. After H₂ reduction, both catalysts were rust in colour and contained large Ag⁰ particles. The extent of reducibility of 2%Ag/CZA was greater as seen from the peak area represented for the reduction (table 3.12). The 2% Ag was considered as the optimum loading of Ag onto CZA support due to its greater ease of reduction and greater extent of reducibility. This helped in providing the stored oxygen in ceria, at lower temperatures, for soot oxidation.

The intensity of the low temperature reduction peak was found to be influenced by the increase in surface area of the ceria support as observed from table 3.12. ZrO₂ incorporation into CeO₂ further facilitated the surface and bulk reduction process of CeO₂ [25]. Oxygen storage capacity of ceria was greatly enhanced in the presence of a metal such as Ag alongside structural modification by the introduction of defects with incorporation of ZrO₂ and Al₂O₃ into the lattice.

Table 3.12 Physical properties of Ag/CZA catalysts

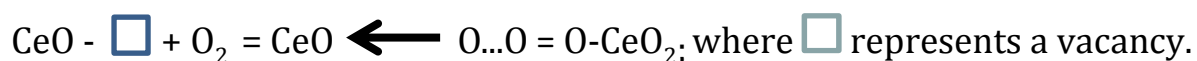
Sl.No	Catalyst	Surface area (m ² g ⁻¹)	2θ	Crystallite size (nm)	Peak temperature (reduction) °C	H ₂ consumption (μmol g ⁻¹)
1.	1%Ag/CZA	89	28.68	6.4	146	853.31
2.	2%Ag/CZA	87	28.66	6.7	138	938.52
3.	5%Ag/CZA	70	28.69	6.8	128	729.97

There was a decrease in surface area observed upon impregnation of the metal salt onto the CZA support. This generally occurs in the case of some metal supported catalysts, where the metals are buried in the bulk of the support, resulting in a loss of the adsorptive and catalytic properties. In the case of the fluorite structured CeO₂, the cationic sub-lattice provides a large activation barrier for the migration of metal atoms into the bulk. The metal crystallite tends to anchor onto the surface oxygen vacancies of ceria created by high temperature reduction. This property of the CZA support provides

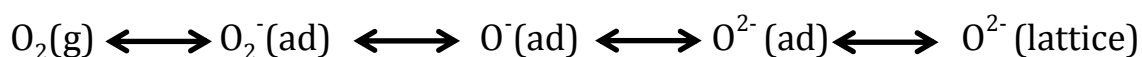
its resistance to sintering, and therefore there is not much change in the adsorptive or catalytic properties of metal impregnated CeO₂ [14,32].

There was a synergistic metal support interaction observed in this case. The catalytic activity may have been influenced by oxygen storage capacity, Ce⁴⁺/Ce³⁺ redox couple and defects such as anionic vacancies at the metal–ceria interface. Ceria influences the catalytic property of the supported metal by metal-support interaction. In turn the metal in this case silver tends to influence the physico-chemical properties of ceria support such as the OSC and reducibility. There is also a possibility of superoxide species being formed due to Ag-CeO₂ interaction that were molecularly adsorbed in bent end-on geometry on the silver surfaces. These could be key active species in enhancing the mechanism of the oxidation. This probability was not investigated in this study and is a potential area for future investigation [26]. This is necessary as the understanding of this interaction would help to explain a plausible mechanism of soot oxidation.

The role of silver surface was to increase the O₂ mobility of CeO₂ by creating a large concentration of structural defects thereby enhancing the reducibility and to weaken the Ce-O bond located nearby, thus promoting the exchange between lattice O₂ and adsorbed O₂ as shown below:



The various oxygen vacancies would have led to the reduced ceria surface that promoted the activation of adsorbed oxygen to form superoxide, even in the lattice as was shown by Machida *et.al*. Thus there could be a formation of superoxide species of O₂ formed along with several forms of O₂ such as O₂(g) [26]. This is a possible mechanism suggested in literature.



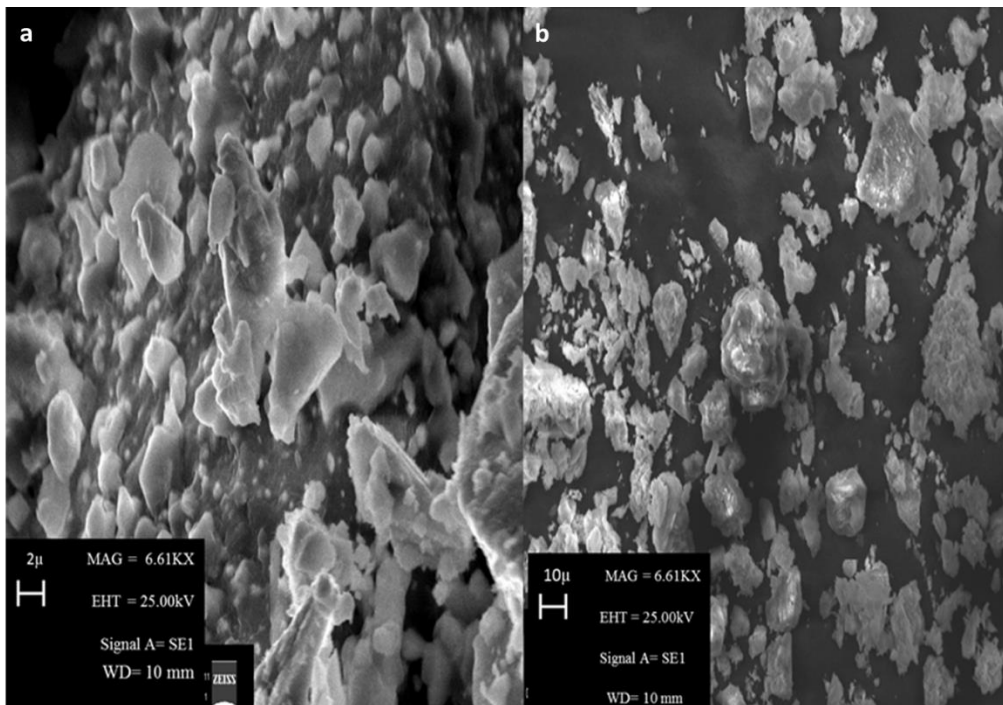


Figure 3.30 SEM micrographs for 2% Ag/CZA catalysts – a) 6.61KX-coprecipitation, b) impregnation

Figure 3.30a represented the 2%Ag/CZA-co-precipitation (prepared upon co-precipitation of Ag with CZA) and b was 2%Ag/CZA-impregnation. From the figure 3.30 it was evident that the 2% Ag/CZA prepared by co-precipitation of the precursors were made of ordered particles that were spherical in shape. Smaller particles of $2\mu\text{m}$ agglomerated together to give rise to large particles of around $10\mu\text{m}$. There was no distinct Ag phase observed as bright spots due to the low weight loading. In the case of Ag/CZA impregnation, the particles were larger, of around $10\text{-}30\mu\text{m}$. In this case there was no ordered arrangement of particles but they were present as clumps of Al_2O_3 on CZ surface as proven by EDX analysis.

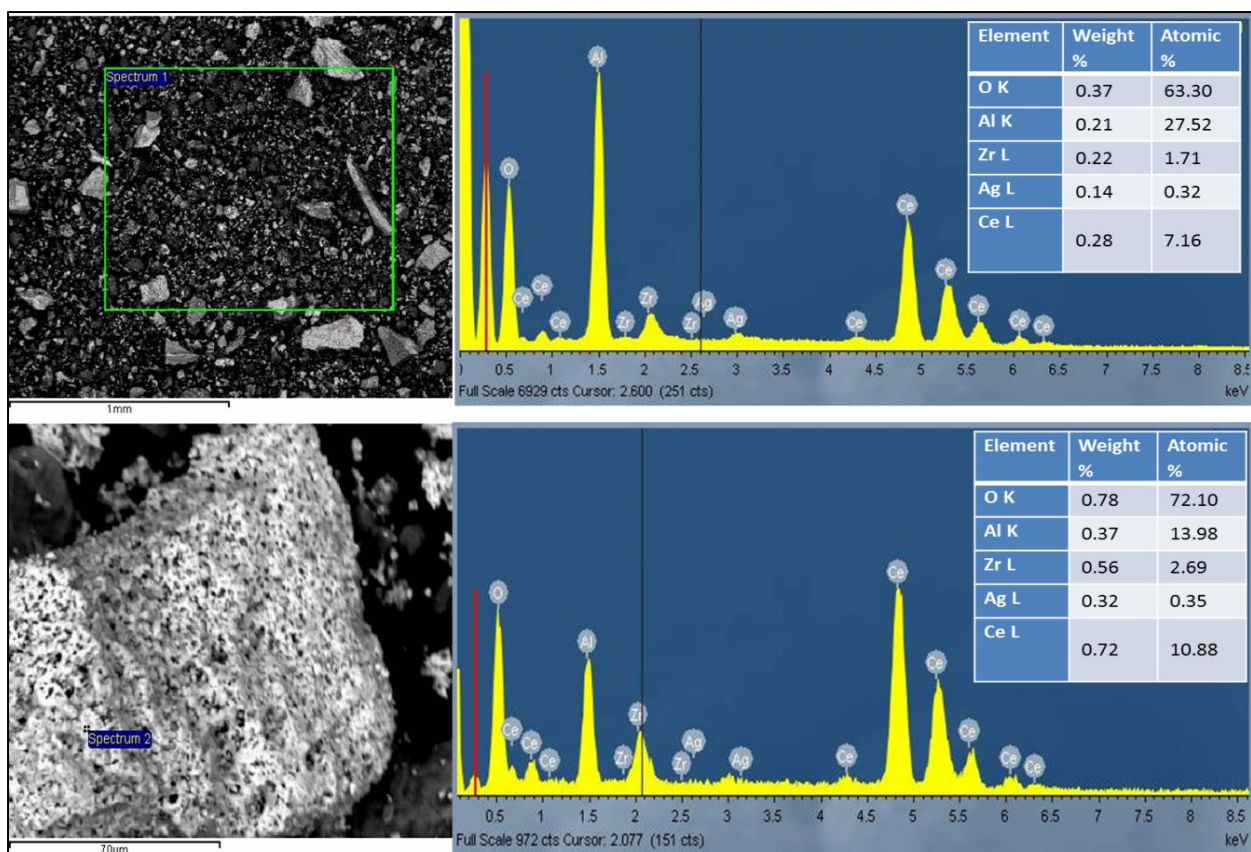


Figure 3.31 EDX point and area analysis of 2% Ag/CZA- impregnation

A scan of a region consisting of several particles had shown that Al_2O_3 impregnation led to as a distinct phase that was not very clearly evident from XRD (figure 3.31). Also, the particle sizes were around $70\mu\text{m}$. It was difficult to determine the state of the Ag as both XRD and EDX were unable to detect such low concentrations of Ag on the CZA.

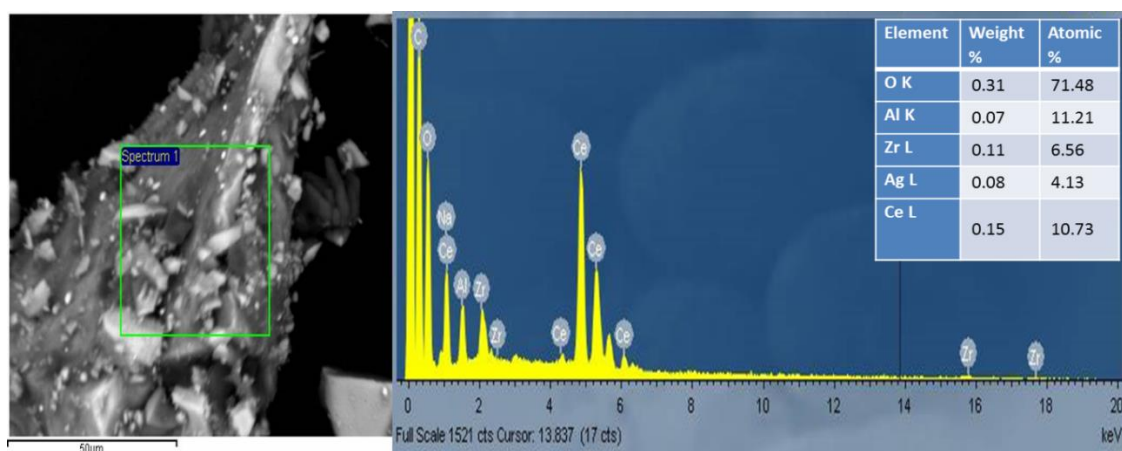


Figure 3.32 EDX area analyses for 2%Ag/CZA-co-precipitation

3.4.2 Soot oxidation activity

The results for soot oxidation activity, in the presence of Ag supported catalysts indicated that 2wt % Ag on CeO₂-ZrO₂-Al₂O₃ (Impregnation) had lower oxidation temperatures compared to 1 and 5 % Ag/CZA. The catalyst was tested under both loose (using a spatula to mix the soot and catalyst in the 10: 3 ratio) and tight (mixing in a pestle and mortar) contact conditions in the range of 300-600°C (figure 3.33). The onset temperature, under tight contact conditions was 396°C and combustion was complete by around 632°C, for the 2% Ag/CZA catalyst. These temperatures were far better than that reported for the CZA- impregnated support alone as shown previously.

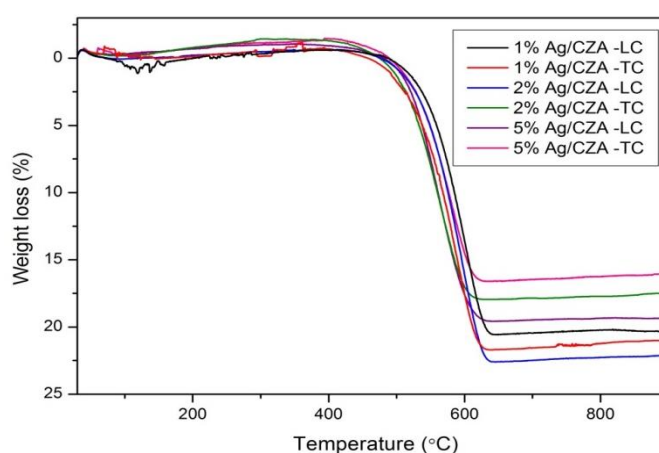


Figure 3.33 Soot oxidation activity – Ag catalysts under tight and loose contact with soot

The reasons for the better activity of 2%Ag/CZA could be based on the characterisation results shown above. There was a possibility of Ag⁰ species being predominantly present in the 2% Ag loaded catalyst, that could be highly dispersed on the surface of the support, while in the case of other weight loadings (1,5%Ag), the Ag⁺ phase could be present. There may be other surface species such as Ag_n responsible in the case of higher loading of silver onto the CZA support. Ag-CeO₂ interaction (as seen from XRD) causes the formation of superoxide species capable of oxidizing the soot particles as described above

Table 3.13 Soot oxidation activity- Ag/CZA- loose and tight contact conditions (CZA-Al₂O₃ impregnation)

Sl.No.	Catalyst	Onset Temperature(T _{on}) (°C)	Extrapolated Onset Temperature(T _{eo})(°C)	T _p (°C)	T _f (°C)
1	1wt%Ag-CZA-TC	409.3	478.3	589	646
2	2wt%Ag-CZA-TC	395.5	465	564.4	632.1
3	5wt%Ag-CZA-TC	456	475.4	537.2	607
4	1wt%Ag-CZA-LC	420	504.11	603	651.03
5	2wt%Ag-CZA-LC	402	503.88	596	647.11
6	5wt%Ag-CZA-LC	408	483	583	640

From the TPR results shown in figure 3.28, it was observed that the Ag on CZA reduced the CeO₂ at a lower temperature of 130°C, providing stored oxygen CeO₂ more readily for soot combustion. The ease with which the oxidation occurred was dependent on the greater extent of reducibility of the CeO₂ to provide the stored oxygen in it, for the combustion of soot.

Contact is a very important criterion for soot oxidation as this process is driven by surface phenomenon when the catalyst and soot come together in a catalytic filter. There was a small increase in the oxidation temperatures, under loose contact conditions, arising from the poor contact between the soot and the catalyst, so that the onset temperature was 402°C and final combustion occurred at around 640°C. The loose contact is generally considered to be representative of real conditions in an exhaust filter, while the tight contact (which gives lower oxidation temperatures) is often used to screen potential catalysts.

3.5 Alkali metal promotion over CZA

3.5.1 Characterization - Varying different alkali metal (K) salts and their effects on different support

Impregnation of CZA- Na_2CO_3 co-precipitated support with various potassium precursors retained the cubic fluorite structure of CeO_2 . The various salts of potassium were K_2CO_3 , KOH , KCl and KNO_3 . This variation of precursor salts was to identify the effects of the K^+ cation and anions on the properties of the support (CZA). A loading of 10% K_2CO_3 was maintained for all the supports. This weight loading was chosen as it had been frequently used in several reports in literature as a good promoter [27,28].

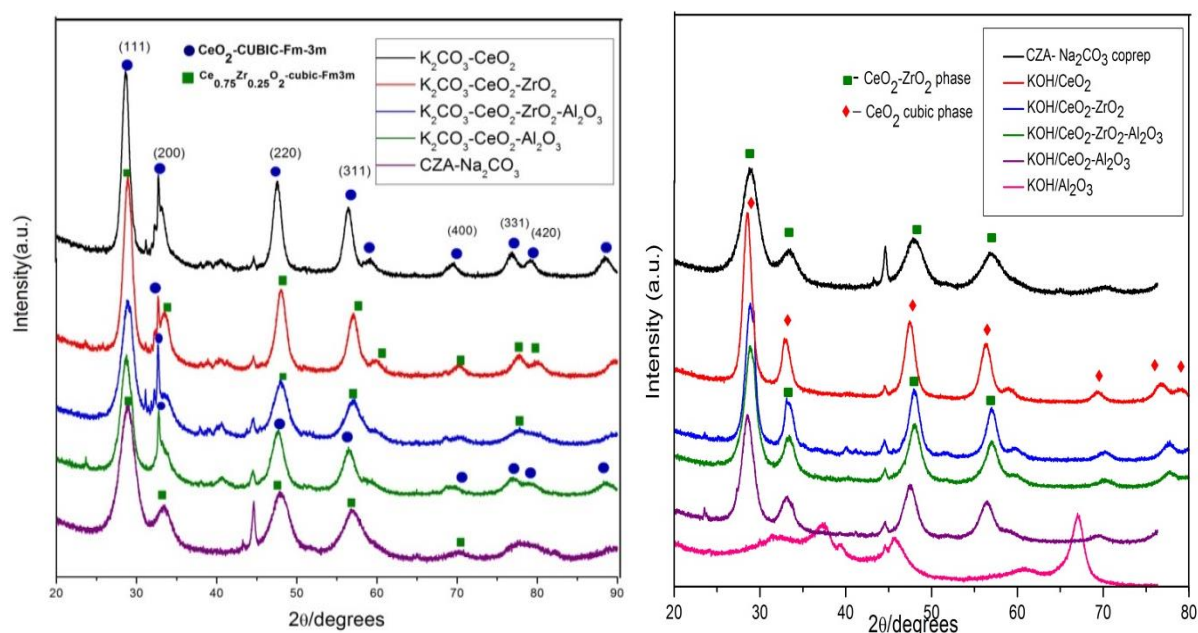


Figure 3.34 - Varying K precursor salts on CZA-a) K_2CO_3 ; b) KOH

On impregnating the alkali metals on various supports the predominant CeO_2/CZ mixed cubic phase was still retained but there was an increase in crystallite size (shown in table 3.15 in page 144), seen as a shift to lower 2θ angles as compared to the support. Surface area values indicated that deposition of alkali metals remarkably reduced the available surface, with the reduction being dependent on the type of metal and on its quantity.

The impregnation of K_2CO_3 showed that there formation of distinct phase with the presence of K on the support. The peak corresponding to the (200) plane at $2\theta=33^\circ$

was split or became irregular, owing to the potassium impregnation. The impregnation on CZ, CA and CZA showed a mixed phase (figure 3.34). Impregnation onto CeO₂ and CA showed increased crystallinity. This suggested that, on incorporation of ZrO₂ into the cubic fluorite CeO₂ lattice, the crystallite size reduced as the Zr⁴⁺ ions were substituted for the Ce⁴⁺ ions, thus creating structural defects. In the case of K₂CO₃/CZA, the crystallites were the smallest as seen from the slightly broader peaks compared to those for the other supports. These small crystallite possessed a slightly higher surface area due to the addition of the Al₂O₃ into the matrix, compared to the other supports.

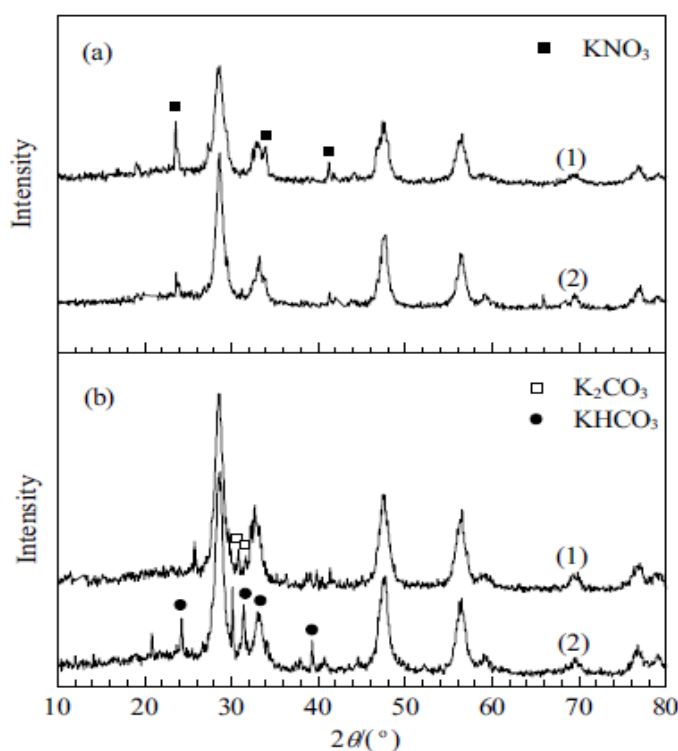


Figure 3.35 X-ray diffractograms indicating KNO₃ and K₂CO₃ phases [27]

The diffraction peaks at 23.52, 33.87 and 41.16° could be indexed to the KNO₃ phase (as seen in figure 3.35) obtained from the JCPDS database (74-2055), as reported by Wenjuan *et al.* in their study on 19% KNO₃/CeO₂ for soot oxidation [27]. This was as seen in my study, varying the precursor salts. They also observed that the KNO₃, upon addition of fresh charge of soot, for three consecutive reactions showed a decrease in the intensity of this phase due to conversion to K₂O or KNO₂ [27]. Also, in the case of K₂CO₃, the peaks were observed at 30.72 and 31.72° as listed in the JCPDS database (71-1466), as seen in figure 3.36.

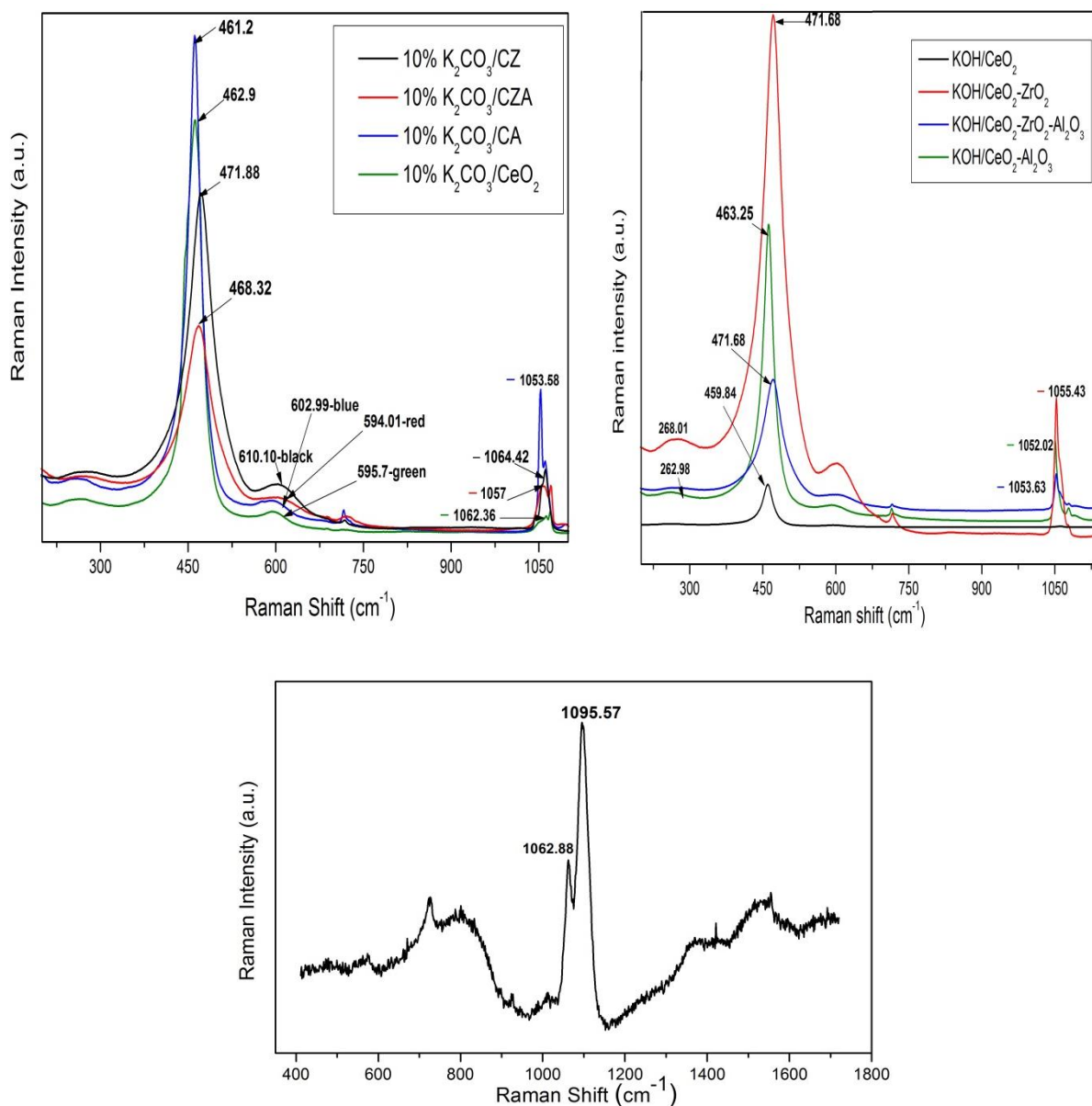


Figure 3.36 K impregnation onto different supports - a) K₂CO₃; b) KOH; c)K/Al₂O₃

K/Al₂O₃ showed only the presence of two peaks at 1062.88 cm⁻¹, attributed to the K₂CO₃ phase and another large peak 1095.57cm⁻¹ due to Na₂CO₃ (precipitating agent). This support possessed crystallites of 71Å (figure 3.36).

3.5.1.1 Study on different supports

Raman spectra also showed that the cubic fluorite CeO₂ phase is maintained but with change in support there was an increase in the distortion of the cubic phase, evident at 600cm⁻¹. The only other change observed, was a small and sharp peak at

1061 cm⁻¹ that could be attributed to symmetric stretching vibrations of CO₃²⁻[28]. This peak confirmed the XRD findings which indicated that potassium was in the form of carbonate, covering the mixed oxides.

K/CeO₂ support showed a very small distorted cubic phase at 600cm⁻¹, represented by the green line (figure 3.36). The black line represented by K/CZ, showed a shift to higher values for the cubic CeO₂ phase at 400cm⁻¹ and the distortion of the phase at 600cm⁻¹. This shift was presumably due to the incorporation of ZrO₂ into the ceria lattice, creating some defects in the structure and resulted in peak broadening with reduction in crystallite sizes. The peaks for K/CZA showed a distinct broadening and reduction in intensity for the ceria phase at 400cm⁻¹. Also, the peak at 600cm⁻¹ showed only a slight distortion to the ceria phase. CZA crystallites were smaller as compared to CeO₂ and CA which possessed lesser peak width and larger crystallites.

Table 3.14 Physical properties of different supports (without K impregnation)

Sl.No	Catalyst	Surface area (m ² g ⁻¹)	Crystallite size (nm)
1.	CeO ₂	7	56.1
2.	Al ₂ O ₃	134	10.3
3.	CeO ₂ -ZrO ₂	13	5.4
4.	CeO ₂ -Al ₂ O ₃	25	4.2
5.	CeO ₂ -ZrO ₂ -Al ₂ O ₃ (Na ₂ CO ₃ coprep)	148	3.1

On comparison of the CA with the CeO₂, it was seen that the Al₂O₃ incorporation into the CeO₂ matrix reduced the growth of the crystallites. But this effect was more evident in the case of CZA, giving the crystallites a smaller size. Here, it was likely that the ZrO₂ facilitated the creation of defects and the Al₂O₃ reduced the growth of the crystals, producing a diffusion barrier between the CZ particles. Upon addition of Al₂O₃, the surface area also increased, as was observed in the case of the mixed oxide supports with Al₂O₃. Thus this support was most ideal with the promotion of K onto its surface. Al₂O₃ as an individual support showed only a distinct K phase at 1062.88 and 1095.97 cm⁻¹ and no other characteristic phases.

Varying the potassium precursor did not alter the phases too much but showed a variation in the crystallite sizes, with change in the support as shown in table. 3.15. The supports were quite similar in terms of crystallite sizes, on comparison with similar supports promoted with different precursor salts. K_2CO_3 promotion onto CZA (Na_2CO_3 coprep) was the most promising catalyst, with small crystallites, high surface area (despite the reduction in area in the presence of K) and good thermal stability (shown in the last part of this chapter).

Temperature programmed reduction profiles showed that the K impregnated onto CZA (Na_2CO_3 coprep.) was more easily reduced as compared to the K on CZ support (figure 3.37). The surface CeO_2 underwent reduction at temperatures of around $450^\circ C$ and in this case there was a possibility of formation of K_2O species on the surface of CeO_2 , that upon melting at $380^\circ C$ could diffuse into the CeO_2 matrix and help in the re-oxidation of the reduced CeO_2 [29].

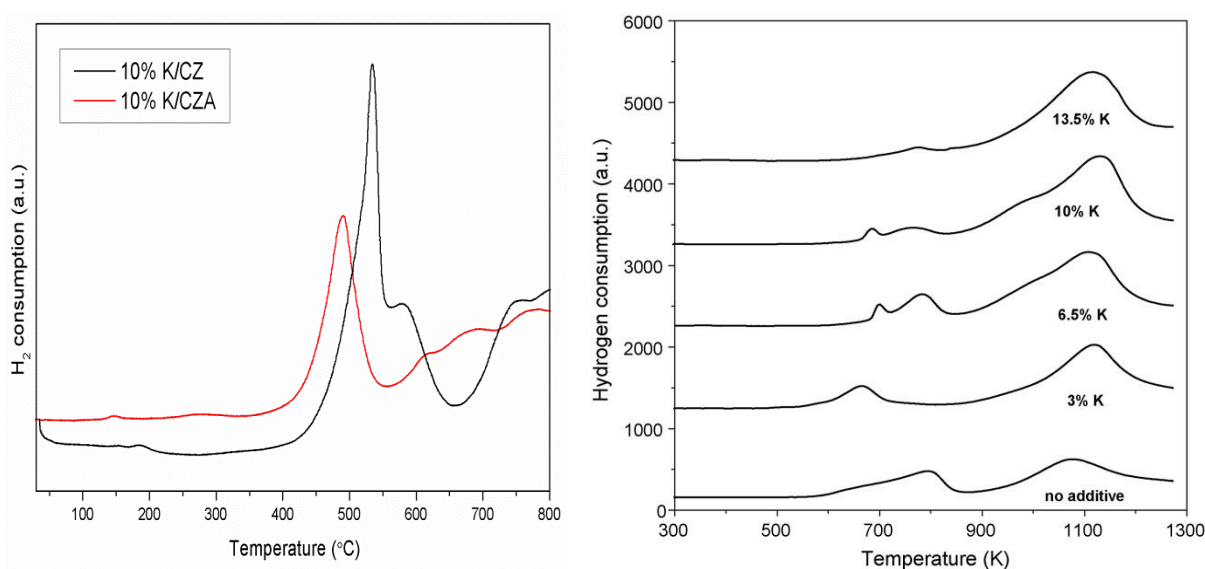


Figure 3.37 TPR profiles- a)K on CZ and CZA; b)varying K/ CeO_2 content from literature [14,29]

The profiles shown for pure CeO_2 and ZrO_2 by Aneggi *et al.* were observed at slightly higher surface and bulk reduction temperatures as compared to the CZ and CZA support. In the case of CeO_2 and K impregnation onto CeO_2 support, the surface reduction was at $527^\circ C$ while bulk reduction was at $830^\circ C$ which was higher than that reported for CZ and CZA as shown in table 3.16 (page 147-148).

Table 3.15 Physical properties of various K impregnated supports

Sl.No	Catalyst	Surface area (m ² g ⁻¹)	2θ (°)	Crystallite size (nm)
1.	KOH-CeO ₂	11	28.66	10.8
2.	KOH-CeO ₂ -ZrO ₂	14	28.68	9.2
3.	KOH-CeO ₂ -Al ₂ O ₃	19	28.46	7.0
4.	KOH- CeO ₂ -ZrO ₂ -Al ₂ O ₃	16	28.95	7.2
5.	KOH-Al ₂ O ₃	93	66.93	5.9
6.	K ₂ CO ₃ -CeO ₂	8	28.76	10.3
7.	K ₂ CO ₃ -CeO ₂ -ZrO ₂	10	28.83	8.1
8.	K ₂ CO ₃ -CeO ₂ -Al ₂ O ₃	12	28.64	8
9.	K ₂ CO ₃ - CeO ₂ - ZrO ₂ -Al ₂ O ₃	17	28.86	5.9
10.	K ₂ CO ₃ -Al ₂ O ₃	32	66.98	8.2

The bare supports such as CeO₂, as shown in table 3.14, were made of small crystallites but possessed a low surface area and they lost their activity at higher temperatures (600°C and above), due to lack of thermal stability and lack of better mode of diffusion of bulk oxygen to the surface for soot oxidation. Thus on incorporating ZrO₂ into CeO₂, oxygen diffusion was favoured by the creation of defects, due to the reduced ionic radii of Zr⁴⁺ as compared to Ce⁴⁺. On introducing Al₂O₃ into the matrix, the crystallites further reduced in size and the surface area also increased due to the high surface area of Al₂O₃. Impregnation of KOH and K₂CO₃ as shown in table 3.15 indicated the trend observed on varying supports and K precursors. The trend as seen from the table 3.15 showed that the impregnation of ZrO₂ and Al₂O₃ leads to shift in XRD peaks to higher 2θ angles resulting in an increased peak width that is due to a decrease in crystallite size. The decrease in crystallite size followed a trend, with K₂CO₃ impregnation as follows-CeO₂> Al₂O₃ >CeO₂-ZrO₂ >CeO₂-Al₂O₃ > CeO₂-ZrO₂-Al₂O₃. A similar trend was observed in the case of KOH, KNO₃ and KCl impregnation(data for

KNO₃ and KCl was not included as they showed a similar trend as the other two precursors. This indicated that the mixed metal oxide supports should be ideal for soot oxidation as these were more thermally stable and possessed smaller crystallites. The surface areas were also higher when Al₂O₃ was added into the CZ lattice. There was an obvious drop in the surface area of the catalysts upon K impregnation. It has been shown from literature that an increase in surface area and decrease in crystallite size through this inverse relationship favours an increase in soot oxidation rate [30] as there is more contact area available for the soot particles, thereby increasing their oxidation.

3.5.2 Soot oxidation activity

3.5.2.1 Variation of potassium salt precursor on CeO₂-ZrO₂-Al₂O₃

K₂CO₃ without any support has shown an onset of 310°C by Zhang *et al.* but due to loss of K at higher temperatures, it needs to be retained within a support material [31]. When various potassium salts (KOH, K₂CO₃, KNO₃, KCl-10wt%) were impregnated on CZA and 10wt%K (K₂CO₃), the onset of soot oxidation was lowered to 295°C from 345°C and the final temperature was 478.3°C, (figure 3.38) as observed in literature for K supported catalysts [32].

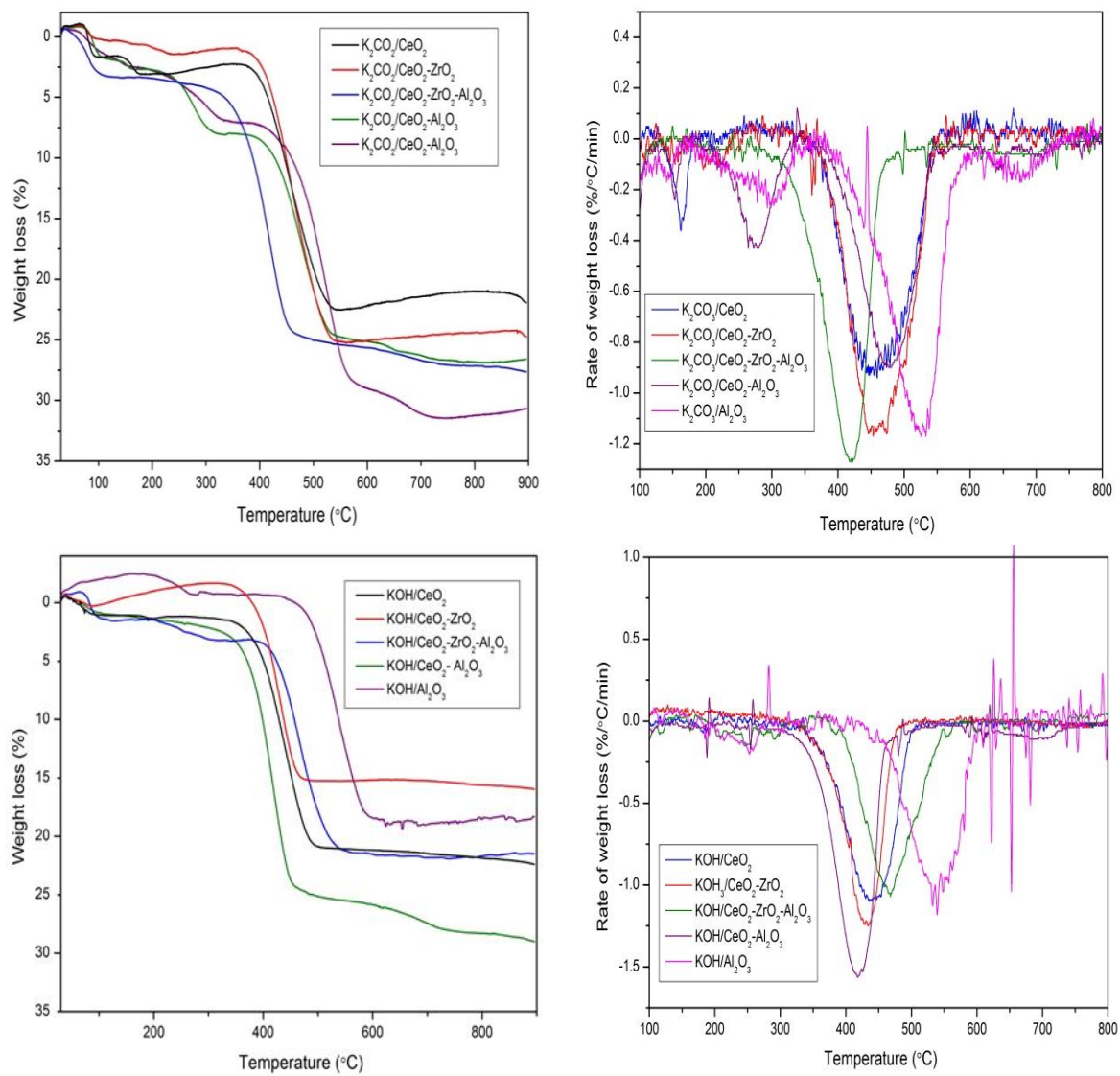


Figure 3.38 Soot oxidation activities for a) K_2CO_3 ; b) KOH supported catalysts

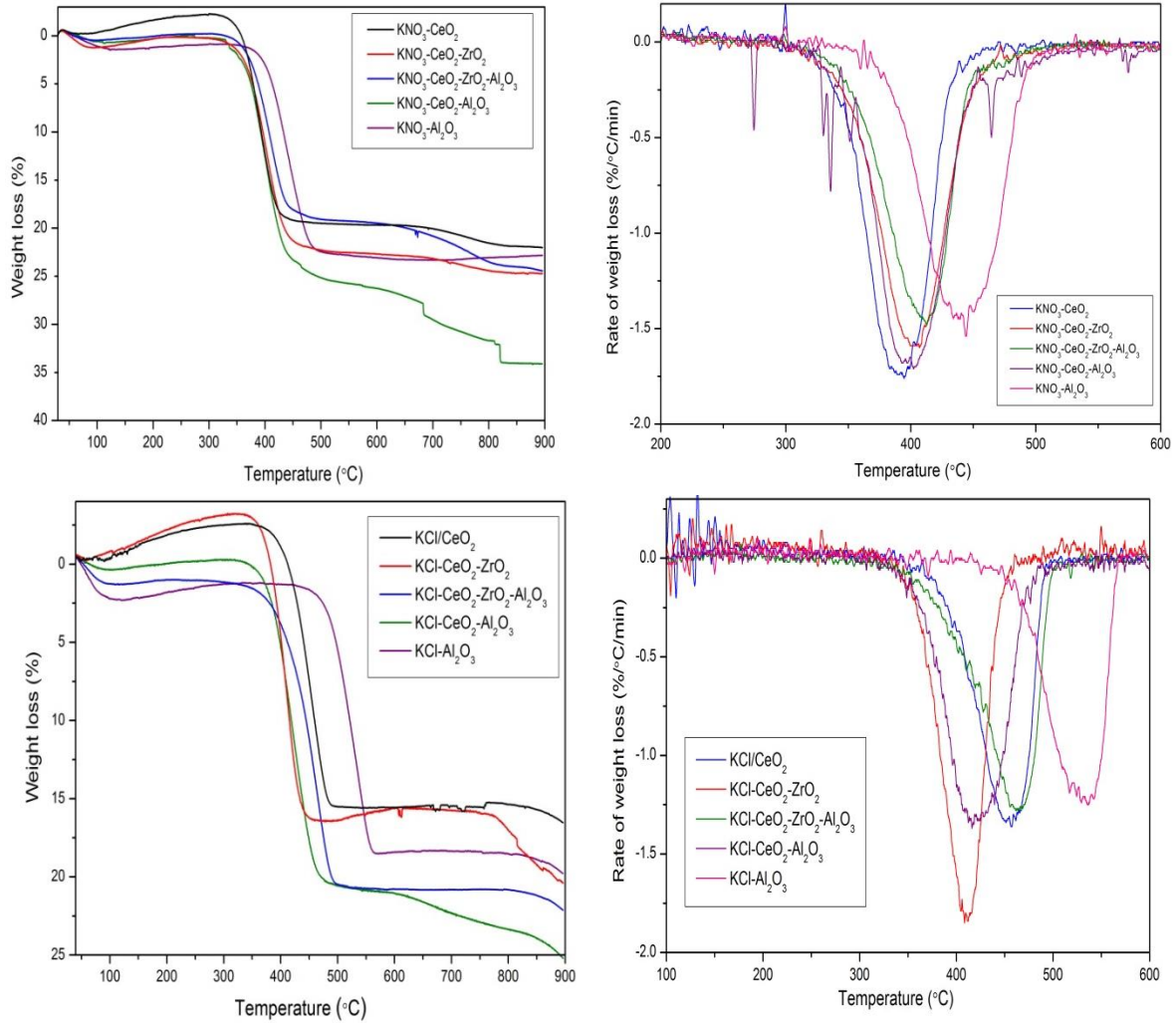
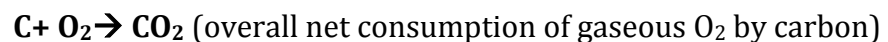
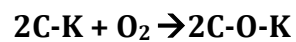
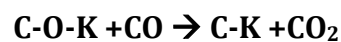


Figure 3.39 Soot oxidation activities for a) KNO₃; b) KCl supported catalysts

It has been previously proposed that the alkali metal favours the chemisorption of molecular oxygen to form a carbon-oxygen complex (C-O-AM) which is the active site, promoting the oxidation of the carbon located near the catalyst. The catalyst helps to transfer the oxygen from the gas phase to the carbon surface. The mechanism can be represented as below:

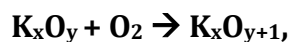


(Some amount desorbed, remaining CO reacts with the oxidized form-Eqn.2)



where, AM is the alkali metal in our case K, C-AM represents the reduced form of the carbon–oxygen complexes and C-O-AM represents the oxidized form of the complex.

In another hypothesis, the alkali metal acts according to the redox cycle of CeO₂ where,



This transfers the oxygen to reduced CeO₂ (Ce₂O₃) to restore CeO₂ that subsequently oxidizes the soot [33, 34]

Table 3.16 Soot oxidation activity of K supported catalysts

Sl.No	Catalyst	Onset temperature (T _{on})(°C)	Extrapolated onset temperature (T _{eo})(°C)	T _p (°C)	T _r (°C)
POTASSIUM HYDROXIDE					
1	KOH-CeO ₂ -Al ₂ O ₃	300.4	349	418.04	485
2	KOH-CeO ₂ -ZrO ₂	311	349	432	492
3	KOH-CeO ₂ -ZrO ₂ - Al ₂ O ₃	317	367	430.2	485
4	KOH- CeO ₂	335.1	370	439.2	518
5	KOH-Al ₂ O ₃	383.2	445.4	537	580.2
POTASSIUM CARBONATE					
1	K₂CO₃ -CeO₂- ZrO₂-Al₂O₃	295	328	415	478.3
2	K ₂ CO ₃ -CeO ₂ - ZrO ₂	310	350.3	427.1	487.33
3	K ₂ CO ₃ -CeO ₂ - Al ₂ O ₃	314.1	338.2	421.13	488.4
4	K ₂ CO ₃ -CeO ₂	306.4	355	438	555.7
5	K ₂ CO ₃ -Al ₂ O ₃	331.03	405	513.1	565.1

POTASSIUM NITRATE					
1	KNO₃ -CeO₂- ZrO₂-Al₂O₃	304	353	418	480
2	KNO ₃ -CeO ₂ - Al ₂ O ₃	326.01	353.2	402	459
3	KNO ₃ -CeO ₂ -ZrO ₂	310	344.1	403.03	472.3
4	KNO ₃ -CeO ₂	390.4	341.2	392.4	457.3
Sl. No	Catalyst	T_{on}	T_{eo}	T_p	T_f
(contd)					
5	KNO ₃ -Al ₂ O ₃	344.11	383.4	441	501
POTASSIUM CHLORIDE					
1	KCl -CeO ₂ -ZrO ₂	325	358	420	462
2	KCl -CeO ₂ - Al ₂ O ₃	318.2	362	419.3	487.01
3	KCl-CeO ₂ -ZrO ₂ - Al ₂ O ₃	320	367	465	505.1
4	KCl-CeO ₂	347.2	385	453	495
5	KCl -Al ₂ O ₃	424	460	535.3	573.1

The results for KCl on various supports showed higher oxidation temperatures (T_{on}-320°C, T_f -505°C) than for K₂CO₃ and KNO₃ (T_{on}-304°C, T_f-457°C). This was in agreement with the observation made by Moulijn and Kapteijn [35], that Cl⁻ anions showed a stronger interaction with K⁺, resulting in the formation of stable salts, and thus the interaction of the K⁺ with the carbon was weaker resulting in the formation of fewer carbonate species that are the active sites for further reaction [36]. Gross *et al.* [36,37] have carried out a few kinetic studies with CeO₂, proposing the mechanism shown in figure 3.38 with the formation of superoxides and peroxides which can then react with soot, generating oxygen vacancies on the surface. The experiments were carried out with K-impregnated (using KNO₃ as potassium source) on ceria and so, the

authors also proposed a coupled cycle in which potassium plays a role during the reaction (figure 3.40).

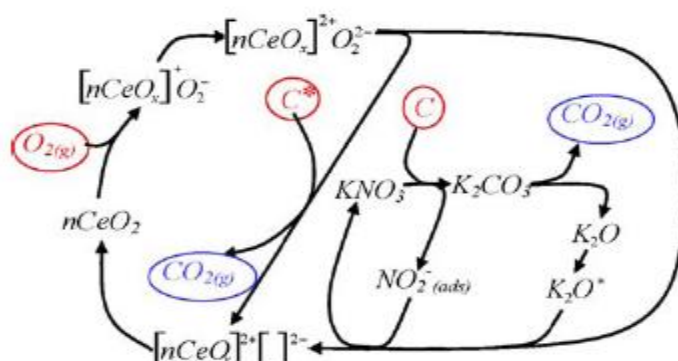


Figure 3.40 Mechanism proposed by Gross *et al.* for ceria-catalysed soot oxidation using K/CeO₂ [37]

It was also observed that CZA was the most ideal support providing oxygen storage from CeO₂-ZrO₂ and providing the mobility of lattice O₂ through the lattice defects. Al₂O₃ provided for the high surface area, thermal stability and prevention of sintering of particles at high temperatures. CeO₂ and Al₂O₃ as individual supports were found to be less active compared to mixed oxide supports from the results above. The best activity was reported for the K₂CO₃ on CZA catalyst indicating that the K₂CO₃ is the best precursor for impregnation as observed from the onset, peak and final temperatures observed for soot oxidation.

3.6 Varying the weight loading of potassium on CeO₂-ZrO₂-Al₂O₃

3.6.1 Characterization

The weight loading of K on CZA was varied from 2-50% K in order to understand the effects of the promoter on soot oxidation. Thus after impregnation onto CZA, the XRD patterns showed that between 2-10% K loading there was no change in the CeO₂ cubic phase of the support.

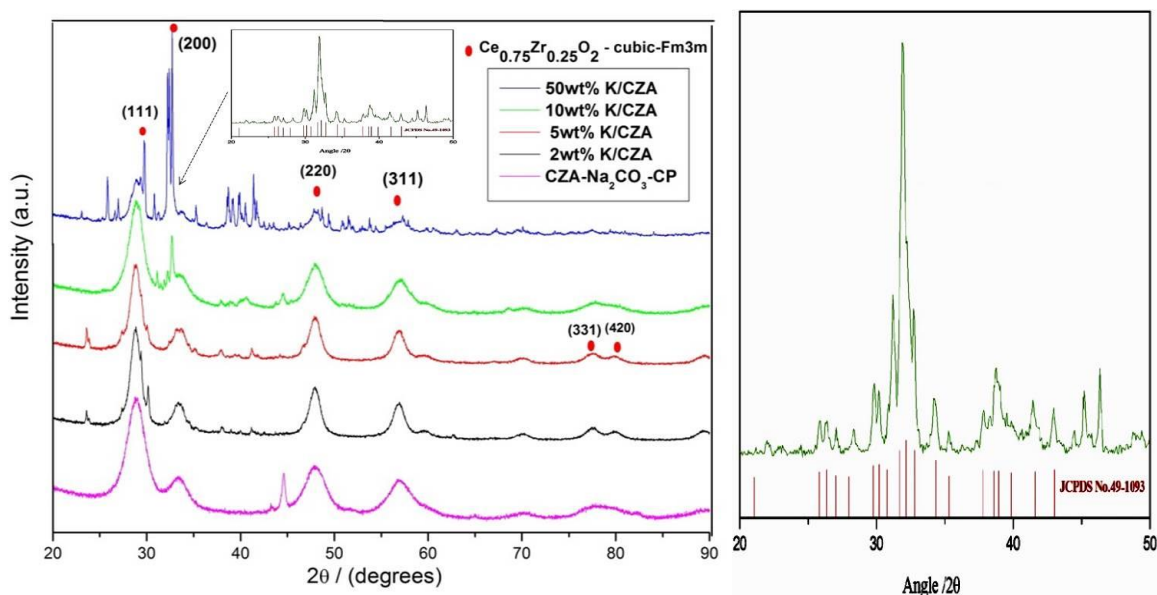


Figure 3.41 X-ray diffractograms - varying the loading of K/CZA

Potassium impregnated (2, 5, 10%) catalysts showed a mixed $\text{CeO}_2\text{-ZrO}_2$ cubic phase represented by the black, red and green lines respectively (figure 3.41). The intensity of the peaks representing these mixed phases, for the 2%K/CZA catalyst was greater than for 5, 10 and 50%K/CZA. Thus larger crystallites were seen to indicate more intense peaks, with a predominant CeO_2 phase. As the weight loading of K increased, the peaks at (111) and (200) were distorted and the peak at (200) was split giving rise to smaller peaks, in the case of 10 and 50% K/CZA. With a drastic increase in loading as in the case of 50%K/CZA, the catalyst lost its cubic fluorite structure; XRD peaks became very sharp and intense. Furthermore, the material underwent sintering to give rise to very large crystallites.

Small peaks appeared on impregnation of K, around $32\text{-}33^\circ$ and $38\text{-}45^\circ$ and they were in agreement with a recent study done with carbonates by Wang *et al.* [14]. They observed peaks in similar diffraction angles for K_2CO_3 as shown in figure 3.41. This observation suggested that potassium remained in the form of carbonate, even after calcination. The same was observed upon K impregnation onto CZ support as well. It has also been studied that K impregnation on different supports with varying Ce:Zr ratios showed an increase in crystallite size with increased Ce content in the support as shown in table. On varying the weight loading of K on CZA the crystallite sizes increased with increase in weight loading, indicated by more intense or sharp peaks. The Al_2O_3 in

the support tends to prevent the sintering of the particles and maintains smaller crystallite sizes producing broader peaks.

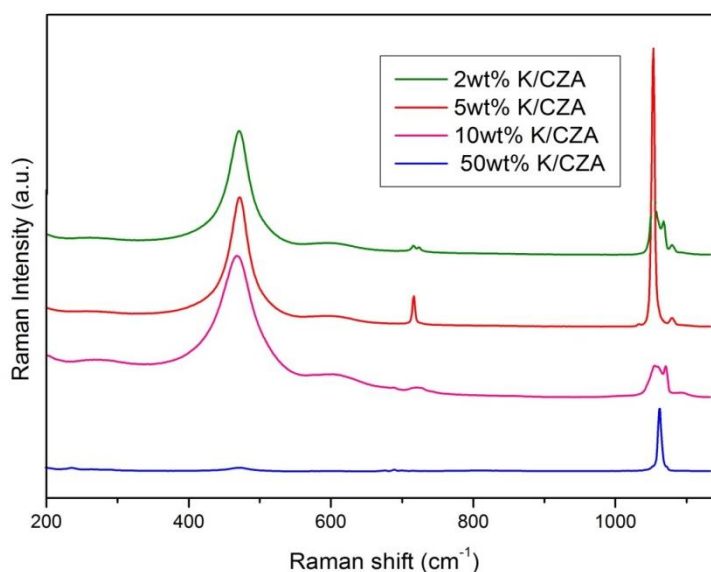


Figure 3.42 Raman spectra - varying the loading of K/CZA (not normalised as the scales for the various spectra are different)

A proof for the loss of cubic structure, with increased potassium promotion, was evident from the Raman spectra shown in figure 3.42. The cubic fluorite symmetry for CeO₂ was lost or was not accessible in the case of 50% K/CZA (high loading), represented by the blue line at 460cm⁻¹. The potassium appeared to create a morphological change in the CZA structure. In the case of the 2, 5, 10% K/CZA catalysts the CeO₂ structure was still maintained. The increased intensity of the peaks with K loading was due to the re-calcination of the calcined support upon impregnation at 500°C. There had been a considerable loss in surface area upon impregnation of K onto the different supports. The crystallite sizes also increased upon increased weight loading of K/CZA following a trend- 50%>10%>5%>2%. The ideal weight loading of K on CZA was 10% with small crystallites (~6nm) and surface area of 17m²g⁻¹. The reduction of the surface area could be attributed to the plugging of the micro pores in the catalyst by K₂CO₃.

Table 3.17 Physical properties of K/CZA- varying the weight loading

Sl.No	Catalyst	Surface area (m ² g ⁻¹)	2θ	Crystallite size (nm)	Peak temperature (reduction) °C	H ₂ consumption (μmol g ⁻¹)
1.	2% K/CZA	3	28.87	4.2	514	2193.55
2.	5% K/CZA	4	28.80	4.4	513	3482.24
3.	10% K/CZA	17	28.86	5.9	490	1240.289
4	50% K/CZA	2	32.69	39.2 (from 2θ=32°) not accurate determination	498	622.5727

The TPR profiles of the catalysts K/Ce_xZr_{1-x}O₂ are reported in figure 3.43. The most remarkable feature was increase in area of the second reduction peak in all the catalysts, indicating the greater extent of reduction. These changes were slightly different from those observed by Aneggi *et al.* for CeO₂ doped with different potassium amounts (3-13.5%) [32]. They observed that an increase in loading of K on the surface led to larger hydrogen consumption of the second peak in the profile and associated this fact to the formation of surface carbonates which could be reduced to CO and H₂O during H₂-TPR, as is seen in the case of the 2 and 5% K/CZA catalysts. But for higher weight loadings the peaks were broad and attain the bimodal pattern, for 10% and 50% K loading, indicating that the carbonates present on these CZA supports decreased the reducibility and the surface area of the supports. The formation of carbonates could be correlated to the XRD and Raman results that have demonstrated the presence of carbonates. This could be responsible for the similarities in the second reduction peaks in these catalysts to the observations made by Aneggi *et al.* The hydrogen consumption values for 10%K/CZA and 50%K/CZA were lower than for the other two catalysts and these follow the bimodal pattern of CeO₂ reduction with a surface reduction at around 480°C and bulk reduction between 700-800°C.

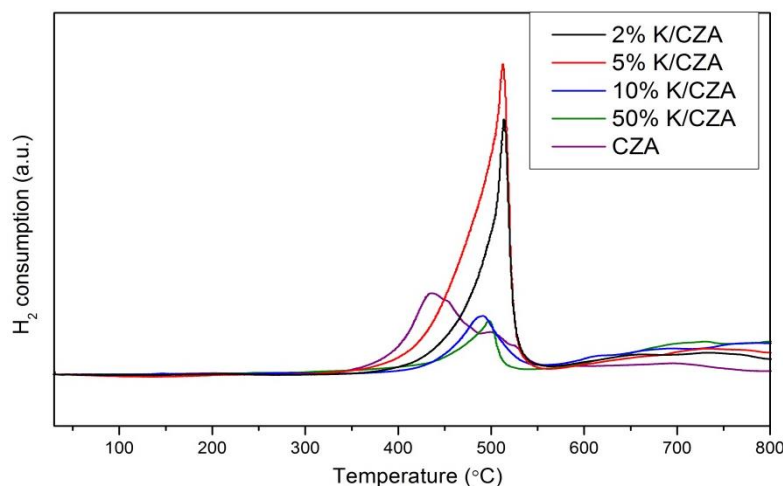


Figure 3.43 TPR profiles- varying K loading on CZA

Figure 3.43 showed that the support material (purple line) reduced at a lower temperature and was therefore easier to reduce than the K doped materials. The support reduced at around 400°C (surface) and 500°C (bulk) while that for 10 and 50 %K it had shifted to slightly higher temperatures. Thus proving that the supports were easily reducible but the extent of reduction was greater for (10, 50%K) impregnated supports (table 3.17).

Comparing K/CZA and K/CZ (CZ supports, with a constant weight loading of 10% as shown in figure 3.44), the values for peak reduction temperatures (from table 3.17), showed that the changes were not very significant, except in case of 10% K/Ce_{0.3}Zr_{0.7}O₂, where the profile showed a broad peak, with consumption of H₂ in the range 500-700°C. A second peak was also observed indicating that the surface and bulk reduction occurred separately. This was similar to the case of K/CZA (10, 50% weight loading).

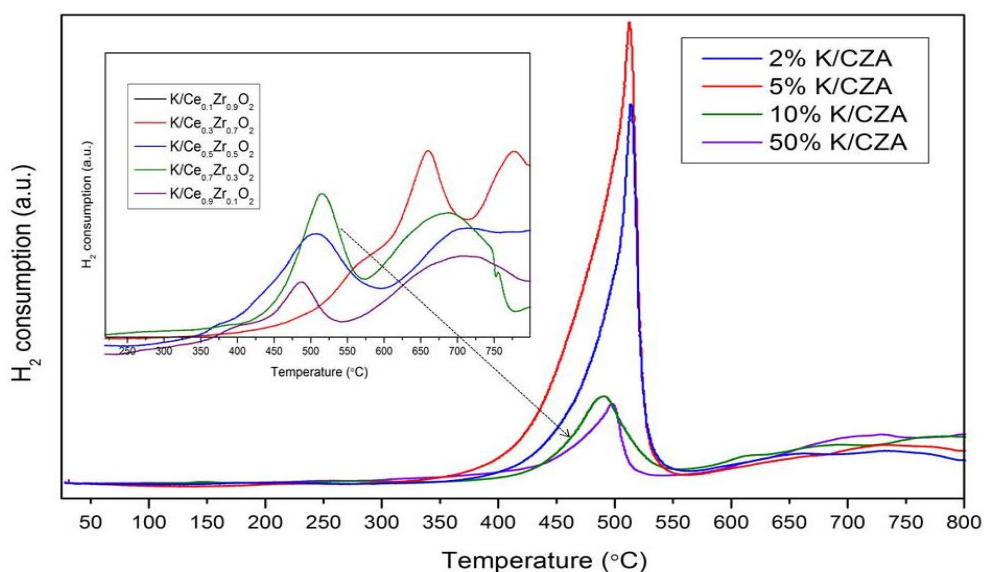


Figure 3.44 TPR profiles- comparison of K/CZA and (inset- K/CZ catalysts)

This could be due to the fact that Ce-content on the low surface area had been covered by K_2CO_3 , making the diffusion of H_2 to reach the reducible ceria more difficult. XPS results showed that 10%K/Ce_{0.3}Zr_{0.7}O₂ had the largest concentration of potassium on the surface and so, it seems that this fact could explain the lower reducibility of Ce⁴⁺.

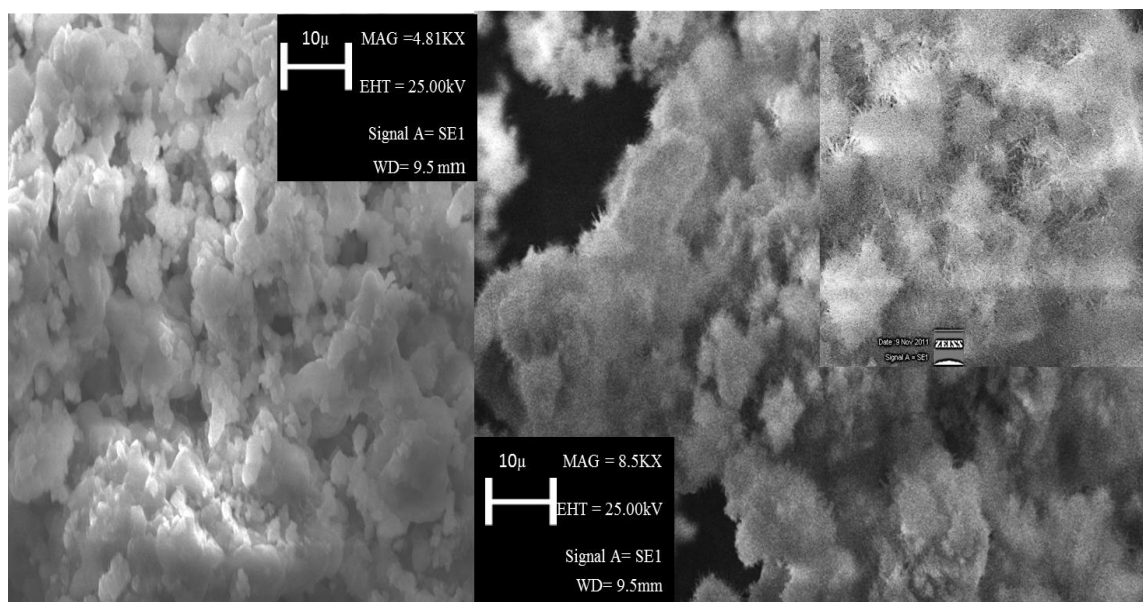


Figure 3.45 SEM micrographs of 2%K/CZA catalysts

SEM shows that the 2% K/CZA did not show much difference from that seen for the CZA support. Upon increasing the concentration of K on CZA, the structure changed. Long needle like fine particles were present on the surface of the CZA structure, arising

from the K_2CO_3 impregnation on CZA. In the figure 3.46 below, the impregnation of K was clearly evident. A particle of $10\mu m$ was seen adjoint to the CZA, formed of hair-like fine structures.

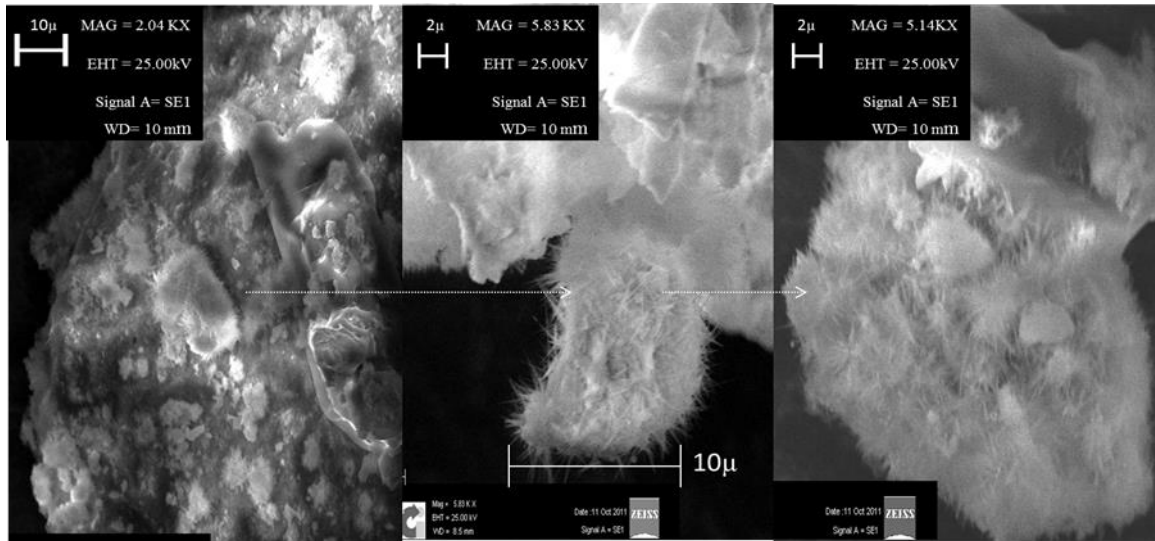


Figure 3.46 SEM micrographs for 10%K/CZA-a) 2.04KX, b) 5.83KX; c) 5.14KX

EDX analysis showed that the K was impregnated on the CZA as it was present as a dominant peak on the CZA. The loading was accurate from the EDX analysed when compared to the preparation method for K_2CO_3 impregnation on CZA.

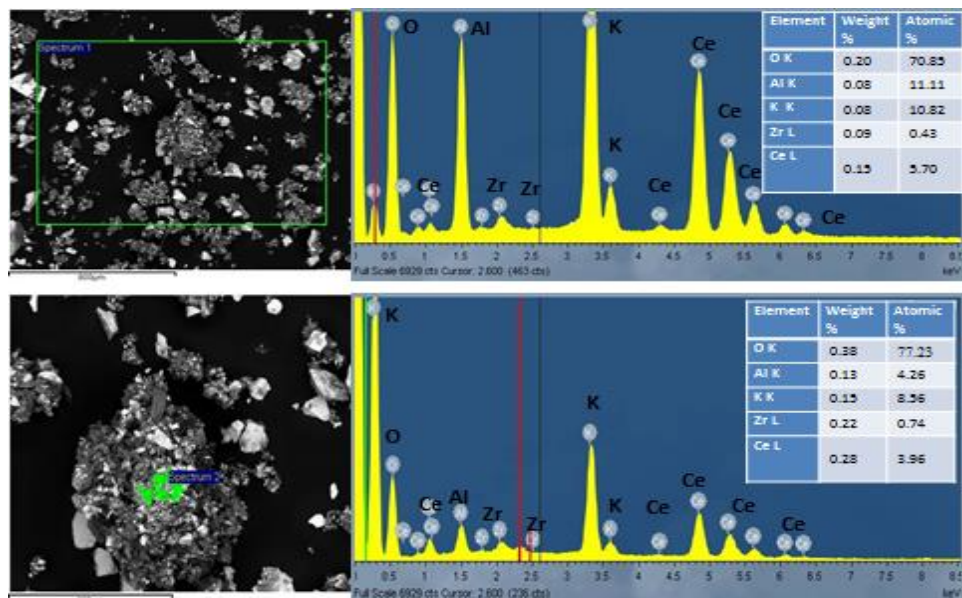


Figure 3.47 a) shows the presence of 10% K distributed on the CZA particles while b) shows the distribution of K on a single particle surface.

XPS for the various weight loadings of K on CZA showed that an increase in content of K_2CO_3 on the surface of CZA, indicating a change in catalyst structure. The CZ was seen to be depleted on the surface as the content of K increased beyond 10%. This effect explained the drop in performance of the catalyst, with loading as high as 50% K, where the surface was completely covered with K_2CO_3 (figure 3.48).

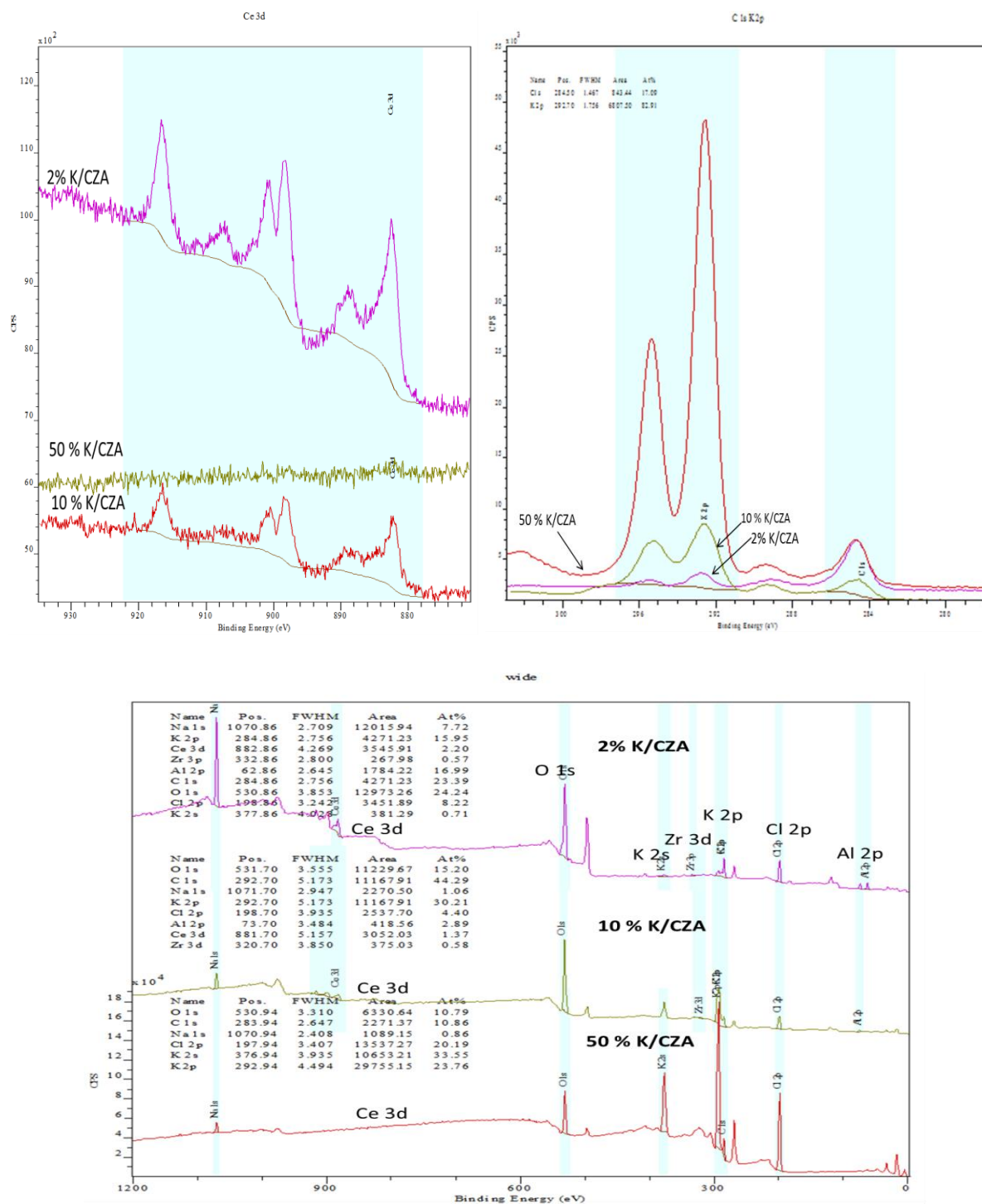


Figure 3.48 Varying K content on CZA a) change of Ce 3d; b) change of K 2p;c)wide scan

Figure 3.48 a) represents change in Ce 3d orbitals with increase in K loading (b) represents the K 2p orbitals on increasing the content from 2-50% and (c) shows the entire spectra for the three different catalysts with a detailed listing of all the elements.

Table 3.18 XPS analyses- Elemental composition – narrow scan

Atomic % narrow scan									
Sl. No	Catalyst	O 1s (531 ev)	Zr 3d (183 ev)	Al 2p (75 ev)	C 1s	K 2s	K 2p (368.1, 374 ev)	Ce 3d (884, 901 ev)	Ce:Zr ratio
1	2% K/CZA	47.34	1.17	19.64	27.0	1.62	2.15	2.74	2.44:1
2	10% K/CZA	29.99	0.65	10.13	46.26	8.65	42.83	1.59	2.34:1
3	50% K/CZA	3.86			55.94	6.59	33.62		

Table 3.18 represented the narrow scan of the elements present on the surface of this catalyst. This helped to understand the change in ratio of Ce: Zr with increase in loading from 2-50% K₂CO₃. The ratio was maintained at 2.4:1 until 10% loading onto CZA, beyond which the CZ lattice was destroyed by K₂CO₃. The increase in loading was observed as was seen from the K 2s and K 2p orbitals. The same was represented in the wide scan too indicated in table. 3.19.

Table 3.19 XPS analyses- Elemental composition – wide scan

Atomic % wide scan										
Sl. No	Catalyst	O 1s (531 ev)	Cl 2p (199 ev)	Zr 3d (183 ev)	Al 2p (75 ev)	C 1s	K 2s	K 2p (368.1, 374 ev)	Ce 3d (884, 901 ev)	Ce:Zr ratio
1	2% K/CZA	24.24	8.22	0.62	16.99	23.29	0.71	15.95	2.20	3.54:1
2	10% K/CZA	15.81	4.36	0.57	2.89	43.48		30.90	1.36	2.38:1
3	50% K/CZA	10.79	10.19			10.86	35.55	29.76		

3.6.2 Soot oxidation

Varying the weight loading of K_2CO_3 on $CeO_2-ZrO_2-Al_2O_3$ (as shown in figure 3.49) showed that 10wt% K was the most active composition, with an onset of 297°C and complete oxidation occurred by around 476°C. In the absence of alkali metal supported catalyst, the oxidation temperatures were around 600°C. The alkali metal tends to decrease the temperature of oxidation through a mechanism explained below. This weight loading was used for the comparative studies between alkali and alkaline earth metals.

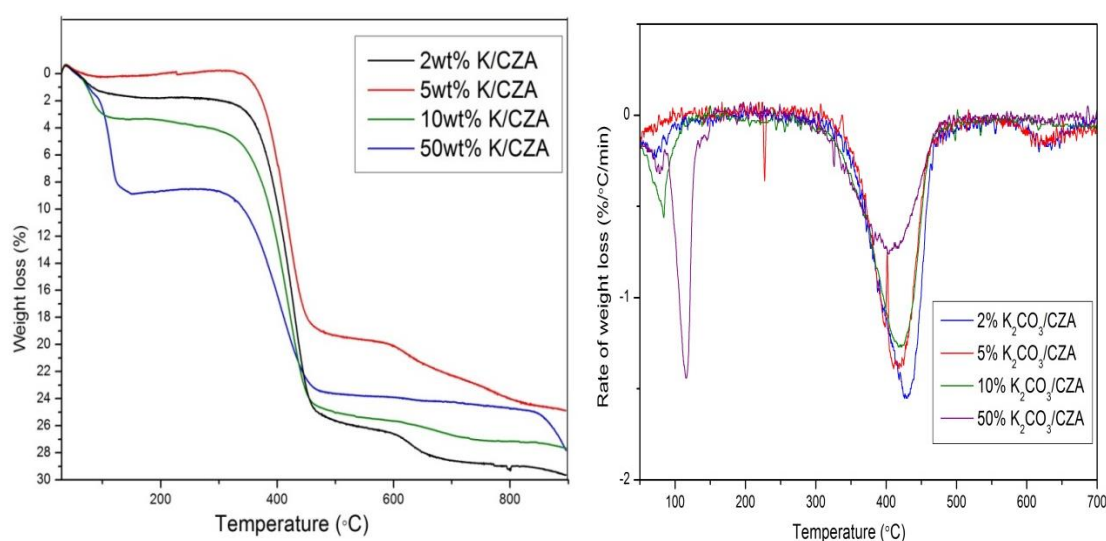
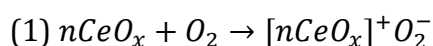


Figure 3.49 Soot oxidation activity- Variation of K content on CZA

In the K-impregnated catalysts, K_2CO_3 has been used as potassium source as this is capable of providing the carbonates necessary for soot oxidation. It has a high melting point, 891°C. XRD diffractograms and Raman spectra indicated the presence of carbonates, indicating that potassium was present as K_2CO_3 , loaded on the mixed oxides $Ce_xZr_{1-x}O_2$. As suggested in the literature [37], the carbonate can form potassium oxide at high temperature (Eq. 5), which would decompose as mentioned before to form potassium superoxide (Eq. 6) at 350°C. This superoxide has a melting point around 380°C, and it could be the responsible for the high surface diffusion of potassium in these systems (Eq. 7). The potassium superoxide is a strong oxidising agent which could be also involved in the restoration of Ce(IV) from Ce(III) to close the well-known redox cycle of cerium oxide (Eq. 1-3).



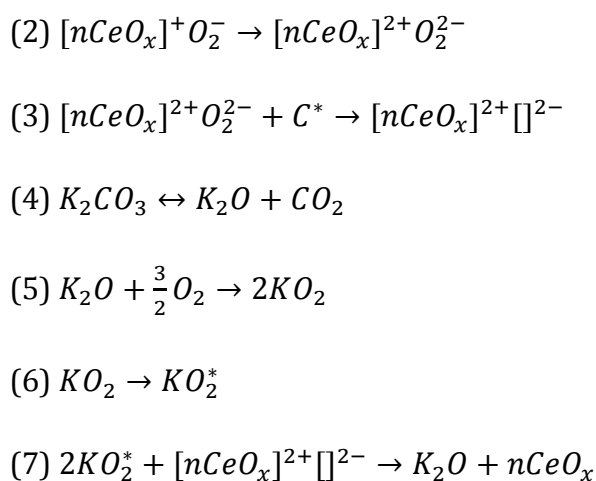


Table 3.20 Soot oxidation activity – varying of K/CZA

Sl.No	Alkali metal on CZA(Na ₂ CO ₃)	Onset temperature (T _{on}) (°C)	Extrapolated onset temperature (T _{eo})(°C)	T _p (°C)	T _f (°C)
1	2% K/CZA	323	342	430.02	475
2	5% K/CZA	311	347.1	414.34	466.23
3	10% K/CZA	297	336.41	421	476.22
4	50% K/CZA	271	304.3	404	483.4

As observed from Table 3.20, the peak temperatures for K-impregnated catalysts were around 380°C (melting point for potassium superoxide) and this observation would be in agreement with the proposed reaction mechanism, suggesting that contact between both reactants, soot and catalyst has been greatly improved after potassium carbonate impregnation. The best activity was demonstrated by the 10%K loaded catalyst, suggesting this to be the optimum loading of K₂CO₃ onto the support. On varying the loading of K (K₂CO₃) on CeO₂-ZrO₂-Al₂O₃ (2, 5, 10, 50wt %), 10 wt% was found to be the most ideal loading for effective soot oxidation. An increase in weight loading of K beyond 10% showed an increase in final temperatures. The 50%K/CZA catalyst was also ideal in terms of the onset and peak temperatures but it was observed that there was a greater loss of weight at the 100°C in the case of this catalyst and upon subjecting this catalyst to a second run with soot the temperatures of oxidation were

very high owing to the loss of the metal (high weight loading of K). The rate of oxidation was also comparatively slower as compared to 10%K/CZA. Quantitative analysis of the reduction profiles for varying K loading on CeO₂, studied by Aneggi *et al.* was reported in Table 3.21, which showed that the amount of oxygen extracted (equivalent to hydrogen removal) increased with the addition of potassium up to a loading of 10 wt%; then a plateau was reached, and for higher amount of potassium loading, the oxygen extracted was almost constant. Analysis of the reaction products from reduction showed that, in the presence of potassium the majority of oxygen extracted was in the form of CO, while modest quantities of CO were formed in the absence of potassium.

Table 3.21 Oxygen extracted in TPR experiments for pure cerium and CeO₂ doped with K as KOH (fresh samples)[32]

Sample	O ₂ extracted X 10 ⁴ (mol/g sample)
CeO ₂	6.40
Ce 3K	7.13
Ce 6.5K	9.58
Ce 10K	10.46
Ce 13.5K	10.16

Table 3.21 showed that on varying the content of K the amount of extractable oxygen from CeO₂ increased but was constant beyond 10%K loading. The soot oxidation temperatures for 10%K/CZA were lower than that observed in literature for K supported on CeO₂ [32]. In the absence of alkali metal supported catalyst, the peak oxidation temperatures were around 600°C, clearly proving that the alkali metal tends to decrease the temperatures by the above mechanisms, acting as a promoter. This weight loading was used for the comparative studies between alkali and alkaline earth metals.

3.7 Comparison of alkali and alkaline earth metals

3.7.1 Characterization

The optimum weight loading of 10% K_2CO_3 (on CZA- Na_2CO_3 coprep.) was used for impregnating different alkali and alkaline earth metals, to understand the effect of these as promoters for soot oxidation. The X-ray diffractograms showed that the cubic CeO_2 phase had been maintained, with an indication of a CZ mixed phase when compared to the JCPDS database. The peak width for all the peaks in case of 10%Na/CZA and 10%Cs/CZA was found to be greater as compared to 10% K/CZA, thus indicating larger crystallites with sharp peaks. There was a clear shift observed to lower values of 2θ on comparison of the support with the impregnated catalysts. On moving down the group, from Li to Cs, the crystallite size decreased (figure 3.50).

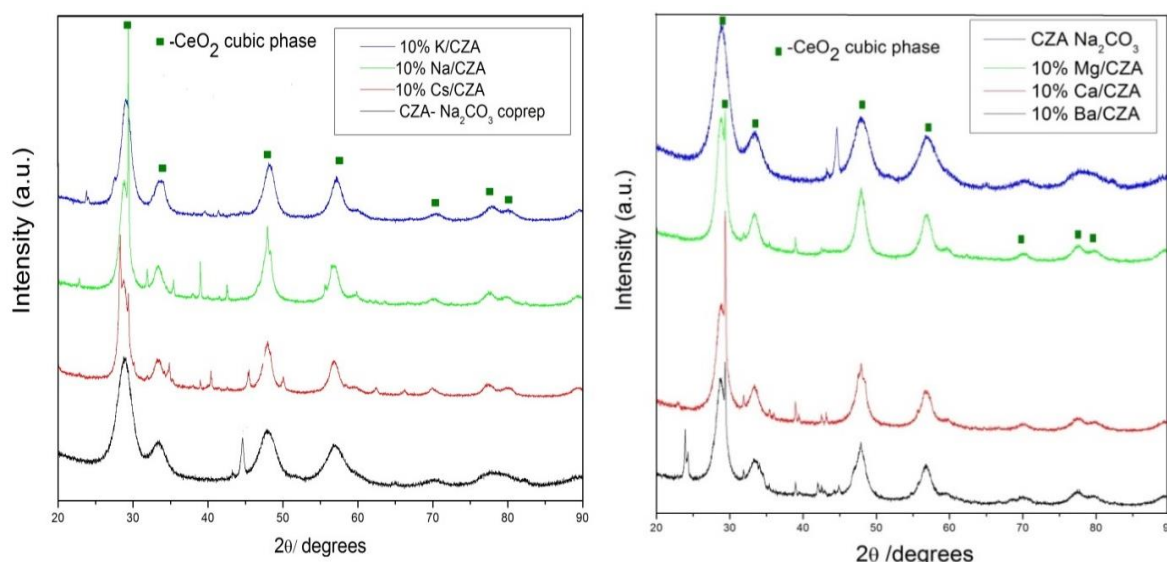


Figure 3.50 X-ray diffractograms for a) alkali metals; b) alkaline earth metals on CZA

Raman spectroscopy revealed that the cubic symmetry of the CeO_2 phase was maintained in the alkali and alkaline earth metal impregnated CZA catalysts. The peak at 460cm^{-1} shifted to slightly higher values as shown in the figure 3.51 for Cs and K impregnated catalysts, indicating that they possess larger crystallites and that the cubic CeO_2 structure was slightly distorted in these cases. In the case of K impregnated catalysts, the peaks were more intense and the peak at 600cm^{-1} representing the distorted cubic CeO_2 , owing to the presence of ZrO_2 in the lattice was also predominant in this case.

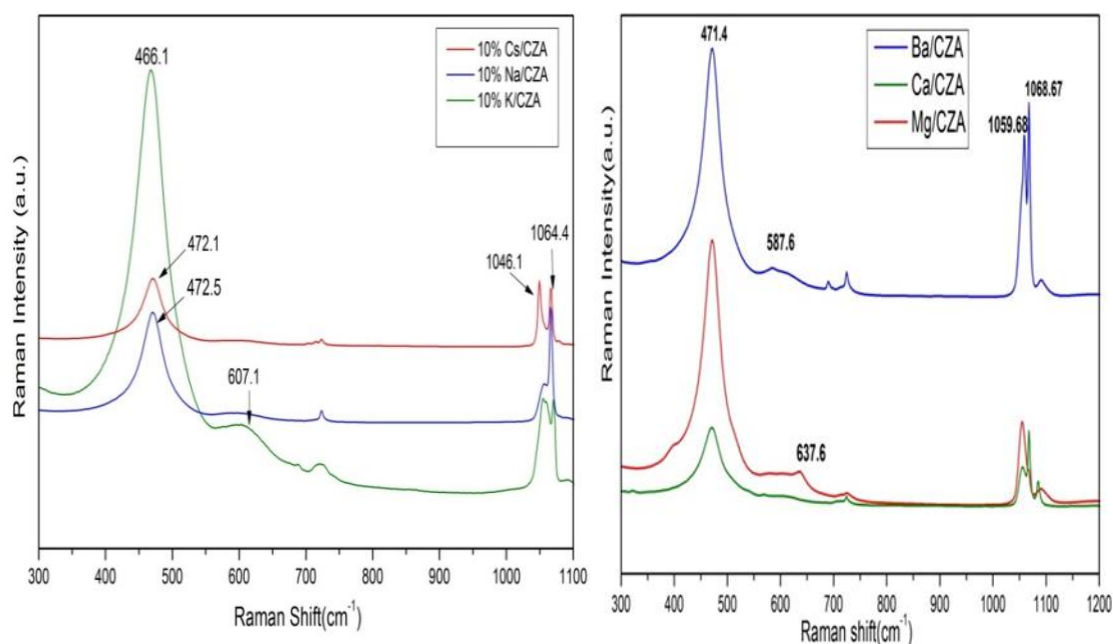


Figure 3.51 Raman spectra – a) alkali metal on CZA; b) alkaline earth metal on CZA

In the case of alkaline earth metal supported on CZA, the peaks represented the cubic phase at 471.4 cm⁻¹ and a distortion at 600cm⁻¹. The additional peaks observed were for the Ba, Ca and MgNO₃ peaks.

Table 3.22 Physical properties of Alkali and alkaline earth metal impregnated catalysts

Sl.No	Catalyst	Surface area (m ² g ⁻¹)	2θ (°)	Crystallite size (nm)	Peak temperature (reduction) °C	H ₂ consumption (μ mol g ⁻¹)
1.	10% Cs/CZA	6	47.92	9.9	555	3819
2.	10% Na/CZA	8	47.90	6.9	552	2574
3.	10% K/CZA	17	48.26	7.2	490	1240
4.	10% Ba/CZA	9	28.72	6.4	512	4158
5.	10%Ca/CZA	12	28.77	6.6	526	4996 821.5
6.	10%Mg/CZA	22	28.69	7.9	500	4165

The crystallite sizes were between 6-8 nm for the alkali and alkaline earth metal oxides. Impregnation of these metals on CZA drastically reduced the surface area due to these large crystallites plugging the pores.

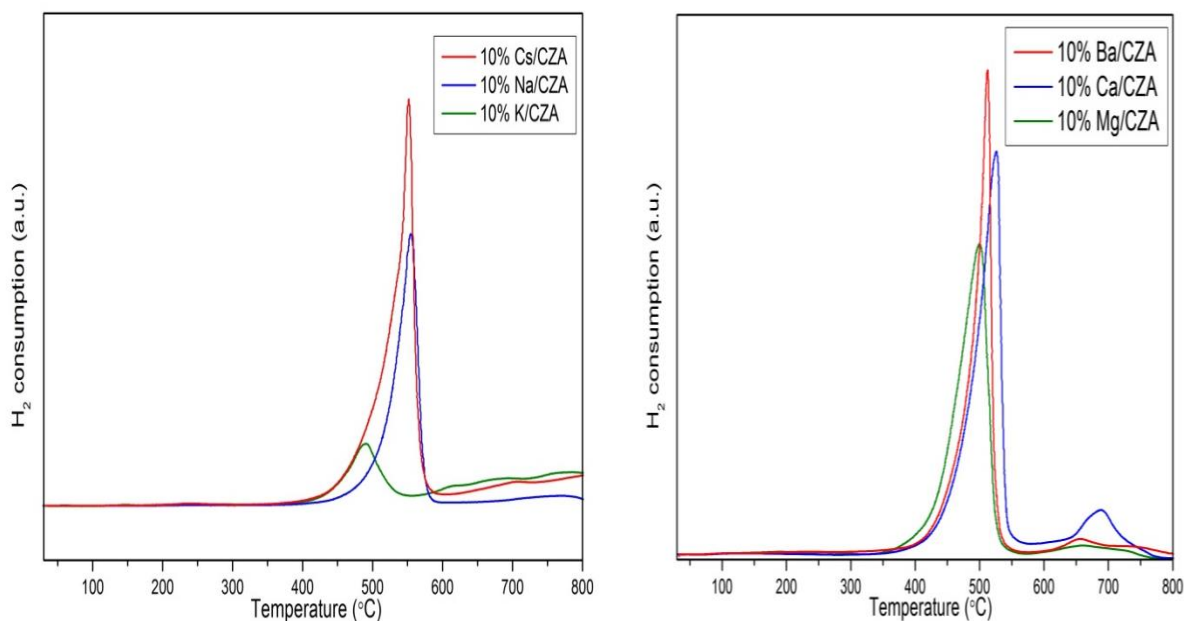


Figure 3.52 TPR profiles – a) alkali metals; b) alkaline earth metal impregnated on CZA

TPR profiles showed that the reduction peak for CeO_2 was at around 450°C with a peak for surface and bulk reduction, while in the case of the alkali metals there was only a single reduction peak that was evident, indicating that the surface and bulk reduction occurred at the same time. The reduction coincided with the onset of soot oxidation. The peak area was smaller for the K/CZA while that for Na and Cs were greater indicating the extent of reduction was in the order - $\text{Cs} > \text{Na} > \text{K}$. But in these cases the nitrates were used for the ease of preparation and the temperatures for soot oxidation for Cs and K were quite similar for reasons described in section.

3.7.2 Soot oxidation activity - Comparison between alkali and alkaline earth metal supported $\text{CeO}_2\text{-ZrO}_2\text{-Al}_2\text{O}_3$

Amongst the alkali metals 10wt% Cs and 10wt% K on $\text{CeO}_2\text{-ZrO}_2\text{-Al}_2\text{O}_3$ showed similar activity and lower oxidation temperatures compared to 10wt%Na (Figure 3.53). It was suggested in literature [8, 38] that under tight contact condition the activity depends on the electro-positivity of the alkali metals and owing to the lower electro-negativity of Cs and K, the dissociative chemisorption of O_2 occurs more readily on the surface of these alkali metals leading to a stronger electrostatic attraction with the surface O_2 , which results in better dispersion. The temperatures of oxidation were lower compared to that observed by Aneggi *et al.* for various alkali metals (10wt %) on CeO_2 [8, 38].

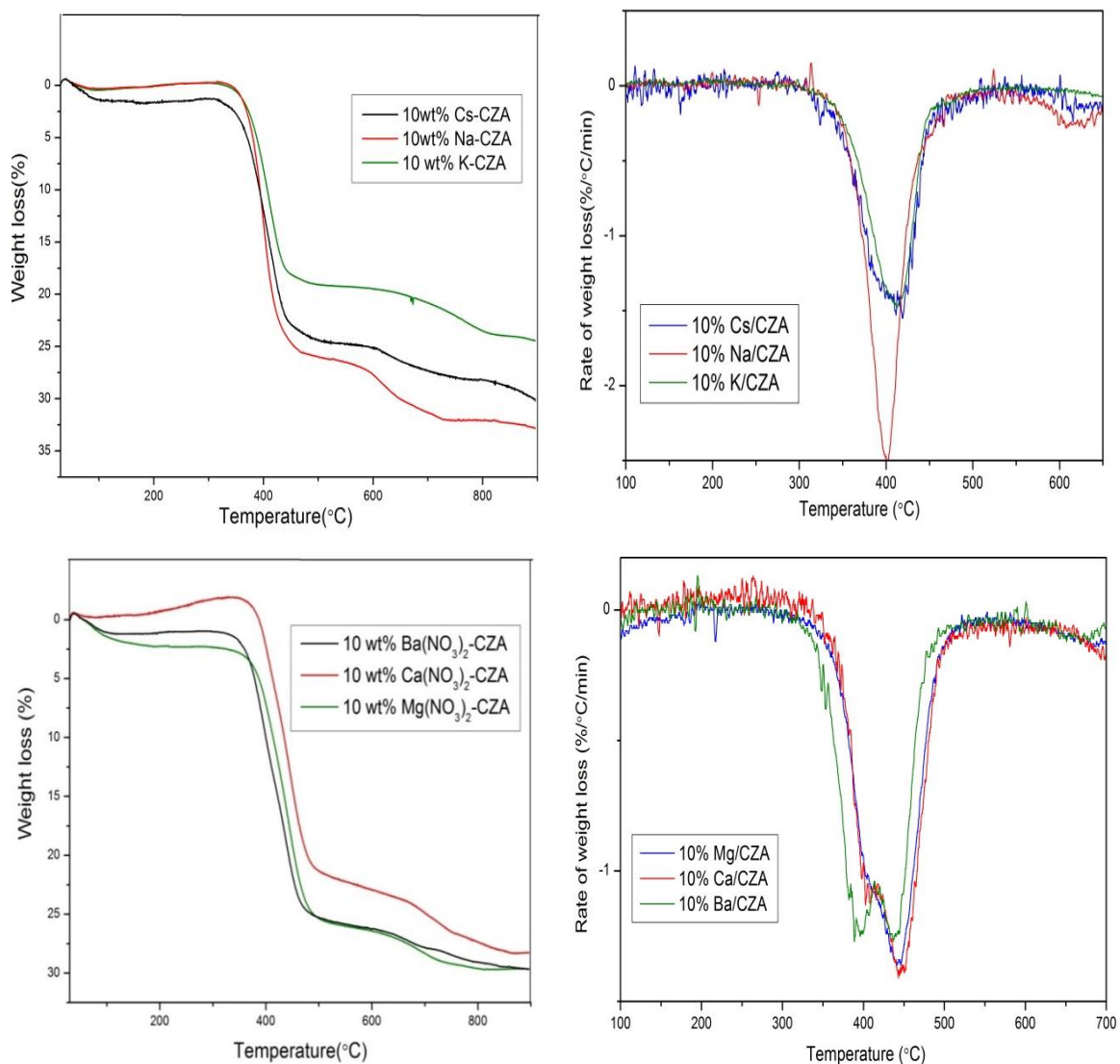


Figure 3.53 Soot oxidation activity – a) alkali metals (top); b) alkaline earth metals (bottom)

Moreover, decreasing along the group, the catalytic activity increased (table 3.23), with caesium hydroxide being the most efficient catalyst in soot oxidation. It has been reported that alkali metals are much more active than metal oxides under tight contact conditions and arranged in order of their activity as Cs >K> Na > Li, which is similar to this investigation [8,32].

Table 3.23 Soot oxidation activity – alkali and alkaline earth metals on CZA

Sl.No	Alkali metal on CZA (Na ₂ CO ₃)	Onset temperature(T _{on})(°C)	Extrapolated onset temperature (T _{eo})(°C)	T _p (°C)	T _f (°C)
ALKALI METAL ON CZA					
1	10%Cs/CZA	292.01	343.01	411	452
2	10%Na/CZA	317	361.3	400.43	470.24
3	10%K/CZA	304.4	350.4	411	458
ALKALINE EARTH METAL ON CZA					
1	10%Ba/CZA	304.3	344.4	414.34	480.11
2	10%Ca/CZA	323	367	443.3	502.3
3	10%Mg/CZA	326.4	361.3	442.1	523.1

3.8 Combination of Silver and Potassium on the support

Silver on CeO₂ has been widely studied in the past with most catalysts being prepared by impregnation. However Yamazaki *et al.* prepared a material with “rice-ball” morphology as is shown in Figure 3.54. This catalyst had high activity for soot oxidation with peak temperatures around 315°C (TC) and 376°C (LC), for a catalyst: soot ratio of 19:1, as compared to the 10:3 used in our analyses study [39].

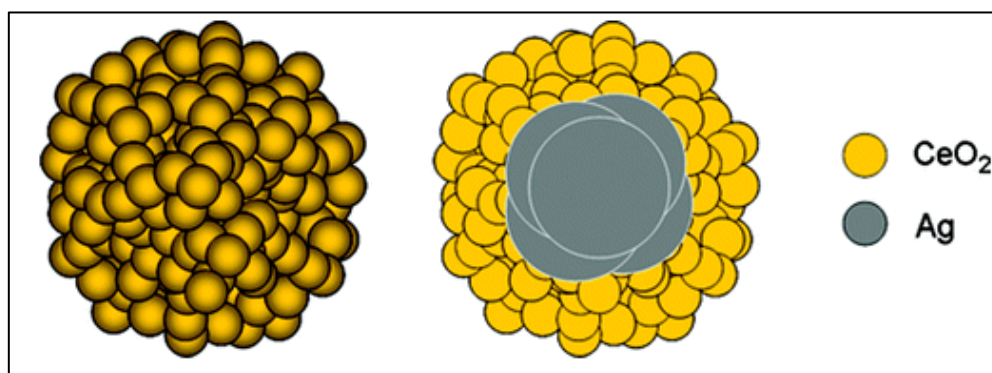


Figure 3.54 Scheme of the structure of a “rice-ball” Ag-CeO₂ catalyst [40]

The synergistic effects between potassium and an active precious metal such as silver, impregnated onto a transition metal oxide surface, with the aim of reducing the

soot combustion temperatures, was studied in this research. Thus the first approach was to synthesise the same rice ball structure, and promote the oxidation with the incorporation of potassium onto the surface. This method helped to keep the silver surrounded by ceria, in an inverted design with respect to the conventional supported catalysts, with potassium impregnated onto the surface, resulting in a material in which potassium and silver would not be in intimate contact.

The method of preparation of this catalyst is mentioned in chapter 2. This was compared with the direct impregnation method of Ag–K onto CZA with a weight loading of 2 and 10% respectively.

3.8.1. Catalyst characterisation

X-ray diffraction and X-ray photoelectron spectroscopy showed that the Ag and ceria did not form a homogeneous mixture. Figure 3.55 showed that all characteristics peaks for ceria were observed with sharp signals that indicated a highly crystalline structure. Also, the crystallite size shown in Table 3.24 was considerably larger than that of the previously studied ceria-zirconia and CZA mixed oxides, suggesting a pure ceria phase. The diffractogram also showed characteristic peaks for Ag, with no other phases being detected. The lattice parameter for metallic Ag was 4.090 Å, with a face-centered cubic structure and this value was almost identical to the value calculated for Ag particles in plane (111). Thus, we can say that the Ag and CeO₂ were not dispersed in the homogeneous mixture.

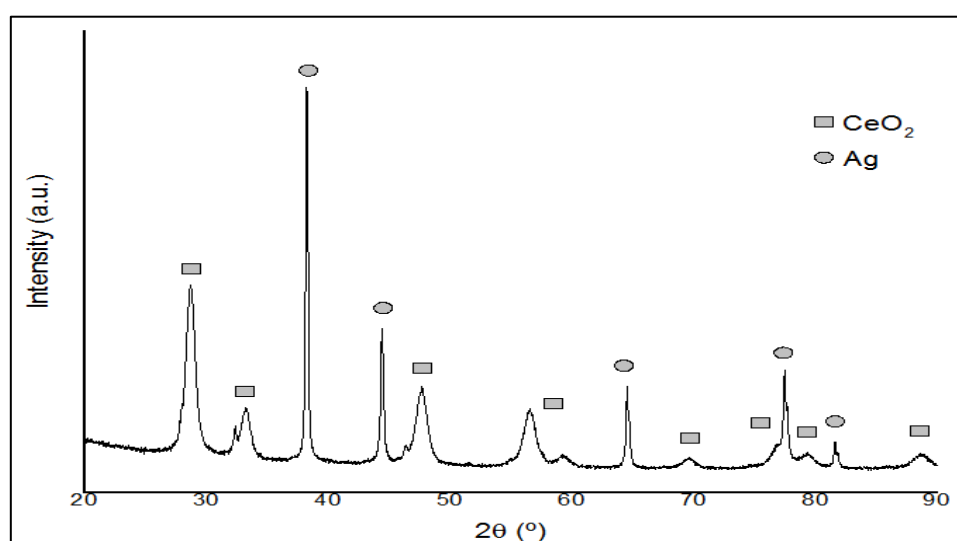


Figure 3.55 XRD diffractogram of Ag-CeO₂.

Table 3.24 Summary of crystallite size and lattice constants for Ag-CeO₂.

Ag-CeO ₂ component	Most intense Bragg angle ^a (°)	Crystallite size ^b (Å)	d _{calc} (Å)
Ag	38.22	176	2.3519
CeO ₂	28.68	118	3.1084

^a Most intense angle corresponds to planes (111) in both cases; ^b Crystallite sizes were calculated by means of Scherrer equation.

Table 3.25 summarised the XPS data for the Ag/CeO₂ catalyst that confirmed that Ag was present on the surface as metal, Ag⁰. The binding energies for Ag⁰ and Ag⁺, studied from literature [41] showed that the silver of AgNO₃ was successfully reduced by Ce(III) species upon co-precipitation. The XPS spectra for Ce 3d showed that the Ce (III) nitrate used as precursor had been oxidized to Ce (IV). This was confirmed by the TGA results, given at the end of this chapter, showing the formation of the respective oxides from the precursors, similar to that occurring during calcination.

Table 3.25 Summary of surface composition on Ag-CeO₂.

Catalyst	C _{1s} ^a (At%)	Ce _{3d} (At%)	O _{1s} (At%)	Ag _{3d} (At%)
Ag-CeO ₂	56.89	6.76	32.37	3.23

^a The value for C and O on the surface has hugely affected the percentages for Ce and Ag, and it is mainly due to 'atomic' carbon from the atmosphere.

This indicated that the rice-ball morphology was not achieved as the amount of silver on the surface was a significant amount as compared to the cerium. To prove this was not the case the exact molar ratio, in a homogeneously distributed Ag-CeO₂ catalyst was compared with that obtained through XPS.

AgNO₃ (0.7408 g, 169.87 g/mol) and Ce(NO₃)₃·6H₂O (1.2623 g, 434.22 g/mol) were used as precursors:

$$M_w(\text{Ag}) = 107.87 \text{ g/mol}, \quad M_w(\text{CeO}_2) = 172.12 \text{ g/mol}$$

$$m_{\text{Ag}} = \frac{0.7408 \text{ g AgNO}_3}{169.87 \frac{\text{g}}{\text{mol}} \text{ AgNO}_3} \times 107.87 \frac{\text{g}}{\text{mol}} \text{ Ag} = 0.47 \text{ g Ag} \rightarrow n_{\text{Ag}} = 4.36 \text{ mmol Ag}$$

$$m_{CeO_2} = \frac{1.2623 \text{ g } Ce(NO_3)_3 \cdot 6H_2O}{434.22 \frac{\text{g}}{\text{mol}} Ce(NO_3)_3 \cdot 6H_2O} \times 172.12 \frac{\text{g}}{\text{mol}} CeO_2 = 0.50 \text{ g } CeO_2 \rightarrow \rightarrow n_{CeO_2}$$

$$= 2.90 \text{ mmol } CeO_2$$

Hence, the mol% Ag and weight % Ag was calculated for the prepared catalyst, Ag-CeO₂:

$$Ag \text{ (weight\%)} = \frac{0.47 \text{ g } Ag}{0.50 \text{ g } CeO_2 + 0.47 \text{ g } Ag} \times 100 = 48.45 \text{ w\%}$$

$$Ag \text{ (mol\%)} = \frac{4.36 \text{ mmol } Ag}{2.90 \text{ g } CeO_2 + 4.36 \text{ mmol } Ag} \times 100 = 60.06 \text{ m\%}$$

Now, a ratio CeO₂/Ag was obtained for easier comparison. This value was equivalent to the number of CeO₂ molecules per silver atoms in the whole catalyst:

$$\text{Atomic ratio } \frac{Ce}{Ag} \text{ in the catalyst} = 2.90/4.36 = 0.66 : 1$$

From the XPS data collected in Table 3.25, the amount of Ag was given, and the amount of CeO₂ could be calculated, assuming that all surface cerium is as CeO₂ on the surface. The XPS results for Ce 3d suggested a huge predominance of Ce⁴⁺ therefore the error was not going to be important.

$$\%Ag \text{ (surface)} = 3.23\%$$

$$\%Ce \text{ (surface)} = 6.76\%,$$

The ratio CeO₂/Ag on the surface was obtained and compared with the atomic ratio in the catalyst.

$$\text{Atomic ratio } \frac{CeO_2}{Ag} \text{ on the surface} = \frac{6.76}{3.23} = 2.09 : 1$$

$$\frac{\text{Surface ratio}}{\text{Catalyst ratio}} = \frac{2.09}{0.66} = 3.16 : 1$$

Thus, it could be said that there was nearly 3 times more CeO₂ on the surface than in the whole catalyst. This fact was supporting the idea of a “rice-ball” catalyst. Upon impregnating this catalyst with 10% K₂CO₃ on the surface, to improve the activity, the ratio of the CeO₂: Ag was calculated.

Table 3.26 Elemental composition –Ag/CeO₂ through XPS

Name	Position	FWHM	R.S.F.	Area	% Conc.
Ce 3d	894.41	4.859	8.808	34556.54	13.89
O 1s	525.41	2.442	0.78	10298.2	46.74
Ag 3d 5/2	364.01	1.215	3.592	2369.69	2.34
C 1s	281.21	1.642	0.278	2268.52	28.89
K 2p	288.91	1.64	1.466	3374.74	8.15

From table 3.26, we obtained the data for the atomic % of Ce and Ag = 13.89/2.34= 5.93:1 ~ 6:1 (narrow spectra as shown in table) or 10.43/2.1=4.96:1 from the wide spectra shown in figure 3.56d. The K₂CO₃ on the surface of the CeO₂ @ Ag core shell structure caused a depletion in the content of the Ag and CeO₂ on the surface, as was seen from the drop in atomic concentrations in the two cases shown in table 3.26 and the inset table in figure 3.56d.

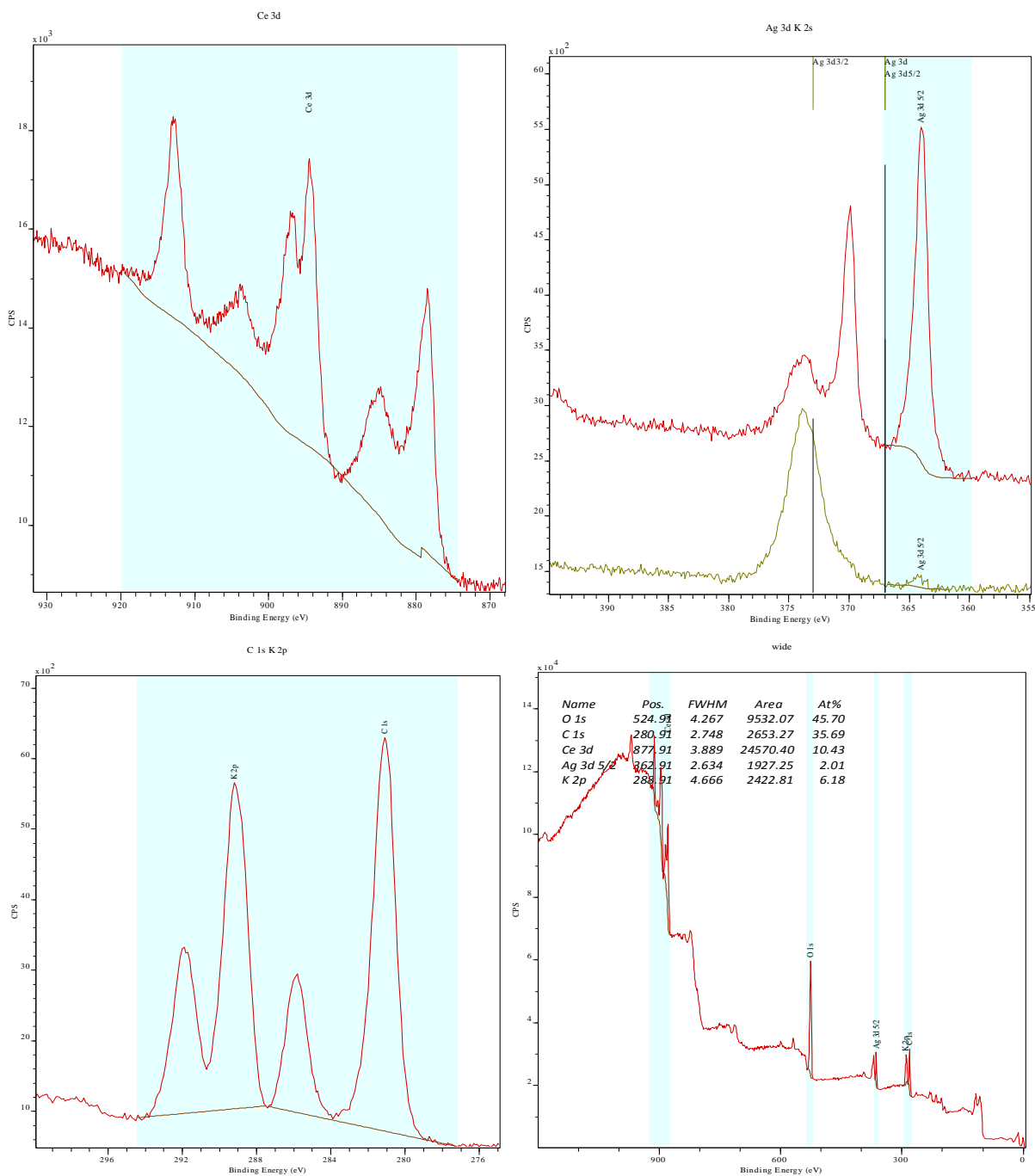


Figure 3.56 a) Ce-3d spectra; b) Ag 3d and K 2s; c) C 1s and K 2p; d) Wide scan spectrum

Thus from the XPS data it could be concluded that the catalyst took the form of a layered structure with the central core containing Ag and a shell surrounding it made of CeO₂, followed by an impregnation of K₂CO₃ on the surface of this core shell structure. The depth of this layered structure was not beyond the XPS electron penetration/profiling depth of 20Å. The bulk of the catalyst had been studied using EDX.

Figure 3.57 shows the EDX-mapping of K/CeO₂@Ag. This showed the core is made of up Ag, surrounded by the CeO₂ shell on the outside of the particle. The formation of the oxide was also clearly evident from the vast expanse of the oxygen on the catalyst. This particle was chosen with a carbon background to indicate the contrast as could be seen from the C Ka1 image, clearly indicating this contrast between the particle under study and the carbon background from the carbon disc. K as K₂CO₃ was also present as the distinct bright white spots on the CeO₂ shell as clusters of small particles. Existence of K₂CO₃ in the carbonate phase was confirmed from XPS C 1s for carbonate peak. This distribution was more or less even as can be seen from the figure3.57, thus enhancing the active sites on the catalyst.

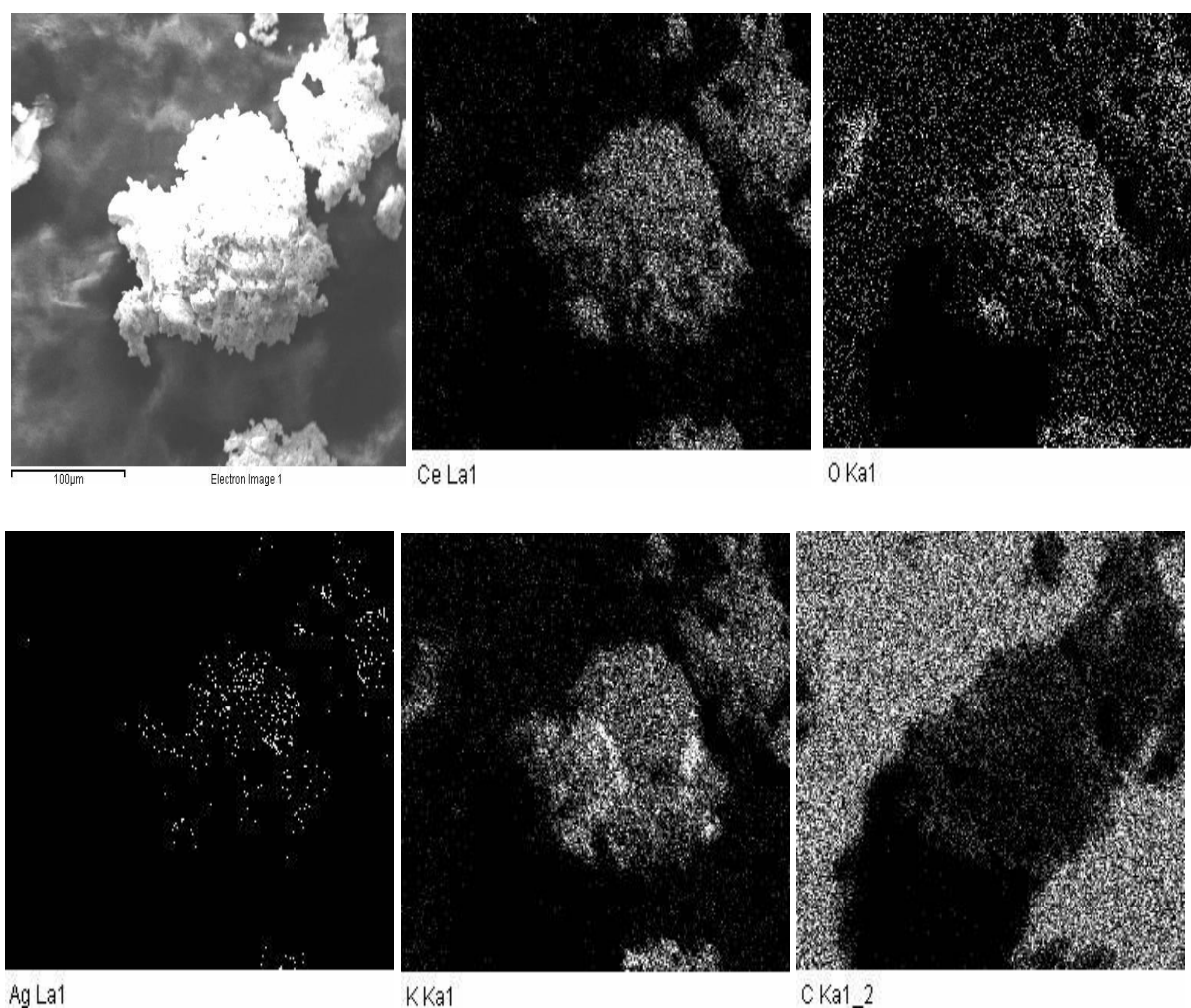


Figure 3.57 EDX mapping of a particle of K impregnated CeO₂@Ag core shell structure

A similar trend was seen in another particle being mapped. This indicated the synergism between Ag and CeO₂ phases in the rice ball structure of an Ag core and a

CeO₂ shell, as shown below in figure 3.58. The striking contrast from the background was evident as in the above case, with the presence of the C Ka1_2 highlighting the contrast. K was present on the surface as aggregates of tiny K₂CO₃ particles, indicated by the bright white patches as shown in figure 3.58.

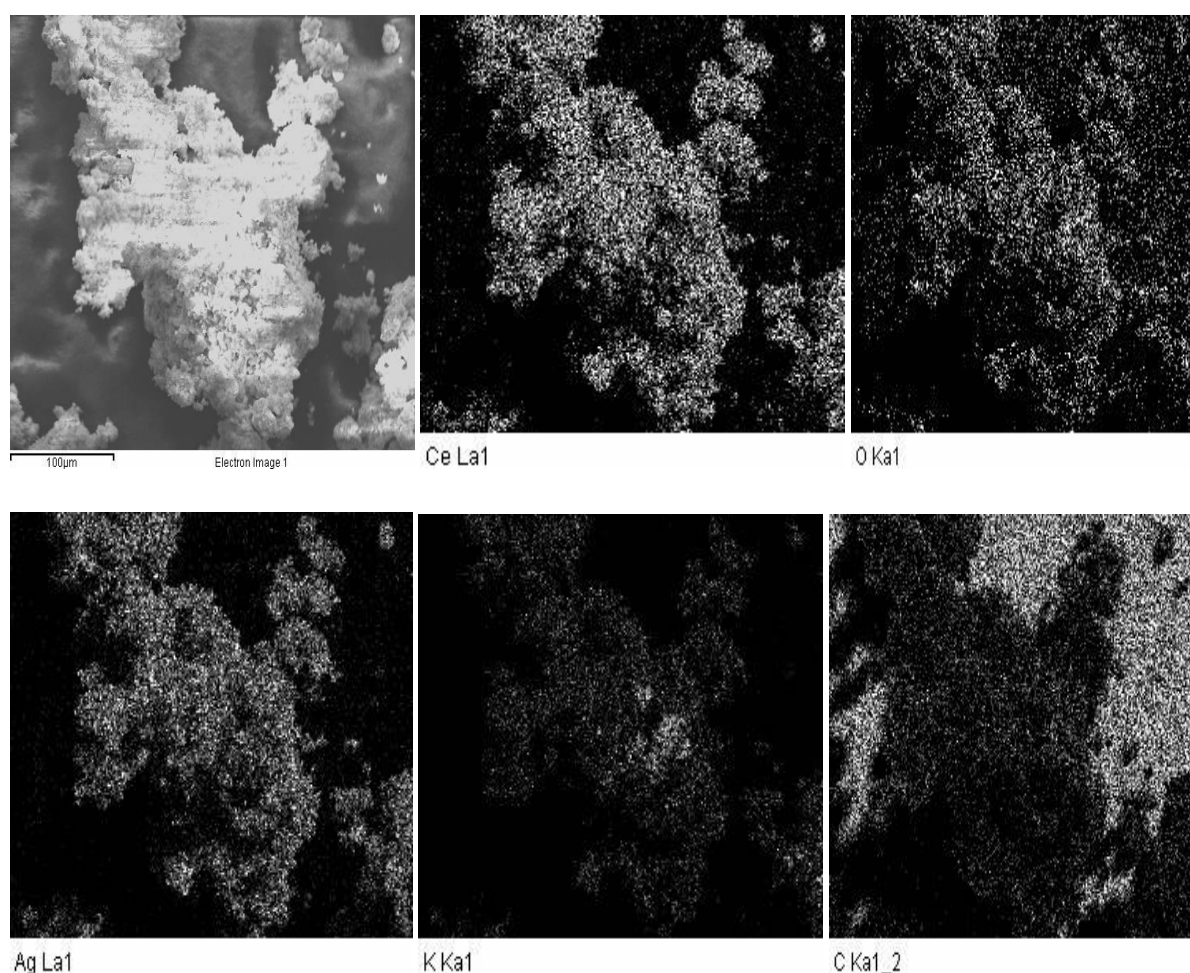


Figure 3.58 EDX mapping of a particle of K impregnated CeO₂@Ag core shell structure

SEM micrographs indicated the structure of K/CeO₂@Ag. The tiny K₂CO₃ hairlike particles were seen on the surface of the ceria particles. EDX mapping as above, and EDX area analysis showed the distribution of the various elements in the catalyst (figure 3.59).

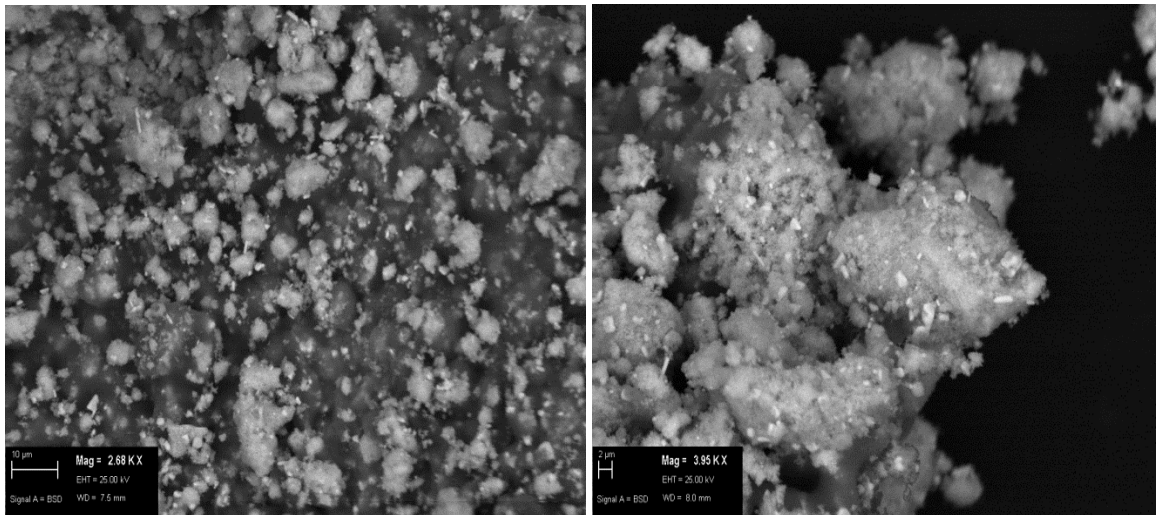
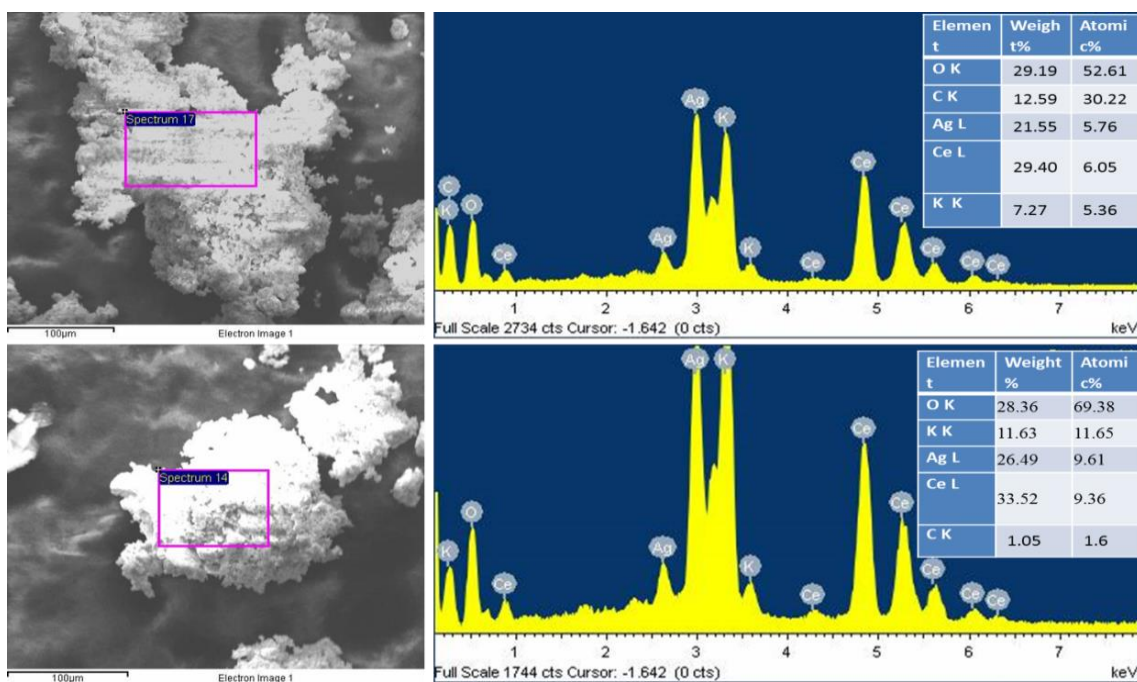


Figure 3.59 SEM indicating the CeO₂@Ag core shell structure

The area analyses shown below for the catalyst indicated a Ag phase with a loading of Ag almost equivalent to that used in the preparation (EDX, XPS). The ceria shell surrounded this silver completely as explained in detail above. This kind of geometry gave a defined structure for the catalyst and thus could make the migration of the oxygen through this matrix easier, thus providing a good storage of it as well, in the matrix. The Ag-K synergism on the surface, where the K₂CO₃ was present needed further speculation. There is a possibility that the Ag species migrated through the ceria matrix, and along with the K₂CO₃ helped in the oxidation.



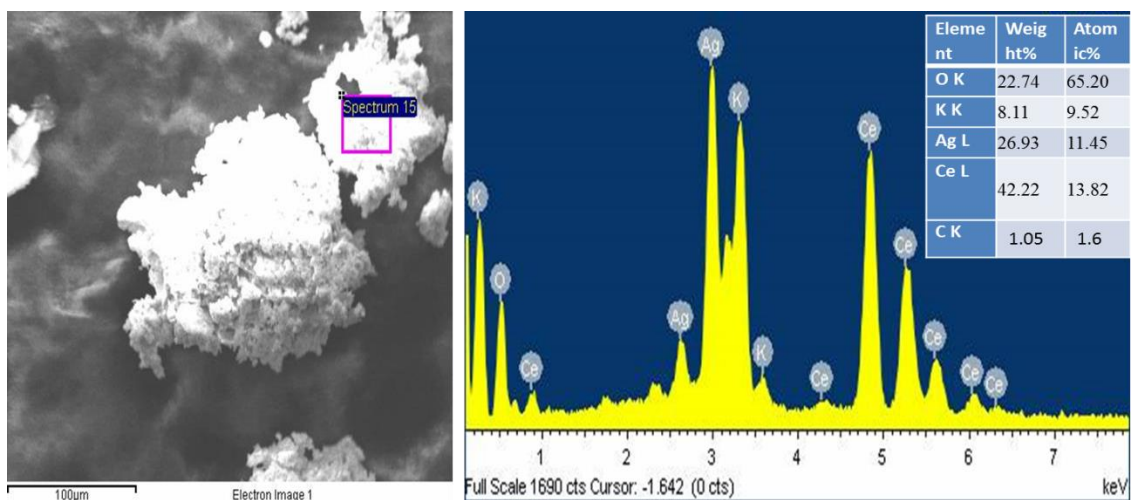


Figure 3.60 Area analyses of different particles of CeO₂@Ag

XPS and EDX were used to understand the formation of the oxides. The three different area scans indicated a similar distribution of the elements on the surface with vast concentrations of CeO₂-Ag present. TEM showed that the CeO₂@Ag rice ball morphology had been formed as could be evidently seen from figure 3.61 with a central Ag core and surrounding CeO₂.

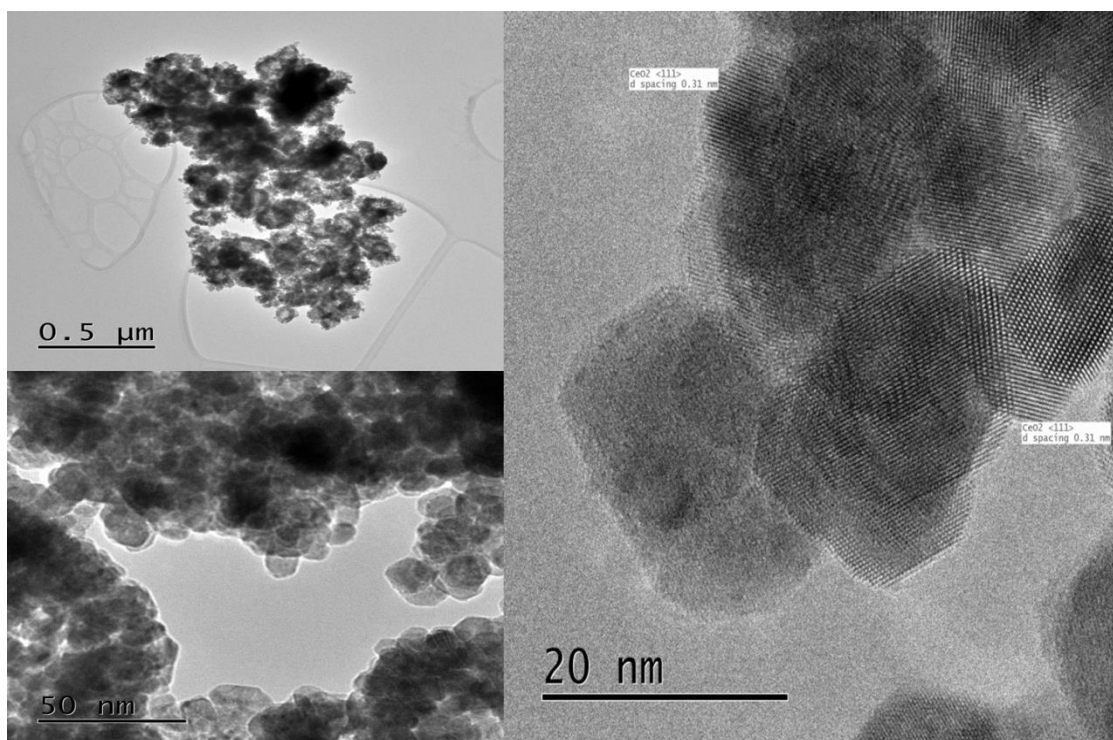


Figure 3.61 TEM images for CeO₂@Ag rice ball catalysts with focus on the lattice planes

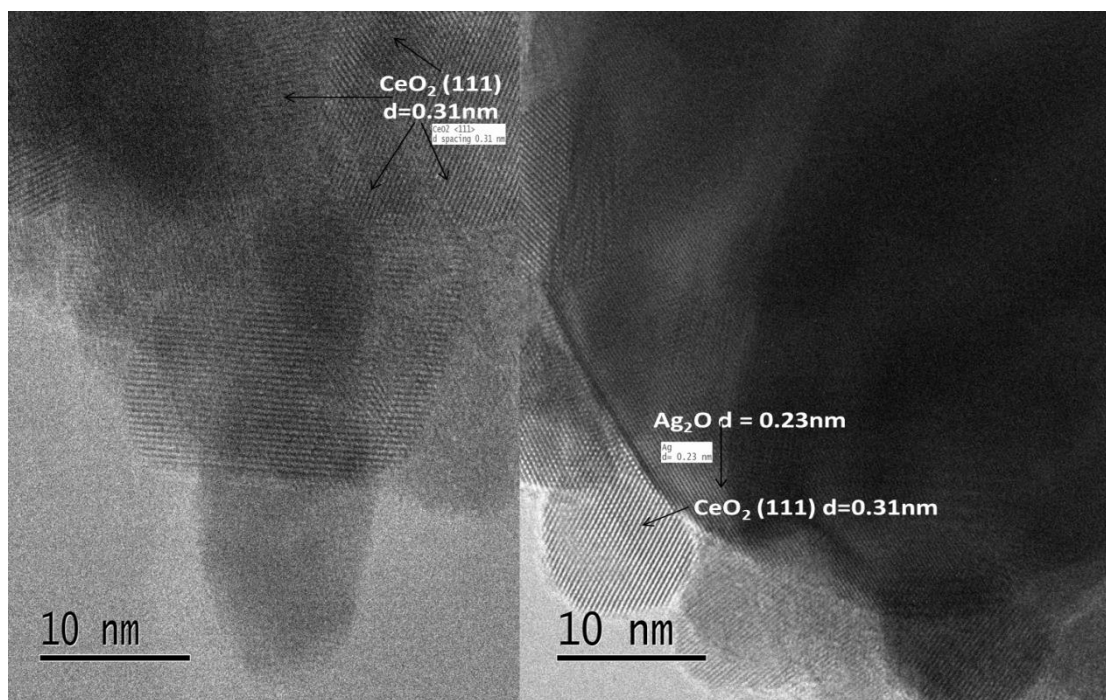


Figure 3.62 CeO₂@Ag with lattice planes of Ag₂O and CeO₂

The TEM images showed how the Ag core consisting of Ag₂O and Ag⁰ species, was surrounded by CeO₂ nanoparticles, giving a core shell like appearance (figure 3.62). The evidence of K on the surface was seen from the EDX analyses using the dark field imaging (STEM-EDX). The region chosen showed a small concentration of K on the surface and the weight percentage of Ag and Ce were seen to match that of the preparation, with an excess of CeO₂ surrounding the Ag core. K appeared as bright green spots and Ag clusters appeared as shown by bright blue in the EDX maps (figure 3.63).

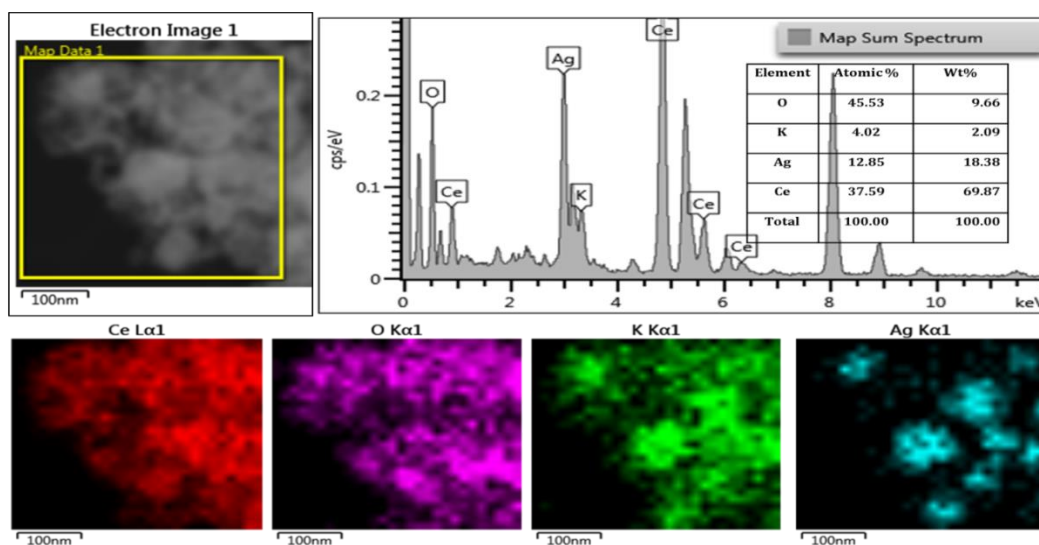


Figure 3.63 CeO₂@Ag -EDX mapping

3.8.2 Soot oxidation activity for $\text{CeO}_2@\text{Ag}$ and $\text{K}/\text{CeO}_2@\text{Ag}$ catalysts

The $\text{Ag}-\text{CeO}_2$ and the impregnated $10\% \text{K}/\text{Ag}-\text{CeO}_2$ catalysts were tested for soot oxidation using TGA experiments, under the same conditions as used in the previous sections, and the results were as seen in table 3.27. The $\text{Ag}-\text{CeO}_2$ showed a lower peak temperature as compared to the $\text{Ce}_x\text{Zr}_{1-x}\text{O}_2$ and K/CZ or K/CZA catalysts, but the final oxidation temperature was slightly higher than those of K/CZ or K/CZA .

Table 3.27 Soot oxidation activity of $\text{CeO}_2@\text{Ag}$ and K impregnated $\text{CeO}_2@\text{Ag}$

Catalyst	Contact mode	T_{on} (°C)	T_{eo} (°C)	T_{p} (°C)	T_{f} (°C)
$\text{Ag}-\text{CeO}_2$	LC	403	405	483	587
	LC	382	413	470	570
10%K/Ag-CeO₂					
10%K/Ag-CeO₂	TC	292	323	382	508

Yamazaki and co-workers suggested that the effect of this morphology and the synergism between Ag and CeO_2 were crucial in stimulating the formation and migration of active oxygen species on silver surface. The proposed mechanism for soot oxidation was illustrated in figure 3.64.

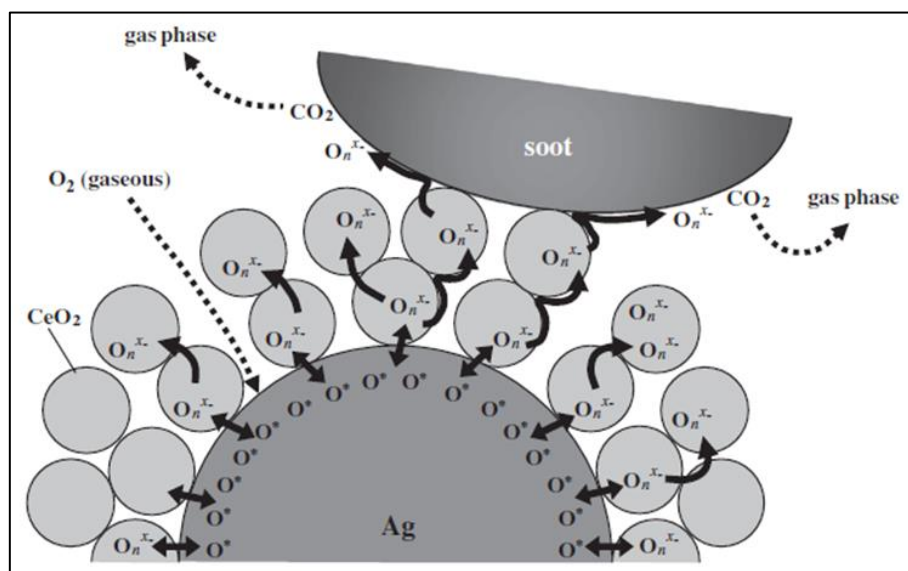


Figure 3.64 Soot oxidation mechanism illustrated by Yamazaki *et al.* for $\text{CeO}_2@\text{Ag}$ [39]

They stated that Ag at the surface led to the formation of the atomic oxygen by molecular oxygen adsorption, assisted by the synergistic effect of Ag-CeO₂ and the large interface between silver and ceria particles. Subsequently, the atomic oxygen species migrated to CeO₂ surface through the maximised interface and generated active oxygen species. These species were very mobile in nature and migrated onto the soot particle surfaces ultimately oxidising the soot to CO₂.

These hypotheses could explain the high activity observed for Ag-CeO₂ with peak oxidation temperature of 483°C and final temperatures of 587°C, temperature which was slightly higher than those obtained with K-impregnated ceria-zirconia mixed oxides (535-579°C) or K/CZA (421-478.3). These observations suggested the rapid formation/migration of active oxygen species, with a catalyst-soot contact that could be improved on. The value for the onset temperature, 382 °C, was in agreement with the mechanism. This suggested that the intermediates (KO₂) having a melting point of 380°C were responsible for improving the contact between catalyst and soot, in these kind of materials. The relatively high peak and final temperatures was probably due to greater difficulties for molecular oxygen to diffuse from the ceria lattice, through the K surface, onto the soot. These diffusion limitations could be responsible for decrease in formation of atomic oxygen species on silver that could have aided in the improved soot-catalyst oxidation.

3.8.3 Ag-K direct impregnation on CZA- characterization

The catalyst prepared by impregnating 2% Ag and 10% K onto CZA-Na₂CO₃ coprep. was explained in the experimental chapter. The X-ray diffraction patterns showed that the CeO₂-ZrO₂ mixed phase with a cubic lattice structure was present. The impregnation of Ag onto the CZA support showed that there was an Ag⁰ phase with a reflection from the Ag (111) plane at 2θ=38.16°. The large crystallite sizes for the Ag impregnated catalysts meant that the peaks width was less and shifted to lower angles of 2θ. Thus the crystallite sizes for these were comparatively larger than those for the supports (CZA-impreg and CZA - Na₂CO₃ co-precipitation). The impregnation of K distorted the cubic CeO₂ phase as mentioned above (figure 3.53).

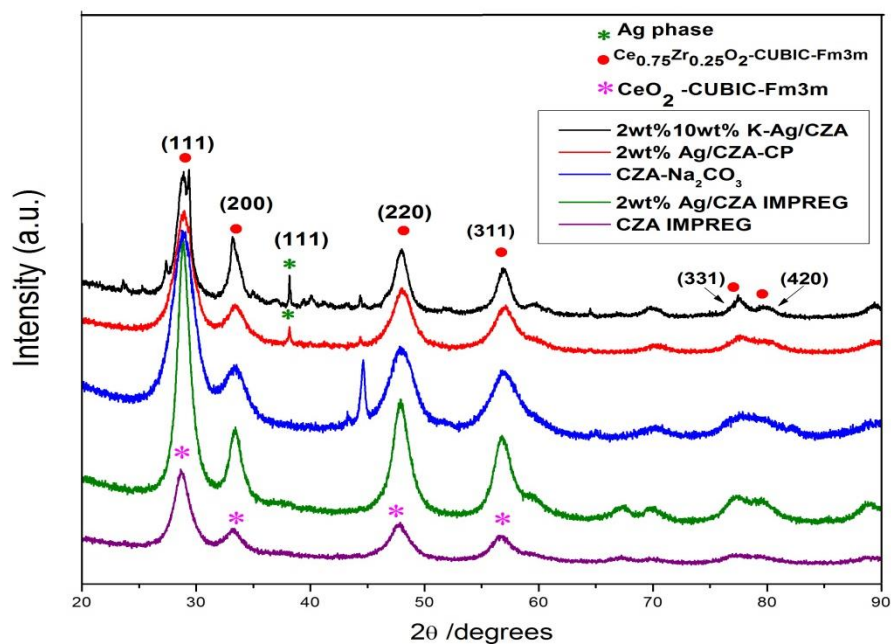


Figure 3.65 X-ray diffractograms for Ag, K impregnation on CZA as a comparison with CZA

3.8.3.1 Optimization of the catalyst

The activity of the 2% Ag 10% K/CZA catalyst was modified by varying the calcination regime, to optimize it for soot oxidation. The regime followed was described in the experimental chapter. The dry catalyst precursors were subjected to different temperatures, heating rates and time so as to understand the change in catalyst composition over the entire range.

a) Variation of calcination temperature

The calcination precursors were subjected to different temperatures between 200-750°C. X-ray diffractograms revealed the increased peak intensity or crystallinity with increase in temperature. At higher temperatures (750°C), the cubic phase of the catalyst tend to sinter which was observed as the increased crystallinity in the cubic structure, alongside a shift to lower 2θ angles. The phases for the various calcined samples revealed the cubic CZ mixed phase as seen from the JCPDS database with an evident distortion of the phases due to the impregnation of potassium on the surface of the support. This was in the form of K_2CO_3 as described in section 3.5. This may be absent in the case of the catalyst calcined at 750°C due to increased sintering of the particles at such high temperatures. The Ag^0 phase (111) observed at 38.16, 44.38 and 64.58 indicated formation of metallic silver and the peak intensity increased with increase in temperature. No evidence for the presence of Ag_2O crystallites were

obtained from XRD profiles. The optimum calcination temperature for the synthesis of the Ag-K/CZA catalyst was 500°C where the cubic CZ mixed phase was intact, the Ag⁰ was present on the CZA surface and potassium could be present as the K₂CO₃ on the support (suggested by table 3.28). This could bring about a good synergy between the Ag and K and thus enhanced its interaction with the CZA support (figure 3.66).

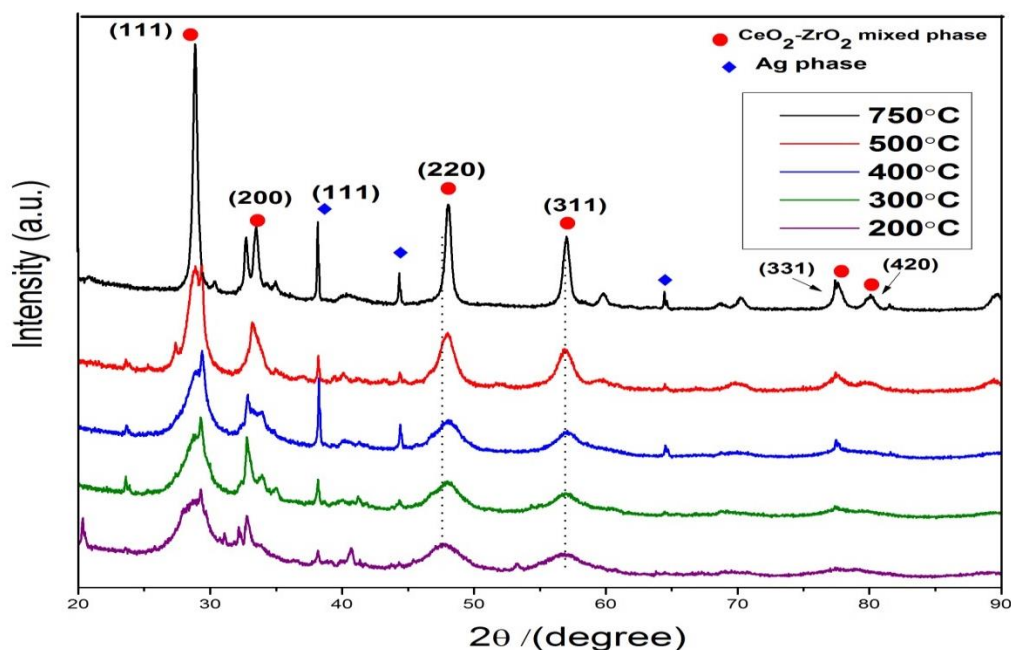


Figure 3.66 X-ray diffractograms for Ag-K/CZA - varying the calcination temperature

Raman spectroscopy indicated that the cubic CeO₂ phase was maintained when calcined at lower temperatures (figure 3.67). At higher temperatures the incorporation of ZrO₂ into the CeO₂ lattice was predominant and the cubic symmetry was distorted at 500°C (600cm⁻¹). The peaks had shifted to higher 2θ angles at lower temperatures. The peaks indicating the cubic symmetry at 472.2cm⁻¹ became sharper, more symmetrical and were slightly shifted to a higher wavenumber, when the calcination temperature was increased from 200 to 750°C. This could be due to better crystallinity of CZA at higher calcination temperatures, which was in consistency with the XRD observation. This was observed both in the case of CZA-500°C and CZA-750°C.

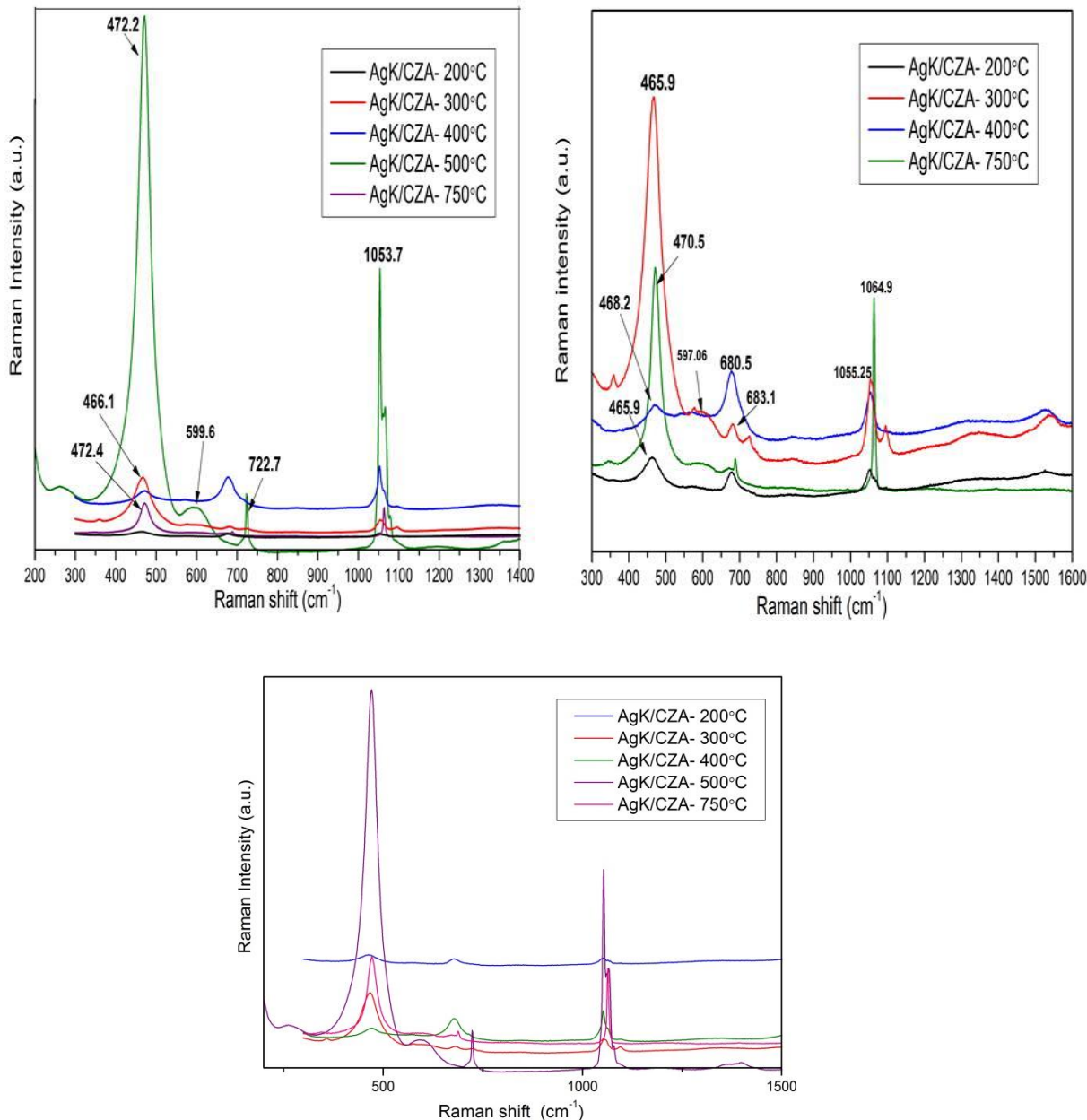


Figure 3.67 Raman spectra for Ag-K/CZA - varying the calcination temperature

Thus the crystallite sizes in these cases tended to increase with increase in calcination temperature. It is plausible that the shift in 2θ value could have been caused by the transformation of Ce^{3+} (0.114 nm) into Ce^{4+} (0.097 nm) at high temperature. The distinction of the cubic ceria phase from the distorted tetragonal symmetry of ZrO_2 was evident in these cases, from Raman spectroscopy. There is a kind of asymmetrical broadening in the other cases, which could be due to the size effect in smaller crystallites. The increase in intensity of the peaks at higher temperatures was as a consequence of sintering of particles, with a possibility of growth of the CZ particles.

The Al₂O₃ usually acts as a diffusion barrier and prevents growth of these particles but this property is lost at higher temperatures [42].

Table 3.28 Physical properties of Ag/CZA catalysts- varying calcination regime

Sl. No.	Catalyst	Surface area (m ² /g)	2θ	Crystallite size (nm)	Peak reduction temperature (°C)	H ₂ consumption (μmol/g)
Varying calcinations temperatures						
1.	200°C	14	47.74	3.3	212 302	1740 1049
2.	300°C	14	29.11	6.7	266	3384
3.	400°C	10	29.36	9.8	300	3433
4.	500°C	11	28.69	7.7	316	4595
5.	750°C	2	28.	11	700	104
Varying calcinations rates-at 500°C						
6.	1°C/min	2	29.32	13.1	310	3108
7.	5°C/min	11	28.69	7.7	316	4595
8.	10°C/min	7	48.02	6.1	316	4779
9.	20°C/min	5	57.07	10	331	5423
Varying calcinations time- at 500°C, 5°C/min						
10.	4 hrs	9	48.08	20	274	3272
11	5hrs	11	28.69	7.7	316	4595
12.	6hrs	9	28.80	9.7	305	2993

The optimization of the catalyst showed that on calcining the catalyst at lower temperatures between 200-400°C, the formation of the CeO₂-ZrO₂ mixed oxide phase was incomplete (based on TGA analyses) but at 500°C this was attained, thus proving this to be the ideal temperature for the formation of the mixed metal oxides from their nitrate precursors. The crystallite sizes were very small at 200°C and gradually

increased with increase in calcination temperature. This was due to the fact that the particles began to sinter at higher temperatures. There was also a drop in surface area of the catalysts with increase in calcination temperatures. The calcination rates tend to influence the size of the crystallites to an extent. Extremely slow ($1^{\circ}\text{C min}^{-1}$) and rapid ($20^{\circ}\text{C min}^{-1}$) heating rates to 500°C produced larger crystallites, as the formation of the oxides could be effected due to delayed or rapid formation of crystallites under an atmosphere of air, for the formation of the oxides from the nitrates. The calcination time did not have too much effect on the crystallite size. The effect of crystallite size on the soot oxidation activity has been previously discussed. The optimized conditions for the preparation of 2% Ag 10% K -CZA were 500°C , $5^{\circ}\text{C min}^{-1}$ and 5 hrs under flowing air.

Addition of Ag onto the CZA resulted in a drop in surface area with a loading of 2% Ag and 10% K onto the support. This kind of approach is typical of a high surface area supported metal oxide possessing high specific weight and low porosity. This effect tends to get more pronounced at higher loadings as observed in the case of 1, 2, 5 % Ag loadings on CZA. The presence of K decreased the surface area. A minimum amount of promoter (10%) was needed for efficient soot combustion. The addition of potassium stabilized the activity of CeO_2 upon calcination, irrespective of the loss of surface area on its addition. Thus compromising surface area for activity was a rational approach in the case of soot oxidation as the process is a contact driven one, where the kinetics of the reaction occur quite rapidly. The catalyst tends to operate efficiently at low temperatures and also tends to preserve activity at high temperatures as is observed in the activity data reported above.

Scanning electron microscopy coupled with EDX indicated the morphology of the catalyst along with the description of the elemental composition. The back scatter detector was used to obtain the elemental composition for the Ag-K impregnated catalyst as Ag was detected as bright spots on the detector and proved for more accurate elemental determination. The different analyses carried out on the catalyst included, map scans to determine the nature of distribution of various elements on a particle, point analyses helped to identify individual particle distributions and area analyses gave a more in-depth concentration distribution of the elements.

The images below indicated a map scan of a particle of Ag-K/CZA. This showed how (figure 3.68) the elements were spread throughout the surface coverage. This indicated that the support mainly consisting of CZA covered the vast expanse of the particle with impregnation of K_2CO_3 on the surface. There was an evident homogeneous distribution of the CeO_2 and Al_2O_3 phases with fine distribution of ZrO_2 in the matrix, providing a good mobility for the surface oxygen species. K was present as K_2CO_3 as could be observed from the XPS. Ag was present on the surface and in the bulk. It was observed as bright spots as seen from figure 3.68. The concentration of Ag was lower on the surface but there was a good spread around the particles

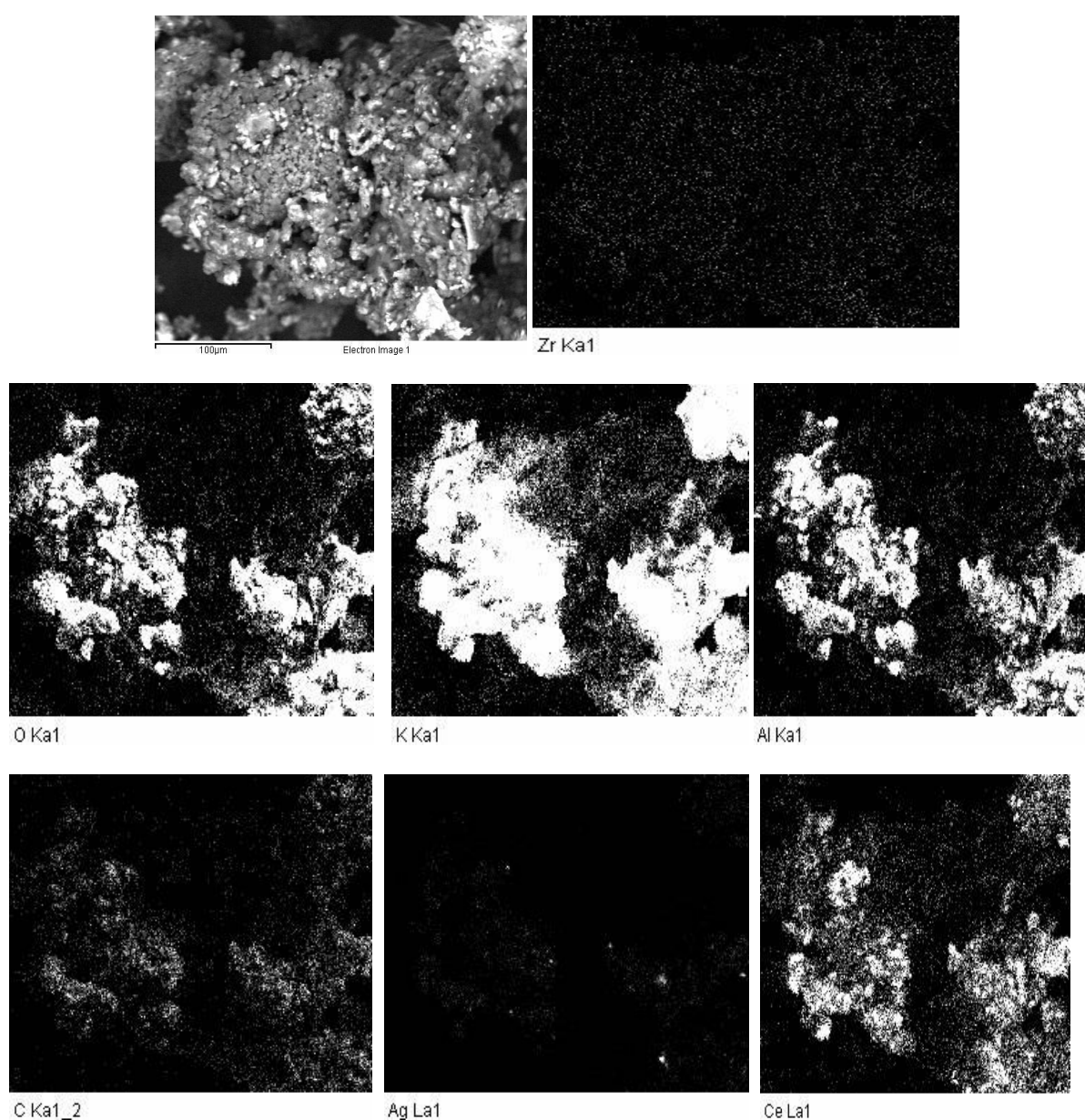


Figure 3.68 EDX mapping of Ag-K /CZA catalyst particle-1

Figure 3.69 also shows another particle of Ag-K/CZA being mapped. The image for O Ka1, K Ka1 and Al Ka1 showed that the major spread along this particle was from these elements indicating the dominance of these phases. The clusters of Ag could be observed as spots, as in the previous case. The CZ lattice was well spread on the particle, with Al₂O₃ excess giving the support more thermal stability and resistance to sintering.

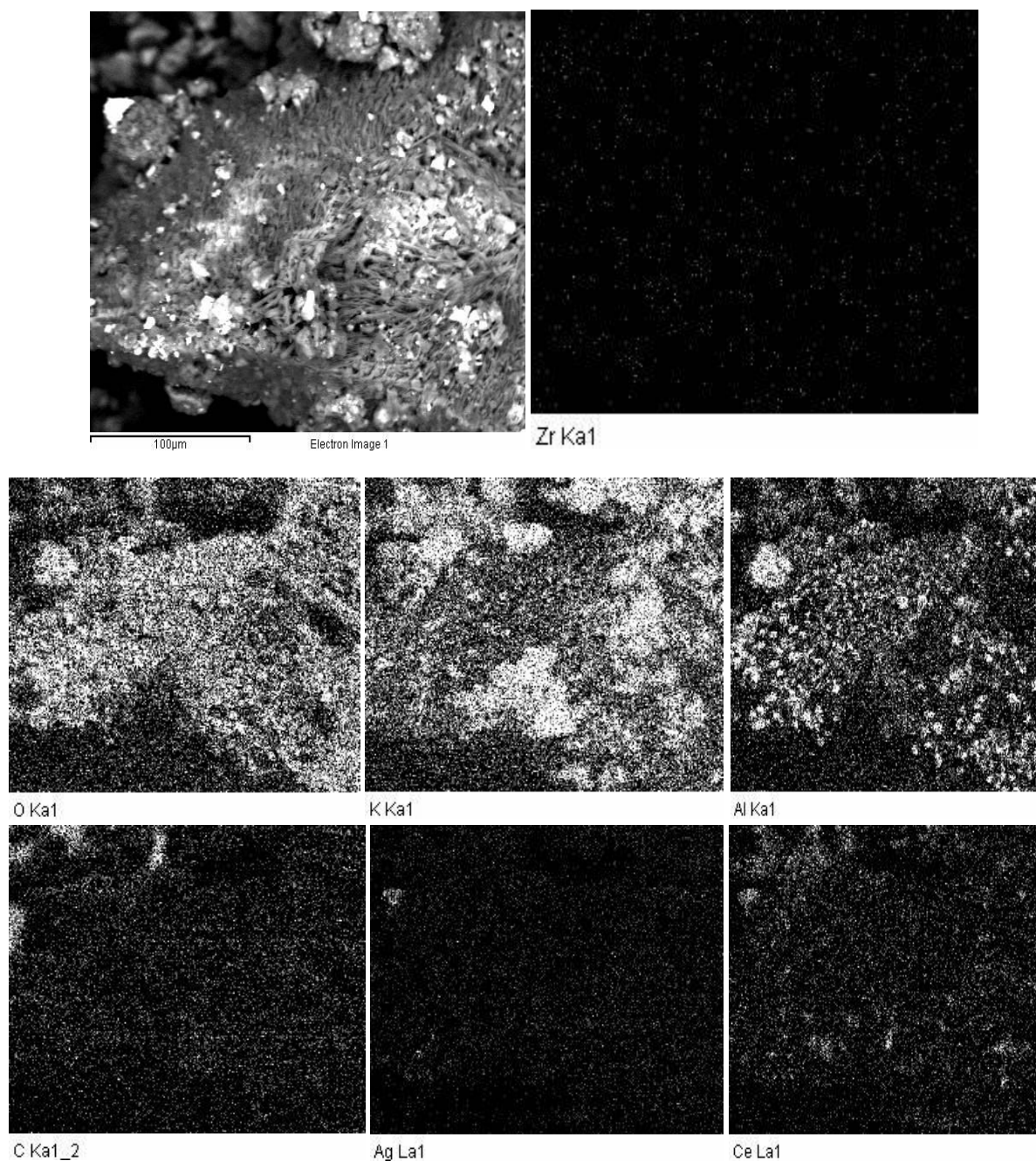


Figure 3.69 EDX mapping of Ag-K /CZA catalyt particle-2

Area scans as seen in figures 3.70 a,b showed the elemental distribution on the CZA. K₂CO₃ was present as a dominant phase on the support (EDX). In an area scan, the

concentrations of different elements was quite high compared to that observed in the point scans as this is a cumulative of several concentrations of various particles. The atomic and weight percentages were indicated in the table as an inset on figure 3.70. The ratio of Ce: Zr as indicated by the weight ratios was $0.28/0.11=2.5:1$, which was the same as that observed from XPS data previously mentioned.

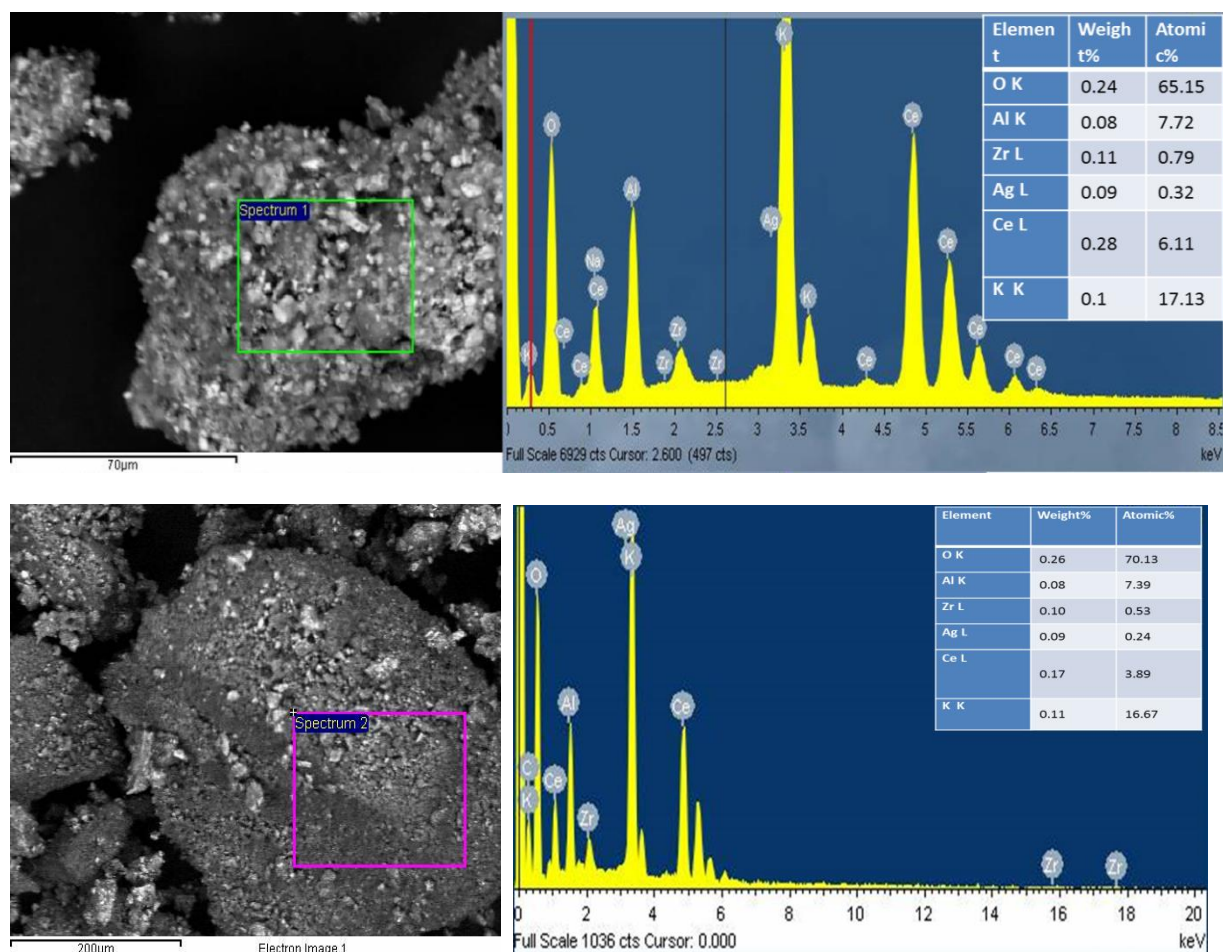


Figure 3.70 Area scans using EDX of Ag-K/CZA

The two different area scans indicated different distribution of the particles but the predominance of K was the key factor in both cases (figure 3.70). On observing the two particles separately it was evident that the presence of CZ varied in different areas. The elemental concentrations were similar to those used in the experimental preparation of the catalyst. The oxide formation was also clearly indicated from XPS and EDX.

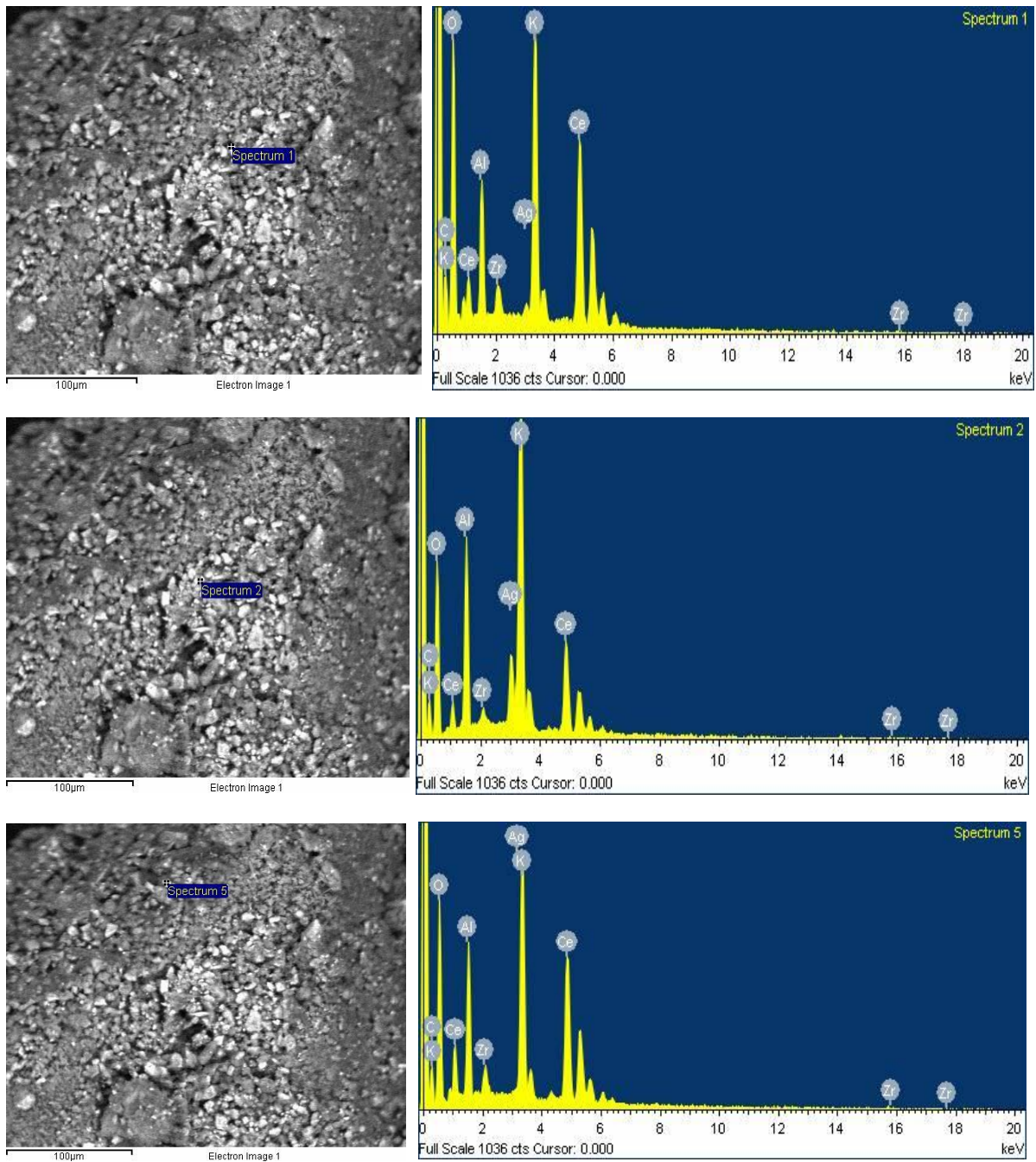


Figure 3.71 Point scan using EDX of Ag-K/CZA-particle 1

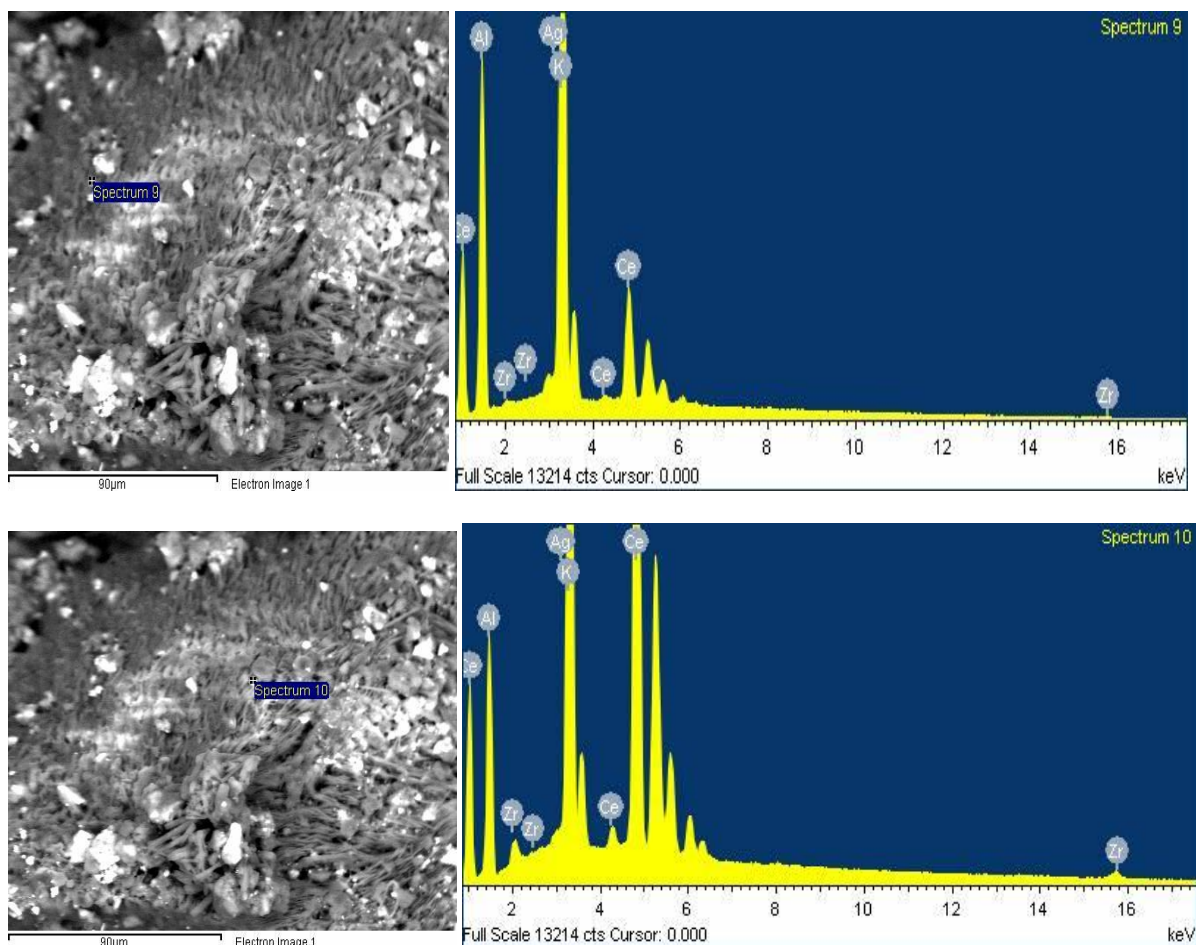


Figure 3.72 Point scan using EDX for particle 2 of Ag-K/CZA

Two separate particles were analysed using the back scattered detector and several point scans were taken to show the distribution of the various elements (figure 3.71, 3.72). The concentrations of the different phases showed a predominance of $\text{CeO}_2\text{-Al}_2\text{O}_3$ on the substrate level and an even cover of K as K_2CO_3 on the surface (XPS). The Ag was present on the surface too but the concentration varied from point to point on the surface.

The particle size distribution was analysed using SEM with the use of the back scatter detector to identify the precious metals impregnated onto the support. Several images were analysed for this purpose and then using the Image-J software, the particles were individually marked and the particle size recorded for around 400-500 such particles. These were termed as ferrets on the software and the ferret size/particle size distribution was calculated using the software. Figure 3.73 indicated the particles marked for analysis and figure 3.74 showed the particle size distribution. The Ag existed as Ag^0 on the surface.

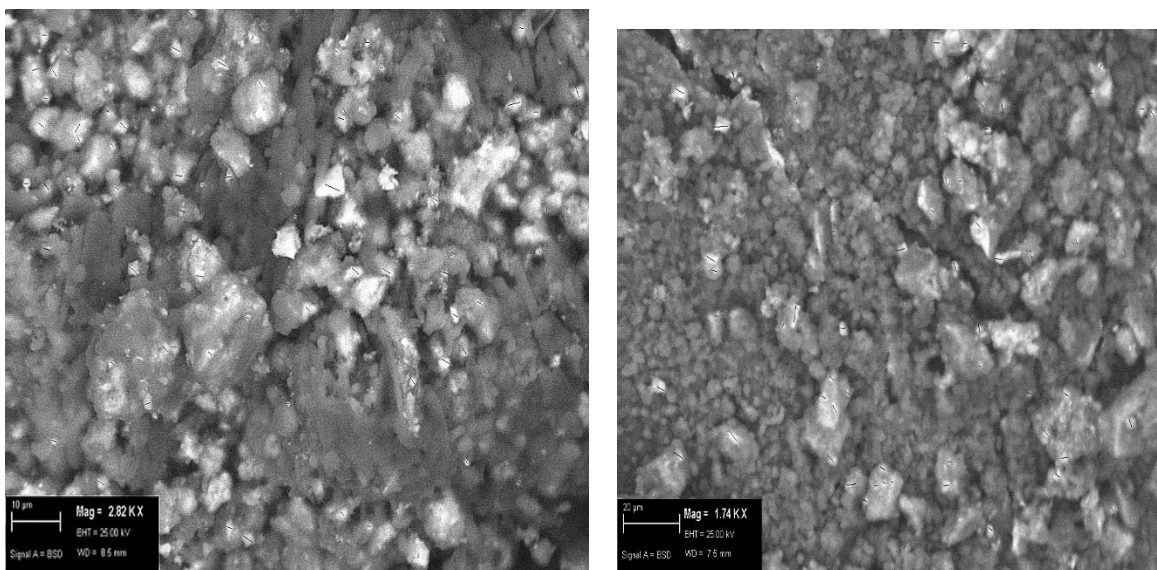


Figure 3.73 SEM images used to calculate particle size distribution-Ag-K/CZA

The particle size distribution showed that the Ag particles were spread across, through the surface of the support. They formed small clusters varying in size. The particles ranged from as small as 0.2 nm to as large as 6.7 nm. The concentration of the small particles between 0.5-0.9 μ m were maximum as shown in table 3.29. There were considerable number of particles between 1.5-2 μ m (50%)

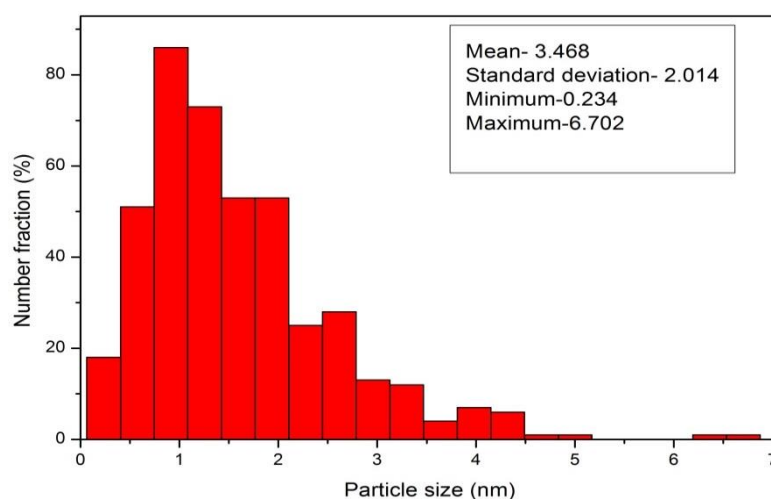


Figure 3.74 Particle size distribution of Ag particles on Ag-K/CZA catalysts

In the case of the uncalcined precursor, the ratio for Ce:Zr was calculated in terms of their atomic percentages. Atomic % of Ce-0.98, Zr-0.39 giving a ratio of 0.98/0.39 =**2.51:1**. This was also confirmed from the *area : RSF* measurement:

Ce- Area/R.S.F=4380/8.808= 497.27; Zr- area/R.S.F = 510.3/2.576 = 198.09

Thus ratio of Ce:Zr = 497.27/198.09 = **2.51:1**

Table 3.29 Elemental distribution in Ag-K/CZA catalyts- wide scan spectrum-uncalcined

Name	Position	FWHM	R.S.F.	Area	% Conc.
Ce 3d	878.61	2.168	8.808	4380.23	0.98
O 1s	527.84	1.828	0.78	15790.77	40.07
O 1s	526	1.828	0.78	1462.63	3.71
O 1s	529.46	1.828	0.78	1759.06	4.46
Ag 3d 5/2	364.71	1.311	3.592	971.31	0.54
K 2p	289.21	1.52	1.466	8575.24	11.58
C 1s	281.21	1.448	0.278	3847.17	27.39
Zr 3d	178.21	1.264	2.576	510.3	0.39
Al 2p	70.51	1.491	0.193	1060.15	10.87

On looking at the wide spectrum of the elements present on the surface of the precursor, we observed that there was an excess of Al as compared to that in the calcined sample. Also, the Ce:Zr ratio from this spectrum gave, $0.84/0.37 = 2.27:1$ which was approximately the ratio obtained above and matched that used for the preparation of the support. Thus indicating that the impregnation did not alter this Ce:Zr -7:3 ratio as this was vital for the catalyst to exhibit good redox properties.

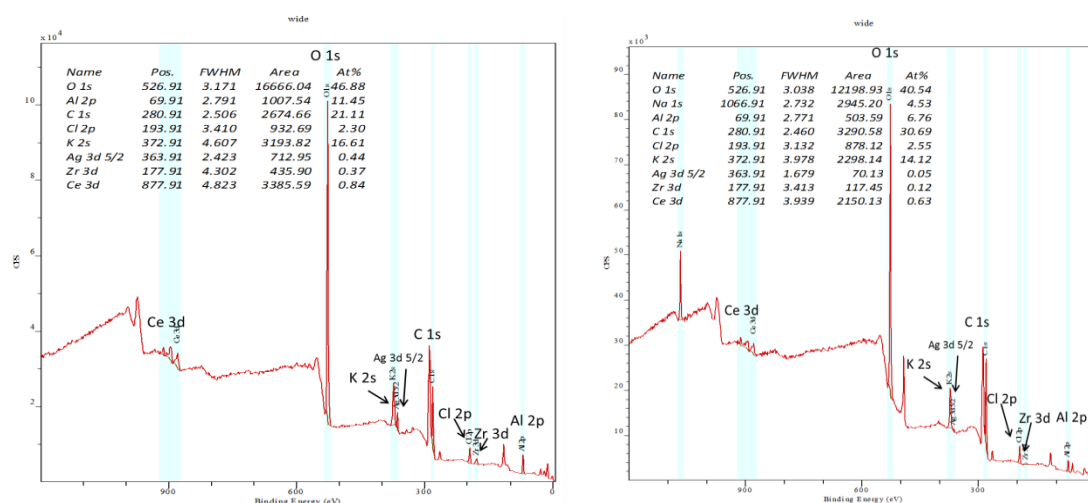


Figure 3.75 Wide scan spectra showing elemental distribution of Ag-KCZA- a)precursor; b) calcined

As for the calcined catalyst, the Ce:Zr ratio from the narrow scan yielded $0.57/0.15 = 3.8:1$, while that from the wide scan yielded $0.63/0.12 = 5.2:1$. The ratio was slightly higher than in the case of the supports and precursor. It was observed that

there was a depletion of CZA on the surface upon impregnation of Ag and K , followed by calcination. The change in the ratio could be due the formation of two different phases of ZrO₂ observed, one at Zr 3d-181.6 ev which was indicative of the stoichiometric ZrO₂, confirmed from literature, while the other at Zr 3d - 180.7eV owing to the non-stoichiometric ZrO₂.

Table 3.30 Elemental distribution in Ag-K/CZA catalyts- wide scan spectrum-calcined

Name	Position	FWHM	R.S.F.	Area	% Conc.
Ce 3d	893.91	1.341	8.808	2081.44	0.57
O 1s	527.59	1.801	0.78	11963.16	37.04
O 1s	525.32	1.165	0.78	443.63	1.37
O 1s	529.14	1.801	0.78	1216.49	3.77
Ag 3d 5/2	364.01	0.727	3.592	57.39	0.04
K 2p	289.11	1.589	1.466	6652.82	10.96
C 1s	281.21	1.296	0.278	4605.76	40.01
Zr 3d	178.11	1.109	2.576	160.53	0.15
Al 2p	70.61	1.59	0.193	487.07	6.09

Figure 3.76a showed the effect of impregnation of K on CZA, and the decrease in intensity upon calcination. The C 1s peak indicated a slight increase in intensity owing to the carbonate peak from the K₂CO₃ that was present on the surface of the CZA support. The impregnation of Ag showed a distinct Ag 3d 5/2 peak at 364.3ev and a Ag 3d 3/2 peak at 373.9 eV, in the case of the precursor and calcined sample respectively, but the peak at 364.3eV reduced in intensity drastically, upon calcination, indicating that the surface concentration of Ag reduced from 0.54-0.04% (observed from table 3.29 and 3.30), suggesting that it had become dispersed throughout the bulk.

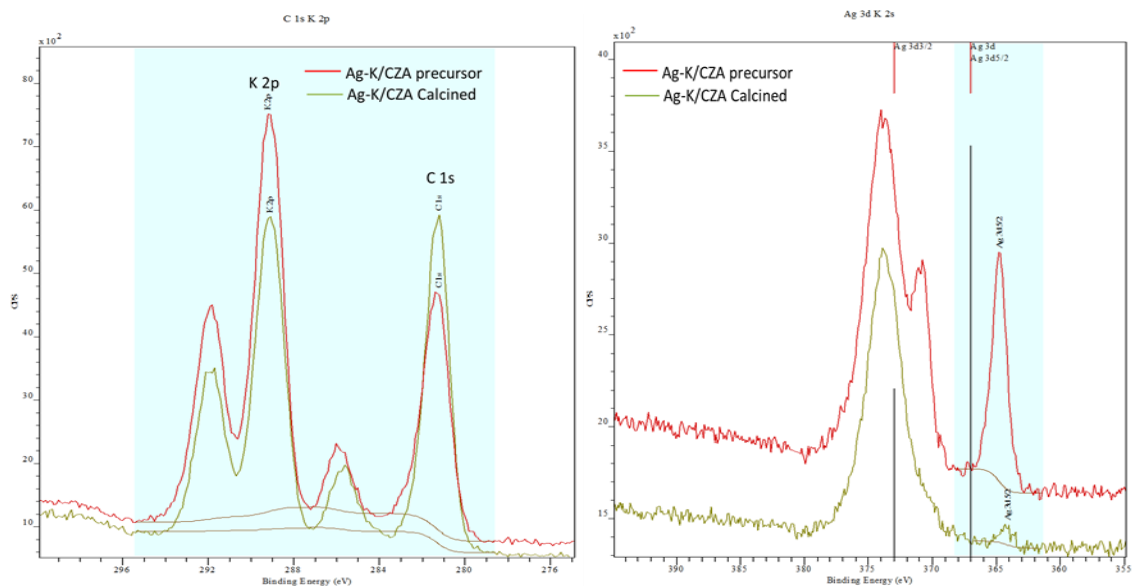


Figure 3.76 XPS spectra –precursor and calcined- a)K 2p, C 1s; b) Ag 3d K 2s

The O 1s spectra showed the different kinds of species present in the catalyst. The surface oxides and hydroxides were present at 531 and 529eV respectively, while the carbonates were present at 532 eV (figure 3.77). The oxides arose from the CeO_2 , ZrO_2 , Al_2O_3 and partly from the Ag_2O and K_2O phases. The remaining oxygen was from the atmosphere at 527eV. The carbonates were present from the K on the CZA lattice. There were few traces of Na and Cl present in the lattice, either as contaminant from the preparation (present in the precursor salt/in the water used to wash the precursor).

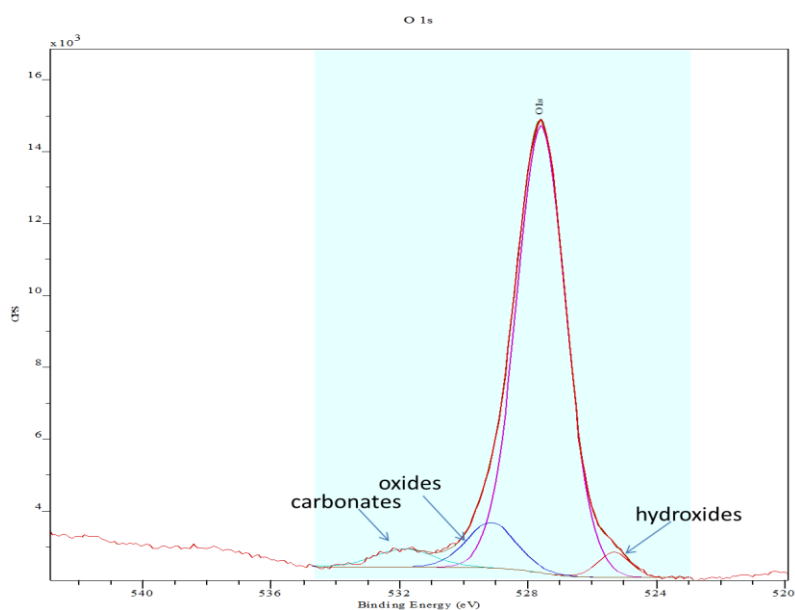


Figure 3.77 XPS spectra –precursor and calcined- O 1s

Figure 3.78 displayed the FT-IR spectra of the CZA precursor and calcined catalyst, alongside the Ag-K impregnated precursor and calcined samples. The peaks located at 3450, 1628(33), 1585(3), 1534(6), 1474 and 1450(1), 1352, 1325, 1039, 933(44), 654 cm^{-1} were assigned to the $\nu\text{O-H}$, $\nu\text{H-O-H}$, $\nu\text{C=O}$, $\nu\text{C=C}$, $\nu\text{C=O} + \delta\text{C-H}$, νNO_3 , $\nu\text{C-CH}_3$, πCH_3 , $\nu\text{C-CH}_3 + \nu\text{C=O}$, $\pi\text{CH}_3 + \text{ring distortion} + \nu\text{Zr-O}$, respectively[43]. The stretching vibration of H-O-H was almost certainly due to the water from the precursor solutions of $\text{Al}(\text{NO}_3)_3 \cdot 9\text{H}_2\text{O}$, $\text{ZrO}(\text{NO}_3)_2$ and $(\text{NH}_4)_2\text{Ce}(\text{NO}_3)_6$. The vibrations were far more pronounced with increase in calcination temperature.

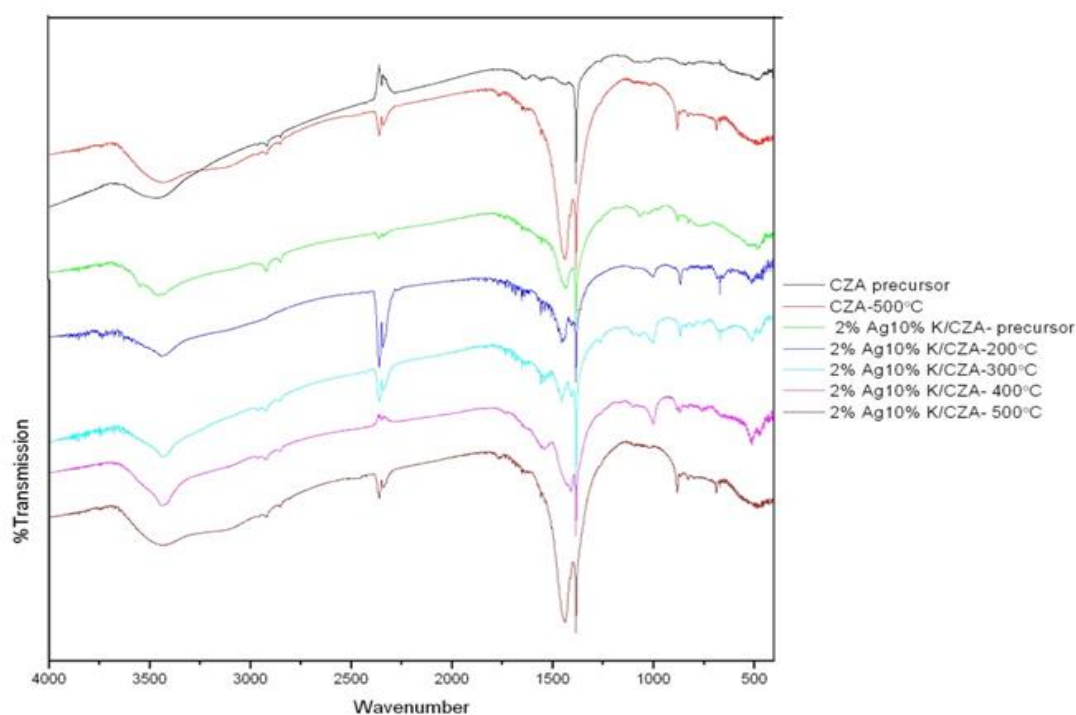


Figure 3.78 FTIR spectra for Ag-K/CZA catalysts- varying calcination temperature

Temperature programmed reduction profiles showed that the catalyst when calcined at 500°C had the maximum H_2 consumption values as indicated in the table 3.28. The reduction took place at temperatures lower than that observed for the support (CZA) and for the K impregnated CZA (figure 3.79). The impregnation of Ag onto CZA was known to bring down the reduction temperatures of CeO_2 surface and bulk reduction as shown in previously. The reduction temperature profiles indicated that the addition of K increased amount of extractable oxygen essential for soot oxidation, as a function of the reduction of the CeO_2 in the support. The surface and bulk reduction profiles for the catalyst calcined at temperatures as high as 750°C, showed a

shift to higher temperatures and the bimodal profile was distorted. The ease of reduction was observed in the case of the catalyst calcined at 500°C, with greatest extent of reducibility given in terms of the amount of H₂ consumed (from TPR analyses).

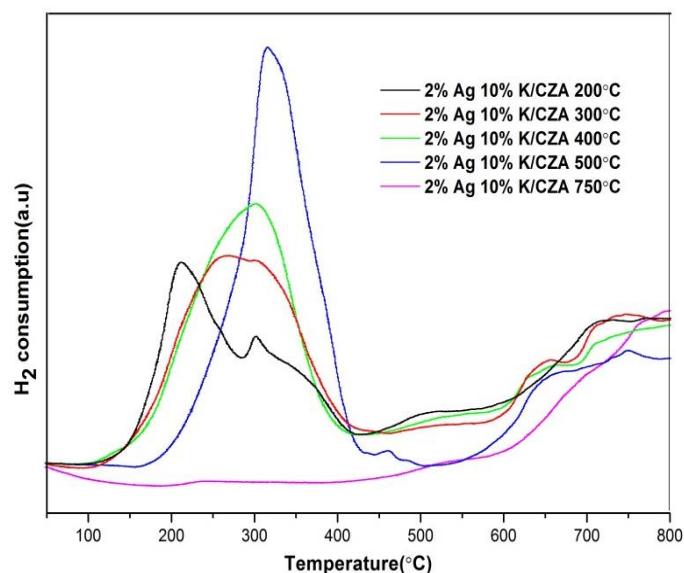


Figure 3.79 TPR profiles for Ag-K/CZA –varying calcination temperatures

Soot oxidation tests as shown in table 3.29, indicated that the lowest onset, peak and final oxidation temperatures were reported for the catalyst calcined at 500°C. This could be understood from the characterization of this catalyst that explained the formation of the CZA mixed oxide at this temperature with an impregnation of the Ag and K on the surface. Reduction profiles indicating maximum reducibility for this catalyst also suggested that the bulk oxygen was transferred to the surface and was available for the soot as the oxidation rate increased, with a maximum rate at 440°C.

Upon calcination at higher temperatures there was a change in structure of the catalyst and this caused the particles to sinter or grow in size, restricting the activity of soot oxidation. The impregnation of Ag and K onto CZA had improved the reducibility of the catalyst and in turn its activity for soot combustion. On calcining at lower temperatures, the onset of the oxidation was also pushed to slightly higher oxidation temperatures as there was insufficient oxygen availability from the catalyst surface needed to maintain the redox mechanism of CeO₂. This appeared to be that is vital in accelerating the rate of the reaction.

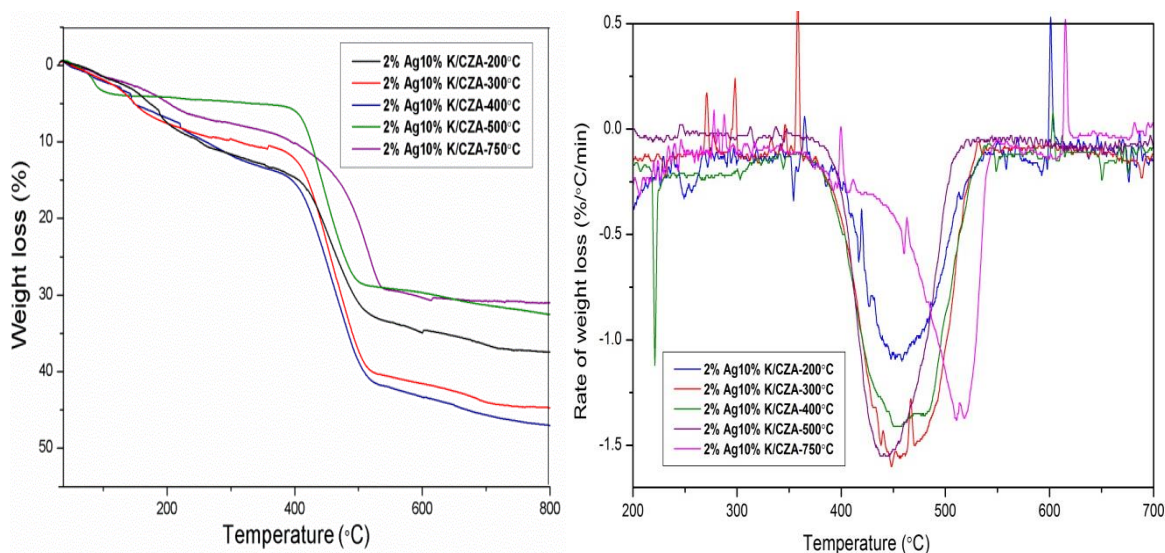


Figure 3.80 Soot oxidation activities for Ag-K/CZA catalysts- varying calcination temperatures

a) Variation of calcination rates

The catalysts prepared by varying the rate of calcination, between 1-20°C min⁻¹, showed no significant change in the structure. The distortion of the cubic fluorite symmetry due to the presence of K₂CO₃ on the surface was very clearly observed in all cases despite varying the rate of calcination. There was a slight increase in crystallinity when the rate of calcination was very slow, as in the case of 1°C min⁻¹, and the Ag (111) phase was distinct at 38°. With an increase in the rate of calcination, the peaks were seen to shift to higher 2θ angles with a greater peak width, indicated presence of smaller crystallites.

Figure 3.81 showed that calcining the catalysts at 500°C at 5°C min⁻¹ was the optimal rate for calcination, as the peaks indicated that the phases were less distorted and more crystalline. The Ag⁰ phase was observed on the CZA support, with slight distortion due to the K promotion. The crystallite sizes also tend to vary only very slightly with increase in calcination rates.

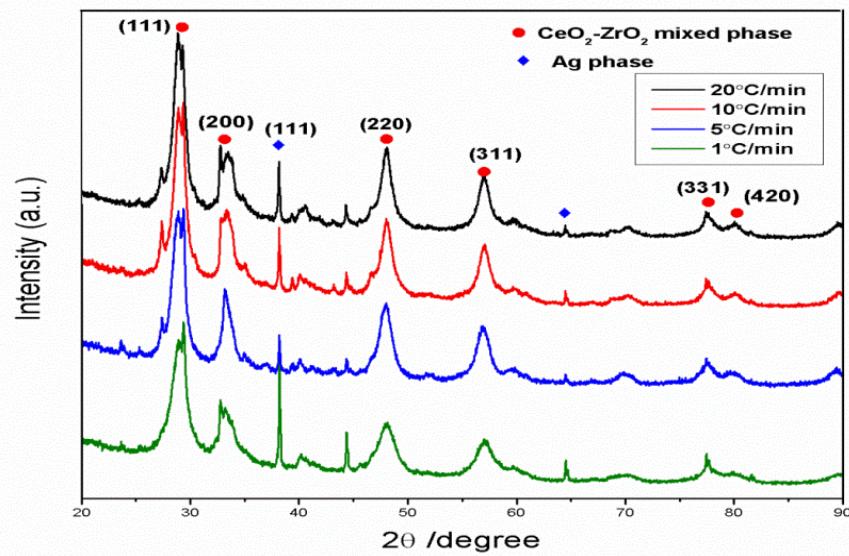
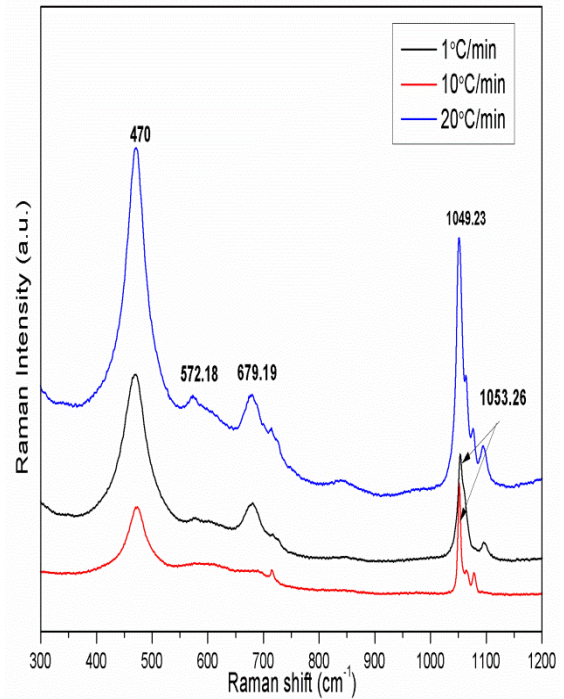
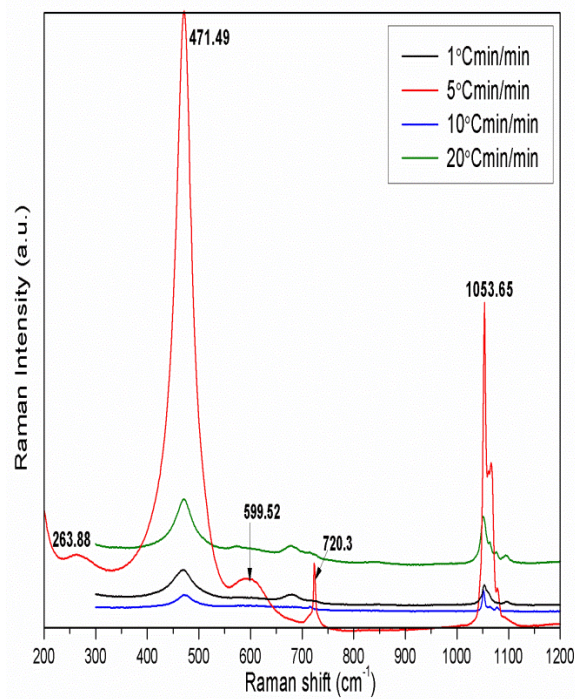


Figure 3.81 X-ray diffractograms for Ag-K/CZA- varying calcination rates

There was no distinct phase separation (as shown in the figure 3.81) with the formation of a mixed phase as indicated. This showed that a homogeneous mixture was formed upon calcination at 500°C, with an optimum calcination rate of 5°C min⁻¹.



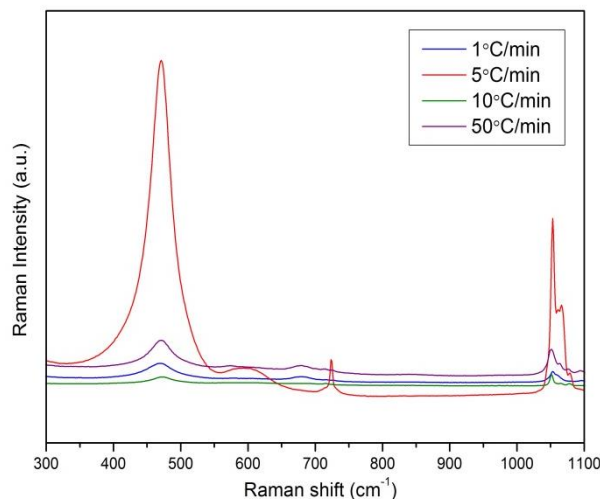


Figure 3.82 Raman spectra for AgK/CZA – varying calcination rate-a) entire spectra;b) zoomed in spectra

The Raman spectra for varying calcination rates of Ag-K/CZA (500°C) showed that the cubic CeO₂ phase was maintained in the case of the 5°C/min calcined catalyst as compared to the other rates. This could be concluded from the intensity of the cubic phase as shown in figure 3.82 (a) when compared to that observed for the other rates. The distortion of the cubic symmetry due to the ZrO₂ incorporation was also evident with bands seen at 268.88, 600 and 720 cm⁻¹. The peak at 1053.65cm⁻¹ represented the K₂CO₃ impregnation on the surface of CeO₂-ZrO₂-Al₂O₃.

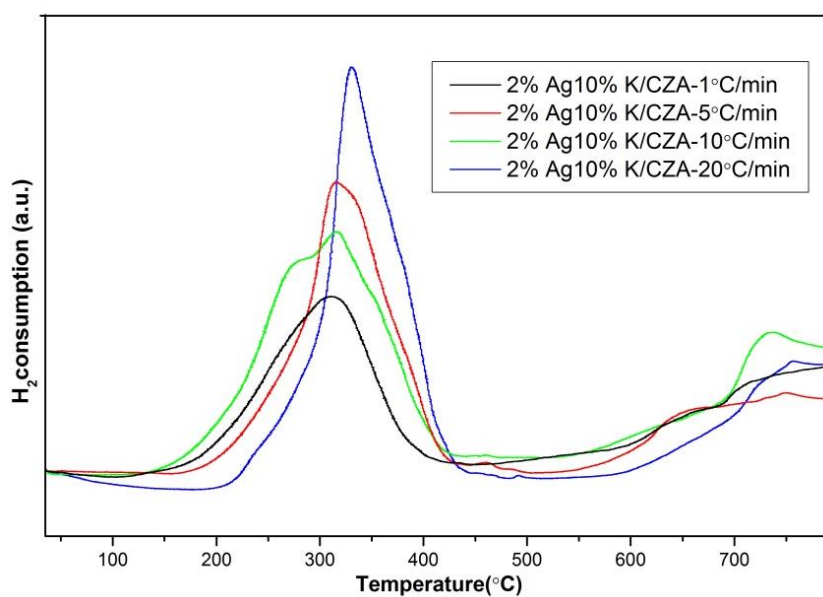


Figure 3.83 TPR profile for Ag-K/CZA – varying calcination rate

H₂ consumption values, from the table 3.28, indicated that the reducibility from the peak area for H₂ consumption was maximum when the rate of calcination was 20°C min⁻¹ but this occurred at temperatures slightly higher than for the other rates. There was only one single reduction peak observed, that consisted of the surface and bulk reduction of CeO₂. This was due to the incorporation of Ag that caused the overall reduction profile to shift to lower temperatures. The H₂ consumption values can be correlated to the amount of extractable O₂ from the lattice of CeO₂, and this was seen to be a maximum at a calcination rate of 5°C min⁻¹. The availability of the O₂ stored in CeO₂ was essential for the oxidation of the soot during the onset. This corresponded to the reduction temperatures of CeO₂ at 320°C, as seen in the figure 3.83.

The rate of calcination of the catalyst was therefore vital in optimising the catalyst preparation. The oxidation temperatures as seen from table 3.29 indicated that the calcination rate of 5°C min⁻¹ was ideal for the preparation as this showed lowest onset, peak and final combustion temperatures (figure 3.84). This could be explained by more incorporation of oxygen into the lattice of the catalyst, which allowed the Ag and K₂CO₃ to bind to the support more effectively. The role of alkali metals was probably to promote the dissociative chemisorption of oxygen. The promotion might be independent of the interaction between ceria and the metal occurring through a redox cycle, instead it is correlated to surface carbonate complexes that are formed after deposition of alkali metals. The presence of ZrO₂ in the mixed metal oxide support plays an important role in creating structural defects necessary for the transport of the lattice oxygen from the bulk to the surface, irrespective of being irreducible in nature.

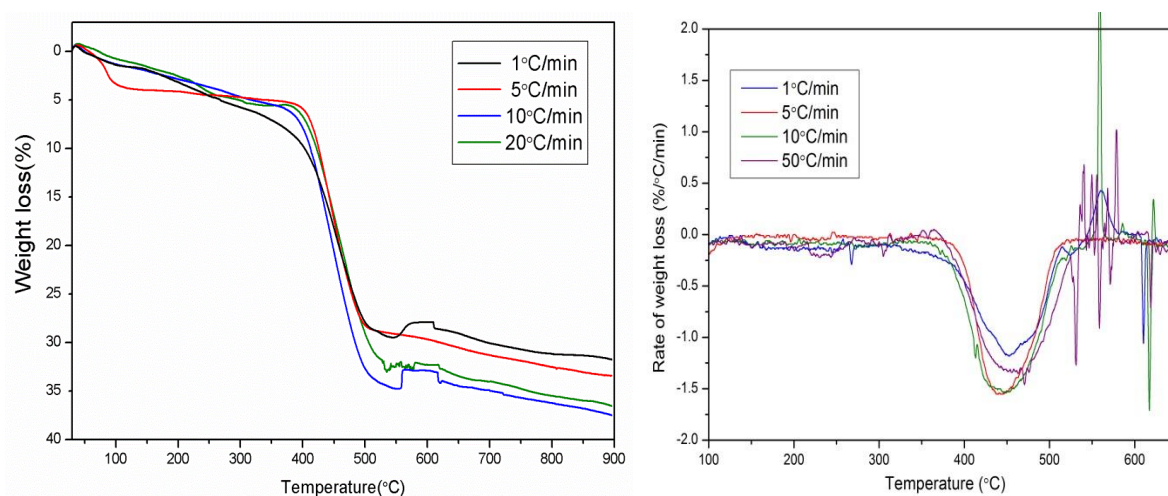


Figure 3.84 Soot oxidation activity of Ag-K/CZA- varying calcination rates

b) Variation of calcination time

X-ray diffractograms for Ag-KCZA (500°C , $5^{\circ}\text{C min}^{-1}$) showed that on varying the duration of calcination between 4, 5 and 6 hours not much change is seen in the structure of the catalyst (figure 3.85). The Ag (111) phase was slightly more intense when calcined for 4hr. The homogeneous cubic $\text{CeO}_2\text{-ZrO}_2$ mixed phase was retained irrespective of the calcination times. The crystallite sizes were quite similar as seen from table 3.28. The crystallite sizes increased with decrease in peak width.

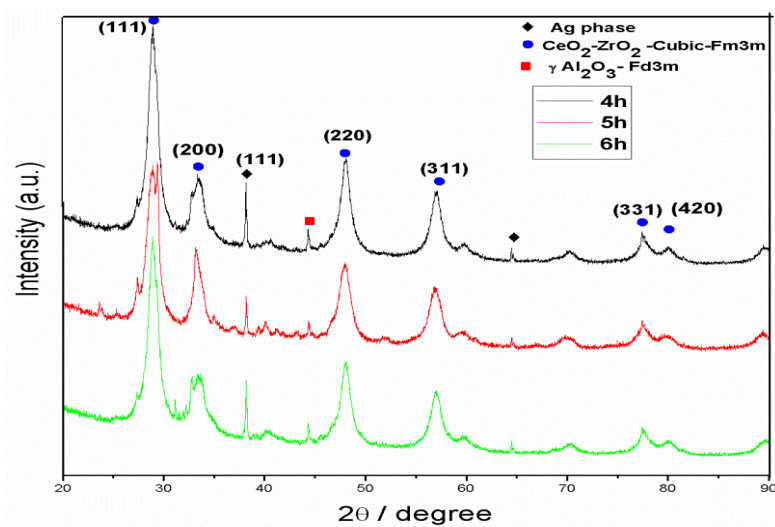


Figure 3.85 X-ray diffractograms for Ag-K/CZA-varying calcination time

Raman spectroscopy showed that the cubic fluorite CeO_2 phase was maintained and a mixed phase was evident with ZrO_2 incorporation as seen in figure 3.86.

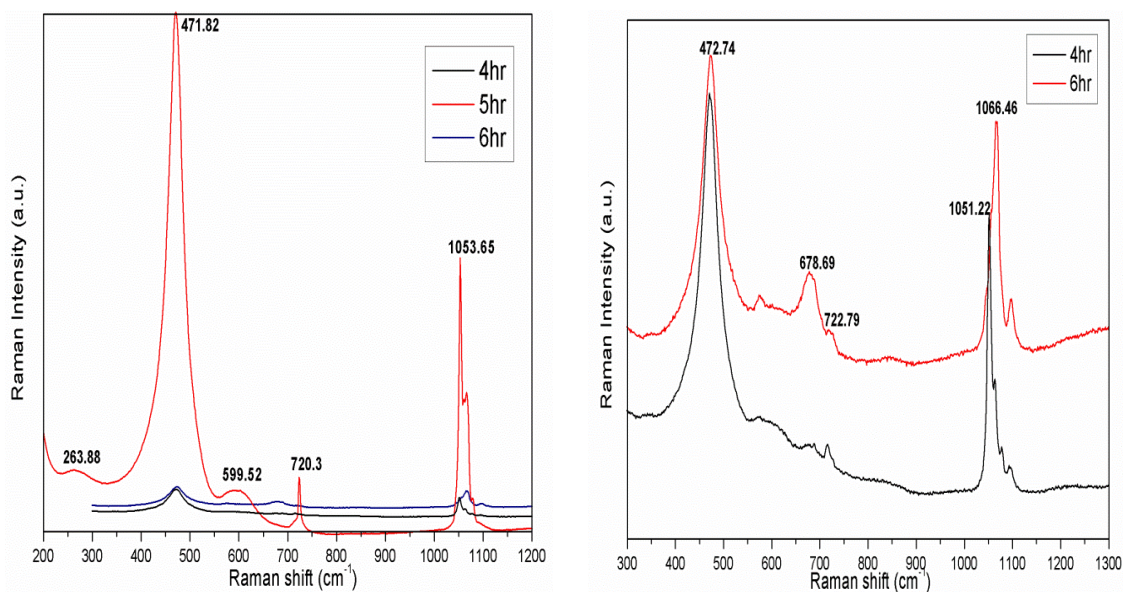


Figure 3.86 Raman spectra for AgK/CZA – varying calcination time-a) entire spectra;b) zoomed in spectra

The intensity of the cubic phase for the Ag-K/CZA (500, 5°Cmin⁻¹, 5hrs) was stronger than that for 4 and 6 hour calcinations. There was a slight shift in the peak positions towards greater 2θ angles with increase in calcination times as was observed in the case of the peaks for the cubic CeO₂ phase and for the K₂CO₃ phase, indicating smaller crystallites with peak broadening. Thus the calcination regime with a 5 hour calcination resulted in the optimized catalyst.

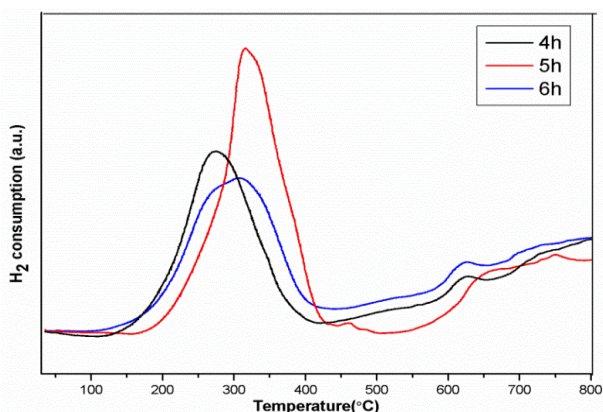


Figure 3.87 TPR profiles for 2% Ag-10% K/CZA – varying calcination time

Temperature programmed reduction also showed that the maximum extent of reducibility followed upon calcination at 500°C, 5°C min⁻¹ for 5 hours as seen in table 3.28. This reduction coincided with the temperatures for the onset of soot oxidation, thereby suggesting that the soot was provided with lattice oxygen stored in the catalyst. The single reduction profile indicated the simultaneous surface and bulk reduction of the CeO₂ in the catalyst (figure 3.87).

The potassium-modified soot oxidation catalyst, synthesised by impregnation exhibited excellent soot oxidation activity, with a decrease of over 100°C in the final temperatures as compared to pure CZ mixed oxides. Calcination times for the catalyst preparation are also vital in understanding the nature of the catalyst. After calcining at a relatively slow rate of 5°C min⁻¹ for about 5 hours, the soot oxidation rate was rapid due to sufficient storage of oxygen in the catalyst that was required to oxidise the soot and aid in its complete oxidation by 500°C (figure 3.88). This was observed in the data shown in table 3.29.

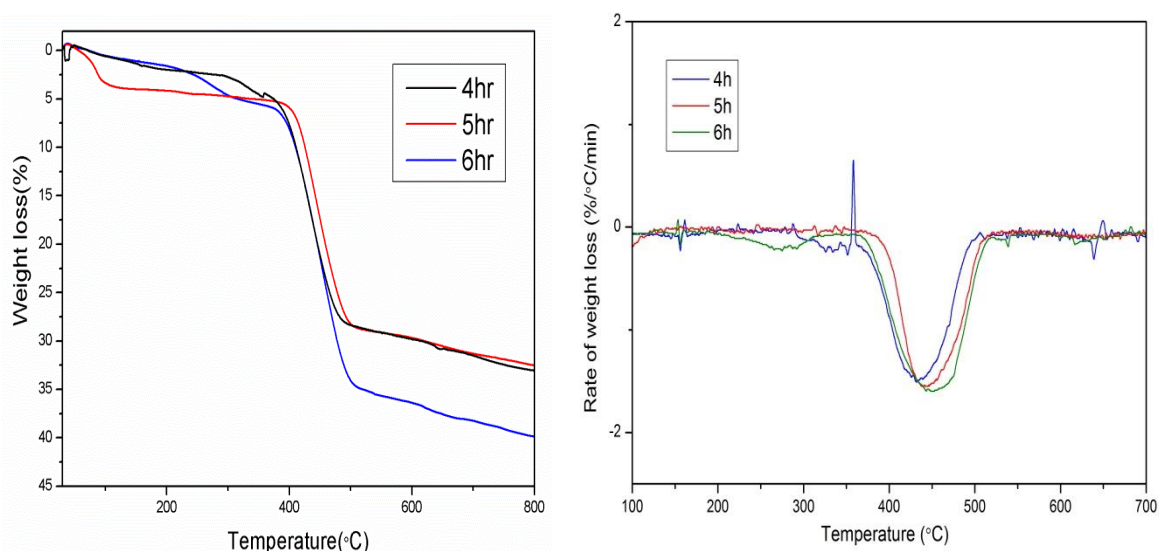


Figure 3.88 Soot oxidation activities for 2%Ag-10%K/CZA – varying calcination time

Table 3.29 Soot oxidation activity for Ag-K/CZA – varying calcination regime

Sl. No.	Catalyst	Onset temperature (T _{on})(°C)	Extrapolated Onset Temperature(T _{eo}) (°C)	Peak temperature (T _p) (°C)	Final Temperature (T _f) (°C)
Varying calcinations temperatures - 2%Ag10%K-CZA					
1.	200°C	394.3	403	453.4	550
2.	300°C	378	394.3	466.4	532.3
3.	400°C	364.3	405.2	457	531.4
4.	500°C	360.2	394	440.1	518
5.	750°C	359.2	443	518	551
Varying calcination rates					
6.	1°C/min	352.3	381.4	451.3	520
7.	5°C/min	360.2	394	440.1	518
8.	10°C/min	360.2	381	449.2	529.4
9.	20°C/min	364	375	462.4	523.1
Varying calcination time					
10.	4 hrs	358.2	366	437	506.4
11.	5hrs	360.2	394	440.1	518
12.	6hrs	366	376	451.3	520

Figure 3.90 represented the different morphologies of the 2% Ag 10% K/CZA catalyst calcined at 200, 300, 500 and 750°C. At 200°C, the presence of K₂CO₃ was not clearly evident and the structure resembled the CZA support. On increasing the calcination temperature, the impregnated K₂CO₃ was more evident as needle like whiskers present on the surface of CZA. This was partially evident at 300°C (figure

3.90b) while at 500°C (figure 3.90c) there was a distinct formation of the impregnated K_2CO_3 and Ag_2O on CZA. This morphology has been described in detail in section above.

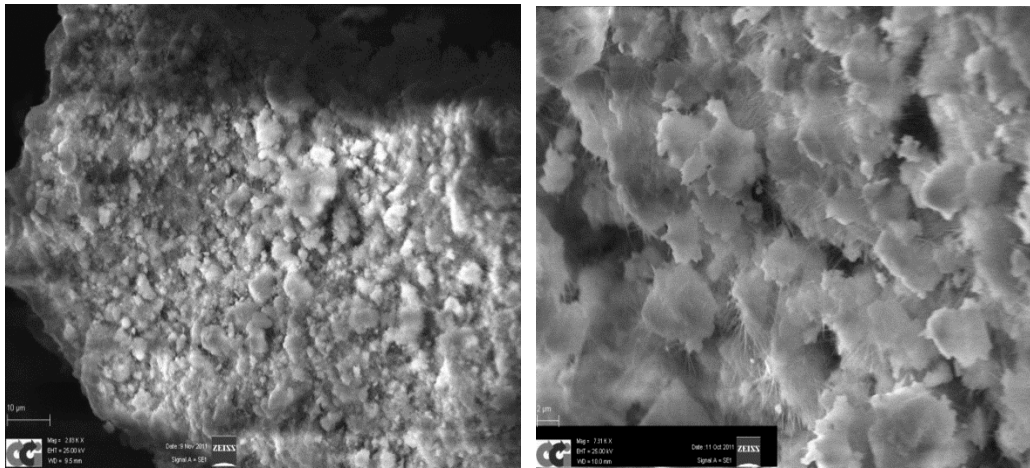


Figure 3.89 SEM images for 2%Ag10%K/CZA-500°C

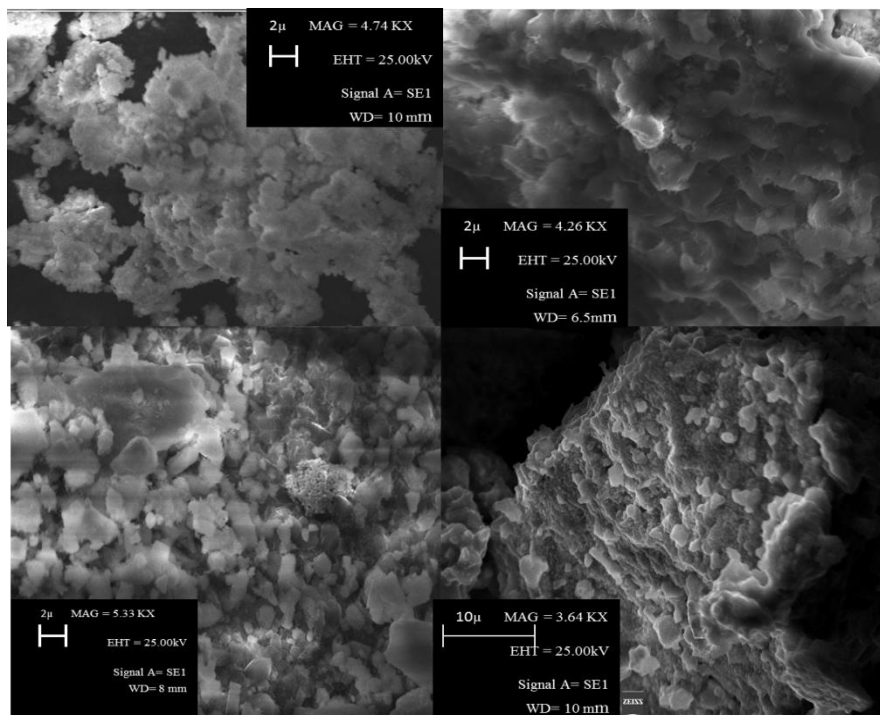


Figure 3.90 SEM images for Ag-K/CZA- a)200; b)300; c)500; d)750°C

Upon calcination at 700°C, the morphology changed, and the needle-like K_2CO_3 tends to decompose due to sintering (observed as bright spots) at such high temperatures. This was shown in the figure 3.91.

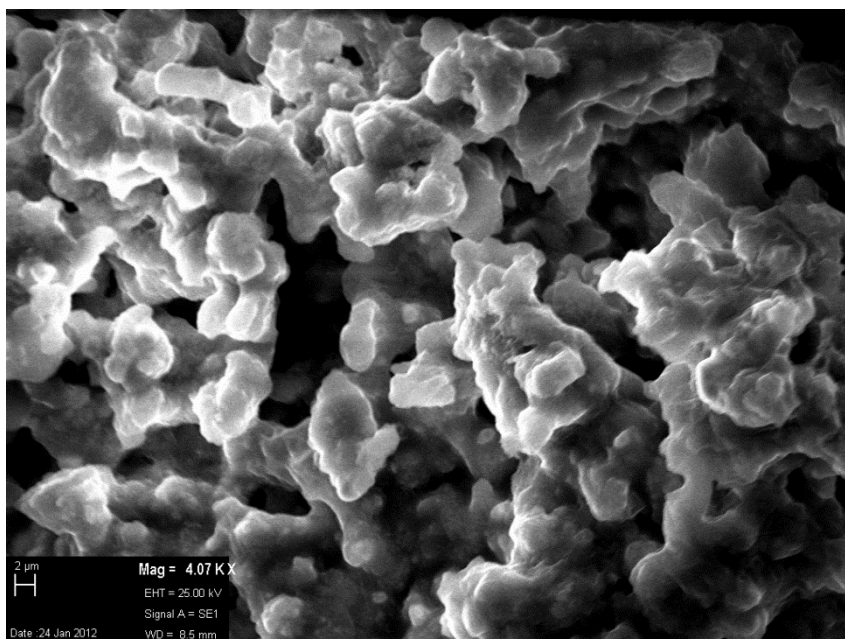


Figure 3.91 SEM images for 2%Ag10%K/CZA-750°C

3.9 Variation in the content of Ag-K on CZA (Na_2CO_3)

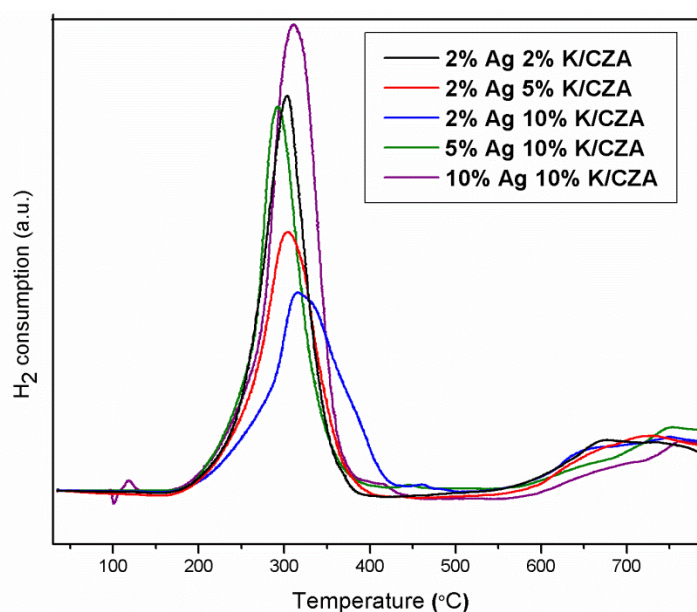


Figure 3.92 TPR profiles for varying Ag and K content on CZA

TPR profiles seen in figure 3.94 showed that on varying the loading of Ag and K on the CZA support, catalysts with 10% Ag and 10% K loading had greatest ease of reduction and maximum extent of reducibility, as indicated by the amount of H_2 consumed (shown in table 3.30). The peak temperature at which this occurred was around 320°C, where the onset of soot oxidation occurred, thus providing for the lattice oxygen stored in the catalyst through ceria reduction. The bimodal reduction profile

was modified upon Ag and K impregnation, resulting in a single reduction peak. The 10% Ag 10%K/CZA catalyst showed lowest activity as compared to the other weight loaded Ag-K/CZA catalysts (table 3.31). The reducibilities of the 2% Ag 2% K/CZA and 5% Ag 10%K/CZA also showed high reduction capabilities, but the synergy between Ag-K on CZA was not optimal for these loadings to promote the soot oxidation at low temperatures. The soot oxidation rate was maximum at around 440°C for these catalysts.

Table 3.30 Physical properties of AgK/CZA-varying Ag and K content on CZA

Sl.No	Alkali metal on CZA (Na ₂ CO ₃)	Surface area (m ² g ⁻¹)	Crystallite size (nm)	H ₂ consumption (μmol g ⁻¹)
1	2%Ag 2%K/CZA	9	9.3	6023.116
2	2%Ag 5%K/CZA	5	10.9	4896.364
3	2%Ag 10%K/CZA	12	7.7	4595.703
4	5% Ag 10%K/CZA	6	8.6	5490.975
5	10%Ag 10%K/CZA	2	12.7	7693.631

Table 3.30 shows a decreasing surface area with increase in content of Ag and K on CZA. Increased loading also led to increase in crystallite sizes due to sintering and decomposition of the K on CZA. Although impregnation of K₂CO₃ decreased the surface area, it was still an efficient promoter of soot oxidation. Retaining this in the catalyst composition was vital and thus the optimum composition in terms of the morphology and activity of these catalysts was 2%Ag 10%K/CZA (figure 3.93). The reduction profiles showed an increased H₂ consumption in the case of increased K loading, indicating that the amount of O₂ stored was more in the case of increased loading of Ag and K. Also a low loading of Ag at 2% showed this same effect. Thus a combination of these two factors gave an optimized composition for storage of O₂ in the lattice, that could be used during soot oxidation.

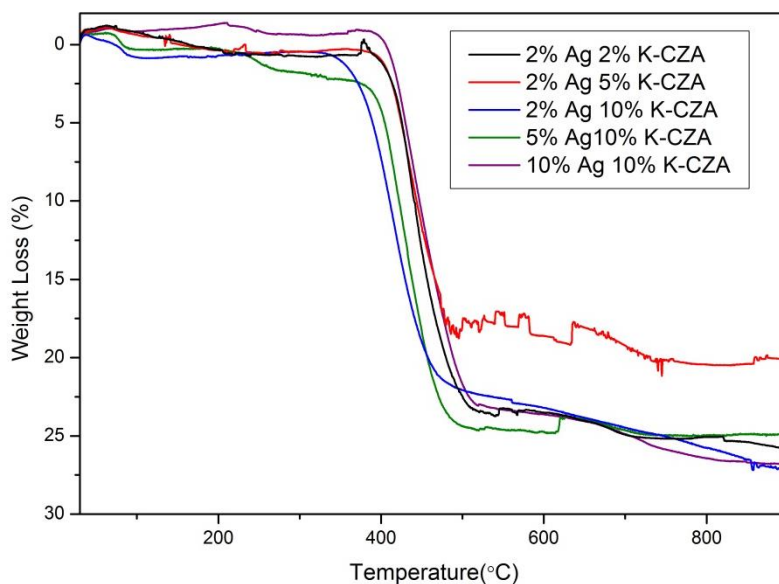


Figure 3.93 Soot oxidation activity for Ag-K/CZA- varying Ag, K content

Although 2% Ag 10%K/CZA showed poor reducibility in terms of the amount of H₂ consumed, this occurred at the onset of soot oxidation (320°C) and thus the Ce⁴⁺/Ce³⁺ redox occurred at this stage to provide the lattice oxygen in the catalyst. Also, the bulk reduction took place in the temperature range between 320-380°C, thus supplying the soot with a large amount of stored oxygen from the ceria, through the diffusion along the CZA lattice, with incorporation of the defects introduced by addition of ZrO₂.

Table 3.31 Soot oxidation activity of Ag-K/CZA- varying content of Ag and K

Sl.No	Alkali metal on CZA (Na ₂ CO ₃)	Onset temperature(T _{on}) (°C)	Extrapolated onset temperature (T _{eo}) (°C)	T _p (°C)	T _f (°C)
1	2%Ag 2%K/CZA	367.2	398.4	439.6	521.6
2	2%Ag 5%K/CZA	384.8	393.2	435.6	510.4
3	2%Ag10%K/CZA	324.8	350.8	410.8	491.6
4	5% Ag 10%K/CZA	364.4	384.8	430	508
5	10%Ag 10%K/CZA	382	401	439.6	521.6

3.10 Catalyst durability

The 2%Ag-10%K/CZA (calcined at 500°C, 5°C/min, 5hrs) showed extremely good soot oxidation activities with onset of 324°C and final oxidation occurring at 492°C. The high activity could be attributed to the high surface area and high reducibility. This catalyst was ideal for soot oxidation and should be suitable for exhaust gas aftertreatment as CZA supports are already widely used in three way catalysts. The catalysts were re-tested and the results were reproducible for 2wt%Ag-10wt%K/CZA as shown in figure 3.96a and 10%K/CZA in figure 3.96b.

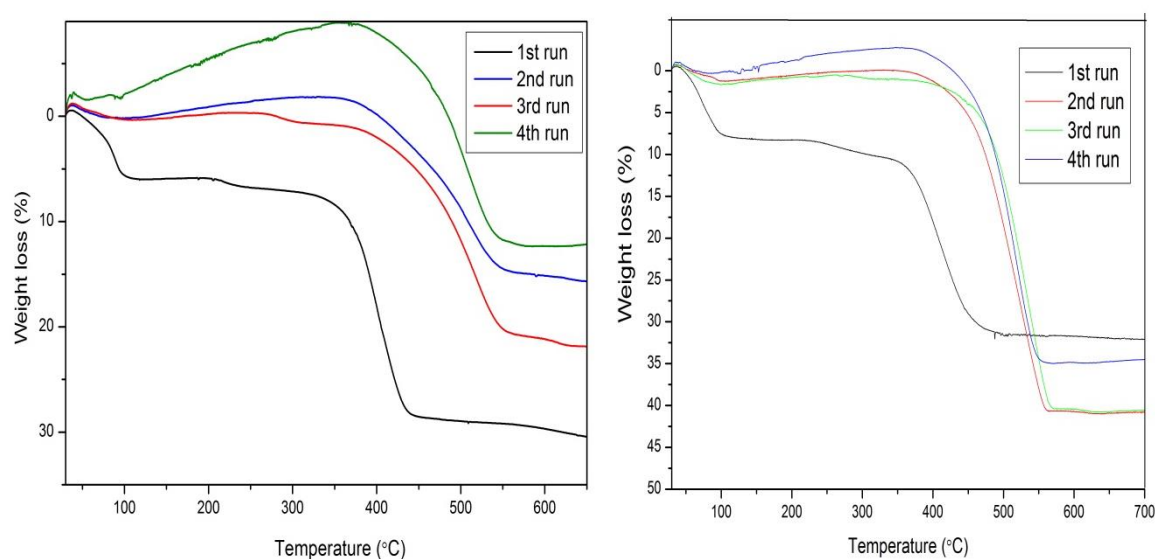


Figure 3.96 Soot oxidation activity-reproducibility –a)2%Ag10%K/CZA; b) 10%K/CZA

The results indicated that both catalysts promoted the combustion of soot very efficiently, along a temperature range of 300-550°C, even after subjecting the catalyst to four consecutive oxidations using fresh batch of soot each time, while keeping the catalyst amount unaltered. The first run in both cases showed that the catalyst oxidized the soot by 420°C and 470°C for 2%Ag10%K/CZA and 10%K/CZA respectively, but on subjecting them to three more subsequent runs, the oxidation temperatures shifted to slightly higher temperatures with a difference of about 100°C. The oxidation began at around 450°C in the 2nd, 3rd and 4th runs and was complete by 550°C, indicating a more rapid rate in oxidation of the soot as could be seen from the slopes in the curves from figure 3.96. The catalyst had not been sintered despite subjecting it to such high temperatures as seen from repeated TGA soot oxidation analyses on the same catalyst. Figure 3.97 indicated the efficiency in terms of the rate of soot oxidation, in the

presence of the Ag-K/CZA catalyst, under loose and tight contact conditions as opposed to pure soot oxidation. The catalyst helped reduce the temperatures of oxidation by nearly 200°C. The catalyst was ideal under both loose and tight contact conditions enabling it to be used in diesel filters.

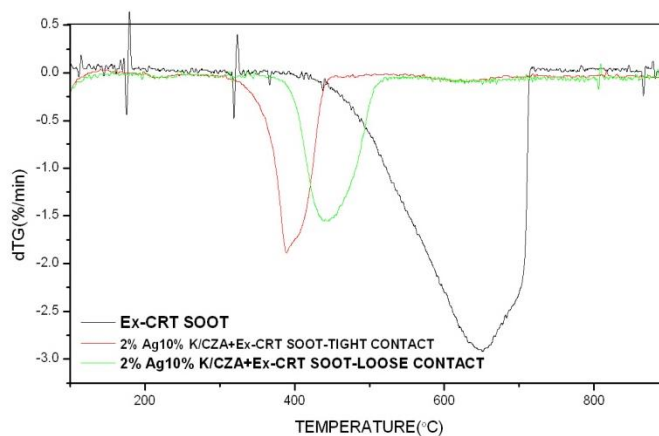


Figure 3.97 Rate of soot oxidation in the presence of 2%Ag-10%K/CZA under loose and tight contact with soot

This catalyst was studied in more detail under N_2 and air atmosphere in order to understand the decomposition pattern of the catalyst under an inert and oxidative atmosphere. The supports were also subjected to this treatment. Figure 3.98 indicated that the decomposition of the CZA precursors under air and N_2 (indicated by the blue and pink lines respectively), began at around 100°C with a loss of water from the precursors at this temperature.

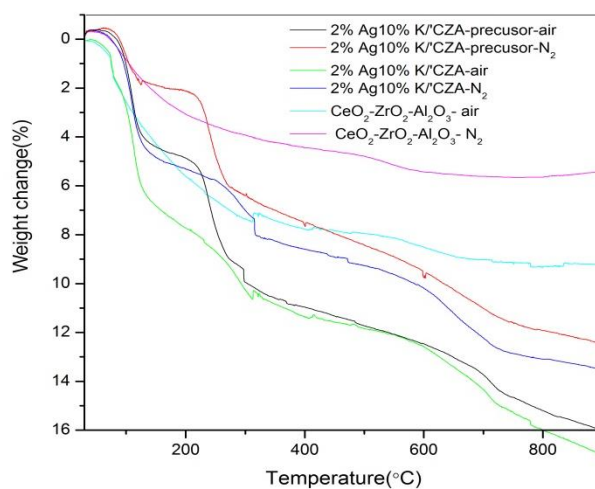


Figure 3.98 a) Decomposition of CZA and AgK/CZA air/ N_2

There was a subsequent weight loss at 300°C and it was complete by around 500°C, which indicated the oxidation of the support under air but under N₂ there was only decomposition at 100-150°C owing to water loss, physisorbed CO₂ and/or bicarbonate species, the latter being formed upon reaction of basic OH groups with CO₂ (from the . Above 150°C, the more firmly bonded CO₂ species, such as bidentate carbonates and carboxylates in various configurations/structures tend to get desorbed together with some of the less stable OH groups. The mass losses observed in the 600–900 °C range were caused by both by the release of water, by more complete dehydroxylation and/or by the removal of polycarbonates species, and other contaminants trapped in the bulk structure of the ceria-zirconia [44].

In the case of the precursors for Ag-K/CZA, initial weight loss at 100°C was due to the water loss and thereafter a clear loss occurred at 300-600°C, owing to the formation of the oxides and the dispersion of K₂CO₃ on CZA. Under N₂ atmosphere, this catalyst seemed to show a loss of the oxygen from the lattice leading to ceria reduction at 300°C which probably aids in the soot oxidation. This could be accounted as the oxygen storage capacity of the catalyst. This was given from the figure 3.99 that represented the reduction of this catalyst under H₂/Ar to indicate the ceria reduction profile followed by its oxidation and second reduction to form ceria again.

Table 3.32 Reduction capabilities of Ag-K/CZA post TPR-TPO-TPR

Sl.No	Catalyst	H ₂ consumption (μ moles/g)
1	AgK/CZA-reduction -1	4965.3
2	AgK/CZA-reduction -2	558.8

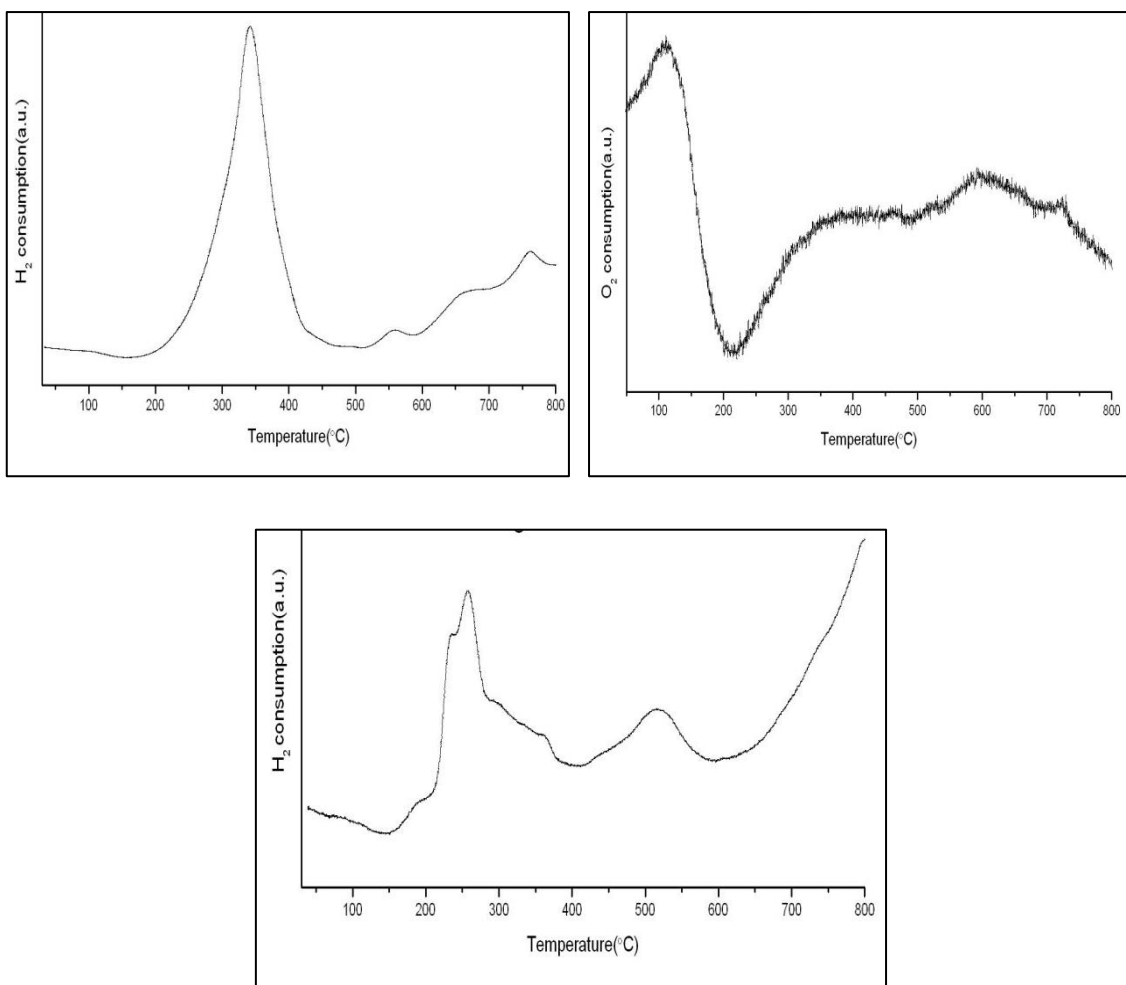


Figure 3.99 Redox of AgK/CZA catalyst indicating consecutive reduction-oxidation-reduction cycle

There was a drop in the reduction of the ceria in the catalyst during a successive TPR-TPO-TPR run due to the fact the ceria undergoes reduction from Ce^{4+} to Ce^{3+} and then back to Ce^{4+} . This utilised $4965.3 \mu \text{ moles/g}$ of H_2 for this process and then oxidation was carried out to give the initial form again as shown in figure 3.99. The Ce^{4+} then was reduced to see how much of the oxygen stored in the catalyst was utilised for the second reduction after the re-oxidation of the catalyst. This showed an amount of $558.8 \mu \text{ moles/g}$, indicating that this was the oxygen stored that was released upon second reduction as $559 \mu \text{ moles/g}$, which could be utilised by the soot of the consecutive oxidations of soot as in the above cases. This shows how the oxygen stored in the lattice of the catalyst is used for the soot oxidation. The initial reduction of the catalyst provides the oxygen stored for soot oxidation and upon reoxidation (as in the

case of gaseous oxidation of reduced CeO_2) the catalyst comes back to its original state. A second reduction was carried out to show a typical oxidation cycle of soot.

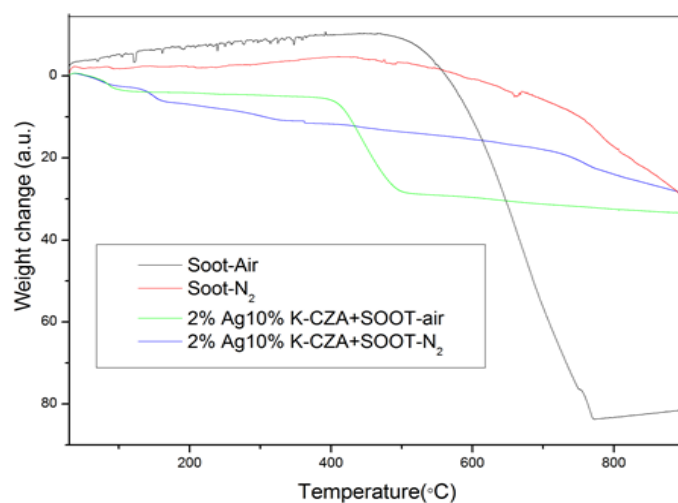


Figure 3.100 Catalysed and uncatalysed soot oxidation under N_2 and air

This figure 3.100 indicated that the oxidation of soot occurred in the absence of the catalyst at very high temperatures in the presence of oxidative atmosphere, through a very slow process that begins at temperatures above 500°C and is complete by 750°C . In the presence of the catalyst this temperature was lowered under oxidative atmospheres. In the presence of N_2 , the stored O_2 could be used as shown above, upon reduction of the ceria to oxidize the soot. Thus this catalyst showed considerable promise for the direct oxidation of trapped soot in automotive applications.

Conclusions: Several analyses on the CZA supports revealed that the best method of preparation was coprecipitation using Na_2CO_3 as a precipitating agent with a calcination under flowing air at 500°C , $5^\circ\text{C}/\text{min}$ for 5 hours. Modified wet impregnation of 2wt% Ag onto CZA helped to reduce the temperatures of soot oxidation by effecting the reducibility of CeO_2 in the catalyst at low temperatures of 120°C . Also, 10%K impregnation(wet impregnation) onto CZA acted as a promoter for soot oxidation drastically reducing the soot oxidation temperatures, almost 200°C lower than uncatalysed oxidation.

References

1. D. Terribile, A. Trovarelli, J. Llorca, C. de Leitenburg, G. Dolcetti, *Catalysis Today*, 43, (1998), 79
2. L. Katta, P. Sudarsanam, G. Thrimurthulu and B. M. Reddy, *Applied Catalysis B-Environmental*, 101, (2010), 101-108.
3. L. N. Ikryannikova, A. A. Aksenov, G. L. Markaryan, G. P. Muravieva, B. G. Kostyuk, A. N. Kharlanov, E. V. Linina, *Applied Catalysis A*, 210, (2001), 225
4. D. H. Prasad, J. Lee, H. Lee, B. Kim, J. Sung Park, *Journal of Ceramic Processing Research*, 10,6, (2009), 748-752
5. M. Fernandez-García, A. Martínez-Arias, A. Iglesias-Juez, C. Belver, A. B. Hungría, J. C. Conesa, J. Soria, *Journal of Catalysis*, 194, (2000), 385
6. P. Fornasiero, J. Kašpar, M. Grazini, *Journal of Catalysis*, 167, (1997), 576
7. G. L. Markaryan, L. N. Ikryannikova, G. P. Muravieva, A. O. Turakulova, B. G. Kostyuk, E.V. Lunina, V.V. Lunin, E. Zhilinskaya, A. Aboukais, *Colloids Surfaces A*, 151, (1999), 435.
8. A. Trovarelli, *Catalysis Review Science and Engineering*. 38, (1996), 439
9. F. Giordano, A. Trovarelli, C. de Leitenburg, M. Giona, *Journal of Catalysis*, 193, (2000), 273
10. C. F. Oliveira, F. A. C. Garcia, D. R. Araujo, J. L. Macedo, S. C. L. Dias, J. A. Dias, *Applied Catalysis A-General*, 413, (2012), 292-300
11. I. Atribak, A. Bueno-Lopez, A. Garcia-Garcia, *Journal of Catalysis*, 259, (2008), 123-132.
12. L. N. Ikryannikova, A. A. Aksenov, G. L. Markaryan, G. P. Murav'eva, B. G. Kostyuk, A. N. Kharlanov, E. V. Lunina, *Applied Catalysis A-General*, 210, (2001), p225-235.
13. J. Kašpar, P. Fornasiero, N. Hickey, *Catalysis Today* 77, (2003), 419
14. A. Trovarelli, C. de Leitenburg, M. Boaro, G. Dolcetti *Catalysis Today*, 50, (1999) 353.
15. V. Perrichon, A. Laachir, G. Bergeret, R. Frety, L. Tournayan, *Journal of the Chemical Society. Faraday Transactions*, 90, (1994) 773
16. H. C. Yao, Y. F. Y. Yao, *Journal of Catalysis*, 86, (1984), 254
17. M. Pijolat, M. Prin, M. Soustelle, O. Touret, P. Nortier, *Journal of the Chemical Society-Faraday Transactions*, 91, (1995), 3941-3948
18. B. M. Reddy, A. Khan, Y. Yamada, T. Kobayashi, S. Loridant, J. C. Volta, *Journal of Physical Chemistry B*, 107, (2003), 11475-11484
19. G. Neri, A. Pistone, C. Milone, S. Galvagno, *Applied Catalysis B: Environmental*, 38 (2002) 321-329
20. F. Oliveira, F. A. C. Garcia, D. R. Araujo, J. L. Macedo, S. C. L. Dias, J. A. Dias, *Applied Catalysis A-General*, 413, (2012), 292-30
21. N. Nejar, M. Makkee, M. J. Illan-Gomez, *Applied Catalysis B-Environmental*, 75, (2007), 11-16

22. J. Zhang, L. Li, X. Huang, G. Li, *Journal of Materials Chemistry*, 22, (2012), 10480
23. L. Kundakovic, M. F. Stephanopoulos, *Journal of Catalysis*, 179, (1998), 203–221.
24. S. Scire, S. Minico, C. Crisafulli, C. Satriano, A. Pistone, *Applied Catalysis. B*, 40, (2003), 43–49
25. G. Ranga Rao, J. Kašpar, S. Meriani, R. D. Monte, M. Graziani, *Catalysis Letters*, 24 (1994) 107.
26. T. Tabakova, F. Boccuzzi, M. Manzoli, J. W. Sobczak, V. Idakiev, D. Andreeva, *Applied Catalysis A*, 298, (2006), 127–143.
27. S. Wenjuan, Y. Lihua, M. A. Na, Y. Jiali, *Chinese Journal of Catalysis*, 33, (2012), 970-976
28. P. Sipos, L. Bolden, G. Hefter and P. M. May, *Australian Journal of Chemistry*, 53, (2000), 887-890
29. D. R. Lide, *CRC Handbook of Chemistry and Physics, 86th Edition*, CRC Press, (2005),43
30. S. Yeqin, Z. Ying, L. Hanfeng , Z. Zekai, C. Yinfei, *Chinese Journal of Catalysis*, 34, (2013) 567–577
31. Y. Zhang , X. Zou *Catalysis Communications* 8, (2007), 760–764
32. E. Aneggi, C. de Leitenburg, G. Dolcetti, A. Trovarelli, *Catalysis Today*, 136 (2008) 3–10
33. Z. H. Zhu, G. Q. Lu, *Journal of Catalysis*, 197, (1999), 262.
34. Z.H. Zhu, G.Q. Lu, R.T. Yang, *Journal of Catalysis*, 192, (2000), 77.
35. J. A. Moulijn, F. Kapteijn, *Carbon* 33, (1995), 1155.
36. R. J. Lang, *Fuel* 65, (1986), 1324.
37. M. S. Gross, M. A. Ulla, C. A. Querini, *Applied Catalysis A-General*, 360, (2009), 81-88
38. L. Castoldi, R. Matarrese, L. Lietti, P. Forzatti, *Applied Catalysis B: Environmental*, 90 (2009) 278–285
39. K. Yamazaki, T. Kayama, F. Dong and H. Shinjoh, *Journal of Catalysis*, 282, (2011), 289-298
40. T. Kayama, K. Yamazaki, H. Shinjoh, *Journal of the American Chemical Society*, 132, (2010), 13154-13155
41. X. Zhu, R. Bai, K. H. Wee, C. Liu , S. L. Tang, *Journal of Membrane Science*, 363, (2010), 278-286.
42. L. Hongmei, Q. Hu, Y. Li, M. Gong, Y. Chen, J. Wang, Y. Chen, *Journal of Rare Earths*, 28, (2010), 79–83
43. L. Y. Zhu, G. Yu, W. W. Qin, X. Q. Wang, D. Xua, *Journal of Alloys and Compounds*, 492, (2010), 456–460
44. L. Zenboury, PhD thesis (2009), Metz.

Chapter 4

Soot oxidation studies-quantitative analysis

4.1. Introduction

Diesel particulate filters (DPF) are monolith structures used to trap soot particulate matter (PM) from engine exhausts. One such system is known as the continuously regenerated trap (CRT) which uses NO_x in the exhaust for NO_2 -assisted soot combustion, since NO_2 is far more oxidising than O_2 and NO , with reaction proceeding at around 200°C with NO_2 while over 500°C is required with O_2 . This mechanism helps to solve the problem of poor contact between the catalyst and soot. The CRT however needs a sufficient NO_2 production source and a technique for the optimal usage of NO_2 with a requirement of high temperatures in the exhaust in order to help assist the reaction at a rapid rate.

The problem is further exacerbated as modern day diesel engines do not produce enough NO_x for successful application of the CRT in some circumstances. Thus there is a need to develop catalysts that can activate O_2 to form highly reactive oxygen species, or can store the NO_x necessary for the rapid increase in rate of combustion. Thus CeO_2 based formulations have been evaluated but the utilisation of the active oxygen species was restricted by the contact between the soot and the catalyst.

This study aimed at evaluating the effect of oxidising agents such as NO_x , CO , CO_2 alongside trying to utilise O_2 , the most abundant oxidising agent in the diesel exhaust, to understand the process of soot oxidation occurring in the exhaust. This study was carried out using the optimised Ag-K/CZA and Pt/SiC catalysts. Some of the characteristics of soot through compositional analyses have also been highlighted to try and understand the mechanism of the oxidation in more detail.

The work presented in this chapter was focussed on mainly understanding the possible mechanisms of diesel soot oxidation under different conditions of the exhaust. The study showed how varying concentrations of oxygen feed could affect the rate of soot oxidation, as in the lean and rich conditions of the exhaust. Norit charcoal and graphite have been studied as models for soot oxidation with the aim of understanding the oxidation of solid carbonaceous components of soot and volatile aromatic compounds.

4.2 Soot characterization

4.2.1 TEM /STEM

The diesel soot used in this study was subjected to TEM analyses and the structures were as seen in figure 4.1. The diameter of the primary particles using TEM was found to be 22.6 ± 6.0 nm for diesel soot. These primary particles of diesel soot showed an onion-shell structure of nanocrystalline graphite with domain sizes between 2–3 nm. The soot particles were constituted mostly of carbon atoms, with a C: H ratio around 10:1. They had a chain structure composed up to 4000 of smaller spherical particles known as *spherules*. These spherules tend to agglomerate in clusters and possess between 10^5 to 10^6 carbon atoms. The agglomerate sizes varied from 10 to 1000 nm with a surface area around $200 \text{ m}^2\text{g}^{-1}$ [1, 2, 3].

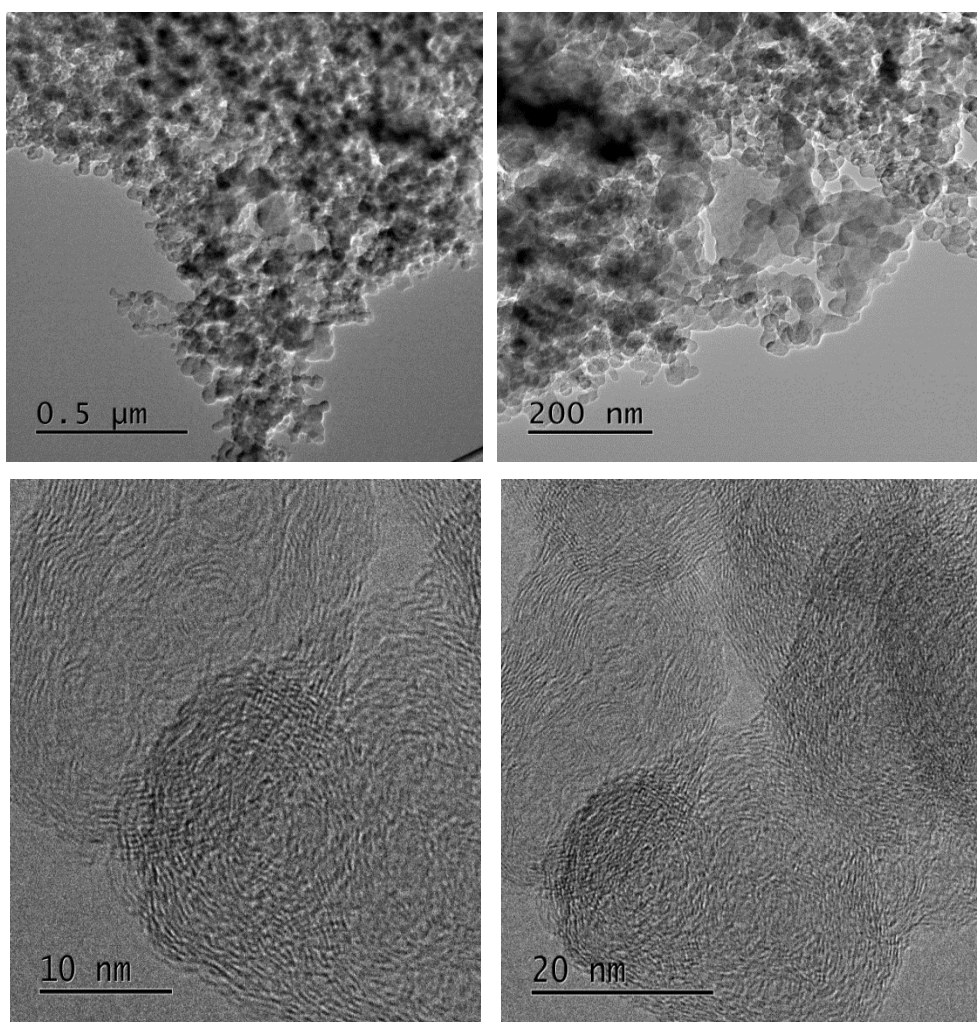


Figure 4.1 TEM images of soot particles

The agglomerates made up of nanoparticles were more or less spherical with a diameter typically from 10 to 80 nm, most of them lying in the range of 15-30 nm as

suggested by Amann and Siegl. The energy-dispersive X-ray spectra of diesel soot showed a silicon peak along with a dominating carbon peak [1, 4, 5].

Studies from literature showed that these spherules constituted of concentrate lamellate structure arranged around the centre that were identical to the carbon black or graphite structure. The carbon atoms bonded together in hexagonal face-centred plane arrays or as *platelets*. The space between two platelets was 0.355 nm in average which was slightly higher than graphite. These over layers of 2 to 5 platelets layer to form crystallites, and several such crystallites in disordered layers (turbostratic mode) constituted a spherule as shown in figure 4.2. Soot density was estimated to be close to the graphite, i.e. around 2 gcm^{-3} [6].

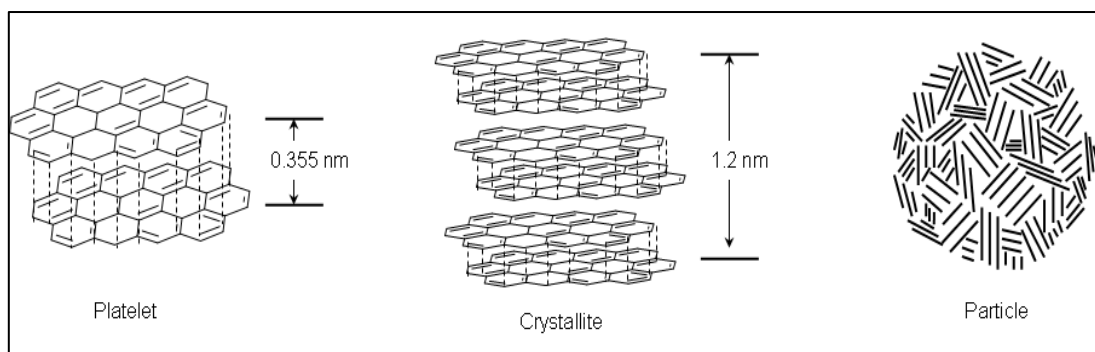


Figure 4.2 Soot particle formation [6]

Figure 4.3 reveals how the soot was formed from the precursors at different parts of the diesel fuel flame. This analysis was conducted by Wilson Merchan *et al.* on different types of soot such as diesel fuel flame soot, biodiesel fuel flame soot [7].

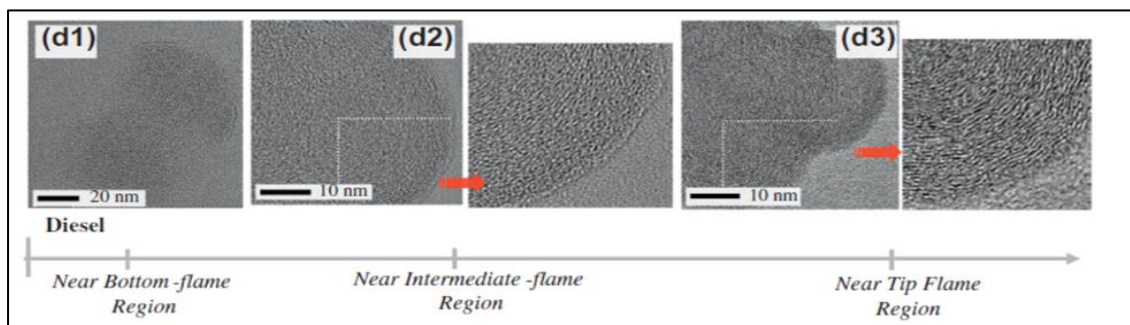


Figure 4.3 Representative HR-TEM images of young and mature soot nanostructure variation from different biodiesels and from diesel fuel near the bottom-flame, intermediate flame, and tip-flame regions [7]

4.2.2 CHNS analyses

Elemental analyses of soot and extracted soot revealed that the following elements were predominantly present in diesel soot. The main constituent was carbon accounting for nearly 92% of the total weight, followed by hydrogen (~1%), and with the remainder made up of nitrogen (~0.2%) and sulphur (~0.2%). The hydrogen was mainly associated with the PAH compounds, as its concentration in the soot reduced post extraction using different extraction methods to obtain the adsorbed hydrocarbons (table 4.1).

Table 4.1 CHNS analyses of soot before and after extraction (remaining percentage is the inorganic ash)

Sl.No	SAMPLE	Total %wt	CARBON (%wt/wt)	HYDROGEN (%wt/wt)	NITROGEN (%wt/wt)	SULPHUR (%wt/wt)
1	SOOT-PRIOR TO EXTRACTION	92.75	91.48	0.95	0.15	0.17
2	SOOT- POST CRUDE EXTRACTION-DCM	87.4	86.39	0.73	0.08	0.2
3	SOOT-POST 4 STEP EXTRACTION/ULT RASONIC-ATION	71.13	70.23	0.61	0.09	0.2
4	SOOT POST- TOLUENE SOXHLET EXTRACTION	70.29	69.54	0.5	0.05	0.2

Elemental analyses of soot was also carried out using EDX and XPS techniques, which showed that there were some other elements present in very small concentrations (ppm levels) that could be detected from these analyses but not with accuracy. These included metallic elements such as Fe, Zn and Cu in very small concentrations (atomic %) which were difficult to quantify. This data was understood from literature and their contributions towards the oxidation are studied from results shown by Docekel *et.al* in 1991 [8] where they detected several elements such as Cd, Cr, Cu, Fe, Mn, Ni, Pb, Se, and V in the sample solutions (from diesel soot) by using a Perkin-Elmer 5000 Zeeman atomic absorption spectrometer equipped with a HGA 500 graphite furnace and an AS-40 autosampler. A Perkin-Elmer 400 atomic absorption spectrometer was also used to identify minor elements such as Ca, Na, and Zn by the flame technique using acetylene: air. The analyses consisted of diluting the samples ten times and a

standard was added to quantify for the concentrations [8]. These concentrations were as given in figure 4.4.

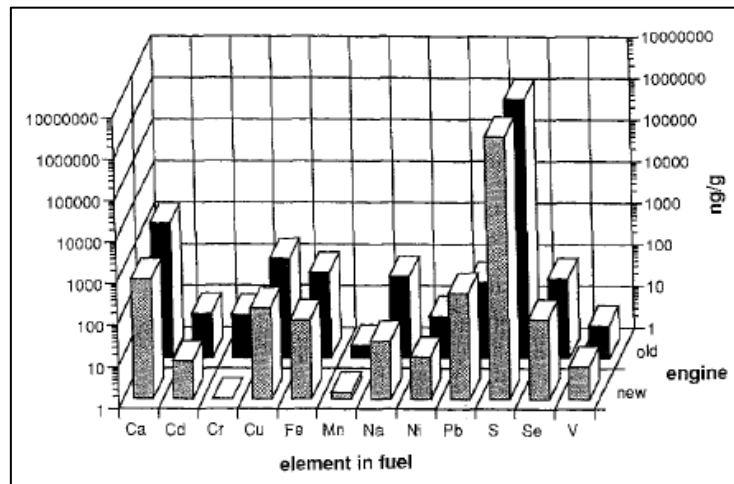


Figure 4.4 Elemental constitution of soot [8]

4.2.3 Raman spectroscopy

Raman spectroscopy was used to understand the nature of the carbon atoms in diesel soot as a comparison to graphite which is a pure form of carbon. The different graphite models were obtained from a company called Haydale and these were described below.

- a) GT graphite: formed by chemical vapour deposition method where Mg was reacted with CO₂ to give the sp² carbon. The particles had a SSA of around 450m²/g and were made up of minuscule platelets which were around 50nm-200nm in diameter, but typically agglomerated into small bundles around 500 nm to 2 microns.
- b) XGNP GRAPHENE NANOPATELETS: GRADE M (XGM-5) are unique nanoparticles consisting of short stacks of graphene sheets having a platelet shape. Each grade contained particles with a similar average thickness and surface area. Grade M particles were made of an average thickness of approximately 6 nm and a typical surface area of 120 to 150 m²/g. Grade M possessed average particle diameters of 5, 15 or 25 μm. This was shown in figure 4.5 [9].
- c) XGNP GRAPHENE NANOPATELETS: GRADE C (XGC 750)- These had an average thickness of a few nanometres and a particle diameter of less than 2μm. Their average surface areas were 300, 500 and 750 m²/g [10].

These were compared with soot and extracted soot in order to understand the contribution towards the D and G band, thereby giving an understanding of the amount of impurities or defects in the carbon in soot as compared to that from pure graphite. Raman spectra in the range $1000\text{-}2000\text{cm}^{-1}$ showed the D and G bands for carbon samples. The D band at 1350 and G band at 1582cm^{-1} indicated the two main characteristic peaks and the ratio of which gave the purity of the carbon sample. The G band is the primary Raman active mode for sp^2 bonded carbon atoms present in a planar configuration while the D band represents the disorder or defects. From the figures 4.6 a, b and c for soot, Norit, extracted soot, respectively, the D band was intense and the ratio of D: G was higher thus indicating more defects in these samples than in graphitic samples.

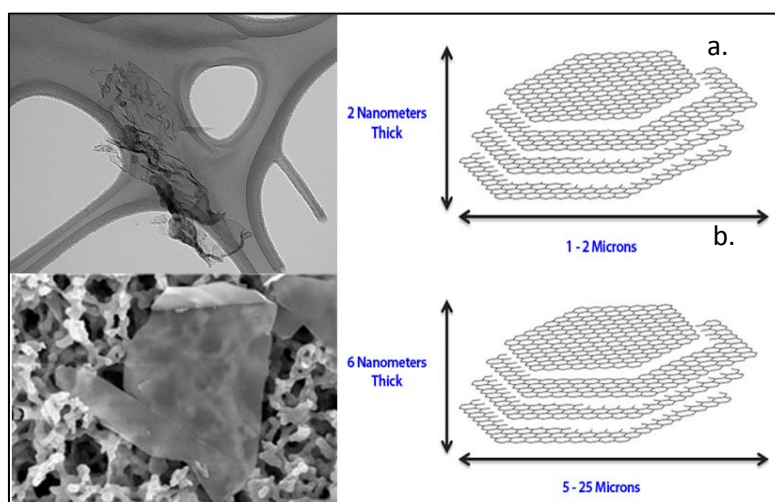


Figure 4.5 Graphene nanoparticles- a) grade C; b) grade M [9,10]

The Raman spectra for the various carbon samples were shown in figure 4.6. The variation in the D and G character of the two bands has been indicated. Raman spectroscopy is an ideal technique for comparison of the purity of the carbon species in the various samples.

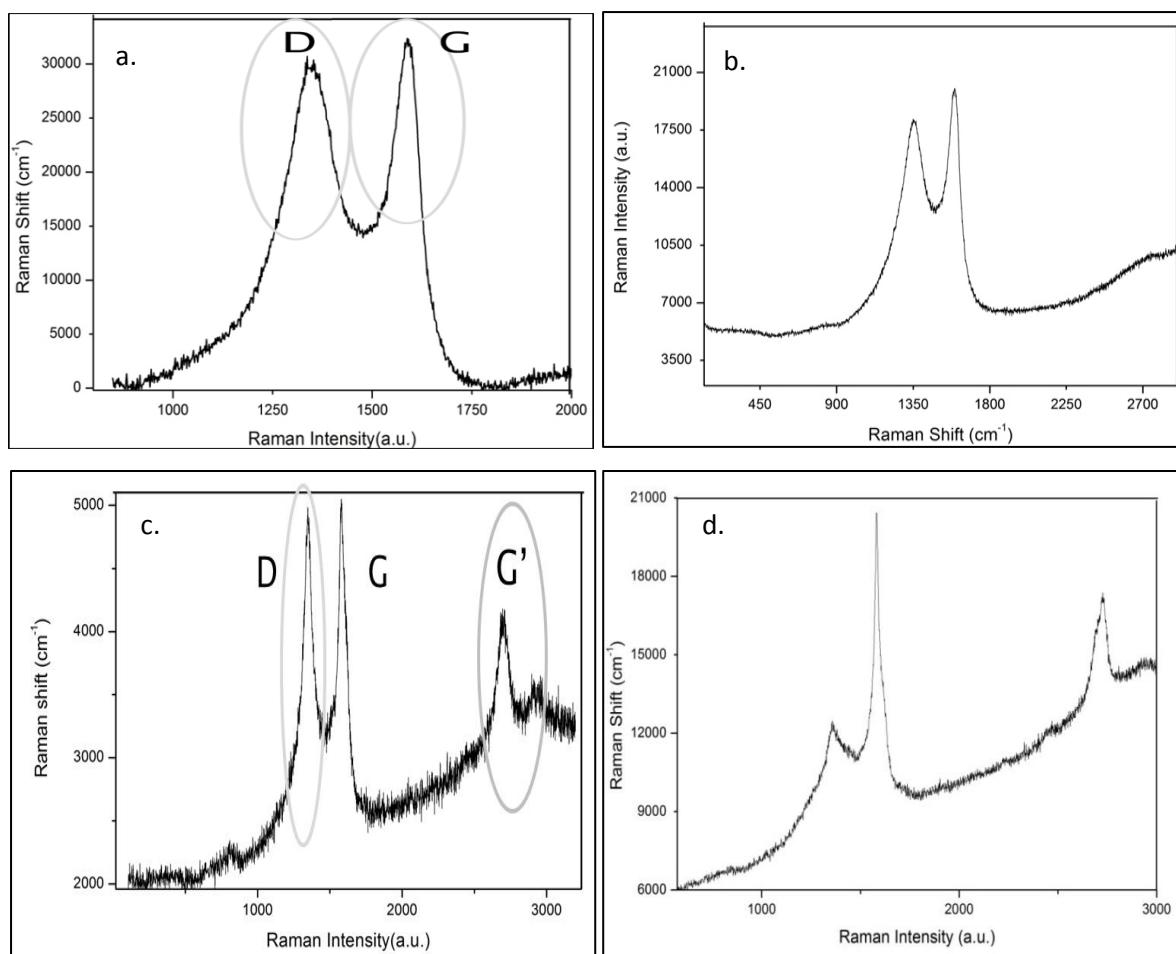


Figure 4.6 a) Soot; b) extracted soot; c) graphene nanoparticles grade C and d) grade M

Soot and extracted soot showed an intense D band and their ratio of D/G was higher than for the pure graphitic forms, as shown in table 4.2, indicating that there were far more defects in these than in the pure graphitic samples.

Table 4.2 D/G ratios of carbon samples for comparison of defects

Sl.No	Sample	D/G ratio
1	Soot	1.622
2	Extracted soot	1.845
3	Graphite-GT	1.561
4	Graphene nanoparticles-grade C	1.435
5	Graphene nanoparticles-grade M	1.573

There was a connection between the D/G ratio affecting the impurity and the activity during combustion. TGA analyses for the onset peak and final temperatures of

combustion were compared and this showed that the samples with a large D-band peak have a low combustion temperature and greater impurities as is the case for soot and extracted soot, shown in table 4.3 [11].

Table 4.3 Soot combustion activity for carbon samples

Sl.no	Catalyst	Onset temperature (T_{on}) (°C)	Extrapolated onset temperature (T_{eo}) (°C)	Peak temperature (T_p) (°C)	Final temperature (T_f) (°C)
1	GT-Graphite- DP255- UNTREATED	404.3	422.2	502.3	607.1
2	XGC 750 graphite	264.1	470.1	656.1	680
3	XGM5-graphite	321.1	544	693	720
4	Soot extract acetone	404.3	462.2	656.1	886
5	Soot ex-CRT	419.3	461.2	652.3	717.1

4.2.4 NMR

Soot was also analysed using a 600MHz NMR equipment in order to that to understand the nature of aromatics in their initial phase to their oxidation between 400-550°C. The spectra also showed the aliphatics present in soot and their oxidation as seen from figure 4.7. A large proportion of soot was made up of aliphatics (the concentrations were not quantified in this study) that tend to undergo oxidation to CO₂ at higher temperatures. The aromatics underwent oxidation in the temperature range 300-700°C, as was evident from the reduction in intensity of the signals, between 1-2ppm, with increase in temperature.

The spectrum in green, for the soot extracted in acetone and mixed with deuterated acetone, showed that the aromatics in the soot present on the soot were mainly desorbed around 300°C (figure 4.7) and were collected as products in acetone although a significantly large concentration remained on the surface of soot (figure 4.9). Over higher temperatures the concentration of aromatics on the surface gradually decreased, indicating their oxidation to CO₂, which is the primary product of soot oxidation.

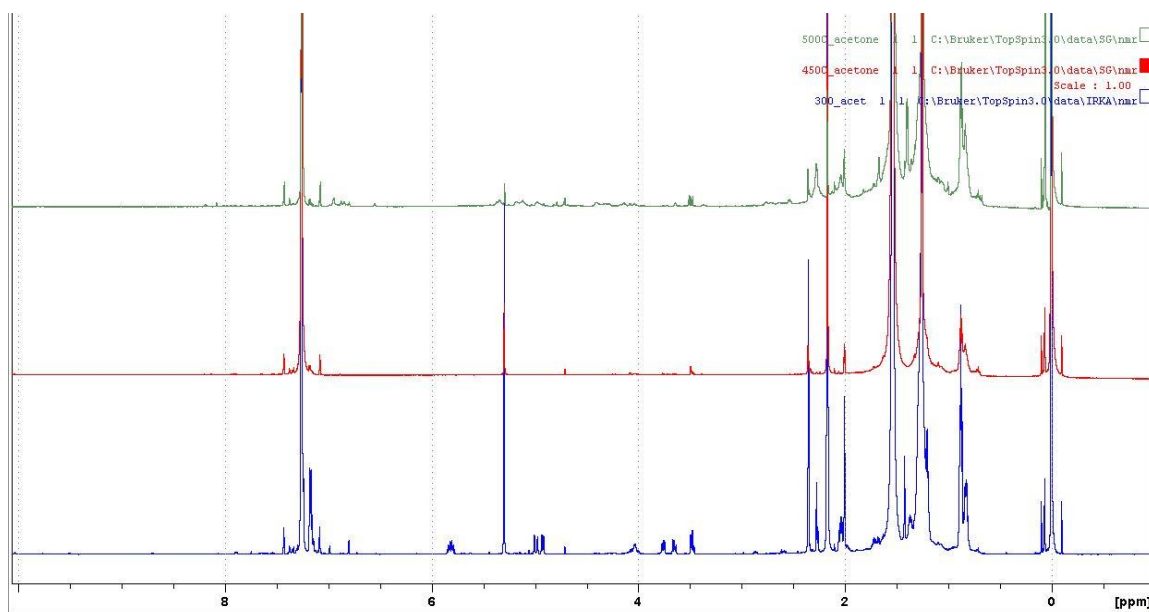


Figure 4.7 ¹H-NMR analysis of soot post oxidation at different temperatures-**Spectrum in blue**- Soot extraction in acetone-300°C, **spectrum in red**- Soot at 400°C-extracted in acetone, **spectrum in green**- Soot post reaction at 550°C-extracted in acetone

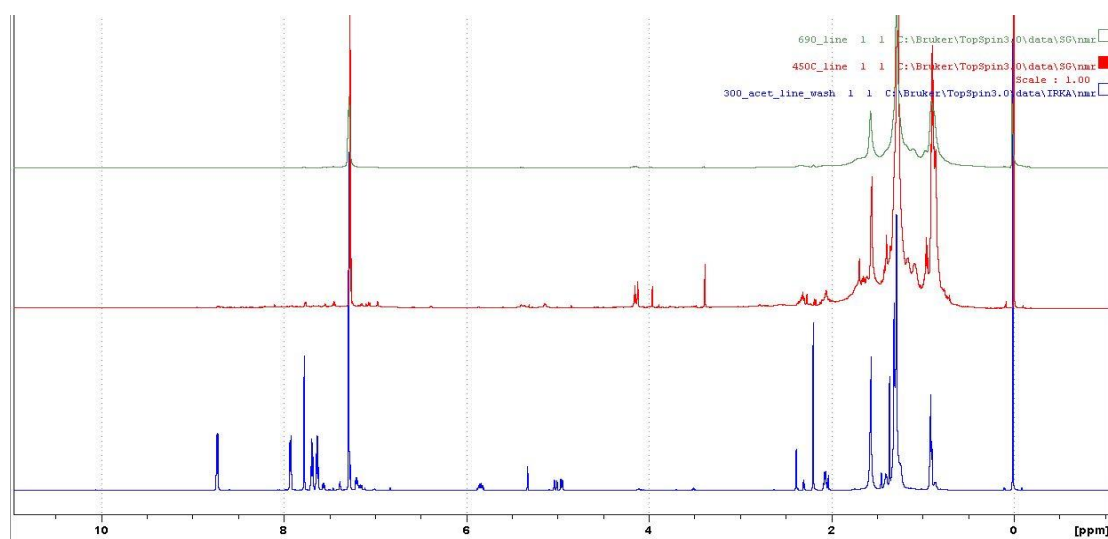


Figure 4.8 ¹H-NMR analysis of soot post oxidation at different temperatures-**Spectrum in blue**- Products condensed in line-300°C, **spectrum in red**- Products in line at 400°C-post reaction, **spectrum in green**- Products in line at 600°C

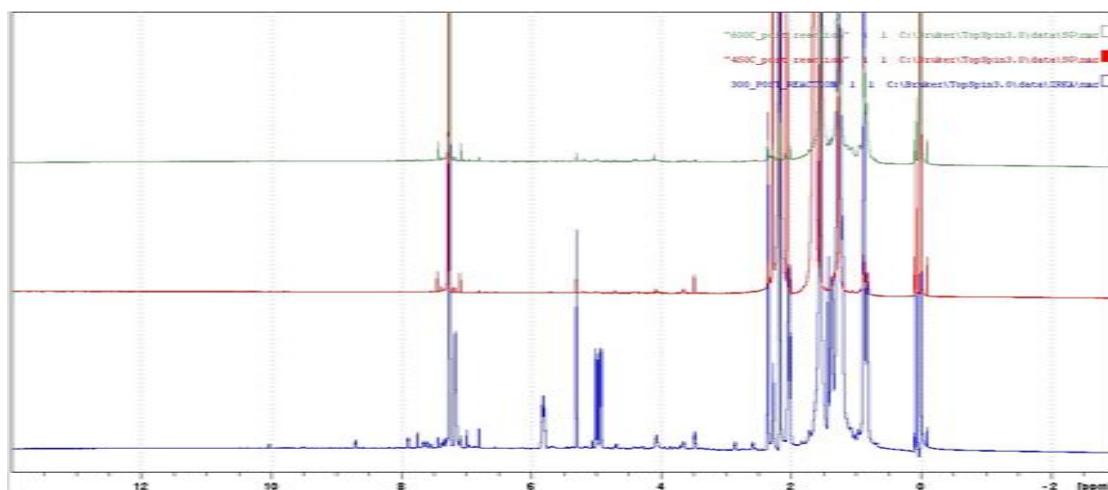


Figure 4.9 $^1\text{H-NMR}$ analysis of soot post oxidation at different temperatures- **Spectrum in blue**- Soot post reaction-300°C, **spectrum in red**- Soot at 400°C-post reaction, **spectrum in green**- Soot post reaction at 600°C

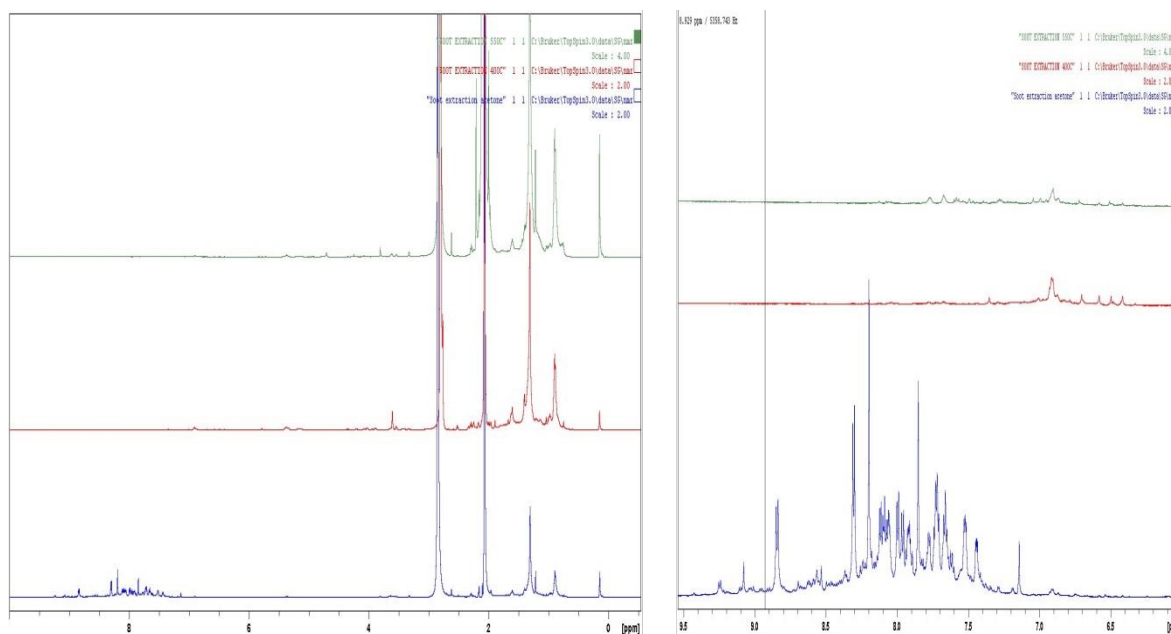


Figure 4.10 $^1\text{H-NMR}$ analysis of soot -**Spectrum in blue**- Soot prior to oxidation, **spectrum in red**- Soot at 400°C-post reaction, **spectrum in green**- Soot post reaction at 600°C

Figure 4.10a represents the soot before and after oxidation, indicating very distinctly the aromatic oxidation at higher temperatures which was visible in figure 4.10b and in an enlarged image in figure 4.10a. The different hydrogen present in the sample were the following: The main assigned groups were hydrogen on aromatic rings (H_α , 6.5 -9.0 ppm); hydrogen of $-\text{CH}$, $-\text{CH}_2$, $-\text{CH}_3$ groups on carbon atoms in β position aromatic rings (H_β , 1.0- 2.0 ppm); and methyl hydrogen on carbons γ , δ or higher

position to aromatic rings, as well as methyl hydrogen of alkanes, cyclo alkanes and naphthenic rings (H γ , 0.5-1.0 ppm). The products were seen to have significant aliphatics with predominance of methyl and methylene groups on β and γ positions of aromatic rings. It was important to observe that there was a significant fraction of hydrogen on the γ position at 0.864 ppm, which suggested the existence of large aliphatic chains or saturated rings joined to different types of aromatic ring, as suggested by Manoj *et al.* [12].

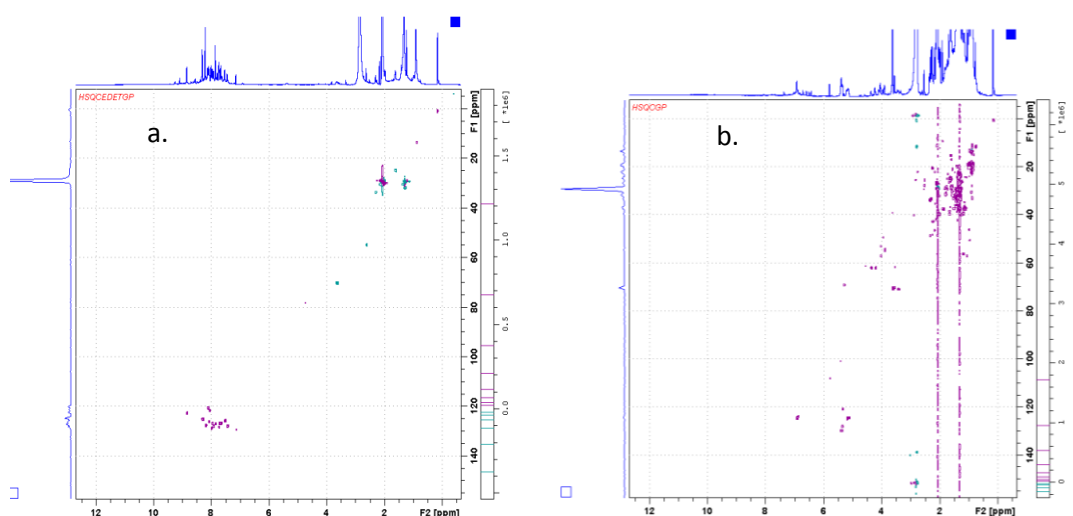


Figure 4.11 a) HSQC spectrum-Soot extraction in acetone-prior to oxidation; b) Soot post reaction at 400°C-extracted in acetone

Soot oxidation was analysed using the HSQC spectra which indicated that there was an increase in aliphatics during the oxidation. Figure 4.11a shows that soot was constituted of aromatics which broke down into smaller partially oxygenated species and then were converted to CO₂. The aliphatics concentrations tend to increase at higher temperatures as seen in figure 4.11b.

4.2.5 IR

The most intensive absorption features could be attributed to oxygenated functionalities, such as -C-O, aromatic and carboxylic groups. Aromatic -C-H bonds were observed at 3050 cm⁻¹ and the C=O from the carboxylic and aromatic species was seen at 1720 and 1600 cm⁻¹.

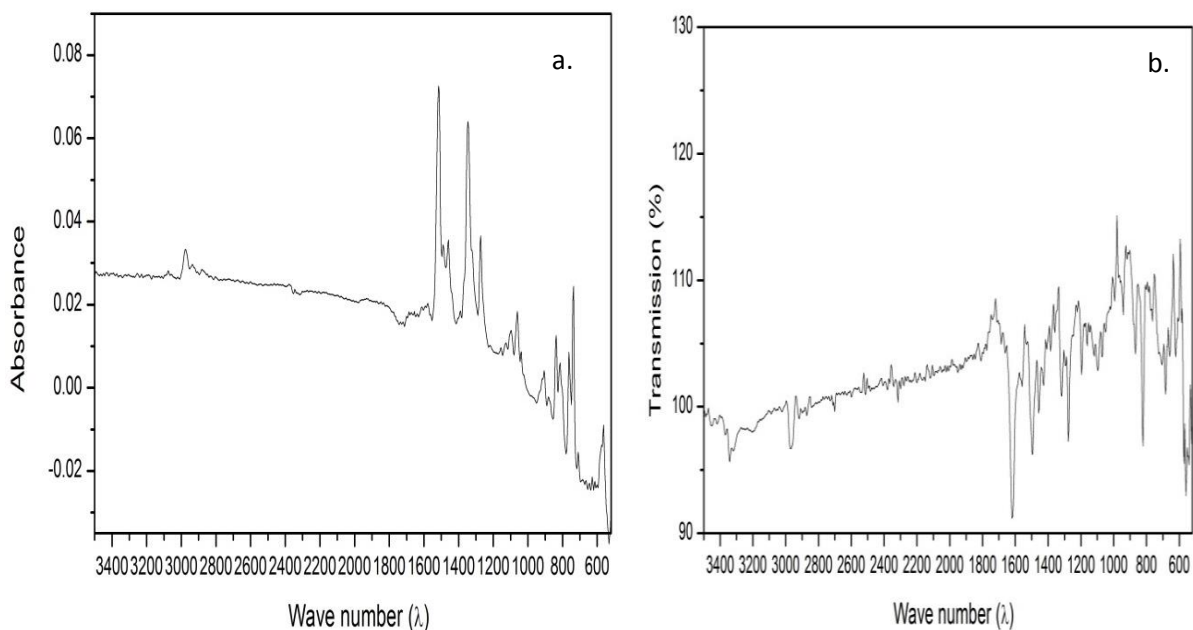


Figure 4.12 IR spectra of unreacted soot- a) absorbance mode; b) transmission mode

There was a broad combination of peaks between $800\text{-}1600\text{cm}^{-1}$ which could be from the reaction products, with trace gases produced during aerosol formation along the exhaust. This was a result of the incomplete hydrocarbon combustion. This was attributed to the carbon skeleton i.e. the -C-C- and -C=C- groups. The peaks at 880 , 840 , and 760 cm^{-1} were characteristic of substituted aromatics, as seen in the figure 4.12a and b [12, 13].

4.2.6 Porosimetry

Diesel soot was analysed for its surface area and pore structure using the Autosorb/porosimeter as described in chapter 2. This showed that the soot had a relatively high surface area ($75\text{m}^2/\text{g}$). The particles had a pore size distributed in the mesoporous range of $2\text{-}5\text{ nm}$, as seen in figure 4.13. Some pores were between $5\text{-}10\text{nm}$. The average pore size was 37.49\AA . The soot consisted of mesoporous particles that aggregate together. The optimised catalyst in use had a very low surface area of $3\text{m}^2/\text{g}$. The catalyst helped in oxidizing the soot as the contact between the catalyst and soot was vital in governing the rate and completion of combustion. The oxidation occurred on the interface of the catalyst and soot as described in chapter 3. The adsorption-desorption isotherms indicated the adsorption and desorption of N_2 onto the pore sites,

that helped to calculate the pore size distribution, pore volume and average pore diameter (table 4.4).

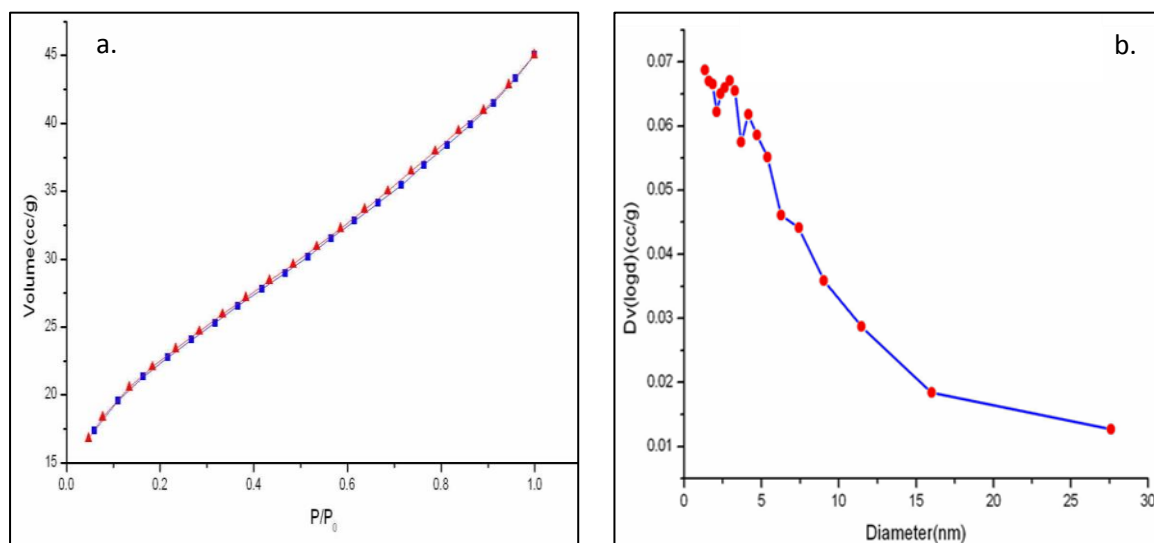


Figure 4.13 Adsorption-desorption isotherm; b) pore size distribution

Table 4.4 indicates the physical properties of soot, Norit and the most efficient catalyst for soot oxidation. This gave an idea of the pore sizes of soot and the catalyst. The catalyst pores were much smaller compared to the soot particles. Thus sometimes this could lead to the plugging of the pores by these fine particles. Despite this effect, the catalyst: soot contact was vital in determining the kinetics of the reaction.

Table 4.4 Physical properties of soot, model soot and catalyst

Sl.No	Sample	Average Pore size(Å)	Total Pore volume (cc/g)	Surface area (m ² /g)
1.	Soot	37.49	0.08	74.5
2.	Norit	24.7 2	0.083	134.4
3.	Catalyst-2%Ag10%K/CeO ₂ - ZrO ₂ -Al ₂ O ₃	58.48	0.004	3

4.3 Rate of uncatalysed soot oxidation in the presence of synthetic air flow

Soot oxidation in the absence of the catalyst was studied under an oxidative atmosphere of synthetic air (20%O₂/He) from 30-700°C at 5°Cmin⁻¹ and the production of CO₂ was monitored every three minutes by gas chromatography (GC). The GC was

calibrated for CO₂ and the amount of CO₂ produced from the soot oxidation was quantified using a response factor derived from the calibration. Calculations from the area counts have been described in chapter 2. The rates of the CO₂ formation (CO₂ molar flow rate) were also calculated as described in the appendix. The rates were calculated taking into account the mmols of CO₂ produced along the entire temperature range of carbonaceous soot oxidation.

Figure 4.14 shows the rate of the uncatalysed soot oxidation in mmols of CO₂ produced. The reaction rate started off very slowly and then picked up at around 450°C, corresponding to the peak temperature as shown by the TGA data for soot oxidation. The rate reached its maximum around 600°C. The production of CO₂ ceased at around 690°C which indicated the completion of oxidation. The concentration of CO₂ (in ppm) as a function of temperature was also shown in figure 4.14b. The total amount of CO₂ produced was also calculated in mmols, between 300-700°C and was used to calculate the conversion of initial amount of carbon in soot to CO₂ (section 4.62)

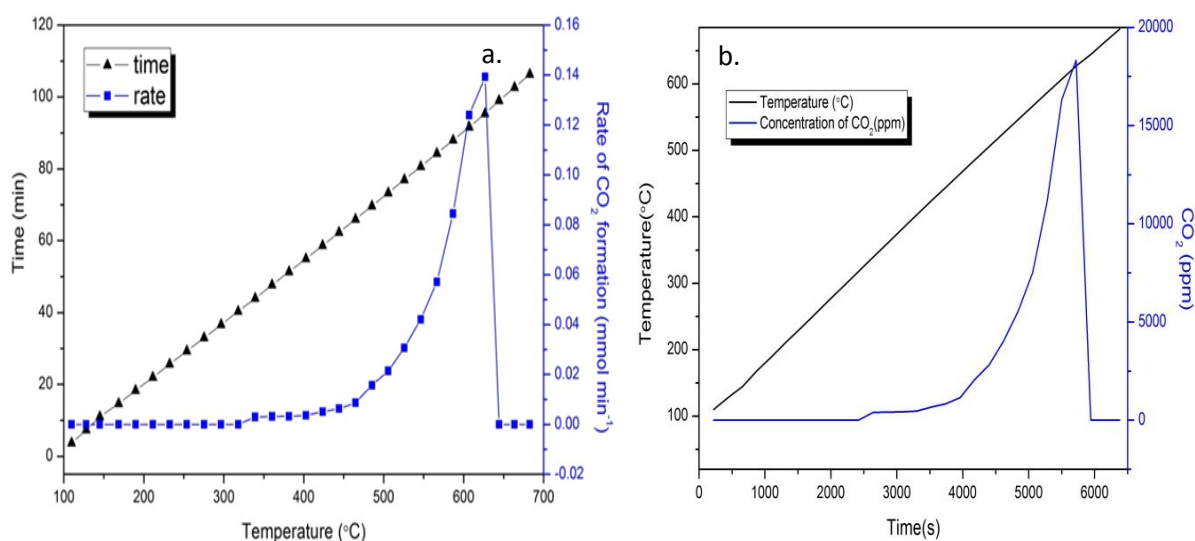


Figure 4.14 Rate of uncatalysed soot oxidation

Experimental conditions-50ml min⁻¹ of 20% O₂/He flow, uncatalysed reaction- soot mass- 0.0254g

4.3.1 Varying O₂/He flow rate

The flow rates of O₂/He for the above analysis was fixed at 50 ml min⁻¹ but in order to understand the effect of flow rate, various analyses were carried out between low flow rates of 50ml min⁻¹ (10ml O₂ : 40 ml He) and highest of 500 ml min⁻¹ O₂/He. This was to understand the reactivity of soot to the oxidative atmosphere. Figure 4.15a

showed the rate of soot oxidation, as a function of flow rate between 500>200>50 ml min⁻¹. This showed that the higher the flow rate of O₂, the faster was the rate of the oxidation and increased production of CO₂. The GHSV were kept constant throughout all analyses at 30,000h⁻¹. Thus the rate increased and a considerable increase in the CO₂ concentration was also detected from figure 4.15b. The concentration of CO₂ produced was seen to reach a maximum of 27500ppm when the reaction was maximum between 580-600°C. The temperatures for complete oxidation of uncatalysed soot were higher compared to catalysed soot oxidation, as explained previously from TGA results in chapter 3.

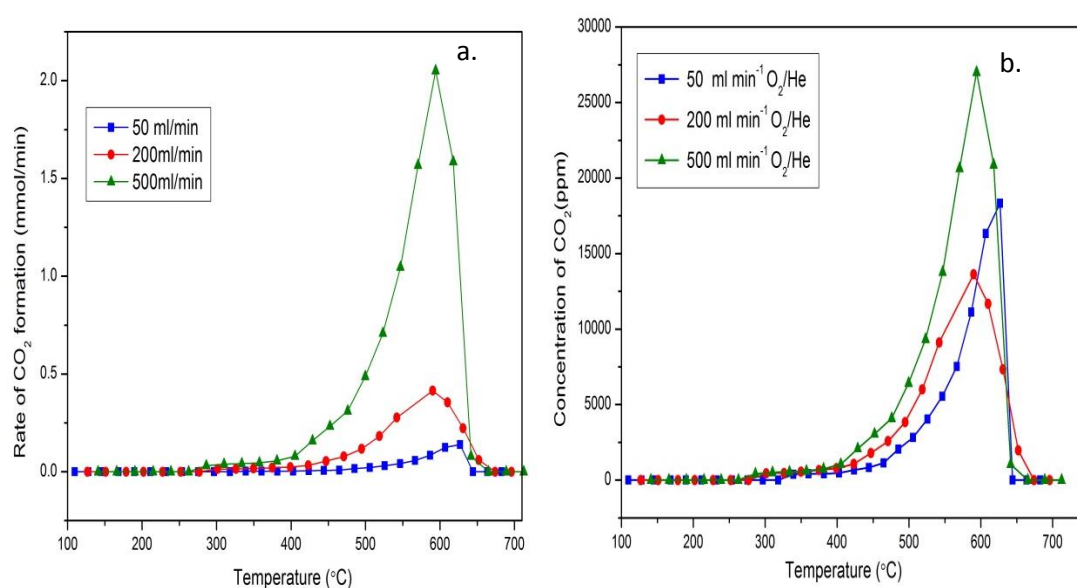


Figure 4.15 Varying the flow rate of O₂/He - a) rate of the reaction; b) concentration of CO₂

The oxidation occurred most rapidly in the presence of an excess flow of 500ml min⁻¹ O₂/He feed with the oxidation complete in 80mins, indicating a relatively longer span of time as opposed to the catalysed oxidation (60mins). The amount of CO₂ produced from the 50ml min⁻¹ O₂/He feed as compared to the 200ml min⁻¹ feed was lower and took longer, for the oxidation to occur as was observed from both the figures 4.15a,b.

4.3.2 Varying O₂/He concentrations

The concentrations of O₂/He were varied to understand the effect of an oxidative environment in more detail. The diesel exhaust was seen to have a continual oxygen rich feed. Thus understanding the kinetics under these conditions was essential for a better understanding of the mechanism of soot oxidation. Figure 4.16a represented the rate of CO₂ formation on varying the O₂ content of the feed. Thus the O₂ content in the

feed or in the exhaust is an important criteria in determining the rate of soot oxidation. These tests were carried out under a 50ml min^{-1} flow of O_2/He for the ease of understanding. The extremely low (10% O_2) and extremely high O_2 feed (100% O_2) were not suitable in producing large concentrations CO_2 from the soot as the low concentration led to a rapid rate but produced CO_2 over a higher temperature range. The reaction started at 460°C and produced less CO_2 over the temperature range and took longer (90mins) for complete oxidation.

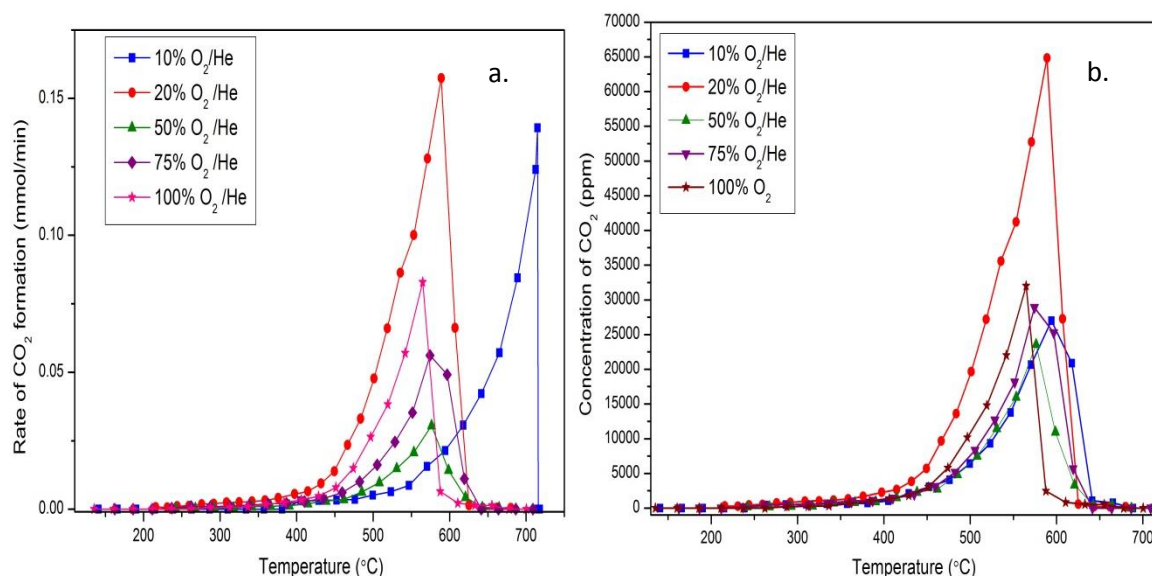


Figure 4.16 Varying the concentration of O_2/He - a) rate of the reaction; b) concentration of CO_2

The ideal conditions lie between 50-75% O_2/He that provided considerable amounts of CO_2 observed from figure 4.16b in shorter span of time (65-70min for 50% O_2/He and 75 mins for 75% O_2/He from Figure 4.3a, represented by green and purple lines). 20% O_2/He helps produce maximum amounts of CO_2 as seen from the red line but takes longest span of time to produce it, indicating the slowest rate. Thus it is necessary to understand the effect of oxygen concentration on the rate of the reaction to improve the understanding of the mechanism, in the presence and absence of a catalyst.

4.4 Study on the rate of catalysed soot oxidation in the presence of synthetic air flow

The catalyst used for this purpose was the catalyst that yielded the best results for soot oxidation under the TGA, which was the 2%Ag-10%K/CZA catalyst with onset temperatures of 320°C and final temperature of combustion at around 550°C .

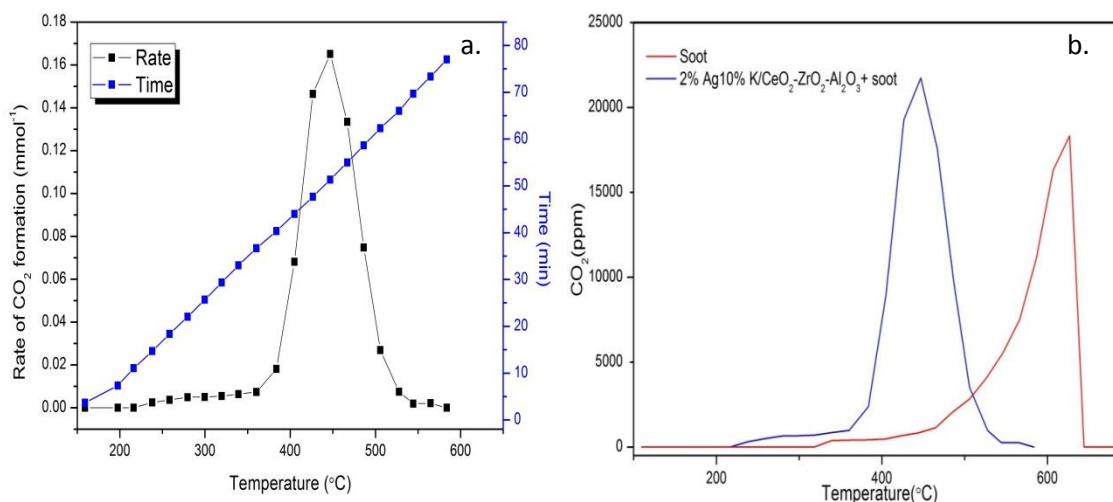


Figure 4.17 Rate of catalysed soot oxidation

Experimental conditions-50ml min⁻¹ of 20% O₂/He flow, uncatyalsed reaction- soot mass-0.0254g;

Catalysed reaction-Catalyst mass-0.0091g; soot mass-0.0023g, GHSV-30,000h⁻¹

On comparing figure 4.14a and 4.17a, in presence of catalyst, the oxidation temperatures was drastically reduced. The total concentration of CO₂ produced was higher for catalysed soot compared to the uncatyalsed oxidation.

4.4.1 Varying O₂/He flow rates

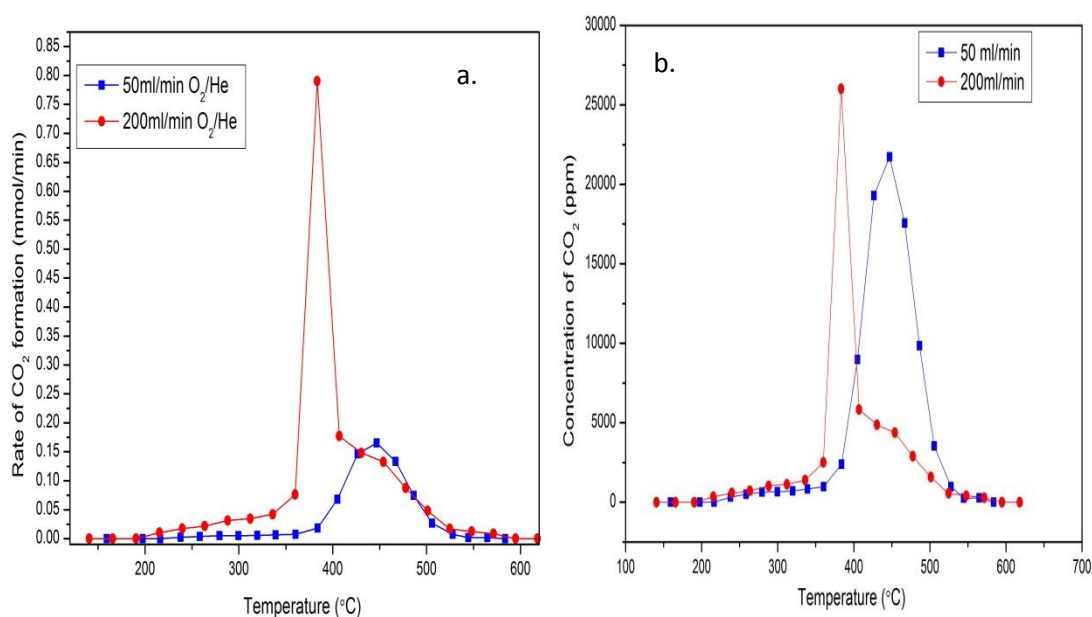


Figure 4.18 Varying the flow rate of 20% O₂/He - a)rate of the reaction; b)concentration of CO₂

Under higher flow rate of O₂/He(200ml min⁻¹), the rate of catalysed soot oxidation was rapid, with a sharp increase touching its maximum at 42mins and 390°C. The oxidation was complete by 520°C. The amount of soot converted to CO₂ was higher at a higher flow of 200ml min⁻¹ of O₂ as seen in figure 4.18a,b. The rate of CO₂ formation

was slower under 50ml/min as compared to that observed in the case of 200ml min⁻¹ O₂/He flow (figure 4.18a) indicating that the increase in oxidant in the feed enhances the rate of oxidation. The amount of CO₂ produced is also greater under higher oxidant flow.

4.4.2 Variation of O₂/He concentration

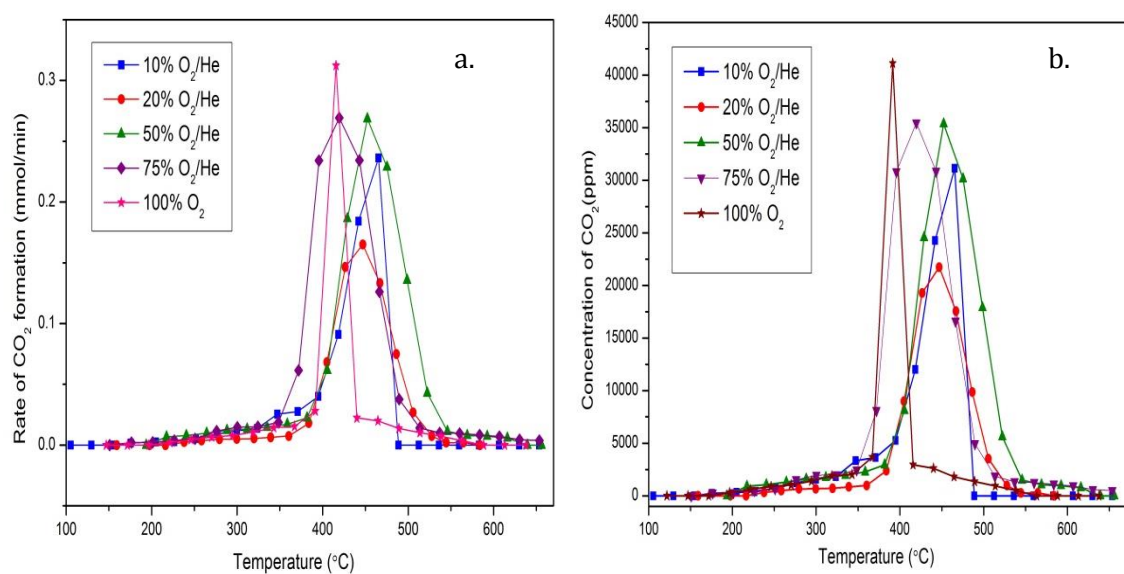


Figure 4.19 Varying the concentration of O₂/He - a) rate of the reaction; b) concentration of CO₂

The variation of the O₂ concentration in the feed showed that the rate of the reaction was maximum under pure O₂ flow (100%) but produced least amount of CO₂ (figure 4.19). This occurred at an increased rate and at lower temperatures (390-450°C) as compared to the other concentrations. Soot was oxidised ideally under a flow of 50-75% O₂/He, where the rate was relatively high and the amount of CO₂ produced was also higher (between 350-550°C) compared to that under the other concentrations. The oxidation under 10-20%O₂ (with less oxidant in the feed) did not improve the rate of oxidation and produced relatively low concentrations of CO₂ as observed from the figures above.

4.4.3 Soot oxidation- N₂ atmosphere-rate of reaction

This analysis was carried out to understand the contribution of lattice oxygen stored in the catalyst towards soot oxidation, in the absence of an oxidative flow. Under N₂ atmosphere, from figure 4.20a, we could observe that the rate of soot oxidation

followed a similar pattern but more amount of CO₂ was produced in the presence of the catalyst as seen in figure 4.20b. The catalyst is capable of providing the O₂ stored in its lattice for soot oxidation at lower temperatures despite the absence of O₂ in the feed.

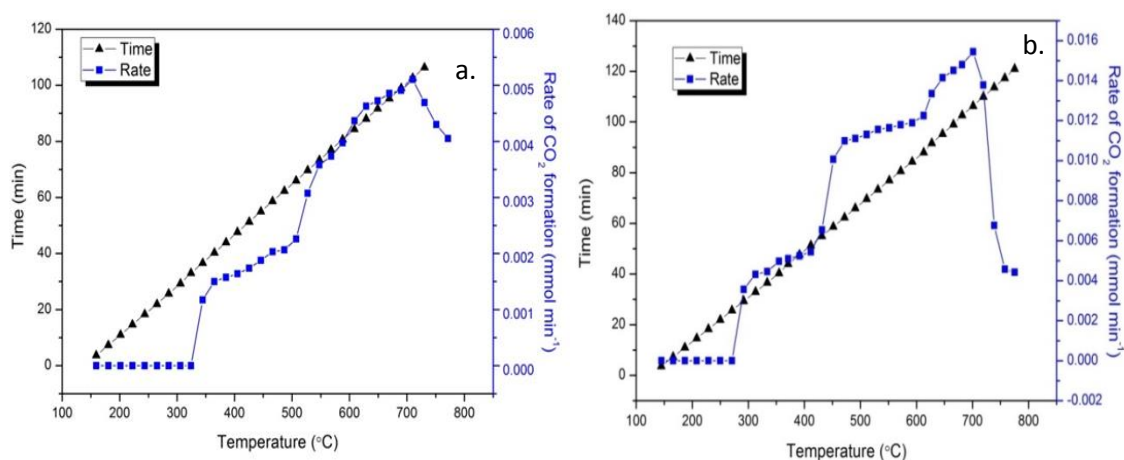


Figure 4.20 Soot oxidation under N₂ flow- a) uncatalysed; b) catalysed

Experimental conditions-50ml min⁻¹ of 100% N₂ flow, uncatalysed reaction- soot mass- 0.0254g;

Catalysed reaction-Catalyst mass-0.0091g; soot mass-0.0023g, GHSV-30,000h⁻¹

4.4.4 Catalysed soot oxidation- effect of catalyst-soot contact

The rates of the reaction showed that under loose contact conditions, the amount of CO₂ produced was more as compared to that under tight contact conditions but this occurred at a slower rate and took longer for complete combustion of the soot (80min- figure 4.21a). The temperature range for the loose contact run was between 350°C and 520°C while that for the tight contact condition was between 420°C and 490°C (figure 4.21b). This could be compared to the TGA results obtained showing similar peak and final temperatures. Total concentration of CO₂ produced under loose contact was 0.67mmol/min while that under tight contact was 6.57mmol/min.

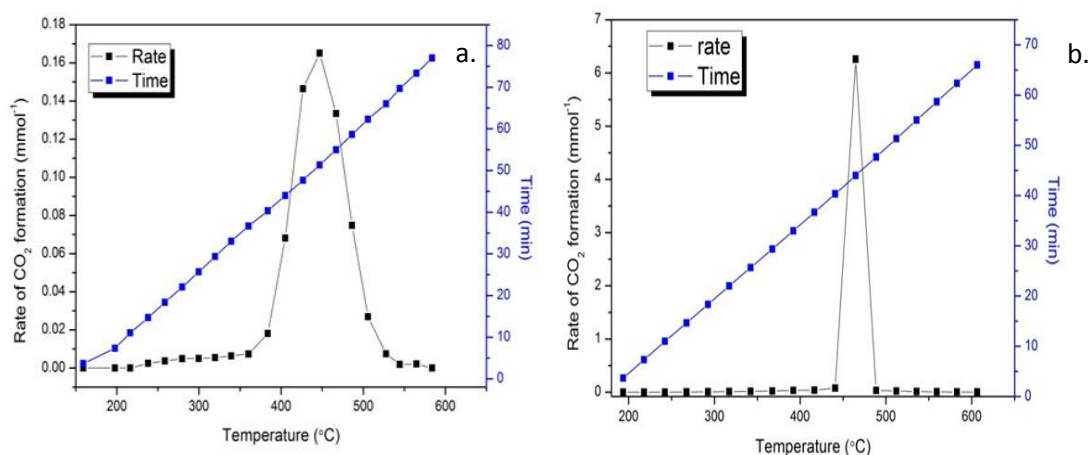


Figure 4.21 Effect of contact: a) loose contact; b) tight contact

Experimental conditions-50ml min⁻¹ of 20% O₂/He flow, Catalyst mass-0.0091g; soot mass-0.0023g, GHSV-30,000h⁻¹

4.4.5 In-situ XRD studies on Ag-K/CZA+soot-O₂/He

In-situ XRD analyses were carried out on a catalyst (2%Ag-10%K/CZA): soot mixture in order to understand the effect of soot oxidation on the catalyst structure. These analyses were carried out under a flow of O₂/He where the catalyst and soot were mixed together in a loose contact condition allowing changes in crystal structure of the catalyst to be monitored as a function of temperature [14]. Figure 4.22 shows the diffractograms for temperatures from 150°C (light green line) to 700°C (pink line). Increased crystallinity was not observed until 600°C, when the catalyst showed intense peaks owing to sintering at such high temperatures. This is very evident from the shift in 2θ angles for this catalyst at 2θ=28.1, 33, 47.5 and 57.5° (owing to the cubic crystal structure of CZA) to lower values and also shift in peaks for the K₂CO₃ at 37.5° and peaks for Ag⁰ at 2θ=43°, thus causing a reduction in peak width. Therefore, from these results it can be concluded that, on the time scale of these experiments, this catalyst resisted sintering until high temperatures of around 500°C. We assume that, since this catalyst combusted the soot by around 600°C, it would not be susceptible to this kind of sintering. However the temperature rise due to the exothermic soot combustion reaction could possibly have led to sintering of the catalyst at high temperatures. Repeated analyses of the catalyst still shows good activity for the Ag-K/CZA catalyst calcined at 500°C, however sintering effect was observed when the catalyst was calcined at 750°C as seen in chapter 3.

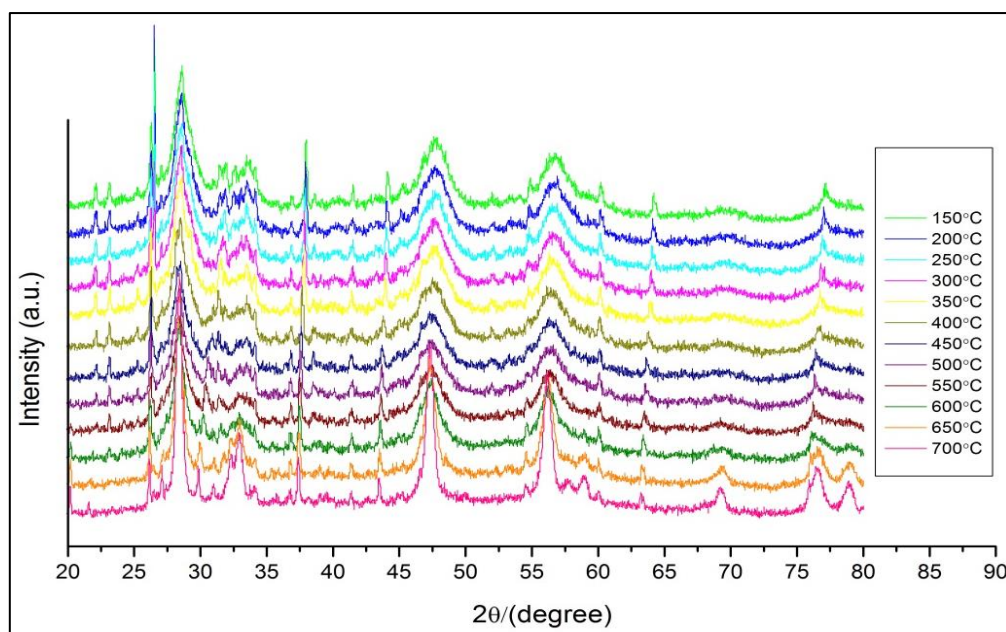


Figure. 4.22 *in-situ* XRD studies on Ag-K/CZA catalyst with soot under O₂/He

4.5 Model soot oxidation

Soot oxidation could be better understood using more pure forms of carbon such as graphite and charcoal that did not contain any adsorbed hydrocarbons. Generally these forms had very high temperatures for oxidation (400-850°C). So they were ideal models to optimise catalysed oxidation of carbonaceous particles.

4.5.1 Norit charcoal-O₂/He

Norit activated charcoal was used to understand the soot oxidation process as a model for this reaction. The temperature of oxidation revealed that the combustion of Norit took place at a higher temperature than diesel soot, at around 600°C. The amount of CO₂ produced as a function of time and temperature was shown in figure 4.23 b where it could be seen that the rate of oxidation was slow until 500°C beyond which the rate rapidly increased after one hour of exposure to O₂/He (50ml/min). The rate reached a maximum at 580°C, and beyond this the oxidation was complete by 625°C. The amount of CO₂ produced (mmols) is indicated in figure 4.23a.

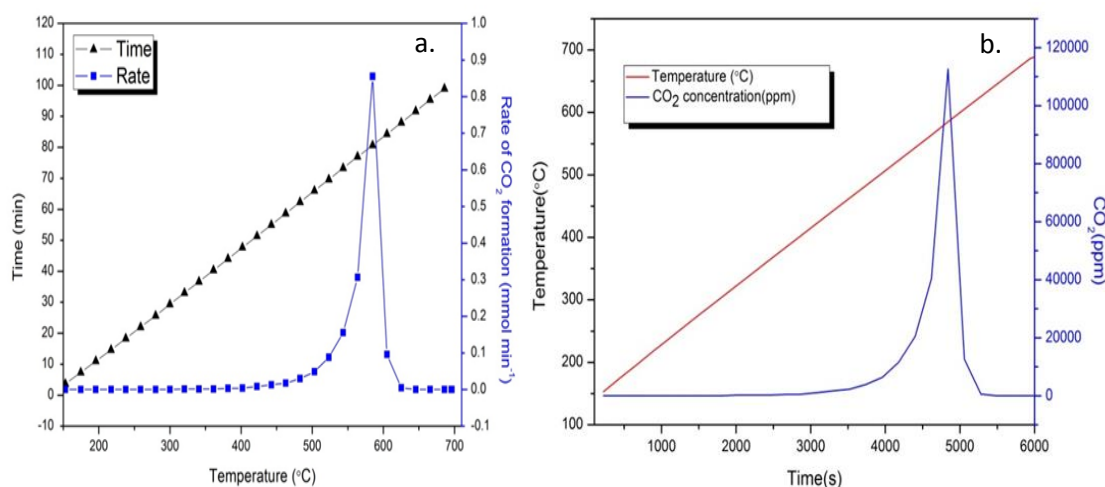


Figure 4.23 Norit oxidation- a) rate; b) Quantification of CO₂

Experimental conditions-50ml min⁻¹ of 20% O₂/He flow, GHSV-30,000h⁻¹

4.5.2 Graphite - O₂/He

Graphite was used to understand the combustion of soot with respect to the carbon content in it. Graphite chosen for this study was free of PAHs and this was used to understand the contribution of CO₂ from a carbon source similar to the carbonaceous soot oxidation. The graphite was also mixed with phenanthrene in the proportion that is typically present in soot to understand the contribution of phenanthrene towards CO₂ production as discussed in section 4.5.3.

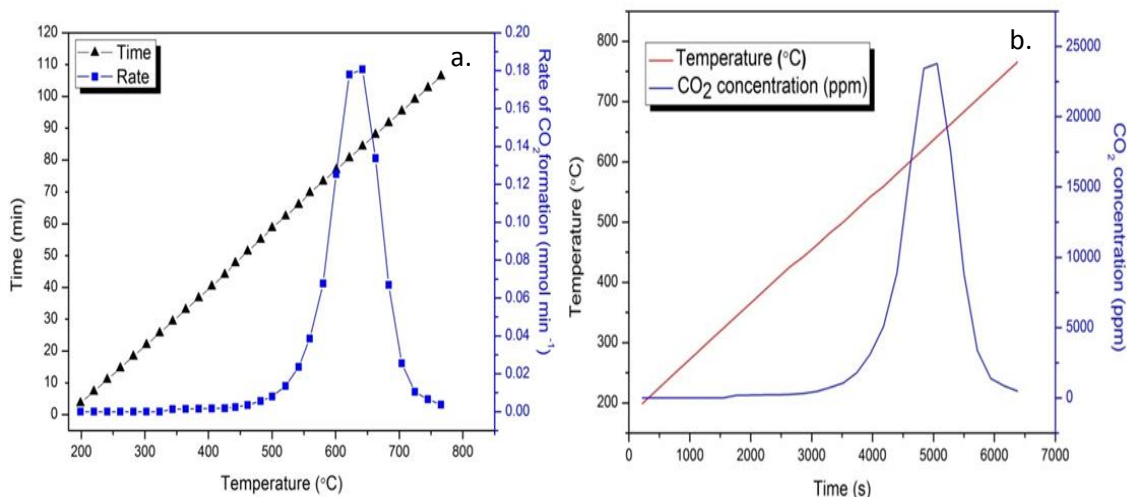


Figure 4.24 Graphite oxidation- a) rate; b) Quantification of CO₂

Figure 4.24a shows the rate of CO₂ production from graphite which suggested that it combusted at very high temperatures (800°C), with an increase in rate of the reaction around 520°C. It increased rapidly thereafter until 680°C, beyond which the rate began to decrease and the combustion was complete by 800°C. The amount of CO₂ produced as a function of time and temperature is indicated in figure 4.24b. This could be compared to the soot oxidation temperatures, although the final temperature of combustion was slightly higher than that of soot.

4.5.3 Phenanthrene-graphite model- O₂/He

The concentration of phenanthrene in diesel soot was studied using HPLC and has been described in detail in chapter 5. In order to investigate the behaviour of three ring aromatics, which appear to be the greatest challenge to oxidise, a 'simplified soot' mixture consisting of phenanthrene mixed with graphite was prepared. The composition of the mixture, 0.09g phenanthrene in 1 g graphite, was chosen to reflect the average composition of CRT soot, based on the Soxhlet extraction process.

4.5.3.1 Contributions of graphite, phenanthrene towards CO₂ production in the presence and absence of catalysts

The phenanthrene-graphite model described above was studied to understand its contribution towards the oxidation process. Thus individual concentrations of phenanthrene, graphite and the mixture of the two were subjected to oxidation under synthetic air feed. The analysis was repeated three times to obtain the contribution of

CO₂ as an average of the three runs. This oxidation was considered similar to the carbonaceous soot in the absence of the catalyst. Figure 4.25a shows the three runs on graphite carried out at three different instances. The amount of CO₂ produced in mmols has been summed up and are presented in table 4.5. The temperatures for the oxidation of the graphite were lower than that for the phenanthrene-graphite mixture indicating that PAHs are more difficult to combust.

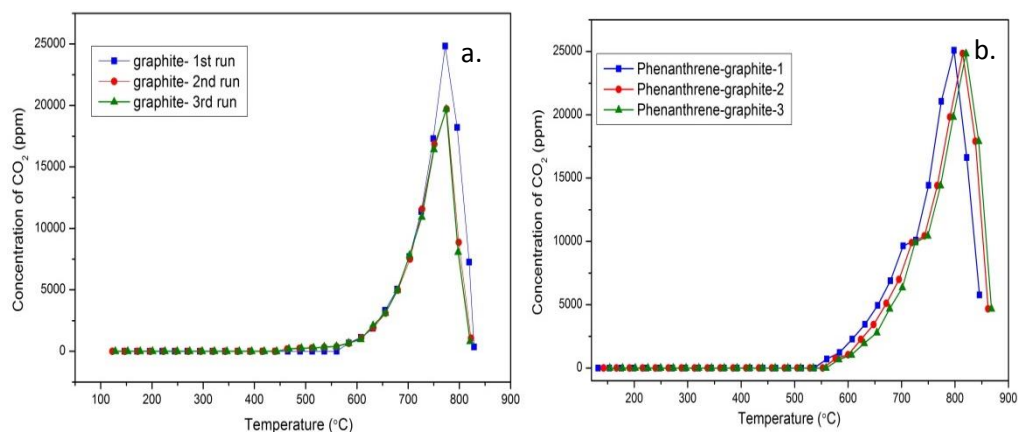


Figure 4.25 Quantification of CO₂-a) graphite; b)phenanthrene-graphite

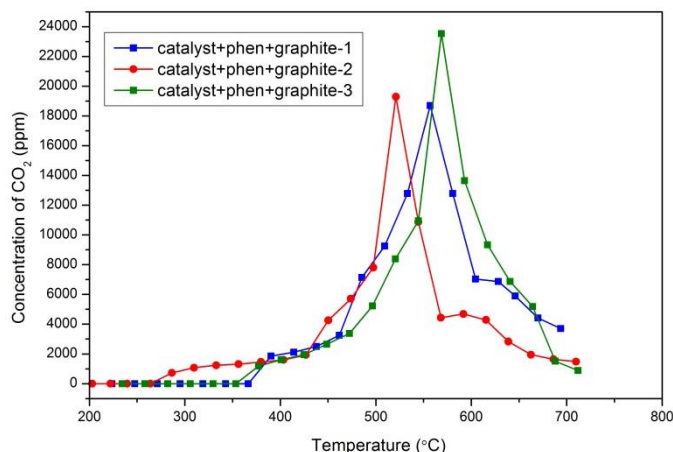


Figure 4.26 Catalysed phenanthrene-graphite oxidation- Quantification of CO₂

The rates of oxidation were quite similar in both cases with combustion, starting at 550°C and then rapidly increasing to a maximum at 750°C and then completion by 810°C for graphite and 870°C for phenanthrene-graphite mixture. In the presence of the catalyst, these temperatures dropped down between 350-700°C as indicated in figure 4.26. These tests were repeated thrice for reproducibility to yield the CO₂ production in mmols/min as shown in table 4.5.

Table 4.5 Quantification of CO₂ under catalysed and uncatalysed conditions using graphite and phenanthrene-graphite

Sl.No	Sample	Total amount of CO ₂ produced (mmol)		
1	Graphite	3.01	2.39	2.33
2	Phenanthrene-graphite	3.71	3.69	3.62
3	Catalyst+phenanthrene-graphite	2.98	2.60	2.92
4	Catalyst +graphite	3.50	3.19	3.24

Table 4.5 shows the contributions of graphite and phenanthrene-graphite in the presence and absence of catalyst towards soot oxidation. The total number of milli moles of CO₂ produced was higher in the presence of the catalyst for pure graphite oxidation. The catalyst helped to oxidize phenanthrene to CO₂ to a large extent as mentioned in chapter 5 (as seen in figure 4.26). The contribution of phenanthrene towards CO₂ yields was calculated theoretically based on the initial amounts used in the reaction. This has been described in detail below:

0.09g of phenanthrene was mixed with 1g of graphite (as is present in soot).

i.e. 90 mg of phenanthrene in 1000 mg, thus 2.287 mg was present in 25mg of the mixture (0.0254g was used for the analyses of soot/graphite/phenanthrene-graphite oxidation). This 2.286mg of phenanthrene is equivalent to 1.284×10^{-5} mol.

If $1 \text{ mol C}_{14}\text{H}_{10} + \text{O}_2 \longrightarrow 14 \text{ moles of CO}_2$,

Then, 1.284×10^{-5} mol gives $1.79710^{-4} \text{ mol} \sim \mathbf{0.179 \text{ mmol CO}_2}$. This was the contribution of phenanthrene towards CO₂ production.

From the analyses above it can be seen that oxidation of graphite alone gives an average of *2.58 mmols* of CO₂ and phenanthrene with graphite oxidation resulted in production of *3.67mmols* (average from table 4.5.) Thus subtracting these two values the contribution of phenanthrene towards CO₂ can be calculated and it is equal to 1.09mmols.

From the results, it was seen that a significant proportion of the phenanthrene did not get oxidized to CO₂ but was desorbed off the surface of the soot as phenanthrene. These desorbed concentrations accounted for the difference in theoretical and experimental contributions of phenanthrene. The desorption data is given in chapter 5.

4.6 Testing using synthetic exhaust mix

These tests were carried out to quantify the two primary products of carbonaceous soot oxidation-CO₂ and CO under a synthetic diesel exhaust gas.

4.6.1 Uncatalysed soot oxidation- exhaust gas mix-with 300 ppm NO

The soot oxidation was carried out in a reactor with an FTIR gas analyser as described in chapter 2. The synthetic diesel exhaust feed consisted of 230ppm CO, 100ppm propane, 300ppm propene, 9% O₂ with N₂ as balance

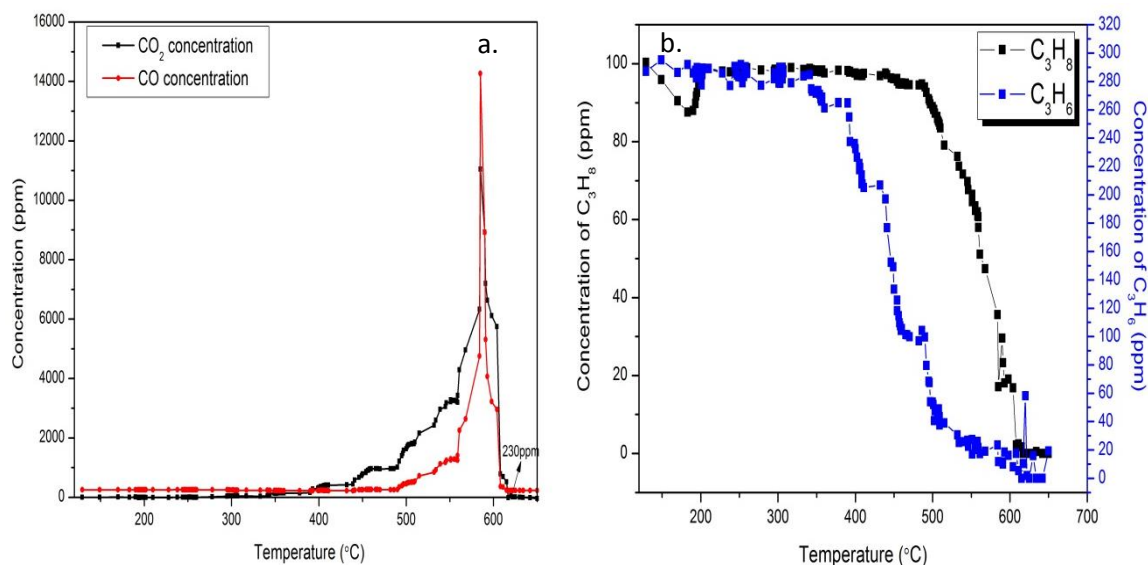


Figure 4.27 a) Quantification of CO₂ and CO; b) Quantification of C₃H₆, C₃H₈-uncatalysed soot oxidation

The CO₂ yields were shown in Figure 4.27a. These indicated that there was a sharp increase in CO₂ production starting at approximately 380°C, reaching a peak at approximately 520°C and then decreased to 620°C, when the combustion was complete. This was in close agreement with the results obtained from TGA analysis. FTIR analyses also helped to obtain the concentration of CO produced during soot oxidation as another important primary product of combustion. The figure showed that the production of CO began at temperatures higher than that for CO₂ formation under this exhaust gas feed. The production of CO started at 500°C, gradually increased until about 550°C. The rate rapidly increased soon after, reaching a maximum at 580°C. The production of CO then decreased between 580-600°C, when the oxidation is nearing completion. The initial feed of CO (130ppm) was maintained until the soot combustion began to contribute towards its increase at 500°C.

The propane (black line-figure 4.27b) in the feed could also undergo oxidation to form CO₂, which is the most probable oxidation product of propane combustion, thus

contributing to the CO₂ yield. The initial concentration of the propane (100ppm), from the feed, remained constant until 420°C, but then gradually started to get oxidized beyond this temperature and was completely oxidized to CO₂ by 600°C. This showed a significant drop in the concentration of the feed indicating its oxidation during this temperature range, thus contributing to the CO₂ yield. Propene was converted to CO₂ between 550-600°C.

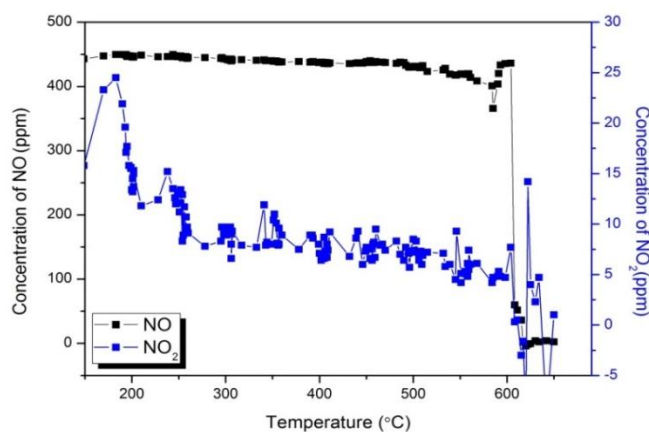


Figure 4.28 Quantification of NO and NO₂ –uncatalysed soot oxidation

In the presence of NO in the feed, at the start of the reaction, at around 200°C, a very small amount of NO was converted to NO₂ (blue line in figure 4.28 shown as an increase in concentration of NO₂), but as the reaction progresses the concentration of NO remained constant until temperatures of 650°C. It remained unreacted and the concentration of NO₂ fell to almost nil. In the absence of the catalyst the NO is incapable of getting oxidized to NO₂, which would help increase the rate of oxidation.

4.6.2 Combustion of soot to CO₂ - Mass balance

The conversion of the total carbon in the soot to CO₂ was calculated from its initial amount obtained from C, H, N, S analyses on soot. This helped to understand the contribution of the solid elemental carbon in the soot towards CO₂ formation as well as an indication of the contribution from the PAHs adsorbed on the surface of the soot. During the process of soot oxidation, desorption and oxidation of these PAHs could occur (as described in detail in chapter 5) alongside the oxidation of the elemental carbon. The calculations were as shown below:

Total moles of CO₂ produced from soot oxidation (uncatalysed) = 0.5262*10⁻³mol.

1 mol =12g of C,

$0.5262 \times 10^{-3} \text{ mol} = 0.5262 \times 10^{-3} \times 12 = 0.00631 \text{ g of C} \sim \mathbf{6.31 \text{ mg}}$

Amount of soot used at the start of the reaction = 0.00814 g.

91.4% of soot is carbon (C, H, N, S analysis of soot reveals this value – section 4.2.2)

$$\frac{91.4}{100} * 0.00814 = 0.00743 \text{ g} = \mathbf{7.43 \text{ mg}}$$

$$\frac{6.314}{7.439} * 100 = \mathbf{84.88 \sim 85\%}$$

Thus 85 % of the 91.4% carbon in the soot is converted to CO₂. The remaining percentage could be accounted for the desorbed products that are not oxidized to CO₂. The contribution of CO and the hydrocarbon conversion could not be accounted for using the GC due to certain limitations.

4.6.3 Catalysed soot oxidation- exhaust gas mix (100 ppm propane, 230 ppm CO, 300 ppm propylene, 9% O₂, ≥ 90.93% N₂) with and without NO feed

4.6.3.1 Ag-K/CZA+soot-loose contact

CASE 1. With NO in the gas feed

As intended, the catalysed soot oxidation occurred at much lower temperatures than in the uncatalysed reaction. The concentration of CO₂, as shown for the catalysed oxidation was nearly twice that of the uncatalysed oxidation and CO was almost 8-10 times lower in concentration as compared between figures 4.27a and 4.29a. This clearly indicated that the drop in CO concentration was due to its conversion to CO₂. This occurred when the rate of catalysed soot oxidation was at a peak between 350-400°C. The CO from the feed was 230 ppm. The CO₂ and CO formed a similar profile with a sudden increase in CO concentration to 1700 ppm alongside an increase in CO₂ concentration to 32000 ppm at 400°C, which was the point at which the rate was maximum. CO was also produced from the soot at this stage; beyond this point the concentrations of both drastically fall to the minimum indicating complete oxidation. The concentrations of CO₂ were seen to increase at 400°C due to two factors which included contribution from soot and from the oxidation of CO and hydrocarbons.

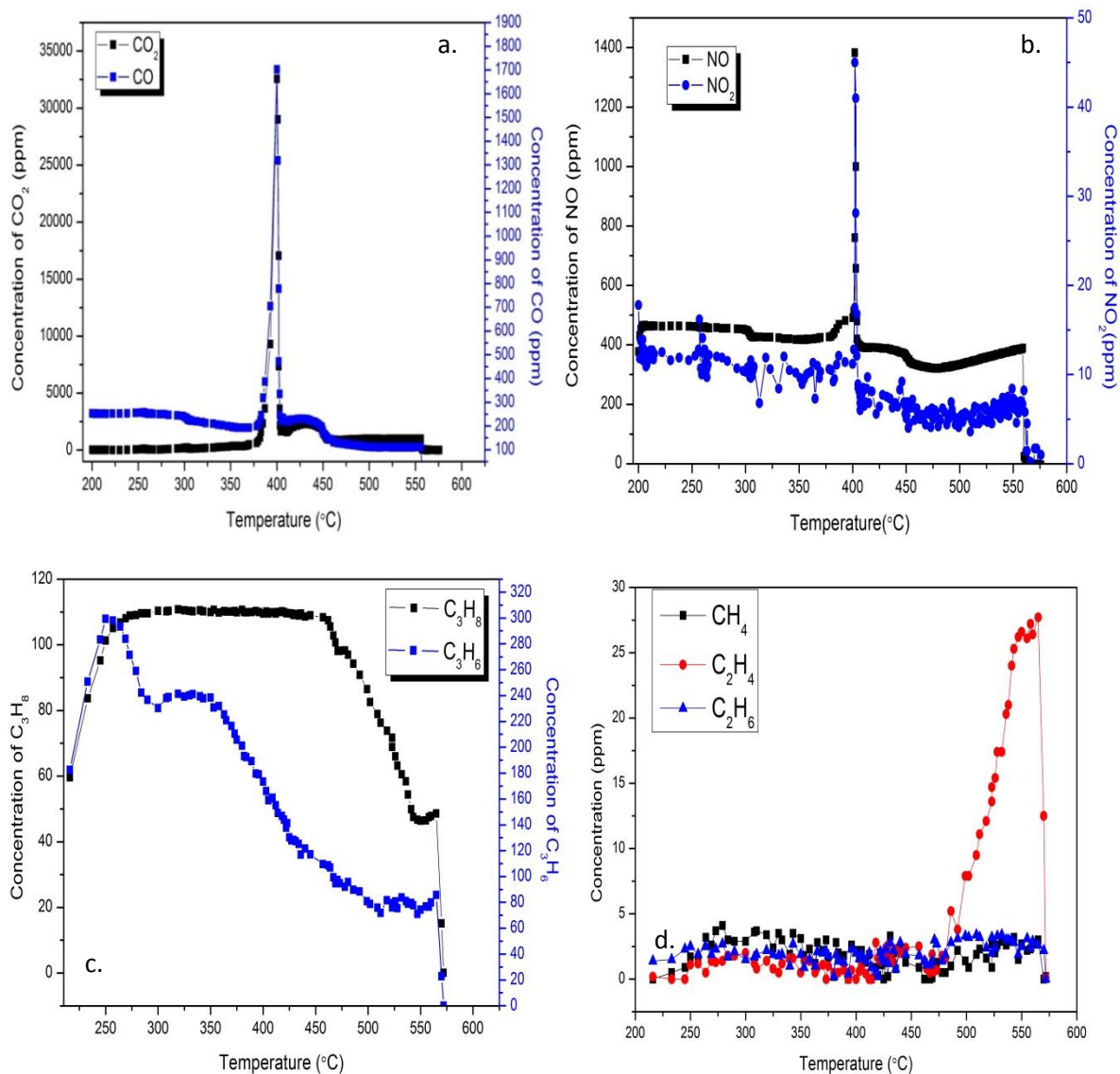


Figure 4.29 a) Concentrations under Ag-K/CZA+soot oxidation *under exhaust +NO feed* - a) CO₂/CO; b) NO/NO₂; c) C₃H₈/C₃H₆; d) CH₄/C₂H₄/C₂H₆

In the presence of NO, (black line on figure 4.29b), the initial concentration of NO remains constant (as from the feed) with only a small percentage being converted to NO₂ (blue line-~10ppm). It is noteworthy that at the peak temperature of soot oxidation, there was a sudden increase in the concentration of NO and NO₂, indicating that the NO was converted to NO₂. NO₂ aids in enhancement of the oxidation and as the thermodynamic equilibrium of NO oxidation was reached, the NO₂ concentration dropped. This has been studied by several researchers such as Hurtado *et al.* [15] who applied NO chemisorption onto several CeO₂ based oxides in order to understand these material's ability to convert the NO to NO₂. Although this reaction is thermodynamically

favoured, it is kinetically restricted at low temperatures in the absence of the catalyst. Using this catalyst, alongside a consecutive increase in temperature they observed effective conversion of NO to NO₂.

Mueller *et al.* [16] also conducted several studies on different kinds of soot to understand the effect of NO₂ addition into the feed, leading to enhancement of CO₂ production at lower temperatures and oxidation at more rapid rates as per the equations : $C(s) + NO_2 \rightarrow CO + NO$; $CO + NO_2 \rightarrow CO_2 + NO$; $NO + O_2 \rightarrow 2NO_2$.

Also some other studies on the NO/NO₂ effect suggested that the active oxygen from the CeO₂-ZrO₂ mixed oxide (in this case CZA) is transferred not only to soot but also to NO to yield NO₂. On the other hand, Setiabudi *et al.* [17] suggested that the formation of active oxygen in CeO₂ was initiated by NO₂ in the gas phase, which was governed by the fact that active oxygen was desorbed from the ceria surface as a consequence of previous interaction with NO₂. A synergism was observed between the NO₂-assisted and the active oxygen promoted soot combustion for the Ce-Zr catalysts studied [6].

At low temperatures, before the start of the oxidation (250°C) the gas-feed concentration of propane was 100ppm and propene was 300ppm. The propane concentration remained at 100ppm until around 450°C, beyond which the concentration started to drop gradually to 90ppm and then quite rapidly to 45ppm leading to oxidation to CO₂ by 575°C. There was a possibility of propane dehydrogenation to propene. The concentration of propene rapidly fell right from the start (300 ppm at 250°C to 230 ppm at 300°C) and then gradually reduced to 80ppm between 350-575°C beyond which it was probably oxidized to CO₂. There was conversion to small concentration(25-30ppm) of ethylene.

Case 2. In the absence of NO feed

There was a clear drop in the concentration of CO₂ and CO in the absence of NO, indicating that NO was a key contributor in soot combustion (figure 4.30). The CO₂ concentration very slowly increased between 450-520°C as oxidation gradually increased and finally dropped in concentration after complete combustion of the soot by 575°C.

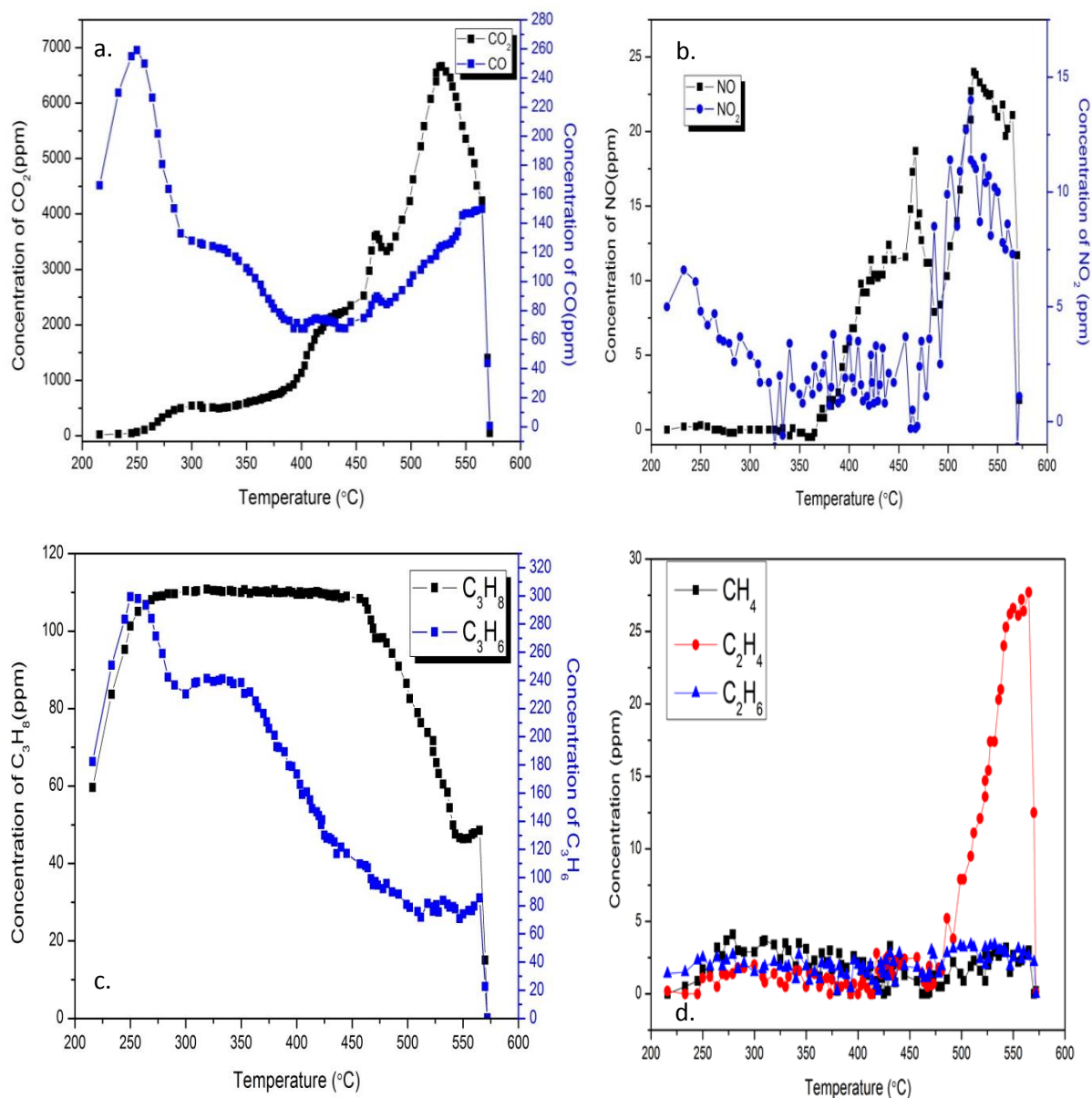


Figure 4.30 a) Concentrations under Ag-K/CZA+soot oxidation *under exhaust feed-*
a) CO₂/CO; b) NO/NO₂; c) C₃H₈/C₃H₆; d) CH₄/C₂H₄/C₂H₆

The concentration of CO fell rapidly at the start from 260 ppm to 140 ppm between 250-300°C and then to 60 ppm by 450°C due to its conversion to CO₂, beyond this the concentration increased to 160 ppm, showing that the CO cannot be further oxidized to CO₂. The NO and NO₂ appeared in the product stream at between 350-500°C (around 15-20 ppm). This was probably formed during the oxidation of nitrated PAHs in soot. The O₂ from the lattice could be oxidizing this to NO₂ leading to a slight increase in NO₂ concentration. The formation of ethane at 450°C probably as a result of cracking of propane.

4.6.3.2 Pt/SiC

Case 1. With NO in the feed

On the basis of TGA analysis, it was found that this catalyst was not ideal for soot oxidation, as the peak of oxidation occurred at temperatures as high as 560°C. This catalyst is a good NO_x storage source as it holds the NO on the surface from 250-300°C (figure 4.31b). The Pt/SiC was prepared as according to the procedure described in chapter 2. As it did not contain CeO₂, it was not expected to have any oxygen storage capacity. Therefore, even in the presence of NO feed, the concentration of CO₂ did not increase as much as in the previous case. The initial concentration of CO very rapidly fell from 260ppm to 10ppm at 250°C (onset of oxidation). This catalyst was capable of adsorbing CO on its surface, from the start of the oxidation, showing that CO concentrations reach only maximum of 10ppm and was oxidized in the presence of O₂ from the feed to CO₂. This led to a significant increase in CO₂ concentration in soot (figure 4.31a) to 1000ppm (contribution from soot oxidation, CO oxidation and hydrocarbon oxidation). This concentration started to increase at 520°C to reach a maximum of 14000ppm at 550°C. This contribution was a combination of CO oxidation and soot combustion.

There was a clear decrease in the concentration of NO and between 300-400°C. These changes could be assigned to the oxidation of NO to NO₂ on the surface of this catalyst. This aided in the increase in rate of soot oxidation, showing an increase in NO₂ concentration. Beyond 450°C, there was steady decrease in the concentration of NO₂ and rapid increase in NO concentration to that from the feed.

The propane concentration in the gas stream was seen to decrease steadily along the oxidation of soot between 300-600°C. (Figure 4.31c). However, there was negligible concentration of cracking products (ethene and methane). Moreover, the concentration of propene decreased at the start of the analysis thus suggesting an oxidation of both propane and propene. Propane gradually decreases to negligible concentrations along the entire temperature range of oxidation, suggesting its dehydrogenation to propene and oxidation to CO₂, while propene was seen to be oxidized more rapidly to CO₂ at lower temperatures (between 250-300°C).

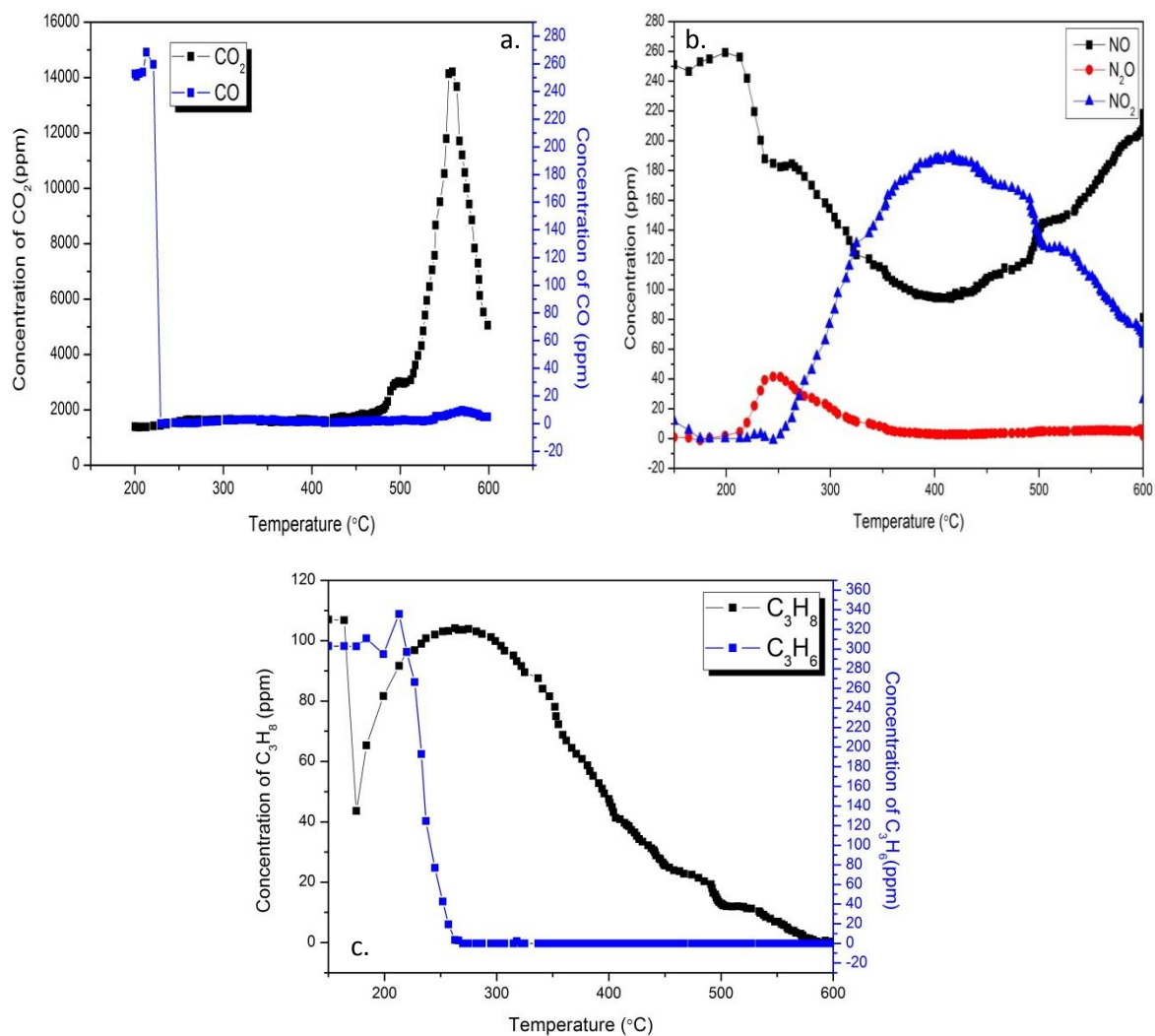


Figure 4.31 Concentrations under Pt/SiC + soot oxidation *under exhaust with NO feed*-
a) CO₂/CO; b) NO/NO₂; c) C₃H₈/C₃H₆;

Case 2. Without NO in the feed

In the absence of NO in the feed, the peak amount of CO₂ produced was reduced as compared to the previous case, reinforcing the fact that contributed to the NO₂, converting the carbon in the soot to CO₂, thereby increasing its concentration. The concentration of CO₂ due to the soot combustion was gradually increasing along the entire temperature range of 300-600°C (figure 4.32a). The initial concentration of CO was seen to fall between 200-300°C and beyond this point it was totally converted to CO₂, in the presence of oxygen from the feed. The concentration of propane from the feed gradually dropped between 300-500°C, indicating its oxidation to CO₂ or dehydrogenation to propene (beyond 400°C). This was clearly observed from the rise in

propene concentration between 500-550°C followed by oxidation to CO₂, where the concentration of CO₂ was at its peak.

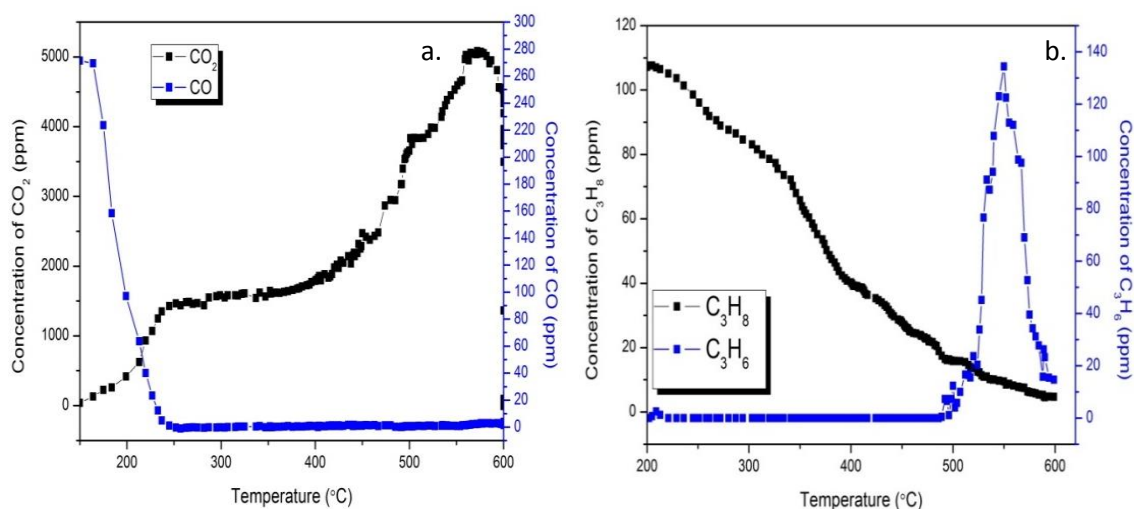


Figure 4.32 a) Concentrations under Pt/SiC +soot oxidation *under exhaust feed-*
a) CO₂/CO; b) C₃H₈/C₃H₆

Pt/SiC was ideal for oxidising CO and hydrocarbons but it could also dehydrogenate propane. The Pt/SiC catalyst is not active for the cracking of hydrocarbons.

4.6.3.3 Ag-K/CZA+Pt/SiC

The procedure for preparation of this catalyst has been described in chapter 2, illustrating the need for such a catalyst for combined PAH-soot oxidation. The best ratio of Pt/SiC: Ag-K/CZA-1:2 was soot oxidation, based on TGA studies as described in chapter 5.

Case 1. With NO in the feed

The concentrations of CO and CO₂ were seen to increase to a maximum of 10,000ppm with the increase in rate of soot oxidation. The CO was converted to CO₂ in the presence of O₂ from the feed. The combustion rate is at a peak of approximately 460°C (Figure 4.33a). The NO and NO₂ were initially seen to touch a concentration of 2260ppm and 70ppm respectively, probably due to the desorption of nitrated aromatic species undergoing desorption at around 320°C. The NO then rapidly adsorbed onto the catalyst and was converted to NO₂, and this was not stored on the catalyst but rapidly

converted the soot to CO₂. Thus this catalyst shows low concentrations of both NO and NO₂ indicating that the NO₂ is reduced back to NO through a redox cycle. The NO₂ concentration slowly increased at 500°C to a small amount (40ppm), indicating that the catalyst effectively utilised the NO₂ to oxidise soot completely beyond (500°C). The levels of NO₂ tend to increase only slightly and the NO remains unreacted from the feed gas, beyond 500°C. This is further evidenced by the NO level displaying a minimum concentration of 120ppm throughout analysis, suggesting a practical maximum amount of NO, which can be stored on the catalyst or utilised for soot combustion (figure 4.33b).

Propane remained constant at the feed level of 100ppm up to approximately 500°C (Figure 4.33c). At temperatures above 550°C there was a small degree of propane cracking observed (as seen previously) indicated by rise in the levels of ethene and methane (Figure 4.33d), alongside a degree of dehydrogenation to propene as well as total oxidation to CO₂, contributing to its increase in concentration, is observed. The propene concentrations were similar to those measured in analysis under exhaust gas only (without NO), where it remains high at low temperatures and gets adsorbed onto the catalyst at approximately 300-500°C. The rise in concentration at 500°C could be due to the desorption from catalyst surface resulting in the fall in concentration of both propene and propane at 600°C due to total oxidation.

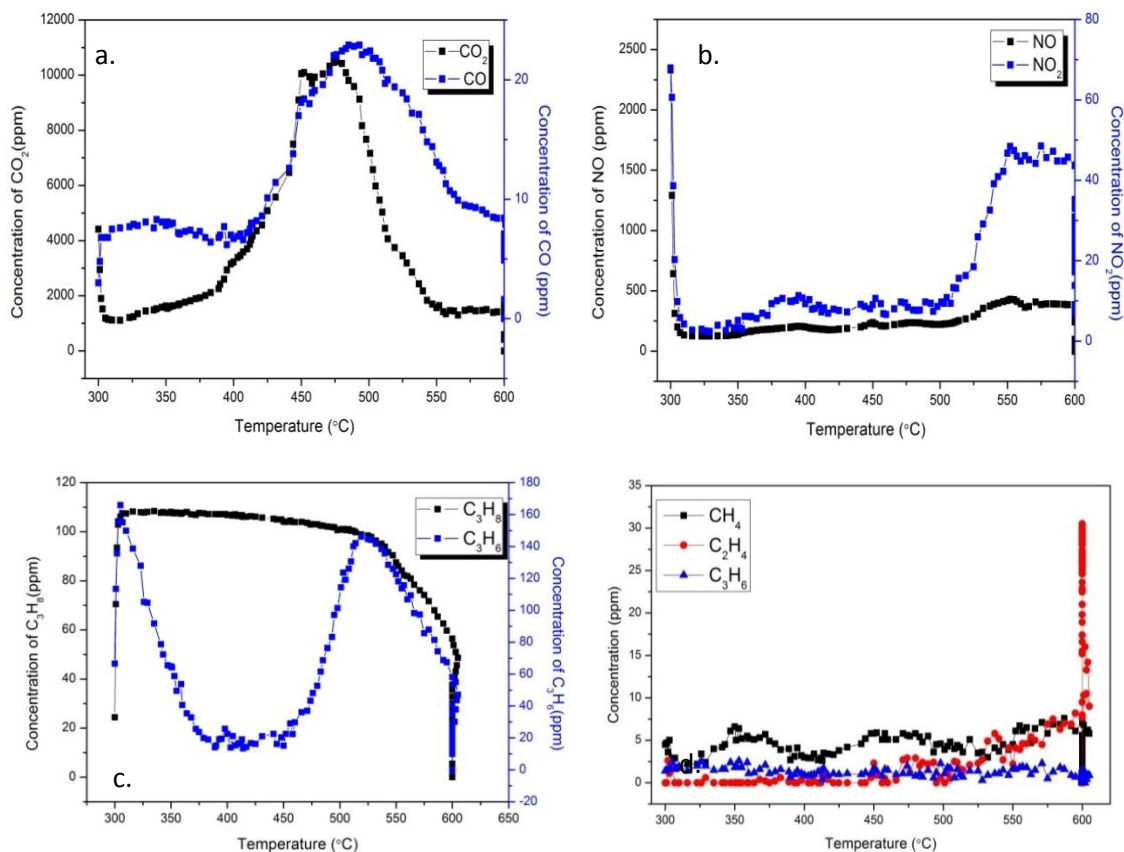


Figure 4.33 a) Concentrations under Ag-K/CZA+Pt/SiC +soot oxidation *under exhaust feed+NO* a)CO₂/CO; b)NO/NO₂; c)C₃H₈/C₃H₆; d)CH₄/C₂H₄/C₂H₆

Case 2. Without NO in the feed

In the absence of NO feed, peak CO₂ production occurred at 460°C (Figure 4.34a), signifying that soot combustion was occurring at a lower temperature than was achieved under a He/O₂ mix. The CO₂ arose from the oxidation of soot and propane oxidation alone. The levels of CO₂ and CO were comparatively lower in the absence of NO in the exhaust compared to that in the presence of it. This was seen from the concentration of CO that showed a sharp decrease at the start of the oxidation, leading to the formation of CO₂. This occurred on the surface of the Pt/SiC catalyst that stored the CO and oxidized it to CO₂, later around 400-500°C. There was negligible concentration (~70ppm) of NO and NO₂ (10-15ppm) formed from the combustion of soot, indicating its occurrence from combustion of PAHs (figure 4.34b).

The propane concentration in the gas stream remained constant (figure 4.34c) until approximately 500°C where a steady fall was observed resulting in a rise in the concentrations of cracking products, methane and ethene (Figure 4.34d), but not enough to account for the total reduction in propane concentration. This suggested that the catalyst transforms aliphatic hydrocarbon and aids in total combustion at higher

temperatures. Dehydrogenation of propane to propene accounted for the spike in propene concentration at the temperatures close to 550°C, however the concentration rapidly dropped as temperature in the reactor increased, indicating either adsorption/storage on the catalyst or total oxidation, resulting in a concurrent rise in CO₂ concentration.

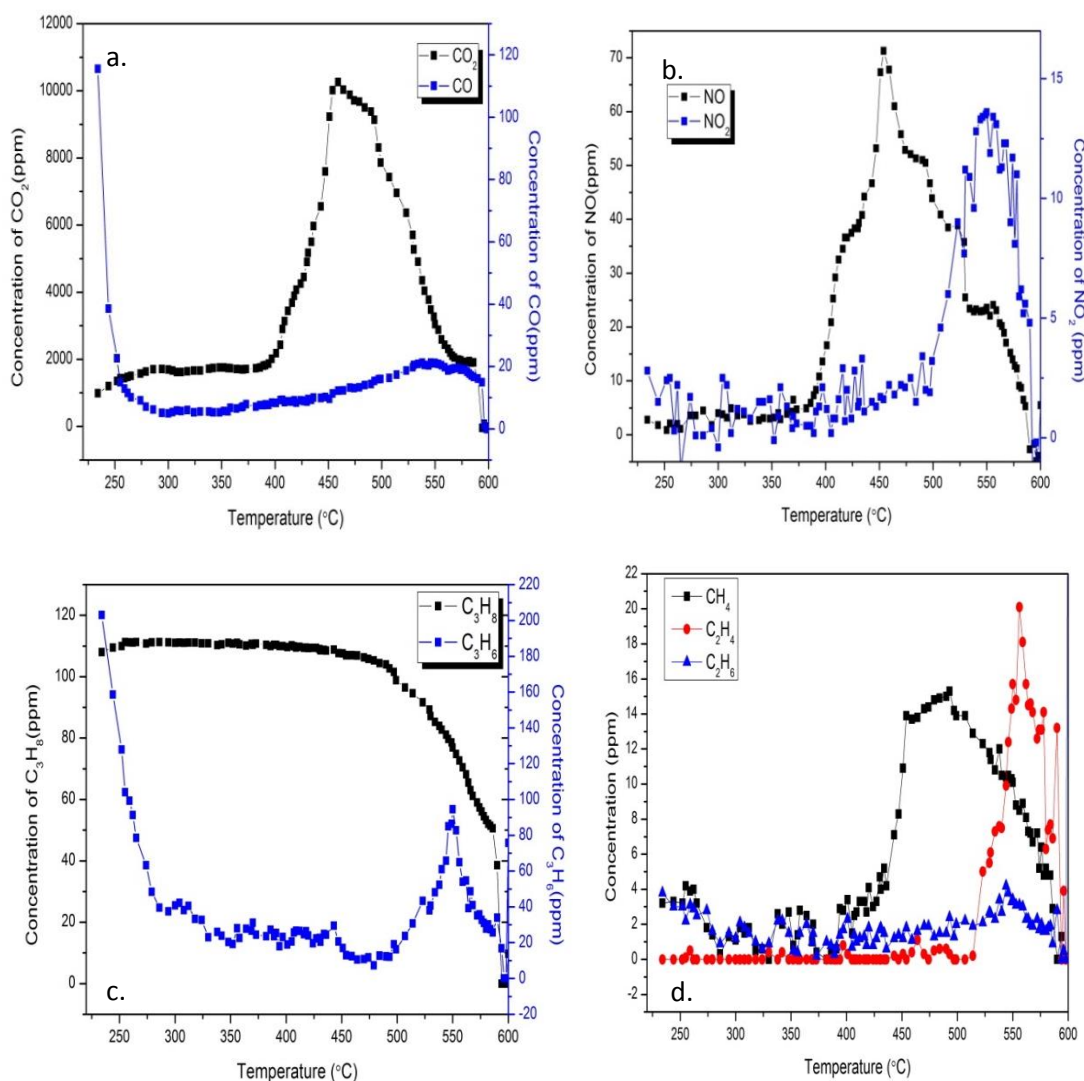


Figure 4.34 a) Concentrations under Ag-K/CZA+Pt/SiC + soot oxidation under exhaust feed a) CO₂/CO; b) NO/NO₂; c) C₃H₈/C₃H₆; d) CH₄/C₂H₄/C₂H₆

4.6.4 Extracted soot- with and without NO

The studies on extracted soot were conducted to understand the oxidation of soot upon removal of the VOCs and PAHs from the surface of the soot. The extracted soot is obtained post Soxhlet extraction process. The concentrations of CO and CO₂ are very high from extracted soot. The oxidation occurs at high temperatures between 450-

600°C. The CO and CO₂ formed from the soot oxidation and from propane and propene oxidation resulted in the massive increase in concentrations. After the PAHs were removed from the soot, the carbonaceous particles tend to react at higher temperatures in the absence of the catalyst. The CO and CO₂ levels increased at the temperatures close to 450°C and then decreased by 500°C. Later, in the presence of more NO₂, along with propane oxidation occurring simultaneously, it resulted in the further increase in concentration at 550°C. The production of CO and CO₂ was not constant and varied with increase in temperature of the exhaust for the extracted soot as shown in figure 4.35a. The contribution of soot (prior to extraction), towards CO and CO₂ production was higher as compared to that produced from the extracted soot as the contribution of PAHs increased the concentration of CO and CO₂.

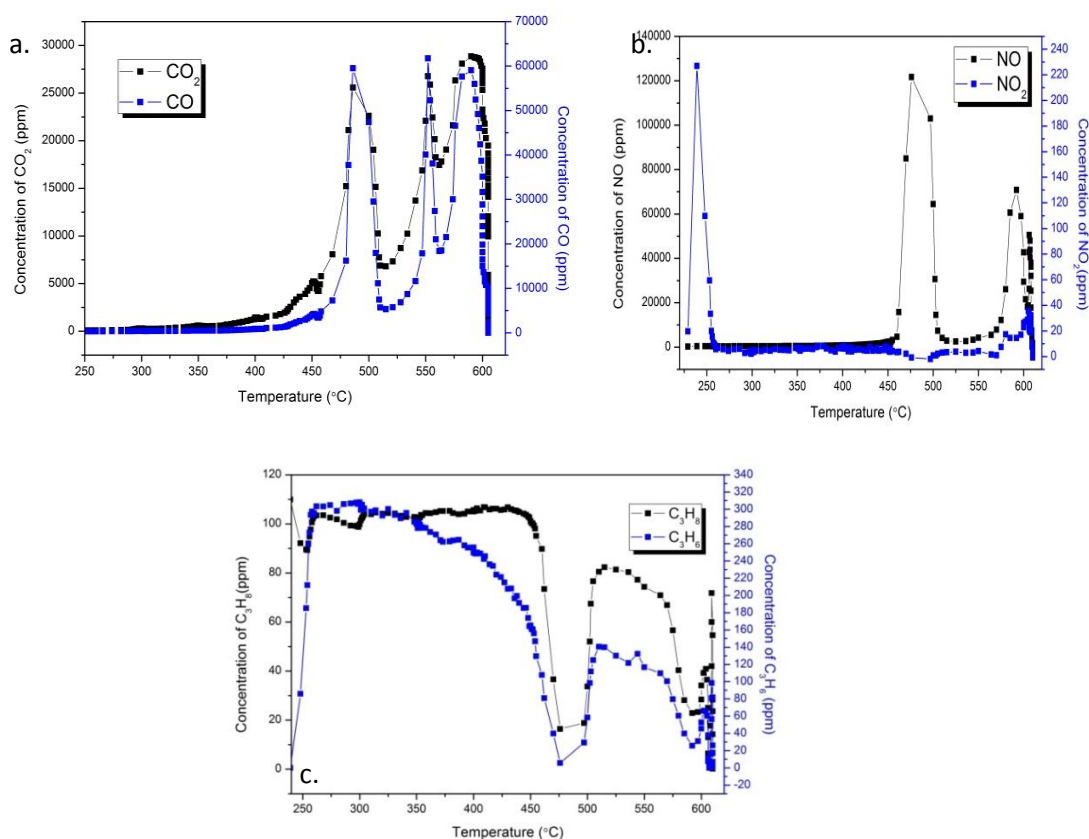


Figure 4.35 a) Concentrations under extracted soot oxidation under exhaust feed –with NO a) CO₂/CO; b) NO/NO₂; c) C₃H₈/C₃H₆;

In the presence of NO in the feed there was a constant adsorption of NO onto the surface of soot and this led to the formation of NO₂ at the start of the test, followed by increase in rate of the soot oxidation through a NO₂ assisted mechanism, beyond which by 500°C, the NO was not adsorbed anymore on the soot surface, leading to an increase in its concentration (figure 4.35b). Propane combustion occurred rapidly at 475°C and

propene was combusted gradually around 375-475°C. The concentrations dropped to a minimum and then picked up again between 500-550°C (figure 4.35c). The loss of volatile organics that were adsorbed on the surface of soot, upon extraction, resulted in the increase in a peculiar trend in combustion. Similar trends were observed in the absence of NO feed with increased CO₂ and CO concentrations as shown in figure 4.36a,b.

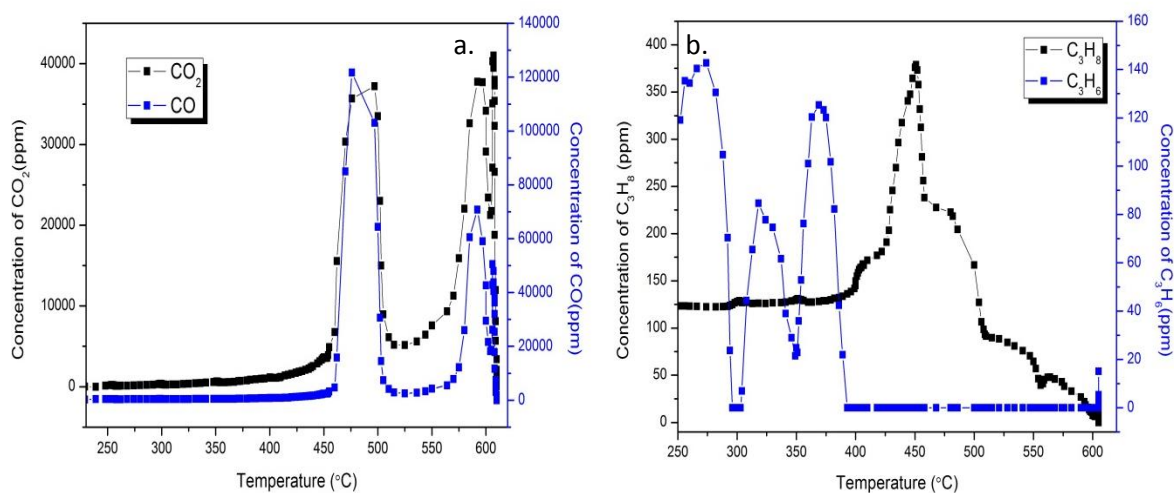


Figure 4.36 a) Concentrations under extracted soot oxidation under exhaust feed-without NO
a) CO₂/CO; b) C₃H₈/C₃H₆

In the absence of NO feed, the peak concentration of CO₂ was seen to be slightly lower than in the presence of it (figure 4.36a). The concentrations were higher as the conversion to CO₂ was not very easy. The contributions only arose from the CO and CO₂ of the carbonaceous soot, at around 480°C A significant trend in the increase, followed by a decrease and subsequent increase in concentration of both CO and CO₂ could arise due to the nature of extracted soot, behaving like a pure graphitic carbon source. The exotherms for combustion were probably higher. Propane concentration increased was oxidised beyond 450C, with complete oxidation at 600°C (figure 4.36b).

4.7 Catalyst characterization

4.7.1 Pt/SiC

The Pt/SiC catalyst was a good CO adsorber as shown above and was characterised to understand its physical properties. Figure 4.37 showed that silicon carbide used as the catalyst support was a highly crystalline material, giving well defined peaks in XRD analysis. Upon impregnation and calcination, new peaks were

seen at $2\theta = 40.0^\circ$, 46.5° and 67.8° , these phases corresponded to a Pt^0 phase. These results were confirmed through XPS shown in figure 4.39a.

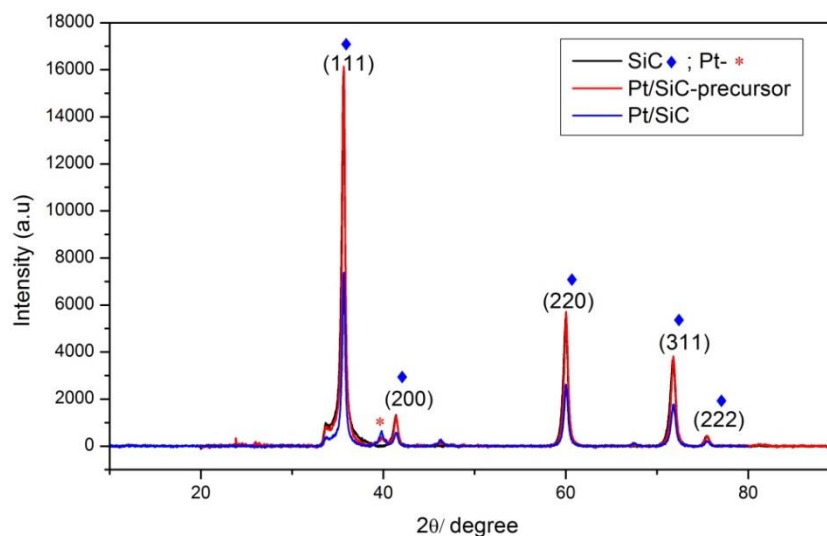


Figure 4.37 X-ray diffractograms for Pt/SiC catalyst

The Pt 4f showed a doublet peak present as Pt^0 (71eV) and Pt^{4+} (74eV) states (seen in figure 4.39), and confirmed from literature [18]. XPS data for Pt/SiC, from the narrow scan, showed the following elemental composition: a peak at 102.9 eV for SiO_2 and at 100.5 eV for SiC. The carbide formation was indicated by C 1s at 282.5eV (figure 4.38a,b). This was as listed in table 4.6 giving the atomic concentrations (%).

Table 4.6 Atomic concentration of Pt/SiC

Sl. No	Catalyst	C 1s (%)	Pt 4f (%)	Si 2p (%)
1	Pt/SiC precursor	59.47	0.72	39.67
2	Pt/SiC	55.64	0.55	43.81

Upon calcination was clearly visible that the content of Pt reduced on the surface and the concentration of Si increased slightly. Calcination could probably be responsible for the conversion of the Pt^0 to Pt^{4+} , causing it to move deeper into the SiC lattice. On calculating the ratio of Si: C for calcined Pt/SiC, from the atomic percentages we get, Si: C is $43.81:55.64 = 0.78:1 \sim 1:1$. From the area ratios we get, C area = 12492 and Si area = 1824, dividing area by the R.S.F we get;

$$C = 12492 / 0.278 * 4 = 1797.4; Si = 1824 / 0.328 * 32.5 = 1807.31$$

$$\text{Thus Si: C} = 1807.31 / 1797.4 = 1:1.$$

The Si 2p is present as 24.03 % of Si 2p carbide and 20.02 % oxide character.

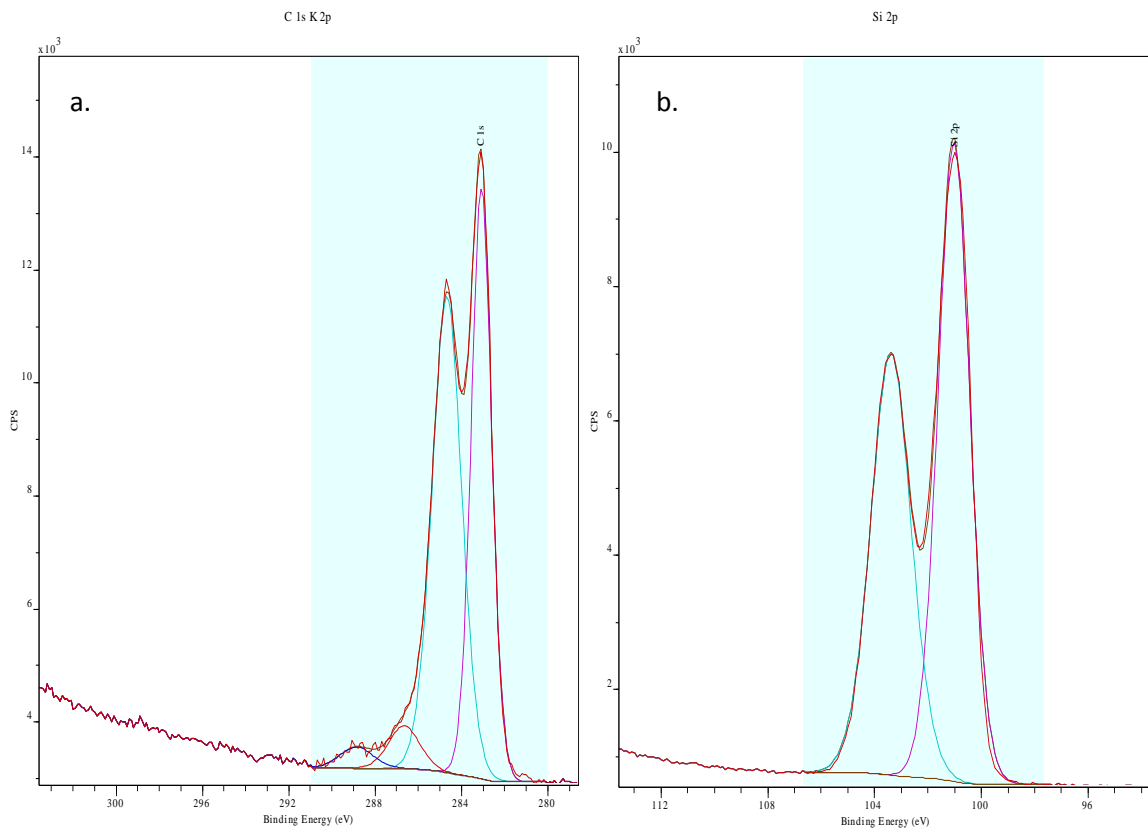


Figure 4.38 XPS spectra for calcined Pt/SiC - a) C 1s spectra; b) Si 2p spectra

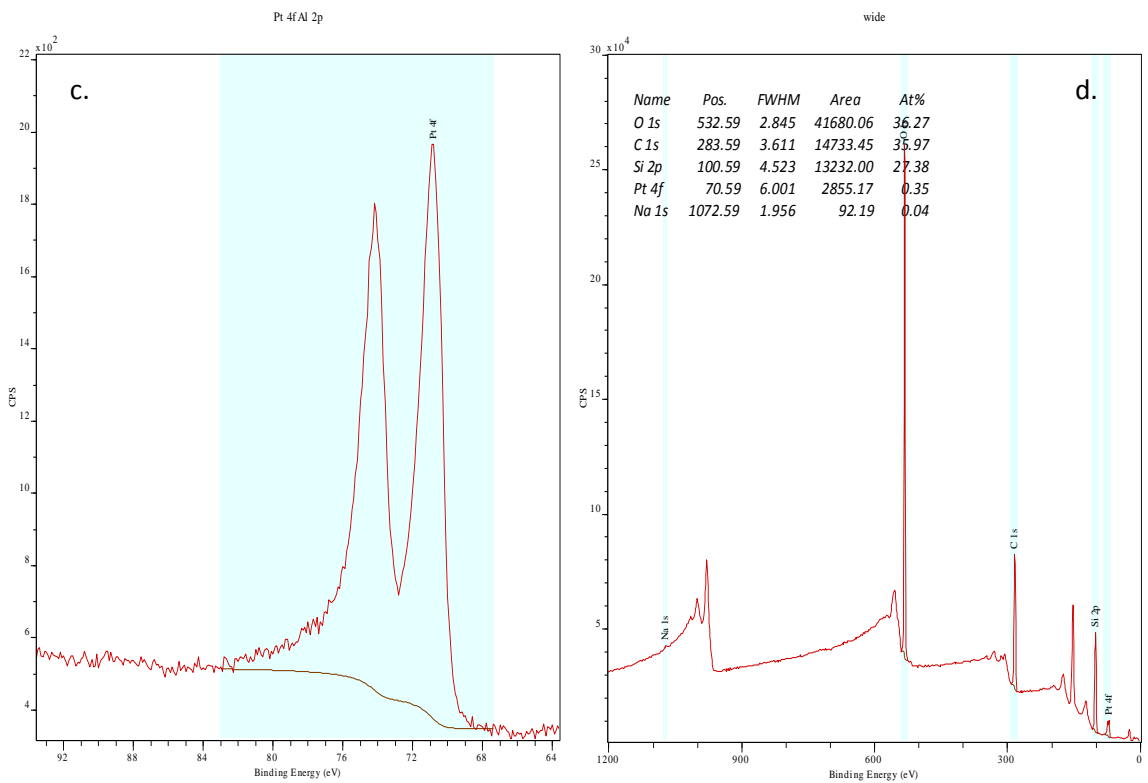


Figure 4.39 XPS spectra of calcined Pt/SiC- a) Pt 4f spectra; b) wide scan spectrum

SEM micrographs revealed that the Pt had been dispersed onto the SiC surface directly. The Pt particles were not spread across the SiC matrix as can be seen from figure 4.40a. They were localized onto certain SiC particles seen as bright spots of Pt as shown in figure 4.40a, b. This is due to the nature of incipient wetness impregnation. SiC appeared to have a fluffy cotton ball like appearance. The SiC particles were around 10-20 μm while Pt particles on top of the SiC were smaller than 5 μm .

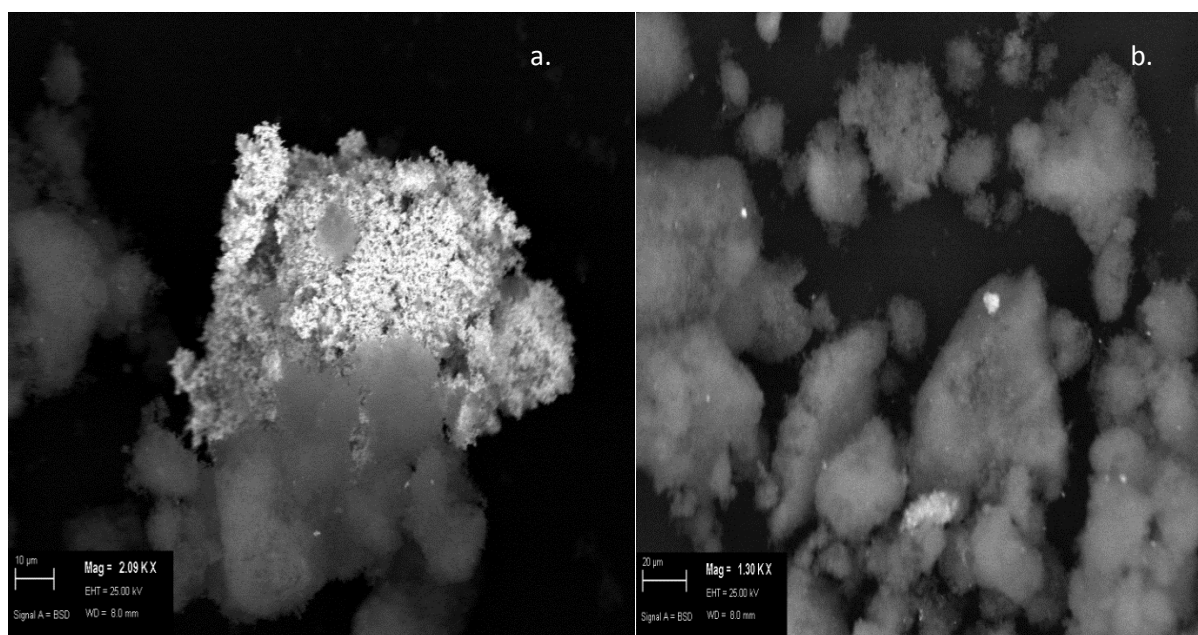


Figure 4.40 SEM micrographs of Pt/SiC- a) single particle-2.09KX; b) spread around particles 1.30KX

TEM showed that the tiny Pt⁰ (2-10nm) particles were localised on the SiC support. These particles were seen as small dark black spots on the large particles in the background which represented the SiC particles (figure 4.41a, b). The different crystal planes for Pt and SiC could be distinguished (as shown in figure 4.41c,d) which showed the d spacing for SiC as 0.25nm and for Pt⁰ as 0.225nm, indicating that the Pt⁰ particles were over seen to be dispersed inhomogeneously onto the SiC lattice (seen from figure 4.41a,b). There was also a spherical layer of SiC seen to cover the Pt particles. It was confirmed after several close examinations of several images of different Pt/SiC particles that it was not an artefact but a spherical coating of SiC around each Pt particle. This can be seen from figure 4.41c and d. These Pt particles were tiny nanomaterials of approximately 2-10nm. There were a large number of these particles on the SiC surface.

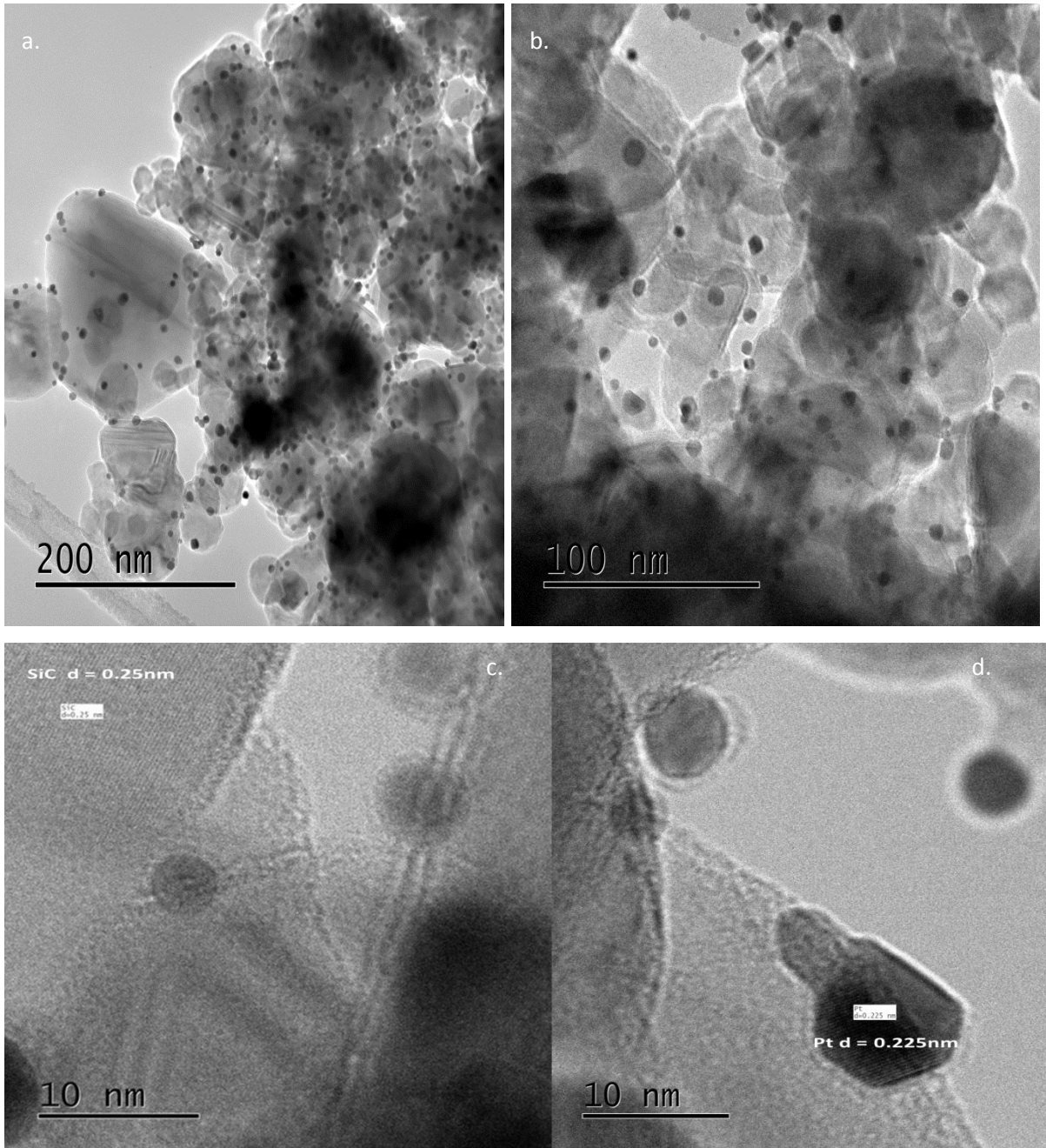


Figure 4.41 TEM images for Pt/SiC- bright field-a) 200nm; b) 100nm; c) SiC planes; d) 10nm Pt planes

EDX mapping was carried out using dark field imaging/STEM images and elemental composition was identified as shown in figure 4.42.

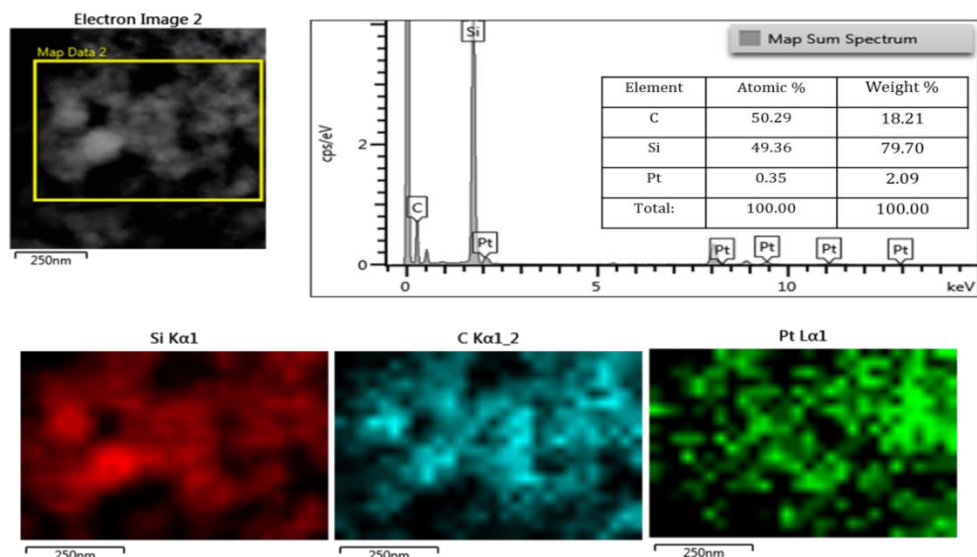


Figure 4.42 EDX mapping of elemental composition in Pt/SiC

The EDX elemental scan along the region shown as an inset image in figure 4.42 showed that the atomic concentration of Pt, (as percentage) was of 2 % which is in agreement with the preparation of these particles. The SiC revealed a good spread of the SiC particles as seen on the map for Si K α 1. The main bright spots revealed the Si clusters (indicated by dark red). The C K α 1_2 revealed the spread of carbon from SiC, as bright blue spots, in similar regions of Si K α 1. This confirmed the spread of SiC. The Pt was spread throughout the surface giving a 2% distribution, indicated by the bright green spots. The same result was shown using SEM/EDX maps, as seen in figure 4.43, that showed the distribution of the Pt⁰ and SiC on a single particle, with a background of from the carbon disc. The bright spots covering the fluffy white SiC particles were Pt⁰.

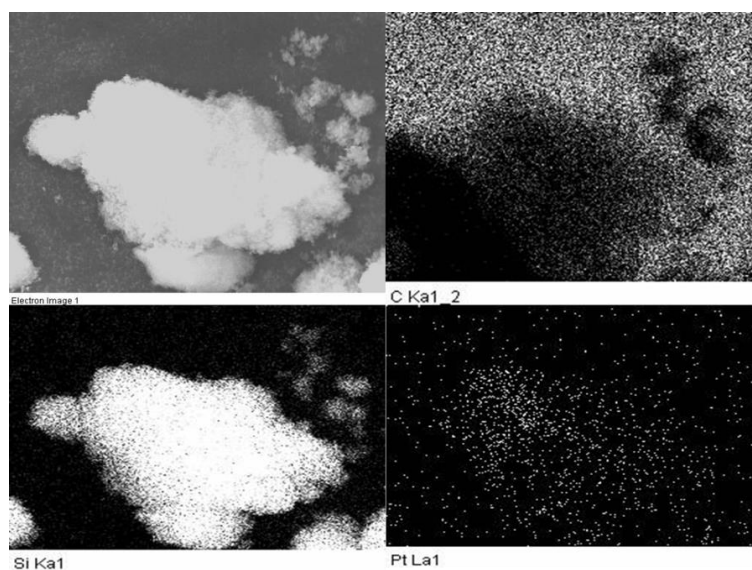


Figure 4.43 SEM -EDX mapping for Pt/SiC

4.7.2 Pt/SiC+Ag-K/CZA

The two catalysts prepared were mixed together mechanically in different ratios as described in chapter 2 and the Pt/SiC : Ag-K/CZA – 1:2 ratio was the most active among the ratios for soot oxidation and this is described in detail in chapter 5. Porosimetry measurements for pore size distribution utilising the BJH method suggested that the mixed catalyst exhibited a small degree of microporosity as shown in the figure 4.44, with a significant distribution of pores, with a diameter between 5 and 8 nm. Average pore size calculations gave an average pore diameter of 25 nm, suggesting that the material also has a large number of mesopores present in it. This suggested that the mechanical mixing of the two catalysts yielded a range of particles of variable sizes and a varied distribution of pore sizes, efficient to tackle the various sizes of soot particles in their pores.

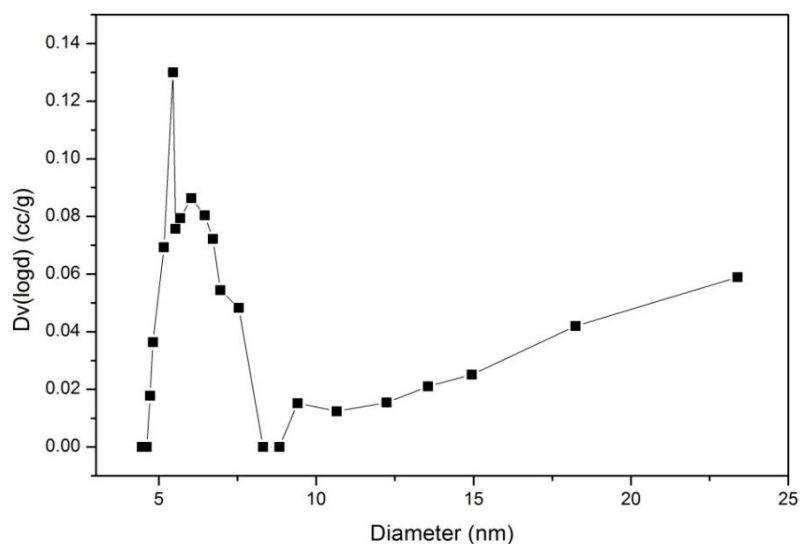


Figure 4.44 Pore size distribution in Pt/SiC+Ag-K/CZA

Table 4.7 BET surface areas of catalysts and supports

Catalyst	BET surface area (m ² /g)
PtSiC+AgKCZA-1:2	28
CZA support	148
Ag-K/CZA	25
SiC support	29
Pt/SiC (incipient wetness impregnation)	29

BET surface area (Table 4.7) showed that there was a significant reduction in surface area upon impregnation of the active metal phases for Ag, K onto CZA. This was

presumably due to the blocking of pores in the support material by the high loading of impregnated K (present as K_2CO_3), and to a lesser extent, Ag. SiC and Pt/SiC were negligibly different in their surface areas, suggesting that there was little to no pore blocking upon impregnation which indicated that the fairly large Pt particles were formed on the surface, as formation of smaller particles with high dispersion would be expected to increase metal surface area significantly. This is due to the incipient method of impregnation. The mixed catalyst showed a surface area with an average of its constituent parts, suggesting there was no change in morphology or pore blocking upon mechanical grinding of the catalysts.

XPS showed that the peak for Ce 3d was insignificant in comparison to the other dominant peaks. indicating that the surface might contain less of the ceria. The oxide peaks shown in figure 4.45, indicate the formation of oxides at 531eV and also presence of the carbonates from K_2CO_3 at 532eV.

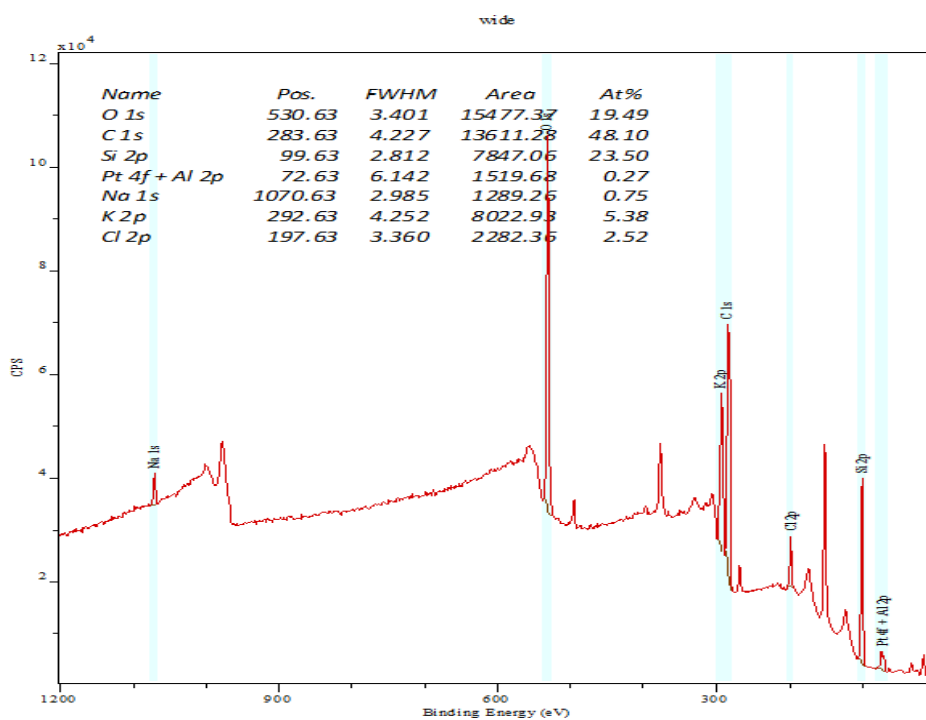


Figure 4.45 Wide scan spectrum for Pt/SiC+Ag-K/CZA

The Si 2p peak indicated the SiC phase and a small concentration of the SiO_2 phase as well. The physical mixing led to an overlap of the Al 2p and Pt 4f peaks. Thus quantification of Al in this case was difficult. 86% of the Al 2p orbital is mostly tightly

held and there is less chance of photoemission in this case as compared to the Pt containing d orbitals that give rise to increased photoemission.

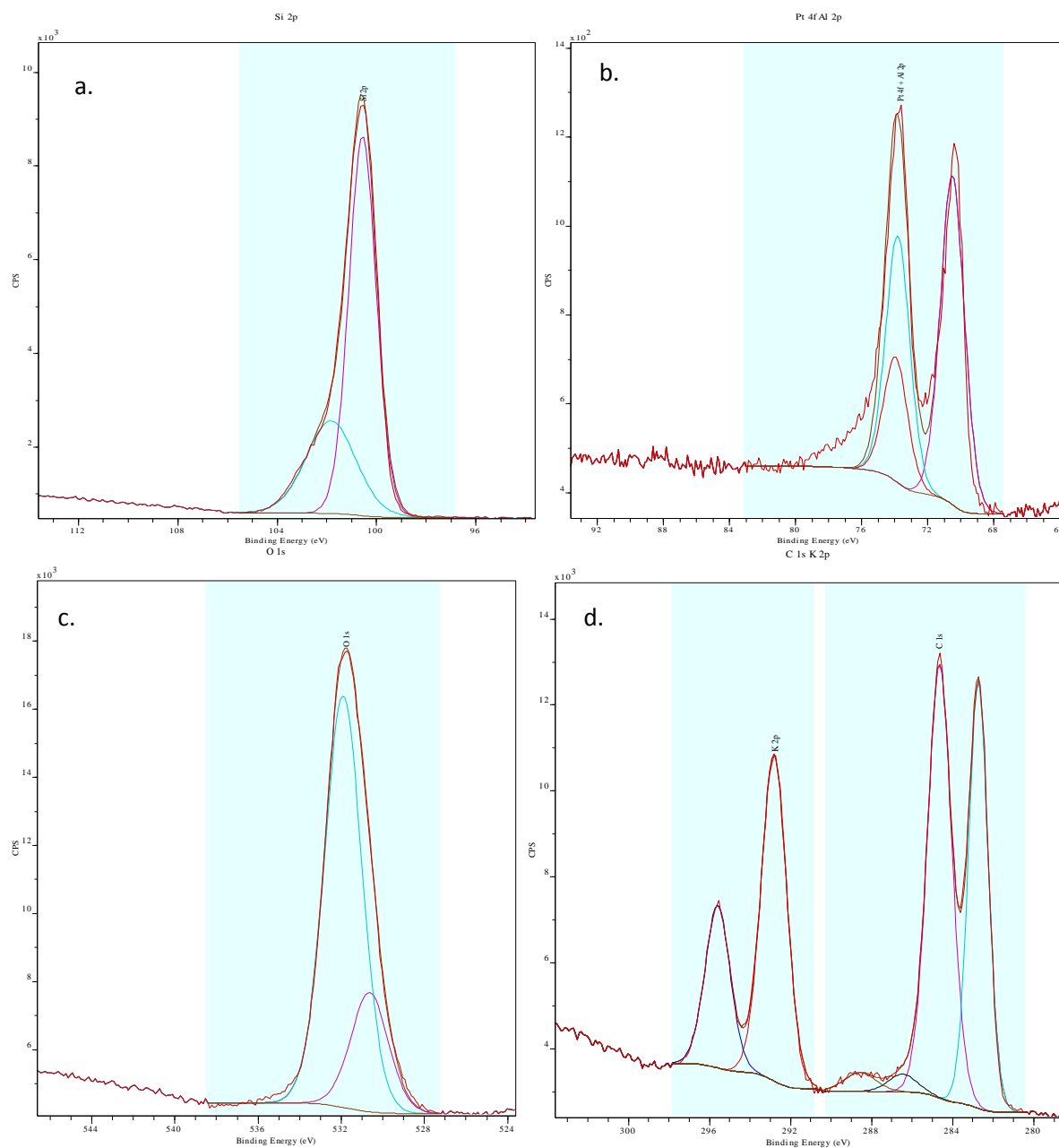


Figure 4.46 XPS spectra for a) Si 2p; b) Pt 4f; c) O 1s d) C 1s K 2p

The Pt/Al/Ag was present as an over layer, indicating good contact between the two catalysts. The O 1s peaks indicated the formation of the oxides at 530.9 eV and a distinct peak for the carbonates from K_2CO_3 at 532eV. The peaks for Ce and Zr 3d were not visibly present on the surface as these may have been mixed thoroughly with the Pt/SiC, yielding a greater percentage of SiC on the surface. The first peak of the C 1s spectra at 282eV was due to the SiC in the catalyst and the second peak at 286eV was

due to the carbon from the atmosphere. Pt 4f was present as Pt⁰ and Pt⁴⁺ states as indicated from the binding energies, corresponding to 71 and 74 eV respectively (figure 4.46) [12].

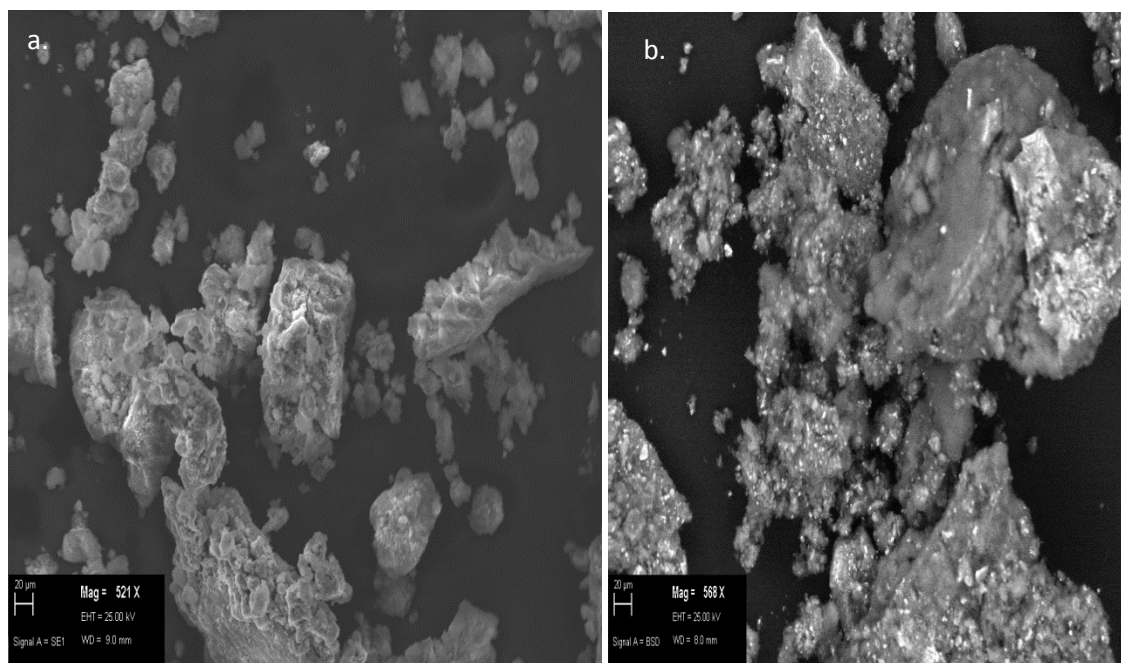


Figure 4.47 SEM micrographs for the mixed catalyst-Pt/SiC: Ag-K/CZA- 1:2- a)SE detector; b) back scatter detector

SEM images indicated that the two catalysts had been mixed thoroughly, with presence of the Ag-K/CZA catalyst structure alongside the SiC from the Pt/SiC spread throughout the catalyst. The presence of Pt and Ag was indicated by the bright spots on the support as can be seen from the figure 4.47b. In addition to SEM, EDX was employed to understand the composition of the elements in the mixed catalyst. Figure 4.47b showed the image under the back scatter detector chosen for the study. The map indicated the presence of the elements in the particle chosen. This showed that the particle under study is thoroughly covered by SiC (figure 4.48). The background of this image was shown as carbon, clearly indicated by C Ka1_2. There was also considerable distribution of CeO₂-Al₂O₃ oxides present along the regions of SiC and faint traces of ZrO₂ indicating that the CZA catalyst had mixed well with the Pt/SiC. On observing the Pt and Ag, these were present as small clusters around the particles with a greater spread of Pt on this particle. The potassium had a well dispersed spread around the particle, suggesting that the promoter has an even distribution, thereby providing more active sites for the soot to react.

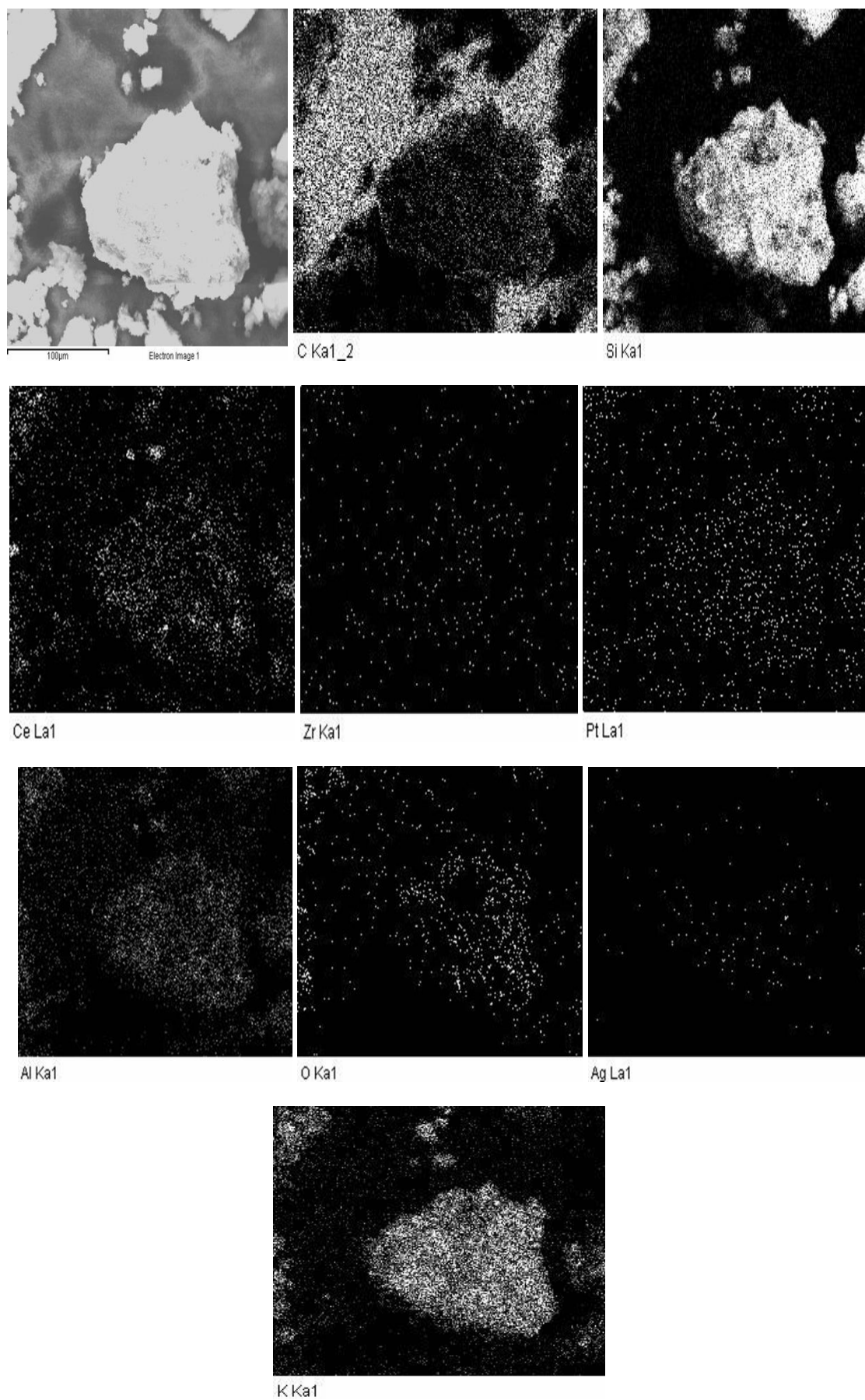


Figure 4.48 EDX mapping of the mixed catalyst-Pt/SiC: Ag-K/CZA - mapping of a particle

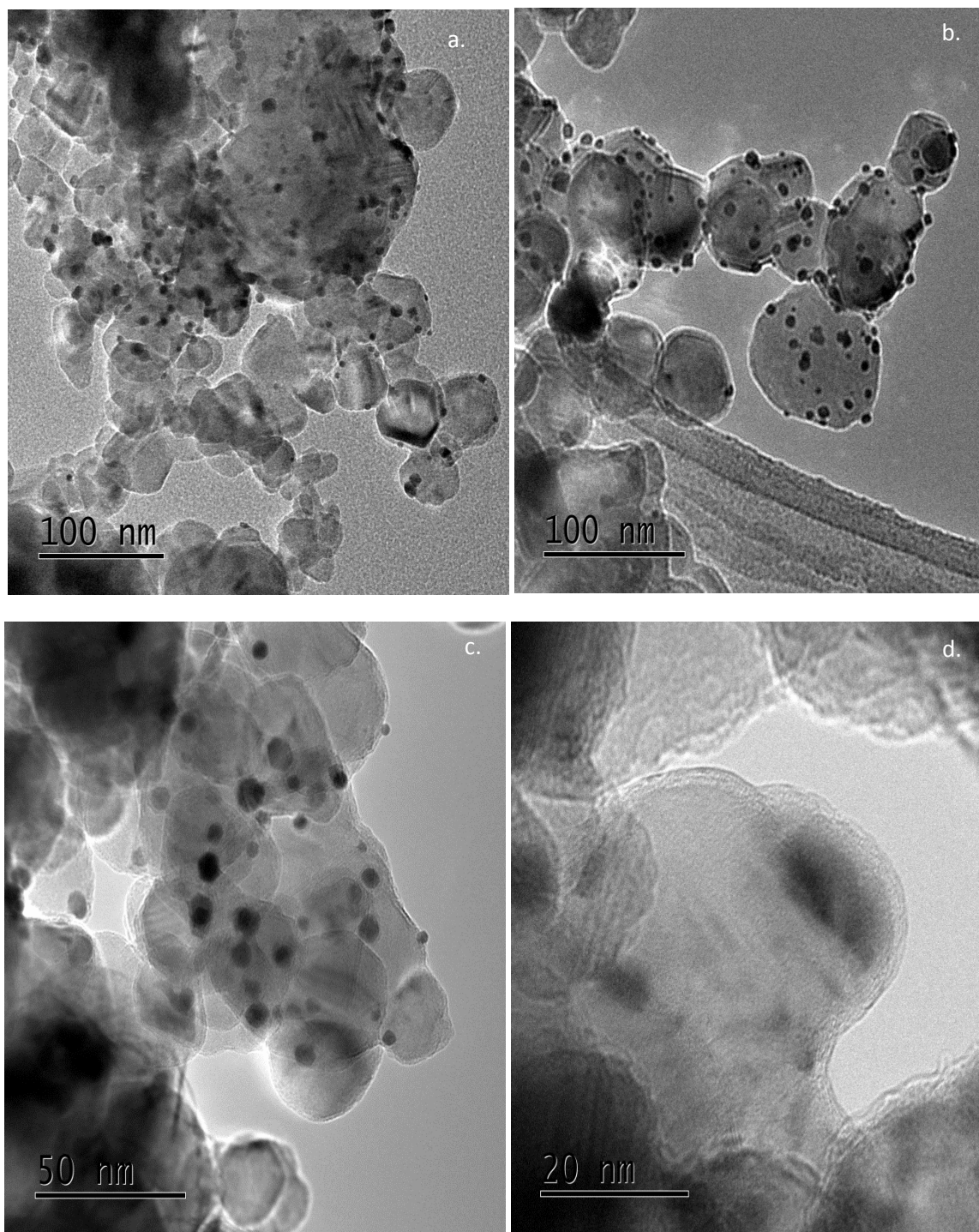


Figure 4.49 TEM images –mixed catalyst- a and b- particles of Pt/SiC and Ag-K/CZA well dispersed in the lattice; c) resolved image showing the distribution of particles; d) K_2CO_3 around the Ag/CZA particle

The TEM images showed that the Ag-K/CZA and Pt/SiC particles were well dispersed in the catalyst and the lattice planes for the CeO_2 and SiC supports were seen to be present together with an impregnation of the Ag and Pt nanoparticles, seen as bright spots on them (figure 4.49a,b). There was a clear coating of the K_2CO_3 present

around the Ag-CZA particles and was seen to spread into the entire matrix of the catalyst, indicating good spread of the promoter. This was thought to be an artefact initially, but from several analyses on different particles this was proven to be incorrect and that the coating or layer around these particles was from the K_2CO_3 . The lattice planes showed that the Ag was present as the oxide and metallic forms on the CZA lattice as was seen from the figure 4.51. The d spacing for Ag^0 was 0.24 and that for Ag_2O was 0.25nm. Thus it was evident that both these forms existed together. The Pt was present in the metallic form on the SiC as shown in figure 4.50. The K_2CO_3 was also clearly evident, seen surrounding the Ag metallic and oxidic phases on the CZA.

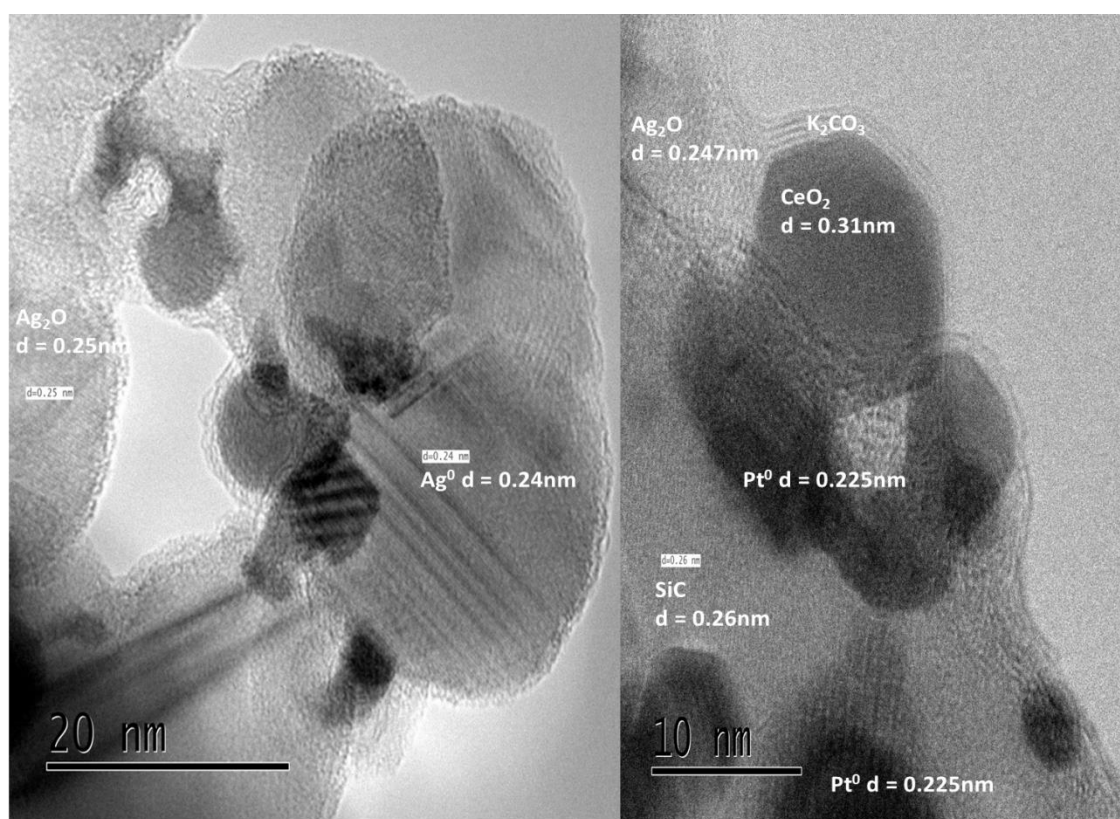


Figure 4.50 TEM images for mixed catalyst-Pt/SiC+Ag-K/CZA

EDX mapping using dark field imaging with STEM-EDX indicated the presence of a mixed phase of both the catalysts. There was predominance of SiC (red) in some places over CZA, as could be seen in the case of this area under observation, with formation of the mixed oxides at different locations indicated in pink. Pt was seen to be distributed as bright light green clusters on the SiC matrix.

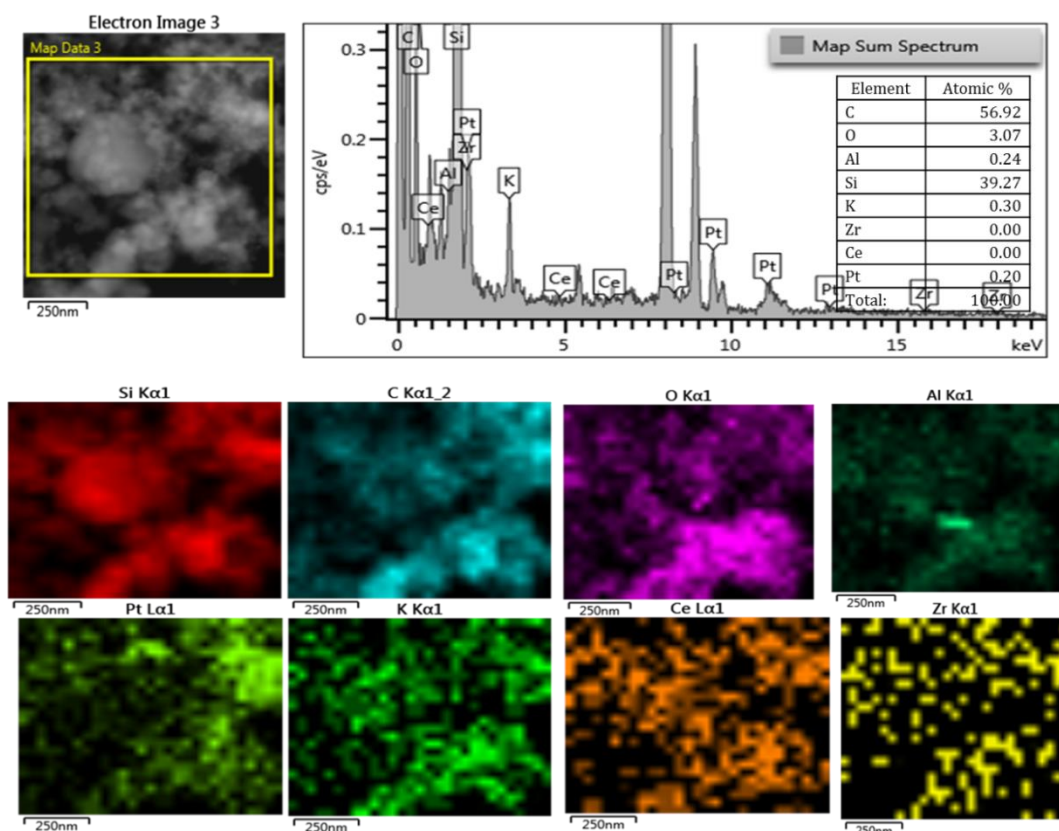


Figure 4.51 EDX mapping using STEM-EDX for Ag-K/CZA+Pt/SiC

4.8 Conclusions

Soot was characterised using several analytical techniques before extraction to try and understand its physical properties and understand the various mechanisms of its oxidation. Analysis through TEM, SEM-EDX, Raman and porosimetry gave a good description of the morphology, constitution of particles and their distribution in terms of particle sizes. NMR was a useful technique in understanding the aromatic and aliphatic components adsorbed onto soot that undergo a modification during soot oxidation. The aromatics on soot were analysed in detail in chapter 5. The conversion of total carbon in the initial amount of soot used in the reactor to CO_2 was quantified. The contribution of the most predominant aromatic, phenanthrene towards CO_2 production was also quantified. This model helped to understand the contribution of the small concentration of aromatics towards increased CO_2 yield.

It has been reported that CeO_2 and its mixed oxides can catalyse the reduction of NO_x by soot, removing both diesel pollutants, soot and NO_x simultaneously. Pisarello *et al.* have studied the simultaneous removal of NO_x and soot using catalysts made of

supports such as MgO, La₂O₃ and CeO₂ impregnated with Co, K or Ba [19]. The goal of this study was to explore the potential of CZA catalysts to accomplish soot combustion and in particular to identify the conditions under which this active oxygen-assisted mechanism contributes/prevails with regard to the NO₂-assisted combustion. In order to achieve this goal, soot combustion experiments were carried out with O₂ or with O₂+NO_x mixtures with several models and real soot samples of very different reactivities. Varying oxygen feed was understood to influence the rate of soot oxidation.

A relatively high flow rate of O₂ (200ml min⁻¹) increased the rate of soot oxidation but a considerably lower flow rate (50ml min⁻¹) and concentration of 50-75% of O₂ in the feed helped convert more soot to CO₂, in the presence of the Ag-K/CZA catalyst. The catalyst was capable of providing the O₂ stored in its lattice for soot oxidation as was observed in the case of inert gas analyses. The contact between the catalyst and soot was vital in improving the rate of oxidation.

Different catalysts were compared which included ceria-zirconia mixed oxides with similar composition but very different surface areas, bulk oxygen mobility and surface properties, which meant varied active oxygen production capacity, and a Pt catalyst with high NO₂ production capacity. Contribution of active oxygen from Ce-Zr mixed oxides to soot combustion with regard to the NO₂-assisted mechanism tends to become more important as temperature in the exhaust increases. The CZA catalysts were more effective than the Pt/SiC catalyst for soot combustion due to the contribution of active oxygen-assisted mechanism.

A synergistic effect was seen between NO₂ assisted and active oxygen promoted mechanism for soot oxidation using the combined Pt/SiC-Ag-K/CZA catalyst. Under loose contact conditions between catalyst and soot, it was noticed that the gas phase O₂ did not react directly with the soot instead the active oxygen species on the catalyst surface was transferred to the soot or aided the conversion of NO to NO₂ that propagated the soot oxidation. This mixed catalyst has been studied in further detail for PAH oxidation in chapter 5 and this has proven to be efficient for oxidation of the predominant three ringed PAHs and in oxidizing some of the heavier and more toxic aromatics.

References

1. B. Oger, Soot characterisation in diesel engines using laser-induced incandescence, University of Brighton, Ph.D. thesis, **2012**
2. C. A. Amann, D. C. Siegl, *Aerosol Science and Technology*, 1, (**1981**), 73 - 101.
3. R. L. Vanderwaal, *Combustion and Flame*, 112, (**1998**), 607-616.
4. M. Wentzela, H. Gorzawskib, K. H. Naumannc, H. Saatho, S. Weinbruchb, *Aerosol Science*, 34, (**2003**), 1347–1370
5. A. Braun, N. Shah, F. E. Huggins, K. E. Kelly, A. Sarofim, C. Jacobsen, S. Wirick, H. Francis, J. Ilavsky, G.E. Thomas, G. P. Huffman, *Carbon*, 43, (**2005**), 2588–2599
6. I. Atribak, F. E. López-Suárez, A. Bueno-López, A. García-García, *Catalysis Today* , 176, (**2011**), 404– 408
7. W. Merchan-Merchan, S. G. Sanmiguel, S. McCollam, *Fuel*, 102, (**2012**), 525–535
8. B. Docekal, V. Krivan, N. Pelz, *Fresenius Journal of Analytical Chemistry*, 343, (**1992**), 873-878
9. <http://xgsciences.com/products/graphene-nanoplatelets/grade-m/>
10. <http://xgsciences.com/products/graphene-nanoplatelets/grade-c/>
11. N. T. Thanh Tam, N. X. Nghia, N. T. Quynh, P. H. Khoi, P. N. Minh, *Journal of the Korean Physical Society*, 52, (**2008**), 1382-1385
12. B. Manoj, S. Sreelaksmi, A. N. Mohan, A. G. Kunjomana, *International Journal of Electrochemical Science*, 7 (**2012**) 3215 – 3221
13. U. Kirchner, V. Scheer, R. Vogt, *Journal of Physical Chemistry. A*, 104, (**2000**), 8908-8915
14. N. Guilhaume, B. Bassou, G. Bergeret, D. Bianchi, F. Bosselet, A. Desmartin-Chomel, B. Jouguet, C. Mirodatos, *Applied Catalysis B: Environmental*, 119– 120, (**2012**), 287– 296
15. N. Guillén-Hurtado, I. Atribak, A. Bueno-López, A. García-García, *Journal of Molecular Catalysis A: Chemical*, 323, (**2010**), 52–58
16. J. Oliver Müller, B. Frank, R. E. Jentoft, R. Schlögl, D.S. Su, *Catalysis Today*, 191, (**2012**), 106–111
17. A. Setiabudi, J. Chen, G. Mul, M. Makkee, J.A. Moulijn, *Applied Catalysis B*, 51, (**2004**), 9.
18. <http://www.lasurface.com/database/elementxps.php>
19. M. L. Pisarello, V. Milt, M. A. Peralta, C. A. Querini, E. E Miro', *Catalysis Today*, 75, (**2002**) 465–470

Speciation of diesel soot: Identification and quantification of polyaromatic hydrocarbons

5.1 Introduction

Polycyclic Aromatic Hydrocarbons (PAHs) are a group of Volatile Organic Compounds (VOCs), which have serious health problems associated with their emission into the atmosphere. The process of catalytic oxidation is an effective abatement process to control these PAH emissions. The different types of PAHs are ubiquitous pollutants in the atmosphere and they can react with atmospheric oxidants such as O_3 , NO_x ($NO + NO_2$), OH radicals and undergo photochemical reactions forming by-products, such as hydroxy-PAH, nitro-PAH, PAH-quinones, ketones, aldehydes, acids etc., that are highly toxic and carcinogenic. It is worth emphasizing that their mutagenicity has been shown to increase relative to their parent compounds. The oxidized forms are more toxic as these hydrophilic molecules can be easily adsorbed into the alveoli [1].

Three and four-ring PAHs are semi-volatile in nature [2] and these compounds partition between the gas and solid phases in the atmosphere while the five ringed PAHs and heavier ones tend to be mainly associated with particles having size $<1 \mu m$ [3,4]. Phenanthrene is one of the most abundant PAHs in the ambient air and is representative of VOCs in the atmosphere [5, 6]. A study in the city of Manchester, UK from the period of 1991 to 1998, measured phenanthrene concentrations in the range of $20-50 \text{ ngm}^{-3}$ [7]. Under ambient conditions, because of its high vapour pressure ($1.6 \times 10^{-2} \text{ Pa}$, 298 K) phenanthrene tends to exist primarily in the gas phase and it undergoes atmospheric oxidation in the gas-phase through reaction with the OH radical, with an atmospheric lifetime of $\sim 6-9$ hours [8]. Wang *et al.* investigated the formation of 9, 10-phenanthrenequinone from the reactions of gas-phase phenanthrene with OH radicals and ozone [6]. The existence of these high concentrations of phenanthrene and oxidized forms is more in the gaseous phase compared to that on the particulate phase. However it is still essential to understand the reactions in the particulate phase, as PAHs tend to get desorbed at high exhaust temperatures.

5.2 Soot - Direct insertion into the Mass Spectrometer

In this study, direct insertion of the soot into the mass spectrometer was carried out as mentioned in the experimental section and revealed that there were several PAHs adsorbed on the surface of the carbonaceous agglomerates [9]. These ranged from two ringed naphthalene to eight membered ringed structures, such as benzocoronene. The specific PAHs as shown in figure 5.1 included, naphthalene (128.06 gmol^{-1}), phenanthrene (178.08 gmol^{-1}), fluoranthene (202.08 gmol^{-1}), chrysene (226.08 gmol^{-1}), perylene (252.08 gmol^{-1}), indeno(1,2,3-cd)pyrene (276.08 gmol^{-1}), coronene (300.10 gmol^{-1}), dibenzo(ghi)perylene (326.11 gmol^{-1}) and benzo(a)coronene (350.11 gmol^{-1}) [10].

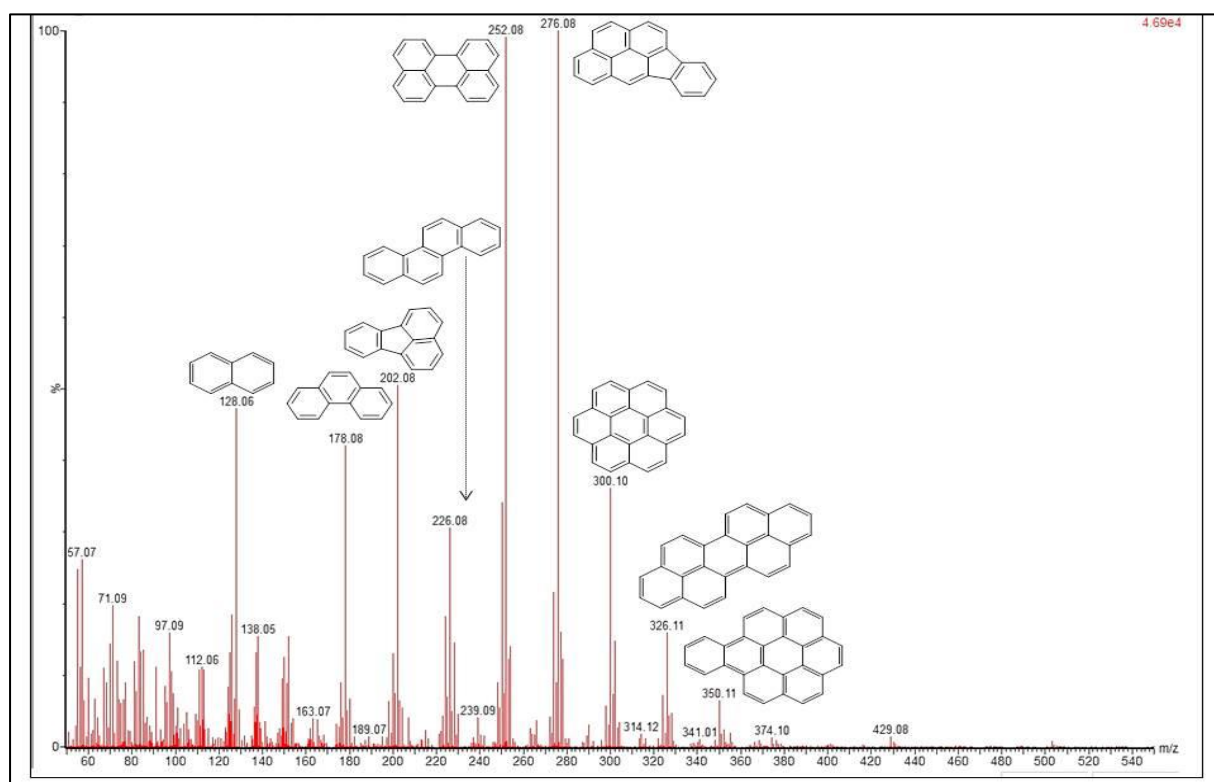


Figure 5.1 PAHs detected from direct soot insertion into Mass spectrometer

(PAH structures were drawn using ChemDraw Pro 13.0 and exported onto the image file for clarity of images)

5.3 Diesel soot extraction techniques

Extraction can be carried out on solid samples that contain volatile components. This is often a better approach than the use of evolved gas analysis, which can lead to

the volatile components undergoing reactions (such as cracking or cyclisation) during heat treatment. A number of extraction techniques have been widely used to extract the PAHs from environmental samples. These include Soxhlet extraction [11, 12], supercritical fluid extraction [13, 14], microwave assisted extraction [15, 16], ultrasonic assisted extraction [17, 18], accelerated solvent extraction, pressurized fluid extraction [19, 20] and sub-critical water extraction [21, 22]. The choice of extraction method depends on several factors such as type of analyte, available equipment, time etc. Different techniques can yield different results, however, due to incomplete or selective extraction. In this study several techniques have been probed starting with a simple approach of crude extraction down to a complex Soxhlet extraction technique that involved more efficient extraction over longer duration.

5.3.1 Crude extraction using DCM and acetone

The PAH components in diesel soot from a continuous regenerating trap of a diesel engine vehicle in USA were speciated by treating it with 15ml of acetone in a vial, shaking it thoroughly and extracting the products using a simple Buchner funnel. The products thus obtained were analysed by Gas Chromatography-Mass Spectrometry (GC-MS). The same procedure was carried out with a less polar solvent such as dichloromethane (DCM). The solvent was evaporated until complete dryness. About 0.8ml of deuterated acetone was then added as a solvent for Nuclear Magnetic Resonance (NMR) spectroscopic analysis (results seen in Chapter 4).

5.3.2 Minimising experimental error

In order to avoid sample-to-sample variability, a larger quantity of soot (1g) was extracted using 100ml of acetone as mentioned above. The solvent was allowed to evaporate and 5ml of DCM was added, from which an aliquot was analysed using GC-MS. The soot remaining was extracted three more times using 100ml of acetone each time and the process was repeated as above. The same process was repeated using DCM as the solvent for extraction. These samples were analysed using GC-MS.

5.3.3 GC-MS analysis on crude soot extracts

The GC-MS analysis of diesel soot reveals several polyaromatic hydrocarbons such as *naphthalene* (128.17g mol^{-1}), *acenaphthene* (154.21g mol^{-1}), *fluorene* (166.23g mol^{-1}), *phenanthrene* (178.011g mol^{-1}), *fluoranthene* (202.04g mol^{-1}), *pyrene* (202.25g mol^{-1}) and *cyclopenta (c, d) pyrene* (226.09g mol^{-1}) as seen in figure 5.2. These matched up to the results seen from mass spectrometric analyses by direct soot insertion.

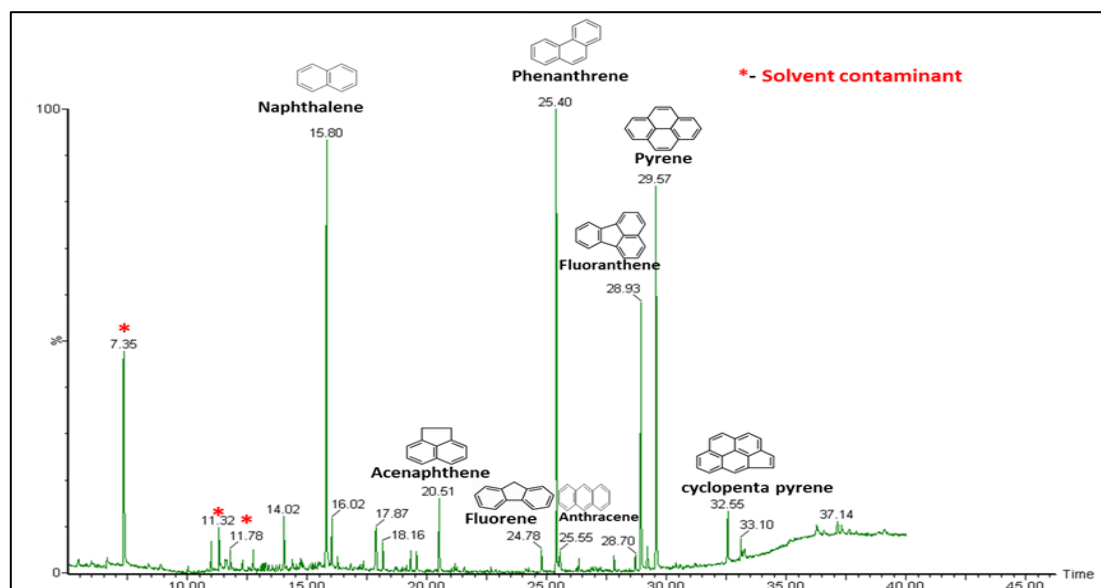


Figure 5.2 PAHs identified from crude extraction of diesel soot using GC analysis

These originate as a result of incomplete combustion of some of the hydrocarbons in diesel fuel forming the soot particulates at higher temperatures. Soot nucleation and growth results in the formation of these large hydrocarbons alongside some smaller ones.

The spectra in figure 5.3 revealed the products extracted in acetone from 1g of soot. The products were extracted four times using 100ml of acetone each time. The aromatics observed includes *toluene* (R.T-5.13, M.W-91.04), *naphthalene* (R.T-15.80, M.W-128.05), *acenaphthylene*(R.T-19.30, M.W-152.19), *acenaphthene* (R.T-20.52, M.W-154.21), *fluorene* (R.T-24.77, M.W-166.23), *phenanthrene* (R.T-25.40, M.W-178.01), *anthracene* (R.T-25.54, M.W-178.01), *fluoranthene* (R.T-28.91, M.W-202.04), *pyrene* (R.T-29.56, M.W-202.04) and *cyclo-penta(c,d)pyrene* (R.T-32.54, M.W-226.06). There was a gradual increase in the number of rings from toluene (1ring) to cyclopenta(c,d)pyrene (>5rings). This showed how the soot nucleates have grown to form

larger aggregates of polycyclics. The intensity of the peaks gradually reduced after the first extraction. Some of these could probably arise directly from diesel fuel used in engines.

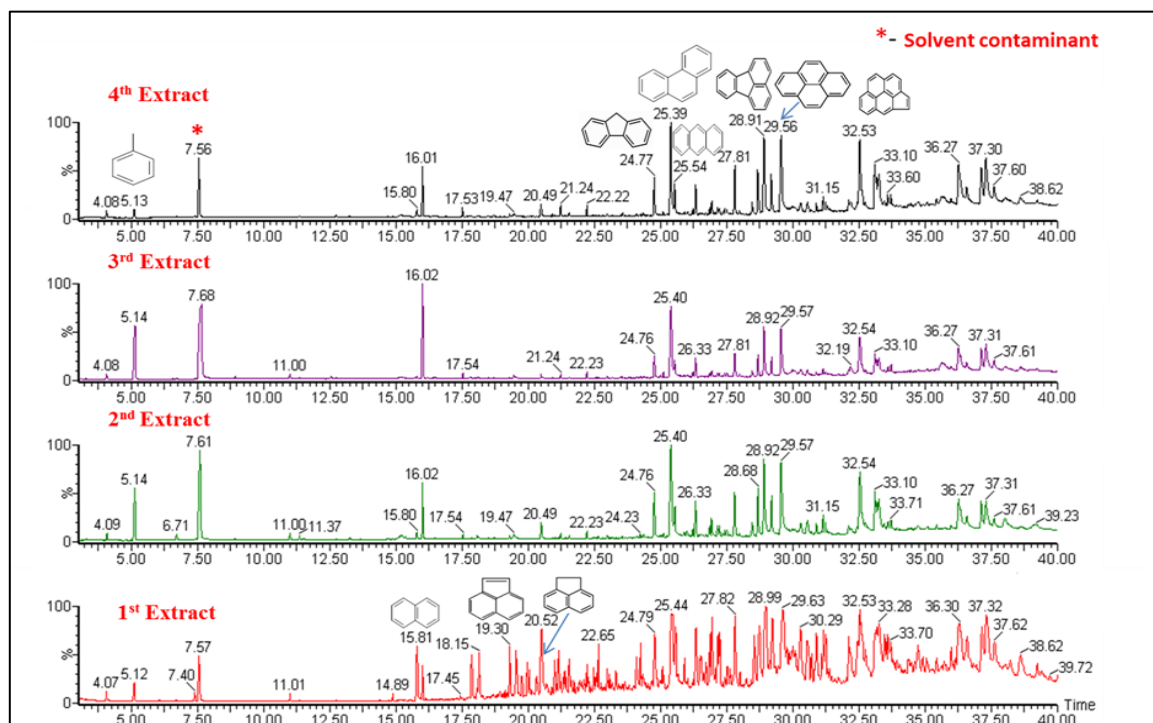


Figure 5.3 PAHs identified upon repeated extraction of soot using acetone – GC analyses

Similar products were observed in the spectra in figure 5.4 for the extraction of soot in DCM. Some PAHs were seen only in the acetone extract when compared to that in the less polar solvent extraction (DCM). Naphthalene, fluorene, phenanthrene, pyrene were the predominantly observed polyaromatics in diesel soot. Several extractions of the soot were required to obtain some of the products observed such as acenaphthylene and acenaphthene. This suggested that these hydrocarbons were present as a multilayer on the surface of the carbonaceous agglomerates. Thus even after repeated extraction of the same batch of soot, four times, several aromatics, mainly phenanthrene, were still present in relatively large concentrations. This also suggested that the efficiency of detection of the heavier PAHs through GC-MS was not very efficient as compared to that seen from the direct insertion of soot into the mass spectrometer. Thus a more sophisticated technique was needed for the analyses, which was chosen to be HPLC and LC-MS. Also a more efficient method of extraction was needed for complete extraction of the PAHs.

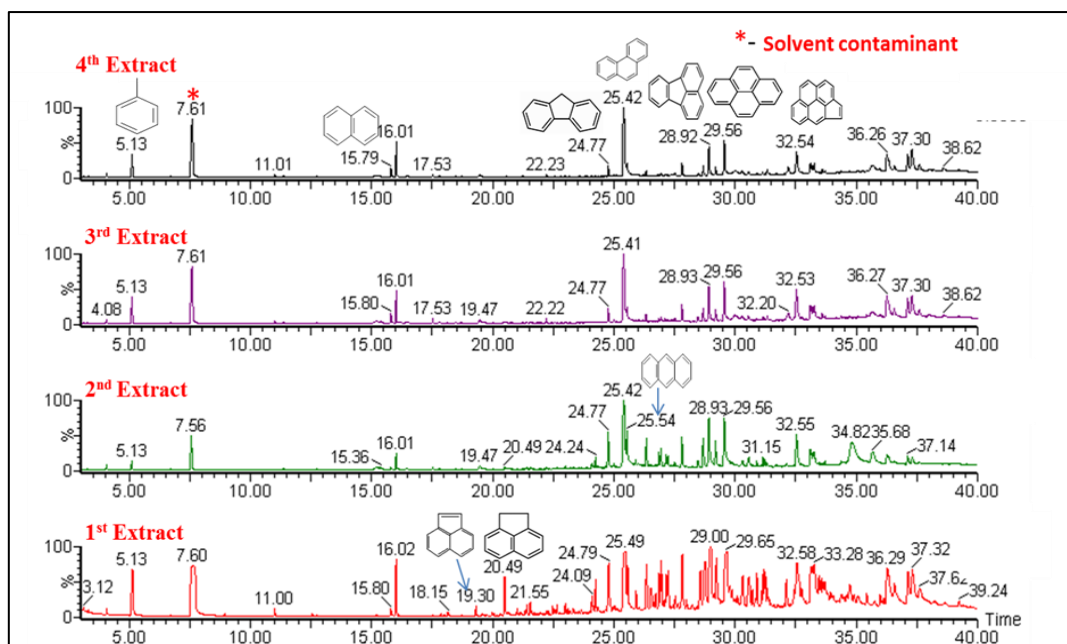


Figure 5.4 PAHs identified upon repeated extraction of soot using DCM – GC analyses

5.3.4 HPLC - Identification of polyaromatic hydrocarbons

5.3.4.1 HPLC analysis of the Polyaromatic hydrocarbon standard

A standard that consisted of 10 μ g each of 16 polyaromatic compounds in 1ml of the solution as described in the experimental section in chapter 2 was used for quantification of the aromatics in diesel soot. This was carried out using HPLC on a Zorbax Eclipse Plus phenyl hexyl column (4.6 x 150mm, 3.5 μ sized particles) fitted with an Agilent Zorbax Eclipse Plus phenyl hexyl analytical guard column (4.6 x 12.5mm, 5 μ), with water (A) and acetonitrile (B) being the mobile phases. A UV detector was applied to detect the compounds with absorbance observed at 254 nm. A gradient program was used for the efficient separation of the aromatics as described in detail in chapter 2.

Figure 5.5 identified the various PAHs present in the standard as per those observed in the data sheet. Table 5.1 showed the various compounds and their retention times.

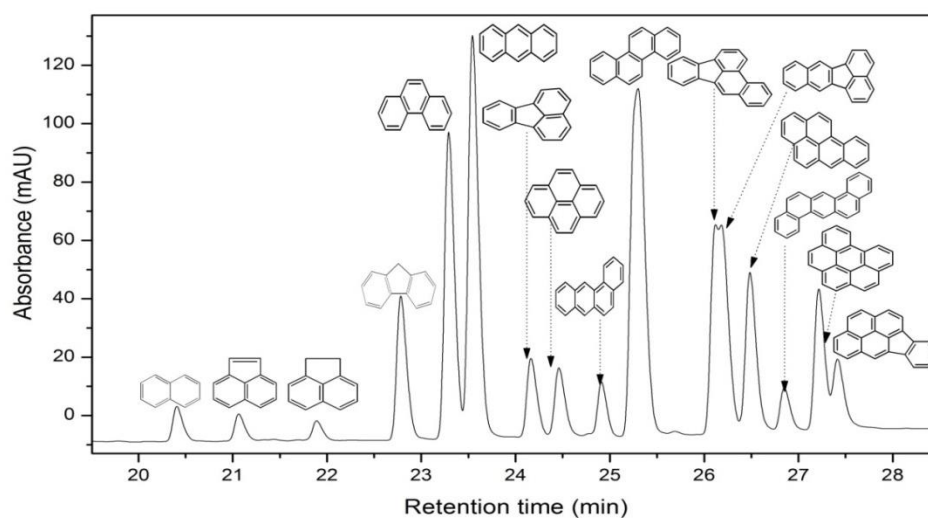


Figure 5.5 PAHs identified in the standard from Sigma Aldrich

A list of the various PAHs present in the standard has been listed along with their retention time and molecular weights.

Table 5.1 PAHs and their corresponding retention times and molecular weights

Sl.No	Compounds	Retention time (min)	Molecular weight (g mol ⁻¹)
1	Naphthalene (C ₁₀ H ₈)	20.4	128.05
2	Acenaphthylene (C ₁₂ H ₈)	21.06	152.19
3	Acenaphthene (C ₁₂ H ₁₀)	21.89	154.21
4	Fluorene (C ₁₃ H ₁₀)	22.78	166.23
5	Phenanthrene (C ₁₄ H ₁₀)	23.29	178.01
6	Anthracene (C ₁₄ H ₁₀)	23.54	178.01
7	Fluoranthene (C ₁₆ H ₁₀)	24.16	202.04
8	Pyrene (C ₁₆ H ₁₀)	24.46	202.04
9	benzo(a)anthracene (C ₁₈ H ₁₂)	24.9	228.28
10	Chrysene (C ₁₈ H ₁₂)	25.29	228.28
11	benzo(b)fluoranthene (C ₂₀ H ₁₂)	26.12	252.30
12	benzo(k)fluoranthene (C ₂₀ H ₁₂)	26.18	252.31
13	benzo(a)pyrene (C ₂₀ H ₁₂)	26.48	252.31
14	dibenzo(a,h)anthracene (C ₂₂ H ₁₄)	27.41	278.34
15	benzo(ghi)perylene (C ₂₂ H ₁₂)	26.84	276.33
16	indeno(1,2,3-cd)pyrene (C ₂₂ H ₁₂)	27.21	276.33

5.3.4.2 HPLC analysis on 4 step extracted soot combined with ultrasonication

This process was carried out using 1g of soot. The first solvent for the extraction was n-heptane, for which 50ml of the solvent was used, followed by ultrasonication for 15 minutes at each stage. This helped in efficient mixing of the solvent and soot particles leading to good extraction. This was followed by toluene (60ml), assisted by ultrasonication. The third stage involved the use of chloroform-ethanol (69.3ml Chloroform + 0.7ml Ethanol) and finally methanol (50ml) was used.

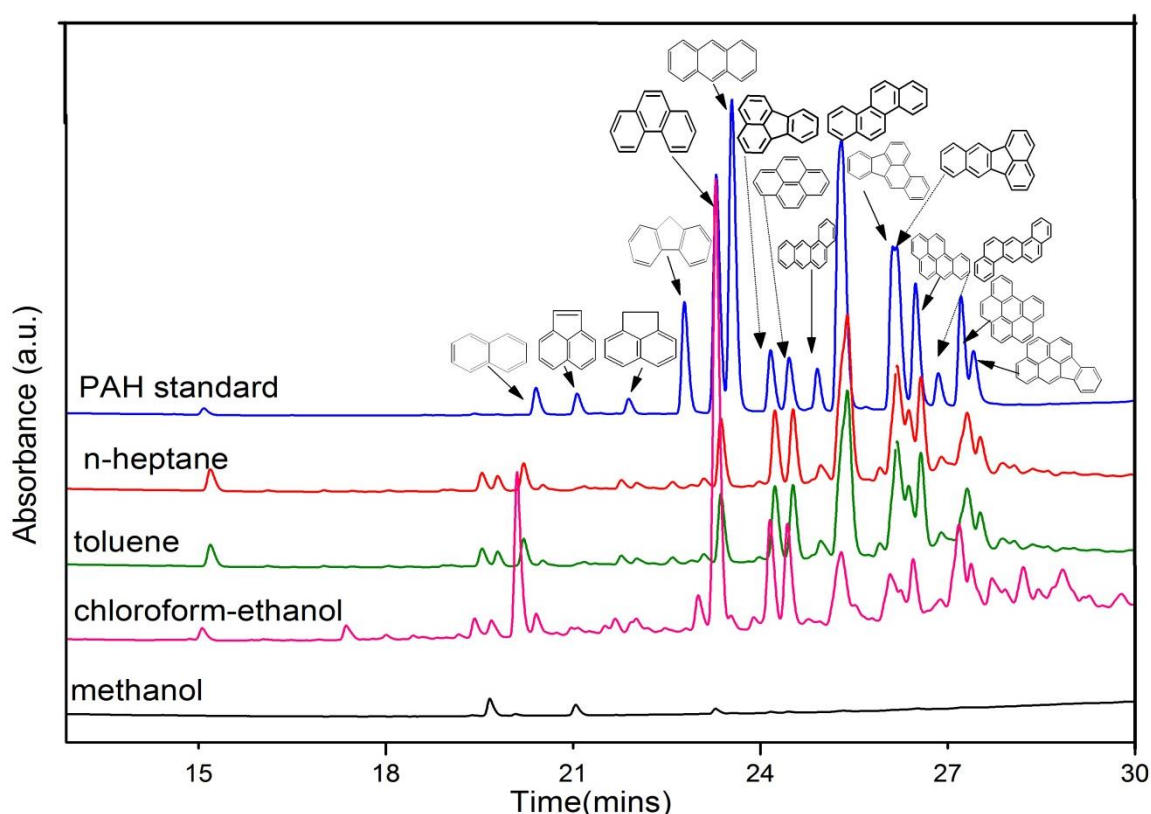


Figure 5.6 HPLC analyses: PAHs observed on 4 step extraction of diesel soot

Figure 5.6 showed that the compounds present in the standard (represented in blue) matched up with several peaks present in the extracts mentioned above, of which toluene and chloroform-ethanol were the most efficient solvents for this purpose. The major peaks were observed for naphthalene, phenanthrene, pyrene, chrysene, benz(a)anthracene, chrysene, benzo (b) and (k) fluoranthene, benzo(a)pyrene, dibenzo anthracene, benzo(ghi)perylene and indeno(1,2,3-cd) pyrene, alongside some unknown compounds. These compounds matched the findings by several researchers working on soot formation and oxidation [23-25].

5.3.4.3 HPLC analysis on Soxhlet extracted diesel soot

This was carried out in a Soxhlet apparatus using toluene (85ml) for 1 g of soot. The process consisted of heating the solvent until it evaporated, the vapours rose to the level of soot in the thimble causing the extraction of the hydrocarbons in soot and this then was condensed back into the round bottom flask, through the siphon arm, once it was completely filled with the solvent. This process occurred continuously for several such cycles over a 16 hr time period, leading to efficient extraction of the soot. Toluene and chloroform have been widely used for this purpose.

The concentration of hydrocarbons by toluene Soxhlet extraction of 1g of soot is 0.15mg (0.015% of the total soot). The figure 5.7 below shows that the majority of aromatics are extracted using toluene. The efficiency of the extraction depends on the type of solvent, the time period and the kind of aromatic species present in soot.

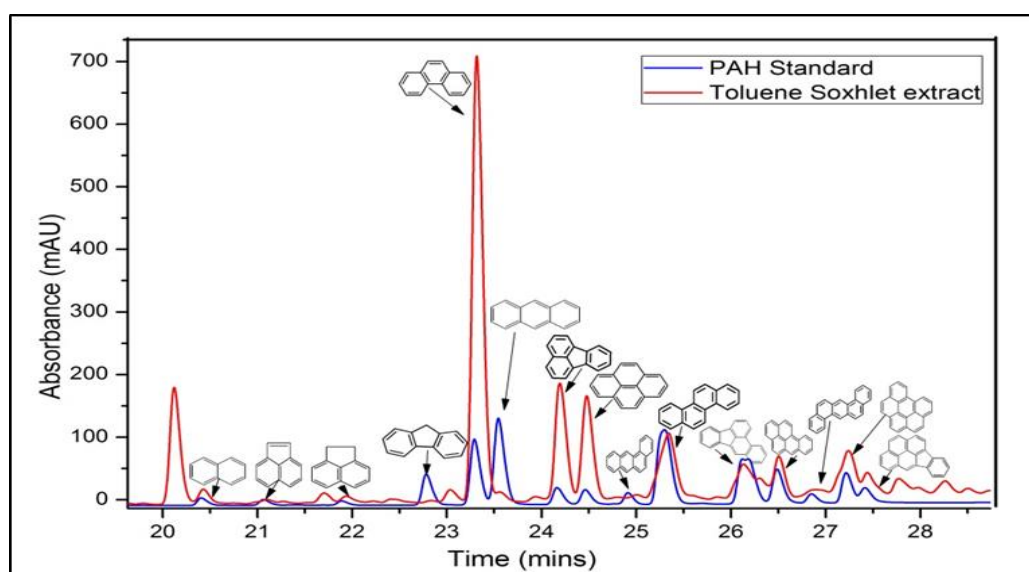


Figure 5.7 HPLC analyses: PAHs observed on Toluene-Soxhlet extraction of diesel soot

On using chloroform-ethanol solvents, similar PAHs were extracted. The concentration of the PAHs from this extraction was significant (0.12 mg/0.012% of the total soot) but lower when compared to the toluene Soxhlet extract. Several unknown compounds have been identified which could indicate the presence of hydrocarbons with different functionalities such as oxygenated/nitrated/sulphated polyaromatics. Again, phenanthrene was detected as the major PAH present in the soot. From the scale seen in figure 5.7 and figure 5.8, it was noted that the concentrations of the aromatics

were twice as high in the case of toluene Soxhlet compared to the chloroform Soxhlet extracts.

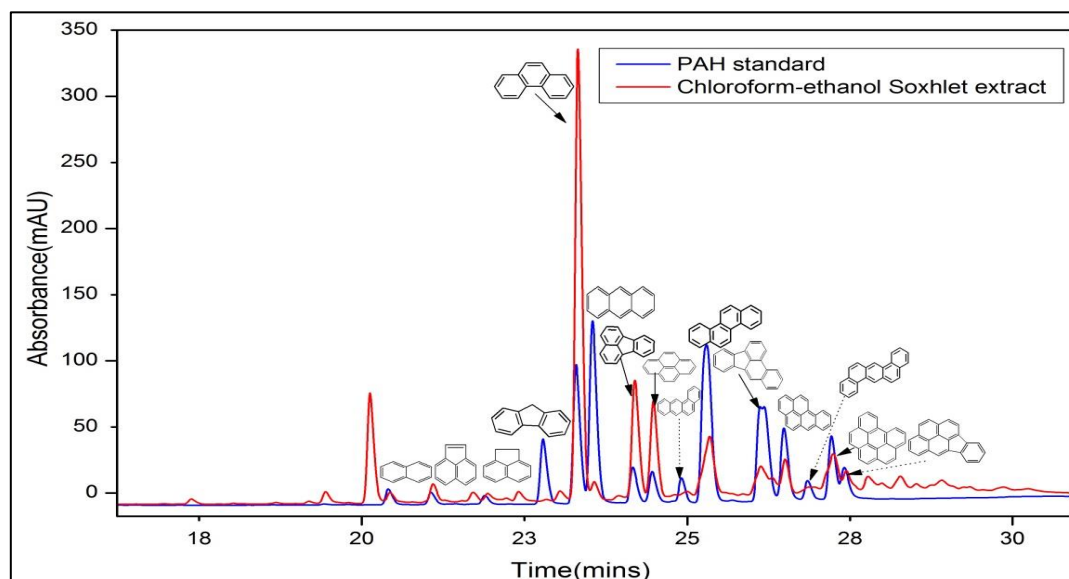


Figure 5.8 HPLC analyses: PAHs observed on chloroform-ethanol Soxhlet extraction of diesel soot

The extraction efficiencies have been summed up in the table 5.2. 1g of soot was repeatedly extracted using the crude extraction technique. The ultrasonication helped improve extraction to an extent and using different solvents with the aim of extracting different functionalities on these aromatics was the key factor in determining the efficiency of extraction. Soxhlet extraction was a cumbersome process involving long durations (16hours) but yielded most of the aromatics adsorbed on the soot. It has been observed later in this chapter that the desorption of the aromatics from the surface of the soot was faster and more efficient upon thermally inducing desorption, by heating the soot over a temperature range.

Table 5.2 Extraction efficiencies of PAHs in diesel soot by various methods and solvents

Sl. No	Extraction method	Concentration of PAHs in 1g soot (g)	Extraction efficiency (%)
1	Toluene Soxhlet	0.15	0.015
2	Chloroform-ethanol Soxhlet	0.12	0.012
3	4 step extraction with ultrasonication	0.02	0.002
4	Crude extraction - acetone- 4 times	0.048	0.0048
5	Crude extraction - DCM- 4 times	0.054	0.0054

5.4. Quantification of Polyaromatic hydrocarbons

5.4.1 Quantification of PAHs in soot – Extraction

The concentration of the individual PAHs in soot were measured on comparison with the standard obtained from Sigma Aldrich. The standard was diluted and then injected into the HPLC to obtain the area counts for the 16 compounds, as shown in chapter 2. The calculation for the calibration factor, in order to calculate the concentration of each of these 16 compounds was shown in the appendix.

Table 5.3 showed the concentration of the various PAHs in soot identified as a comparison with the standard. This showed that the best method of extraction, yielding maximum concentration of the PAHs was toluene Soxhlet extraction. The concentrations were calculated as explained in chapter 2.

Table 5.3 Total Concentrations of the PAHs extracted from the various extractions of diesel soot

Sl.No	Method of extraction	Total concentration of PAHs (mM)/g of soot
1.	Toluene Soxhlet	1.6874
2.	Chloroform Soxhlet	0.8992
3.	4 step extraction	
1 st step	n-heptane	0.422
2 nd step	toluene	0.9055
3 rd step	Chloroform-ethanol	0.667
4 th step	methanol	0.061
	total	2.055

The four step extraction was capable of obtaining maximum concentration of the aromatics (2.055mM/g of soot) as shown from the table above, however this involved a more complicated set-up for extraction compared to the Soxhlet extraction method. Toluene and chloroform-ethanol are by far the best solvents in either case of extraction thus proving that most of the aromatics are extracted in a nonpolar solvent. This analysis was adapted from a finding by H. J. Gitze, J. Schneider and H. G. Herzog in 1994 [26,27]. They were able to use a modified Soxhlet extraction technique called Soxtec extraction wherein the sample was extracted during the process of boiling the solvent as opposed to the that in the condensed solvent, as in the case of Soxhlet extraction. In the second phase the lifted extraction thimble was washed out nearly quantitatively by

the refluxed solvent and in the third phase the clean solvent was collected in the upper part of the system for the next analysis, while the sample was concentrated in the lower part. In total only 4h (2h boiling, 1h wash-out and 1h concentration) gave a well reproducible recovery that was similar to that of Soxhlet-extracts which was a 16h long procedure.

In their study they used soot particles from exhaust fumes, collected by blowing through a self-constructed collection apparatus with a borosilicate/glass fibre extraction thimble inside subjected to a load of 1400 r.p.m, and 460 kW into the by-pass line of the exhaust gas. The eluents were exchanged from heptane/benzene to chloroform and methanol and the compounds were fractionated into the different classes, wherein the aliphatic compounds were fractionated using heptane while the nitro-PAH were fractionated using chloroform. The same concept was applied here but using these as solvents for extraction [26]. The identification of aliphatic compounds was done using NMR as shown in chapter 4.

The various polyaromatic hydrocarbons fell into 4 categories - two ringed structures 2R-naphthalene, three ringed structures 3R-acenaphthylene, acenaphthene, fluorene, phenanthrene, anthracene, four ringed PAHs 4R- fluoranthene, pyrene, chrysene), five ringed structures 5R-benzo(b)fluoranthene, benzo(k)fluoranthene, benzo(a) pyrene, dibenzo(a,h)anthracene and six ringed PAHs 6R-benzo(ghi)perylene, indeno(1,2,3-cd)pyrene. Figure 5.9 represents the concentrations of the PAHs from various extractions of soot using different techniques as listed in table 5.4. It clearly showed that the toluene Soxhlet extraction had maximum concentration of these aromatics in a one-step extraction process involving a longer duration and more efficient contact of the solvent with the soot. The four step process involved a thorough extraction of several functional groups linked to the aromatics alongside the major PAHs as was shown by Gittze *et al.* in their work on the extraction of soot [27]. Higher concentration of the non-polar aromatics, were extracted using non polar solvents such as toluene and chloroform. A combination of chloroform (non-polar) and ethanol (polar) was used to extract the different functionalities separately and more efficiently. Thus in the presence of this combination several unknown compounds were also identified.

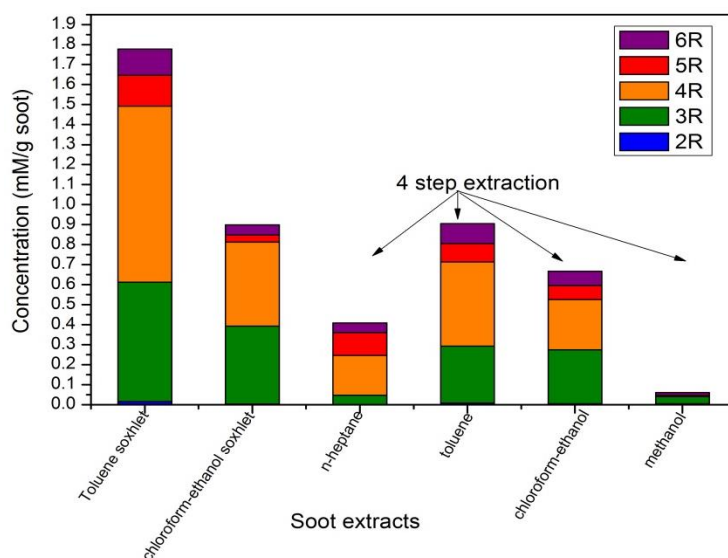


Figure 5.9 HPLC analyses: Quantification of various PAHs from different extractions of soot

Major concentrations of these PAHs were the three ringed and four ringed structures, mainly phenanthrene, as was detected from HPLC on quantification. Heavier five and six membered ring PAHs were present only in very small concentrations as shown in table 5.4. Table 5.4 represented the individual concentrations of the PAHs in diesel soot matched to the standards and a concentration of the total PAHs present in mmol/g of soot.

Table 5.4 Concentrations of individual PAHs observed on different extractions of diesel soot

Sl.No	Compounds	Retention time	Response factor	SOXHLET EXTRACTION		4 STEP EXTRACTION-ULTRASONICATION			
				Concentration-Toluene (mM)/g soot	Concentration-Chloroform-Ethanol (mM)/g soot	n-heptane (mM)	Toluene (mM)	Chloroform ethanol (mM)	Methanol (mM)
1	Naphthalene	20.407		0.0154	0.0032		0.0085	0.005	0.005
2	Acenaphthylene	21.064	875.22		0.090				0.034
3	Acenaphthene	21.89		0.092	0.064	0.047	0.080	0.105	
4	Fluorene	22.782	4732.4		0.001		0.021	0.025	
5	Phenanthrene	23.29	10723	0.505	0.229		0.183	0.138	0.001
6	Anthracene	23.543	16161		0.005	0.013		0.002	
7	Fluoranthene	24.163	3204.6	0.431	0.21	0.077	0.204	0.11	
8	Pyrene	24.46	2905.4	0.396	0.189	0.081	0.183	0.123	
9	Chrysene	25.298	22222	0.052	0.021	0.041	0.034	0.018	
10	benzo(b)fluoranthene	26.121	17002	0.066	0.026	0.004	0.054	0.024	
11	benzo(k)fluoranthene	26.183	7968.6	0.024	0.009	0.054		0.009	
12	benzo(a)pyrene	26.485	7654.8	0.066		0.040	0.038	0.025	0.008
13	dibenzo(a,h)anthracene	26.849	2554.5			0.016		0.012	
14	benzo(ghi)perylene	27.215	7254.3	0.083	0.033	0.029	0.066	0.044	
15	indeno(1,2,3-cd)pyrene	27.413	5066.8	0.047	0.019	0.020	0.034	0.027	0.013
16	Total			1.68	0.89	0.42	0.90	0.66	0.06

Toluene is an ideal solvent for extraction of the small two ringed naphthalene, more complex three ringed phenanthrene, larger four membered structures such as fluoranthene and pyrene and also heavier PAHs such as benzo(b) and (k)fluoranthene, benzo(a)pyrene (highly carcinogenic) alongside six membered benzo(ghi)perylene and indeno(1,2,3-cd)pyrene. The detection of these compounds through GC-MS analysis also showed the presence of these compounds, as shown in section 5.3.3. These data have been verified by comparison with studies in literature that have shown toluene to be an ideal solvent for extraction. The four step method of extraction was useful in proving this fact as shown from the extraction efficiencies of toluene over the other solvents. A general practice of extraction, using different solvents, followed by filtration and a clean up procedure was carried out in the analysis of atmospheric samples prior to HPLC analysis. Quantification of benzo(a) anthracene was not possible as the standard and dilutions showed very insignificant peaks for this compound thereby making the analysis difficult. This compound was not identified in the extracts of soot and was therefore not analysed further.

5.4.2 Quantification of PAHs in soot during oxidation

Qualitative and quantitative analyses of PAHs emitted during soot combustion was performed at 300, 400, 500 and 600°C (uncatalysed soot - 690°C) as mentioned in the experimental chapter 2, by passing 200 ml min⁻¹ of various gas feeds for 1 hour over a catalyst and/or soot reactor bed. The catalyst and soot mixture were mixed in a 10:3 weight ratio, maintaining a GHSV of 30,000 h⁻¹, for which 0.0850 g of catalyst and 0.0254 g soot were mixed together in a vial establishing a loose contact, representative of the real exhaust scenario. These conditions were used for each experiment. For uncatalysed soot oxidation, the mass used was 0.0254g for each experiment. The products desorbed through the process of combustion of soot were trapped in-line into a vial containing acetone held in an ice-acetone bath. In addition to in-line trapping, the spent catalyst/unreacted soot mixture post reaction was analysed for adsorbed PAHs by solvent extraction with HPLC grade dichloromethane. These analyses were carried out using the following gas mixtures: He (100%); He (80%) O₂ (20%); He (80%) CO₂ (20%); He (91.85%) O₂ (8%) NO (0.15%) and exhaust gas mix (A synthetic exhaust gas mixture containing O₂ (8%), CO (1%), C₃H₈ (0.01%), C₃H₆ (0.024%), NO (0.03%) and N₂ (90.936%)).

The products collected during the combustion, in acetone, and PAHs still adsorbed to the catalyst/soot surface, post reaction, were evaporated and the condensed PAHs were dissolved in acetonitrile (1 ml). The samples were then analysed by high performance liquid chromatography (HPLC) on an Agilent Technologies 1200 series chromatograph as mentioned in chapter 2. Selected samples were also analysed by liquid chromatography-mass spectrometry (LC-MS) as mentioned in chapter 2, with the aim of identifying any products of partial oxidation of PAHs.

5.5 Desorption of Polyaromatic hydrocarbons on thermal treatment

5.5.1 Desorption upon soot treatment with helium

This analysis was carried out on a batch of soot under a flow of 100% He (200ml min⁻¹) and the products collected in acetone were analysed according to the procedure described in section 5.42. The sample post reaction was also analysed in a similar manner. Figure 5.10 showed the products trapped in acetone. This revealed that a large proportion of the volatile components in the diesel soot were three ringed PAHs consisting of acenaphthylene, acenaphthene, fluorene, anthracene and mainly phenanthrene. The major contribution was from phenanthrene. This was seen to increase with increase in temperature until 600°C.

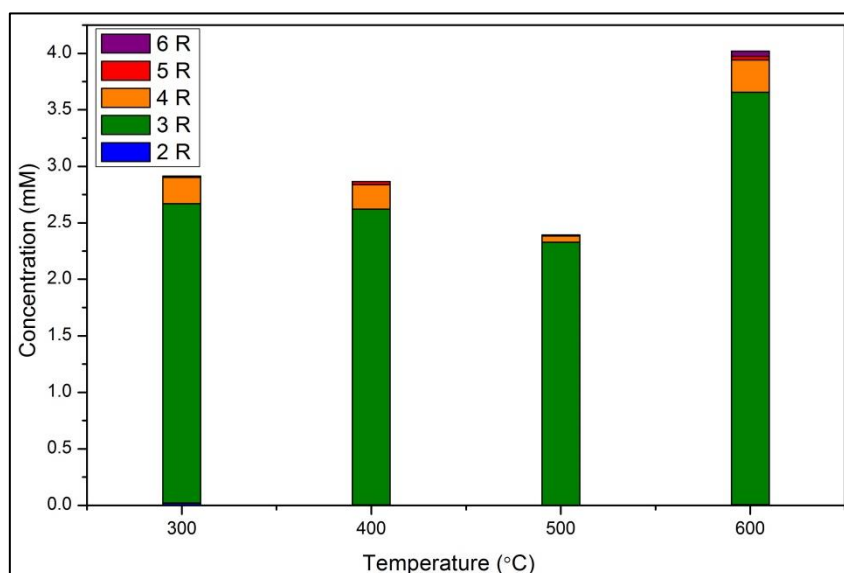


Figure 5.10 HPLC analyses: Qualitative analysis of trapped PAH combustion products from soot (0.0254 g) under 200 ml/min flow of He –Products in acetone

Table 5.5 Concentrations of PAHs desorbed under helium atmosphere-products in acetone (0.0254 g soot)

Temperature (°C)	2 rings (mM)	3 rings (mM)	4 rings (mM)	5 rings (mM)	6 rings (mM)
300	0.02	2.6	0.2	0.01	0
400	0.003	2.6	0.2	0.03	0
500	0.003	2.3	0.05	0.005	0.004
600	0.006	3.6	0.3	0.031	0.05

Heavier PAHs tend to desorb only at higher temperatures as was seen from table 5.5, for the five and six membered ring structures as compared to smaller PAHs (2, 3, 4 ringed structures). The three ringed PAHs desorbed more slowly because of their lower volatility. This test, in the absence of catalyst and O₂ feed gives an indication of the PAHs desorbed from the surface of the soot. The concentration of aromatics desorbed from the surface of the soot was found to be almost twice that on the surface of the soot post reaction as seen in figure 5.11. This concentration was also higher than that extracted from soot at room temperature, indicating that most of these three ringed aromatics tend to get desorbed from the surface of the soot only at higher temperatures. At temperatures of around 550-600°C, the PAHs were completely desorbed off the surface of the soot and were collected in acetone.

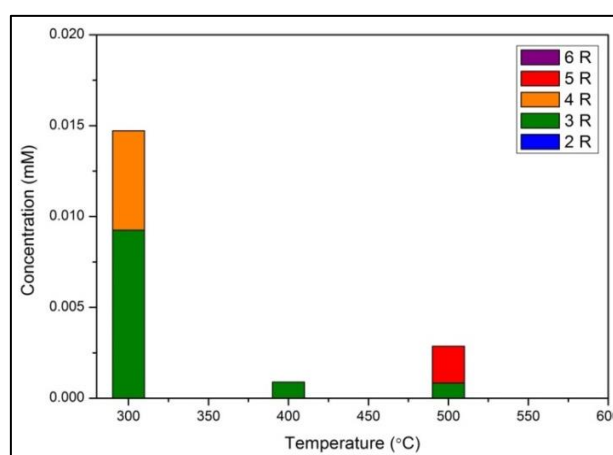


Figure 5.11 Qualitative analysis of trapped PAH combustion products from soot (0.0254 g) under 200 ml/min flow of He –soot post reaction

The soot used in these experiments was collected from a CRT filter and is not a model soot such as carbon black. It represented an inhomogeneous concentration of PAHs present. Thus the small differences in the concentrations of PAH combustion products collected in further analyses may be simply due to inconsistencies in the composition of the soot since the sample size here is small. Table 5.6 represented the decrease in the concentration of phenanthrene present on the surface of the soot observed post reaction with increase in temperature.

Table 5.6 Concentrations of PAHs desorbed under helium atmosphere - soot post reaction

Temperature (°C)	2 rings (mM)	3 rings (mM)	4 rings (mM)	5 rings (mM)	6 rings (mM)
300	-	0.009249	0.005468	-	-
400	-	0.000891	-	-	-
500	-	0.000839	-	0.002021	-
600	-	-	-	-	-

Table 5.7 indicated the highest concentrations of PAH represented by phenanthrene (3rings), followed by pyrene (4rings) and the highly carcinogenic benzo(a)pyrene (5rings). These PAHs were quite difficult to desorb off the surface and this process occurred only at higher temperatures (600-700°C)

Table 5.7 Concentrations of phenanthrene (most abundant), pyrene (second most abundant) and benzo(a)pyrene (highly carcinogenic) on desorption under helium

Temperature	3R			4R		5R	
	Products in acetone (mM)	Soot post reaction (mM)	Total	Products in acetone (mM)	Soot post reaction (mM)	Products in acetone (mM)	Soot post reaction (mM)
300	2.6	0.009	2.5	0.1	-	0.01	-
400	2.5	0.002	2.5	0.1	-	0.03	-
500	2.2	0.0004	2.2	0.05	-	0.007	0.002
600	3.4	-	3.4	-	-	-	-

Several scientists have tried to understand the desorption of PAHs from the surface of soot samples. Guilloteau *et al.* have studied the desorption of three ringed PAHs such as phenanthrene, anthracene, four ringed pyrene, fluoranthene and five ringed benzo(k) fluoranthene, present in the soot produced from a premixed flame of liquid fuels consisting of decane, propyl benzene and propyl cyclohexane in the ratios 74:15:11. This was done using HPLC offline analysis as was the case our study [27]. The same kind of analyses was carried out by Bedjanian and co-workers for the five and six membered ring structures such as benzo(ghi)perylene (BghiP), indeno(1,2,3-cd)pyrene (IdP), anthanthrene (Antha), dibenz(ah)anthracene (DBahA), dibenzo(ae)pyrene (DbaeP) [28].

This study was identical to that carried out in our research using a fixed bed reactor. The soot source was from a real diesel exhaust trap that introduced complexities with respect to the change in concentrations along the desorption process with increase in temperature. The process of PAH desorption under helium was similar to the studies conducted by the above groups but the fixed bed reactor set-up and the realistic exhaust soot, used in our study was indicative of the kinetics involved in a real diesel engine. Also, the PAHs on the kerosene soot (used by Guilloteau and Bedjanian *et al.* were known to form a monolayer on the carbonaceous soot as opposed to a multilayer formation in the case of diesel soot [27, 28]. In the case of kerosene/flame soot, there was a homogeneous desorption of PAH continuously from the surface of the soot as opposed to a heterogeneous desorption of PAHs from the diesel soot (our study). The rates of soot oxidation have been studied in detail in chapter 4.

5.5.2 Desorption of PAHs during soot oxidation under 20% O₂/He

The uncatalysed soot oxidation led to the desorption of several PAHs with increase in temperature. Most of PAH desorption occurred between 400-500°C, where the rate of the soot oxidation was maximum as shown in figure 5.12(a). The major concentration arose from the three membered ring structures, predominantly phenanthrene as could be seen from the analysis of products condensed in the line. The line connected the reactor head to the trap and is of a very short path length, heated upto around 120°C. This was believed to prevent the condensation of the PAHs. But on analysing the products from the line (figure 5.12 b) a large concentration was seen to be

condensed into the line. This could be due to their less volatile nature. Most of the volatiles in the presence of the oxidising atmosphere were being oxidised either to partial oxygenated products and then to CO₂ or directly to CO₂ as opposed to merely being desorbed.

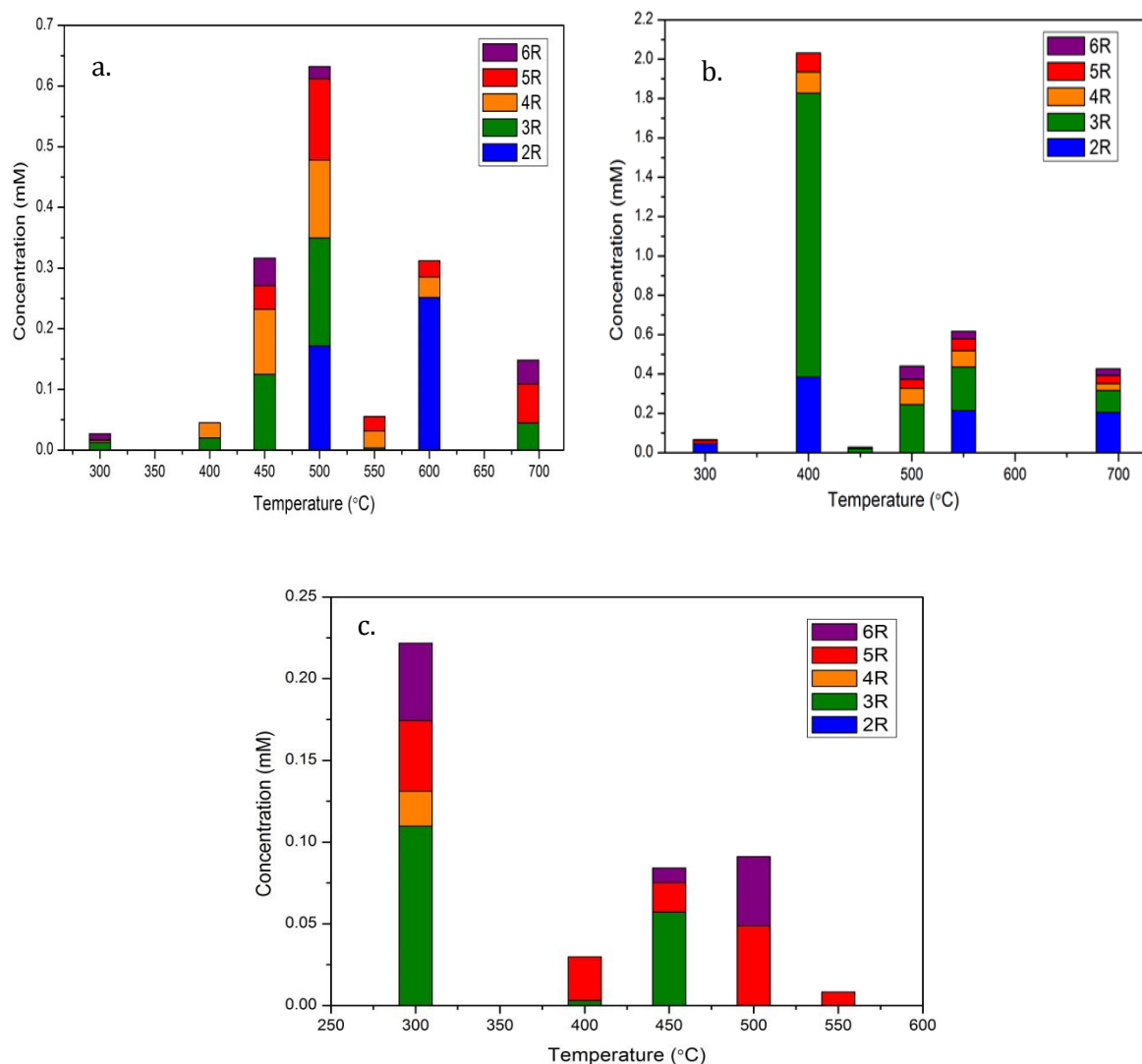


Figure 5.12 Concentration of PAHs upon desorption from uncatalysed soot oxidation under 20% O₂/He, 200 ml/min - a) products in acetone, b) line wash, c) post reaction

On analysing the surface of the soot (figure 5.12c), it was observed that there was a small concentration of the three ringed phenanthrene still present at 300 and 450°C. This was later completely desorbed by 700°C. There was a steady decrease in the PAHs observed on the surface of the soot post reaction, as thermal desorption and oxidation took place.

In the presence of the catalyst, a completely new situation arose as was observed from the products in acetone and those condensed in the line (figure 5.13 a, b). This indicated that there was a significant drop in concentration of the desorbed aromatics (mainly heavier 4/5/6 aromatics) compared to that observed in the case of uncatalysed soot oxidation. This indicated that the catalyst was capable of oxidising the PAHs to smaller partially oxygenated species such as 9, 10 phenanthredione etc., which is described in the later part of this chapter.

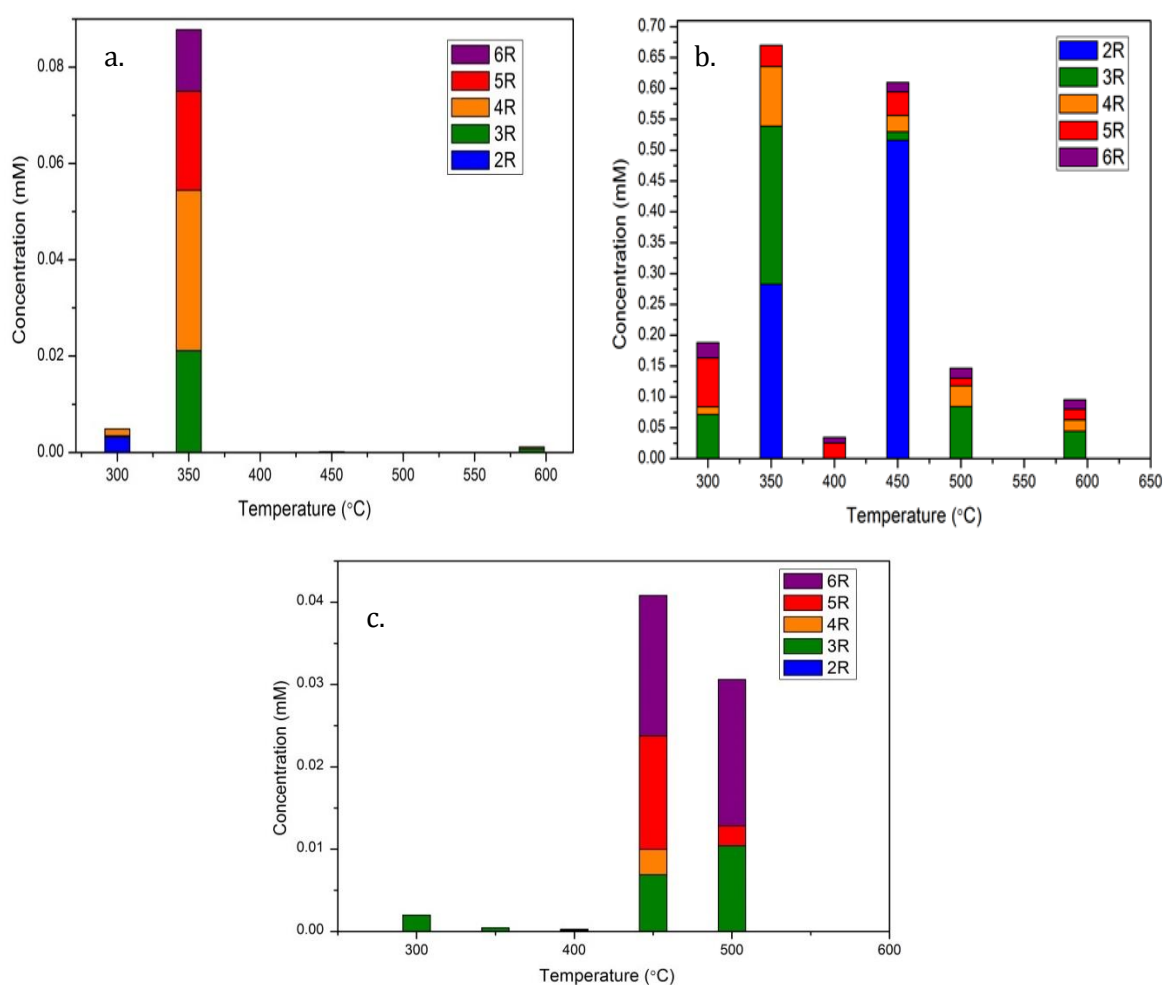


Figure 5.13 Concentration of PAHs upon desorption from catalysed soot oxidation under 20% O₂/He, 200 ml/min - a) Products in acetone, b) line wash, c) post reaction

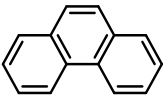
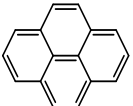
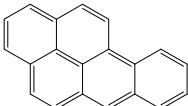
Three and four ring aromatics decreased in concentration between 350-500°C, as observed from the products in acetone (figure 5.13a), however, significant concentrations remained on the surface between 450-500°C, suggesting some difficulty in the oxidation of these species. Only a small concentration of the heavy five and six membered ring structures were easily desorbed from the surface of the soot, while most

of it tends to still remain on the surface until 500°C (figure 5.13 c). A similar situation was observed in the case of uncatalysed soot oxidation as seen from figure (5.12 c), reflecting the fact that these heavy aromatics were non-volatile and required a lot of thermal energy to be desorbed or oxidised to CO₂. On observing the soot post reaction at 550 and 600°C, in the presence of catalyst, there were no PAHs observed indicating either complete desorption or more probably complete oxidation of the PAHs to CO₂ compared to uncatalysed oxidation.

Phenanthrene was seen to condense in the line as seen from figure 5.13(b), from the surface of the soot. Pyrene was readily desorbed from the surface at low temperatures (300-400C). The inhomogeneity of soot was clearly evident from the varied concentrations of benzo(a)pyrene desorbed from the surface of the soot in the presence of an oxidative atmosphere. Fairly high concentrations were evolved even at very high temperatures indicating that the heavy aromatics were not easily oxidisable.

The results for catalysed soot oxidation as shown in table 5.8 showed that there could be rapid oxidation of several PAHs to CO₂, in the presence of O₂. The concentrations of phenanthrene, pyrene and benz(a)anthracene desorbed from the surface was very low indicating that these molecules might have been totally oxidised to CO₂ or formed partial oxygenated products that led to CO₂ formation. The process of oxidation was complete by 600°C indicating that the catalyst has been efficient not just in carbon combustion but also in PAH combustion. Only extremely small amounts of phenanthrene (~nil) were desorbed and collected at 590°C. This data was in good correlation with the maximum activity of soot shown in TGA and oxidation results as shown in chapter 3.

Table 5.8 Concentrations of Phenanthrene, pyrene and benzo(a)pyrene desorbed under 20%O₂/He in presence of a catalyst

Temperature (°C)									
	Products in acetone (mM)	Line wash	Soot post reaction (mM)	Products in acetone (mM)	Line wash	Soot post reaction (mM)	Products in acetone (mM)	Line wash	Soot post reaction (mM)
300	0.0002	0.01	0.0002	-	0.01	-	-	-	-
350	0.02	0.3	0.0004	0.02	0.04	-	0.009	0.01	-
400	-	-	0.0001	-	-	-	-	0.01	-
450	0.0001	0.01	0.004	-	0.01	-	-	0.005	-
500	-	-	0.005	-	0.006	-	-	-	-
590	0.0007	0.002	-	-	0.006	-	-	-	-

A table showing the concentration of phenanthrene desorbed under an oxidative atmosphere expressed as a percentage of the its desorption under helium atmosphere was described in the appendix section. On increasing the flow rate of O₂/He feed from 50 ml/min to 200ml/min, it was observed that the amount of PAHs desorbed was less (compare figures 5.13 and 5.15), indicating that the rate of oxidation was more rapid at higher flow rate of oxygen due to availability of more oxygen for the PAH-oxidation. There was more rapid conversion of the PAHs to CO₂. The concentration for the products in acetone (figure 5.15a) showed a maximum of 0.18mM at 400°C, for the experiment at 200ml min⁻¹ O₂/He feed while it touched a maximum of 2mM for O₂/He feed of 50ml min⁻¹ (figure 5.13a). Post reaction analysis revealed a further decrease in the concentrations of the PAHs due to rapid oxidation of PAHs (figure 5.15c). The PAHs on the surface of the soot from 300-500°C are negligible owing to this rapid rate of soot oxidation. Figure 5.14 showed the concentrations of the aromatics desorbed from the soot during the uncatalysed oxidation under a higher flow of oxygen. These were lesser than that desorbed under 50ml flow of oxygen, indicating more oxidation. But this was still higher than that observed in the presence of the catalyst.

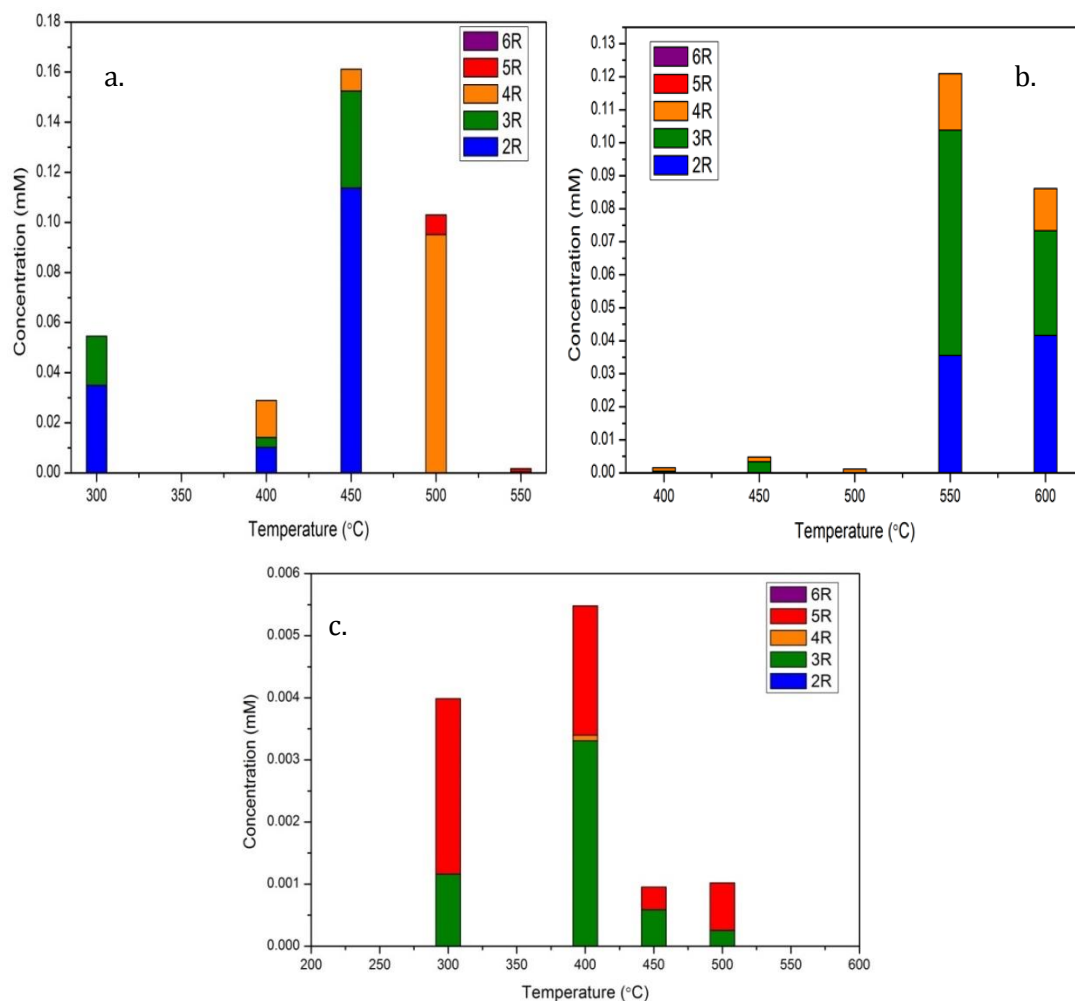


Figure 5.14 Concentration of PAHs upon desorption from uncatalysed soot oxidation (0.0254 g) under 20% O₂/He (200ml/min) - a) Products in acetone, b) line wash, c) post reaction

The catalysed soot oxidation under a higher flow of O₂/He showed the efficiency of the catalyst in oxidizing the aromatics to CO₂. The rapid rate of the oxidation between 350-450°C showed that the heavier aromatics were totally oxidized and only very small concentrations of the three and four ringed PAHs, mainly phenanthrene remained on the soot. These were probably oxidized by 500°C to CO₂. The route to formation of CO₂ was difficult to understand, as PAHs could undergo oxidation through the formation of partial oxygenated products or through a dimerization route or direct combustion to CO₂. This has been investigated using LC-MS as seen in last section of this chapter.

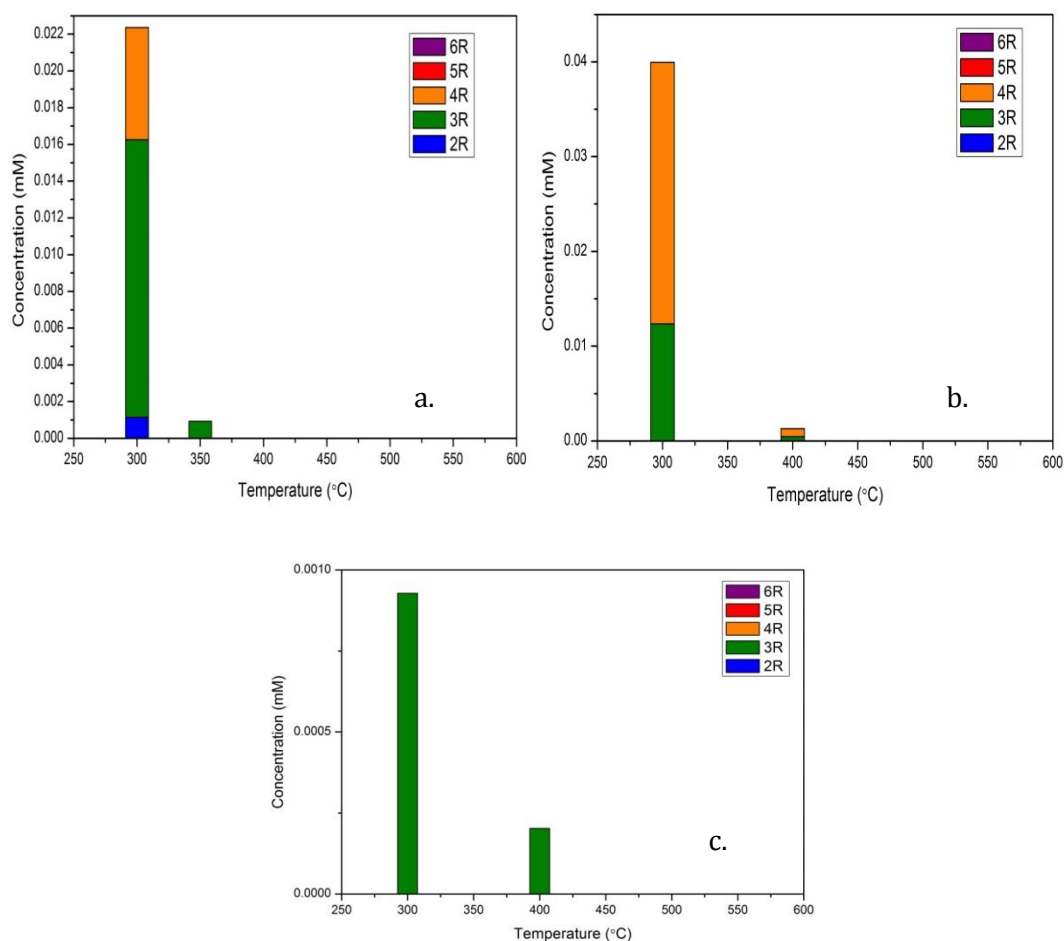


Figure 5.15 Concentration of PAHs upon desorption from catalysed soot oxidation under 20% O₂/He (200ml/min) - a) Products in acetone, b) line wash, c) post reaction

5.5.3 Desorption of PAHs during soot oxidation under CO₂ atmosphere

Soot oxidation was carried out under various oxidative environments in order to understand the effect of individual oxidants in the exhaust on soot. The soot oxidation (catalysed and uncatalysed) was studied under varying concentrations of CO₂ between 20% CO₂/He and 100% CO₂, at a fixed flow of 50ml min⁻¹ in both cases. The analyses under CO₂ was carried out as this was a primary oxidant in the exhaust. A modification was carried out in the reactor setup in order to collect products as they were desorbed to avoid condensation in the line. It was observed that the major concentration of phenanthrene was obtained under a flow of 100% CO₂, in the presence of the catalyst. The desorption of products were similar in both cases, between 400-500°C but heavier PAHs desorbed faster, to higher extent, in the presence of pure CO₂ feed as observed from the products collected in acetone. This indicated that the feed propagated

desorption above 20% CO₂ (figure 5.16). These tests were not completely reproducible due to the variability in the composition of soot.

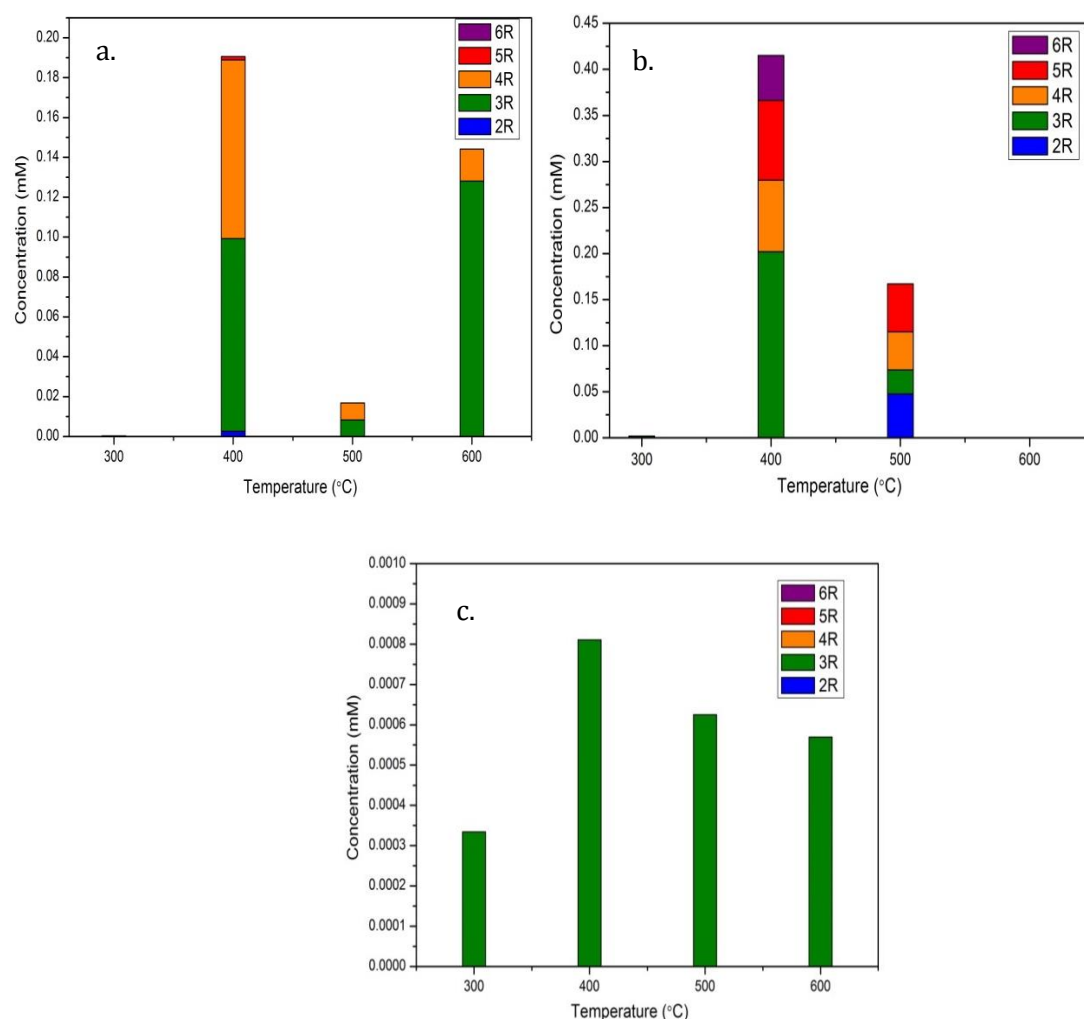


Figure 5.16 Concentration of PAHs upon desorption from uncatalysed soot oxidation (0.0254 g) under CO₂ (200ml/min) - a) Products in acetone 20%CO₂/He, b) Products in acetone -100%CO₂, c) post reaction-20%CO₂/He

Post reaction products showed only a negligible amount of phenanthrene remaining on the surface of the soot under 20% CO₂/He feed while all the PAHs in the presence of 100% CO₂ were desorbed off the surface completely (figure 5.16c).

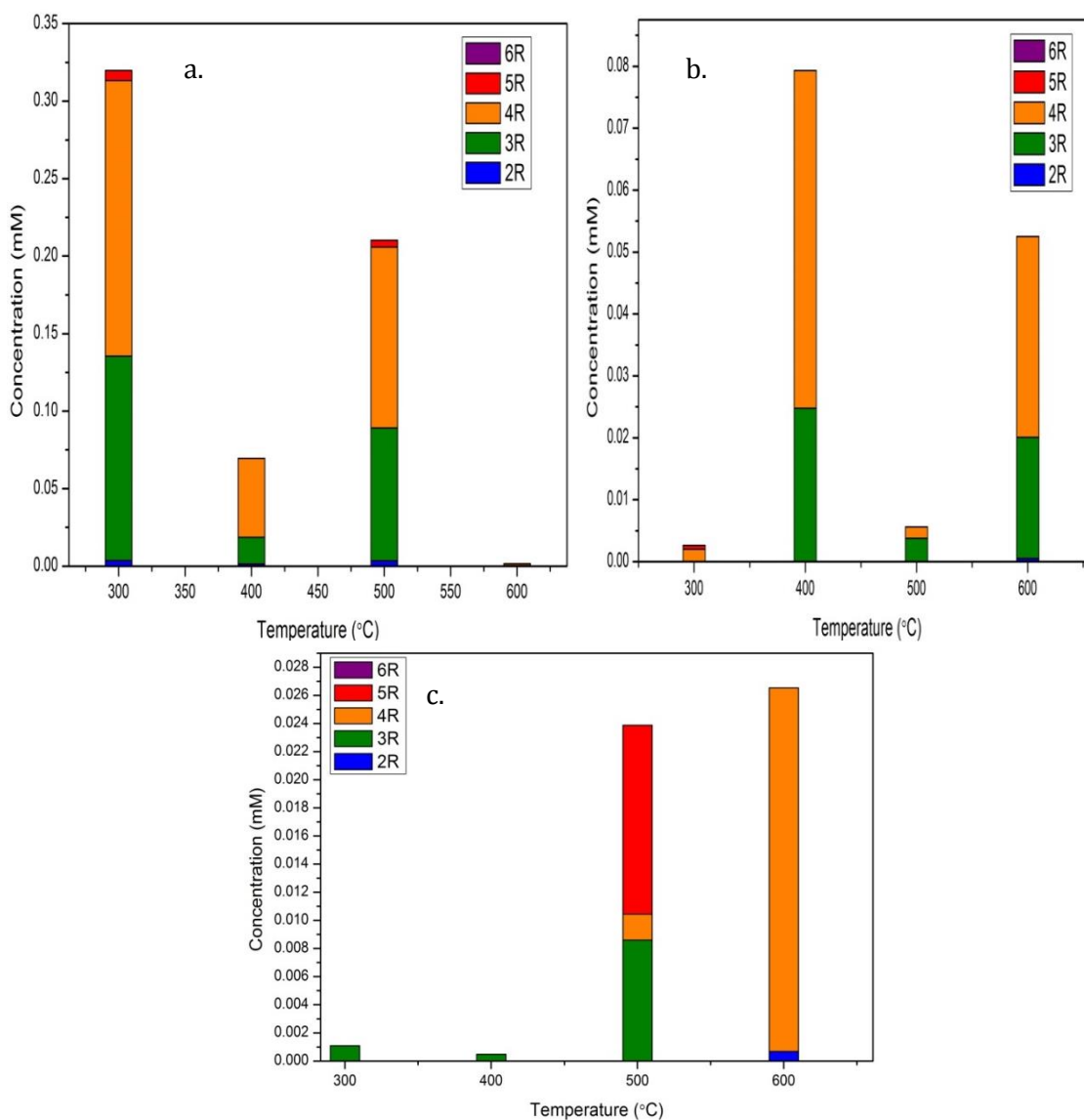


Figure 5.17 Concentration of PAHs upon desorption from catalysed soot oxidation under CO₂ (200ml/min) - a) Products in acetone 20% CO₂/He, b) Products in acetone - 100% CO₂, c) post reaction-20% CO₂/He

The catalysed soot oxidation yielded the same concentration of PAHs (3 and 4 ring) as that in the case of uncatalysed oxidation, in the presence of 20% CO₂/He but facilitated the desorption at lower temperatures of 300°C (onset of catalysed soot oxidation) and also completely desorbed the PAHs from the surface by 550°C. A small fraction of four ring PAHs remained on the surface until 600°C (figure 5.17). This could be due to the less volatile nature of these aromatics. In the presence of a pure CO₂ atmosphere, the concentration of the PAHs was lower than for uncatalysed soot oxidation, (as shown in table in the appendix) indicating that the PAHs were oxidised in

the presence of the pure CO₂ feed in the presence of a catalyst. The catalyst helped to provide the O₂ required for the soot oxidation from the lattice upon reduction of the ceria at 350°C, beyond which the concentration of desorbed phenanthrene slowly started to increase around 400°C and reached a maximum when the rate of the reaction was maximum between 400-500°C, when it starts getting oxidized to CO₂. The feed of CO₂ helped to provide the oxygen for the continuous oxidation of soot, and the oxygen stored in the lattice of CZ was obtained as it passed through the defects created in the structure by the incorporation of smaller ions such as Zr⁴⁺ and Al³⁺ into the CeO₂ cubic fluorite structure. Thus by the Mars van Krevlen mechanism shown in figure 5.18 (explained in chapter 3), soot was oxidised by CeO₂ using lattice oxygen produced on its reduction to Ce₂O₃ and also through the feed of CO₂ that forms CO+O₂, providing the O₂ for the oxidation of these aromatics at higher temperatures. As the reaction was under air conditions, the external oxygen was able to re-oxidise Ce(III) to Ce(IV) and it could oxidise again C in soot or CO to form CO₂. There was also a possibility of the CO₂ reoxidising the CeO₂ in the catalyst. This was not investigated in this study but is a scope for future analyses.

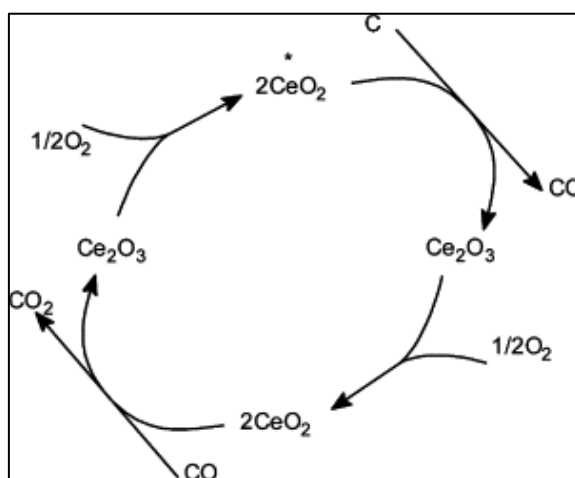


Figure 5.18 Representation of the Mars vanKrevlen mechanism for CeO₂ redox

In the presence of the alkali metal, the K₂CO₃ in this case formed a kind of molecular oxygen complex by utilizing the available oxygen from the CO₂ on forming CO and O₂. The catalyst then helped to transfer the oxygen from the gas phase to the carbon surface. The mechanism was explained in detail in chapter 3. The Ag in the Ag-K/CZA was present as Ag₂O and Ag⁰ (chapter 3) that may have formed surface oxygen species in the presence of the O₂ from the CO₂ feed (on forming CO+O₂) and this helped to

oxidise the soot further. This explained the activity of the catalyst towards diesel soot oxidation, in a CO₂ rich environment.

5.5.4 Desorption of PAHs during soot oxidation under NO atmosphere

In the presence of NO (300ppm) and O₂ (8%) feed there was more desorption of heavier PAHs (5,6 rings) and a larger concentration of these aromatics was observed to be collected at temperatures between 400-600°C as the oxidation proceeds. The concentration of 3, 4 and 5 membered ring structures mostly arose from phenanthrene, pyrene, benzo(a) pyrene and indeno(1,2,3-cd)pyrene respectively (figure 5.19). NO₂ produced from the NO oxidation, in the presence of O₂ (8%) helped in oxidation of these aromatics to CO₂, alongside the carbonaceous soot particles at high temperatures, in the absence of the catalyst (650-700°C) but the catalyst helped to lower these temperatures by supplying additional stored oxygen from the lattice, leading to rapid oxidation rates.

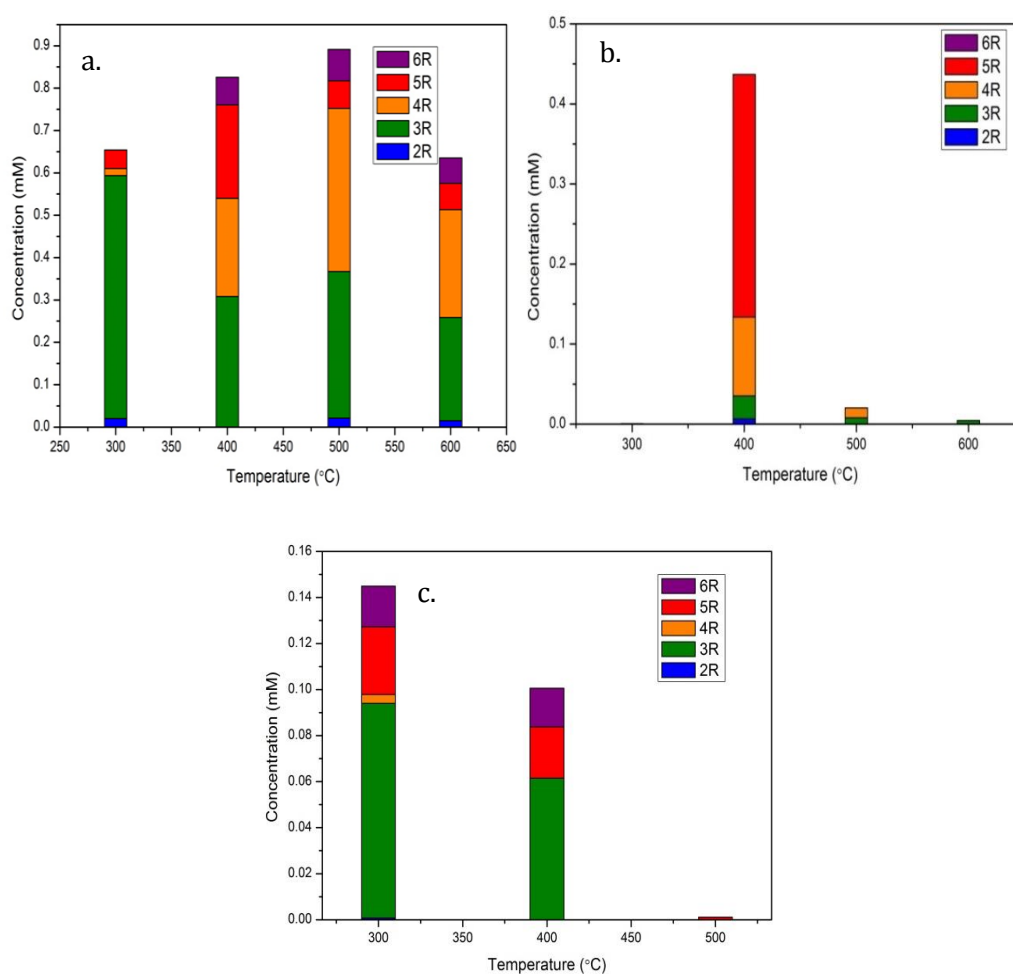


Figure 5.19 Concentration of PAHs upon desorption from uncatalysed soot oxidation under 300ppm NO/O₂/He (200ml/min) - a) Products in acetone, b) Line wash c) post reaction

In the presence of the catalyst some interesting observations were made. The concentrations of the heavy PAHs desorbed from the surface was lower (0.23mM -300-400°C) when compared to that observed during uncatalysed oxidation (0.98mM-400-500°C) indicating that these aromatics were being oxidized in the presence of the catalyst (figure 5.20). Also, the concentration of these PAHs decreased with increase in temperature, owing to the formation of NO₂ through the oxidation of NO and O₂ that proved to be vital in enhancing the oxidation of soot. A mechanistic explanation was provided for the reaction of some of the PAHs with NO₂ was shown in figure 5.20 and 5.21 for fluorene and pyrene nitration, respectively.

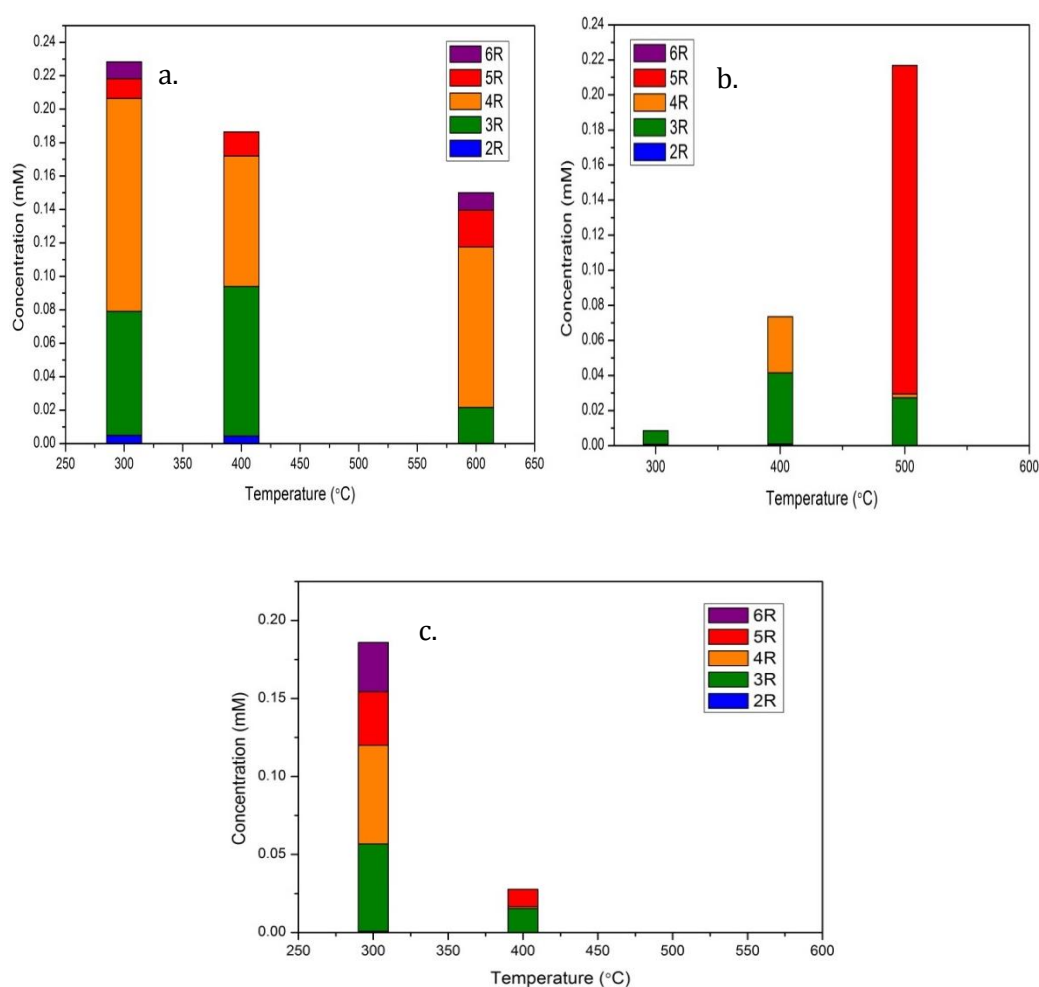


Figure 5.20 Concentration of PAHs upon desorption from catalysed soot oxidation under 300ppm NO/O₂/He (200ml/min) - a) Products in acetone, b) Line wash c) post reaction

The soot post reaction was observed to have only a small amount of heavy five and six membered aromatics adsorbed on the surface at around 300 and 400°C in the presence of the catalyst, under oxidative conditions of NO/O₂/He. Beyond this, as the

rate increased, they tend to break down into simpler and smaller aromatics with the major concentration of the carbon in soot finally undergoing oxidation to CO₂ by 600°C.

Fluorene, a three ringed PAH has been identified and measured in the emissions from diesel and gasoline engines, gas turbine engines [29,30]. In ambient air it exists in the gaseous phase owing to its vapour pressure. This was present in significantly high concentrations in the diesel soot analysed used in our study. A mechanism was proposed by Nielsen *et al.*, to explain the preferential OH radical attack on the position(s) of the highest electron density which is the preferred position of electrophilic substitution (2-position) in the case of fluorene, the addition of which leads to the formation of a hydroxycyclohexadienyl-type radical intermediate as shown in the figure 5.50. This is then followed by an NO₂ addition on the ortho position to the OH group which are the 1- and 3- positions in fluorene. The formation of 1- and 3-nitrofluorene which were the two main isomers formed by removal of H₂O. Upon analyses of 200mg of diesel particulates with a spiked concentration of the 1,2,3,4-nitrofluorene isomers, it was observed that there was a significant concentration of these isomers in the exhaust [31,32].

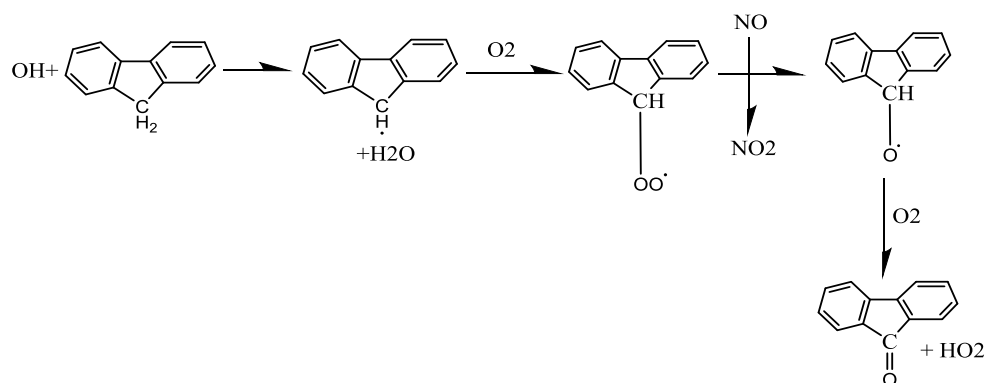


Figure 5.21 Fluorene oxidation pathway in the presence of OH radical [31]

Pyrene, a four ringed aromatic present in diesel soot was studied for nitration as shown by Miet *et al.* according to the following mechanism, through a HONO departure as shown in many heterogeneous reaction studies of NO₂. NO₂ was added to the electrophilic carbon (position 1) and a second NO₂ molecule is added to the alpha position leading to the departure of -HONO that occurs by the abstraction of a hydrogen atom from position 1. Addition of OH radical at the 1-position is seen as in the case of NO₂ addition as shown in figure 5.22.

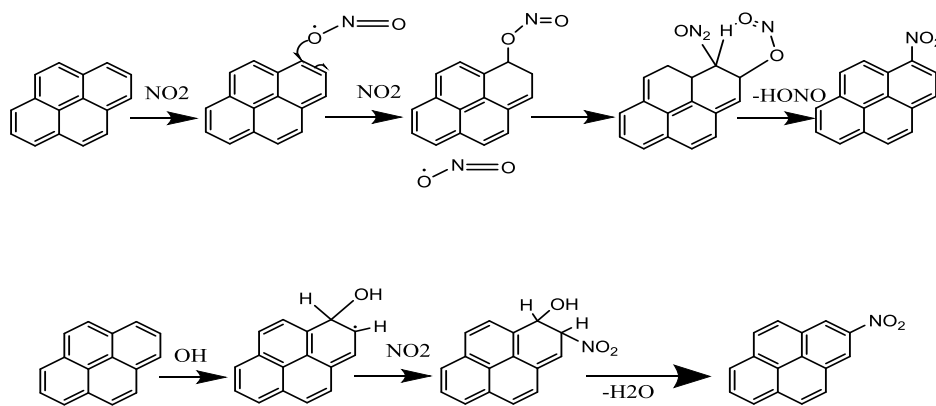


Figure 5.22 Pyrene oxidation pathway in the presence of NO_2 [33]

5.5.5 Desorption of PAHs during soot oxidation under exhaust gas atmosphere

These conditions chosen to mimic the real scenario in diesel engines and to understand the effects of various contributors in the feed towards the oxidation process. A constant desorption of products was observed in the presence of this mix, from the surface of the soot, in the absence of the catalyst. The major products that came off the surface were the three and four membered ring structures as observed in the previous cases. A large concentration was seen to still remain on the surface of the soot between 400-600°C, indicating the oxygen feed was quite lean for the process of conversion of these aromatics to CO_2 . This was probably due to the lack of available O_2 . This oxygen would have probably been sufficient to oxidize the carbon in the soot to CO_2 and for the NO conversion to NO_2 in the feed further enhancing the reaction of the carbonaceous soot particulates, making the oxidation of aromatics difficult. This would need further investigation.

The products collected in acetone revealed that the concentration of three and four ringed aromatics was greater than that of the other aromatics in diesel soot (figure 5.23). The most significant three ringed PAH present was phenanthrene, as previously observed. The other three ringed structures included acenaphthene, acenaphthylene, fluorene and anthracene, present in slightly lower concentrations in diesel soot. These aromatics desorbed off the surface right from the onset of the oxidation at 300°C, with maximum concentrations in the absence of the catalyst, under the exhaust mix conditions (0.32mM). This concentration tends to reduce to 0.25mM at 500°C with the rapid increase in the rate of soot combustion as indicated by the figure 5.23. The

combustion was complete by 500°C in the case of catalysed soot oxidation in the presence of the exhaust mix.

The soot post reaction indicated the incapability of the PAH (3/4membered rings) to get desorbed off the surface or oxidised to CO₂ in the absence of the catalyst (figure 5.23c). Under the presence of the exhaust conditions, the five and six membered ring structures were not desorbed during, both catalysed and uncatalysed soot oxidation. This was probably due to the fact that the exhaust feed tends to convert these large compounds to smaller compounds as soon as they are formed, thereby increasing the concentration of lighter aromatics. The percentage of desorption was given in table 5.9.

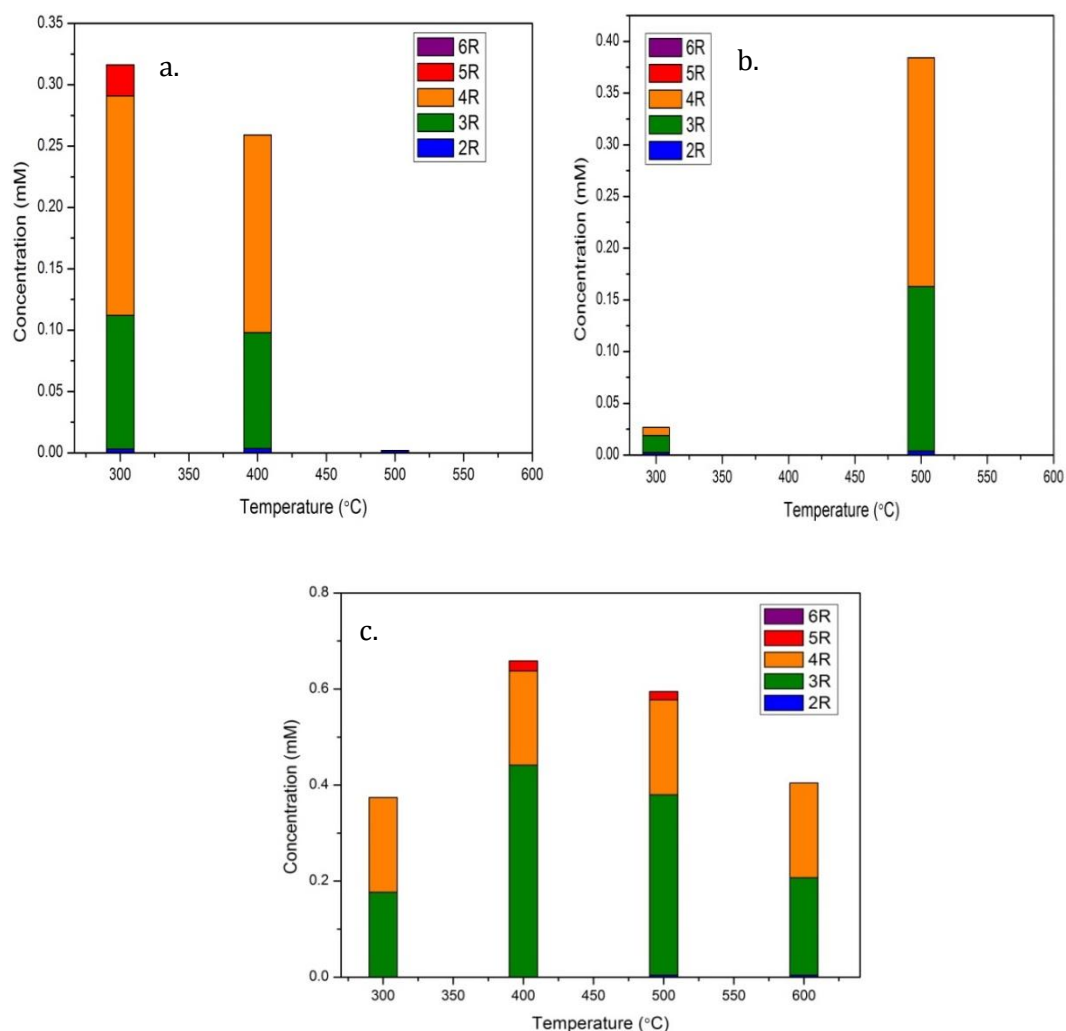


Figure 5.23 Concentration of PAHs upon desorption from soot oxidation under real exhaust gas feed- a) Products in acetone-uncatalysed, b) Products in acetone-catalysed, c) post reaction-uncatalysed

In the presence of an excess NO atmosphere in the exhaust and absence of O₂ (300ppm NO/He), it was observed that, during the uncatalysed soot oxidation the PAHs tend to remain on the surface of the soot itself and a large concentration of the heavier five and six membered ring structures were more difficult to drive off the surface, thus delaying their oxidation due to the absence of an oxidative atmosphere. This was observed from the concentration of PAHs on the soot post reaction until 700°C. While in the presence of the catalyst, the oxidation was more favourable, as the stored oxygen from the lattice was available at 350°C for the soot oxidation. The lattice oxygen probably reacted with the NO in the feed to give NO₂, and so helped improve the rate of the oxidation at lower temperatures (figure 5.24).

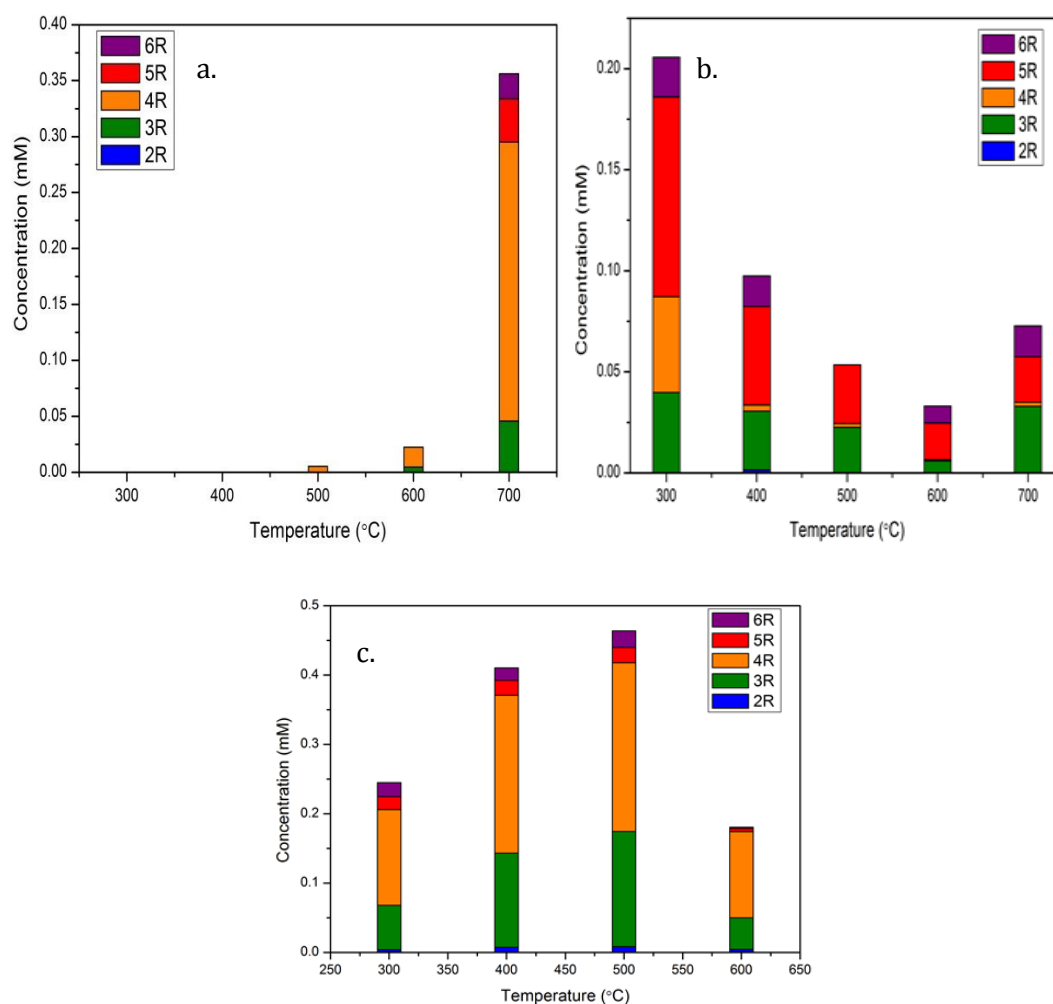


Figure 5.24 Concentration of PAHs upon desorption from uncatalysed soot oxidation under 300ppm NO/He (absence of O₂ feed) - a) Products in acetone, b) Line wash c) post reaction

The PAHs, mainly the difficult to oxidize PAHs (3 and 4 rings), were desorbed from the surface of the soot between 400-500°C. The complete desorption followed by oxidation was seen to occur by 600°C. In the case of the NO/O₂/He, NO/He and typical diesel exhaust conditions, the catalyst functioned well and helped to provide the oxygen needed for the NO_x assisted soot combustion. This is why in the case of 300ppm NO/He, despite a lack of O₂, the catalyst provided the stored O₂ the lattice for the conversion of the NO to NO₂, while the K promoter significantly favoured the formation of the carbonate species that also provided a rapid increase in the reaction rate. The Ag₂O also underwent subsequent reduction to Ag⁰ and helps in converting the O₂ to oxide or superoxide species, to form the CO₂ as the final oxidation product, thus oxidizing the heavier components in soot. Varying the concentration of NO/O₂/He from 300 to 1500ppm, also caused an increase in desorption at higher temperature and rapid increase in rate of oxidation, thereby leading to the complete oxidation of the soot by 550-600°C.

5.5.6 Conclusions

1. *Influence of O₂ atmosphere*: It was observed from table 5.9, that the concentration of most of the three, four and five ringed PAHs desorbed in the absence of a catalyst was greater as opposed to that in the presence of a catalyst under synthetic air flow (between 300-500°C). The major three membered constituent of diesel soot has been found to be phenanthrene, which is quite difficult to combust under O₂ rich conditions of the exhaust. The GC-MS and HPLC data for the catalysed soot oxidation in the presence of 20% O₂/He showed that the catalyst helped in reducing the temperatures for the combustion but a small trace of phenanthrene was still present in the line at 600°C. Combination of thermal desorption and oxidation in the presence of the catalyst is essential for the oxidation of the soot. The reaction pathways for the oxidation of polycyclic aromatic hydrocarbons present in soot particles in presence O₂ have been investigated using DFT by several groups [30,31].

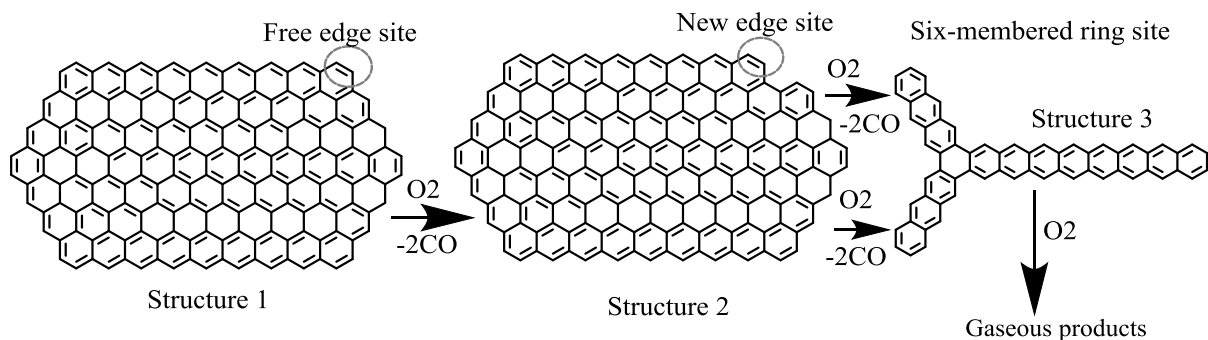


Figure 5.25 PAH oxidation scheme under O_2 atmosphere shown using DFT modelling

In the literature, several soot models from flames have been described and most of them state that the soot oxidation takes place through the reactive “free-edge” site as shown in figure 5.25 [34,35]. There are several free edge and zig-zag sites present on the PAH surface. There is a formation of a new free-edge site on the structure upon removal of a free-edge site from structure 1 by O_2 (seen on structure 2). This process continues until all the free-edge sites on soot are completely exhausted, beyond which the six membered rings undergo complete combustion as depicted in structure 3 [36]. A significant mass loss of 65% is observed upon free-edge site oxidation at around 176 C atoms in structure 1 were found to be reduced to 62 C atoms. Thus this is chosen as a preferred site for model soot oxidation reactions [37]. DFT also allows the determination of the rate of reactions for soot oxidation by O_2 and this is assumed to be the same as the rate for the conversion of 4-pyrenyl (a pyrene radical) by O_2 to form 4-phenanthryl (figure 5.26)[38].

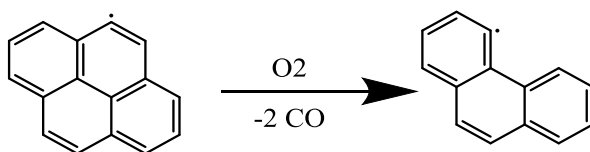


Figure 5.26 Oxidation of 4-pyrenyl to 4-phenanthryl indicating oxidation of soot PAH.

2. Influence of CO_2 atmosphere: There is a balance between the desorption and oxidation processes taking place in the exhaust. Upon varying the concentrations of the CO_2 in the feed, it was observed that in the presence of less CO_2 there was more desorption favoured over oxidation. An increase in the CO_2 concentration to 100% caused more oxidation of the aromatics, in the presence of the catalyst. The gases are recycled through the engine but the exhaust reaching the filter will still contain a lot of oxygen.

The effect of CO₂ addition to ethylene/air fuel rich premixed laminar flames yielding an ethylene/O₂/N₂/CO₂ flame was studied by Mancarella *et al.* in order to understand the role of these components in the kinetic pathways leading to the formation of PAHs. The soot trapped on a PTFE filter was analysed using TGA and the PAHs were analysed using HPLC. The addition of CO₂ reduced PAH and soot emissions in laminar premixed ethylene flat flames, wherein it promoted the reaction, CO₂+H→CO+OH. The higher OH radical post-flame concentration helped in the PAH and soot oxidation by the direct oxidative attack of their gaseous hydrocarbon precursors, especially acetylene and benzene [39,40].

CO₂ as explained was converted to CO and OH· Radical, and the O₂ from the lattice of the catalyst added to the oxygen, thus enhancing the oxidation. In the presence of a lower concentration of CO₂, the desorption was higher as compared to a pure CO₂ atmosphere. This was due to an obvious decrease in the oxidant in the gas feed necessary for soot oxidation. There were several pathways proposed in literature (as mentioned in chapter 3) in order to understand the mechanism and these involved several stable intermediates with embedded O atoms. Some of the partial oxygenated species formed during the oxidation of soot have been observed in our study as well (shown towards the last part of this chapter).

3. Influence of NO (with and without O₂) atmosphere: In the presence of an NO₂ atmosphere provided by the oxidation of NO and O₂ from a feed of 300 ppm NO/O₂/He, the desorption rates were higher compared to a CO₂ atmosphere and is almost similar to that under O₂ atmosphere indicating that the CO and O₂ are stronger oxidants as compared to NO₂. This could be due to the fact that the oxidising agents (NO₂ and O₂) were reacting with the solid carbon which released the adsorbed PAHs. But the catalyst was still active to an extent and favoured the oxidation to CO₂, probably through the formation of partial oxidised products. In the presence of a diesel exhaust mix, the rate of desorption was less. The catalyst helped in oxidising the soot to CO₂ at lower temperatures as compared to the uncatalysed soot oxidation. At the start of the oxidation the desorption rates may have been slightly higher (300°C) but over a temperature range the oxidation rate was higher.

Some interesting observations showed that, in the presence of a greater amount of NO/O₂ as in the case of 1500ppm NO/O₂/He compared to 300ppm NO/O₂/He, the rate of oxidation was rapid and the concentration of the products was more than for a simple O₂/He atmosphere. Also, the catalyst helped to oxidize the three ring structures mainly phenanthrene to a larger extent under different oxidative atmospheres.

Different reactive sites as shown in figure 5.27, were studied to understand the non-catalytic interaction of soot with NO by Raj *et al.* [41,42], wherein several reaction pathways were suggested for this process, taking into account the reaction energetics and kinetics using DFT and TST modelling approaches. This gave rise to a new rate for the formation of CO from soot. The pathways helped in understanding the PAH growth model and in the oxidation of the PAH-soot to CO, N₂ and N₂O. The soot site and temperature of the reaction were taken as key factors in the NO-soot reaction. Under isothermal conditions it was found that the number of O₂ atoms remaining on the surface of the soot decreased with an increase in temperature for a given reaction time. This reaction is found to stop after a point due to the formation of pyrrolic, pyridinic and pyridonic fragments on the surface of the soot. The reaction of soot with NO₂ is faster than with NO, as the NO₂ tends to add O₂ to the surface of the soot with the re-formation of NO that subsequently can take part in the further oxidation of soot.

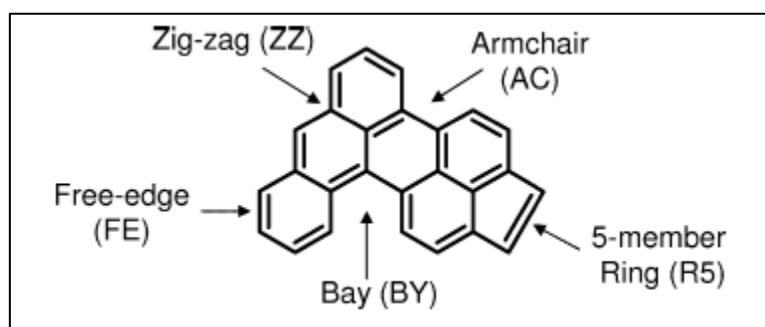


Figure 5.27 Image indicating various sites on a PAH molecule capable of undergoing oxidation, shown using DFT

In the past, theoretical models were used to understand this phenomenon taking into consideration the zig-zag sites found on the soot. The study by Kyotami and Tomita [43] alongside the study by Raj *et al.* showed that the NO addition to PAH had two possible thermally favourable orientations:

- a) N-O bond axis is parallel to the reactive site.

b) N-O bond axis is perpendicular to the reactive site with the N atom close to the PAH.

One of the proposed pathways was shown in figure 5.29. In this above pathway, the two NO molecules were chemisorbed onto the ZZ sites of the pentaphene molecule, of which one of the PAH bonds break (CS3). Thereby, the two N atoms on the arm chair site formed a bond resulting in a more stable species (CS4). One of the C-N bonds broke resulting in a N₂ chain. The N₂ molecule then gets desorbed from the PAH surface. The remaining two O atoms as seen in CS6 tend to oxidize the PAH molecule through CO formation as seen in figure 5.28 [44]. Several such pathways have been proposed from DFT based on different reactive sites on the PAHs.

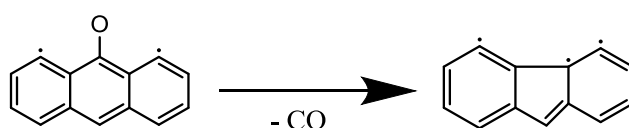


Figure 5.28 CO formation pathway formed upon PAH oxidation [44]

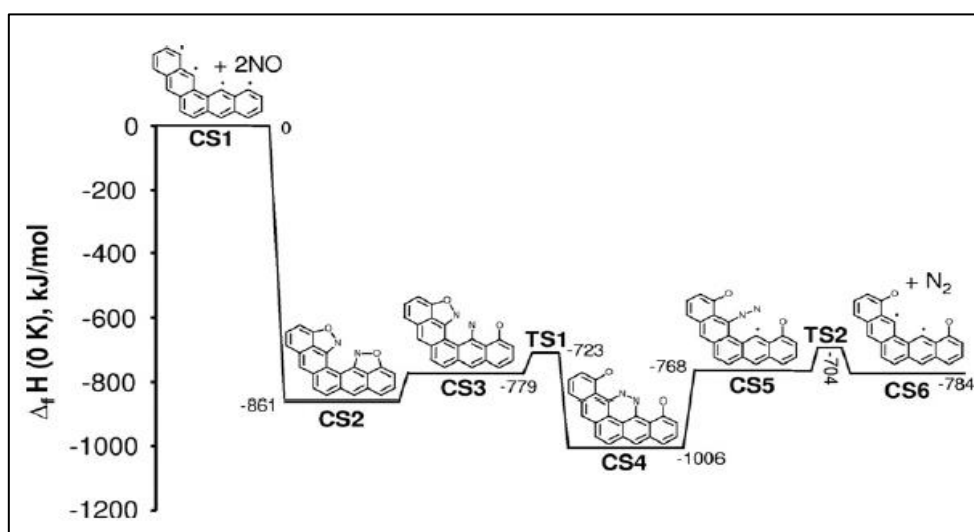


Figure 5.29 Reaction pathway for PAH oxidation expressed using DFT under NO atmosphere [37,39]

On observing the soot post reaction, under 300ppm NO/He, the rate of oxidation was very slow, in the absence of a catalyst as opposed to an increase in rate in presence of the catalyst. The three membered ring structures remained on the surface of the soot until 700°C without being oxidised or desorbed.

Effect on four membered ring structures- The study on four membered ring structures showed that the concentration of these were also significantly high, with fluoranthene

and pyrene being the major contributors to the PAH concentration, followed by chrysene. At the onset of soot oxidation at 300°C, in the case of the catalysed soot oxidation, there was a significant amount of thermal desorption observed under the realistic exhaust conditions, 1500ppm NO/O₂/He and under 300ppm NO/He. However, an atmosphere containing 300ppm NO/He did not provide the soot enough oxygen to convert the heavy aromatics and thus the benzo(a)pyrene tends to remain on the soot surface under these conditions until 700°C and beyond without getting oxidized, in the absence of the catalyst. The same atmosphere in the presence of catalyst caused these aromatics to dissociate into smaller aromatics by providing the oxygen stored in the CeO₂ with a peak reduction temperature of 350°C for the Ag-K/CZA catalyst.

Effect on heavier PAHs – The mechanism for oxidation of six membered ring structures is a complex one. Soot oxidation (uncatalysed) began at 400°C and these aromatics tend to get desorbed to a large extent between 400-500°C in the presence of 300ppm NO/O₂/He atmosphere. The presence of the catalyst helped to break down these aromatics to smaller aromatics, and thus only very small amounts of the six membered rings desorbed from the surface of the soot while most of them were oxidised to smaller ring structures. These large aromatics were not found in large concentration in the diesel soot, but the predominant among the two was indeno(1,2,3-cd)pyrene, which was considered to be a probable human carcinogen. The catalyst was capable of eliminating these heavy aromatics as well, in both oxidative environments such as 1500ppm NO/O₂/He and in the absence of an oxidative environment as in the case of NO/He.

4. Influence of real exhaust conditions - Soot oxidation in the presence of the Ag-K/CZA catalyst under the realistic exhaust conditions showed that these PAHs break down to form smaller aromatics at temperatures above 450°C. On analysing these products, we observed that, in the absence of the catalyst, desorption of the aromatics from the surface occurred only between 400-500°C, in the presence of 300 ppm NO/O₂/He and under realistic exhaust conditions, where the rate of reaction was maximum as observed from the TGA results. In this case the oxidation to form smaller PAHs was not possible and thus only desorption occurred at higher temperatures. While in the presence of the catalyst, the PAHs not only desorbed from the surface, but oxidation also occurred quite significantly as several unknown compounds were

identified alongside the ones that have been quantified, indicating that these heavier ring structures at higher temperatures tend to broke down to form smaller ring structures.

Traces of the pyrene and fluoranthene were observed on the surface of the soot until 700°C in the absence of the catalyst, under 300ppm NO/He, proving that the catalyst was vital in oxidising such heavy ringed structures into smaller ones. The five membered ring structures observed in soot included benzo(b)fluoranthene, benzo(k) fluoranthene, benzo(a) pyrene-highly carcinogenic and dibenzo(a,h) anthracene, with major contributions to the collected products from benzo(a)pyrene followed by benzo(b)fluoranthene. These were toxic compounds, which if emitted out of the exhaust, would be extremely detrimental to human health and the environment. The products trapped in acetone showed that the concentration of these heavy aromatics was not as high when compared to the three and four membered ring structures. A similar trend was followed as in the case of the three and four membered ring structures. Only a small concentration of benzo(k)fluoranthene was observed to have desorbed from the surface at low temperatures from the uncatalysed soot under realistic exhaust mix.

Table 5.9 Percentage of thermal desorption as a concentration of desorption under Helium atmosphere

Temper-ature (°C)	O ₂ /He (%)		CO ₂ (%)				300ppm NO/O ₂ /He (%)		Exhaust mix (%)	
	Soot	Catalyst+ soot	100% CO ₂		20% CO ₂ /He		Soot	Catalyst+ soot	soot	Catalyst+ soot
			Soot	Catalyst+ soot	soot	Catalyst+ soot				
300	42.3	29.1	6	0.02	0.12	3.4	38.4	59	2	7
400	52.8	18.3	2.4	1	2.3	0.8	0.5	2.1	2.1	6
500	4.9	7	0.12	0.4	0.6	2.05	0.7	0.1	4.4	10.1
600	-	0.1		0.52	3.2	0.01	0.8			4

Each analyses involved the use of a fresh batch of soot with or without catalyst depending on the condition. These are individual analyses at each temperature and thus cannot be totalled. Percentages were calculated as shown in the appendix.

It can be seen from table 5.9 that the amount of thermal desorption under different conditions could be expressed as a percentage of the desorption under helium.

The desorption under helium was considered to be pure desorption, involving no oxidation. Thus expressing the concentrations under an oxidative atmosphere was calculated as shown in the appendix. The percentage of desorption was quite high (40-50%) in the absence of a catalyst and under an oxidative environment such as 20%O₂/He (synthetic air) while in the presence of a catalyst the desorption was lower clearly indicating that the catalyst promoted the oxidation of these aromatics. In the presence of CO₂ atmosphere, this percentage was far lower, with smaller concentrations of desorption in the presence of a catalyst and faster oxidation of the PAHs on the soot, alongside the carbon in the soot at lower temperatures. In the presence of an NO₂ atmosphere there was still a considerable amount of desorption but only at around 300°C, beyond which the oxidation of these PAHs occurred, as the rate increased in the presence of the NO₂ aided mechanism. Under exhaust conditions the percentage of thermal desorption was quite low indicating oxidation of the PAH species.

5.5.7 Comparison of extracted soot and pre-treated soot during oxidation

Several oxidative tests under 20% O₂/He were carried out using the soot and extracted soot to try to understand the oxidation regime in the presence or absence of PAHs. Figure 5.30a indicated that the majority of three ringed structures, predominantly phenanthrene, was obtained from the surface of the soot between 400-600°C, until then it was seen on the surface of the soot. Upon extracting the PAHs from soot using toluene Soxhlet extraction, the PAH concentration remaining adsorbed on the soot (post extraction) was very low and indicated the efficiency of extraction. A significant concentration was observed from the extracted soot surface at 600°C (0.1mM). But major contributions arose from the uncatalysed soot prior to extraction, reaching a maximum of 0.18mM of three ringed PAHs at 500°C. Post reaction analyses showed how the concentration on the surface of the soot gradually reduced with increase in temperature (figure 5.30b).

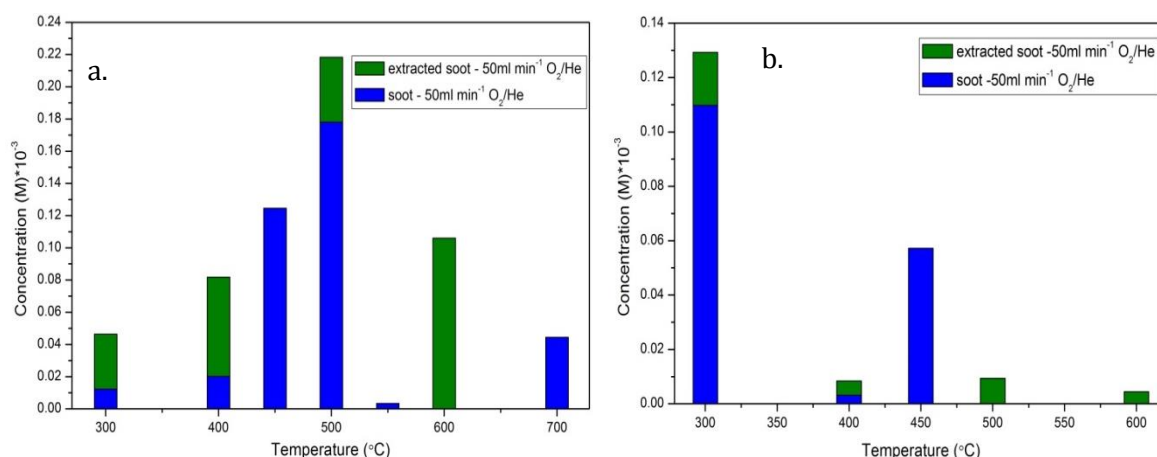


Figure 5.30 HPLC analyses: 3 ringed PAHs desorbed from soot and extracted soot a)products in acetone, b)post reaction

On observing the soot for four ringed PAHs, the major contributions arose from the soot prior to the extraction (blue bars-figure 5.31a) and on observing the soot post oxidation, concentrations of ~0.2mM were seen to be adsorbed on the soot surface (not extracted-blue bars-figure 5.31b), even at high temperatures.

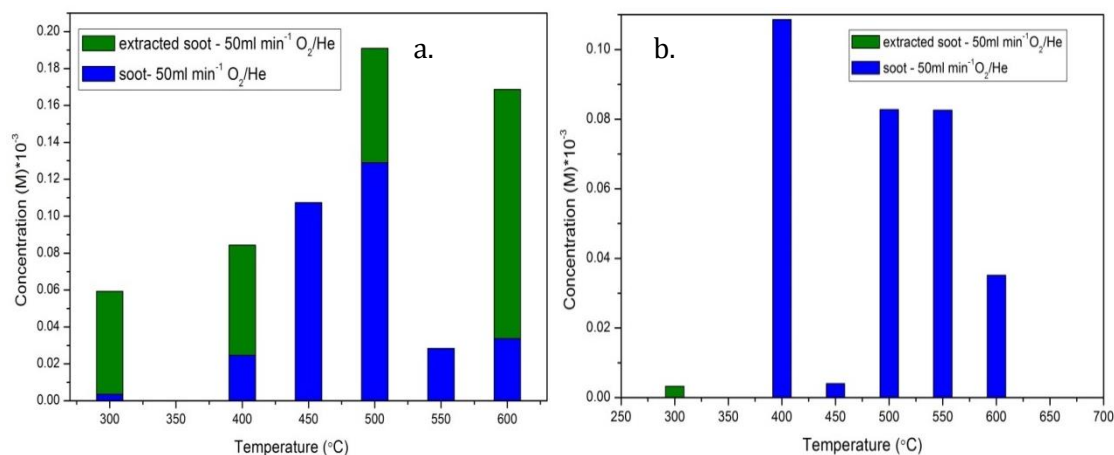


Figure 5.31 HPLC analyses: 4 ringed PAHs desorbed from soot and extracted soot- a)products in acetone, b)post reaction

Heavier PAHs were seen to be strongly adsorbed on the surface of the soot (prior to extraction) as was observed from the post reaction analysis throughout the oxidation range. These need to be desorbed from the surface and oxidized in the presence of the catalyst (as shown in figure 5.32a,b). The extracted soot in all the analyses showed very low to nearly negligible amounts of PAHs due to the efficiency in extraction of the PAHs.

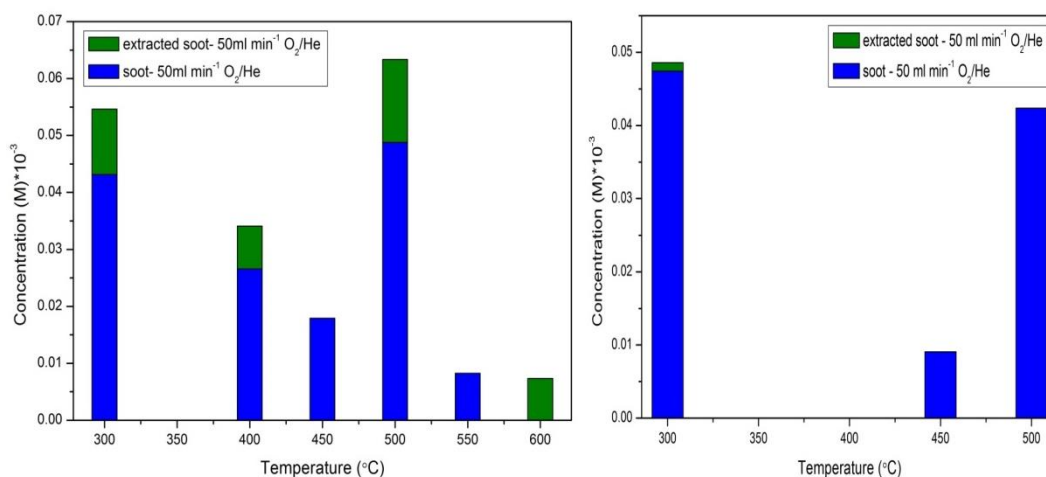


Figure 5.32 HPLC analyses: 5 and 6 ringed PAHs desorbed from soot and extracted soot-
a) products in acetone, b) post reaction

5.6 Modification of catalyst for total PAH combustion

A Pt/SiC catalyst prepared according to the procedure described in Chapter 2, was tested for naphthalene oxidation as described in the section below.

5.6.1 Testing for Pt/SiC for naphthalene oxidation

The Pt/SiC aromatic-oxidation catalyst prepared by wet impregnation according to Sellick *et al.* [45] showed slightly different activity compared to that reported in their study, achieving T_{100} and T_{50} for naphthalene consumption at 275°C and 195°C respectively (Figure 5.33a), as opposed to the T_{100} - 250°C and T_{50} - 212.5°C, previously reported. A Pt/SiC catalyst prepared by incipient wetness (Figure 5.33 b) required the same temperature to reach T_{100} , however it showed greater activity for naphthalene consumption at lower temperatures, with a T_{50} at 170°C (~20°C lower than the above catalyst). This increase in activity was suspected to be due to a higher metal loading; Although both catalysts were prepared with the aim of achieving 2.5 wt% Pt loading, it was observed that on evaporation of solvent in the incipient wetness impregnation preparation, there was a visible separation of precursor Pt salt from the support, possibly leading to a loading lower than 2.5 wt%.

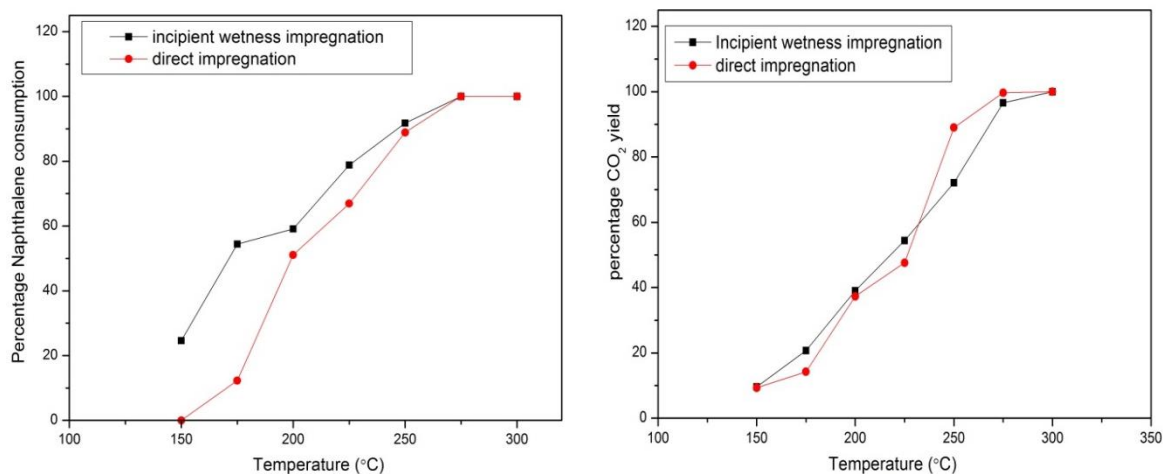


Figure 5.33 Pt/SiC (incipient and direct impregnation – a) naphthalene oxidation b)CO₂ formation

The results from these tests proved that the incipient wetness impregnation showed better performance for naphthalene oxidation, thus was taken as a benchmark catalyst for PAH combustion. This catalyst was then combined with the 2%Ag-10%K/CZA catalyst in ratios of 2:1, 1:1 and 1:2 (Pt/SiC: Ag-K/CZA) by manual grinding using a mortar and pestle.

5.6.2 Optimization of the ratio of Pt/SiC : Ag-K/CZA- for efficient PAH combustion

The above mentioned mixed catalysts, prepared by manual grinding (10 mg) were individually combined with soot and subjected to thermo-gravimetric analysis, under flowing air, over a temperature range of 30-900°C. This analysis showed that the ratio of 1:2 (Pt/SiC: Ag-K/CZA) was the most ideal for soot oxidation (from the values of the onset, the peak and final temperatures shown in table 5.10). This method was used as a method to screen the catalysts in order to choose an ideal catalyst for combined PAH-soot oxidation.

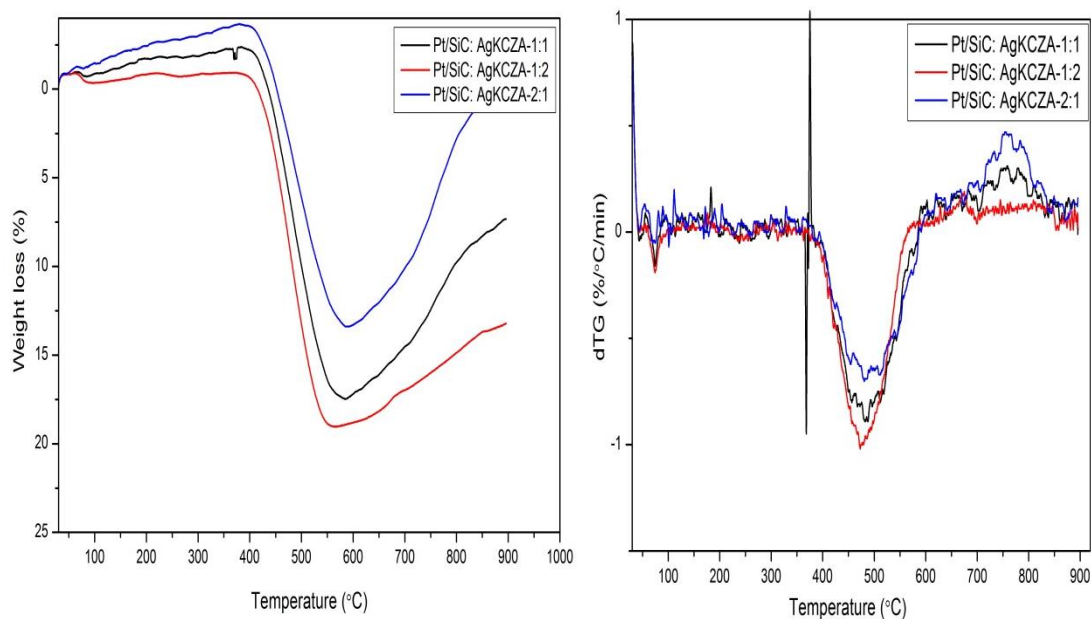


Figure 5.34 TGA plots showing activity of different ratios of Pt/SiC: Ag-K/CZA for soot oxidation

These mixed catalysts were tested for soot oxidation, with the aim of choosing an optimised ratio of mixed catalyst and soot for further testing.

Table 5.10 Activity of different ratios of Pt/SiC: Ag-K/CZA towards soot oxidation

	Ratios		
	2:1	1:1	1:2
Onset temperature (°C)	385	380	375
Extrapolated onset temperature (°C)	390	395	385
Peak temperature (°C)	490	480	475
Final temperature (°C)	590	590	565

The TGA plots (Figure 5.34) indicated the onset, peak and final temperatures as shown in (Table 5.10). From these results it was observed that the mixed catalyst consisting of Pt/SiC:Ag-K/CZA combined in a 1:2 ratio (henceforth referred to as 'mixed catalyst') exhibited the lowest onset temperature (the temperature at which soot combustion is initiated), peak temperature (the temperature at which soot combustion rate is maximum) and final temperature (the temperature of complete combustion).

Ag-K/CZA has been proven to be a very good soot oxidation catalyst exhibiting very high activity. Thus the mixed catalyst with a greater amount of Ag-K/CZA would be ideal for soot oxidation combined with the Pt/SiC for hydrocarbon oxidation. Thus for further analyses, this ratio of (1:2) was used. Thermal stability is also a very vital

feature for an automotive exhaust catalyst. Thus this was tested using a certain amount of catalyst and soot for the oxidation and this was retested with fresh charge of soot for three consecutive runs as shown in figure 5.35.

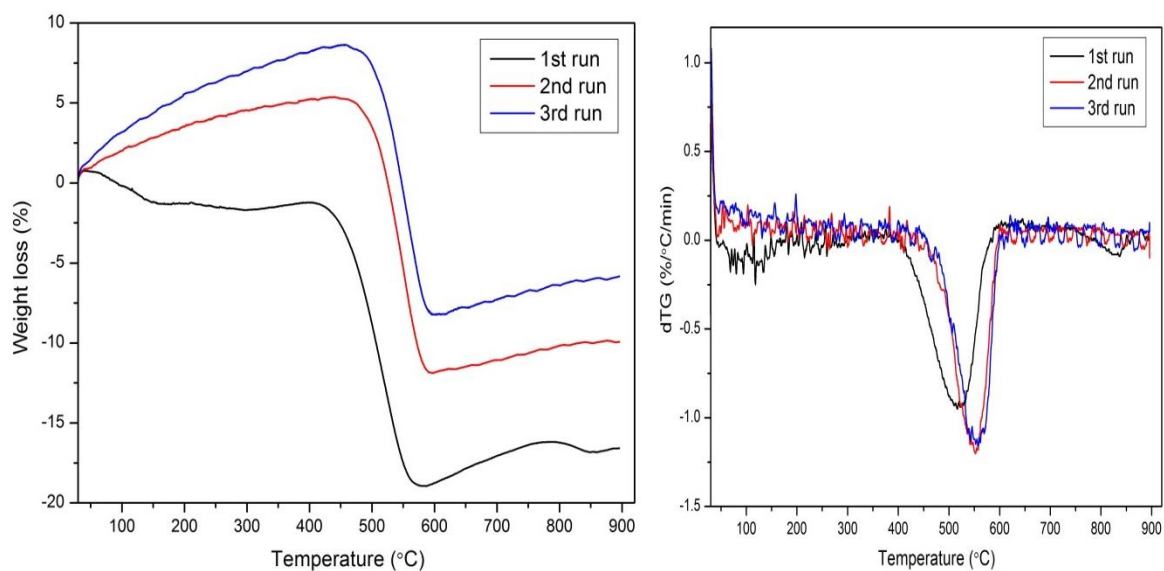


Figure 5.35 Reproducibility of Pt/SiC-AgKCZA-1:2 during three consecutive tests for soot oxidation

The first run displayed highest activity with subsequent two runs displaying lower but stable activity with an onset of 440°C and peak temperature of 550°C. The combustion was complete by 600°C. It appeared that the catalyst structure underwent a change in structure at higher temperatures, leading to a slight change in activity. This suggested sintering at higher temperatures, thus leading to a decrease in active surface of the metal and in turn its performance for soot oxidation.

5.6.3 Desorption of PAHs during soot oxidation under 20%O₂/He

The soot with the mixed catalyst was tested under 20% O₂/He and this showed a significant decrease in the concentration of the PAHs desorbed from the surface compared to that under the Ag-K/CZA catalyst. Two ring PAHs appeared to be totally oxidised, as would be expected from the performance of the catalyst in naphthalene oxidation. The majority of PAHs desorbed were the three ringed PAHs only, indicating that the heavier aromatics were probably oxidized more easily in the presence of this catalyst and a high concentration of O₂ feed. (Figure 5.36a)

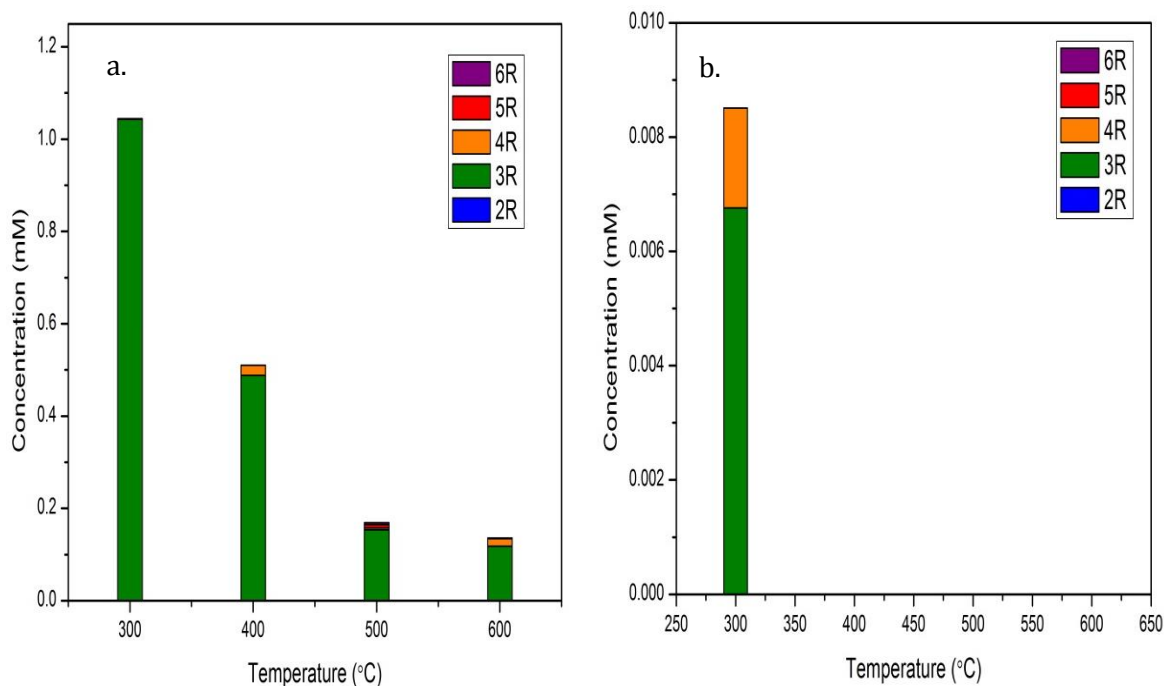


Figure 5.36 PAH desorption under 20%O₂/He – a)products in acetone, b)post reaction

Analysis under line not needed as the products were collected as soon as they were formed

There was a decrease in desorption concentration over higher temperatures. However, there was a significant concentration of phenanthrene observed on the soot post reaction at 300 °C, suggesting some difficulty in the oxidation of these species. Heavier PAHs with higher molecular weights were present in very small amounts as compared to those seen in the case of using the single component Ag-K/CZA catalyst for PAH oxidation, suggesting good activity for oxidation of these species by the mixed catalyst. However, the soot desorption results suggested, there not much desorption of higher molecular weight PAHs from the soot. The soot post reaction on extraction showed low PAHs (Figure 5.36 b), thus it may be concluded that all surface PAHs had desorbed or most of them were oxidised. There was a significant increase in activity of the catalyst for PAH combustion with temperature, as would be expected. Total combustion of the carbonaceous soot particles occurred by 600 °C, in the presence of the catalyst but the PAHs took longer to get oxidised, despite an excess oxygen in the feed, indicating that there was still modification required in the structure of the catalyst towards three ring (phenanthrene) oxidation.

5.6.4 Desorption of PAHs during soot oxidation under CO₂/He

In the presence of a CO₂-rich atmosphere, the combustion of carbonaceous soot particles was possible but the results shown in figure 5.37a showed that the combustion of the three ringed PAHs, in the presence of the catalyst was not efficient. Under such conditions the mixed catalyst performed slightly better than the individual Ag-K/CZA catalyst as the heavier aromatics were oxidised but the three ring PAHs especially phenanthrene are found to be very difficult to oxidise.

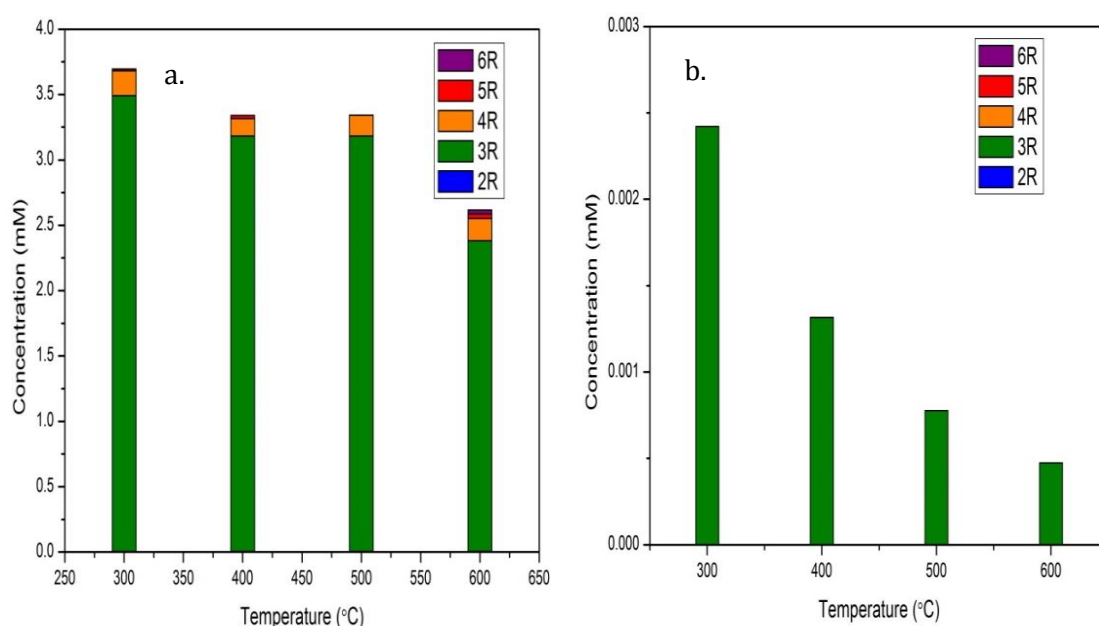


Figure 5.37 Desorption of PAHs under 20%CO₂/He – a)products in acetone, b)post reaction Analysis under line not needed as the products were collected as soon as they were formed

There was a high concentration of phenanthrene desorbed under this atmosphere that tends to decrease with temperature. But there was a significant concentration of phenanthrene being desorbed at 600°C (~2mM), indicating the inability or slow oxidation of phenanthrene oxidation using this catalyst. The utility of CO₂ for combustion was not a particularly desired pathway as the combustion of carbonaceous species with CO₂ could release poisonous CO into the exhaust stream. Soot post reaction shown in figure 5.37b showed continuous desorption of the aromatics from the surface with increase in temperature.

5.6.5 Desorption of PAHs during soot oxidation under NO atmosphere

The combustion of PAHs under NO/O₂/He showed a reduction in the concentration of PAHs desorbed from the surface of the soot compared to that under CO₂ and pure desorption of PAHs under helium but there was a significant increase in desorption compared to that collected after combustion under O₂ (figure 5.38)

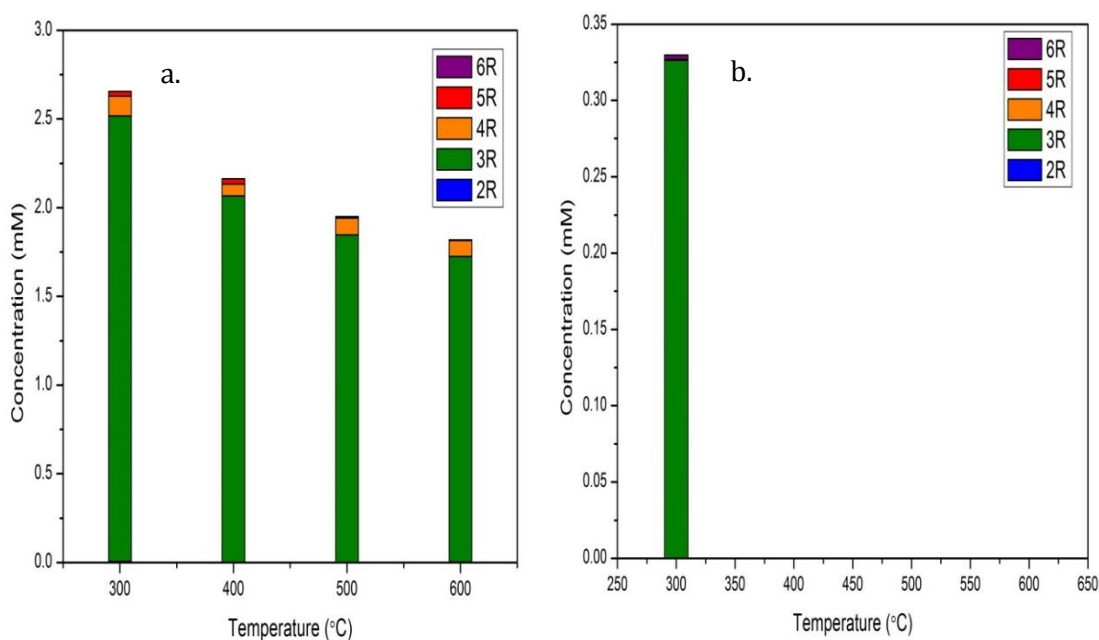


Figure 5.38 Desorption of PAHs under 300ppm NO/O₂/He – a)products in acetone, b)post reaction, Analysis under line not needed as the products were collected as soon as they were formed

In these analyses 8% O₂ was used in the feed to reflect a typical exhaust gas composition while in the case of the analyses under O₂ and He, 20%O₂ was used to reflect a synthetic air composition. Thus it may be concluded that an increase in catalytic activity towards PAH combustion was observed in the presence of an excess O₂ in the gas stream.

In the analyses under 300 ppm NO/O₂/He, the soot was combusted totally by 500°C, which was in agreement with the qualitative analysis under exhaust gas conditions shown in figure 5.39, containing similar concentrations of O₂ and NO. The soot was combusted by 500°C and the temperature at which the rate of oxidation reached a maximum was seen at 460°C. Again it was observed that the PAH concentration profile of the combustion products was dominated by three ring PAHs, suggesting difficulty in oxidising this species.

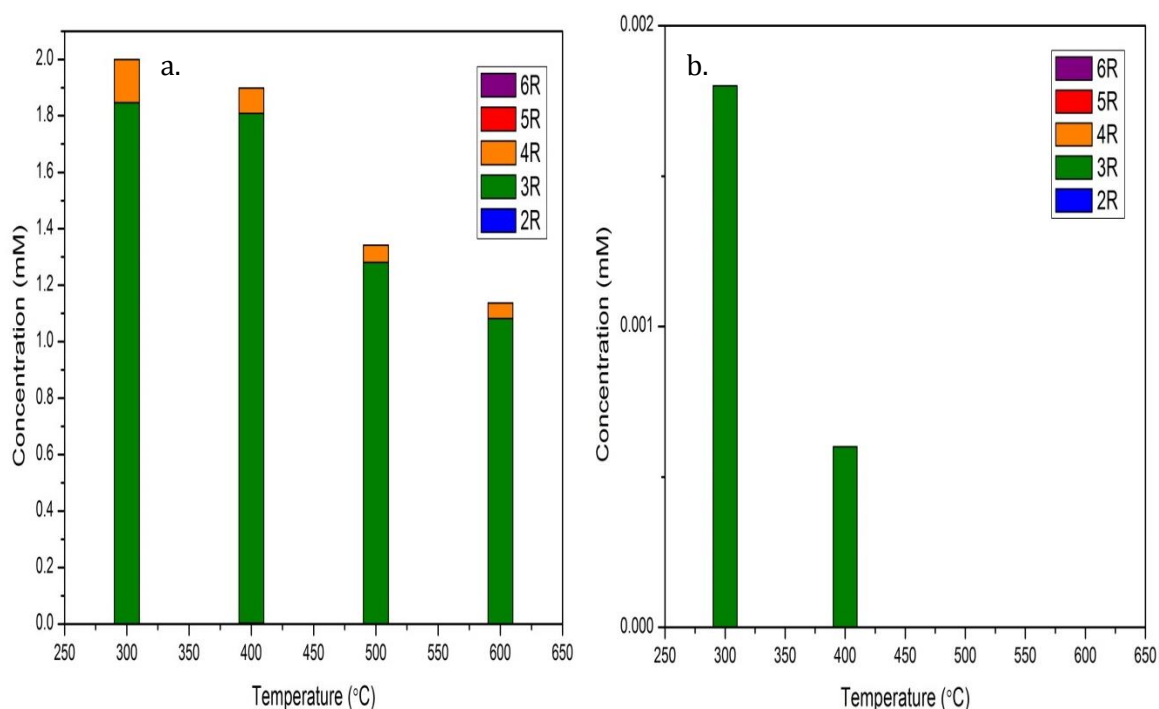


Figure 5.39 Desorption of PAHs under exhaust gas – a)products in acetone, b)post reaction

Analysis under line not needed as the products were collected as soon as they were formed

The concentration of PAHs collected from the gas phase under realistic exhaust gas (as shown in Figures 5.39 a and b), revealed that the main products desorbed are the three ringed structures. The distribution was similar to that collected from analyses under NO/O₂ as the concentrations of these principal oxidants were identical in both cases. The oxidation of PAHs was easier in the presence of the mixed catalyst as compared to the individual Ag-K/CZA, thereby oxidising the heavier aromatics quite easily. The concentration of desorbed products decreased with increase in temperature, most of which was desorbed by 450-600°C

The rates of desorption of phenanthrene were higher in the presence of the mixed catalyst as compared to the Ag-K/CZA catalyst for soot oxidation as can be observed from table 5.9 and table 5.11. The mixed catalyst proved to be capable of oxidising the other components better, as the desorption concentrations of the two, four, five and six membered rings were near negligible in this case, indicating a complete oxidation of these molecules to CO₂. The three membered rings especially phenanthrene were difficult to oxidize in the presence of this catalyst. The need was thus to

understand this system better with respect to phenanthrene for which a model has been created to try and understand the progress of the reaction.

Table 5.11 Percentage of thermal desorption as a concentration of desorption under Helium atmosphere

Temperature (°C)	O ₂ /He		CO ₂		300 ppm NO/O ₂ /He		Exhaust mix	
	Soot	Catalyst+ soot	soot	Catalyst+ soot	Soot	Catalyst +soot	soot	Catalyst +soot
300	42.3	54	0.12	20.62	38.4	91.86	2	69.65
400	52.8	19.1	2.3	49.71	0.5	76.6	2.1	70.03
500	6.8	7	0.6	-	0.7	80.2	4.4	54.89
600	-	3	3.2	67.99	0.8	48.60	-	30.977

Each analyses involved the use of a fresh batch of soot with or without catalyst depending on the condition. These are individual analyses at each temperature and thus cannot be totalled. Percentages were calculated as shown in the appendix.

The desorption increased in the presence of the mixed catalyst {as was seen from tables 5.9 (Ag-K/CZA) and 5.11 (Pt/SiC+Ag-KCZA)}. The desorption was maximum under the NO/O₂ atmosphere and this was seen to decrease with increase in temperature. The oxidation in these cases probably takes places post desorption off the surface, into the gas stream, in the presence of the O₂ from the feed to give rise to partially oxygenated products.

5.7 Phenanthrene bound to graphite: An ideal soot model

This model was prepared with the concentrations of phenanthrene as seen in the soot extracts, mixed with graphite. This was subjected to oxidation under synthetic air so as to understand the formation of partially oxygenated species formed upon phenanthrene oxidation. The graphite chosen for the study was free off any adsorbed PAHs.

5.7.1 Desorption of PAHs during soot oxidation under 20% O₂/He atmosphere

Uncatalysed oxidation of phenanthrene-graphite mixture showed a large amount of three ringed phenanthrene being desorbed from the surface of soot. This increased with an increase in temperature as in the case of the exhaust, probably due to the greater desorption rate at higher temperatures (figure 5.40a). In the absence of the catalyst this phenomenon was bound to occur, as this indicated increased desorption, but less oxidation. The presence of higher molecular weight PAHs indicated that the reaction pathway followed a proposition suggested by Zhang *et al.* [47], involving the polymerisation of smaller PAHs to form larger species. The graphitic surface analysed post reaction showed that the concentrations of the phenanthrene decreased with an increase in temperature and was negligible around 450-500°C, indicating that the desorption was quite rapid at this point coinciding with the rate of maximum oxidation of the carbonaceous soot moieties (figure 5.40b). The synthetic air mixture was used for these analyses for the ease of understanding the kinds of aromatic species formed during the oxidation of these PAHs.

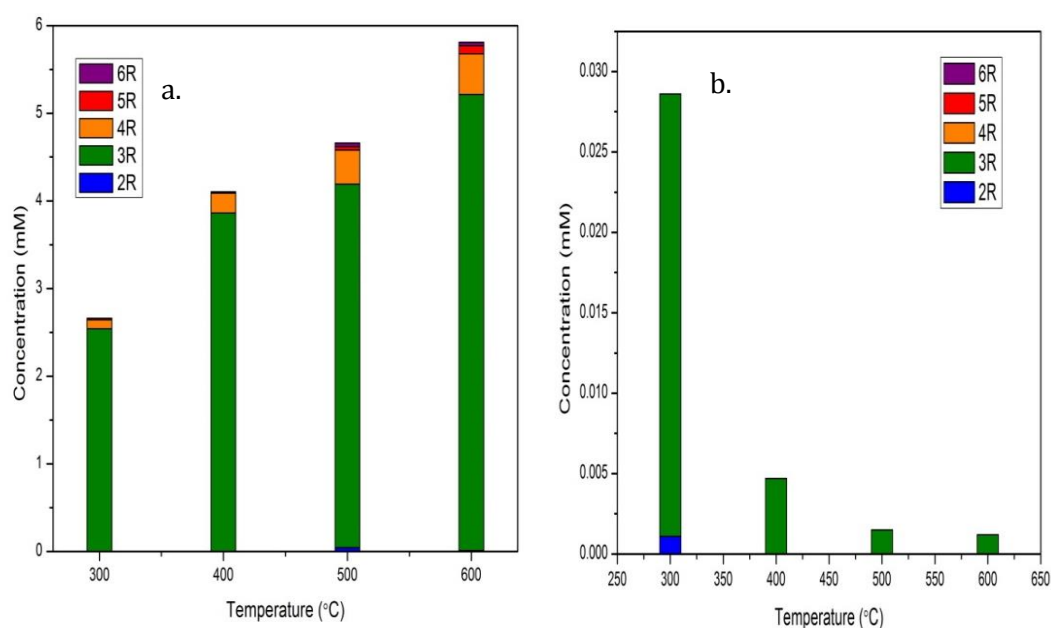


Figure 5.40 Desorption of Phenanthrene under 20% O₂/He- uncatalysed phenanthrene-graphite oxidation – a)products in acetone, b)post reaction

The catalytic combustion products of phenanthrene/graphite as represented in figure 5.41 showed a considerable decrease in the concentration of three ring aromatics as compared to non-catalysed combustion products, as was previously observed. The

decrease in heavier PAHs indicated that the oxidation process was favoured over desorption, suggesting that the catalyst accelerated direct oxidation pathways, but not polymerisation pathways, perhaps even suppressing these.

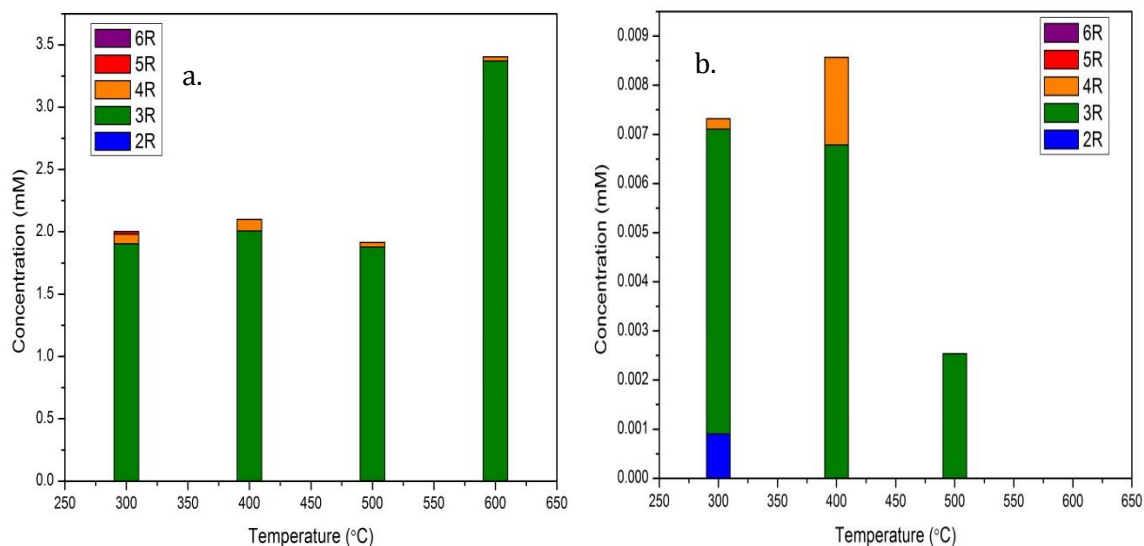


Figure 5.41 Desorption of Phenanthrene under 20% O₂/He - catalysed phenanthrene-graphite oxidation – a)products in acetone, b)post reaction

Table 5.12 indicated the percentage of thermal desorption in the absence and presence of a catalyst for phenanthrene oxidation. This showed that the mixed catalyst was capable of oxidising phenanthrene in the phenanthrene-graphite mixture into partially oxygenated compounds as shown below. Observing the soot post reaction we could see that the phenanthrene-graphite was probably oxidized to CO₂ by 600°C, in the presence of the catalyst but it was not fully combusted in the absence of it, until higher temperatures. The contribution of phenanthrene and graphite towards CO₂ formation was studied in detail in chapter 4.

Table 5.12 Desorption percentages of Phenanthrene from phenanthrene-graphite in the presence and absence of catalyst

Temperature (°C)	O ₂ /He	
	Phenanthrene+graphite (%)	Phenanthrene+catalyst+graphite (%)
300	19.38	14.02
400	28.8	15.34
500	31.7	14.24
600	30.9	25.15

This could be understood in more detail from analysis using LC-MS. The products from for uncatalysed phenanthrene-graphite and catalysed phenanthrene-graphite oxidation were obtained by trapping them in acetone similar to the previous cases. Partially oxidised products from phenanthrene oxidation when analysed using LC-MS, showed an M+H⁺ ion peak at 10 min, owing to the formation of 9,10-phenanthrene quinone with the formation of a dimer with a molecular weight of 416 and a Na adduct addition of M.W-22. This gave the 2M+Na⁺ peak – 436 (Figure 5.42). This was a commonly occurring oxidation product of phenanthrene. Dimerisation has been reported as a common phenomenon occurring in these PAHs at high temperatures [47].

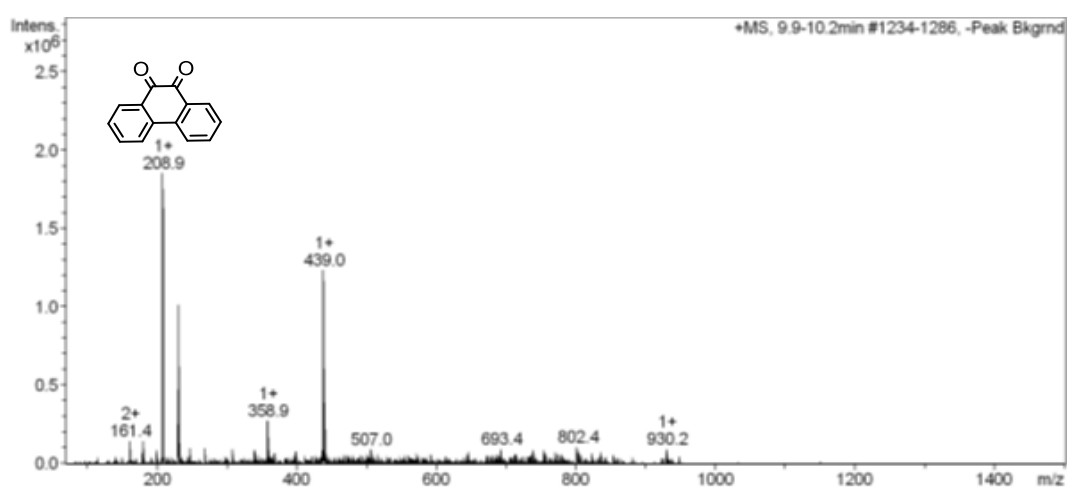


Figure 5.42 LC-MS analyses: Partial oxidation product-Phenanthrene-graphite oxidation-uncatalysed - 600°C- 9,10-phenanthrene quinone

The spectrum below represented that of a compound with molecular weight 241 which from literature indicates the possibility of a nitro-PAH such as 2-nitrodibenzopyranone or 4-nitrodibenzopyranone. This peak was observed at a retention time of 6.2min (figure 5.43).

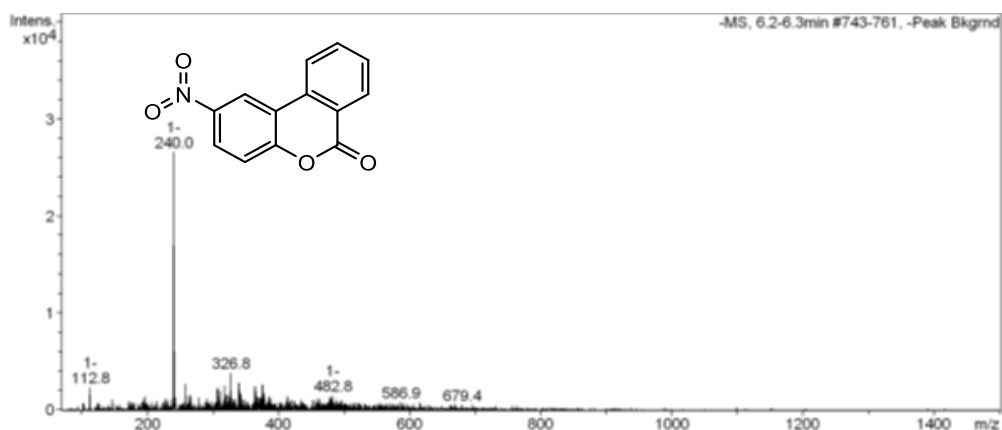


Figure 5.43 LC-MS analyses: Partial oxidation product-Phenanthrene-graphite oxidation-uncatalysed - 600°C- 2-nitrodibenzopyranone

The presence of nitro- functional groups on PAH such as phenanthrene is not expected. These functionalities are commonly present in soot formed from diesel fuel. Peaks of 2-nitroanthracene, 9-nitroanthracene, and 1-nitropyrene have been identified in diesel soot by Harvey *et al.* in their study on diesel and biodiesel soot [46-48]. They arise from chemical reactions of PAHs with different nitrogen containing molecules, such as NO_x or O_x (Alebic-Juretic *et al.*, 1990; Fan *et al.*, 1995; Pitts *et al.*, 1978; Xu and Burlingame, 1988). It was reported that some of these nitro-PAHs contribute to the mutagenicity of diesel exhaust particulates and these included 1,3-, 1,6- and 1,8-dinitropyrenes, 1-nitropyrene, 4-nitropyrene, and 6-nitrochrysene. Therefore, several researchers have investigated the chemical and physical properties of particulate matter in diesel exhaust according to the development of diesel technology and emissions regulation [49,50].

Another partially oxidized product was observed at 7.6min with a M+H⁺ peak = 240.9 which was attributed to biphenyl-2,2'-dicarboxylic acid with a molecular weight of 240. This indicated that the ring opening of phenanthrene to form corresponding acids from ketonic forms occurs at higher temperatures (figure 5.44).

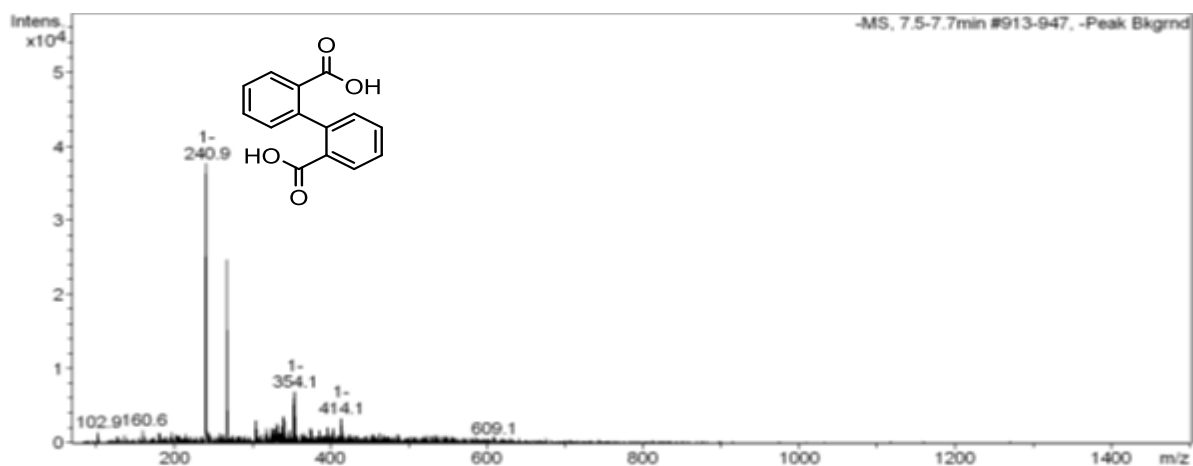


Figure 5.44 LC-MS analyses: Partial oxidation product-Phenanthrene-graphite oxidation-uncatalysed - 600°C- biphenyl-2,2' dicarboxylic acid

These partially oxidised products were formed only at higher temperatures such as 550-600°C in the exhaust.

In the presence of the catalyst, the following oxidative products were formed. The $M+H^+=226.7$ ion peak below represented 2-(2-formyl phenyl benzoic acid) with a molecular weight of 228. This was formed at 300°C, indicating the activity of the catalyst and its capability to oxidise the phenanthrene at lower temperatures (figure 5.45).

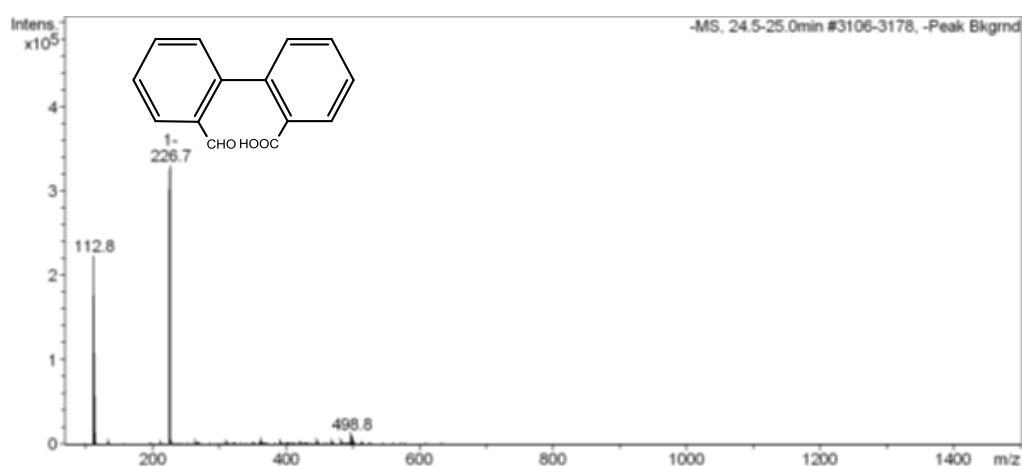


Figure 5.45 LC-MS analyses: Partial oxidation product-Phenanthrene-graphite oxidation-catalysed - 300°C - 2-(2-formyl phenyl benzoic acid)

The same product was obtained at 400°C (figure 5.46) probably indicating almost complete oxidation of phenanthrene to CO₂ through the formation of corresponding

acids. This study needs further investigation to understand the conversion to CO₂. There was a possibility of a dimer formation in this case, with a Cl⁻ adduct.

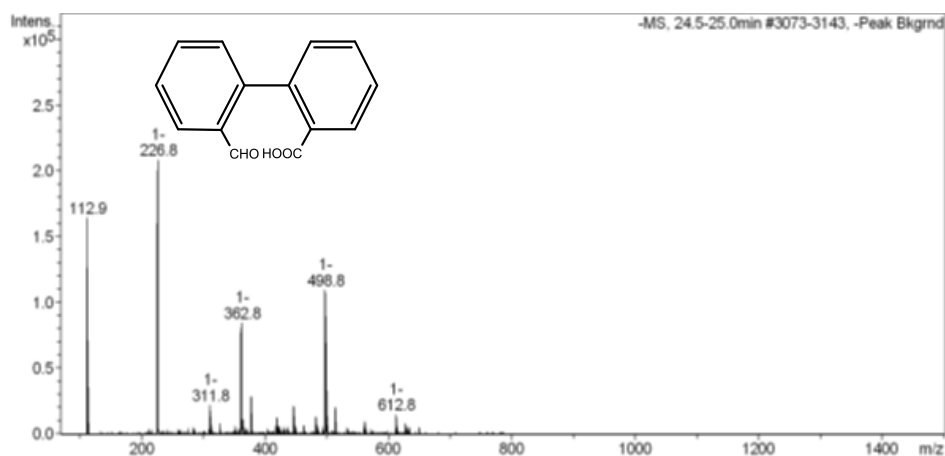


Figure 5.46 LC-MS analyses: Partial oxidation product-Phenanthrene-graphite oxidation-catalysed - 400°C - 2-(2-formyl phenyl benzoic acid)

An M-H⁺=288.1 peak indicating an oxidative product with molecular weight 287 was found in both EI-positive and EI-negative modes and was seen to form a dimer(576) along with a Na adduct (574+22=596). This product is present in the catalysed and uncatalysed soot oxidation along the entire temperature range between 300-600°C (figure 5.47).

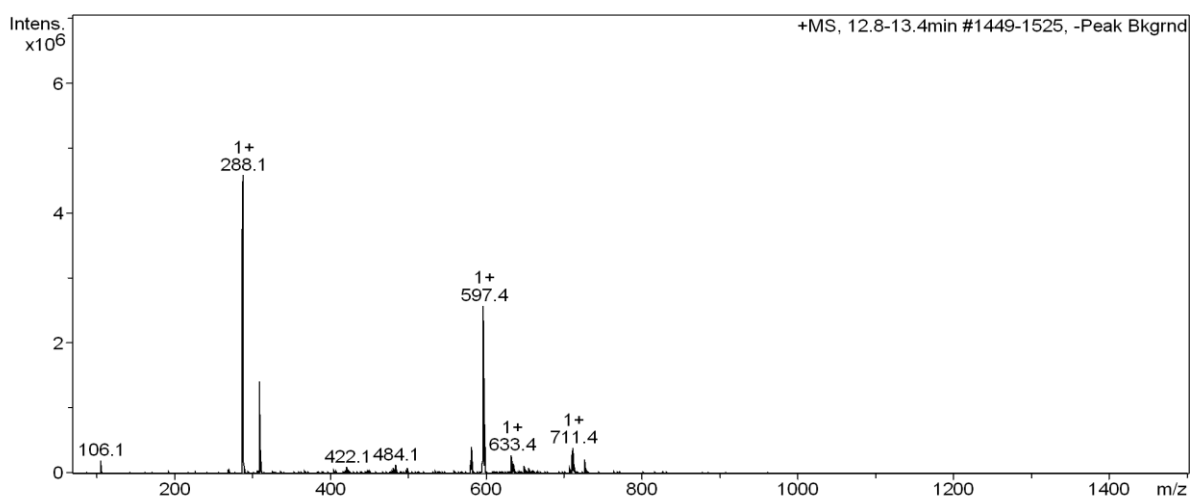
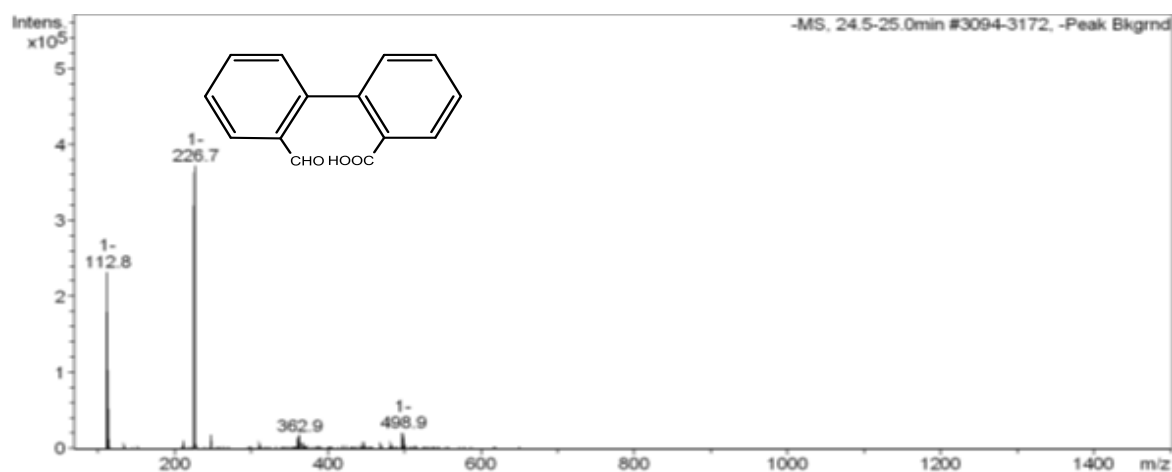
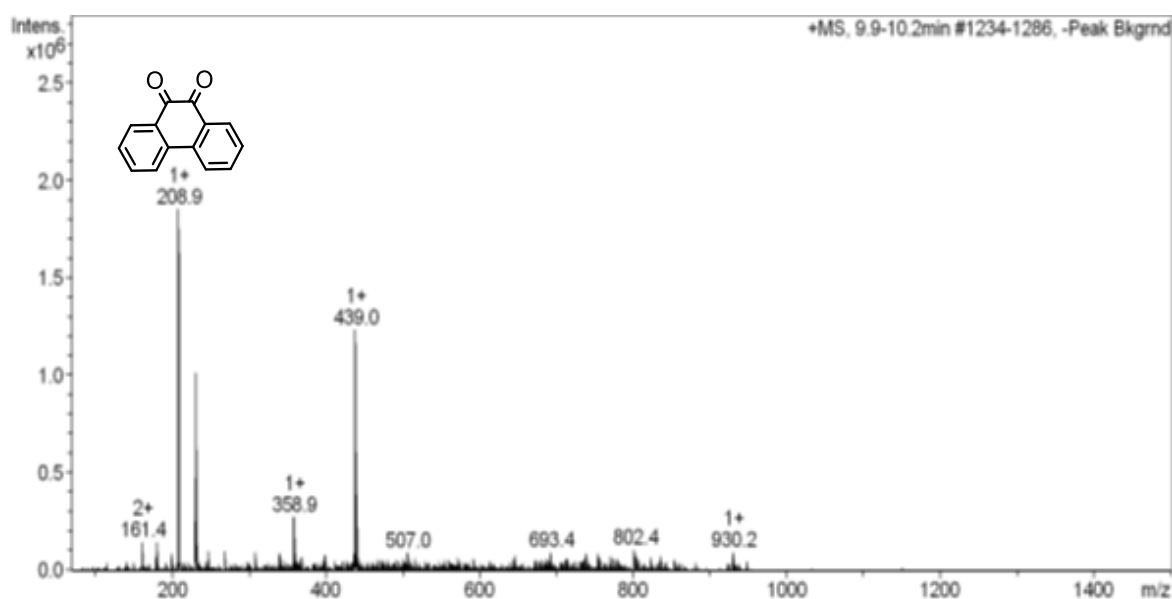


Figure 5.47 LC-MS analyses: Partial oxidation product-Phenanthrene-graphite oxidation-catalysed - 300°C – 600°C - unknown

The partial oxidation products from the oxidation of phenanthrene-graphite, in the presence of a catalyst was much reduced compared to that from the uncatalysed

oxidation, indicating that phenanthrene was completely converted to CO₂ under the O₂ atmosphere and at lower temperatures (complete oxidation by 600°C). The products seen during soot oxidation were quite complex to analyse but under the same oxidation conditions, in the presence of a 20% O₂/He feed, a few of these compounds from phenanthrene oxidation were present, such as 2-(2-formyl phenyl benzoic acid) and the compound with molecular weight 287 at 300, 400, 500 and 600°C but in the presence of the catalyst these compounds were not detected, indicating complete oxidation.



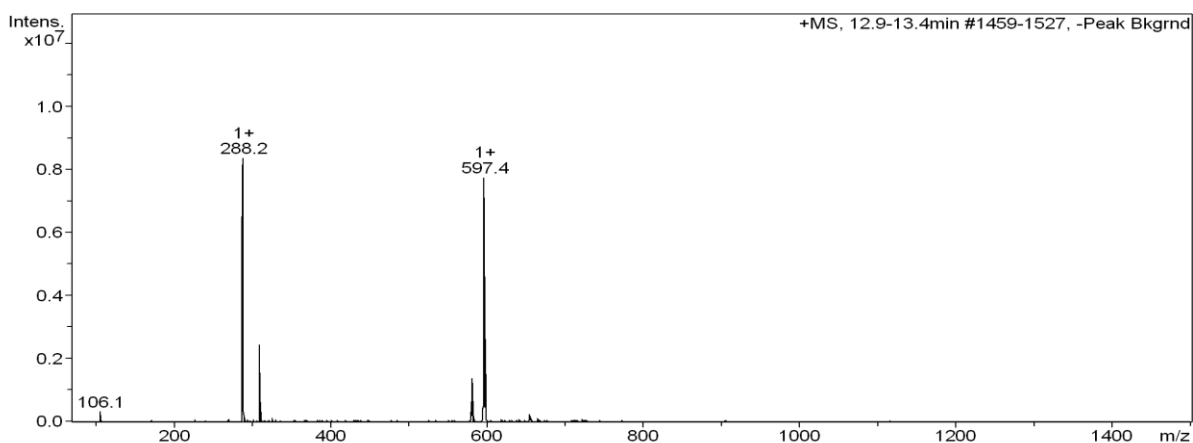


Figure 5.48 LC-MS analyses: Common Partial oxidation product - Phenanthrene-graphite oxidation-catalysed/uncatalysed oxidation

Results thus tend to indicate that there were no (or negligible quantities of) low molecular mass, partially-oxygenated products present in both catalysed and non-catalysed test samples. If similar mechanisms to those proposed by Zhang for naphthalene oxidation (Figure 5.48) were taking place, then the decomposition-oxidation pathway of phenanthrene would be expected to form partially-oxygenated intermediates such as phenanthrene 9,10-dione, naphthalic anhydride and smaller carboxylic acids, aldehydes and esters. The fact that these species were present suggests that once this pathway has been initiated, there is rapid progress to total oxidation for the majority of these molecules. This needs to be investigated in more detail under the reaction conditions used in this study.

5.8 Mechanisms of certain PAHs under various oxidative atmospheres

LC-MS indicated the presence of small amounts of the larger oxygenated molecules, formed by dimerization of some of the intermediates in the decomposition-oxidation pathway of phenanthrene, possibly with methylation also occurring. These large oxidative products possessed molecular weights beyond 300. This appears to again be analogous with the naphthalene dimerization and methylation pathway proposed by Zhang *et al.* [51] as shown in figure 5.49 and 5.50. Naphthalene-decomposed intermediates (Figure 5.49) were obtained mainly from the formation of phthalic anhydride, eventually leading to esterification and other oxidation processes. The main contributors to the formation of naphthalene derivatives were dimerisation (Figure 5.50a) and methylation mechanisms (Figure 5.50b). An initial growth of naphthalene

prior to its decomposition during the catalytic oxidation process, accounted for the formation of heavy PACs [51].

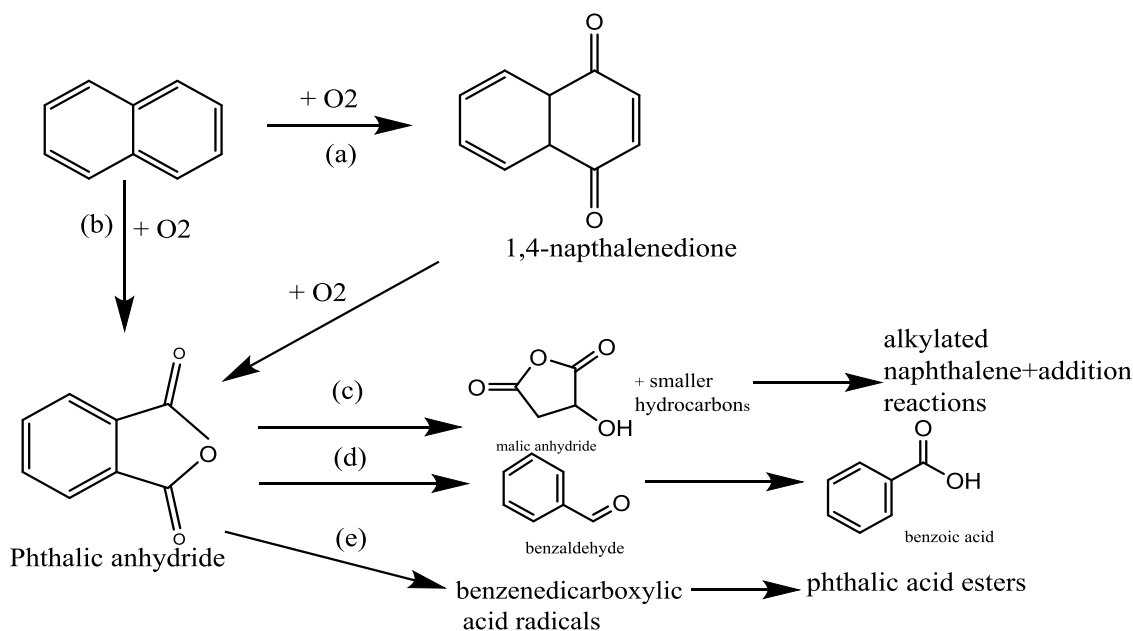


Figure 5.49 Naphthalene oxidation pathways [51]

These dimerised/methylated species have been identified in small amounts in both catalysed and uncatalysed phenanthrene/graphite combustion products. The formation of methylated or dimers was not significantly higher in the presence of a catalyst suggesting the oxidation may not totally depend on this route. However as there were lower concentrations of total PAHs detected in the catalysed combustion products (Figure 5.39) versus non-catalysed combustion products (Figure 5.40) it could be concluded that the rate of total oxidation of PAHs, likely via the decomposition-oxidation pathway, was enhanced in the presence of the mixed catalyst.

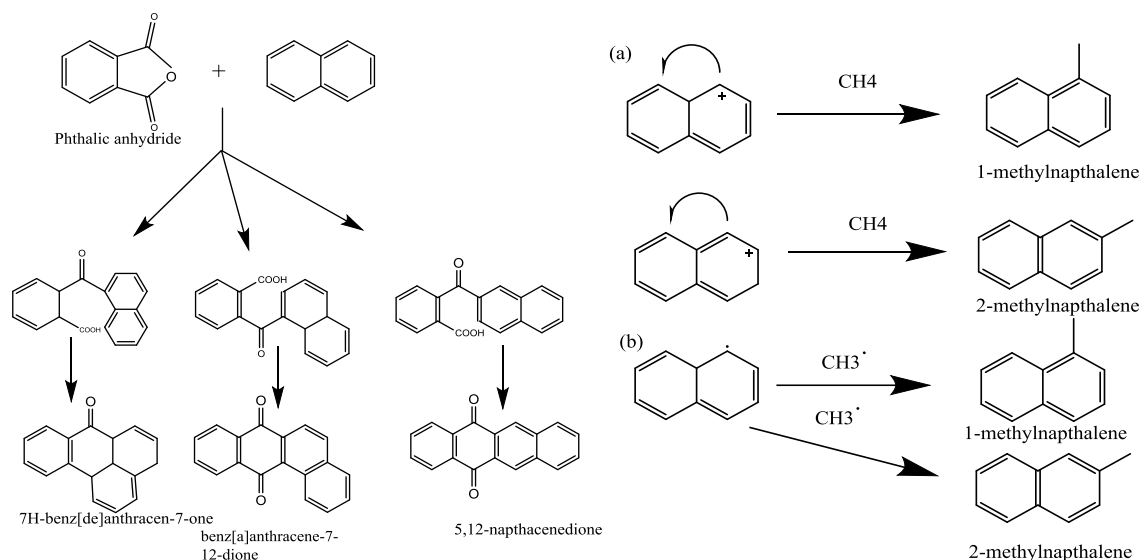


Figure 5.50 Naphthalene oxidation pathway- a) dimerization, b) methylation

In the case of phenanthrene oxidation with OH radical, it was observed that the 9-fluorenone, dibenzopyranone, 9,10-phenanthrenequinone, and 2,2'-diformylbiphenyl seen by GC-MS analyses of SPME in a study by Wang *et al.* were in agreement with Helmig and Harger (1994) [5,6]. 9,10-phenanthrenequinone was formed through the 9-hydroxyphenanthrene radical upon OH addition leading to further oxidation products. 9-fluorenone, dibenzopyranone, 9,10-phenanthrenequinone, 2,2'-diformylbiphenyl and traces of diphenic acid anhydride were observed as the major reaction products of an NO₃ radical initiated reaction of phenanthrene identified by SPME sampling/GC-MS analyses as shown below in figure 5.51. These studies by various researchers holds relevance to this study as these partially oxygenated species formed during the oxidation of soot are similar to that formed in the different studies conducted by these researchers, thus giving evidence and fortifying the probable mechanisms of PAH-soot oxidation, taking into account its complexity.

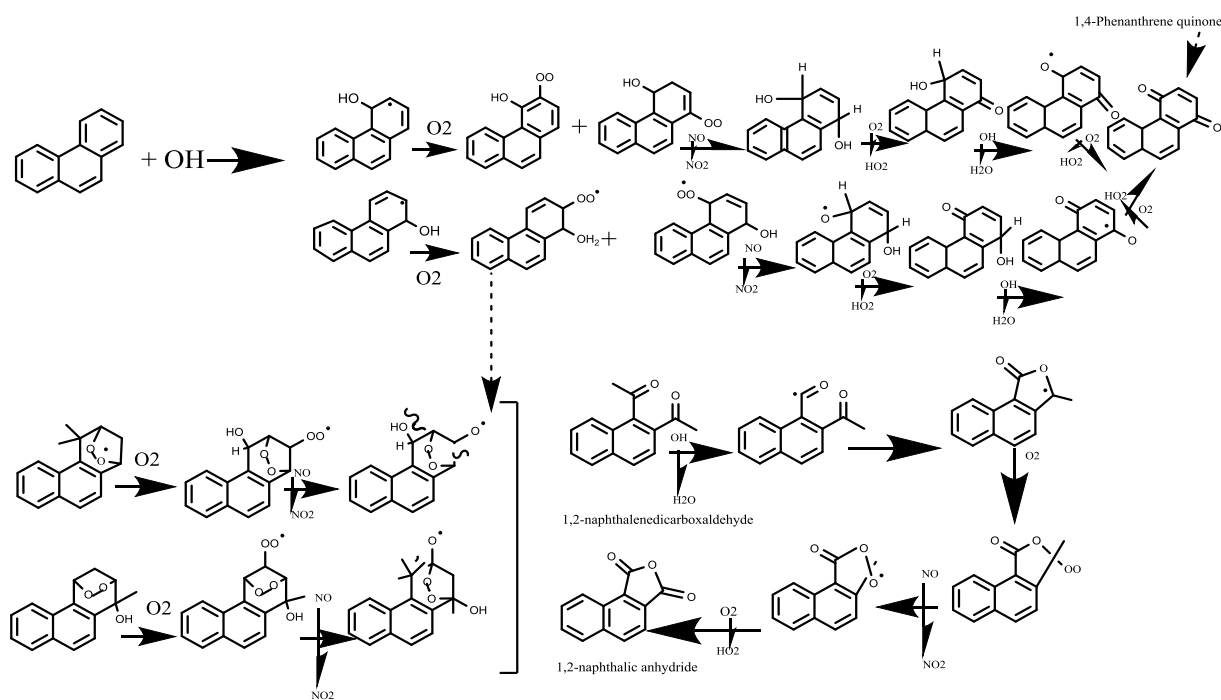


Figure 5.51 Phenanthrene oxidation pathway in the presence of OH radical [5]

In a study by Atkinson and Arey (2007) they showed that the OH radical addition pathway to form an OH-aromatic adduct tends to dominate in the case of simple aromatic compounds such as benzene, toluene and the xylenes [52]. Formation of 1,2-naphthalenedicarboxaldehyde and 1,2-naphthalic anhydride from the reaction of OH-[Phen-O₂] radical with O₂ is depicted in figure 5.51. 1,2-naphthalenedicarboxaldehyde possessing an intra-carbon double bond as a ring opening product loses one of its hydrogen atoms through an attack by OH radicals and forms a formyl radical. The intra-aldehyde group then attacks the formyl radical and leads to formation of 1,2-naphthalic anhydride through cyclization and loss of a hydrogen atom. 1,4-phenanthrene quinone can be formed from phenanthrene by further reactions of some OH-Phen-O₂ peroxy radicals as shown in the figure 5.51. This study showed formation of some of the partially oxygenated species during phenanthrene oxidation. These were similar to those observed in our study but the reaction with various radicals such as OH[•] needed more investigation.

The reaction products of phenanthrene oxidation were found to be 9-fluorenone, 1,2-naphthalic anhydride, 2,2'-diformylbiphenyl, dibenzopyranone, 1, 2, 3, 4 and 9-phenanthrols, 1, 2, 4 and 9-nitrophenanthrenes, 1,4-phenanthrenequinone, 9,10-

phenanthrenequinone and 2- and 4-nitrodibenzopyranones. From the measurement of gas/particle partitioning of products, it was apparent that the phenanthrene quinones, phenanthrols, nitrophenanthrene and nitrobenzopyranone existed mainly in the particle phase. Thus, these oxidized products should be found in SOA in the atmosphere and may, therefore, have an impact on human health. Recent studies have shown that the quinones are highly toxic to humans and the other oxidized products might be also considered to be toxic pollutants. The oxidation of phenanthrene shown by several scientists as mentioned above takes place through an attack on the outer ring, thereby oxidising it as opposed to that observed in our case, where the middle ring undergoes attack by the oxygenated species, forming the corresponding partially oxygenated compounds such as 9,10-phenanthrene quinone and 2-(2-formyl phenyl) benzoic acid. These over the course of further oxidation lead to the formation of CO₂. This kind of attack on the middle ring tends to maintain the aromaticity of the other rings.

Several studies in our research group on homogeneous catalytic oxidation of phenanthrene have shown similar approaches. It was shown by Nowicka *et al.* using a monophasic solvent system, the oxidation of phenanthrene was carried out giving rise to biphenyl 2,2'-dialdehyde while the oxidation of pyrene led to the production of phenanthrene-4,5-dialdehyde via the control of reaction time and the use of quenching [53]. Thus this kind of preferential attack on the middle ring as in the case of phenanthrene is not common but leaves more scope for investigation in the future.

5.9 Conclusions

This chapter showed the presence of various PAHs in diesel soot through several extraction techniques, the best being Soxhlet extraction using toluene. This chapter also highlights the use of the 2%Ag-10%K/CZA catalyst (ideal for soot oxidation) for PAH oxidation. The main observation was that, the process of desorption and oxidation occurred in the exhaust based on the absence or presence of an oxidative atmosphere. This catalyst was capable of oxidising the three ringed PAHs to a large extent. It was incapable of oxidising the heavier aromatics that were constantly being desorbed without being oxidised. The oxidation under CO₂ showed that the PAHs were oxidised more efficiently rather than being desorbed off the surface. The rate of desorption was higher in the presence of oxidants such as NO₂, O₂ and under realistic exhaust mix.

These oxidants could be reacting with the solid carbon, thereby releasing the adsorbed PAHs.

Modification to the catalyst structure as explained in this chapter, helped to bring a mix between a good soot oxidation catalyst (Ag-K/CZA) and a good PAH oxidation catalyst (Pt/SiC). This mixed catalyst showed that the heavier five and six ringed PAHs were oxidised very efficiently as there were no traces of desorption seen in these cases. The total combustion of the carbonaceous soot occurred by 600°C, in the presence of this catalyst but a small concentration of the PAHs were still adsorbed onto the soot surface beyond these temperatures in the absence of the catalyst, indicating the difficulty of oxidation of these species. Thus there was a need for catalyst modification to help in the oxidation of PAHs such as phenanthrene in a more efficient manner. The combustion of aromatics such as benzene over Pt catalysts was studied by Dryakhlov *et al.* [54] and they found that the benzene was converted by a heterogeneous-homogeneous mechanism with certain steps occurring in gas phase. Beyond this several authors then investigated the oxidation reactions of benzene and toluene over Pt catalysts [55,56]. It was shown that the aromatics tend to strongly adsorb onto the Pt surface. There is not much information on this kind of adsorption of these aromatics onto the surface but it is believed that it may occur both via the aromatic ring or alkyl groups present on the soot. This study gives an insight on the probable modes of adsorption of the PAHs onto Pt catalysts as used in our study, thus giving a better understanding of the catalyst-soot interaction.

The factors governing the reactivity of these PAHs are: a) the loss of aromaticity which explains how the partially or fully hydrogenated compounds are more reactive than the starting materials ; b) formation of partially oxygenated or selective oxidation products that are believed to be the intermediates in the total combustion process of these PAHs. Thus it is necessary to understand these intermediates and their reactivity in order to unveil the mechanism of PAH-soot oxidation. This chapter also focused on the oxidation of phenanthrene (the predominant aromatic in soot). A model of phenanthrene with graphite helped to an extent in understanding the complexity of phenanthrene oxidation pathways and showed the occurrence of oxidation (in the presence of the mixed catalyst) through an attack on the middle ring, yielding partially oxygenated species that were later oxidised to CO₂.

Several studies were conducted on these Pt catalysts to understand the effect of the catalyst and structure activity correlations to explain the mechanism. The most widely used catalyst for the various analyses of PAH oxidation was a well dispersed Pt/Al₂O₃ (~1nm). These oxidation reactions with the aliphatics and aromatics on the soot depended on the surface structure and particle size of these Pt particles. Studies by Diehl *et al.* have revealed that the light alkanes and the aromatics tend to oxidize easily on the big particles while O₂ activation process involving the adsorption/desorption and dissociation was easier on the 5-10nm Pt particles. Thus the catalyst structure is a vital factor in determining the progress of the oxidation [57]. The Pt/SiC and Pt/SiC+Ag-K/CZA catalyst structures have been understood in detail in chapter4.

References

1. J. Arey, R. Atkinson, B. Zlelinska, P. A. McElroy, *Environmental Science and Technology*, 23, (1989), 321-327.
2. L. E. Sitaras, E. B. Bakeas, P. A. Siskos, *Science of the Total Environment* 327,(2004), 249-264.
3. T. F. Kahan, N. O. A. Kwamena, D. J. Donaldson, *Atmospheric Environment* 40, (2006), 3448-3459
4. J. N. Pitts, D. M. Lokensgard, P. S. Ripley, K. A. Vancauwenberghe, L. Vanvaeck, S. D. Shaffer, A. J. Thill, W. L. Belser, *Science*, 210, (1980),1347-1349
5. D. Helmig, W. P. Harger, *Science of the total environment*, 148, (1994), 11-21.
6. L. Wang, R. Atkinson, J. Arey, *Atmospheric Environment* 41, (2007), 2025-2035.
7. K. Prevedouros, E. BrorströmLunde, C. J. Halsall, K. C. Joens, R. G. M. Lee, A. J. Sweetman, *Environmental Pollution*, 1128, (2004),17-27.
8. T. F. Bidleman, *Analytical Chemistry*, 56, (1984),2490-2496.
9. N. Klempier, H. Binder, *Analytical Chemistry*, 55, (1983), 2104-2106
10. Neff (1979) and Handbook of Chemistry and Physics (Weast, 1968).
11. D. Bodzek, K. Luks-Betlej, L. Warzecha, *Atmospheric Environment, Part A:General Topics*, 27A(5), (1993), 759-64
12. D. J. T Smith, R. M. Harrison, *Atmospheric Environment*, 30, (1996), 2513-2525.
13. T. Paschke, S. B. Hawthorne, D. J. Miller, B. Wenclawiak, *Journal of Chromatography. A*, 609(1-2), (1992), 333-40.
14. B. A. Benner, *Analytical Chemistry*, 70(21), (1998), 4594-4601
15. V. Lopez-Avila, R. Young, W. F. Beckert, *Analytical Chemistry*, 66, (1994),1097-106.

16. P. Bruno, M. Caselli, G. de Gennaro, M. de Rienzo, A. Traini, *Journal of Environmental Monitoring*, 2, (2000), 223-227.
17. A. H. Miguel, J. B. De Andrade, *International Journal of Environmental Analytical Chemistry*, 35, (1989), 35-41.
18. C. H. Marvin, L. Allan, B. E. McCarry, D. W. Bryant, *International Journal of Environmental Analytical Chemistry*, 49(4), (1991), 221-230.
19. B. E. Richter, B. A. Jones, J. L. Ezzell, N. L. Porter, N. Avdalovic, C. Pohl, *Analytical Chemistry*, 68, (1996), 1033-1039
20. O. P. Heemken, N. Theobald, B. W. Wenclawiak, *Analytical Chemistry*, 69, (1997), 2171-2180
21. K. J. Hageman, L. Mazeas, C. B. Grabanski, D. J. Miller, S. B. Hawthorne, *Analytical Chemistry*, 68(22), (1996), 3892-3898
22. S. B. Hawthorne, S. Trembley, C. L. Moniot, C. B. Grabanski, D. J. Miller, *Journal of Chromatography A*, 886, (2000), 237-244.
23. A. Eiroa, V. Leroy, P. Dagaut, Y. Bedjanian, *Chemosphere*, 78, (2010), 1342-1349
24. H. A. Claessens, L. G. D. Lammerts van Bueren, P. M. Van De Ven, *Journal of Aerosol Science*, 17, (1986), 639-642,
25. B. B. Chakraborty, R. Long, *Environmental Science and Technology*, 1, (1967), 82
26. H. J. Gitze, J. Schneider, H. G. Herzog, J. Fresenius *Analytical Chemistry*, 340, (1991) 27-30
27. A. Guilloteau, Y. Bedjanian, M. L. Nguyen, A. Tomas, *Journal of Physical Chemistry A*, 114, (2010), 942-948
28. Y. Bedjanian, M. L. Nguyen, A. Guilloteau, *Journal of Physical Chemistry A*, 114, (2010), 3533-3539
29. D. Helmig, J. Arey, R. Atkinson, W. P. Hager, P. A. McElroy, *Atmospheric Environment*, 26, 9, (1992), 1735-1745,
30. T. E. Jensen, R. A. Hites. *Analytical Chemistry* 55, (1983), 594-599.
31. T. Nielsen, B. Seitz, T. Ramdahl, *Atmospheric Environment*, 18, (1984), 2159-2165
32. J. N. Pitts, J. A. Sweetman, B. Zielinska, A. M. Winer, R. Atkinson, *Atmospheric Environment*, 19, (1985), 1601-1608
33. K. Miet, K. Le Menach, P. M. Flaud, H. Budzinski, E. Villenave, *Atmospheric Environment*, 43 (2009), 837-843
34. M. Frenklach, H. Wang, *Proceedings of Combustion Institute*, 23, (1990), 1559-1566
35. A. Raj, M. Celnik, R. Shirley, M. Sander, R. Patterson, R. West, M. Kraft, *Combustion and Flame*, 156, (2009), 896-913,
36. J. F. Orrego, F. Zapata, T. N. Truong, F. Mondragon, *Journal of Physical Chemistry A*, 113, (2009), 8415-8420
37. J. Appel, H. Bockhorn, M. Frenklach, *Combustion and Flame*, 121, (2000), 122-136,

38. C. Y. Lin, M. C. Lin, Paper 7, Presented at the Fall Technical Meeting of the Eastern States Section of the Combustion Institute, Gaithersburg, Maryland, November **1987**.
39. S. Mancarella, A. Sully, M. Derudi, R. Rota, S. Granata, T. Faravelli, E. Ranzi, *Chemical Engineering transactions*, 10 (**2006**), 523
40. D. X. Du, R. L. Axelbaum, C. K. Law, *Combustion and Flames*, 102, (**1995**), 11-16
41. A. Raj, Z. Zainuddin, M. Sander, M. Kraft, *Carbon*, 49 (**2011**) 1516-1531
42. M. Sander, A. Raj, O. Inderwildi, M. Kraft, S. Kureti, H. Bockhorn, *Carbon*, 47, (**2009**), 866–875
43. T. Kyotani, A. Tomita *Journal of Physical Chemistry B*, 103, (**1999**), 3434–3441.
44. K. Sendt, B. S. Haynes, *Combustion and Flames*, 143, (**2005**), 629–43.
45. D. R. Sellick *et al.*, *Applied Catalysis B: Environmental*, 132, (**2013**), 98-106
46. L. Li-bin, L. Yan, L. Jin-ming, T. Ning, H. Kazuichi, M. Tsuneaki, *Journal of Environmental Sciences*, 19, (**2007**), 1–11
47. C. D. Havey, R. R. Hayes, L. R. McCormick, K. J. Voorhees, *American Chemical Society, Divisions of Fuel Chemistry*, 50(1), (**2005**), 333
48. F. Portet-Koltalo, N. Machour, Diesel Engine - Combustion, Emissions and Condition Monitoring, Edited by Saiful Bari, ISBN 978-953-51-1120-7, Hard cover, 266 pages, Publisher: InTech
49. H. A. Bamford, D. Z. Bezabeh, M. M. Schantz, S. A. Wise, J. E. Baker, (**2003**), *Chemosphere*, 50: 575–587
50. X. Yang, K. Igarashi, N. Tang, J. M. Lin, W. Wang, T. Kameda, A. Toriba, K. Hayakawa, *Mutation Research*, 695, (**2010**), 29–34.
51. X. W. Zhang, S. C. Shen, K. Hidajat, S. Kawi, L. Yu, K. Y. Simon, *Catalysis Letters*, 96, (2004), 87
52. R. Atkinson, J. Arey, *Polycyclic Aromatic Compounds*, 27, (**2007**), 15-40
53. E. Nowicka, Selective oxidation of Polynuclear aromatic hydrocarbons, Ph.D. Thesis, **2012**
54. A. S. Dryakhlov, S. L. Kiperman, *Kinetics of Catalysis*, 22, (**1981**), 159–163.
55. S. Ordoñez, L. Bello, H. Sastre, R. Rosal, F.V. Diez, *Applied Catalysis B: Environmental*, 38 (**2002**)139–149
56. A. A. Barresi, M. Cittadini, A. Zucca, *Applied Catalysis B: Environmental*, 43, (**2003**),27–42
57. F. Diehl, J. Barbier, D. Duprez, I. Guibard, G. Mabilon, *Applied Catalysis B: Environmental*, 95, (**2010**), 217–227

Chapter 6

Conclusions and future work

6.1 Final Conclusions

The main aim of this study was to synthesise optimized catalysts capable of lowering the temperatures of soot oxidation and in oxidising the PAHs adsorbed onto the surface of the soot. Several catalysts have been studied with the aim of utilizing the oxygen stored in the lattice of these catalysts for the purpose of soot oxidation either by a spill over or redox mechanism as mentioned in chapter 1. The wide range of catalysts prepared as seen in chapter 2 ranged from efficient redox supports such as CeO_2 , $\text{CeO}_2\text{-ZrO}_2$, $\text{CeO}_2\text{-ZrO}_2\text{-Al}_2\text{O}_3$ and $\text{CeO}_2\text{-Al}_2\text{O}_3$ to silver and potassium impregnated CZA catalysts that were capable of promoting the combustion at faster rates and at lower temperatures.

The optimization of the CZA catalysts was described in detail in chapter 3 where different methods were employed to understand the influence of the preparation on the structural and physical properties of the catalysts. The co-precipitation of the precursor solutions of CeO_2 , ZrO_2 and Al_2O_3 all together, using a base such as Na_2CO_3 , followed by calcination at 500°C , 5°C min^{-1} for 5 hours under flowing air was ideal in preparing tiny crystallites of CZA. These upon impregnation with different percentages of silver nitrate, with an ideal loading of 2%Ag, led to a decrease in the soot oxidation temperatures ($T_{\text{on}}\text{-}402^\circ\text{C}$, $T_{\text{f}}\text{-}647^\circ\text{C}$). This promotion of soot oxidation correlates with reduction of the ceria in the catalyst at lower temperatures, by $100\text{-}150^\circ\text{C}$ due to the silver impregnation allowing the oxygen stored in the CZ crystal lattice to be used for combustion. Similarly, the impregnation of the K_2CO_3 onto the CZA surface resulted in significant decrease in oxidation temperatures and enhanced activity towards soot oxidation, showing that alkali metals act as promoters in the reaction. Alkali and alkaline earth metals on CZA were tested for soot oxidation and were both found to be ideal promoters. As expected, the loading played a key factor in determining the promotional activity of K on the CZA support for soot oxidation ($T_{\text{on}}\text{-}304^\circ\text{C}$, $T_{\text{f}}\text{-}458^\circ\text{C}$). The optimum loading of K that led to the decrease in surface area of the CZA supports and gave rise to crystallites of considerable sizes as mentioned in chapter 3, was found to be 10%. The K_2CO_3 functioned by a carbon-oxygen-K complex mechanism that helped

to oxidized the carbon from the soot efficiently to CO₂. Upon using various other K salts such as KCl, KNO₃, KOH, different mechanisms were seen to take dominance but best results were produced in the presence of K₂CO₃ and KNO₃ on CZA supports. A combination of the alkali metal promotion and Ag, to produce smaller nanoparticles ideal for soot oxidation resulted in a simple approach of direct impregnation of Ag and K on CZA. This resulted in a drastic increase in rate of the reaction and the surface area of this catalyst was slightly higher than that of the pure K impregnated catalysts. The Ag⁰ and Ag₂O species alongside the K₂CO₃ was responsible for the providing the oxygen species to soot and aids in lowering the oxidation temperatures (T_{on}-324°C, T_f-390°C).

The major products of soot combustion, CO₂ and CO were quantified using GC and FTIR analyses. The influence of different oxidative conditions, in the presence and absence of the catalyst, on the rate of the reaction was analysed was studied in detail in chapter 4. The influence of NO₂ on the promotion of soot combustion was also studied by testing the Ag-K/CZA, Pt/SiC and Pt-SiC+Ag-K/CZA catalysts, in the absence and presence of NO feed under a realistic exhaust gas feed. The Ag-K/CZA was found to be a good redox catalyst with a good oxygen storage capacity owing to the nature of the ceria-zirconia in the lattice while the Pt/SiC was a good NO_x storage source that helped to oxidize the soot by providing the NO₂ adsorbed to its surface to the catalyse the soot oxidation faster. The mixed catalyst Pt/SiC+Ag-K/CZA helped to oxidise the soot and the PAHs adsorbed on the soot surface. The NO₂-assisted mechanism and also the redox property of ceria, functioning by the Mars van Krevlen mechanism were vital in determining the rate of the reaction. The active oxygen and NO₂-assisted mechanisms occurred based on the condition prevalent in the exhaust.

The aim of the work described in Chapter 5 was to speciate the PAHs present in diesel soot, using various solvent extraction techniques. The major component identified was phenanthrene, which allowed a realistic model soot formulation to be created in order to understand the catalytic reactions taking place. The phenanthrene, which was bound to graphite in concentrations typical of real soot, was oxidised in the presence of an oxidative atmosphere to form partial oxygenated products (such as 9,10-phenanthrenedione) as well as CO₂. The concentration of the desorbed products under realistic exhaust gas feed, O₂, CO₂ or NO/NO₂ atmosphere was calculated as a percentage of the of the desorption products under helium atmosphere. The Ag-K/CZA

was capable of oxidising the aromatics very efficiently under various oxidative atmospheres, especially under CO₂-rich atmosphere. There was a difficulty in oxidising the heavier aromatics in the presence of this catalyst. This was possible in the presence of the mixed catalyst. This catalyst helped to oxidise the phenanthrene to partially oxygenated species and finally to CO₂. This study has been successful in understanding different aspects of soot oxidation taking into account its complexity. The 2%Ag-10%K/CZA has proven to be an efficient catalyst and is ideal for a scale up, to be used for commercial purposes. This catalyst is a very stable one showing good reproducibility over several successive runs, with fresh charge of soot.

6.2 Future Work

This study has led to several intriguing results that need more investigation. The catalyst structure in terms of the synergism between the Ag species and K on CZA need to be studied in more detail, so as to give a suitable explanation for the mechanism of catalysed soot oxidation. The changes in catalyst with oxidation need to be understood through in-situ FTIR or EPR studies. There is scope for synthesis of a more efficient PAH-soot combustion catalyst that is capable of oxidising the aromatics at lower temperatures, alongside the carbonaceous soot oxidation.

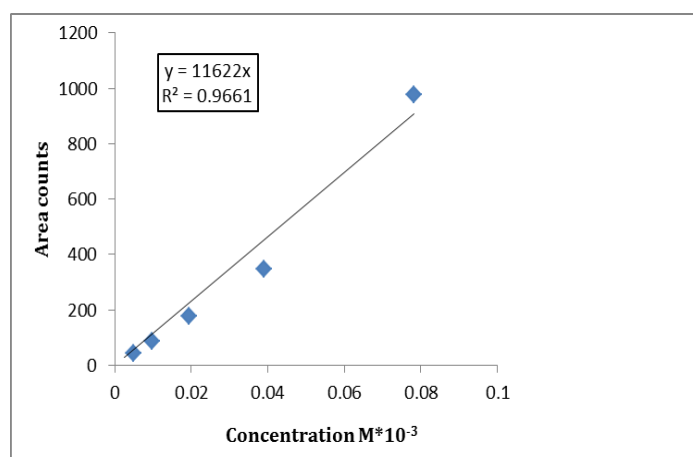
The oxidation of the other aromatics models such as phenanthrene-graphite could be used to effectively understand the formation of partially oxygenated species through an in-line mass spectrometer. Comparison of different soot samples from different points in the exhaust was necessary in order to understand the distribution of PAHs in the diesel exhaust. Understanding of the mechanisms for soot oxidation based on the situation in the exhaust needs more attention, for which constant in-line gas analyses using the FTIR-MS techniques would help in quantifying and understanding different products evolved.

7. Appendix

1. HPLC calibration plots for the 16 compounds from the standard injection into HPLC

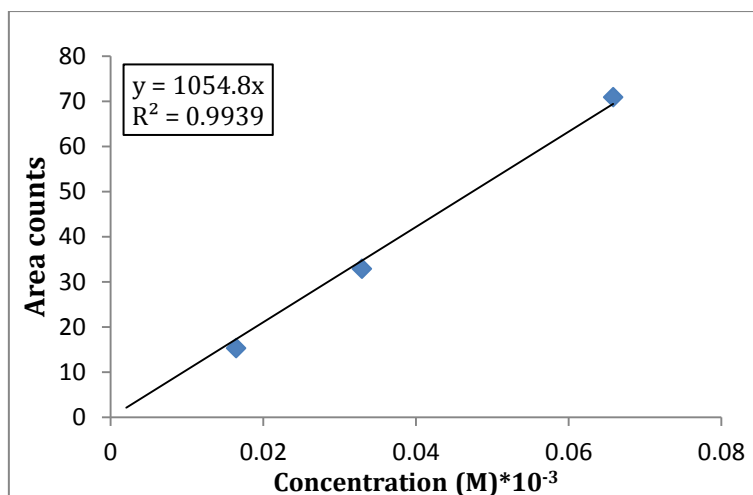
i) Naphthalene

concn(mol/l)	concn (mol/l*10 ⁻³)	area
7.81774E-05	0.0781774	978.807
3.90887E-05	0.0390887	346.8
0.000019544	0.019544	176.9
9.7721E-06	0.0097721	88.1
0.000004886	0.004886	44.7
0.000002443	0.002443	



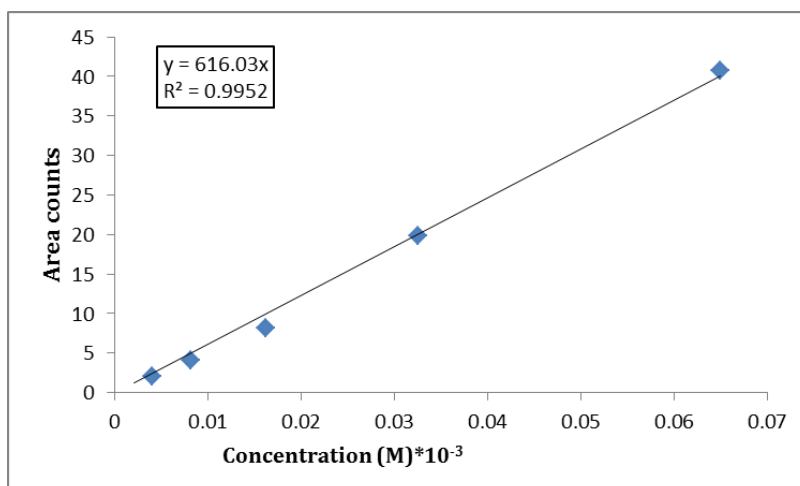
ii) Acenaphthylene

Sl.No	Concentration(M)	Concentration M (*10 ⁻³)	Area counts
1	6.58387E-05	0.065839	70.88773
Diln1	3.29194E-05	0.032919	32.88536
Diln2	1.64597E-05	0.01646	15.28358
Diln3	8.22984E-06	0.00823	
Diln4	4.11492E-06	0.004115	
Diln5	2.05746E-06	0.002057	



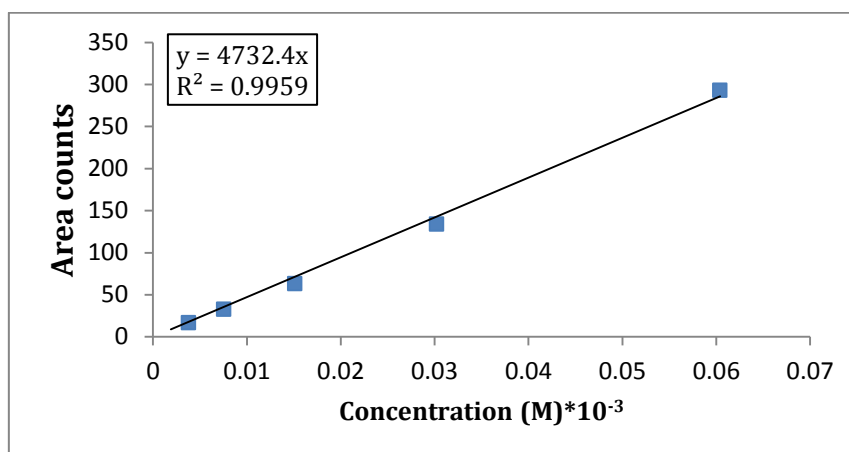
iii) Acenaphthene

Sl.No	Concentration (M)	Concentration M(*10 ⁻³)	Area
1	6.49763E-05	0.06497633	40.7353
Diln1	3.24882E-05	0.03248816	19.7827
Diln2	1.62441E-05	0.01624408	8.2217
Diln3	8.12204E-06	0.00812204	4.05748
Diln4	4.06102E-06	0.00406102	2.05035
Diln5	2.03051E-06	0.00203051	



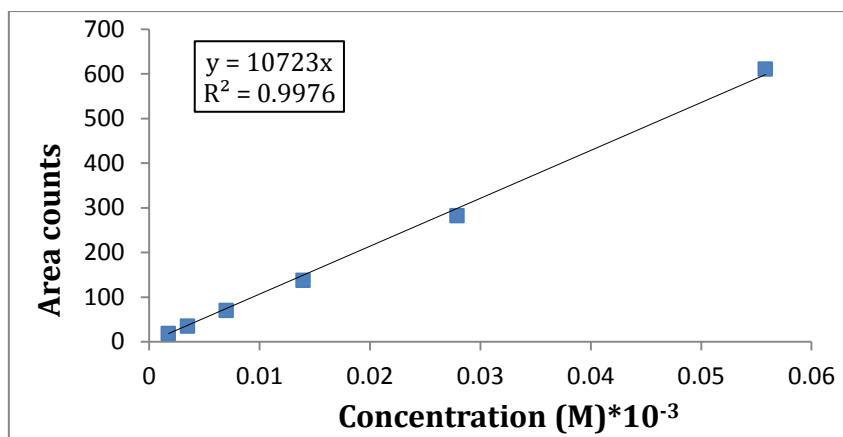
iv) **Fluorene**

Sl.No	Concentration (M)	Concentration M(*10 ⁻³)	Area
1	0.0000604	0.0604	292.8272
Diln1	3.02003E-05	0.0302003	133.8898
Diln2	1.51001E-05	0.0151001	63.28279
Diln3	7.54978E-06	0.00754978	32.75503
Diln4	3.7748E-06	0.0037748	16.86382
Diln5	1.88744E-06	0.00188744	



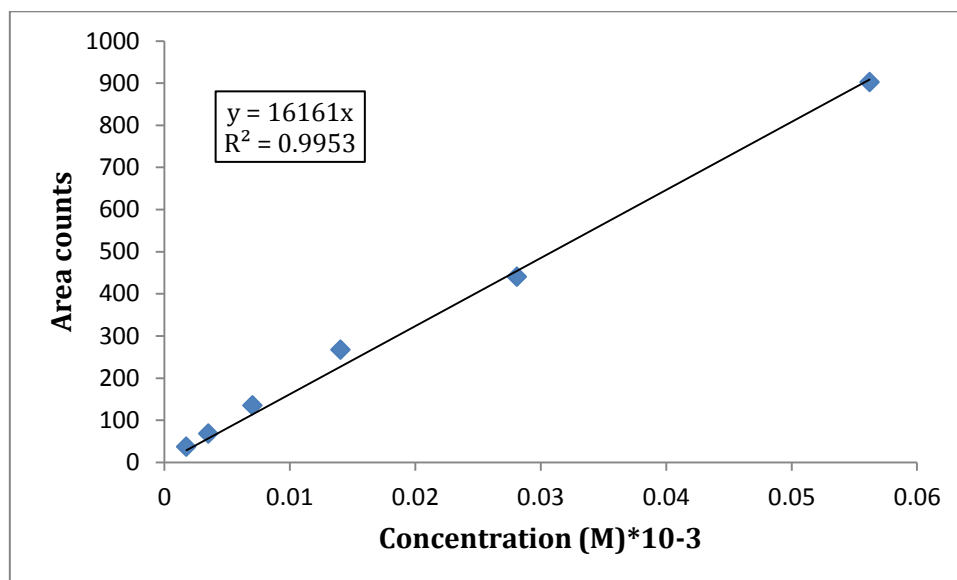
v) **Phenanthrene**

concentration in moles /l	concnmol/l(*10 ⁻³)	area
0.000055826	0.055826	610.772
0.000027913	0.027913	282.5131
0.000013956	0.013956	137.6536
6.97834E-06	0.00697834	70.03932
3.4891E-06	0.0034891	34.96241
1.74459E-06	0.001744585	18.66044



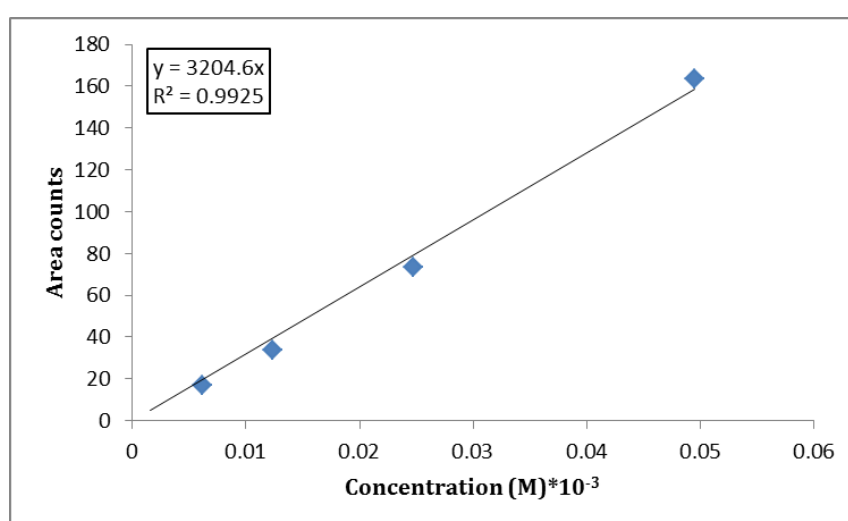
vi) Anthracene

Sl.No	Concentration (M)	Concentration M(*10 ⁻³)	Area
1	0.000056219	0.056219	902.20874
Diln1	0.000028109	0.028109	439.72318
Diln2	0.000014054	0.014054	267.15207
Diln3	7.02743E-06	0.00702743	134.90869
Diln4	3.51371E-06	0.00351371	67.83804
Diln5	1.75685E-06	0.00175685	36.89619



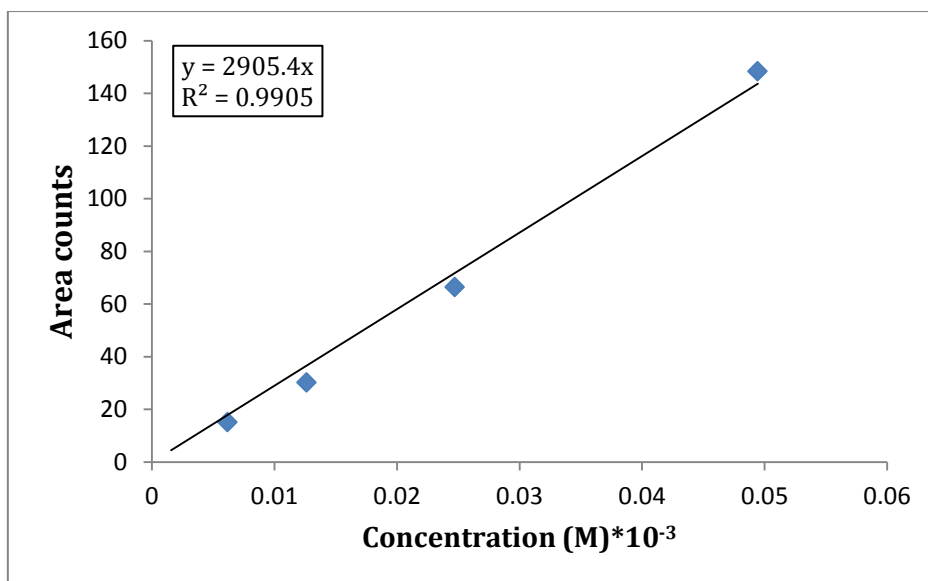
vii) Fluoranthene

Sl.No	Concentration (M)	Concentration M(*10 ⁻³)	Area counts
1	0.00004954	0.04954	163.41656
Diln1	0.00002477	0.02477	73.64005
Diln2	0.000012385	0.012385	33.93755
Diln3	6.19252E-06	0.00619252	17.01391
Diln4	3.09626E-06	0.00309626	
Diln5	1.55122E-06	0.00155122	



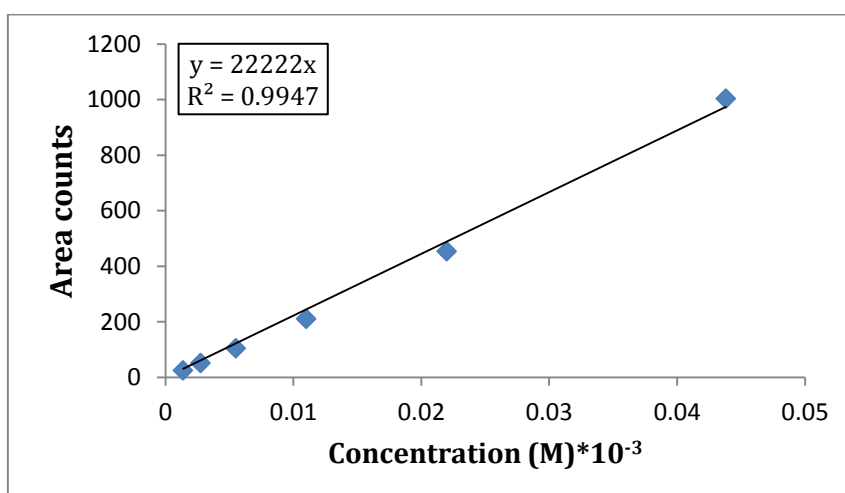
viii) Pyrene

Sl.No	Concentration (M)	Concentration (M)*10 ⁻³	Area
1	0.000049443	0.049443	148.3756
Diln1	2.47218E-05	0.0247218	66.36184
Diln2	0.000012609	0.012609	30.1925
Diln3	6.18046E-06	0.00618046	15.16296
Diln4	3.0902E-06	0.0030902	
Diln5	1.54512E-06	0.001545117	



ix) Chrysene

Sl.No	Concentration (M)	Concentration (M)*10 ⁻³	Area
1	0.00004381	0.04381	1002.85352
Diln1	0.00002199	0.02199	453.67685
Diln2	1.09952E-05	0.0109952	210.1317
Diln3	5.49763E-06	0.00549763	103.70542
Diln4	2.74881E-06	0.00274881	50.90343
Diln5	1.3744E-06	0.0013744	24.80263

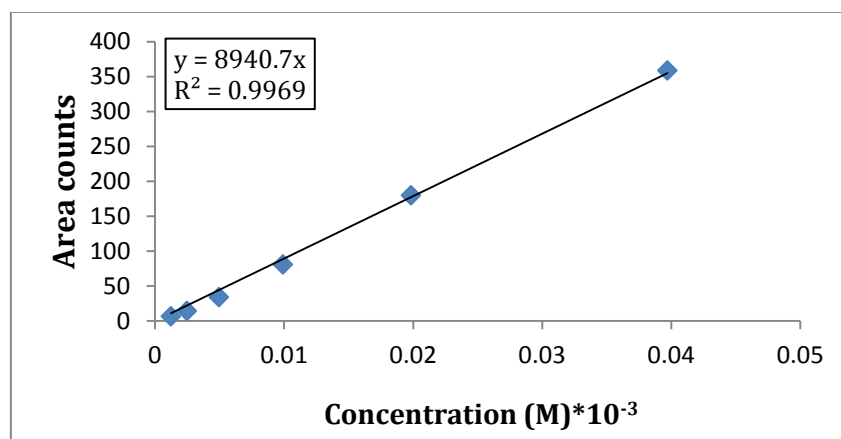


x) **benzo(a) anthracene**

Sl.No	Concentration (M)	Concentration M(*10 ⁻³)	Area
1	4.39796E-05	0.04397955	3.98213
Diln1	0.000021989	0.021989	1.63549
Diln2	1.09948E-05	0.0109948	
Diln3	5.49744E-06	0.00549744	
Diln4	2.74872E-06	0.002748722	
Diln5	1.37436E-06	0.001374361	

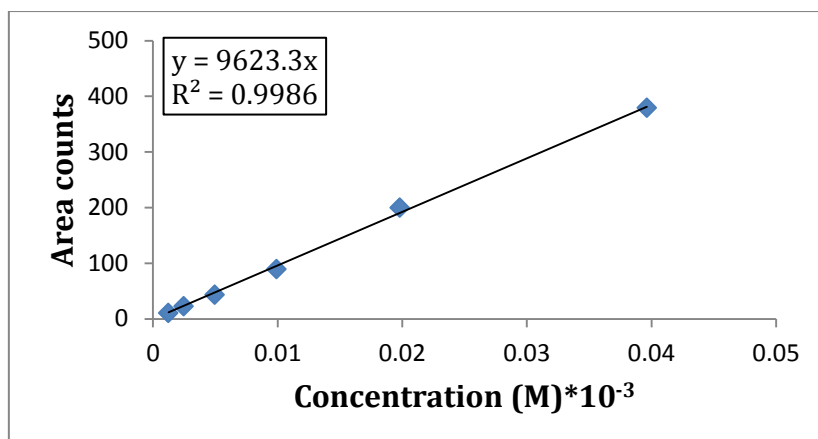
xi) **benzo(b)fluoranthene**

Sl.No	Concentration (M)	Concentration M(*10 ⁻³)	Area
1	3.97136E-05	0.03971361	358.069
Diln1	1.98565E-05	0.0198565	179.721
Diln2	9.92829E-06	0.00992829	80.3029
Diln3	4.96415E-06	0.004964145	33.6943
Diln4	2.48207E-06	0.002482073	14.198
Diln5	1.24104E-06	0.001241036	6.38833



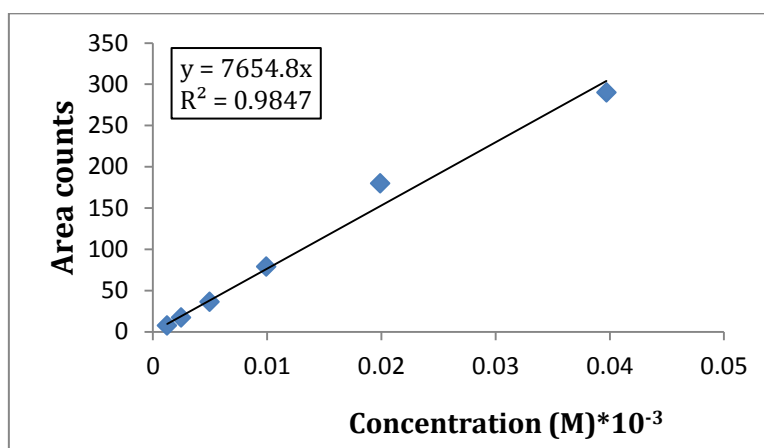
xii) **benzo(k) fluoranthene**

Sl.No	Concentration (M)	Concentration M(*10 ⁻³)	Area
1	3.96338E-05	0.03963378	379.068
Diln1	1.98169E-05	0.01981689	199.673
Diln2	9.90844E-06	0.00990844	89.4749
Diln3	4.95422E-06	0.00495422	43.2599
Diln4	2.47711E-06	0.002477111	22.6458
Diln5	1.23856E-06	0.001238555	10.3866



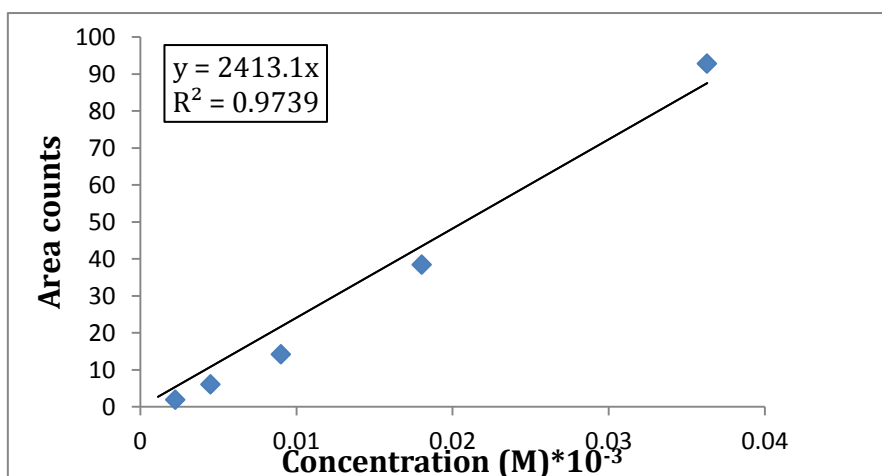
xiii) benzo(a) pyrene

Sl.No	Concentration (M)	Concentration M (*10 ⁻³)	Area
1	3.97031E-05	0.03970305	290.004
Diln1	1.98961E-05	0.0198961	179.494
Diln2	9.92826E-06	0.009928262	78.8473
Diln3	4.96416E-06	0.004964161	36.1414
Diln4	2.48207E-06	0.002482066	16.9804
Diln5	1.24103E-06	0.001241033	7.46669



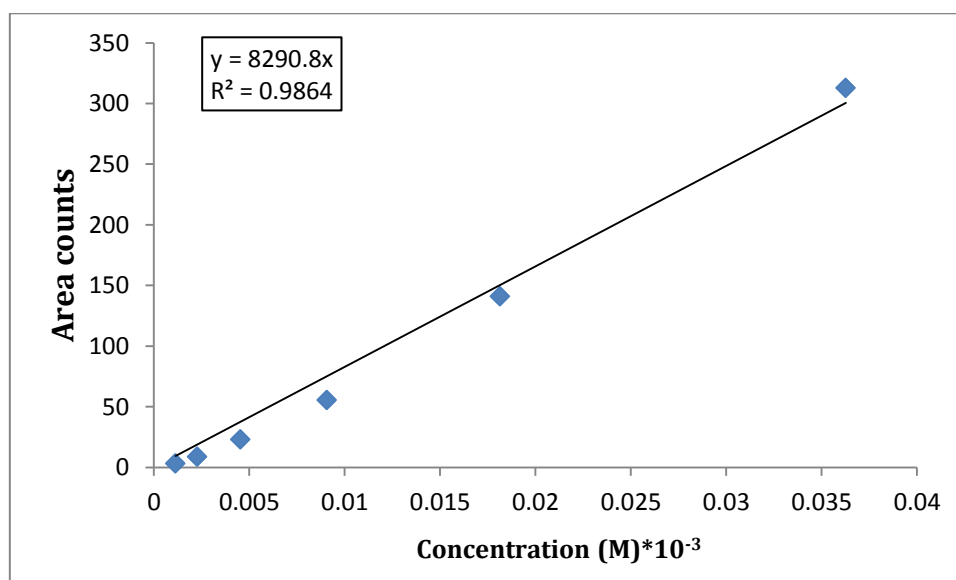
xiv) dibenzo(a,h) anthracene

Sl.No	Concentration (M)	Concentration M (*10 ⁻³)	Area
1	3.6307E-05	0.036307013	92.8433
Diln1	1.80351E-05	0.01803506	38.4371
Diln2	9.01753E-06	0.009017534	14.1582
Diln3	4.50877E-06	0.004508767	6.02087
Diln4	2.2472E-06	0.002247198	1.93977
Diln5	1.12719E-06	0.001127191	



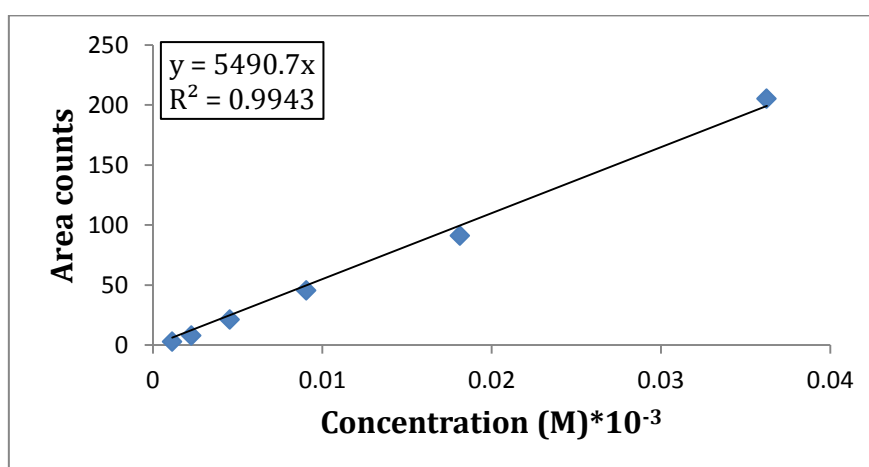
xv) **benzo(ghi)perylene**

Sl.No	Concentration (M)	Concentration M (*10 ⁻³)	Area
1	3.62609E-05	0.0362609	312.903
Diln1	1.81305E-05	0.01813045	140.88
Diln2	9.06523E-06	0.009065225	55.5241
Diln3	4.53261E-06	0.004532612	23.0327
Diln4	2.26631E-06	0.002266306	8.62201
Diln5	1.13315E-06	0.001133153	3.22234



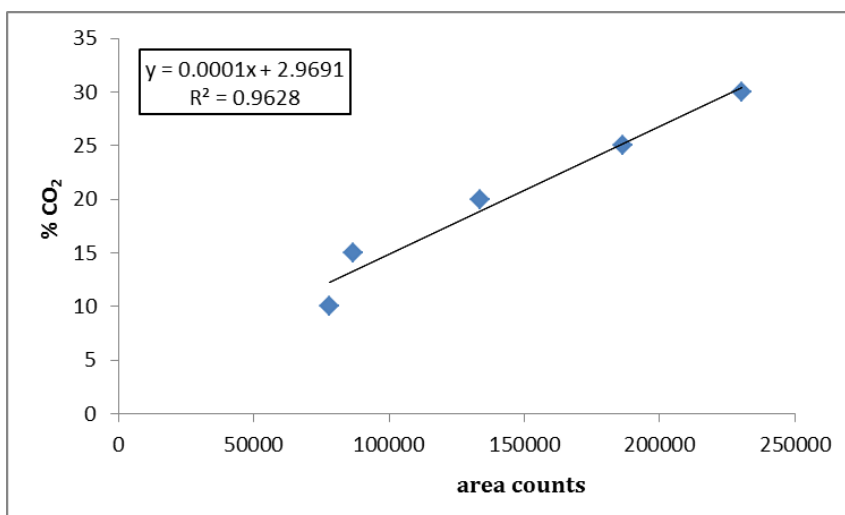
xvi) indeno(1,2,3-cd)pyrene

Sl.No	Concentration (M)	Concentration M (*10 ⁻³)	Area
1	3.62609E-05	0.0362609	205.184
Diln1	1.81305E-05	0.01813045	91.1378
Diln2	9.06523E-06	0.009065225	45.6588
Diln3	4.53261E-06	0.004532612	21.1427
Diln4	2.26631E-06	0.002266306	8.02881
Diln5	1.13315E-06	0.001133153	2.80501



2. Calculation of CO₂ concentrations- Calibration on GC

% CO ₂	Area	response factor
10	77906.5	0.000128
15	86852	0.000173
20	133792	0.000149
25	186590.5	0.000134
30	230263	0.00013
Response factor		0.000143



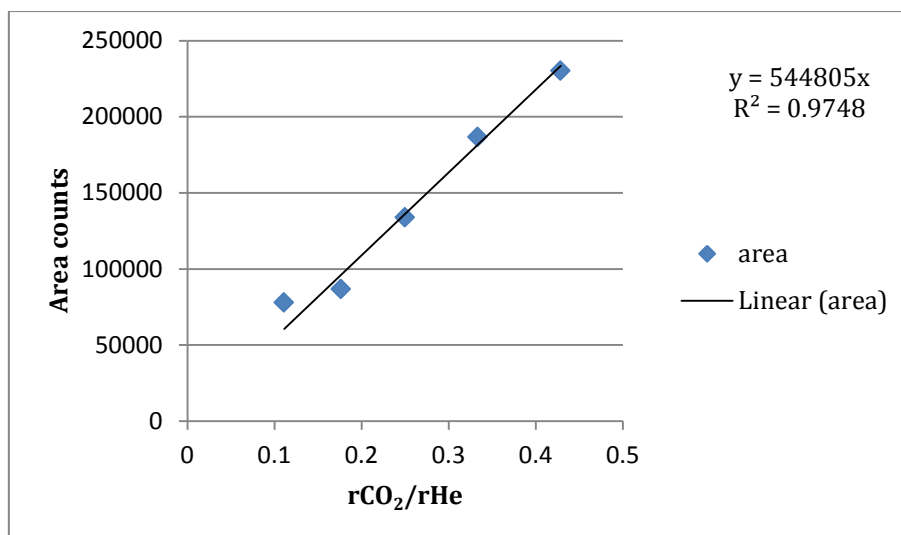
3. Calculation of CO₂ concentrations- rate of the reaction

The calibration for the rate of CO₂ formation was calculated using the ratios of flows for CO₂ to that for Helium versus the area counts.

$Y=AX$, $X = r_{CO_2}/r_{He}$; where r_{CO_2} and r_{He} are the flows of the two gases respectively

rco2/rhe	area
0.1111	77906.5
0.1764	86852
0.25	133792
0.3333	186590.5
0.4285	230263

The flow of CO₂ was diluted in helium flow. Thus $X=r_{CO_2}/r_{He}$. Thus there is no variation of gas flow rate. The various dilutions of CO₂/He are 10,15,20,25,30% CO₂/He.



Thus $rCO_2 = X \cdot rHe$ and this is the flow of CO_2 in ml/min.

1ml at 25°C, 1 bar atmospheric pressure, using $PV = nRT$

1ml = 0.040342 mmol of gas

$rCO_2 \times 0.040342 \text{ mmol} = nCO_2/\text{min}$ mmol CO_2 produced in 1 minute.

Therefore, $\text{Area}/\text{slope} \times rHe = rCO_2$

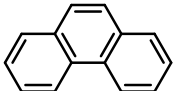
$rCO_2 \times 0.040342 = \text{concentration of } CO_2 \text{ produced in mmol/min.}$

4. Calculation of desorption percentages from Pt/SiC+Ag-K/CZA and phenanthrene-graphite oxidation

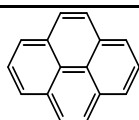
In the case of Pt/SiC-Ag-K/CZA the concentrations of desorption were expressed as a percentage of the desorption under helium and that for phenanthrene-graphite has been described in the section ahead.

a. Pt/SiC-Ag-K/CZA+soot

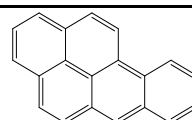
1. O₂/He-soot-Pt/Sic+Ag-K/CZA

Temperature	 Concn (mM) under soot-Helium	Desorbed concentration (mM)	% desorption	Concentration remaining on surface (mM)	Concentration remaining on surface (mM)	Total %
300	2.578	0.00953	0.36	0.0092	0.00386	41.95
400	2.5269	1.33492	52.82	0.0021	0.00317	
500	2.262	0.15308	6.76	0.0004	0.00556	
600	3.459					

2. Catalysed soot ox-O₂/He

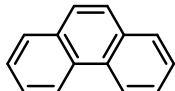


Concn in soot=0.396mM/g soot

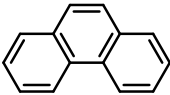


Concn in soot=0.066mM/g soot

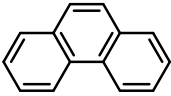
Temperature	Concentration (mM)	% desorption	Concentration (mM)	% desorption
300	0.004	3.03	0.001	9.9
400	0.07	53.03	0.04	
500	0.11		0.06	
600	0.05	38.46	0.03	

Temperature	 Concn in soot mM	Desorbed concentration (mM)	% desorption	Concentration remaining on surface (mM)	Concentration remaining on surface (mM)	% remaining on the surface
300	2.578	0.01286	0.498	0.0092	0.00264	28.69
400	2.5269	0.27748	10.981	0.0021	0.000154	7.33
500	2.262	0.15308	6.767	0.0004	0.00504	
600	3.459	0.002797	0.08			

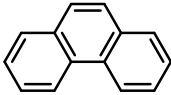
3. Soot-100%CO₂

Temperature	 100%CO ₂ Concn in soot (mM)	Desorbed concentration (mM)	% desorption	Concentration remaining on surface (mM)	Concentration remaining on surface (mM)	% remaining on the surface
300	2.578	0.0746	2.89	0.0092	0.000274	2.97
400	2.5269	0.0390	1.54	0.0021	-	-
500	2.262	0.002637	0.116	0.0004	-	-
600	3.459				-	-

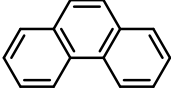
4. Soot - 20% CO₂

Temperature	 Concn in soot mM	Desorbed concentration (mM)	% desorption	Concentration remaining on surface (mM)	Concentration remaining on surface (mM)	% remaining on the surface
300	2.578	0.000317	0.122	0.0092	-	-
400	2.5269	0.057447	2.273	0.0021	-	-
500	2.262	0.01039	0.459	0.0004	-	-
600	3.459	0.1071	3.096			

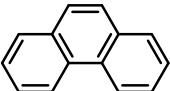
5. Cat-soot- 100% CO₂

Temperature	 100%CO ₂ Concn in soot (mM)	Desorbed concentration (mM)	% desorption
300	2.578	0.000633	0.024
400	2.5269	0.01725	0.682
500	2.262	0.006291	0.278
600	3.459	0.0181	0.523

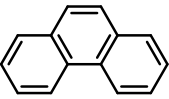
6. Cat-soot-20% CO₂/He

Temperature 20%CO ₂	 Concn in soot (mM)	Desorbed concentration (mM)	% desorption
300	2.578	0.06563	2.54
400	2.5269	0.01716	0.679
500	2.262	0.043104	1.905
600	3.459	0.000326	0.0094

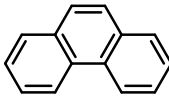
7. Soot- NO/O₂/He

Temper ature	 Concn in soot mM	Desorbed concentration (mM)	% desorption	Concentrati on remaining on surface (mM)	Concentration remaining on surface (mM)	Total %
300	2.578	0.0429	1.664	0.0092	0.003329	36.18
400	2.5269	0.0125	0.494	0.0021	0.007279	
500	2.262	0.0144	0.636	0.0004		
600	3.459	0.0263	0.76			

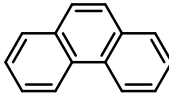
8. Cat-soot- NO+O₂/He

Temperature	 Concn in soot mM	Desorbed concentration (mM)	% desorption	Concentration remaining on surface (mM)	Concentration remaining on surface (mM)	Total %
300	2.578	0.003913	0.151	0.0092	0.005319	57.815
400	2.5269	0.0432	1.709	0.0021		
500	2.262	0.002287	0.101	0.0004		
600	3.459					

9. Soot- exhaust mix

Temperature	 Concn in soot mM	Desorbed concentration (mM)	% desorption
300	2.578	0.047048	1.82
400	2.5269	0.054239	2.144
500	2.262	0.100093	4.424
600	3.459		

10. Cat-soot-exhaust mix

Temperature	 Concn in soot mM	Desorbed concentration (mM)	% desorption
300	2.578	1	6.46
400	2.5269	0.481581647	4.988
500	2.262	0.150424322	9.681
600	3.459	0.094190059	2.977

b. Phenanthrene-graphite model

Calculation of phenanthrene concentrations were calculated as shown below:

Considering the concentration of phenanthrene desorbed at 300°C from the phenanthrene-graphite surface (0.00248mM)

i.e. 2.4871mmol present in 1 l solution.

Approximately 15ml used to collect the products in acetone,

i.e., 2.4871mmol in 1000ml , so xmmol in 15ml, $x=0.037305$ mmol phenanthrene.

But the amount used for the analyses was 0.5ml.

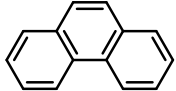
Thus in 0.5ml, 0.0012435mmol of phenanthrene is present and in **1ml =0.00248mmol**

The initial amount of phenanthrene in the phenanthrene-graphite mixture has been calculated to be **0.01283mmol**

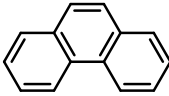
Thus the percentage of desorption at 300C is $0.00248/0.01283 \times 100 = 19.384\%$

The percentages of desorption for the different temperatures was calculated using this calculation.

1. Phenanthrene-graphite-without catalyst

Temperature	 Concn in soot mM	Desorbed concentration (mM)	Concentration remaining on surface (mM)	Concentration remaining on surface (mM)	Total %
300	0.01283	0.00248	19.38	0.00002605	0.203
400		0.0036962	28.809	0.000004668	0.03
500		0.00407	31.728	0.000001545	0.012
600			30.977		

2. Phenanthrene-graphite-with catalyst

Temperature	 Concn in soot mM	Desorbed concentration (mM)	Total %	Concentration remaining on surface (mM)	Concentration remaining on surface (mM)	Total %
300	0.01283	0.0017994	14.024	0.0092	0.000005402	0.0421
400		0.001969	15.347	0.0021		
500		0.0018271	14.241	0.0004	0.000000309	0.0024
600		0.003226	25.151			